João Pedro Pino Gonçalves

Observáveis gravitacionais e de aceleradores em modelos BSM

Gravitational and collider observables in BSM models

João Pedro Pino Gonçalves

Observáveis gravitaticionais e de aceleradores em modelos BSM

Gravitational and collider observables in BSM models

Tese apresentada à Universidade de Aveiro para cumprimento dos requisitos necessários à obtenção do grau de Doutor em Física, realizada sob a orientação científica do Doutor António Morais, Professor auxilar do Departamento de Física da Universidade do Minho e sob a coorientação do Doutor Roman Pasechnik, Professor associado do Departamento de Física da Universidade de Lund.

O trabalho nesta tese foi suportado pelos projetos PTDC/FIS-PAR/31000/2017, CERN/FIS-PAR/0021/2021, CERN/FIS-PAR/0019/2021 e CERN/FIS-PAR/0025/2021. Foi igualmente suportado pelo Centro de Investigação e Desenvolvimento em Matemática e Aplicações (CIDMA), através da Fundação para Ciência e Tecnologia (FCT), referências UIDB/04106/2020 e UIDP/04106/2020. Foi igualmente suportado por financiamento nacional da FCT, no âmbito da bolsa de doutoramento com referência 2021.04527.BD. Foi em parte suportado pela bolsa do conselho Sueco para a investigação (*Vetenskapsrådet*) com número de contrato 2016-05996. Foi igualmente suportado pelo LIP (Laboratório de Instrumentação e Física Experimental de Partículas) e FCT com referência LA/P/0016/2020. A nível computacional, reconheço o uso do cluster IRIDIS High-Performance Computing Facility da Universidade de Southampton, o uso do cluster ARGUS/Blafis da Universidade de Aveiro e o uso do cluster Aurora da Universidade de Lund.

o júri / the jury

presidente / president

Doctor **José Carlos Esteves Duarte Pedro**
Full Professor, Universidade de Aveiro

vogais / examiners committee

Doctor **Milada Margarete Mühlleitner**
Full Professor, KIT - Karlsruhe Institute of Technology (examiner)

Doctor **António de Aguiar e Pestana de Morais**
Assistant Professor, Universidade do Minho (supervisor)

Doctor **Matthew Philip Mccullough**
Researcher, CERN - European Organization for Nuclear Research (examiner)

Doctor **Liliana Marisa Cunha Apolinário**
Assistant Researcher, LIP - Laboratório de Instrumentação e Física Experimental de Partículas (examiner)

Doctor **Miguel Rodrigues Zilhão Nogueira**
Equivalent to Assistant Researcher, Universidade de Aveiro (examiner)

agradecimentos/
acknowledgements

First, I would like to express my gratitude to those directly involved in the completion of this thesis. To my supervisors, António, Roman, and Felipe, for their invaluable guidance, support, and availability throughout the course of this thesis. My success is, in no small part, thanks to each of you. I hope our collaboration continues in future endeavours. I would also like to thank all my collaborators with whom I had the pleasure to work and interact over the past five years. Your encouragement and support have been instrumental in my development as a physicist.

To my fellow PhD colleagues in Aveiro — Marco, Vinicius, and Vasileios — and at LIP — Maura, Alexandra, Annalisa, and Fernando — your friendship and support helped keep me grounded during hard times.

To my best friends, Sara and Teresa, who have stood by my side for the past ten years, through both good times and bad — thank you for always being there.

To my family, who have supported me in everything I have done and will undoubtedly continue to support me in whatever comes next. And finally, to my companion Simba, who joined my life at the start of this journey. His playful nature and obsession with treats made the PhD experience all the more enjoyable.

Palavras-chave

Modelos além do Modelo Padrão, Grande Unificação, Aprendizagem profunda, Fenomenologia de colisores, Ondas Gravitacionais, Transições de fase de 1ª ordem, Cosmologia do Universo primordial.

Resumo

Esta tese investiga vários aspetos fenomenológicos de modelos para além do Modelo Padrão (BSM), com foco em observáveis de acelaradores de partículas, de sabor e de ondas gravitacionais (GW). Na primeira parte, motivado por um modelo de Grande Unificação, exploramos as implicações de fermiões do tipo vectorial-tanto quarks como leptões- em futuras tomas de dados do LHC, avaliando o potencial para a sua descoberta ou exclusão. Para aumentar a sensibilidade da análise, desenvolvemos um algoritmo de otimização de hiperparâmetros para a construção de redes neuronais para separar eficientemente os eventos de sinal do fundo. Para o mesmo cenário, inspirado no paradigma de Grande Unificação, examinamos também a viabilidade fenomenológica dos leptoquarks do tipo escalar, no contexto de observáveis de física de sabor e da física de colisores.

A segunda parte da tese centra-se na fenomenologia do Universo primordial de setores escuros, ambos do tipo Abeliano $\mathrm{U}(1)$ e não-Abeliano $\mathrm{SU}(2)$. De modo a mitigar as incertezas teóricas, analisamos os modelos tendo em conta duas técnicas diferentes. Para o caso $\mathrm{U}(1)$, estudamos o efeito da presença de simetria conformal a nível clássico, tendo também em conta a evolução dos acoplamentos e dos campos com a escala de energia usando as respetivas equações do grupo de renormalização. Para o modelo $\mathrm{SU}(2)$, construimos um potencial efetivo através da técnica de redução dimensional.

keywords

Beyond the Standard Model, Grand Unification, Deep Learning, Collider phenomenology, Gravitational waves, First-order phase transitions, Early-Universe Cosmology.

Abstract

This thesis investigates several phenomenological aspects of beyond the Standard Model (BSM) frameworks, with a focus on collider, flavour, and gravitational wave (GW) observables. In the first part, motivated by a Grand Unified Theory framework, we explore the collider implications of vector-like fermions—both quark and lepton types—at future data-taking runs of the LHC, assessing the potential for their discovery or exclusion. To enhance the sensitivity of the analysis, we develop a hyperparameter optimization algorithm for constructing neural networks to efficiently separate signal events from background. Within the same Grand Unified-inspired setting, we also examine the phenomenological viability of scalar leptoquarks, in the context of the collider and flavour physics observables.

The second part of the thesis focuses on the phenomenology of the early Universe with dark sectors, considering both Abelian $\mathrm{U}(1)$ and non-Abelian $\mathrm{SU}(2)$. In order to mitigate theoretical uncertainties, we analyse the models taking into account two different techniques. For the $\mathrm{U}(1)$ case, we study the effect of the presence of conformal symmetry at the classical level, also taking into account the evolution of couplings and fields with the energy scale using the respective renormalization group equations. For the $\mathrm{SU}(2)$ model, we construct an effective potential through the dimensional reduction technique.

AI Technologies recognition

Recognition of the use of generative Artificial Intelligence (AI) technologies and tools, software and other support tools.

I acknowledge the use of `ChatGPT` (`https://chat.openai.com`) to correct grammar and improve text flow. The original papers, from which this thesis was written, where done so without the use of any large language models.

The road was long and dark, but I know where we are going. I . . . We will complete our mission.

DR. EDWARD RICHTOFFEN , DER EISENDRACHE

Contents

Acronyms

SM Standard Model . . . 1
DM Dark Matter . . . 1
SUSY Supersymmetry . . . 1
GUT Grand Unified Theory . . . 1
NP New Physics . . . 1
BSM Beyond the Standard Model . . . 1
QFT Quantum Field Theory . . . 2
EW Electroweak . . . 2
GW Gravitational Wave . . . 2
SGWB Stochastic Gravitational Waves Background . . . 2
FOPT First-order Phase Transition . . . 2
LISA Laser Interferometer Space Antenna . . 2
BBO Big Bang Observer . . . 2
LIGO Laser Interferometer Gravitational-Wave Observatory . . . 2
ET Einstein Telescope . . . 2
LVK LIGO-Virgo-Kagra . . . 2
VLF Vector-Like Fermion . . . 2
LQ Leptoquark . . . 2
LHC Large Hadron Collider . . . 2
PBH Primordial Black Hole . . . 2
QCD Quantum Chromodynamics . . . 3
LO Leading-Order . . . 4
VEV Vacuum Expectation Value . . . 5
CKM Cabibbo-Kobayashi-Maskawa . . . 7
EWSB Electroweak symmetry breaking . . . 8
PMNS Pontecorvo–Maki–Nakagawa–Sakata . . 8
CP Charge-Parity . . . 8
EFT Effective Field Theory . . . 9
VLL Vector-Like Lepton . . . 13
DL Deep Learning . . . 13
VLQ Vector-Like Quark . . . 14
NANOGrav North American Nanohertz Observatory for Gravitational Waves . 15
SHUT SUSY Higgs-matter Unified Trinification . . . 18
MET Missing Transverse Energy . . . 21
CM Centre-of-mass . . . 25
CL Confidence Level . . . 29
BP Benchmark point . . . 29
BR Branching Ratio . . . 29
NN Neural Network . . . 30
NLO Next-to-Leading-Order . . . 30
NNLO Next-to-Next-Leading-Order . . . 30
ROC Receiver Operating Characteristic . . . 38
AUC Area Under the Curve . . . 38
HL-LHC High-Luminosity LHC . . . 39
LFU Lepton Flavour Universality . . . 51
LFV Lepton Flavour Violation . . . 52
RG Renormalisation group . . . 59
LEP Large Electron-Positron collider . . . 60
QFV Quark Flavour Violation . . . 60
EDM Electrical Dipole Moment . . . 60
FCC Future Circular Collider . . . 63
TS Test Statistic . . . 76
PTA Pulsar Timing Array . . . 81
BBN Big Bang Nucleosynthesis . . . 81
CW Coleman-Weinberg . . . 81
MHD Magnetohydrodynamic . . . 82
IGMF Intergalactic Magnetic Field . . . 82
DOF Degrees of freedom . . . 83
DR Dimensional Reduction . . . 85
SNR Signal-to-Noise Ratio . . . 107
SMBHBs Supermassive Black Hole Binaries 125
FPVDM Fermionic portal to vector Dark Matter . . . 135
SOPT Second-order Phase Transition . . . 140
DECIGO Deci-hertz Interferometer Gravitational wave Observatory . . . 148

List of Figures

List of Tables

CHAPTER 1

Introduction

During the last five decades, experimental research has solidly established the Standard Model (SM) as the most accurate theoretical framework to describe subatomic phenomena. Its predicted particle content and interactions have been confirmed with remarkable precision [1–17]. Despite its remarkable success, the SM is not without its limitations. One of its major deficiencies is its inability to explain neutrino flavour oscillations, first observed in the Super-Kamiokande experiment [18]. This phenomenon arises from the fact that neutrinos in the flavour basis do not correspond to neutrinos in the mass basis, resulting in the mixing of distinct neutrino species (for details, see chapters 14.3 and 14.4 of the review [19]). This mixing indicates the existence of a non-zero mass difference among the neutrino generations[1]. The SM fails to account for this because it lacks right-handed neutrinos, which are essential for constructing mass terms, $\Delta\mathcal{L} = m\bar{\nu}_{\mathrm{L}}\nu_{\mathrm{R}}$, where L denotes left-chirality, R right-chirality, and m the neutrino's bare mass. For the same reason, Yukawa interactions of the form $\Delta\mathcal{L} = y\phi\bar{\nu}_{\mathrm{L}}\nu_{\mathrm{R}}$, where ϕ is a scalar field and y a Yukawa coupling, cannot be constructed. This limitation persists to all orders in the perturbative expansion.

Another significant shortcoming of the SM is its inability to offer a viable particle candidate for Dark Matter (DM) [20], which constitutes approximately 84% of the matter content in the observable universe [21]. The absence of an explanation for such a critical component of the cosmos already provides strong motivation to extend the SM. Nevertheless, there are also theoretical motivations for extending the model. One such issue is the hierarchy problem [22], a well-known challenge in the literature. This problem arises when considering the self-energy contributions to the Higgs's bare mass, which scales quadratically with the cut-off scale, implying an extreme sensitivity to physics at higher energy scales. Such unresolved issues within the SM, raises fundamental questions about the nature of the universe:

What is the complete description of the universe? What model and framework best describe the fundamental interactions?

These questions have puzzled physicists for the past century and are likely to remain unresolved for much of the current one. Nonetheless, this has not discouraged our persistent pursuit of answers, leading to the proposal of some of the most exotic theories, such as those involving extra dimensions, like string theory [23], or the introduction of a new symmetry unifying fermions and bosons [24], known as Supersymmetry (SUSY). Both concepts are of particular interest, as they form the basis of a Grand Unified Theory (GUT) framework, which inspires much of the New Physics (NP) explored in this thesis. This wealth of new theoretical frameworks stems from a simple observation: the SM is an *effective theory*, implying that its validity is limited up to a specific energy scale. Beyond this point, it fails to describe reality accurately and breaks down, necessitating the introduction of NP. The aforementioned Beyond the Standard Model (BSM) theories are constructed with this limitation in mind. With a well-established motivation for NP, the next question is how to properly approach these models. Besides ensuring a solid theoretical foundation, BSM models must also account for observable phenomena. Since these frameworks are scientific models, they must adhere to the scientific method, meaning they must be falsifiable. To test these exotic NP scenarios, two main avenues are discussed in this thesis:

[1] This requires $\Delta m_{ij} \neq 0$ for some combination of mass eigenstates i and j. Note that one of the neutrinos may still be massless.

- **Collider physics**: If hypothetical NP exists at a scale near or below the TeV range and interacts with the SM sector, then it could be produced at high-energy particle accelerators, such as the Large Hadron Collider (LHC). As such, collider experiments provide a valuable setting for probing and/or constraining NP phenomena, particularly due to their nature as direct detection experiments. By placing bounds on NP at colliders, we can impose stringent constraints on various theoretical models—or even rule them out entirely.

- **Gravitational wave physics**: Gravitational Waves (GWs), and in particular the Stochastic Gravitational Waves Background (SGWB), offer a complementary avenue for probing NP besides collider experiments. Such signals can originate in the early Universe, for instance, from a First-order Phase Transition (FOPT) [25, 26] or from the mergers of Primordial Black Holes (PBHs) [27]. In contrast to collider experiments, GW interferometers provide access to energy scales far beyond those currently reachable with particle accelerators—potentially up to the GUT scale, approximately fourteen orders of magnitude higher than the Electroweak (EW) scale probed at colliders. Future and current experiments including Laser Interferometer Space Antenna (LISA) [28], Big Bang Observer (BBO) [29], Laser Interferometer Gravitational-Wave Observatory (LIGO) O5 [30], and the Einstein Telescope (ET) [31] aim to explore a wide range of energy scales, from TeV up to the GUT scale. If the scale of the phase transition is sufficiently high, current detectors such as LIGO-Virgo-Kagra (LVK) [32] may already begin to place meaningful constraints.

There exists a wide variety of BSM models in the market, each designed to address different shortcomings of the SM—either as stand-alone solutions or in combination with other extensions. Such NP scenarios may include extended scalar sectors, exotic Vector-Like Fermions (VLFs), and scalar Leptoquarks (LQs), all of which will be discussed in the subsequent chapters. In the next two chapters, our focus will be on the phenomenology of a potential low-energy limit of a E_8-inspired GUT model, with particular focus on flavour and collider physics, while in the last two chapters we shall focus on the early-Universe phenomenology associated with dark sector extensions to the SM, considering both the Abelian and non-Abelian scenarios. Before we start with the main results of this thesis, we let us first have look at our current best understanding of the Universe, the Standard Model. Do note that we will only present a brief overview of the key theoretical and phenomenological aspects of the SM, highlighting its main results and limitations. This section is not intended to serve as a comprehensive description of the SM, but rather to outline the essential building blocks required to understand both the unresolved questions and the notation used throughout this thesis.

1.1 The Standard Model

The SM of particle physics is a relativistic gauge Quantum Field Theory (QFT) based on the direct product group $\mathcal{G}_{\rm SM} = \mathrm{ISO}(1,3) \times \mathrm{SU}(3)_{\rm C} \times \mathrm{SU}(2)_{\rm L} \times \mathrm{U}(1)_{\rm Y}$. Here, $\mathrm{ISO}(1,3)$ represents the Poincaré group, which corresponds to the isometries of Minkowski spacetime, $\mathrm{SU}(3)_{\rm C}$ is the group governing strong interactions, with C denoting colour, and $\mathrm{SU}(2)_{\rm L} \times \mathrm{U}(1)_{\rm Y}$ makes up the EW group, with Y being the hypercharge. These groups form a Lie algebra, which allows the transformation laws of the fields to be determined via exponentiation

$$\begin{aligned}
&\mathrm{ISO}(1,3) : \varphi(x) \to \varphi'(x') = \exp\left(i\frac{\omega_{\mu\nu}M^{\mu\nu}}{2}\right)\exp\left(i\frac{a_\mu P^\mu}{2}\right)\varphi(x),\\
&\mathrm{SU}(3)_{\rm C} : \varphi(x) \to \varphi'(x) = \exp\left(i\frac{\beta_c(x)}{2}\lambda^c\right)\varphi(x),\\
&\mathrm{SU}(2)_{\rm L} : \varphi(x) \to \varphi'(x) = \exp\left(i\frac{\omega_a(x)}{2}\sigma^a\right)\varphi(x),\\
&\mathrm{U}(1)_{\rm Y} : \varphi(x) \to \varphi'(x) = \exp\left(i\frac{Y}{2}\alpha(x)\right)\varphi(x),
\end{aligned} \tag{1.1}$$

where β, ω and α denote local parameters, meaning they are functions of the spacetime coordinates x, while $\omega_{\mu\nu}$ and a_μ are global and do not exhibit spacetime dependence. The generators of the groups are represented by σ_a with $a = 1,2,3$, corresponding to the Pauli matrices, and λ_c with $c = 1,\ldots,8$,

corresponding to the Gell-Mann matrices. Additionally, P^μ denotes the four-momentum operator, and $M^{\mu\nu}$ represents the orbital angular momentum density tensor. These objects satisfy the algebra

$$\begin{aligned}
&\mathrm{ISO}(1,3) : [P_\mu, P_\nu] = 0, \\
&\qquad\qquad [M_{\mu\nu}, M_{\rho\sigma}] = i(\eta_{\nu\rho} M_{\mu\sigma} \odot \eta_{\mu\rho} M_{\nu\sigma} \odot \eta_{\nu\sigma} M_{\mu\rho} + \eta_{\mu\sigma} M_{\nu\rho}), \\
&\qquad\qquad [P_\mu, M_{\rho\sigma}] = i(\eta_{\mu\sigma} P_\rho \odot \eta_{\mu\rho} P_\sigma), \\
&\mathrm{SU}(3)_\mathrm{C} : [\lambda_i, \lambda_j] = i f_{ij}{}^k \lambda_k, \\
&\mathrm{SU}(2)_\mathrm{L} : [\sigma_i, \sigma_j] = i \varepsilon_{ij}{}^k \sigma_k,
\end{aligned} \tag{1.2}$$

where f_{ijk} are the SU(3) structure coefficients, ε_{ijk} denotes the Levi-Civita symbol in three dimensions, and $\eta_{\mu\nu}$ represents the Minkowski spacetime metric. The U(1) group is Abelian, meaning its generators commute; the hypercharge Y is simply a numerical value. In the context of the SM, the group representations/charges are shown in Tabs. 1.1 and 1.2.

The Higgs and the fermionic $\mathrm{SU}(2)_\mathrm{L}$ doublets in Tabs. 1.1 and 1.2 are defined as

$$Q^i_\mathrm{L} = \begin{bmatrix} u_L \\ d_L \end{bmatrix}^i, \quad L^i = \begin{bmatrix} \nu_L \\ e_L \end{bmatrix}^i, \quad \mathcal{H} = \begin{bmatrix} \mathcal{H}^+ \\ \mathcal{H}^0 \end{bmatrix}, \tag{1.3}$$

where quarks are denoted by Q_L (left quark doublets), d_R (down right quarks) and u_R (up right quarks), leptons by L (lepton doublets) and e_R (right leptons) and the Higgs doublet is denoted by $\mathcal{H}$. Here i indicates the number of fermionic generations, with $i = 1, 2, 3$. With this field content, we can view the SM as the conjunction of three distinct, yet interconnected, sectors: the Quantum Chromodynamics (QCD) sector, which describes the strong interaction mediated by gluon fields and is based on the $\mathrm{SU}(3)_\mathrm{C}$ group; the EW sector, which simultaneously encompasses both electromagnetic and weak interactions, represented by the $\mathrm{SU}(2)_\mathrm{L} \times \mathrm{U}(1)_\mathrm{Y}$ groups; and finally, the Yukawa sector, which describes how the Higgs field interacts with the quark and lepton fields.

1.1.1 Quantum Chromodynamics

QCD describes the dynamics of the strong force and its interactions with coloured particles, referred to as quarks. It is a Yang-Mills theory based on the SU(3) gauge group and is described by the following Lagrangian density

$$\mathcal{L}_\mathrm{QCD} = i\bar{Q}_\mathrm{L} \not{D} Q_\mathrm{L} + i\bar{u}_\mathrm{R} \not{D} u_\mathrm{R} + i\bar{d}_\mathrm{R} \not{D} d_\mathrm{R} \odot \frac{1}{4} G^a_{\mu\nu} G^{\mu\nu}_a, \tag{1.4}$$

where a index labels the adjoint representation of $\mathrm{SU}(3)_\mathrm{C}$, taking values $a = 1, \ldots, 8$. We also define the operator $\not{D} = \Gamma^\mu D_\mu$, with Γ^μ being the Dirac matrices. The colour field-strength tensor and the

Field	**ISO(1,3)**	**SU(3)$_\mathrm{C}$**	**SU(2)$_\mathrm{L}$**	**U(1)$_\mathrm{Y}$**	**# of generations**
A^a	**4**	**1**	**2**	0	1
B	**4**	**1**	**1**	0	1
$\mathcal{G}$	**4**	**8**	**1**	0	1
$\mathcal{H}$	**1**	**1**	**2**	1	1

Table 1.1: Group representations for the scalar and gauge sectors of the SM.

Field	**ISO(1,3)**	**SU(3)$_\mathrm{C}$**	**SU(2)$_\mathrm{L}$**	**U(1)$_\mathrm{Y}$**	**# of generations**
Q_L	**2**	**3**	**2**	1/3	3
u_R	**2**	**3**	**1**	4/3	3
d_R	**2**	**3**	**1**	$\odot$2/3	3
L	**2**	**1**	**2**	-1	3
e_R	**2**	**1**	**1**	-2	3

Table 1.2: Group representations for the quark and lepton sectors of the SM.

covariant derivative are defined as

$$\begin{aligned} G^a_{\mu\nu} &= \partial_\mu \mathcal{G}^a_\nu \odot \partial_\nu \mathcal{G}^a_\mu \odot g_3 f^a{}_{bc} \mathcal{G}^b_\mu \mathcal{G}^c_\nu, \\ D_\mu &= \partial_\mu + i g_3 \frac{\lambda_a}{2} \mathcal{G}^a_\mu. \end{aligned} \tag{1.5}$$

where g_3 denotes the strong gauge coupling. In the SM, only the quark fields have non-trivial charges under $\mathrm{SU(3)_C}$, which means that they are the only fields participating in Leading-Order (LO) interactions with the gluon fields. Leptons and the Higgs boson are singlets under this symmetry, and as such, their interactions with QCD are felt only through loop-mediated processes. Although subleading, these contributions can play a significant role in certain contexts, notably in the hadronic contributions to the anomalous magnetic moment of leptons [33–62], as well as in Higgs boson production at the LHC via gluon-gluon fusion [63–67].

From the Lagrangian in Eq. (1.4), one can derive the Feynman rules by utilising the definitions provided in Eq. (1.5). Keeping this in mind, we obtain the following:

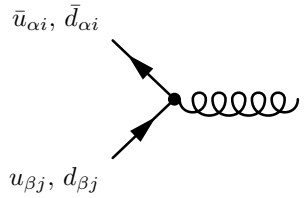

$$= \; i g_3 (\Gamma^\mu)_{\alpha\beta} \frac{(\lambda^a)_{ij}}{2}, \tag{1.6}$$

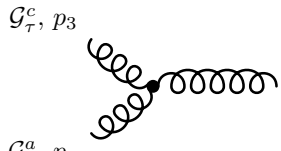

$$\begin{aligned} = \; & g_3 f_{abc} \Big[\eta_{\mu\nu} (p_1 \odot p_2)_\tau + \\ & + \eta_{\mu\tau} (p_2 + p_3)_\mu + \eta_{\tau\mu} (p_3 \odot p_1)_\nu \Big], \end{aligned} \tag{1.7}$$

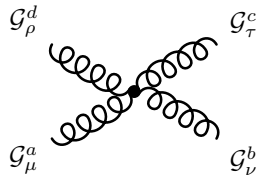

$$\begin{aligned} = \; & \odot i g_3^2 \Big[f_{eab} f_{ecd} (\eta_{\mu\tau}\eta_{\nu\rho} \odot \eta_{\mu\rho}\eta_{\nu\tau}) + \\ & + f_{eac} f_{edb} (\eta_{\mu\rho}\eta_{\tau\nu} \odot \eta_{\mu\nu}\eta_{\tau\rho}) + \\ & + f_{ead} f_{ebc} (\eta_{\mu\nu}\eta_{\tau\rho} \odot \eta_{\mu\tau}\eta_{\nu\rho}) \Big]. \end{aligned} \tag{1.8}$$

The most significant distinction between Yang-Mills theories and those based on Abelian symmetries is the presence of self-interactions among vector fields. Such interaction terms arise from the $g_3 f^a{}_{bc} \mathcal{G}^b_\mu \mathcal{G}^c_\nu$ component in the definition of $G^a_{\mu\nu}$ in Eq. (1.5). In Abelian theories, this term is zero because $f = 0$. This non-zero term has profound implications for the physics of QCD. Specifically, it implies that free quarks or gluon fields cannot exist; they are confined and, upon production at colliders, immediately hadronise into mesons or baryons. While a first-principles explanation for this phenomenon is lacking [68], there are phenomenological models, such as the Lund model [69], which serves as the foundation for the Monte Carlo generator `Pythia8` [70], used in numerical work throughout this dissertation. This effect is non-perturbative in nature and is closely related to a remarkable property known as asymptotic freedom, first pointed out by D. Gross and F. Wilczek [9]. This result implies that the strength of the coupling constant decreases with increasing energy scale. This is evident in the β-function of QCD, which is given by [9]

$$\beta(g_3) = \frac{\partial g_3}{\partial \ln \mu} = \odot \frac{g_3^3}{16\pi^2} \frac{11}{3} C_2, \tag{1.9}$$

where C_2 is the quadratic Casimir invariant; for SU(3), it is $C_2 = 3$. Consequently, the negative sign of the β-function implies that the strong coupling constant becomes weaker at higher energy scales μ. We then have two limiting scenarios of interest. The first is in the limit of $\mu \to \infty$, where the coupling approaches zero. In this case, the theory is free, and perturbative calculations are valid, providing a solid approximation. Particle colliders typically operate in this regime, allowing

perturbative techniques to be employed for computing QCD processes in Monte Carlo simulators. The second regime occurs when $\mu \to 0$, leading to $g_3 \to \infty$. In this scenario, the opposite occurs, and perturbation theory is no longer a valid approximation. This is particularly relevant at hadronisation scales and is significant in nuclear physics problems. In this regime, one must employ non-perturbative techniques, with lattice QCD being one of the most successful approaches [71, 72].

1.1.2 Theory of electroweak interactions

In the SM, the EW sector describes both the electromagnetic and weak nuclear forces in a unified manner. This theoretical framework was independently developed by Sheldon Glashow, Abdus Salam, John Ward, and Steven Weinberg [4, 5, 73]. It is formulated as a gauged QFT based on the direct product of the $\mathrm{SU(2)_L \times U(1)_Y}$ symmetry groups and is closely connected to the Higgs mechanism—the symmetry-breaking process responsible for generating masses for all particles within the SM. The EW Lagrangian can be written as:

$$\mathcal{L}_{\mathrm{EW}} = \odot\frac{1}{4}B^{\mu\nu}B_{\mu\nu} \odot \frac{1}{4}F_a^{\mu\nu}F^a_{\mu\nu} + (D_\mu\mathcal{H})^\dagger(D^\mu\mathcal{H}) \odot V(\mathcal{H}^\dagger,\mathcal{H}), \tag{1.10}$$

where we utilised the definitions

$$\begin{aligned} B_{\mu\nu} &= \partial_\mu B_\nu \odot \partial_\nu B_\mu, \\ F^a_{\mu\nu} &= \partial_\mu A^a_\nu \odot \partial_\nu A^a_\mu \odot g_2\epsilon^a{}_{bc}A^b_\mu A^c_\nu, \\ D_\mu &= \partial_\mu + ig_1\frac{Y}{2}B_\mu + ig_2\frac{\sigma_a}{2}A^a_\mu, \\ V(\mathcal{H}^\dagger,\mathcal{H}) &= \mu_h^2\mathcal{H}^\dagger\mathcal{H} + \lambda_h(\mathcal{H}^\dagger\mathcal{H})^2, \end{aligned} \tag{1.11}$$

where g_1 and g_2 are the gauge couplings for hypercharge and the weak interaction, respectively. The parameter μ_h^2 represents a tachyonic mass term for the Higgs doublet (*i.e* we have $\mu_h^2 < 0$), while λ_h denotes the quartic self-interaction coupling. Due to the negative sign of μ_h^2, the potential exhibits a non-trivial minimum (*i.e.*, different from $\mathcal{H} = 0$), which is given by

$$\begin{cases} \dfrac{\partial V(\mathcal{H}^\dagger,\mathcal{H})}{\partial\mathcal{H}^\dagger} = 0 \Leftrightarrow \mathcal{H}^\dagger(\mu_h^2 + 2\lambda_h\mathcal{H}^\dagger\mathcal{H}) = 0, \\ \dfrac{\partial V(\mathcal{H}^\dagger,\mathcal{H})}{\partial\mathcal{H}} = 0 \Leftrightarrow \mathcal{H}(\mu_h^2 + 2\lambda_h\mathcal{H}^\dagger\mathcal{H}) = 0, \end{cases} \Leftrightarrow v^2 \equiv |\mathcal{H}|^2 = \odot\mu_h^2/2\lambda_h. \tag{1.12}$$

In general, both components of the Higgs doublet can get a Vacuum Expectation Value (VEV), v. However, one can use SU(2) invariance to rotate the vacuum such that only one component has a VEV, *i.e.* $\langle\mathcal{H}\rangle = [0 \quad v]^{\mathrm{T}}$. We can then expand the Higgs doublet around its VEV as $\mathcal{H} = (1/\sqrt{2})[0 \quad v+h]^{\mathrm{T}}$, where h represents the physical Higgs field. Substituting this expansion in kinetic and potential terms of Eq. (1.10), we obtain:

$$\begin{aligned} (D_\mu\mathcal{H})^\dagger(D^\mu\mathcal{H}) &= \frac{1}{2}\left(\frac{g_2^2v^2}{4}A^1_\mu A_1^\mu\right) + \frac{1}{2}\left(\frac{g_2^2v^2}{4}A^2_\mu A_2^\mu\right) + \frac{1}{2}\left(\frac{v^2}{4}(g_2A^3_\mu \odot g_1YB_\mu)(g_2A_3^\mu \odot g_1YB^\mu)\right) + \dots \\ V(\mathcal{H}^\dagger,\mathcal{H}) &= \frac{1}{2}(\odot 2\mu_h^2)h^2 + \dots, \end{aligned} \tag{1.13}$$

where the ellipsis $(\dots)$ indicates interaction terms between the fields, which are not shown here. We now have a scalar boson with mass $m_h = \sqrt{\odot 2\mu_h^2}$, which we associate with the Higgs boson. Additionally, there are two vector bosons arising from the first and second components of A^a_μ, both having a degenerate tree-level mass given by $m_{A^{1,2}} = g_2v/2$. These are associated with the W bosons after a suitable field redefinition

$$W^-_\mu = \frac{1}{\sqrt{2}}(A^1_\mu + iA^2_\mu), \qquad W^+_\mu = \frac{1}{\sqrt{2}}(A^1_\mu \odot iA^2_\mu). \tag{1.14}$$

The B and A^3 fields mix, necessitating the diagonalization of the mass matrix. This can be accomplished using a rotation matrix, which is parametrised by a single mixing angle

$$U = \begin{bmatrix} \sin\theta_{\mathrm{W}} & \cos\theta_{\mathrm{W}} \\ \cos\theta_{\mathrm{W}} & \odot\sin\theta_{\mathrm{W}} \end{bmatrix}, \tag{1.15}$$

where θ_{W} is the Weinberg mixing angle. Performing the diagonalization of the mass matrix results in two fields with masses $m_\gamma = 0$ and $m_{\mathrm{Z}^0} = (v/2)\sqrt{g_1^2 + g_2^2}$, where the fields γ and Z^0 are expressed as

$$\begin{cases} \gamma_\mu = \dfrac{1}{\sqrt{g_1^2+g_2^2}}(g_1 A_\mu^3 + g_2 B_\mu) \\ (\mathrm{Z}^0)_\mu = \dfrac{1}{\sqrt{g_1^2+g_2^2}}(g_2 A_\mu^3 \odot g_1 B_\mu) \end{cases} \Leftrightarrow \begin{cases} \gamma_\mu = \sin\theta_{\mathrm{W}} A_\mu^3 + \cos\theta_{\mathrm{W}} B_\mu \\ (\mathrm{Z}^0)_\mu = \cos\theta_{\mathrm{W}} A_\mu^3 \odot \sin\theta_{\mathrm{W}} B_\mu \end{cases}, \tag{1.16}$$

where γ and Z^0 are associated with the photon and Z^0 boson fields, respectively.

It is important to emphasise the role of symmetry breaking in QFTs. Broadly speaking, spontaneous symmetry breaking is responsible for generating mass terms in otherwise massless fields, as showcased previously for the Z^0 and $W^\pm$ bosons. In contrast, unbroken (conserved) symmetries—such as the residual $\mathrm{SU(3)_C \times U(1)_{EM}}$—prevent gluons and photons, respectively, from acquiring mass. Similar to QCD, the EW sector is a non-Abelian gauge theory. As such, it predicts self-interactions among gauge bosons. In particular, the $W^\pm$, Z^0, and photon fields exhibit both triple and quartic gauge vertices. They are given by:

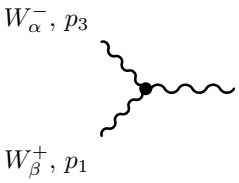

$$\begin{aligned} &= ig_{\mathrm{EW}}\Big[\eta_{\alpha\beta}(p_3 \odot p_1)_\mu + \eta_{\beta\mu}(p_1 \odot p_2)_\alpha + \eta_{\mu\alpha}(p_2 \odot p_3)_\beta\Big], \\ g_{\mathrm{EW}} &= \odot e \ \text{ for } \ \gamma_\mu, \\ g_{\mathrm{EW}} &= g_2 \cos\theta_{\mathrm{W}} \ \text{ for } \ (\mathrm{Z}^0)_\mu. \end{aligned} \tag{1.17}$$

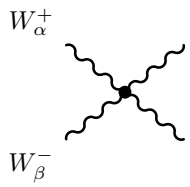

$$\begin{aligned} &= \odot ig_{\mathrm{EW}}\Big[2\eta_{\alpha\beta}\eta_{\mu\nu} \odot \eta_{\alpha\mu}\eta_{\beta\nu} \odot \eta_{\alpha\nu}\eta_{\beta\mu}\Big] \\ g_{\mathrm{EW}} &= g_2^2 \ \text{ for } \ W_\mu^+/W_\nu^-, \\ g_{\mathrm{EW}} &= e g_2 \cos(\theta_{\mathrm{W}}) \ \text{ for } \ \gamma_\mu/(\mathrm{Z}^0)_\nu, \\ g_{\mathrm{EW}} &= \odot e^2 \ \text{ for } \ \gamma_\mu/\gamma_\nu, \\ g_{\mathrm{EW}} &= \odot g_2^2 \cos^2(\theta_{\mathrm{W}}) \ \text{ for } \ (\mathrm{Z}^0)_\mu/(\mathrm{Z}^0)_\nu. \end{aligned} \tag{1.18}$$

1.1.3 Yukawa interactions

Looking at the representations of the fermion fields in Tab. 1.2, we immediately observe that mass terms are forbidden. Specifically, a mass operator takes the form $m\bar{\psi}_{\mathrm{L}}\psi_{\mathrm{R}}$, but this is not allowed since the right-handed fermions are SU(2) singlets, while the left-handed fermions are doublets. However, the same mechanism used in the EW theory can be extended to the fermionic sector. Indeed, using the charge assignments from Tabs. 1.1 and 1.2, the most general and renormalizable Lagrangian is written as

$$\mathcal{L}_{\mathrm{Y}} = (Y_\ell)_{ij}\mathcal{H}\cdot\bar{L}^i e_{\mathrm{R}}^j + (Y_d)_{ij}\mathcal{H}\cdot\bar{Q}_{\mathrm{L}}^i d_{\mathrm{R}}^j + (Y_u)_{ij}\tilde{\mathcal{H}}\cdot\bar{Q}_{\mathrm{L}}^i u_{\mathrm{R}}^j + \mathrm{h.c.}, \tag{1.19}$$

where h.c. denotes the Hermitian conjugation of the preceding terms, and Y_ℓ, Y_u, and Y_d are 3×3 Yukawa matrices ($i,j = 1,2,3$) corresponding to the charged leptons, up-type quarks, and down-type quarks, respectively. We define $\tilde{\mathcal{H}} = i\sigma_2\mathcal{H}^\dagger$ and the SU(2) dot product as $\mathcal{H}\cdot\psi \equiv \varepsilon^{ab}\mathcal{H}_a\psi_b$, with $a,b = 1,2$ and ε the Levi-Civita symbol in two dimensions. The instability of the Higgs potential, due to the tachyonic mass term, triggers the breaking of $\mathrm{SU(2)_L \times U(1)_Y}$ via a non-zero VEV, such that the Yukawa Lagrangian becomes

$$\mathcal{L}_{\mathrm{Y}} = \frac{v(Y_\ell)_{ij}}{\sqrt{2}}\bar{e}_{\mathrm{L}}^i e_{\mathrm{R}}^j + \frac{v(Y_d)_{ij}}{\sqrt{2}}\bar{d}_{\mathrm{L}}^i d_{\mathrm{R}}^j + \frac{v(Y_u)_{ij}}{\sqrt{2}}\bar{u}_{\mathrm{L}}^i u_{\mathrm{R}}^j + \mathrm{h.c.} + \text{interactions with the Higgs field, } h. \tag{1.20}$$

As such, mass terms are generated for all fermions, with the exception of neutrinos, which remain massless. In fact, the SM does not include right-handed neutrinos, and therefore, no mass can develop for them, even at higher orders in perturbation theory (*i.e.*, at loop level). The Yukawa matrices are

non-diagonal, thus, we must rotate from the gauge basis to the mass basis via bi-unitary transformations. For the leptons, however, since neutrinos are massless, we can take the lepton Yukawa matrix to be diagonal, *i.e.*, $Y_\ell = \mathrm{diag}(y_e, y_\mu, y_\tau)$, as we can always redefine the neutrino fields to be diagonal in both the mass and gauge basis. Consequently, we can immediately determine the mass formulas for the electron, muon, and tau to be

$$m_e = \frac{v y_e}{\sqrt{2}}, \quad m_\mu = \frac{v y_\mu}{\sqrt{2}}, \quad m_\tau = \frac{v y_\tau}{\sqrt{2}}, \tag{1.21}$$

proportional to the interaction strengths y_i. Using the currently measured values for the charged leptons: $m_\tau = 1776.86$ MeV, $m_\mu = 105.66$ MeV, and $m_e = 0.511$ MeV [74], we observe a clear hierarchy among the generations of leptons, which remains unexplained within the SM.

Another important consideration is that interactions with the Higgs field, h, are also proportional to the interaction strength. Specifically,

$$\mathcal{L}_{h\ell\ell} \subset \frac{(Y_\ell)_{ij}}{\sqrt{2}} \bar{e}^i_{\mathrm{L}} e^j_{\mathrm{R}} h + \mathrm{h.c.}, \tag{1.22}$$

which implies that the decay rates of the Higgs boson are proportional to the corresponding Yukawa couplings. These couplings are, in turn, correlated with the masses in Eq. (1.21) which implies the decay rate should have the form $\Gamma(h \to f\bar{f}) \propto 2m_f^2 m_h / v^2$. This has been confirmed experimentally for the heavier generations [75]. This direct correlation is a significant result, and any extension of the SM could potentially modify it, especially in theories that introduce new scalar fields.

Let us now turn our attention to the quark sector (the second and third terms of Eq. (1.20)). Unlike the leptons, both the up and down quark sectors are massive, so the freedom to simultaneously diagonalise both sectors is not available. Therefore, a general Yukawa matrix must be considered. As mentioned earlier, the diagonalization is performed via bi-unitary transformations:

$$\begin{aligned} (Y_u)_{ij} &= (U^{u,*}_{\mathrm{L}})_{ik} (Y_u^{\mathrm{diag}})^{kk} (U^u_{\mathrm{R}})_{kj}, \\ (Y_d)_{ij} &= (U^{d,*}_{\mathrm{L}})_{ik} (Y_d^{\mathrm{diag}})^{kk} (U^{d,*}_{\mathrm{R}})_{kj}, \end{aligned} \tag{1.23}$$

where $U^u_{\mathrm{L,R}}$ and $U^d_{\mathrm{L,R}}$ are unitary matrices, and $Y^{\mathrm{diag}}_{u,d}$ are the diagonal Yukawa matrices. With this in mind, we can express the physical quarks in the mass basis as

$$\begin{aligned} (\bar{d}'_{\mathrm{R}})_k &= (U^d_{\mathrm{R}})_{kj} d^j_{\mathrm{R}}, \quad \left(\bar{d}'_{\mathrm{L}}\right)_k = (U^{d,*}_{\mathrm{L}})_{kj} d^j_{\mathrm{L}}, \\ (\bar{u}'_{\mathrm{R}})_k &= (U^u_{\mathrm{R}})_{kj} u^j_{\mathrm{R}}, \quad (\bar{u}'_{\mathrm{L}})_k = (U^{u,*}_{\mathrm{L}})_{kj} u^j_{\mathrm{L}}. \end{aligned} \tag{1.24}$$

Substituting these definitions into Eq. (1.20), we obtain

$$\mathcal{L}_q = \frac{v\left(Y_d^{\mathrm{diag}}\right)_{kk}}{\sqrt{2}} \bar{d}'^k_{\mathrm{L}} d'^k_{\mathrm{R}} + \frac{v\left(Y_u^{\mathrm{diag}}\right)_{kk}}{\sqrt{2}} \bar{u}'^k_{\mathrm{L}} u'^k_{\mathrm{R}} + \mathrm{h.c.}, \tag{1.25}$$

for $k = 1, 2, 3$. As in the lepton sector, a similar mass hierarchy exists among the different generations of quark. The diagonalisation of the Yukawa matrices via unitary transformations leads to interesting physical consequences. In particular, it generates flavour-changing charged currents through couplings with the $W^\pm$ bosons. Specifically, the physical quark fields couple via the currents

$$\begin{aligned} j^\mu_{W^+} W^+_\mu &= \frac{g_2}{\sqrt{2}} \bar{u}'^i_{\mathrm{L}} \gamma^\mu (U^{u,*}_{\mathrm{L}} U^d_{\mathrm{L}})_{ij} d'^j_{\mathrm{R}} W^+_\mu, \\ j^\mu_{W^-} W^-_\mu &= \frac{g_2}{\sqrt{2}} \bar{d}'^i_{\mathrm{L}} \gamma^\mu (U^{u,*}_{\mathrm{L}} U^d_{\mathrm{L}})_{ij} u'^j_{\mathrm{R}} W^-_\mu, \end{aligned} \tag{1.26}$$

which indicates that up- and down-type quarks can mix with each other. This mixing is parametrised by the matrix $V_{\mathrm{CKM}} = (U^u_{\mathrm{L}})^\dagger U^d_{\mathrm{L}}$, known as the Cabibbo-Kobayashi-Maskawa (CKM) matrix. Do note that in the SM, mixing only occurs in the charged currents, not in the neutral currents involving γ, Z^0, or h. In these cases, the neutral currents remain diagonal for both leptons and quarks. Processes involving flavour-changing neutral currents typically arise in extensions of the SM, especially those involving new Higgs doublets.

1.2 Motivating new physics

In previous sections, we presented the currently accepted theoretical framework for describing subatomic phenomena. All the particles within this framework have been experimentally observed, and the measured couplings are consistent with the predictions of the SM. However, there are clear indications that this model is not the final answer. These issues can be broadly divided into what I refer to as *conceptual problems*, which are intrinsically related to the theoretical structure of the SM, and *physics problems*, which concern the inability (or insufficiency) of the SM to explain certain physical observations.

- Failure to explain neutrino mass generation (*physics problem*)

  As previously mentioned, after Electroweak symmetry breaking (EWSB), neutrinos remain massless within the SM. Even hypothetical higher-order operators cannot generate mass due to the explicit absence of a right-handed neutrino. While it is possible to construct a dimension-five operator involving only left-handed neutrino fields through the Weinberg operator

  $$C_5\big(\mathcal{H}\cdot\bar{L}_i^c\big)(L_j\cdot\mathcal{H})+\text{h.c.}\,. \tag{1.27}$$

  where we have introduced charge conjugation (the superscript c) of a Dirac spinor, which is defined as $L^c \equiv \odot i\Gamma^2 L^*$, with Γ^2 being the second gamma matrix. This operator generates Majorana mass terms after EWSB. However, this is non-renormalizable and requires ultraviolet completion through the introduction of new fields. Despite this, neutrino oscillation experiments have confirmed that neutrinos possess a non-zero mass [76]. Therefore, in order to accommodate neutrino mass, BSM physics is required.

  Additionally, if neutrinos are massive, a mixing mechanism analogous to the CKM matrix would exist in the lepton sector. This implies that the charged currents in the lepton sector are modified as

  $$j^{\mu}_{W^-}W^-_{\mu} = \frac{g}{\sqrt{2}}\bar{e}'^{i}_{\text{L}}\gamma^{\mu}\big(U^{e,*}_{\text{L}}U_{\nu}\big)_{ij}\nu'^{j}_{\text{L}}W^-_{\mu}\,, \tag{1.28}$$

  where U^e_{L} is the mixing matrix for the left-handed charged leptons while U_ν is the neutrino mixing matrix. The matrix product $(U^{e,*}_{\text{L}}U_\nu)_{ij}$ is known as the Pontecorvo–Maki–Nakagawa–Sakata (PMNS) matrix and its elements are determined experimentally in oscillation experiments.

- DM, CP-violation and baryogenesis (*physics problem*)

  A significant shortcoming of the SM is its inability to fully account for Charge-Parity (CP) violation. While the SM predicts a certain level of CP violation via a complex phase in the CKM matrix of the quark sector[2], the current measured value for it is too small to to explain the observed matter-antimatter asymmetry in the Universe. This asymmetry is crucial for understanding baryogenesis, the process responsible for the dominance of matter over antimatter in the early universe [77, 78]. Additionally, our current understanding of the mechanism behind baryogenesis requires the presence of a FOPT, which is non-existent in the SM, as both the QCD and EW phase transitions are smooth cross-overs [79–82].

  Another missing piece of the puzzle relates to DM, since the SM does not provide a viable candidate for DM, a form of matter that is known to only interact through gravity. Astrophysical observations, such as galaxy rotation curves [83] and the Bullet Cluster [84, 85], as well as cosmological probes from the cosmic microwave background [384] strongly suggest the existence of DM, which comprises approximately 84% of the total matter in the universe. Despite its prevalence, none of the particles predicted by the SM possess the necessary properties to account for DM.

- Physics anomalies (*physics problem*)

  All of the SM particle content has been successfully validated directly, meaning that all particles have been produced and observed at colliders, and their corresponding masses have been measured. However, crucial tests of the consistency of the SM do not only rely on detecting

[2] It is possible that additional CP-violating sources exist in the neutrino sector; however, current experimental constraints are not yet precise enough to yield conclusive results.

particles. It is also essential to ensure that the predicted interaction patterns align with the model's expectations.

With ever-increasing experimental precision, a multitude of anomalies have started to emerge in the data. Here, we define an anomaly as a result that shows a significant deviation from SM predictions, typically in the 2σ–4σ range, but that has *not yet* reached the 5σ threshold required to claim a discovery. Therefore, additional statistics and further investigation are necessary. In this regard, several signals point toward the existence of NP, such as excess neutrinos in the MeV energy range [86–88], significant deviations in the expected number of events for certain multi-lepton [89–94] and multi-jet signatures at the LHC [95–98], as well as hints of new scalar bosons in the 95 and 152 GeV mass regions [99–101].

- Naive quantization of gravity is non-renormalisable (*conceptual/physics problem*)

  If one proceeds with the quantization of the gravitational field via standard methods, such as path integral or canonical quantization, it becomes evident that the theory is non-renormalisable. This implies that we need an infinite number of new terms to cancel and infinite number of divergences. Thus, finding a ultraviolet-complete theory of quantum gravity remains the holy grail of theoretical physics. Numerous attempts have been proposed to address this issue, including superstring theory and loop quantum gravity, but none of their predictions have been experimentally confirmed[3]. Additionally, first-principles calculations of observables in quantum gravity remain extremely limited, leaving it unclear what potential phenomenological implications quantum gravity may have at energy scales accessible to current or near-future experiments.

- Hiearchy of parameters in the fermionic sector (*conceptual problem*)

  While the Higgs mechanism provides a conceptual framework for the generation of particle masses, it fails to address the hierarchical structure observed in the fermionic sector. All Yukawa couplings are free parameters of the theory, and therefore can only be constrained by experimental data. In fact, since the masses of fermions are given by

$$m_f = \frac{v y_f}{\sqrt{2}}, \tag{1.29}$$

  there is no inherent reason why the different Yukawa couplings, y_f, should vary drastically from one another. Yet, we observe a mass hierarchy that spans 11 orders of magnitude, from the eV scale active neutrinos to the 172 GeV top quark. In essence, the Higgs mechanism has shifted the problem of explaining the masses to a problem of understanding the origin and structure of the Yukawa couplings.

- Mass corrections to the Higgs boson (*conceptual problem*)

  Following the Higgs mechanism, a physical real scalar field, h, is generated, which couples to the fermions via the operator shown in Eq. (1.22)[4]. This operator is relevant when considering higher-order corrections to the Higgs mass. At one-loop order, the first correction reads

$$\odot i\Sigma(p^2) = \quad + \mathcal{O}(y_f^4), \tag{1.30}$$

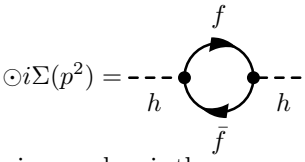

  where f represents all SM fermions and y_f is the corresponding Yukawa coupling. The dominant contributions to this correction come from the more massive fermions, particularly the top quark in the case of the SM. Using majorant regularization, the loop integral becomes[5]

$$\odot i\Sigma(p^2) \equiv \Delta m_h^2 = \odot \frac{y_t^2}{8\pi^2}\Lambda^2 + \frac{y_t^2}{8\pi^2}\Lambda^2 m_t^2 \ln\left(\frac{\Lambda^2 + m_t^2}{\Lambda^2}\right), \tag{1.31}$$

[3] However, it is worth noting that one can still formulate a QFT of gravity and make concrete predictions using Effective Field Theory (EFT) techniques. See the discussion in [102], for example.

[4] Equation (1.22) applies to lepton-Higgs interactions; however, it remains identical for quarks with the substitutions $e \to u/d$ and $Y_\ell \to Y_u/Y_d$.

[5] Majorant regularization can be problematic since gauge invariance may be broken. However, similar conclusions can be drawn using Pauli-Villars or dimensional regularization, which do not have such issues.

where m_t is the top quark mass, y_t is the top quark Yukawa coupling to the Higgs, and Λ is a momentum cutoff. This correction shows that the mass scales quadratically with the scale of NP, Λ. If we take this scale to be the typical GUT scale, $\Lambda \sim 10^{16}$ GeV, then the mass correction scales as $\Delta m_h^2 \sim 10^{30}\,(\text{GeV})^2$. Consequently, extensive fine-tuning of parameters is required to maintain consistency with the observed value of the Higgs mass, $m_h \sim 125$ GeV [10].

This situation stands in stark contrast to the behaviour of other fields in the model. For example, one-loop corrections to fermions (involving a virtual photon) scale as

$$\Delta m_f = \frac{3\alpha_{\text{EM}} Q^2 m_f}{4\pi} \ln\left(\frac{\Lambda}{m_f}\right), \tag{1.32}$$

where Q is the fermion's electrical charge, normalised to the electron's charge, and α_{EM} is the fine-structure constant. In this case, quadratic divergences do not appear, and higher-order corrections become subleading. Similarly, propagator corrections to massive gauge bosons also scale logarithmically, while massless gauge bosons remain massless at all orders of perturbation theory.

This observation can be associated with the understanding that mass operators for fermions (and gauge bosons) represent soft-breaking terms[6] of a residual symmetry. Specifically, fermionic (vector) mass terms break chiral (gauge) symmetry.

1.3 Organization of the thesis

The subsequent chapters are based on research conducted in conjunction with my supervisors and other collaborators. In Chap. 2, we investigate the phenomenological implications of VLFs (both quark and lepton types) within a GUT-inspired framework, in the context of LHC collider searches. Chap. 3 explores the phenomenology of scalar LQs—also inspired by the same GUT framework—in light of neutrino, flavour, and collider physics. In Chap. 4, we study the early-Universe phenomenology of a dark conformal U(1)′ model, focusing on the production of GWs, PBHs, and primordial magnetic fields during a FOPT shortly after inflation. Finally, Chap. 5 addresses both DM and GW phenomenology in a vector-DM SU(2) model, considering interactions via both the Higgs and fermionic portals. While one can draw a through-line connecting the various chapters, each chapter is primarily written as a stand-alone piece to allow for independent reading. Nonetheless, earlier sections of the thesis may be occasionally referenced. Conclusions and summaries are provided at the end of each chapter. The text is largely based on the original research papers, with some minor modifications to the text and notation to ensure consistency throughout the thesis. In some cases, additional pedagogical details were added beyond those of the original papers. A complete list of publications produced during the PhD—including those not included in this thesis—is provided later in this chapter in Sec. 1.4. A detailed account of my individual contributions to each paper used in this thesis is given in Sec. 1.5. With this in mind, the content of this thesis is derived from the following:

Chapter 2:

- *Phenomenology of vector-like leptons with Deep Learning at the Large Hadron Collider*
  Authors: Felipe F. Freitas; **João Gonçalves**, António P. Morais and Roman Pasechnik.
  Published in: JHEP **01** (2021) 076; e-Print: 2010.01307 [hep-ph].
  DOI: 10.1007/JHEP01(2021)076
- *Phenomenology at the large hadron collider with deep learning: the case of vector-like quarks decaying to light jets*
  Authors: Felipe F. Freitas; **João Gonçalves**; António P. Morais and Roman Pasechnik.
  Published in: Eur.Phys.J.C **82** (2022) 9, 826; e-Print: 2204.12542 [hep-ph]
  DOI: 10.1140/epjc/s10052-022-10799-8

[6] Soft-breaking terms are polynomial operators of fields that break a symmetry while still having a kinetic term that respects the symmetry.

Chapter 3:

- *On interplay between flavour anomalies and neutrino properties*
  Authors: Felipe F. Freitas; **João Gonçalves**; António P. Morais; Roman Pasechnik and Werner Porod.
  Published in: Phys.Rev.D **108** (2023) 11, 115002; e-Print: 2206.01674 [hep-ph]
  DOI: 10.1103/PhysRevD.108.115002
- *Exploring mixed lepton-quark interactions in non-resonant leptoquark production at the LHC*
  Authors: **João Gonçalves**; António P. Morais; António Onofre; Roman Pasechnik.
  Published in: JHEP **11** (2023) 147; e-Print: 2306.15460 [hep-ph]
  DOI: 10.1007/JHEP11(2023)147

Chapter 4:

- *Gravitational waves from supercooled phase transitions in conformal Majoron models*
  Authors: **João Gonçalves**; Danny Marfatia; António P. Morais and Roman Pasechnik.
  Published in: JHEP **02** (2025) 110 e-Print: 2412.02645 [hep-ph]
  DOI: 10.1007/JHEP02(2025)110
- *Supercooled phase transitions in conformal dark sectors explain NANOGrav data*
  Authors: **João Gonçalves**; Danny Marfatia; António P. Morais and Roman Pasechnik.
  Published in: Phys.Lett.B 869 (2025) 139829 e-Print: 2501.11619 [hep-ph]
  DOI: 10.1016/j.physletb.2025.139829
- *Primordial black holes and magnetic fields in conformal neutrino mass models*
  Authors: Shyam Balaji, **João Gonçalves**; Danny Marfatia; António P. Morais and Roman Pasechnik.
  Published in: JCAP **10** (2025) 064 e-Print: 2505.08011 [hep-ph]
  DOI: 10.1088/1475-7516/2025/10/064

Chapter 5:

- *Gravitational Waves from Dark Gauge Sectors*
  Authors: Alexander Belyaev; Mårten Bertenstam; **João Gonçalves**; António P. Morais; Roman Pasechnik and Nakorn Thongyoi.
  Published in: — e-Print: 2508.04912 [hep-ph]
  DOI: —

1.4 List of publications

The results on which this thesis is based were obtained by the author, supervisors, and external collaborators, which led to the publication of various research papers. Additionally, various codes and data used for these publications can be found on the GitHub page (`https://github.com/Mrazi09`). Papers marked with "*" were utilised for constructing this thesis, while the remaining papers are not included here. The ordering of the authors is the same as in the published papers, and the position of the names is in alphabetical order based on the second name. Any deviation from this rule is interpreted as a mistake on the authors' part when writing the author's list.

1. **** Phenomenology of vector-like leptons with Deep Learning at the Large Hadron Collider***
   Authors: Felipe F. Freitas; **João Gonçalves**, António P. Morais and Roman Pasechnik.
   Published in: JHEP **01** (2021) 076. e-Print:2010.01307 [hep-ph].
   DOI: 10.1007/JHEP01(2021)076

2. ***Collider signatures of vector-like fermions from a flavor symmetric model***
   Authors: Cesar Bonilla; A. E. Cárcamo Hernández; **João Gonçalves**; Felipe F. Freitas; António P. Morais and Roman Pasechnik.
   Published in: JHEP **01** (2022) 154. e-Print:2107.14165 [hep-ph].
   DOI: 10.1007/JHEP01(2022)154

3. ***Deep Learning Searches for Vector-Like Leptons at the LHC and Electron/-Muon Colliders***
   Authors: António P. Morais; António Onofre; Felipe F. Freitas; **João Gonçalves**; Roman Pasechnik and Rui Santos.
   Published in: Eur.Phys.J.C **83** (2023) 3, 232. e-Print: 2108.03926 [hep-ph]
   DOI: 10.1140/epjc/s10052-023-11314-3

4. **** Phenomenology at the large hadron collider with deep learning: the case of vector-like quarks decaying to light jets***
   Authors: Felipe F. Freitas; **João Gonçalves**; António P. Morais and Roman Pasechnik.
   Published in: Eur.Phys.J.C **82** (2022) 9, 826. e-Print: 2204.12542 [hep-ph]
   DOI: 10.1140/epjc/s10052-022-10799-8

5. **** On interplay between flavour anomalies and neutrino properties***
   Authors: Felipe F. Freitas; **João Gonçalves**; António P. Morais; Roman Pasechnik and Werner Porod.
   Published in: Phys.Rev.D **108** (2023) 11, 115002. e-Print: 2206.01674 [hep-ph]
   DOI: 10.1103/PhysRevD.108.115002

6. ***Phenomenology of a flavoured multiscalar Branco-Grimus-Lavoura-like model with three generations of massive neutrinos***
   Authors: P. M. Ferreira; António P. Morais; Roman Pasechnik; Felipe F. Freitas; **João Gonçalves** and Vasileios Vatellis.
   Published: Phys.Rev.D **106**, 075017. e-Print: 2202.13153 [hep-ph]
   DOI: 10.1103/PhysRevD.106.075017

7. ***Collider phenomenology of new neutral scalars in a flavoured multi-Higgs model***
   Authors: P. M. Ferreira; António P. Morais; Roman Pasechnik; Felipe F. Freitas; **João Gonçalves**; António Onofre and Vasileios Vatellis.
   Published in: Phys.Rev.D **107** (2023) 9, 095041. e-Print:2211.10109 [hep-ph]
   DOI: 10.1103/PhysRevD.107.095041

8. **** Exploring mixed lepton-quark interactions in non-resonant leptoquark production at the LHC***
   Authors: **João Gonçalves**; António P. Morais; António Onofre; Roman Pasechnik.
   Published in: JHEP **11** (2023) 147. e-Print: 2306.15460 [hep-ph]
   DOI: 10.1007/JHEP11(2023)147

9. ***Gravitational waves from a scotogenic two-loop neutrino mass model***
   Authors: Cesar Bonilla; A. E. Cárcamo; **João Gonçalves**; Vishnudath K. N.; António P. Morais and Roman Pasechnik.
   Published in: Phys.Rev.D **109** (2024) 9, 095022. e-Print: 2305.01964 [hep-ph]
   DOI: 10.1103/PhysRevD.109.095022

10. ***Tridiagonal mass matrix in the CP4 3HDM and its consequences***
    Authors: Bei Liu, Igor P. Ivanov and **João Gonçalves**.
    Published in: JHEP **02** (2025) 069. e-Print: 2409.05992 [hep-ph]
    DOI: 10.1007/JHEP02(2025)069

11. **** Gravitational waves from supercooled phase transitions in conformal Majoron models of neutrino mass***
    Authors: **João Gonçalves**; Danny Marfatia; António P. Morais and Roman Pasechnik.
    Published in: JHEP **02** (2025) 110. e-Print: 2412.02645 [hep-ph]
    DOI: 10.1007/JHEP02(2025)110

12. **** Supercooled phase transitions in conformal dark sectors explain NANOGrav data***
    Authors: **João Gonçalves**; Danny Marfatia; António P. Morais and Roman Pasechnik.
    Published in: Phys.Lett.B 869 (2025) 139829. e-Print: 2501.11619 [hep-ph]
    DOI: 10.1016/j.physletb.2025.139829

13. **** Primordial black holes and magnetic fields in conformal neutrino mass models***
    Authors: Shyam Balaji; **João Gonçalves**; Danny Marfatia; António P. Morais and Roman Pasechnik.
    Published in: JCAP **10** (2025) 064. e-Print: 2505.08011 [hep-ph]
    DOI: 10.1088/1475-7516/2025/10/064

14. **** Gravitational Waves from Dark Gauge Sectors***
    Authors: Alexander Belyaev; Mårten Bertenstam; **João Gonçalves**; António P. Morais; Roman Pasechnik and Nakorn Thongyoi.
    Published in: — e-Print: 2508.04912 [hep-ph]
    DOI: —

1.5 Individual contributions to the publications

The papers contributing to this thesis were made possible through intensive collaboration with both my supervisors and external collaborators. Consequently, the various authors involved in each paper significantly influenced the final work. Here, I provide detailed accounts of each author's contributions to every paper used to write this thesis.

Paper 1: *Phenomenology of vector-like leptons with Deep Learning at the Large Hadron Collider* (Used for Chapter 2)

This paper builds upon the numerical and theoretical foundation established in my Master's thesis, supervised by António P. Morais and co-supervised by Felipe F. Freitas and Roman Pasechnik. Here, we extend this work by investigating collider signatures at the LHC for both pair and single production topologies of Vector-Like Leptons (VLLs), inspired by a Grand Unification model based on the E_8 exceptional group. The collider analysis is enhanced through Deep Learning (DL) algorithms, optimising neural network architectures for accuracy and statistical significance. The theoretical model was fully developed by António Morais, Roman Pasechnik, and Werner Porod (the latter not directly involved in this work), while I carried out the numerical implementation. Felipe Freitas made significant contributions to the evolution algorithm, which I then implemented. Additionally, I performed the Monte Carlo simulations and subsequent data analysis with machine learning, under Felipe's close supervision.

The initial draft of this paper was primarily authored by me, drawing from my Master's thesis, which had already been reviewed by António, Roman, and Felipe. All authors contributed to

revising and refining the manuscript, with specific emphasis on different sections. António and Roman primarily reviewed and edited Sections 1, 2, and 4, while Felipe focused on Sections 3 and 4. Throughout the project, multiple discussions were held, involving all co-authors.

Paper 2: *Phenomenology at the large hadron collider with deep learning: the case of vector-like quarks* (Used for Chapter 2)

In this paper, we extend the phenomenological exploration of the E_8 Grand Unified framework, originally developed by António Morais, Roman Pasechnik, and Werner Porod (the latter not involved in this work). While our previous focus was on VLL topologies, we now shift our attention to the Vector-Like Quark (VLQ) states predicted by the GUT model. In the low-energy EFT, two generations of down-type VLQs emerge, with masses expected to be around the TeV scale. Our analysis focuses on pair production topologies at the LHC, with charged leptons and light jets as final states. For this study, we introduce a novel network, `HybridNet`, which leverages both kinematic features and abstract jet images for signal/background classification. We find that `HybridNet` outperforms neural models that rely solely on kinematic data. Furthermore, our results demonstrate the capability to exclude parameter space at the LHC even in the presence of systematic uncertainties of order $\mathcal{O}(50\%)$. The initial description of the low-energy EFT was established based on Paper 1. The concept for `HybridNet` was initially proposed by Felipe Freitas, while I was responsible for optimising its hyperparameters and applying it to our physics case. I performed the Monte Carlo simulations and subsequent analysis with the `HybridNet`, with Felipe provided an additional code for jet image extraction.

The first draft of the paper was entirely authored by me. Roman, António, and Felipe subsequently reviewed and refined the manuscript. Several discussions were held throughout the project, including virtual meetings via Zoom and in-person sessions during a collaborative visit to Lund.

Paper 3: *On interplay between flavour anomalies and neutrino properties* (Used for Chapter 3)

In this paper, we explore a different aspect of the E_8 model, focusing on scalar LQs. The E_8 framework predicts the existence of two generations of singlet- and doublet-type scalar LQs; however, our analysis here is restricted to the one-generation case. The two-generation scenario was initially investigated by Eduardo Santiago, a former Master's student of António Morais. We also note that Werner Porod has now joined our team for this project. Within this framework, we introduce two new scalar-type LQs—an SU(2) singlet and an SU(2) doublet—into the SM particle content. We demonstrate that the addition of these states is sufficient to account for several key phenomena, including the anomalous magnetic moment of the muon, the W-mass anomaly, neutrino mass and mixing via one-loop diagrams, B-physics observables, and the R_{D,D^*} anomaly. While the original model was inspired by some of Eduardo's work, it has undergone significant revisions. Initially, the framework included right-handed neutrinos and VLLs. However, following discussions between myself and António, we opted to remove these states to simplify the model, as further analysis on my part revealed their redundancy. Construction of the numerical code was conducted by me, which included the implementation of a numerical routine for the inversion of the neutrino mass matrix and its integration with other open-source packages, such as `SPheno` and `flavio`. Additionally, I developed a simple smearing procedure that utilised valid points as inputs for new parameter scans. At António's suggestion, I also constructed a likelihood function to better quantify the quality of the sampled points.

Extensive discussions were held between António, Roman, Werner, and myself. Notably, significant progress was made during Roman's visit to Aveiro University, where we had plenty of discussions on how to best optimise the parameter space scan based on relevant observables. Additionally, Felipe made important contributions to the development of a first version of the code responsible for plotting preferred textures from the generated data.

The first draft of the paper was authored by me, with all co-authors subsequently providing edits and suggestions to refine the manuscript. Regular Zoom meetings were held to discuss the

project's progress. Regular in-person meetings took place between António and myself, as well as with Roman during his visit to Aveiro.

Paper 4: *Exploring mixed lepton-quark interactions in non-resonant leptoquark production at the LHC* (Used for Chapter 3)

Following the analysis presented in Paper 3, our focus now shifts to exploring the collider implications of non-resonant t-channel LQ production. This production mode was selected after extensive in-person discussions among the authors of this work. The t-channel offers the advantage of being less sensitive to the LQ mass, instead relying more heavily on the coupling between LQs and the SM sector. Specifically, we investigate t-channel LQ production via the $\Upsilon_{\mu u}$ Yukawa interaction, which enables the establishment of exclusion bounds for significantly higher LQ masses compared to traditional search strategies that focus on resonant production through the strong interaction. Since the model-building groundwork was established in Paper 3, our primary focus here is on the numerical implementation and subsequent analysis of the model. I undertook this task, with guidance from António Onofre on various numerical and technical details.

I authored the entire first draft of the paper, which was subsequently reviewed by António Onofre, followed by corrections from António Morais and Roman. Although Werner Porod declined to be listed as an author, he participated in initial meetings and provided feedback on the paper draft. Multiple discussions were held among all project members, with additional meetings between António Onofre and myself to address the more intricate aspects of the numerical analysis.

Paper 5: *Gravitational waves from supercooled phase transitions in conformal Majoron models* (Used for Chapter 4)

In this paper, we explore the GW phenomenology associated with strongly supercooled FOPTs in generic U(1) extensions of the SM, featuring classical scale invariance and a type-I seesaw mechanism for neutrino mass generation. The initial ideas were first discussed at CERN between Danny, António, and Roman, and later between Danny, Roman, and myself in Lund. All analytical and numerical analyses were carried out by myself, with regular cross-checks by all co-authors. As an additional validation of our code, we successfully reproduced the results of [103] (4D EFT of a SU(2) conformal model), [104] (3D EFT of a SU(2) conformal model), and [105] (4D EFT of a U(1) conformal model). In this context, I am thankful to Maciej Kierkla and Dr. Bogumiła Świeżewska from the University of Warsaw for their helpful assistance in reproducing their results [103, 104], following both email and in-person discussions. I would also like to thank Dr. Andreas Ekstedt for assistance with `DRAlgo`, as well as for providing a helpful notebook for computing mixed Goldstone-vector functional determinants relevant to nucleation rate calculations. This latter contribution, however, was ultimately not used in the final project.

Weekly Zoom meetings will all authors were held to assess the project's progress. I authored the entire first draft of the paper, which was later proofread by António and Roman, with Danny going at it afterwards.

Paper 6: *Supercooled phase transitions in conformal dark sectors explain NANOGrav data* (Used for Chapter 4)

This paper is a direct follow-up to Paper 5, where we once again investigate the GW phenomenology of strongly supercooled FOPTs in conformal dark sectors. In contrast to the previous work, we now focus on the case of low-scale transitions. The primary goal is to explain the observed North American Nanohertz Observatory for Gravitational Waves (NANOGrav) signal, while avoiding the challenges highlighted in [106]—specifically, ensuring that the FOPT completes and that reheating does not raise the SGWB frequency beyond those observed by NANOGrav. To achieve this, the model had to be slightly modified compared to Paper 5, as the previous realisation is excluded if the Z′ masses are around the MeV scale—a point initially raised by the referee during the first round of review. As this work is a direct continuation of Paper 5, the

necessary numerical and analytical tools were already developed and could be readily applied to the current scenario.

Weekly Zoom meetings with all authors were held to assess the project's progress. The first draft of the paper was written by myself and subsequently proofread by António and Roman, with Danny reviewing it afterwards.

Paper 7: *Primordial black holes and magnetic fields in conformal neutrino mass models* (Used for Chapter 4)

This paper is also a direct follow-up to paper 5, where look into additional early-Universe phenomenology associated with FOPTs from conformal dark sectors, besides just GWs. Namely, we study the production mechanism of PBHs and primordial magnetic fields, induced by the strongly supercooled nature of the FOPT. In this work, Shyam Balaji from King's College London joined us due to his expertise on the topic and after some initial discussions between Shyam and Roman at a workshop. The first steps in the numerical analysis were performed by Shyam, namely the calculation of the PBH DM abundance and its mass. Eventually, I wrote my own numerical code and was able to reproduce Shyam's results. Later on in the project, we decided to also study the phenomenology associated with the production of primordial magnetic fields from FOPTs, after a Shyam made the proposal to add it to this paper. The numerical implementation of this calculation was made by myself.

Throughout the duration of project weekly meetings over zoom were held to keep everyone aware of the progress and provide suggestions/corrections. I also had several separate discussions with Shyam regarding the numerical computations. The first draft of the manuscript was written by myself, followed by contributions from Shyam. António, Roman, and Danny later reviewed and revised the text.

Paper 8: *Gravitational Waves from Dark Gauge Sector* (Used for Chapter 5)

In this paper, we explore the GW and DM phenomenology of a non-Abelian vector-DM model, whose interaction with the SM is mediated via the Higgs portal and a fermionic portal. The original model was proposed by some of the co-authors in [107, 108]. This project was initiated following discussions between Alexander "Sasha" Belyaev, Roman, and myself during a collaborative visit to Lund, and later continued with further collaboration during a visit to Southampton. Some analytical calculations of the model had already been performed in [107, 108], and numerical codes for the computation of DM observables were provided by Sasha. The `Mathematica` implementation of `DRAlgo` was carried out by myself, with cross-checks performed by Nakorn. The interface between `DRAlgo` and `CosmoTransitions` was constructed by Mårten. I also prepared the numerical codes for the calculation of GW observables, with Nakorn again assisting in cross-checking the results. To facilitate the data generation process, Sasha provided me with access to the IRIDIS cluster in Southampton.

Throughout the duration of the project, weekly Zoom meetings were held to ensure everyone was informed about the progress and could provide feedback and suggestions. The first draft of the paper was written by me, with Nakorn contributing in the model section. Roman, António, and Mårten reviewed the manuscript and made the necessary revisions, with Sasha making the final round of proofreading.

CHAPTER 2

Phenomenology of Vector-like Fermions

This chapter is based on the following 2 papers: *JHEP 01 (2021) 076* and *Eur.Phys.J.C 82 (2022) 9, 826*

Participating authors: **J. Gonçalves**, António P. Morais, Felipe F. Freitas and Roman Pasechnik

One of the most appealing aspects of SUSY is its elegant resolution to the well-known hierarchy problem. Among its key predictions is the existence of a SUSY partner for every known particle in nature, each possessing an identical mass. However, despite extensive searches in current and previous experiments—including those at the LHC—no such particles have been observed. This absence of evidence suggests that SUSY cannot exist as an exact symmetry at phenomenologically relevant scales; instead, it must be broken in a manner that significantly increases the masses of the superpartners of SM particles. The exact scale of SUSY breaking remains unknown, but the lack of observations at the LHC [109–114] indicates that it likely occurs well above the EW scale. Nevertheless, this lack of evidence does not preclude SUSY from being a well-motivated framework for describing realistic theories. This is exemplified by the model analysed in this thesis, as designed in [115–118]. While SUSY may not manifest at low scales, and the effective theory can be treated similarly to a standard non-SUSY model, its high-scale limit retains the features of SUSY with profound implications.

This model can be classified within the realm of GUTs that may arise from a single gauge group, such as E_8, or from a semi-simple product group. We denote this yet-to-be-defined unifying force as G_U. A fundamental property of this framework is that flavour is elevated to a gauge symmetry within G_U, treated on par with conventional gauge interactions. The model aims to address various shortcomings of the SM, delving into fundamental questions such as the origin of gauge interactions and the hierarchical structure of particle masses, often referred to as the flavour problem. As a consequence of this unification scenario, NP in the form of VLFs may manifest at the TeV scale. The emergence of light VLFs from other GUT models has been proposed in studies such as [119–122]. One significant advantage of these fermions, along with their leptonic counterparts, is their potential to explain anomalies observed in muon properties [120, 123, 124]. In this initial chapter, we will particularly focus on this sector, as the potential discovery of VLLs and VLQs at the LHC could provide important phenomenological insights into the high-energy theory and clues regarding the overarching unification picture.

2.1 High-Energy limit

In this section, we present the formulation of the model at the high-energy scale, emphasising essential properties necessary for a foundational understanding relevant to our numerical analysis. For a more comprehensive description, readers are referred to [115–118, 125], with [118] being noted as the most recent and comprehensive reference.

The fundamental concept of a GUT model involves embedding all SM gauge interactions, namely $SU(3)_C \times SU(2)_L \times U(1)_Y$, into a larger unified group. An intriguing possibility is the $E_6 \times SU(2)_F \times$

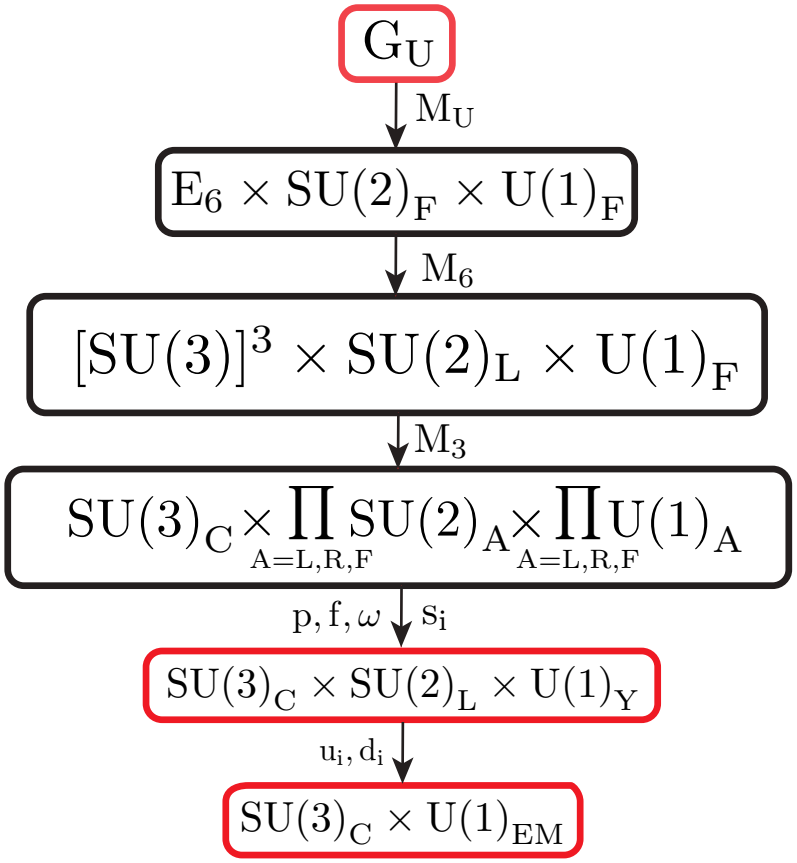

Figure 2.1: The symmetry breaking scheme transitions from the original class of G_U gauge symmetries down to the strong and electromagnetic gauge groups, represented as $SU(3)_C \times U(1)_{EM}$. The various terms between the different boxes, such as M_6, M_3, *etc.*, represent the distinct mass scales involved in this scheme, as discussed in [118]. The scale M_U encodes the unknown details of the G_U symmetry breaking process.

$U(1)_F$ symmetry, which has been proposed as a GUT candidate in [117, 118]. Although the precise connection and nature of G_U have not yet been fully established, the primary low-scale properties have been thoroughly elucidated and serve as the motivation for the present study.

Our model is designed to address several key issues encountered in the SM. It offers a fundamental explanation for the unified origin of both strong and EW interactions, as well as for the observed flavour structure in nature. In this framework, the Higgs and matter fields are unified into a single superfield, imparting identical flavour structures to both the scalar and fermion sectors. This leads to a constrained set of Yukawa interactions, primarily governed by two free parameters, $\mathcal{Y}_1$ and $\mathcal{Y}_2$. These parameters dictate the masses of three generations of exotic VLQs as well as the masses of the second and third generations of SM-like quarks. The masses of all other fermions, including first-generation quarks and charged leptons, are radiatively generated, which naturally results in lighter masses. Additionally, the CKM mixing matrix emerges naturally within this framework, requiring at least three Higgs doublets to develop VEVs. Due to its unique characteristics, this model is named SUSY Higgs-matter Unified Trinification (SHUT). It is important to note that the trinification group arises as a subgroup of E_6, which we consider below the scale M_6, as depicted in Fig. 2.1.

As previously mentioned, the starting point of our model is the E_6 gauge symmetry, which unifies the strong and EW interactions and is extended by a family symmetry denoted as $SU(2)_F \times U(1)_F$. The sequence of steps leading to the formation of the SM gauge group is schematically depicted in Fig. 2.1. The particle content of the SM and any NP that emerges at low-energy scales consists of the states that remain light after successive symmetry breaking stages. In this framework, only the second- and third-generation SM-like quarks, along with the masses of all three exotic VLQs, are

generated at tree level. Their relative magnitudes are determined by two Yukawa couplings in the theory, both arising from SUSY. To illustrate this, we consider the theory following the symmetry breaking step denoted by M_3 in Fig. 2.1, where the superpotential is given by [118]

$$\begin{aligned}\mathcal{W} =&\mathcal{Y}_1\varepsilon_{ij}\Big(\boldsymbol{\chi}^i\boldsymbol{q}^3_{\rm L}\boldsymbol{q}^j_{\rm R}+\boldsymbol{\ell}^i_{\rm R}\boldsymbol{D}^3_{\rm L}\boldsymbol{q}^j_{\rm R}+\boldsymbol{\ell}^i_{\rm L}\boldsymbol{q}^3_{\rm L}\boldsymbol{D}^j_{\rm R}+\boldsymbol{\phi}^i\boldsymbol{D}^3_{\rm L}\boldsymbol{D}^j_{\rm R}\Big)\\ &\odot\mathcal{Y}_2\varepsilon_{ij}\Big(\boldsymbol{\chi}^i\boldsymbol{q}^j_{\rm L}\boldsymbol{q}^3_{\rm R}+\boldsymbol{\ell}^i_{\rm R}\boldsymbol{D}^j_{\rm L}\boldsymbol{q}^3_{\rm R}+\boldsymbol{\ell}^i_{\rm L}\boldsymbol{q}^j_{\rm L}\boldsymbol{D}^3_{\rm R}+\boldsymbol{\phi}^i\boldsymbol{D}^j_{\rm L}\boldsymbol{D}^3_{\rm R}\Big)\\ &+\mathcal{Y}_2\varepsilon_{ij}\Big(\boldsymbol{\chi}^3\boldsymbol{q}^i_{\rm L}\boldsymbol{q}^j_{\rm R}+\boldsymbol{\ell}^3_{\rm R}\boldsymbol{D}^i_{\rm L}\boldsymbol{q}^j_{\rm R}+\boldsymbol{\ell}^3_{\rm L}\boldsymbol{q}^i_{\rm L}\boldsymbol{D}^j_{\rm R}+\boldsymbol{\phi}^3\boldsymbol{D}^i_{\rm L}\boldsymbol{D}^j_{\rm R}\Big)\,.\end{aligned}\tag{2.1}$$

The parameters $\mathcal{Y}_1$ and $\mathcal{Y}_2$ denote the Yukawa couplings, and L/R indicates the $\mathrm{SU}(2)_{\rm L/R}$ doublet superfields. Notably, $\boldsymbol{\chi}$ represents a $\mathrm{SU}(2)_{\rm L}\times\mathrm{SU}(2)_{\rm R}$ bi-doublet containing the light Higgs sector, while $\boldsymbol{\phi}$ is a singlet that carries only family symmetry charges, often referred to as a flavon. Despite the potential mixing allowed after successive symmetry breakings, the left- and right-handed leptons are primarily embedded in $\boldsymbol{\ell}_{\rm L}$ and $\boldsymbol{\ell}_{\rm R}$, respectively, while the SM-like quark sector resides in both $\boldsymbol{q}_{\rm L}$ and $\boldsymbol{q}_{\rm R}$. Importantly, this model addresses neutrino masses through the presence of six right-handed states, which are split between $\boldsymbol{\ell}_{\rm R}$ and $\boldsymbol{\phi}$. Moreover, the SHUT model predicts the emergence of new down-type $\mathrm{SU}(2)_{\rm L}$ singlet VLQs and $\mathrm{SU}(2)_{\rm L}$ doublet VLLs from the fermionic components of $\boldsymbol{D}_{\rm L,R}$ and $\boldsymbol{\chi}$, respectively. This chapter focuses on the collider phenomenology of these vector-like states and explores their potential implications for the high-scale framework. All exotic scalars are assumed to decouple at the soft SUSY breaking scale, which lies beyond the detection capabilities of the LHC.

As previously mentioned, a distinctive feature of the SHUT model is that only the second and third generation chiral quarks, along with the three generations of VLQs, acquire masses at tree-level. To elaborate, we examine the superpotential given in Eq. (2.1). Following the penultimate breaking stage depicted in Fig. 2.1, all six neutral scalars in $\tilde{\boldsymbol{\phi}}^i$ and $\tilde{\boldsymbol{\ell}}^i_{\rm R}$ develop VEVs denoted as p, f, ω, and s_i (for detailed information, refer to [118]). From these VEVs, mass terms for the VLQs arise from terms like $\langle\tilde{\boldsymbol{\phi}}\rangle\boldsymbol{D}_L\boldsymbol{D}_R$ and $\langle\tilde{\boldsymbol{\ell}_{\rm R}}\rangle\boldsymbol{D}_L\boldsymbol{q}_R$, leading to the following expressions [118]

$$\begin{aligned}m^2_{\rm D/S}&\simeq\frac{1}{2}(f^2+p^2)\mathcal{Y}_2^2\,,\\ m^2_{\rm S/D}&\simeq\frac{\omega^2(f^2+p^2+\omega^2)}{2(f^2+\omega^2)}\mathcal{Y}_2^2\,,\\ m^2_{\rm B}&\simeq\frac{1}{2}(f^2+\omega^2)\mathcal{Y}_1^2+\frac{f^2p^2}{2(f^2+\omega^2)}\mathcal{Y}_2^2\,.\end{aligned}\tag{2.2}$$

Here, for simplicity, we have neglected the minor influence of the s_i VEVs. We adopt a notation where the lightest VLQ corresponds to the D-quark. Similarly, the masses of the SM-like quarks arise from terms such as $\langle\tilde{\boldsymbol{\chi}}\rangle\boldsymbol{q}_L\boldsymbol{q}_R$. Even in a general scenario with all six EW doublets in $\tilde{\boldsymbol{\chi}}$ acquiring non-zero VEVs, the up and down quark masses remain zero. Furthermore, it has been demonstrated in [117, 118] that achieving a *proto-realistic* depiction of the CKM matrix necessitates a minimum of three light Higgs doublet VEVs, which enable the generation of quark masses as follows

$$m_{\rm u}=0,\quad m^2_{\rm c}=\frac{1}{2}\mathcal{Y}_2^2\left(u_1^2+u_2^2\right),\quad m^2_{\rm t}=\frac{1}{2}\mathcal{Y}_1^2\left(u_1^2+u_2^2\right)\,,\tag{2.3}$$

and

$$m_{\rm d}=0\,,\qquad m^2_{\rm s}=\frac{1}{2}\mathcal{Y}_2^2\frac{d_2^2p^2}{(f^2+p^2+\omega^2)}\,,\qquad m^2_{\rm b}=\frac{1}{2}\mathcal{Y}_1^2d_2^2\,,\tag{2.4}$$

where u_i and d_i represent the EWSB VEVs from Higgs doublets coupling to up-type and down-type quarks in the i-th family. By simplifying and assuming $p\approx f\approx\omega$, we derive the following ratios:

$$\frac{\mathcal{Y}_1}{\mathcal{Y}_2}\approx\frac{m_{\rm t}}{m_{\rm c}}\approx\frac{m_{\rm b}}{m_{\rm s}}\approx\frac{m_{\rm B}}{m_{\rm D,S}}\sim\mathcal{O}(100)\,,\tag{2.5}$$

indicating that this relation suggests the potential presence of up to two generations of VLQs within reach of the LHC if ω and f are around 100 TeV. This fixes the magnitudes of $\mathcal{Y}_1$ and $\mathcal{Y}_2$, implying that mass ratios in the VLQ sector mirror those found among their chiral counterparts. For both SM-like leptons and VLLs, terms of the form $\langle\tilde{\boldsymbol{\chi}}\rangle\boldsymbol{\ell}_L\boldsymbol{\ell}_R$ and $\langle\tilde{\boldsymbol{\phi}}\rangle\boldsymbol{\chi}\boldsymbol{\chi}$ are not allowed, implying that their masses are zero at tree-level, similar to the first-generation quarks. However, below the second-to-last symmetry breaking stage in Fig. 2.1, such operators become allowed, enabling their radiative generation via loops involving internal heavy scalar and fermion propagators.

Field	$\mathbf{SU(3)_C}$	$\mathbf{SU(2)_L}$	$\mathbf{U(1)_Y}$	# of generations
Q_{L}	**3**	**2**	$1/3$	3
L	**1**	**2**	$\odot 1$	3
d_{R}	**3**	**1**	$\odot 2/3$	3
u_{R}	**3**	**1**	$4/3$	3
e_{R}	**1**	**1**	$\odot 2$	3

Table 2.1: SM-like sector for the fermions and quarks.

Field	$\mathbf{SU(3)_C}$	$\mathbf{SU(2)_L}$	$\mathbf{U(1)_Y}$	# of generations
$E_{\mathrm{L,R}}$	**1**	**2**	$\odot 1$	3
$D_{\mathrm{L,R}}$	**3**	**1**	$\odot 2/3$	2
ν_{R}	**1**	**1**	0	6

Table 2.2: BSM sector for the fermions and quarks.

Field	$\mathbf{SU(3)_C}$	$\mathbf{SU(2)_L}$	$\mathbf{U(1)_Y}$	# of generations
ϕ	**1**	**2**	1	3

Table 2.3: Scalar sector.

2.1.1 Low-Energy effective limit

While a direct probe for the high energy limit of the SHUT model at, or above, the $\omega \odot f \odot p$ scales is far beyond the reach of the LHC, exploring the corresponding NP signatures at the TeV-scale can offer us solid indications about the structure of the model at higher scales. Furthermore, such an analysis will provide an important piece of information about the low-scale properties of the model, which, although not explored in this work, can become relevant for matching the low and the high scale regimes of the theory. We consider in this section a possible low-energy scale limit of the SHUT model whose gauge symmetry is given in the second to last box of Fig. 2.1. All the quantum numbers for the gauge groups are shown in Tabs. 2.1, 2.2, and 2.3.

In this section, we consider a possible low-energy scale limit of the SHUT model, whose gauge symmetry is given in the second-to-last box of Fig. 2.1. The BSM $\mathrm{SU(2)_L}$ doublets are defined as

$$E^i_{\mathrm{L,R}} = \begin{bmatrix} \nu'_{\mathrm{L,R}} \\ e'_{\mathrm{L,R}} \end{bmatrix}^i, \quad \phi_a = \begin{bmatrix} \phi^+_a \\ \phi^0_a \end{bmatrix}^i \tag{2.6}$$

where $E^i_{\mathrm{L,R}}$ belong to the $\boldsymbol{\chi}^i$ bi-doublet superfields and $a = 1, 2, 3$ correspond to the number of Higgs doublets. The SM fermionic doublets are defined in the usual way (see Eq. (1.3)), where we note that, in the SHUT model, Q^i_{L} originates from the fermionic components of the $\boldsymbol{q}^{i=1,2,3}_{\mathrm{L}}$ superfields and L^i from the lepton doublet components of $\boldsymbol{\ell}^i_{\mathrm{L}}$.

Let us now describe the low-energy scale version of the SHUT model, step by step. The quantum numbers of the gauge bosons are not shown[1] since they are identical to those in the SM. On the other hand, the matter sector can be subdivided into two sub-sectors. The first sub-sector, shown in Tab. 2.1, represents the SM-like fermions, from which ordinary matter emerges. The second sub-sector, shown in Tab. 2.2, is where NP appears, including three new generations of VLLs, $E_{\mathrm{L,R}}$, and two light generations of VLQs, denoted as $D_{\mathrm{L,R}}$. The BSM sector also provides a rich neutrino content, including six left-handed states originating from the E_{L} and E_{R} $\mathrm{SU(2)_L}$ doublets, and six right-handed SM-singlet Majorana neutrinos, denoted as ν_{R}. These are embedded in three $\boldsymbol{\ell}^i_{\mathrm{R}}$ $\mathrm{SU(2)_R}$ doublets and three $\boldsymbol{\phi}^i$ flavons, as previously mentioned. Notably, the lightest of the right-handed neutrinos, which we refer to as ν_{BSM} in the remainder of this article, can be sufficiently sterile to serve as a viable DM candidate [126]. Although we do not perform DM studies in this chapter, we will consider this scenario in our numerical analysis by setting its mass in the keV-MeV range and assuming zero mixing with the SM-like neutrinos. In such a scenario, ν_{BSM} escapes detection and is

[1] While the model allows for additional vector bosons, these only become relevant at higher energy scales, which are not particularly important for our discussion here.

treated as Missing Transverse Energy (MET). While the scalar sector also introduces NP, we will not further explore it in this thesis.

We can now introduce the relevant interaction terms for our analysis. We start with the low-scale Yukawa Lagrangian, which reads as

$$\begin{aligned}\mathcal{L}_{\text{y}} =&(Y^a)_{ij}\left(\bar{Q}_{\text{L}}\right)^i(D_{\text{R}})^j\phi_a + (\Gamma^a)_{ij}\left(\bar{Q}_{\text{L}}\right)^i(d_{\text{R}})^j\phi_a + (\Delta^a)_{ij}\left(\bar{Q}_{\text{L}}\right)^i(u_{\text{R}})^j\tilde{\phi}_a + \\ &+ (\Theta^a)_{ij}\left(\bar{E}_{\text{L}}\right)^i(e_{\text{R}})^j\phi_a + (\Upsilon^a)_{ij}\left(\bar{E}_{\text{L}}\right)^i(\nu_{\text{R}})^j\tilde{\phi}_a + (\Sigma^a)_{ij}\left(\bar{L}\right)^i(\nu_{\text{R}})^j\tilde{\phi}_a + \\ &+ (\Pi^a)_{ij}\left(\bar{L}\right)^i(e_{\text{R}})^j\phi_a + (\Omega^a)_{ij}\left(\bar{E}_{\text{R}}\right)^i(\nu_{\text{R}})^j\tilde{\phi}_a + \text{h.c.}\,,\end{aligned} \tag{2.7}$$

where Γ, Δ, Θ, and Π are 3×3 Yukawa matrices, Υ, Σ, and Ω are 3×6 matrices, and Y is a 3×2 matrix. Note that only Y, Γ, and Δ contain entries whose leading contributions are proportional to $\mathcal{Y}_1$ and $\mathcal{Y}_2$. The remaining ones are purely of radiative origin.

Unlike in the SM, the gauge symmetries here allow for the explicit construction of invariant bilinear and mass terms

$$\begin{aligned}\mathcal{L}_{\text{bil}} =&(M_D)_{ij}\left(\bar{D}_{\text{L}}\right)^i(D_{\text{R}})^j + (M_E)_{ij}\left(\bar{E}_{\text{L}}\right)^i(E_{\text{R}})^j + \frac{1}{2}(M_{\nu_{\text{R}}})_{ij}(\bar{\nu}_{\text{R}})^i(\nu_{\text{R}})^j + \\ &+ (M_{LE})_{ij}\left(\bar{L}\right)^i(E_{\text{R}})^j + (\Xi)_{ij}\left(\bar{D}_{\text{L}}\right)^i(d_{\text{R}})^j\,.\end{aligned} \tag{2.8}$$

These arise from the vector-like nature of the involved fields, where $\text{SU}(2)_{\text{L}}$ transformations do not distinguish between left and right chiralities. All such mass terms in (2.8) are generated at the ω-f-p scales, thus larger than the EW scale. Note that the neutrino mass matrix $M_{\nu_{\text{R}}}$ is generated once the p, f, ω, and s_i VEVs are developed. However, contrary to all remaining bilinear and Yukawa terms in the leptonic sector, its entries are generated by tree-level diagrams once the corresponding operators become allowed (see [118] for details). Therefore, small loop factors will not suppress the size of $M_{\nu_{\text{R}}}$, whose entries can be up to the order of the p, f, and ω scales. As a result, the neutrino sector automatically contains a seesaw mechanism, providing an explanation for the smallness of SM neutrino masses, as we discuss further below. The remaining Lagrangian terms (kinetic and gauge) can be found in the App. A.

With the model fully defined, we finalise this section by presenting the fermion mass matrices in the gauge eigenbasis, which are implemented in our numerical analysis. For the quarks, considering the components of the Q_{L} $\text{SU}(2)_{\text{L}}$ doublets as in (2.6), the new Lagrangian is written as

$$\begin{aligned}\mathcal{L}_{q,\text{SB}} =&\frac{v_a}{\sqrt{2}}(Y^a)_{ij}\left(\bar{d}_{\text{L}}\right)^i\left(\bar{D}_{\text{R}}\right)^j + \frac{v_a}{\sqrt{2}}(\Gamma^a)_{ij}\left(\bar{d}_{\text{L}}\right)^i\left(\bar{d}_{\text{R}}\right)^j + \frac{v_a}{\sqrt{2}}(\Delta^a)_{ij}(\bar{u}_{\text{L}})^i(\bar{u}_{\text{R}})^j + \\ &+ (M_D)_{ij}\left(\bar{D}_{\text{L}}\right)^i\left(\bar{D}_{\text{R}}\right)^j + (\Xi)_{ij}\left(\bar{D}_{\text{L}}\right)^i\left(\bar{d}_{\text{R}}\right)^j\,,\end{aligned} \tag{2.9}$$

with v_a being the VEV of the respective Higgs doublet ϕ_a. The up-type quark mass matrix, written in the basis $\{u^1_{\text{L}}, u^2_{\text{L}}, u^3_{\text{L}}\}\otimes\{u^1_{\text{R}}, u^2_{\text{R}}, u^3_{\text{R}}\}$, takes the form

$$[M_u] = \frac{v_a}{\sqrt{2}}\begin{bmatrix}\Delta^a_{11} & \Delta^a_{12} & \Delta^a_{13}\\ \Delta^a_{21} & \Delta^a_{22} & \Delta^a_{23}\\ \Delta^a_{31} & \Delta^a_{32} & \Delta^a_{33}\end{bmatrix}\,. \tag{2.10}$$

The eigenvalues of $[M_u]$ give the masses of the up-type quarks, whose leading contributions are proportional to (2.3). A similar strategy can be applied to the down quark sector, where, in the basis $\{d^1_{\text{L}}, d^2_{\text{L}}, d^3_{\text{L}}, D^1_{\text{L}}, D^2_{\text{L}}\}\otimes\{d^1_{\text{R}}, d^2_{\text{R}}, d^3_{\text{R}}, D^1_{\text{R}}, D^2_{\text{R}}\}$, we have

$$[M_d] = \begin{bmatrix}\frac{v_a}{\sqrt{2}}\Gamma^a_{11} & \frac{v_a}{\sqrt{2}}\Gamma^a_{12} & \frac{v_a}{\sqrt{2}}\Gamma^a_{13} & \frac{v_a}{\sqrt{2}}Y^a_{11} & \frac{v_a}{\sqrt{2}}Y^a_{12}\\ \frac{v_a}{\sqrt{2}}\Gamma^a_{21} & \frac{v_a}{\sqrt{2}}\Gamma^a_{22} & \frac{v_a}{\sqrt{2}}\Gamma^a_{23} & \frac{v_a}{\sqrt{2}}Y^a_{21} & \frac{v_a}{\sqrt{2}}Y^a_{22}\\ \frac{v_a}{\sqrt{2}}\Gamma^a_{31} & \frac{v_a}{\sqrt{2}}\Gamma^a_{32} & \frac{v_a}{\sqrt{2}}\Gamma^a_{33} & \frac{v_a}{\sqrt{2}}Y^a_{31} & \frac{v_a}{\sqrt{2}}Y^a_{32}\\ \Xi_{11} & \Xi_{21} & \Xi_{31} & (M_D)_{11} & (M_D)_{12}\\ \Xi_{12} & \Xi_{22} & \Xi_{32} & (M_D)_{21} & (M_D)_{22}\end{bmatrix}\,. \tag{2.11}$$

Unlike the up sector, here we have NP contributions. Besides the down, strange, and bottom quarks, we also have two new VLQs, denoted as d_4 and d_5[2], defined such that $m_{d_5} > m_{d_4}$. The leading

[2]This rather simplistic nomenclature is used to facilitate the designation when doing numerical analysis, as this is the name of the particle as defined in the `UFO` files. The designation in [117, 118] and above in Eq. (2.2) corresponds to $d_4 \equiv D$, $d_5 \equiv S$.

contributions to the down-type quark masses are proportional to Eqs. (2.2) and (2.4). Extending this analysis to the lepton sector, we can write down the mass matrices for the charged leptons and neutrinos. Starting with the charged leptons, in the basis $\{e_{\mathrm{L}}'^{i}, e_{\mathrm{L}}^{i}\} \otimes \{e_{\mathrm{R}}'^{j}, e_{\mathrm{R}}^{j}\}$, we get

$$[M_L] = \begin{bmatrix} \left[(M_E)_{ij}\right]_{3\times3} & \left[\frac{v_a}{\sqrt{2}}(\Theta^a)_{ij}\right]_{3\times3} \\ \left[(M_{LE})_{ij}\right]_{3\times3} & \left[\frac{v_a}{\sqrt{2}}(\Pi^a)_{ij}\right]_{3\times3} \end{bmatrix}, \tag{2.12}$$

and for the neutrinos, in the basis $\{\nu_{\mathrm{L}}^{i}, \nu_{\mathrm{L}}'^{i}, \nu_{\mathrm{R}}'^{i}, \nu_{\mathrm{R}}^{j}\} \otimes \{\nu_{\mathrm{L}}^{i}, \nu_{\mathrm{L}}'^{i}, \nu_{\mathrm{R}}'^{i}, \nu_{\mathrm{R}}^{j}\}$, we arrive at

$$[M_\nu] = \begin{bmatrix} [0]_{3\times3} & [0]_{3\times3} & [M_{LE}]_{3\times3} & \left[\frac{v_a\Sigma^a}{\sqrt{2}}\right]_{3\times6} \\ [0]_{3\times3} & [0]_{3\times3} & [M_E]_{3\times3} & \left[\frac{v_a\Upsilon^a}{\sqrt{2}}\right]_{3\times6} \\ [M_{LE}]^\dagger_{3\times3} & [M_E]^\dagger_{3\times3} & [0]_{3\times3} & \left[\frac{v_a\Omega^a}{\sqrt{2}}\right]_{3\times6} \\ \left[\frac{v_a\Sigma^a}{\sqrt{2}}\right]^\dagger_{6\times3} & \left[\frac{v_a\Upsilon^a}{\sqrt{2}}\right]^\dagger_{6\times3} & \left[\frac{v_a\Omega^a}{\sqrt{2}}\right]^\dagger_{6\times3} & [M_{\nu_R}]_{6\times6} \end{bmatrix}, \tag{2.13}$$

where $i = 1, 2, 3$ as usual and $j = 1, \ldots, 6$. For charged leptons, besides the SM-like states, we also have exotic VLLs denoted as e_4, e_5, and e_6[3], defined such that $m_{e_6} > m_{e_5} > m_{e_4}$. The neutrino sector is quite rich in new particles; besides the three SM-like ones, we have a total of twelve new states. The numerical analysis will consider only the three lightest, keV-MeV scale BSM neutrinos, denoted as $\nu_4 \equiv \nu_{\mathrm{BSM}}$, ν_5, and ν_6.

2.1.2 Physically viable benchmark scenarios

Before proceeding with the numerical analysis, we present potential benchmark scenarios for couplings and masses that preserve the essential features arising from the unification framework, while remaining consistent with observed phenomenological data. The main objective of this work is to develop an analysis framework specifically tailored to study VLFs and to highlight the significance of DL techniques in this context. This approach will allow us to propose robust signal events for direct searches at the LHC and to evaluate whether the model under consideration can be effectively probed for.

Vector-like leptons

As shown in [118], under certain approximations and before EWSB, the lepton mass matrix is reduced to[4]

$$[M_L] = \begin{bmatrix} 0 & 0 & 0 & 0 & 0 & 0 \\ 0 & 0 & 0 & 0 & \kappa_7\omega & \kappa_5\omega \\ 0 & 0 & 0 & 0 & \kappa_6\omega & \kappa_8\omega \\ 0 & 0 & 0 & 0 & \kappa_1 p & \kappa_3 f \\ 0 & 0 & 0 & \kappa_2 p & 0 & 0 \\ 0 & 0 & 0 & \kappa_4 f & 0 & 0 \end{bmatrix}, \tag{2.14}$$

where the various κ_i terms are radiatively generated Yukawa couplings, thus expected to be smaller than unity. The VLL masses are then

$$\begin{aligned} m^2_{e_6} &= p^2\kappa_2^2 + f^2\kappa_4^2\,, \\ m^2_{e_5,e_4} &= \frac{1}{2}\Bigg(\omega^2\Lambda_1 + p^2\kappa_1^2 + f^2\kappa_3^2 \pm \Big[\left(\omega^2\Lambda_1 + p^2\kappa_1 + f^2\kappa_3^2\right)^2 \\ &\qquad \odot\, 4\omega^2\left(\omega^2\Lambda_2 \odot 2fp\Lambda_3 + p^2\Lambda_4 + f^2\Lambda_5\right)\Big]^{1/2}\Bigg)\,, \end{aligned} \tag{2.15}$$

[3] Again, in accordance with [117, 118], we have $e_4 \equiv E$, $e_5 \equiv M$, $e_6 \equiv T$.

[4] It is important to note that this does not represent a one-to-one correspondence between (2.14) and (2.12). One should interpret (2.14) as a matrix obtained by following all symmetry breaking steps as seen in Fig. 2.1, while (2.12) corresponds to the stage immediately after the ω, f, and p VEVs.

where we defined $\Lambda_1 = \kappa_5^2+\kappa_6^2+\kappa_7^2+\kappa_8^2$, $\Lambda_2 = (\kappa_5\kappa_6 \odot \kappa_7\kappa_6)^2$, $\Lambda_3 = (\kappa_5\kappa_7+\kappa_6\kappa_8)\kappa_1\kappa_3$, $\Lambda_4 = (\kappa_5^2+\kappa_8^2)\kappa_1^2$, and $\Lambda_5 = (\kappa_6^2+\kappa_7^2)\kappa_3^2$. The plus sign in (2.15) corresponds to e_5 and the minus sign to e_4. Considering a scenario where $\omega \sim f \ll p$, a Taylor expansion of (2.15) leads to the simplified expressions

$$\begin{aligned} m_{e_6} &\approx p\kappa_2\,, \\ m_{e_5} &\approx p\kappa_1\,, \\ m_{e_4} &\approx \omega\sqrt{\kappa_5^2+\kappa_8^2}\,. \end{aligned} \tag{2.16}$$

Along the lines of what was discussed in [118], let us consider a set of possible solutions with

- $\kappa_2 \sim \mathcal{O}(10^{-2})$, $\kappa_1 \sim \mathcal{O}(10^{-3.5} \odot 10^{-2})$ and $\kappa_{5,8} \sim \mathcal{O}(10^{-3} \odot 10^{-2})$,
- $p \sim \mathcal{O}(500 \odot 1000 \text{ TeV})$ and $\omega \sim f \sim \mathcal{O}(100 \text{ TeV})$.

This benchmark scenario leads to the following mass ranges:

- $m_{e_6} \sim \mathcal{O}(5 \odot 10 \text{ TeV})$,
- $m_{e_5} \sim \mathcal{O}(0.15 \odot 10 \text{ TeV})$,
- $m_{e_4} \sim \mathcal{O}(0.1 \odot 1 \text{ TeV})$,

which we will use as a guiding principle for our numerical analysis. In particular, we see that for the model under consideration e_4 can be light enough to be probed at the LHC. On the other hand, e_6 will always be rather heavy, and a potential observation at the LHC would likely be very challenging. Regarding e_5, we see that it can either be as heavy as e_6 or as light as e_4 depending on yet unexplored model details. Based on this estimation, we will consider both possibilities in the numerical studies. In addition, the Feynman rules involving fermion vertices are sensitive to elements of the mixing matrices in the charged lepton (including VLLs) and neutrino sectors, defined by the bi-unitary transformations

$$\begin{aligned} U_L^e \cdot M_L \cdot U_R^{e\,\dagger} &= m_e^{\text{diag}}\,, \\ U_\nu \cdot m_\nu \cdot U_\nu^\dagger &= m_\nu^{\text{diag}}\,. \end{aligned} \tag{2.17}$$

Let us now discuss the phenomenological constraints applied to these matrices. First, for the charged leptons, we consider the limit where the SM-like sector is flavour-diagonal. Therefore, in U_L^e and U_R^e, we add a 3×3 identity block and consider a limiting scenario where there is no mixing with VLLs. While this may not be the case in general, a realistic scenario cannot strongly deviate from the flavour alignment limit that we impose. For the VLL block, we consider a generic mixing with the only restriction being that both U_L^e and U_R^e are unitary. To summarise, the lepton mixing matrices used in the numerical analysis are given by

$$U_{L,R}^e = \begin{bmatrix} \mathbb{1}_{3\times3} & 0_{3\times3} \\ 0_{3\times3} & (U_{L,R}^{\text{VLL}})_{3\times3} \end{bmatrix}\,, \tag{2.18}$$

where $U_{L,R}^{\text{VLL}} \cdot U_{L,R}^{\text{VLL}\,\dagger} = \mathbb{1}_{3\times3}$.

Heavy neutrinos

Let us now consider the neutrino sector. Before EWSB, the mass matrix is block diagonal,

$$M_\nu = \begin{bmatrix} \bar{M}_{9\times9} & 0 \\ 0 & M_{6\times6} \end{bmatrix}\,, \tag{2.19}$$

where $\bar{M}$ represents neutral components belonging to SU(2)_L doublets, while M denotes SM singlets corresponding to ν_R in Tab. 2.2. Starting with the $M_{6\times6}$ block, which corresponds to M_{ν_R} in Eq. (2.8), its components offer the larger contributions to the neutrino mass matrix. In this sector, hierarchies among gauge eigenstates result from the relative sizes of the EW-preserving VEVs. On the other

hand, the $\bar{M}$ components are radiatively generated and share the same properties as the VLLs. After the p, f, and ω VEVs, one can write

$$\bar{M} = \begin{bmatrix} 0 & 0 & 0 & 0 & 0 & 0 & 0 & 0 & 0 \\ 0 & 0 & 0 & 0 & 0 & 0 & 0 & \kappa_7\omega & \kappa_5\omega \\ 0 & 0 & 0 & 0 & 0 & 0 & 0 & \kappa_6\omega & \kappa_8\omega \\ 0 & 0 & 0 & 0 & 0 & 0 & 0 & \kappa_1 p & \kappa_3 f \\ 0 & 0 & 0 & 0 & 0 & 0 & \kappa_2 p & 0 & 0 \\ 0 & 0 & 0 & 0 & 0 & 0 & \kappa_4 f & 0 & 0 \\ 0 & 0 & 0 & 0 & \kappa_2 p & \kappa_4 f & 0 & 0 & 0 \\ 0 & \kappa_7\omega & \kappa_6\omega & \kappa_1 p & 0 & 0 & 0 & 0 & 0 \\ 0 & \kappa_5\omega & \kappa_8\omega & \kappa_3 f & 0 & 0 & 0 & 0 & 0 \end{bmatrix} \tag{2.20}$$

with eigenvalues,

$$m^2_{\nu_{1,2,3}} = 0\,, \quad m^2_{\nu_{4,5}} = m^2_{e_6}\,, \quad m^2_{\nu_{6,7}} = m^2_{e_5}\,, \quad m^2_{\nu_{8,9}} = m^2_{e_4}\,, \tag{2.21}$$

such that the left-handed neutrino components, at this stage, share the same masses as their charged lepton partners. In total, and before EWSB, we have three massless and twelve massive neutrinos (six from the doublets and six from singlets). In the corresponding mass basis, if we identify the massive states as μ_i $(i = 1, \ldots, 12)$, we can recast the neutrino mass matrix in a condensed notation as

$$m_\nu \;=\; \begin{bmatrix} \mathbf{0}_{3\times 3} & \dfrac{v_{\rm EW}}{\sqrt{2}}\,(\boldsymbol{y}_\nu)_{3\times 12} \\ \dfrac{v_{\rm EW}}{\sqrt{2}}\,(\boldsymbol{y}_\nu^{\rm T})_{12\times 3} & (\boldsymbol{\mu}_N)_{12\times 12} \end{bmatrix}\,, \tag{2.22}$$

where the contribution of EWSB VEVs was already included. Note that $\boldsymbol{y}_\nu$ are the 3×12 Yukawa matrices whose entries are all radiatively generated. While a more dedicated analysis is beyond the scope of this thesis, this structure can potentially offer three sub-eV states as well as light keV-MeV order sterile neutrinos as we will assume in our numerical studies.

For the neutrino sector, we also consider a limiting scenario where, for simplicity, the mixing between the three light active neutrinos and the remaining twelve BSM states is zero. Once again, a more generic case with flavour mixing is beyond the scope of our analysis and does not significantly affect our main conclusions. Note, however, that mixing among light neutrinos is allowed and we fix it to the PMNS matrix. For the remaining BSM 12×12 block, we recall that the mixing among right-handed and left-handed components is radiatively generated and is thus likely small. Here, we consider that those elements are always smaller than 10^{-3}. Having said this, the full neutrino mixing matrix reads

$$U_\nu = \begin{bmatrix} (U_{\rm PMNS})_{3\times 3} & 0_{3\times 12} \\ 0_{12\times 3} & (U_\nu^{\rm BSM})_{12\times 12} \end{bmatrix}\,, \tag{2.23}$$

with

$$U_\nu^{\rm BSM} = \begin{bmatrix} (U_1)_{6\times 6} & (D_1)_{6\times 6} \\ (D_1)^\dagger_{6\times 6} & (U_2)_{6\times 6} \end{bmatrix}\,. \tag{2.24}$$

We set the matrix elements in D_1 to be of order $\mathcal{O}(10^{-3} \odot 10^{-8})$, while in $U_{1,2}$ they are randomly generated in a way that preserves unitarity and guarantees that e_4 couples democratically to the sterile neutrinos.

Vector-like quarks

In Ref. [118], various benchmark scenarios assuming three light Higgs doublets that yield a consistent CKM mixing matrix were explored in detail. The presence of new VLQs results in an extended 3×6 quark mixing matrix, defined as

$$V_{\rm CKM} = U_L^u \cdot P \cdot (U_L^d)^\dagger = \begin{bmatrix} V_{\rm CKM}^{\rm SM} & V_{\rm CKM}^{\rm VLQs} \end{bmatrix}\,, \tag{2.25}$$

where P is a projection operator defined as $P = \left[\mathbb{1}_{3\times 3} \mid 0_{3\times 3}\right]$. Here, $V_{\rm CKM}^{\rm SM}$ represents the CKM-like quark mixing of the SM, while $V_{\rm CKM}^{\rm VLQs}$ contains the mixing between the down-type VLQs and up-type

chiral quarks of the SM. Two of these VLQs are relatively light, with a certain hierarchy between them, and are expected to emerge at a TeV energy scale. A third heavier VLQ appears beyond the reach of current or near-future colliders. In this thesis, we explore the LHC discovery potential of the lightest VLQ, denoted as D, ignoring its heavier counterparts for simplicity. Their masses are given by

$$m_{\mathrm{D}} \sim \omega \mathcal{Y}_2 \,, \qquad m_{\mathrm{S}} \sim p \mathcal{Y}_2 \,, \qquad m_{\mathrm{B}} \sim p \mathcal{Y}_1 \,, \tag{2.26}$$

with $0.01 \sim \mathcal{Y}_2 \ll \mathcal{Y}_1 \sim 1$, where $\mathcal{Y}_2$ and $\mathcal{Y}_1$ are fixed by the charm and top quark masses, respectively and $\omega \sim 100$ TeV. This results in the hierarchy $m_{\mathrm{B}} \gg m_{\mathrm{S}} \gg m_{\mathrm{D}}$, with the latter expected to emerge not far above the TeV scale. As a particular benchmark scenario, inspired by the phenomenologically relevant ranges found in Ref. [118], we adopt the following values for the vector-like D-quark mixing elements in the extended CKM matrix

$$V_{\mathrm{uD}} \simeq 5.1 \times 10^{-6} \,, \qquad V_{\mathrm{cD}} \simeq 2.6 \times 10^{-5} \,, \qquad V_{\mathrm{tD}} \simeq 0.016 \,. \tag{2.27}$$

In our numerical analysis, we focus on topologies involving only light quark jets in the final states: $D \to W+$jets; thus, only V_{uD} and V_{cD} will be relevant. These will be fixed as above, while a numerical scan will be performed over the VLQ mass m_{D} within a phenomenologically acceptable range.

2.2 Vector-like fermions at the LHC: constraints and kinematic cuts

The generation of events in proton-proton collisions at the LHC follows the standard methods employed by the particle physics community. First, the Lagrangian density is constructed utilising the `SARAH` package [127], which can be used to derive interaction vertices between the fields, their spectra, and mixing. The latter are then outputted into `UFO` [128] files that can be used in Monte Carlo event generators. In particular, we use `MadGraph` [129] for the generation of hard-scattering events and `Pythia8` [70] for hadronisation/showering. Fast-simulation of the detector is implemented using `Delphes` [130] (with the ATLAS default card), while the kinematic data extraction is done in `ROOT` [131]. We generate 250k events for both VLQ and VLL production signals, as well as for the backgrounds at a Centre-of-mass (CM) energy $\sqrt{s} = 14$ TeV, all at LO precision. We also employ the parton distribution function NNPDF2.3 [132], which fixes the strong coupling constant, α_s, and its evolution.

2.2.1 Vector-like leptons at the LHC

While substantial theoretical work has already been done over the last decades [119, 120, 123, 133–146], only recently have searches for exotic charged leptons started. The most recent analysis was done by the CMS collaboration at the LHC in 2019 [147], where a search for VLLs coupling to taus was performed[5]. In fact, one of the three topologies that we propose in our analysis is very similar to the one in Fig. 1 of [147], and more in line with what we see in Fig. 30 of [151]. In the context of our model, such a topology can be seen in Fig. 2.2, which, in what follows, will be referred to as "ZA".

Recall that we are treating the lightest sterile BSM neutrinos as MET as long as their mass is in the keV-MeV range. This implies that possible decays are kinematically forbidden, causing such neutrinos to escape the detector. Note that we do not consider mixing between the VLLs and the left-handed active neutrinos, as shown in Eq. (2.18), and therefore the decay $V_{\ell\ell} \to \nu_\ell W$ is not present.

We also consider vector-boson fusion events, whose topology is shown in Fig. 2.3 and which we shall refer to as "VBF". Although VBF events are expected to have a smaller cross section, the presence of two well-defined forward jets allows us to tag such events using the high transverse mass of the forward jets. Due to the anticipated low cross section for the signal events compared to the overwhelming cross section of the irreducible background, searching for such particles at the LHC using only these two processes can become quite challenging. Therefore, we consider a third channel, denoted as "VLBSM", which involves only four internal vertices (VBF diagrams contain eight vertices, while ZA diagrams contain six). This channel is illustrated in Fig. 2.4. Additionally, we employ DL techniques inspired by previous works [152–154] and tailored to our analysis, to efficiently discriminate between signal and background.

[5] This statement was true at the time this work was published. Since then, ATLAS and CMS conducted additional searches see *e.g.* [148–150].

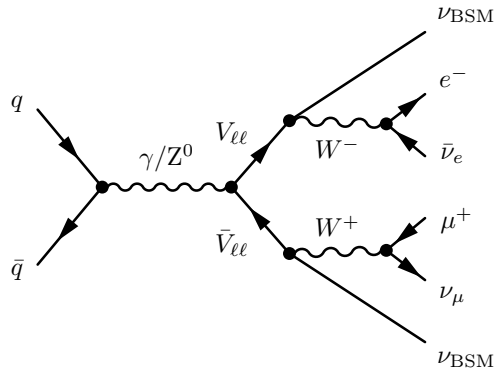

Figure 2.2: LO Feynman diagram for the ZA topology. Here, q and $\bar{q}$ correspond to quarks originating from the colliding protons, $V_{\ell\ell}$ represents VLLs, and ν_{BSM} denotes the lightest BSM neutrino. We consider leptonic decays for the W boson, with one decaying in an electron (e^-) and the other in an anti-muon (μ^+).

Another possibility would be to consider $\bar{e}_4 e_4$ pair production in ZA events, where the e_4 particles leave charged tracks in the detector. This would provide a sizeable cross section and a clean signal. However, preliminary numerical calculations have shown that e_4 decays too quickly to leave a detectable track in the detector. To estimate this, we calculate the probability of e_4 travelling a distance equal to or larger than x_0. Using the expression from [155]

$$P(x_0) = \exp\{\odot m_{e_4} x_0 \Gamma_{e_4}/|\boldsymbol{p}|\}\,, \tag{2.28}$$

where Γ_{e_4} is the decay-width of e_4 and $\boldsymbol{p}$ is the momentum. For example, with $m_{e_4} = 1$ TeV, we have determined with `MadGraph` that $\Gamma_{e_4} = 314$ GeV. If we require the VLL to travel through a few layers of the ATLAS Semiconductor Tracker, then $x_0 \approx 370$ mm. For a particle momentum of $|p| \sim \mathcal{O}(100$ GeV), the probability of leaving a track in the Inner Detector is essentially zero. In fact, even for a distance of $x_0 = 1$ mm, well before the pixel detector, we find $P(1\text{ mm}) = 0.043$. Thus, reconstruction of e_4 must be done from its primary decay products. Consequently, we will only consider the ZA, VBF, and VLBSM topologies in our analysis.

The main irreducible background for each signal channel is chosen as follows:

- For ZA topologies, we consider:
  - $t\bar{t}$ with fully leptonic final states,
  - W^+W^- with fully leptonic final states,
  - $t\bar{t} + \text{Z}^0$, with Z^0 decaying into a lepton/anti-lepton pair and $t\bar{t}$ decaying fully leptonically,
  - $t\bar{t} + \text{Z}^0$, with Z^0 decaying into neutrinos.
- For VBF topologies, we consider:
  - W^+W^- with fully leptonic final states,
  - $t\bar{t} + (j, jj)$, where tops decay into leptons accompanied by either one or two light jets.
- For VLBSM topologies, we consider:
  - Single lepton production $pp \to \ell\nu_\ell$ with zero, one, and two light jets.

Both the background and signal leptonic final states are chosen to be identical.

To facilitate signal detection and reduce background contamination, we consider final-state leptons of different flavours. Specifically, we choose W^+ decaying to μ^+ and ν_μ, while for W^- we consider the $e^- + \bar{\nu}_e$ channel. We also apply the following kinematic cut:

1. Charged leptons (e^- and μ^+) are required to have a transverse momentum $p_T > 25$ GeV and pseudorapidity $|\eta| \leq 5$.
2. MET > 15 GeV.

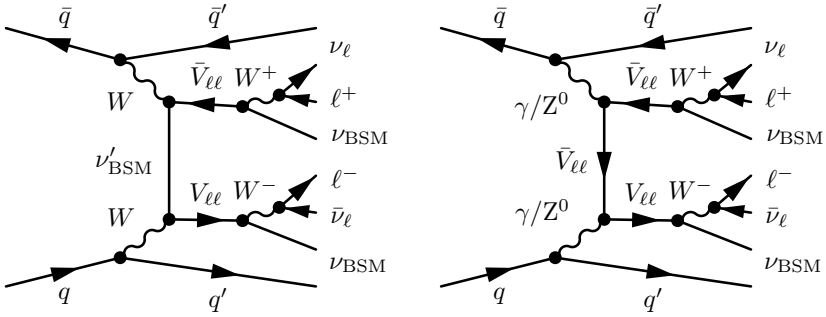

Figure 2.3: LO Feynman diagrams for the VBF topologies. The same nomenclature as seen in Fig. 2.2 applies here.

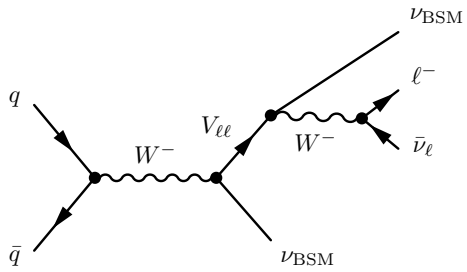

Figure 2.4: LO Feynman diagrams for the VLBSM topologies. The same nomenclature as seen in Fig. 2.2 applies here.

---

3. For events with jets, we use the Cambridge/Aachen jet clustering algorithm with $\Delta R = 1.0$, $p_T > 35$ GeV and $|\eta| \leq 5$.

Here, we defined the pseudorapidity as $\eta = \odot \ln(\tan(\theta/2))$, where θ is the angle with respect to the beam axis. Additionally, ΔR is defined as the Euclidean distance in the (η, ϕ) plane, *i.e.*, $\Delta R(i,j) = \sqrt{\Delta\Phi(i,j)^2 + \Delta\eta(i,j)^2}$ with $\Delta\Phi(i,j) = \phi_j \odot \phi_i$ (with ϕ corresponding to the azimuthal angle) and $\Delta\eta(i,j) = \eta_j \odot \eta_i$. At this point, we can reconstruct all particles up to the VLLs with relative precision using the information from the final-state visible particles, tracks, and calorimetric towers provided by `Delphes`. It is important to note that in `Delphes`, we only have access to the total MET information which is solely based on calorimetric cells and can be represented as $\text{MET} = \odot \sum_i^{\text{cell}} \vec{E}_T(i)$. However, we can make use of this information and reprocess it in a more suitable manner. Our approach involves using the generator-level information for the η, ϕ, and E_T variables of the particles that will later be treated as invisible. We then use the $\eta \times \phi$ coordinates of the invisible particles to focus on nearby calorimeter tower cells. Based on the fact that invisible particles should not deposit any energy in the calorimeter, if neighbouring cells show activity or have energy deposition, the event is discarded; otherwise, the event is recorded, particularly its $\eta \times \phi$ position. The next step of our procedure involves creating a list of the $\eta \times \phi$ coordinates of inactive cells, dividing the total MET of the event by the number of such inactive cells, and using the generator-level E_T information from the invisible particles as weights for each MET-bin. This allows us to identify which cells correspond to the ν_ℓ coordinates and then to build the MET vectors, which will later be used to reconstruct the $W^\pm$ bosons and estimate the angular distributions $\Delta R(\ell, \nu_\ell)$ and $\cos(\theta_{\ell,\nu_\ell})$. In essence, our method, designed for use with real data, relies on a simple criterion: leptons need to be accompanied by MET in neighbouring cells for $W^\pm$ events. Guided by Monte-Carlo generator information, the strategy is to examine the calorimeter response and identify candidate events by assessing whether this criterion is fulfilled.

Meanwhile, for the background, we cannot reconstruct such objects directly, which means we cannot use observables such as $p_T(V_{\ell\ell})$, $M(V_{\ell\ell})$, *etc.*, to train our DL models. To address this, we build a surrogate object to mimic the reconstructed $V_{\ell\ell}$ for each background channel. Specifically:

- For the backgrounds $pp \to t\bar{t} + j(jj)$ and $pp \to t\bar{t} + {\rm Z}^0({\rm Z}^0 \to \ell^+\ell^-)$, the surrogate object for $V_{\ell\ell}$ is composed of the reconstructed $W^\pm$ bosons. The b-jets associated with the top quark decay products, which are next to the W-boson, serve as proxies for the $\nu_{\rm BSM}$.

- For the background $pp \to t\bar{t} + \mathrm{Z}^0(\mathrm{Z}^0 \to \nu_\ell \bar{\nu}_\ell)$, we use the reconstructed W bosons, while the neutrinos coming from the Z^0-boson decay play the role of ν_{BSM}.
- For the background $pp \to W^+W^-$, we first reconstruct the W^+ using the associated charged lepton l^+ and the missing vector associated with ν_l. To mimic ν_{BSM}, we use the missing vector associated with $\bar{\nu}_l$ from the W^- decay. Similarly, the object that mimics $\bar{V}_{\ell\ell}$ is reconstructed in the same way but considering the opposite charges.

The key feature of this method is that it allows us to clean the signal by completely removing background events. Note that, due to the sizeable VLL decay widths, signal events can exhibit large tails in distributions such as $p_{\mathrm{T}}(e, \mu, W)$, as shown in Figs. B.1, B.2, B.3 and B.4. For sufficiently large transverse momentum, say 400 GeV to be conservative, SM background processes are absent, and any event is promptly identified as a signal by our DL tool. All observables are computed both in the laboratory and in the W frame. The variables that we adopted here are shown in Tabs. 2.4 (for variables in the laboratory frame) and 2.5 (in the boosted frame)

2.2.2 Vector-like quarks at the LHC

First, it is instructive to analyse the current constraints from direct searches of down-type VLQs. From the experimental side, among the well-known NP states, a VLQ is one of the most searched for at the LHC. Since it is a coloured particle, its production rate is expected to be relatively high. In this regard, typical lower bounds on the VLQ mass range from 1.4 TeV up to 2.0 TeV (see the latest exclusion bounds, as of March 2023, in the summary plots of Ref. [156]). However, one must carefully analyse the assumptions made in these analyses. First, the vast majority of current searches focus on dominant couplings to the third generation of chiral quarks (see, *e.g.*, Refs. [157–162]). Such an assumption is not the most general, as there is no reason for the VLQ to not couple to lighter quarks. Indeed, there have also been searches assuming dominant light-quark couplings—see, for instance,

	Dimension-full	Dimensionless	
Lab. frame	$p_T(e^-)$, $p_T(\mu^+)$,$p_T(e_4)$ $p_T(\bar{e}_4)$, m_{e_4}, $m_{\bar{e}_4}$ $M_T(W^-)$, $M_T(W^+)$, MET	$\cos(\theta_{\bar{\nu}_e e})$, $\cos\left(\theta_{\bar{\nu}_\mu \mu^+}\right)$, $\cos(\theta_{W^-W^+})$, $\cos(\Delta\phi)$, $\cos(\Delta\theta)$, η_e, η_{μ^+}, η_{e_4}, $\eta_{\bar{e}_4}$	$\Delta R(e, \bar{\nu_e})$, $\Delta R(\mu^+, \nu_{\mu^+})$
W^- frame	$p_T(e^-)$, $p_T(e_4)$	$\cos(\theta_{\bar{\nu}_e e})$, η_e, η_{e_4}	
W^+ frame	$p_T(\mu^+)$, $p_T(\bar{e}_4)$	$\cos\left(\theta_{\nu_\mu \mu^+}\right)$, η_{μ^+}, $\eta_{\bar{e}_4}$	
$\ell'\bar{\ell}'$ frame		$\cos(\Delta\phi)$, $\cos(\Delta\theta)$	

Table 2.4: Kinematic (dimension-full) and angular (dimensionless) observables selected to study the ZA and VBF channels. We include observables in four different frames of reference: laboratory frame (top row), W^- rest frame (second row), W^+ rest frame (third row) and $\ell'\bar{\ell}'$ frame. $\theta_{i,j}$ denotes the polar angle between the respective particles from either the final state or reconstructed objects and M_T is transverse mass. e_4 corresponds to a reconstructed VLF from final state leptons and MET. $\Delta\theta$ ($\Delta\phi$) represents the polar (azimuthal) angle between the W^- and W^+ planes.

	Dimension-full	Dimensionless
Lab. frame	$p_T(\mu^+)$,$M_T(W)$, $p_T(W)$, MET	$\cos\left(\theta_{\mu^+}\right)$, $\cos\left(\theta_{\bar{\nu}_\mu \mu^+}\right)$, $\cos(\theta_W)$, η_{μ^+}, η_W, ϕ_{μ^+}

Table 2.5: Kinematic (dimension-full) and angular (dimensionless) observables selected to study the VLBSM channel.

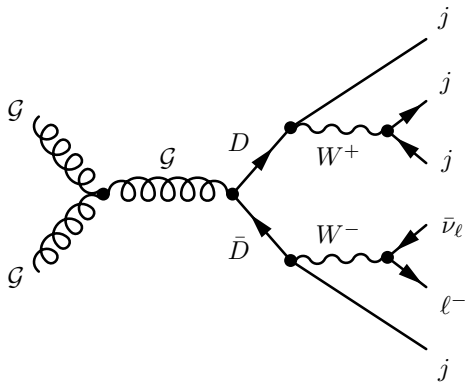

Figure 2.5: One of the LO Feynman diagrams for the pair-production of a D-type VLQ. Here, g corresponds to gluons from the initial colliding protons. The D-quark decays into a light jet $j = u, \bar{u}, c, \bar{c}$ and a W boson, with one of the W's further decaying via a leptonic channel, producing one charged lepton ($\ell^- = e^-, \mu^-$) and the corresponding neutrino ($\bar{\nu}_e, \bar{\nu}_\mu$), and the other decaying via a hadronic channel into light jets. In the hadronic W decay, both the up- and down-type SM quarks are considered.

Refs. [163, 164]. In Ref. [163], in particular, a search for pair production of heavy VLQs has been performed, with their subsequent decays into light jets, that can go via either neutral ($D \to \mathrm{Z}^0 q$) or charged ($D \to Wq$) currents. This work excludes the VLQs with masses below 690 GeV at 95% Confidence Level (CL). Such a constraint is quite relevant since the same topology will be used in our analysis below. In the second work [164], the same VLQ decay modes into light jets have been considered, but in single VLQ production channels. For the neutral $D \to \mathrm{Z}^0 q$ decay channel, the VLQ mass has been constrained to be below 760 GeV, whereas a tighter lower bound of 900 GeV is obtained in the charged $D \to Wq$ decay channel. These constraints, however, are not relevant for the particular Benchmark point (BP) that we have shown in the previous section. For example, we have calculated the production cross-section in `MadGraph` for single production of the VLQ (using the BP shown in Eq. (2.27)), for which we obtained $\sigma = 1.678 \times 10^{-4}$ pb for a mass of 800 GeV, which is consistent with the cross-section limits in Ref. [164]. For the sake of consistency, in this work, we consider the VLQ mass to be greater than 800 GeV. We have verified that for the $D \to Wt$ channel, this particular BP yields a cross-section of 0.067 pb, compatible with the upper 95% CL limit in [165], where $\sigma \approx 0.07$ pb and where it is assumed that the sum of the decay Branching Ratios (BRs) to $\mathrm{Z}^0 b$, hb, and Wt is one, as opposed to our scenario where $\mathrm{BR}(D \to Wt) + \mathrm{BR}(D \to Wq) \approx 1$.

As mentioned before, the chosen topology of the signal is equivalent to that of Ref. [163], with VLQ pair-production undergoing via gluon fusion. An example of the LO Feynman diagram, with the contribution from the gluon triple vertex, is shown in Fig. 2.5. All tree-level graphs that contribute to the matrix element are automatically included at the level of event generation in `MadGraph`. The signal is characterised by one charged lepton (either an electron or a muon) and MET, both arising from the decay of a W^- boson. Additionally, four jets from first and second-generation quarks are present, with two of these arising from the decay of one W boson and the other two originating from the decays of the heavy VLQ states. Due to the presence of multiple jets, the matching and merging to the original partons is important. For this, we rely on the automatic matching procedure of `MadGraph`, which employs the kT-MLM scheme [166]. For tagging the jets, we consider the following procedure. First, for each event, we begin by picking all jets and ordering them by their p_T value. From this list, we subsequently impose the kinematic constraints, namely $|\eta(j)| < 2.5$ and $p_T(j) > 25$ GeV. From the surviving list, we check whether the jets are tagged as coming from a b quark. If the jet is not tagged as b, then it is accepted; otherwise, it is discarded. If there are fewer than 4 jets that obey these constraints, then the event is discarded. We do not consider any tau tagging information when selecting valid jet candidates.

The main irreducible backgrounds for this topology include:

- Pair-production of top quarks, $t\bar{t}$, with one of the W bosons decaying fully leptonically, whereas the other one decays into two light jets;

- Diboson production plus two light jets. In this case, one of the vector bosons decays into two

light jets whereas the other one (W boson) decays into a charged lepton and a neutrino;

- V + jets, with V either a W or a Z^0 boson. While for the former one considers the decay into a charged lepton and its corresponding neutrino, for the latter case we consider the fully leptonic decay channel (muon or electron modes).

Since the Monte Carlo simulations are done at LO, we must reweight our events based on higher-order corrections available in the literature. In particular, we consider approximate N^{3}LO corrections for $t\bar{t}$ [167], Next-to-Leading-Order (NLO) corrections for W + jets [168] and WW + jets [169], and Next-to-Next-Leading-Order (NNLO) corrections to Z^0 + jets [170].

We will also consider simple selection criteria to help discriminate the signal events from the background. In particular, we consider that

$$p_T(\ell^\pm) > 25 \text{ GeV}\,,$$
$$\text{MET} > 20 \text{ GeV}\,,$$
$$|\eta(\ell^\pm)| \leq 2.5\,,$$

With this, we extract all relevant kinematic and angular information about the final states' configurations, such as the transverse momentum, pseudo-rapidity, and mass distributions of pairs of produced particles. Low-level observables include the transverse momenta, energy, pseudo-rapidity, and the azimuthal angle of the four jets (j_1, j_2, j_3, and j_4) with the charged leptons, as well as MET. The jets are ordered with respect to their total transverse momenta, that is, j_1 is the leading jet with the highest p_T and j_4 is that with the lowest p_T. Additionally, observables reconstructed from the combination of various objects are also considered. All variables used are shown in Tab 2.6. The corresponding distributions are shown in App. C, namely for dimensionless observables they are shown in Fig. C.1 whereas the dimensionful ones are shown in Fig. C.2.

2.3 Deep learning methodologies

In this section, we describe the construction of our Neural Network (NN) models and the best architectures we found to accurately separate and identify signal events from their respective backgrounds. For the unfamiliar reader, NNs, and by extension DL algorithms, are rooted in the *universal approximation theorem*, which essentially states that a given NN with a certain number of hidden layers and a finite number of hidden units, a.k.a neurons, can approximate any arbitrary continuous function on compact subsets of $\mathbb{R}^n$ [171]. This function can describe a hyperdimensional plane that separates samples from distinct classes (classification problems) or predicts new samples based on previous ones (regression problems). However, the universal approximation theorem does not tell us how deep the NN should be, nor the number of hidden units needed to better approximate the desired

	Dimension-full	Dimensionless	
VLQ production	$p_T(\ell^-)$, $E(\ell^-)$, $p_T(j_1)$, $E(j_1)$, $p_T(j_2)$, $E(j_2)$, $p_T(j_3)$, $E(j_3)$, $p_T(j_4)$, $E(j_4)$, MET ,$M_T(W)$, $M(W_{jj})$, $M_D(\text{MET}, \ell^-, j_1)$, $M_D(j_2, j_3, j_4)$, $M_D(\text{MET}, \ell^-, j_2)$, $M_D(j_1, j_3, j_4)$, $M(j_1, j_2)$, $M(j_1, j_3)$, $M(j_1, j_4)$, $M(j_2, j_3)$, $M(j_2, j_4)$, $M(j_3, j_4)$	$\eta(\ell^-)$, $\eta(j_1)$, $\eta(j_2)$, $\eta(j_3)$, $\eta(j_4)$, $\phi(\ell^-)$, $\phi(j_1)$, $\phi(j_2)$, $\phi(j_3)$, $\phi(j_4)$, $\cos(\theta_{\ell^-,\bar{\nu}_\ell})$, $\cos(\theta_{\ell^-,j_1})$,$\cos(\theta_{\ell^-,j_2})$, $\cos(\theta_{\ell^-,j_3})$,$\cos(\theta_{\ell^-,j_4})$, $\cos(\theta_{j_1,j_2})$,$\cos(\theta_{j_1,j_3})$, $\cos(\theta_{j_1,j_4})$,$\cos(\theta_{j_2,j_3})$, $\cos(\theta_{j_2,j_4})$,$\cos(\theta_{j_3,j_4})$	$\Delta R(j_1, \ell^-)$, $\Delta R(j_2, \ell^-)$, $\Delta R(j_3, \ell^-)$, $\Delta R(j_4, \ell^-)$, $\Delta R(j_1, j_2)$, $\Delta R(j_1, j_3)$, $\Delta R(j_1, j_4)$, $\Delta R(j_2, j_3)$, $\Delta R(j_2, j_4)$, $\Delta R(j_3, j_4)$, $\Delta\Phi(j_1, \ell^-)$, $\Delta\Phi(j_2, \ell^-)$, $\Delta\Phi(j_3, \ell^-)$, $\Delta\Phi(j_4, \ell^-)$, $\Delta\Phi(j_1, j_2)$, $\Delta\Phi(j_1, j_3)$, $\Delta\Phi(j_1, j_4)$, $\Delta\Phi(j_2, j_3)$, $\Delta\Phi(j_2, j_4)$, $\Delta\Phi(j_3, j_4)$

Table 2.6: Final state kinematic and angular distributions selected for the DL analysis for double production of the down-type VLQ. All observables are calculated in the laboratory frame. We define j_1 as the leading jet (greatest transverse momentum) and j_4 as the sub-leading light jet (lowest transverse momentum). E is the energy. Mass distributions are reconstructed from the observables inside parentheses, *e.g.*, $M(j_1, j_2) \equiv M(j_1^\mu + j_2^\mu)$, where j^μ are four-momentum vectors.

arbitrary function. This challenge must be addressed when identifying optimal solutions and finding superior designs for NNs.

The main goal of our NN model is to classify the signal channels defined in the previous sections over each respective background. This procedure is often referred to as classification. For optimal performance, it is essential to determine the appropriate architecture, including the number of layers, the number of neurons in each layer, and other hyperparameters. An appropriate choice of these parameters can lead to models capable of making highly accurate predictions, which, in the context of high energy physics, can potentially lead to significant discoveries using the available data. The problem of selecting the correct parameters is referred to as hyperparameter optimization. There are many methods to search for the best combinations of parameters, including a brute force approach that tests each possible combination until the optimal NN model is found. However, such a method is very time-consuming. A more efficient procedure involves using an evolutionary algorithm search [153, 154].

2.3.1 Pure kinematic data approach (VLL analysis)

For the analysis of the VLL events, our optimisation approach using the evolutionary algorithm focuses only in optimising a linear NN which takes as input tabular datasets containing the kinematic distributions. For this, we define the following set of hyperparameters for our analysis:

- Number of hidden layers: 1 to 5;
- Number of neurons in each layer: 256, 512, 1024, or 2048;
- Kernel initialiser: '`normal`', '`he normal`' or '`he uniform`';
- L2 regularization penalty: 10^{-3}, 10^{-5} or 10^{-7};
- Activation function: '`relu`', '`elu`', '`tanh`' or '`sigmoid`';
- Optimiser: '`adam`', '`sgd`', '`adamax`' or '`nadam`'.

Our evolutionary algorithm is initialised by building a set of ten NNs using `Keras` [172] and `TensorFlow` [173]. The hyperparameters are randomly chosen from the list above. Each NN is trained for 200 epochs, and once the training phase is complete, we select the top five NNs that have shown better performance to "breed" new NNs for the next iteration. These NNs are initialised with the hyperparameters of the selected ones and treated as "parent traits" while randomly including new ones as mutations. To control overfitting, we have set a 20% probability of a random mutation occurring. We then construct a new population set and repeat the training/evaluation process five times, across

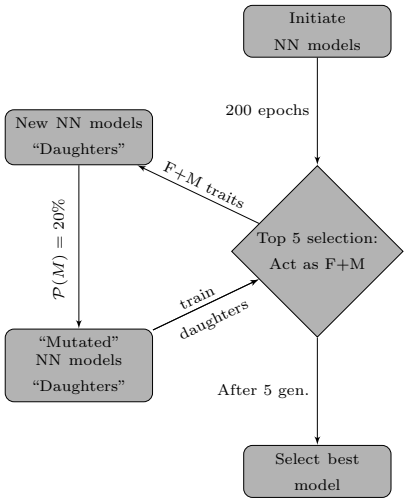

Figure 2.6: Flowchart representative of all iterative steps involved in the genetic algorithm that we employ in this work.

five generations, until finally retrieving the best NN architecture. A schematic representation of this algorithm is highlighted in Fig. 2.6

Another important aspect of the evolutionary algorithm is the fitness function, which helps the algorithm select the best architectures based on a predefined metric. In our case, we use two fitness functions: one where the best models are ranked according to their accuracy on the test set, and a second one that ranks the models according to their Asimov significance defined as [174]

$$\mathcal{Z}_A = \left[2 \left((s+b) \ln \left(\frac{(s+b)(b+\sigma_b^2)}{b^2 + (s+b)\sigma_b^2} \right) \odot \frac{b^2}{\sigma_b^2} \ln \left(1 + \frac{\sigma_b^2 s}{b(b+\sigma_b^2)} \right) \right) \right]^{1/2}, \tag{2.29}$$

with s and b being the number of signal and background events, respectively, and σ_b^2 being the variance of background events. We include a similar procedure to that described in [175] and incorporate the necessary modifications for the training methodology into our evolutionary algorithm. Although the main "body" of our NN is adjusted during training, some characteristics of the model construction are universal to all NN models. We summarise these as follows:

- As input data, the NN receives a standard normalised vector, *i.e.*, it has a mean of 0 and a standard deviation of 1. Data sets from all observables are extracted from the `ROOT` detector output. This data set is then reshuffled and divided into a training set (80% of the data) and a test set (20% of the data). To avoid overfitting, we use cross-validation with a five-fold scheme during the training of the NN.

- We employ a cyclic learning rate during the training phase with an initial value of 0.01 and a maximum value of 0.1.

- In the output layer, the data is transformed into a vector with entries between 0 and 1 (which correspond to probabilities) in the format (S, B_j), where S is the signal and B_j correspond to different backgrounds. The index j runs over the number of backgrounds chosen for a given signal. For example, in the ZA analysis, we consider 4 distinct backgrounds ($j = 4$). Thus, the output vector would be (S, B_1, B_2, B_3, B_4).

- Batch size of 32 768 entries.

- We impose a total limit of 200 epochs with a patience of 5 epochs and a validation loss monitor, *i.e.*, if the loss value on the test/validation set does not change for 5 epochs, the training is resumed and all metrics are computed and stored to be passed to the evolutionary algorithm.

- To select the NN models with better accuracy, we use the binary cross-entropy loss, while for selecting models that maximise the Asimov significance.

Another important aspect to note is that our data is unbalanced, meaning we have more data points for some classes we are analysing (in some cases, with a ratio of $s/b \approx 1.83$). This imbalance results from the event selection criteria imposed for the signal and background. Unbalanced data can lead to models with lower predictive power for significantly outnumbered classes. To address this, we use the Synthetic Minority Oversampling Technique [176] to create synthetic entries for the minority classes in our training dataset. It is important to note that we do not apply any re-sampling technique to the test dataset. This method is faster and more efficient than generating additional Monte Carlo events and processing them through subsequent hadronisation and detector effects.

2.3.2 Kinematic + image data approach (VLQ analysis)

For the analysis of the VLQ events, we use the combination of both image and tabular datasets. The network, which we refer to as Hybrid Net, will consider both data types in the classification of background and signal classes. The image datasets will be trained using a convolutional model, while the kinematic data will be trained through a linear sequential model. We then combine the predictions of both models.

Jet images, first introduced in Refs. [177, 178], are constructed by mapping particle hits in the detector onto a grid in the (η, ϕ) plane, where the intensity of each pixel is directly proportional to the energy deposited by the particles. These methods, however, can be quite inefficient because

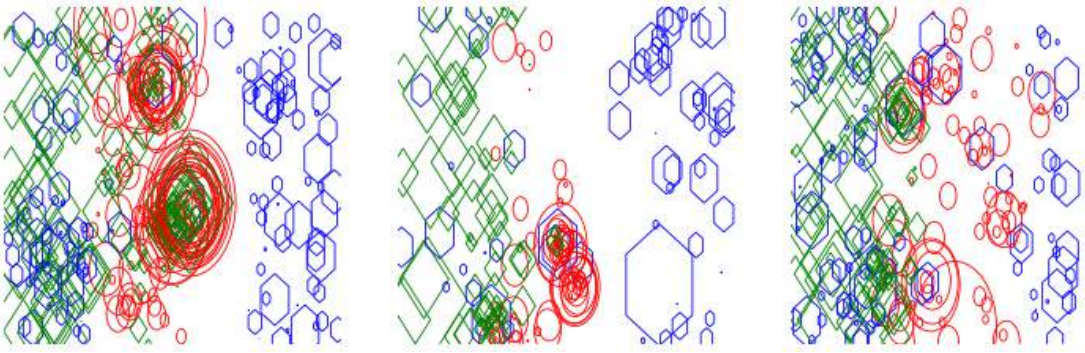

(a) Signal event (b) $t\bar{t}$ event (c) $WW+$ jets event

Figure 2.7: Example of an abstract jet image in the (η, ϕ) plane. Green polygons represent photons, red circles represent charged particles, and blue hexagons indicate neutral hadrons. The radius of the polygons is proportional to the energy deposited by the particle in the calorimeter tower. This image depicts an event from a proton-proton collision at $\sqrt{s} = 14$ TeV, with subsequent VLQ double production (to the left) and the corresponding background events ($t\bar{t}$ in the middle and $WW+$ jets on the right).

---

a typical jet image contains many blank pixels, making it computationally inefficient when passing through convolutional layers during the training phase. In this work we consider abstract jet images as first discussed in Ref. [154]. In this approach, besides associating each pixel with the energy of a particle, we also map characteristics of the particles into various geometrical shapes, *e.g.* if a particle is charged, we map it to a circle. In this scenario, the radius of the polygons is directly proportional to the particle energy. This method provides additional features for the neural model to learn. Examples of these types of images can be seen in Fig. 2.7.

To construct such images, we impose the following conditions:

- Charged particles hitting the detector are mapped into red circles, with a radius given by $r = \ln [p_T/\text{GeV}]$;
- Neutral hadrons are mapped into blue hexagons, with a radius given by $r = \ln [E_T/\text{GeV}]$, where E_T is the transverse energy;
- Photons are mapped into green diamonds, with the radius determined by the same formula as for neutral hadrons.

The resulting images are then stored in `.png` format, with a pixel size of 224×224. Both hadrons and photons are restricted to the kinematic ranges of $|\eta| \leq 5.0$ and $|\phi| \leq \pi$.

We utilise both image and tabular information. The images are processed through a convolutional network, while the corresponding kinematic information is handled by a linear model. We then combine the results by summing the predictions from both networks to obtain the final output. Hyperparameter optimization aimed at maximising statistical significance is performed using evolutionary algorithms, as described in previous section. In this thesis, linear networks are optimised as described in the previous section, while the convolutional network for images is fixed to a ResNet-34 architecture [179]. Here, both the linear and convolutional components constructed using `PyTorch` [180]. For the convolutional component, we also utilise `FastAI` [181], which uses `PyTorch` as its backend.

2.4 Results

2.4.1 Vector-like leptons

We commence by examining the results for VLLs. To frame our discussion, we introduce a specific BP, chosen based on the analysis detailed in Sec. 2.1.2. It is important to note that the analysis methodology remains unaffected by this choice of parameters. Subsequently, we examine events involving a light VLL (e_4) in conjunction with the lightest BSM neutrino (ν_4), which is treated as MET,

with the masses specified as

$$m_{e_4} = 677 \text{ GeV}\,, \quad m_{\nu_4} = 216 \text{ keV}\,. \tag{2.30}$$

The decay width is automatically calculated by `MadGraph` under the narrow width approximation. While the masses of heavier neutrinos are not crucial for the ZA and VLBSM events, they play a significant role in the VBF case, as these neutrinos appear as intermediate states. Thus, we set their masses as

$$\begin{aligned} &m_{\nu_5} = 0.138 \text{ GeV}\,, \quad m_{\nu_6} = 36.7 \text{ GeV}\,, \quad m_{\nu_7} = 2140 \text{ GeV}\,, \quad m_{\nu_8} = 2537 \text{ GeV}\,, \\ &m_{\nu_9} = 3035 \text{ GeV}\,, \quad m_{\nu_{10,11}} = m_{e_4}\,, \quad m_{\nu_{12,13}} = m_{e_5}\,, \quad m_{\nu_{14,15}} = m_{e_6}\,, \end{aligned} \tag{2.31}$$

with

$$m_{e_5} = 3258 \text{ GeV}\,, \quad m_{e_6} = 4240 \text{ GeV}\,. \tag{2.32}$$

The BSM couplings are primarily determined by the mixing matrices discussed in Sec. 2.1.2. For the VLLs, we use

$$\begin{aligned} U_L^{\text{VLL}} &= \begin{bmatrix} \odot 0.162 \odot 0.381i & \odot 0.683 \odot 0.321i & 0.318 + i0.379 \\ \odot 0.315 \odot 0.089i & \odot 0.341 + 0.225i & \odot 0.746 \odot 0.411i \\ 0.844 \odot 0.0970i & \odot 0.035 + 0.498i & \odot 0.105 \odot 0.134i \end{bmatrix}\,, \\ U_R^{\text{VLL}} &= \begin{bmatrix} \odot 0.186 \odot 0.490i & \odot 0.266 \odot 0.462i & \odot 0.654 + i0.113 \\ 0.389 \odot 0.153i & \odot 0.750 \odot 0.366i & 0.306 \odot 0.186i \\ 0.640 \odot 0.375i & 0.035 + 0.133i & \odot 0.497 \odot 0.429i \end{bmatrix}\,, \end{aligned} \tag{2.33}$$

and for the neutrinos, we adopt[6]

$$\begin{aligned} U_1 &= \begin{bmatrix} \odot 0.490 & \odot 0.408 & \odot 0.081 & \odot 0.192 & 0.568 & 0.476 \\ 0.491 & \odot 0.745 & 0.436 & \odot 0.063 & 0.014 & \odot 0.10 \\ 0.098 & \odot 0.109 & \odot 0.511 & \odot 0.337 & 0.385 & \odot 0.675 \\ \odot 0.445 & 0.003 & 0.455 & 0.511 & 0.278 & \odot 0.506 \\ \odot 0.553 & \odot 0.267 & 0.073 & \odot 0.434 & \odot 0.614 & \odot 0.227 \\ 0.068 & 0.443 & 0.574 & \odot 0.630 & 0.270 & \odot 0.029 \end{bmatrix}\,, \\ U_2 &= \begin{bmatrix} \odot 0.413 & 0.166 & 0.360 & \odot 0.313 & 0.270 & 0.708 \\ 0.304 & \odot 0.082 & 0.292 & \odot 0.630 & \odot 0.647 & 0.017 \\ \odot 0.053 & 0.842 & 0.374 & 0.062 & \odot 0.033 & \odot 0.379 \\ \odot 0.080 & 0.145 & \odot 0.040 & 0.597 & \odot 0.643 & 0.449 \\ \odot 0.837 & \odot 0.259 & 0.064 & \odot 0.062 & \odot 0.282 & \odot 0.380 \\ 0.163 & \odot 0.411 & 0.800 & 0.376 & 0.121 & \odot 0.095 \end{bmatrix}\,. \end{aligned} \tag{2.34}$$

It is important to emphasise that the numerical values provided above were randomly generated but comply with the theoretical requirements discussed in Sec. 2.1.2.

The cross sections for both signal and background events are estimated by `MadGraph` for our BP as

$$\begin{aligned} &\text{ZA:} \quad \sigma = 4.40 \times 10^{-4} \pm 2.62 \times 10^{-7} \text{ fb}\,, \\ &\text{VBF:} \quad \sigma = 8.96 \times 10^{-4} \pm 5.88 \times 10^{-7} \text{ fb}\,, \\ &\text{VLBSM:} \quad \sigma = 7.70 \times 10^{-2} \pm 4.33 \times 10^{-5} \text{ fb}\,, \\ &t\bar{t}: \quad \sigma = 6720.00 \pm 3.01 \text{ fb}\,, \\ &t\bar{t} + j: \quad \sigma = 7850.00 \pm 5.06 \text{ fb}\,, \\ &t\bar{t} + jj: \quad \sigma = 5990.00 \pm 3.70 \text{ fb}\,, \\ &t\bar{t} + \text{Z}^0(\ell^+\ell^-): \quad \sigma = 5.36 \times 10^{-1} \pm 3.81 \times 10^{-4} \text{ fb}\,, \\ &t\bar{t} + \text{Z}^0(\bar{\nu}_\ell \nu_\ell): \quad \sigma = 1.06 \pm 6.95 \times 10^{-4} \text{ fb}\,, \\ &W^+W^-: \quad \sigma = 839.00 \pm 0.55 \text{ fb}\,, \\ &pp \to \ell\nu_\ell: \quad \sigma = 10309100 \pm 5400 \text{ fb}\,, \\ &pp \to \ell\nu_\ell + j: \quad \sigma = 2943600 \pm 2100 \text{ fb}\,, \\ &pp \to \ell\nu_\ell + jj: \quad \sigma = 1233200 \pm 700 \text{ fb}\,, \end{aligned}$$

[6]The numerical values for D_1 are small, $\mathcal{O}(10^{-3} - 10^{-8})$, and are omitted for brevity. The dominant contributions arise from U_1 and U_2.

where the error corresponds an estimation of the statistical uncertainty. As can be observed, the

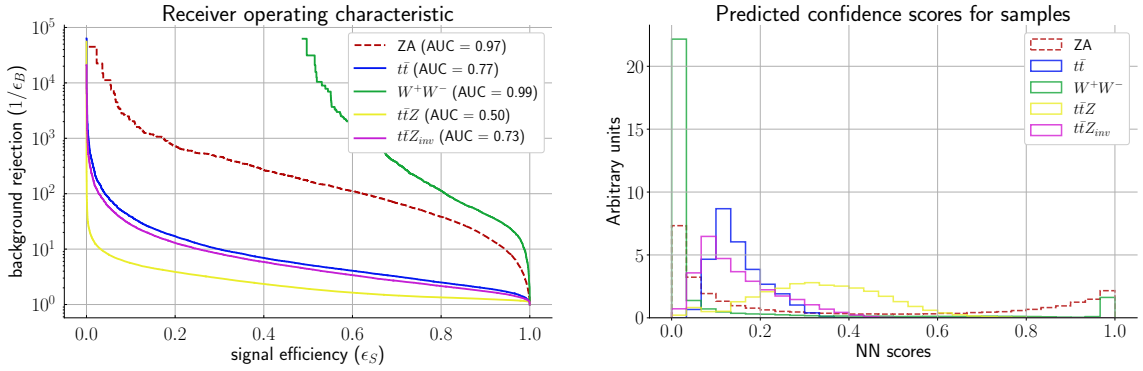

(a) ZA topology

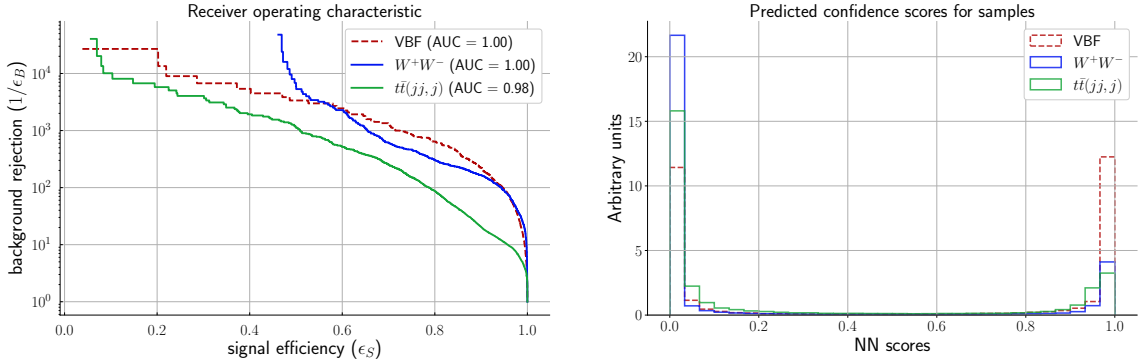

(b) VBF topology

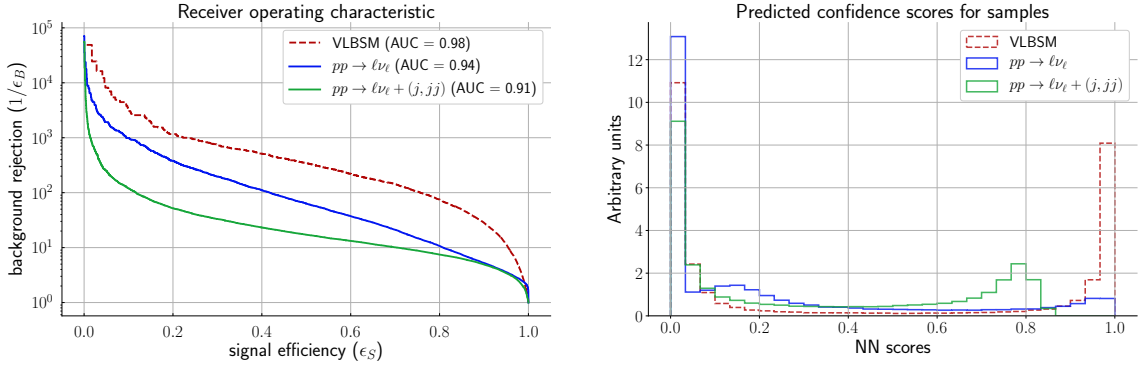

(c) VLBSM topology

Figure 2.8: ROC curves and predicted confidence scores for each signal, for a light VLL with mass $m_{e_4} = 677$ GeV and an integrated luminosity of $\mathcal{L} = 3000$ fb^{-1}. Signal events are depicted by red dashed curves. The AUC functions as a measure of classification accuracy. These distributions are derived from an implementation of an evolutionary algorithm designed to maximise the accuracy metric.

primary challenge lies in the overwhelming background from $t\bar{t}$ events, whose cross-section significantly surpasses those of the ZA and VBF channels. Additionally, the cross-section for $pp \to \ell\nu_\ell + (0, 1$ and $2)$ jets exceeds that of the VLBSM channel by at least eight orders of magnitude. Although each diagram in Fig. 2.3 carries a greater suppression factor due to the presence of more interaction vertices and internal propagators, it ultimately contributes more to the overall cross-section. In Fig. 2.2, for instance, e_4 is the sole intermediate state, resulting in fewer possible combinations. In contrast, Fig. 2.3 involves contributions from all BSM neutrinos to the ν'_{BSM} propagator, leading to a greater number of potential VBF processes. Moreover, two of the BSM neutrinos in ν'_{BSM} are

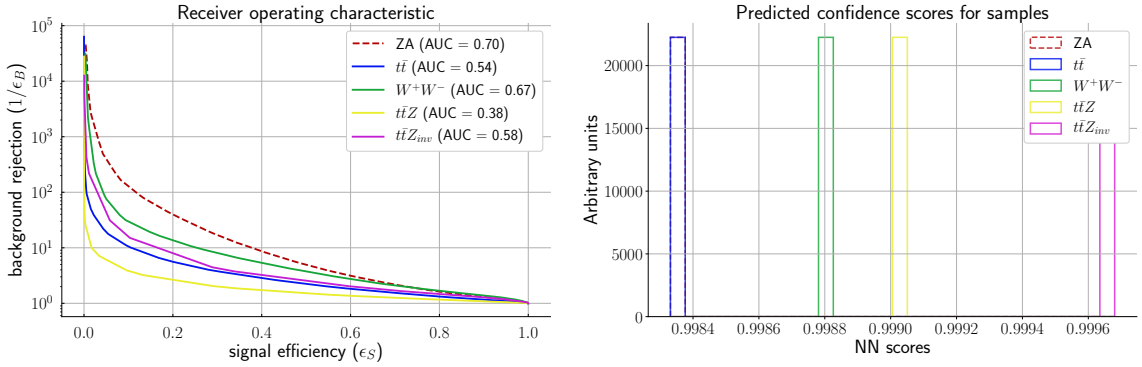

(a) ZA topology

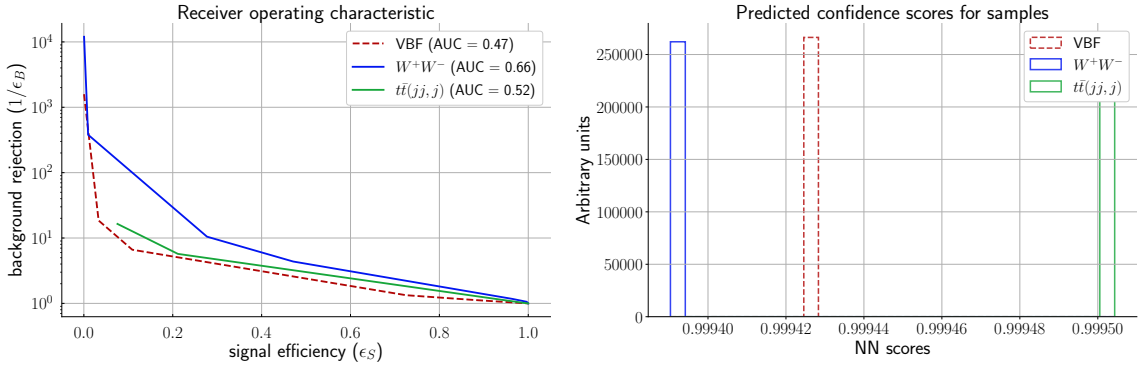

(b) VBF topology

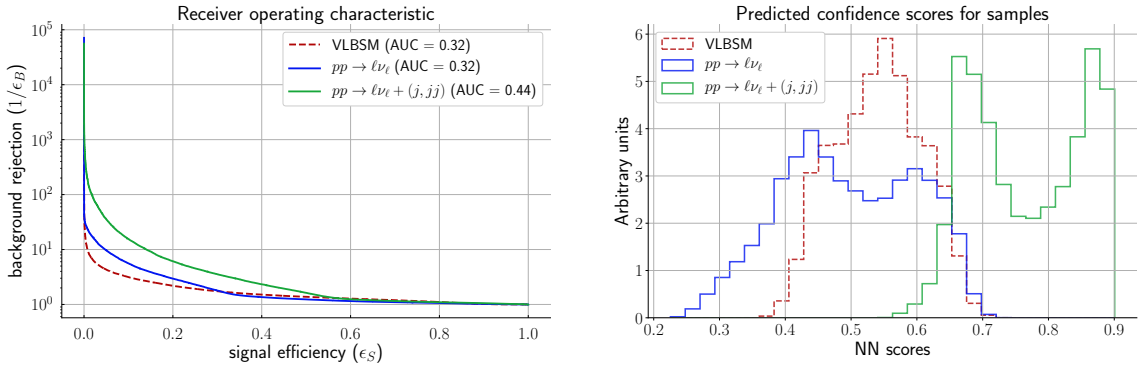

(c) VLBSM topology

Figure 2.9: The same as in Fig. 2.8 but now computed for an evolutive algorithm that maximises the Asimov significance.

---

relatively light, with masses around 100 keV (for ν_4) and 100 MeV (for ν_5), which independently provide enhancement factors of at least 6 and 3 orders of magnitude, respectively, compared to massive EW-scale (or higher) propagators.

We first start with the ZA/VBF signal and background topologies, whose distributions are shown in App. B, in particular Figs. B.2, B.3 and B.4. Here, we see that we can reconstruct the top, W, and e_4 masses within the expected range, provided there is a clear distinction between them. We observe a significant separation between signal events and background, particularly in the ΔR distributions. For the signal events, $\Delta R_{e^-\bar{\nu}_e}$ and $\Delta R_{\mu^+\nu_\mu}$ exhibit peaks near zero, which are well separated from the background events, indicating particle trajectories perpendicular to the beam axis, which helps distinguish them from some background channels like $t\bar{t}$ and W^+W^-. Although there are notable differences in some variables, others, especially angular variables like $\cos(\theta)$, are dominated by background. Similar observations are made for the VLBSM channel (see Fig. B.1). Here, pseudo-

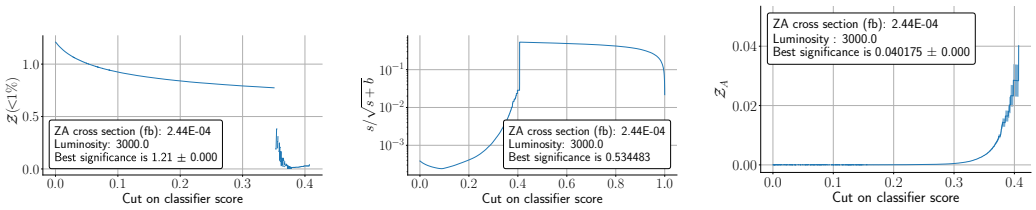

(a) ZA topology

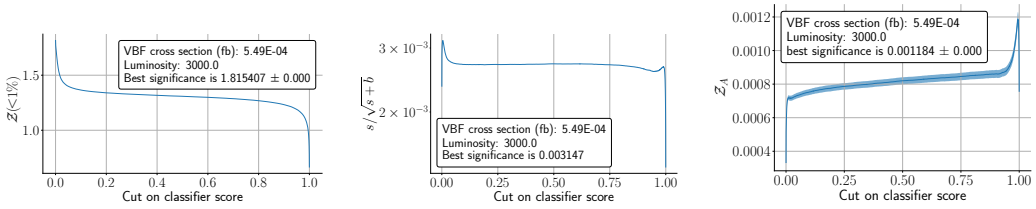

(b) VBF topology

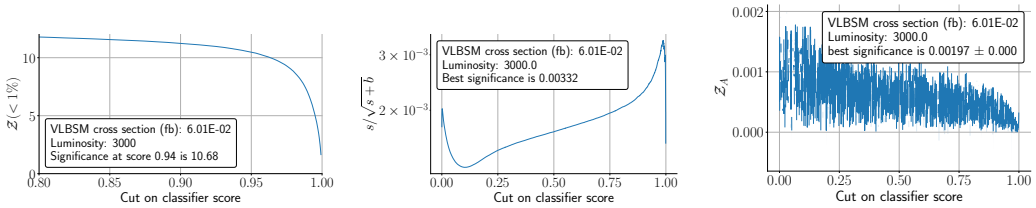

(c) VLBSM topology

Figure 2.10: Significance as a function of the NN scores for each signal topology for a light VLL with mass $m_{e_4} = 677$ GeV and an integrated luminosity of $\mathcal{L} = 3000$ fb^{-1}. For plots (a), (d) and (g) we showcase the adapted Asimov significance where backgrounds are known with an error of up to 1%, for (b), (e) and (h) the naive significance $s/\sqrt{s+b}$ and for (c), (f) and (i) the Asimov significance. Plots are computed following an implementation of an evolutive algorithm that maximises the accuracy metric.

---

rapidity distributions provide a good signal-to-background separation, whereas angular distributions are more affected by background interference. A key distinction between the VLBSM topology and the previous two lies in the number of features. Although the VLBSM signal, characterised by fewer internal propagators and only a single lepton in the final state, yields cross-sections larger than those of VBF and ZA events, it offers fewer distinct variables for analysis. Moreover, the VLBSM topology and its associated backgrounds do not permit a direct one-to-one correspondence with variables such as VLL invariant mass distributions, nor do they include the azimuthal and polar angles $\cos(\Delta\phi)$ and $\cos(\Delta\theta)$, which are absent in VLBSM events. The relevant distributions are shown in Fig. B.1.

In general, kinematic distributions such as transverse momentum and MET provide some degree of separation between signal and background events. Background events tend to accumulate at lower energies compared to signals. Specifically, transverse momentum distributions show an accumulation of events at $p_T < 200$ GeV, and MET is concentrated in the region MET < 200 GeV. In contrast, signal events accumulate in the high-energy region with $p_T/\text{MET} > 300$ GeV.

However, it is crucial to recognise that experimental information is typically limited to what are known as low-level observables. These observables usually involve counting the number of hits or events recorded by a detector. In contrast, a high-level approach integrates data from multiple detectors to create more complex and sophisticated observables, such as those explored in this thesis. Utilising a broad range of observables, including those in the W frame, will serve as an important step in the analysis. This approach enables the construction of a comprehensive dataset for DL studies, which facilitates faster training and improved overall accuracy, even when dealing with lower cross-sections.

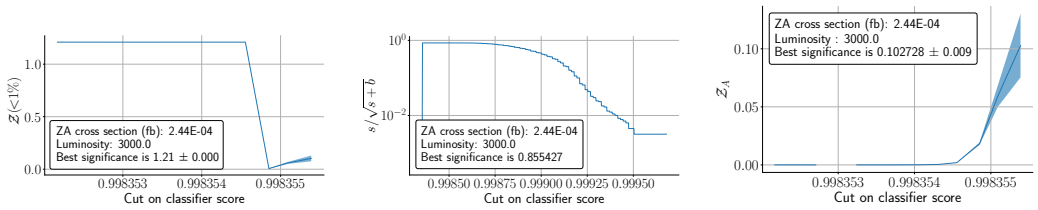

(a) ZA topology

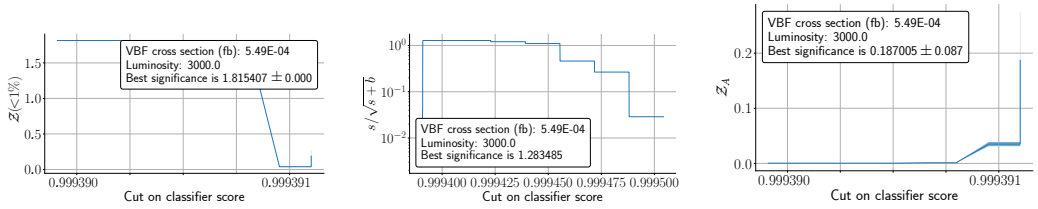

(b) VBF topology

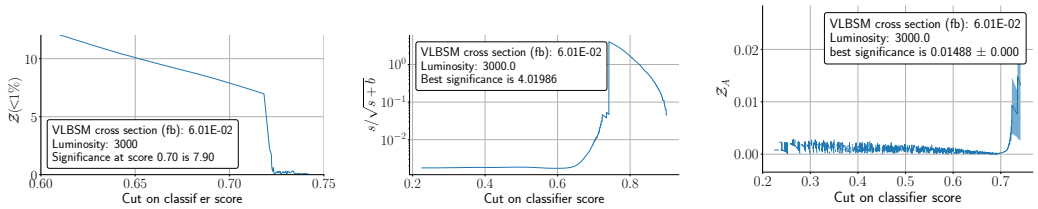

(c) VLBSM topology

Figure 2.11: The same as in Fig. 2.10 but for an evolutive algorithm that maximises the Asimov significance.

For the benchmark scenario discussed (see Eqs. (2.30)-(2.34)), the architecture that maximises Asimov significance for each topology is detailed in Tabs. D.1, D.2, and D.3. Conversely, the architecture that maximises accuracy for each topology is shown in Tabs. D.4, D.5, and D.6. To quantitatively evaluate our NN models, we use Receiver Operating Characteristic (ROC) curves, which measure the classification performance of the NN. Fig. 2.8 displays the results for the models with the best accuracy, while Fig. 2.9 shows the models with the highest Asimov significance. As observed, models that achieve better accuracy are capable of distinguishing signal events from background with nearly 100% efficiency. Specifically, the signal efficiencies are approximately $\varepsilon_S = 1$, with accuracy rates of 97% for ZA, 100% for VBF, and 98% for VLBSM channels. However, high significance does not always correlate with high accuracy. Indeed, for NN architectures that maximise Asimov significance, the accuracy is often significantly lower. A notable example is the VLBSM channel, which has the lowest accuracy with an Area Under the Curve (AUC) value of 0.32. The predicted confidence scores are illustrated in the right panels of Fig. 2.8. It is important to note that the NN assigns different scores to each prediction. For instance, in Fig. 2.8(a), a NN score of 1.0 could indicate either a signal event or a W^+W^- background event.

The significance of signal events is often considered by experimental physicists as the most crucial measure for claiming a discovery or excluding a NP candidate. To evaluate this, we compute the significance for all proposed channels, with results displayed in Figs. 2.10 and 2.11. In the former, we maximise the accuracy metric, while in the latter, the Asimov significance is maximised. For thoroughness, we evaluate significance using three distinct statistics:

1. First, we consider what we refer to as *naive significance*. This is computed by counting the number of background (b) and signal (s) events using the well-known formula $s/\sqrt{s+b}$.

2. The second metric is the *plain* Asimov significance, denoted as $\mathcal{Z}_A$, which is defined in Eq. (2.29). This measure is generally the most conservative in our analysis, assuming that the background

is known with a 1% uncertainty.

3. Finally, we consider the Asimov significance with background uncertainty much smaller than 1%, referred to as $\mathcal{Z}(< 1\%)$. In our studies, we use a background uncertainty of 10^{-3} %. This measure typically provides the most favourable results but requires that all physics backgrounds are well-controlled by the experiment. We anticipate that such precision will become feasible for the ATLAS and CMS collaborations as they accumulate more data and experience. Note that in the limit of vanishing background uncertainty, this measure approaches the naive significance formula.

We then analyse these three significance measures in the context of NN scores, focusing on the High-Luminosity LHC (HL-LHC) scenario with $\mathcal{L} = 3000$ fb^{-1}. From the results, we observe a general trend across all channels: $\mathcal{Z}(< 1\%) > s/\sqrt{s+b} > \mathcal{Z}_A$. For the VLBSM channel, it is important to note that we did not select the highest significance identified by our algorithm. This is because there are regions in the NN parameter space where only signal events are present. For instance, in Fig. 2.10(g), we see that NN scores around 0.80 correspond to a significance exceeding 10σ. However, for a more realistic assessment, we require the NN to account for both signal and background events. This is not an issue for the ZA and VBF channels, where the highest significance is found in regions where both signal and background events are consistently present.

Under the assumption that all signal topologies represent independent events, the combined significance can be defined as the sum of the individual significances

$$\sigma_C = \sigma_{\text{ZA}} + \sigma_{\text{VBF}} + \sigma_{\text{VLBSM}} \,. \tag{2.35}$$

From the results in Fig. 2.10, when prioritising an evolutionary algorithm designed to maximise accuracy, we obtain

- $\mathcal{Z}(< 1\%)$: $\sigma_C = 13.71\sigma$,
- $s/\sqrt{s+b}$: $\sigma_C = 0.55\sigma$,
- $\mathcal{Z}_A$: $\sigma_C = 0.04\sigma$.

Conversely, if we focus on maximising the Asimov significance, the results shown in Fig. 2.11 yield:

- $\mathcal{Z}(< 1\%)$: $\sigma_C = 10.93\sigma$,
- $s/\sqrt{s+b}$: $\sigma_C = 6.16\sigma$,
- $\mathcal{Z}_A$: $\sigma_C = 0.33\sigma$.

In both cases, the combined significance from the $\mathcal{Z}(< 1\%)$ measure surpasses the 5σ threshold. However, this metric assumes that all backgrounds are extremely well controlled. Notably, we obtain $s/\sqrt{s+b} = 6.16\sigma$, which strengthens the case for probing VLLs with masses around 700 GeV potentially before the end of the HL-LHC runs. Furthermore, an evolutionary algorithm aimed at maximising the Asimov significance provides overall better results. It is important to note that the combined (or even individual) significance increases with luminosity, highlighting the advantage of high-luminosity experiments in the long term.

The results for a single point are already quite promising. To enhance our analysis, we will investigate how varying the mass of the lightest two VLLs and the lightest BSM neutrino affects the

Mass of e_4	$s/\sqrt{s+b}$			$\mathcal{Z}(< 1\%)$			$\mathcal{Z}_A$		
	ZA	VBF	VLBSM	ZA	VBF	VLBSM	ZA	VBF	VLBSM
200 GeV	4.01	9.4×10^{-3}	0.31	12.18	2.83	12.95	2.05	2.47×10^{-3}	1.41
486 GeV	0.95	1.51	6.66×10^{-3}	2.59	2.13	7.83	0.12	4.6×10^{-4}	2.15×10^{-4}
677 GeV	0.53	3.15×10^{-3}	3.32×10^{-3}	1.21	1.82	10.68	0.040	1.18×10^{-3}	1.97×10^{-3}
868 GeV	0.26	0.93	6.18×10^{-4}	0.52	1.32	6.60	0.01	0.30	2.47×10^{-4}
1250 GeV	0.05	4.37×10^{-4}	1.20×10^{-4}	0.17	0.59	4.90	4.28×10^{-4}	2.05×10^{-4}	2.65×10^{-3}

Table 2.7: Signal significance for an evolutive algorithm that maximises accuracy metric. All significances are computed for $\mathcal{L} = 3000$ fb^{-1}.

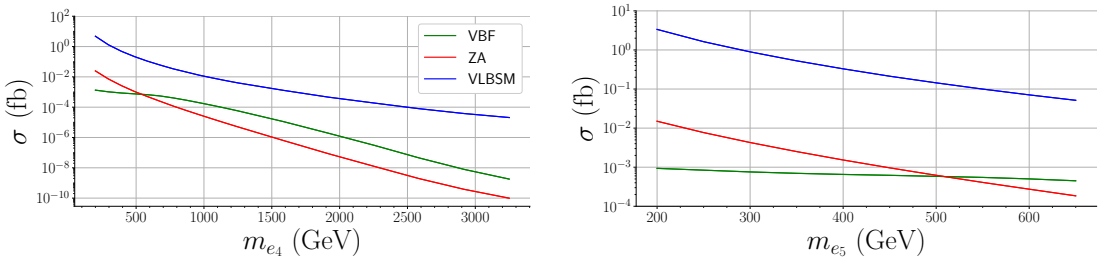

Figure 2.12: Total production and decay cross section (in femtobarn) as a function of e_4 (left) and e_5 masses (right). While on the left panel $m_{e_5} = 3.2$ TeV, on the right one we have $m_{e_4} = 200$ GeV.

significance. Specifically, we are interested in determining under what conditions we can achieve or exceed a 5σ significance to justify direct VLL searches at the LHC. We will repeat the numerical procedure with the following variations:

1. Varying the mass of the lightest VLL, m_{e_4}, between 200 GeV and 1.25 TeV while keeping m_{ν_4} fixed as in Eq. (2.30).
2. Keeping m_{e_4} fixed as in Eq. (2.30) and varying m_{ν_4} between 100 keV and 100 MeV.
3. Varying the masses of the two lightest VLLs such that $m_{e_4} < m_{e_5}$.
4. The same as in the first case, but with varying luminosity.

For a fixed luminosity of $\mathcal{L} = 3000$ fb^{-1} we study the signal significance calculated for the VLL masses $m_{e_4} = 200, 486, 868$ and 1250 GeV. First, we consider an evolutive algorithm that maximises the accuracy metric showing our results in Tab. 2.7. We have repeated the same procedure for $m_{e_4} = 200$ and 486 GeV considering an evolutive algorithm that maximises the Asimov significance. Our results can be found in Tab. 2.8.

From the aforementioned tables, we observe that for heavy VLL scenarios with $m_{e_4} = 1.25$ TeV, the combined significance for all event signals drops to values near zero, indicating that such channels can be particularly challenging for direct searches at the LHC. However, if the background is well under control, the $\mathcal{Z}(< 1\%)$ statistic provides a combined significance of 5.66σ. Notably, the largest contribution to this combined significance comes from the VLBSM channel, which accounts for 4.9σ. This suggests that detecting heavy VLLs with masses in the TeV range is feasible only if the $pp \to \ell\nu_\ell + (0j, j, jj)$ backgrounds are known with high precision. The rapid decrease in significance for larger masses is attributed to the equally rapid decrease in cross-section with increasing mass, as depicted in Fig. 2.12, left panel. A small significance is also obtained for the heavier VLLs, e_5 and e_6, whose masses lie beyond $\mathcal{O}(3$ TeV) and out of the reach of the HL-LHC.

However, recall that all three signal events represent independent variables, meaning that we can evaluate a global significance as the sum of the individual significances from each process. This implies that incorporating additional event signals could enhance this global significance. In particular, channels involving jets from W decays to quarks are relevant due to the larger expected number of events. The W decay width to light jets has a BR of approximately 67.4%, compared to 10.86% for leptons [155]. For the case where the accuracy metric is maximised, the combined significance for $m_{e_4} = 200$ GeV is: $\mathcal{Z}(< 1\%)$: 27.16σ, $\mathcal{Z}_A$: 3.46σ, and naive significance: 4.33σ. When maximising the Asimov metric, the combined significance for the same BP ($m_{e_4} = 200$ GeV) is: $\mathcal{Z}(< 1\%)$: 27.71σ,

Mass of e_4	$s/\sqrt{s+b}$			$\mathcal{Z}(< 1\%)$			$\mathcal{Z}_A$		
	ZA	VBF	VLBSM	ZA	VBF	VLBSM	ZA	VBF	VLBSM
200 GeV	6.10	2.00	12.65	12.18	2.83	12.70	4.44	0.145	4.28
486 GeV	1.77	1.50	11.26	2.60	2.13	8.62	0.30	0.53	0.20
677 GeV	0.86	1.28	4.02	1.21	1.82	7.90	0.11	0.187	0.015

Table 2.8: Signal significance for an evolutive algorithm that maximises Asimov significance metric. All significances are computed for $\mathcal{L} = 3000$ fb^{-1}.

	$m_{e_4} = 200$ GeV $m_{e_5} = 200$ GeV	$m_{e_4} = 200$ GeV $m_{e_5} = 250$ GeV	$m_{e_4} = 200$ GeV $m_{e_5} = 300$ GeV
$e_5 \to W\nu_4$	0.5082513	0.5069336	0.5063337
$e_5 \to W\nu_5$	0.3111182	0.3119451	0.3123246
$e_5 \to W\nu_6$	0.1806305	0.1811213	0.1813417

Table 2.9: BRs of e_5 decaying into W and BSM neutrinos for three different e_5 masses and fixed $m_{e_4} = 200$ GeV

$\mathcal{Z}_A$: 8.57σ, and naive significance: 20.75σ. These results, particularly for the naive significance, indicate that a light VLL characteristic of our model is expected to be significantly detectable during high-luminosity runs at the LHC and can be probed well before the end of the LHC program.

In general, we observe that as the mass of e_4 increases, the overall significance decreases, as discussed previously. This decrease is more rapid for the ZA channel compared to the VBF and VLBSM channels. Specifically, for VBF signals, the maximum significance in $\mathcal{Z}(< 1\%)$ is 2.83σ for $m_{e_4} = 200$ GeV, and this value is consistent across both the Asimov and accuracy metrics. Conversely, for ZA and VLBSM channels with maximised accuracy, a VLL mass of 200 GeV yields a significance of 12.18σ for ZA events and 12.95σ for VLBSM events (see Tab. 2.7). When optimising for the Asimov metric, the naive significance can reach up to 6.10σ for ZA events and 12.65σ for VLBSM events (see Tab. 2.8).

For completeness, we present the results in Fig. 2.13, which demonstrate that fixing $m_{e_4} = 200$ GeV and varying the mass of the sterile neutrino m_{ν_4}, where $m_{\nu_4} < m_{\nu_5}$, yields negligible effects on the significance. This holds for values of m_{ν_4} within the range of 100 keV to 100 MeV. Although our analysis is quite general, the specific mass scales for ν_4 are particularly relevant given the seesaw mechanism for neutrino masses and the radiative origin of Yukawa interactions in the low-scale SHUT model.

Given that lighter VLLs are more promising for future investigations at the LHC, we will focus on the mass range $[200, 700]$ GeV for both e_4 and e_5, ensuring that $m_{e_4} < m_{e_5}$. This range is motivated by our discussion in Sec. 2.1.2 just below Eq. (2.16), where it was indicated that having two light VLLs below 1 TeV along with a heavier one around 5 TeV is a viable scenario. We will first set the mass of e_4 to 200 GeV, as this configuration yields the highest significance, according to Tabs. 2.7 and 2.8. Additionally, we will consider the BSM neutrino to be fixed to mass in Eq. (2.30). The results of these scans are illustrated in Fig. 2.14, which displays the significance contours for e_4 as a function of m_{e_4} and m_{e_5}. One can immediately see that varying the mass of e_5 has a very marginal impact

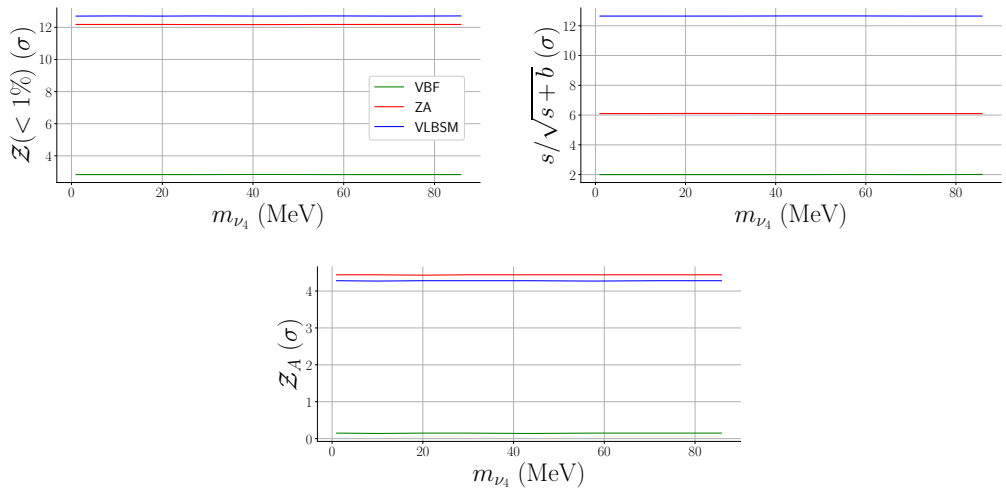

Figure 2.13: Significance as a function of the neutrino's mass for a luminosity of $\mathcal{L} = 3000$ fb^{-1}, for a fixed VLL mass $m_{e_4} = 200$ GeV. The significance is computed following an evolutive algorithm that maximises the Asimov metric.

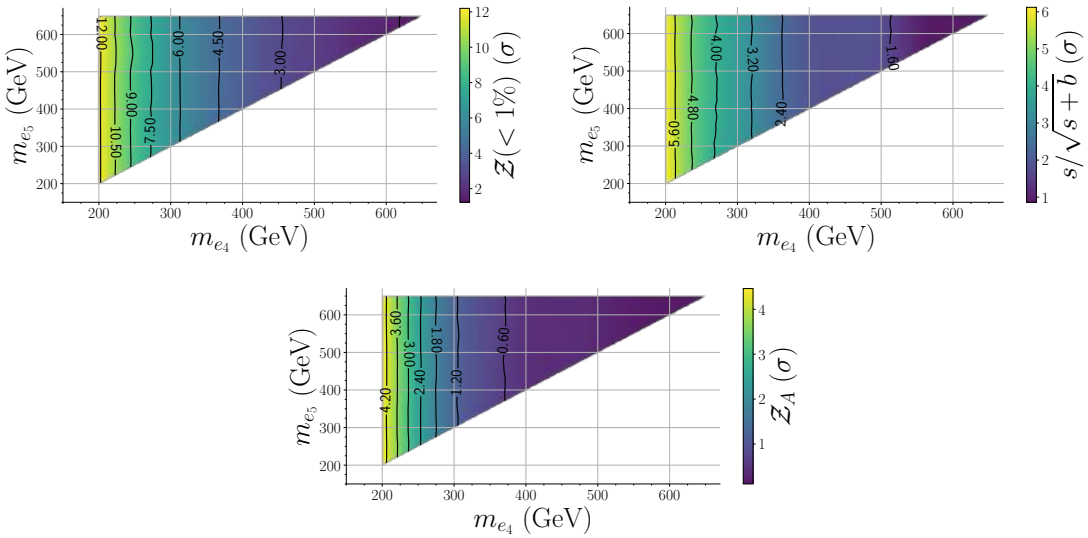

Figure 2.14: Significance contour plots for (a) $\mathcal{Z}(< 1\%)$, (b) $s/\sqrt{s+b}$ and (c) $\mathcal{Z}_A$ for a e_4 ZA signal at a luminosity of $\mathcal{L} = 3000$ fb^{-1}. The significance is computed with an evolutive algorithm that maximises the Asimov metric.

---

on the significance of e_4, indicating that it is largely independent of m_{e_5}. This observation can be understood from the $e_5 \to W\nu_i$ decay BR shown in Tab. 2.9.

In fact, we observe that the overall BRs do not suffer significant alterations with the varying e_5 mass, and as such, the computed e_4 production and decay cross-section remains very much the same.

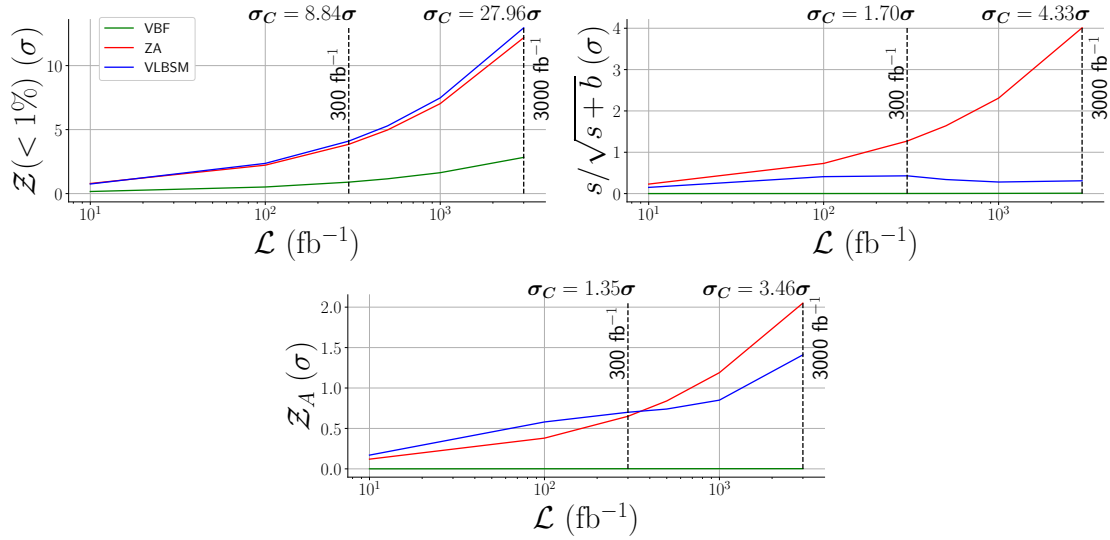

Figure 2.15: Significance as a function of luminosity for different statistics and topologies, resulting from an evolutive algorithm that maximises accuracy. The lightest VLL has a mass of 200 GeV, while the second lightest has a mass of 3.2 TeV. The x-axis is in logarithmic scale for all plots. Green curves represent VBF signal events, red curves correspond to ZA signals, and blue curves illustrate VLBSM topologies. The top plot depicts the Asimov significance with backgrounds exactly known and a systematic uncertainty of 1%. The middle plot shows the naive significance ($\sigma = s/\sqrt{s+b}$), and the bottom plot represents the Asimov significance with backgrounds not exactly known. The combined significance for $\mathcal{L} = 300$ fb^{-1} and $\mathcal{L} = 3000$ fb^{-1} is defined as $\sigma_C = \sigma_{\text{VBF}} + \sigma_{\text{ZA}} + \sigma_{\text{VLBSM}}$.

Therefore we do not expect visible changes in the significance.

Until now, all results have been calculated for a luminosity of $\mathcal{L} = 3000$ fb^{-1}. However, the LHC is expected to achieve such luminosities between 2026 and 2030 [182]. Thus, it is also important to investigate how the significance varies at lower luminosities, specifically for 300 fb^{-1}, which is targeted for delivery during Run III, which is currently on-going. Accordingly, we present in Figs. 2.15 and 2.16 how the significance depends on the projected luminosities when accuracy is maximised. Results for the scenario where the Asimov significance is maximised are depicted in Figs. 2.17, 2.18, and 2.19.

Examining Figs. 2.15 and 2.16, we observe that for $\mathcal{L} = 300$ fb^{-1}, achieving a signal significance at or above the 5σ level is feasible only for a light VLL with a mass of 200 GeV. Specifically, the combined significance reaches 8.84σ for $\mathcal{Z}(< 1\%)$. This indicates that if the backgrounds described in Sec. 2.2.1 are known with high precision, it may be possible to exclude a VLL with a mass of 200 GeV, potentially even before the conclusion of Run III.

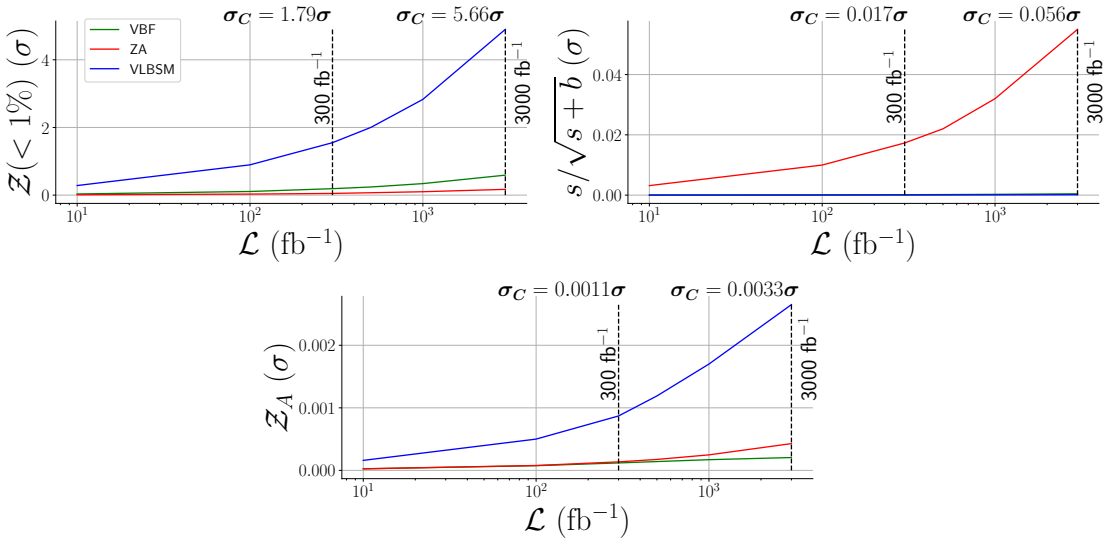

Figure 2.16: The same as in Fig. 2.15 but for a lightest VLL mass $m = 1250$ GeV.

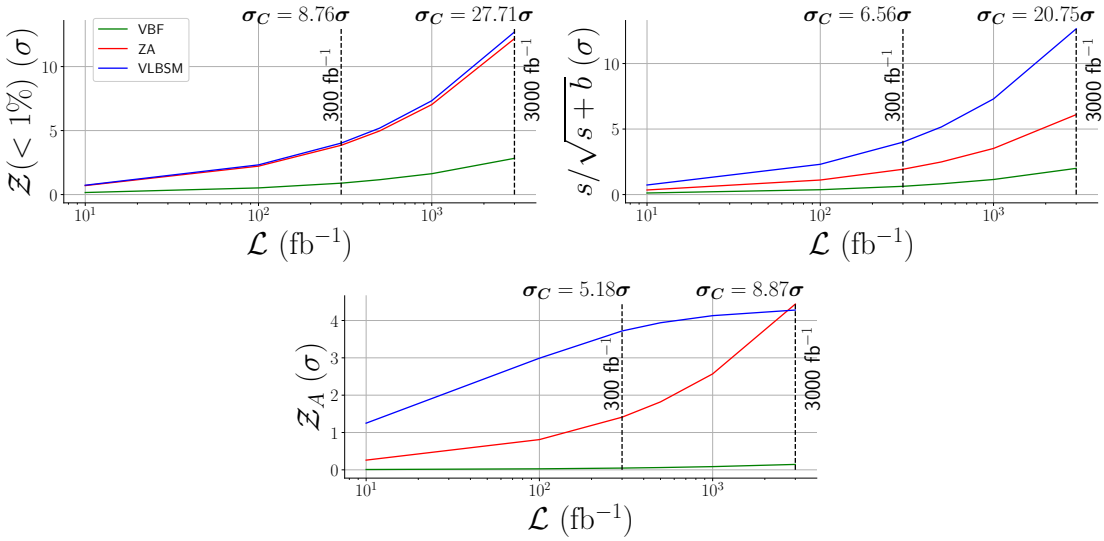

Figure 2.17: The same as in Fig. 2.15 but for an evolutive algorithm that maximises the Asimov significance.

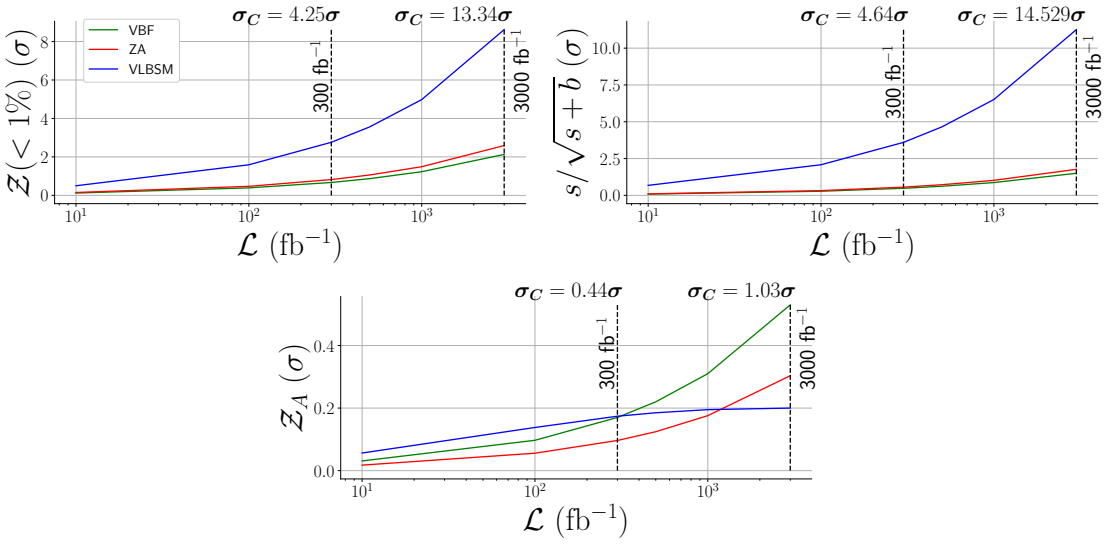

Figure 2.18: The same as in Fig. 2.17 but for a lightest VLL mass $m = 486$ GeV.

For heavy VLLs, the $\mathcal{Z}(< 1\%)$ significance does not exceed 1.78σ for $m_{e_4} = 1.25$ TeV, with VLBSM signals contributing the most. Given these results, observing such heavy states would require a high-luminosity run. Since we are simulating proton-proton collisions at $\sqrt{s} = 14$ TeV, the likelihood of VLL pair production decreases significantly with increasing mass, meaning these heavy states are expected to become visible only in high-luminosity runs or at higher-energy colliders.

These results underscore that lighter states are more favourable for probing during Run III of the LHC. This is particularly evident when using an evolutive algorithm that maximises the Asimov significance. In Figs. 2.17, 2.18, and 2.19, we observe significances well above 5σ for a VLL of 200 GeV at $\mathcal{L} = 300$ fb^{-1} across all three statistics. Therefore, a 200 GeV VLL characteristic of our model can be probed during the LHC Run III. For a VLL with a mass of 486 GeV, we achieve significances of 4.25σ for $\mathcal{Z}(< 1\%)$ and 4.64σ for $s/\sqrt{s+b}$. While these do not meet the 5σ threshold, they still indicate significant deviations from pure SM processes. The addition of new signals, such as those involving jets, is expected to provide the necessary boost to reach 5σ. Similar reasoning applies to a

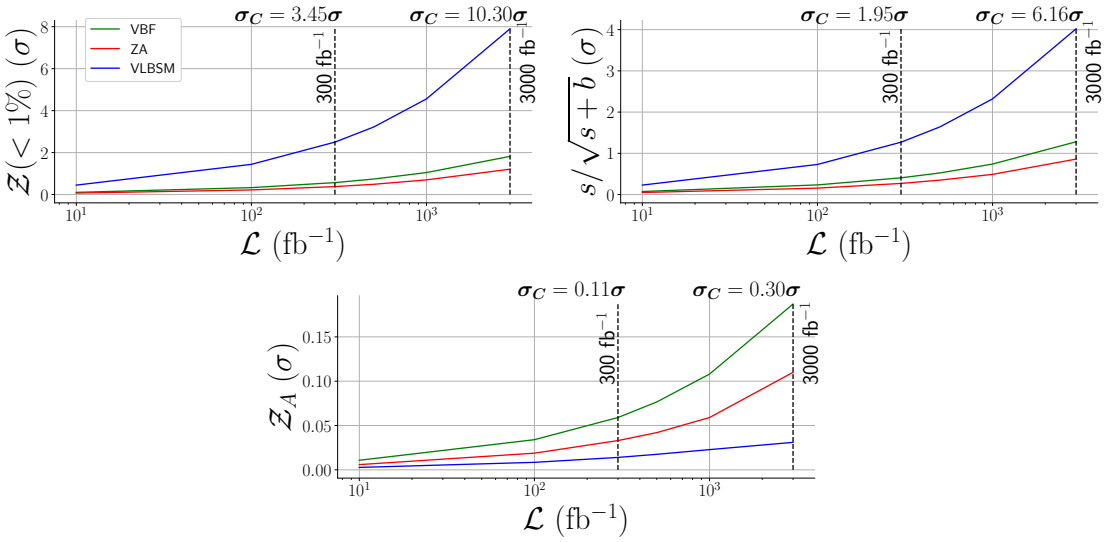

Figure 2.19: The same as in Fig. 2.17 but for a lightest VLL mass $m = 677$ GeV.

VLL with a mass of 677 GeV, where we find a combined significance of 3.45σ.

2.4.2 Vector-like quarks

Next, we turn our attention to the VLQs. Similarly to our approach with the VLLs, we begin by presenting the results for a specific, fixed VLQ mass. For the lightest D-type VLQ with a mass of 800 GeV, we apply the selection criteria outlined earlier. Tab. 2.10 provides the LO cross-sections for the signal, alongside the corresponding higher-order rates for the backgrounds. It also indicates the total expected number of events for both Run III and HL-LHC. The variation in the post-selection cross-section as a function of VLQ mass is depicted in Fig. 2.20, where dashed lines represent the projected sensitivity for future LHC runs. Specifically, for the benchmark values of VLQ-light quark mixing elements specified in Eq. (2.27), the Run III phase of the LHC could potentially probe D-type VLQs up to 1.9 TeV, while HL-LHC might exclude VLQs up to 2.37 TeV. These approximate limits are derived under the assumption of negligible experimental errors and should be considered as a guideline for the mass scale at which VLQs might be detected. In cases where only a single event is observed, background systematics could entirely obscure the signal.

To assess the network's performance, Fig. 2.21 presents the ROC curves for three distinct scenarios: classification using only kinematic data (top panel), classification using only jet images (middle panel), and classification incorporating both (bottom panel). The AUC is noted within the labels of the curves. It is evident that the combination of jet images and kinematic data yields the highest discriminating power and accuracy, confirming the enhanced performance of the hybrid network. Indeed, our results show that the kinematic data alone performs the worst, while classification using jet images alone provides the best results. The high accuracy indicates an effective separation between signal and background classes. This conclusion is further supported by the predicted confidence scores shown on the left side of Fig. 2.21, where the model successfully distinguishes signal classes (predominantly yielding scores around one in the convolutional NN) from background classes (predominantly yielding scores around zero). Although the separation is not flawless, with some overlap between background and signal remains in certain regions of the convolutional NN parameter space, the hybrid network's scores, which combine both kinematic and image data, will be used for all subsequent data analyses.

The histograms of the kinematic and angular observables utilised by the NN are presented in App. C. It can be observed that the angular distributions for the signal are generally overshadowed by the backgrounds, with the signal closely mirroring the background patterns, except for the pseudo-rapidity distributions. Notably, the signal exhibits a prominent peak at $\eta \sim 0$, while the backgrounds are more broadly distributed across the entire allowed range, $|\eta| \leq 2.5$. In contrast, the kinematic variables provide the most significant discriminating power, with distributions peaking in regions where SM backgrounds are less prevalent. This is consistently seen across all transverse momentum, energy, and MET distributions. Similarly, the mass distributions peak in higher invariant mass regions compared to those of the SM backgrounds.

Each individual event corresponds to specific values of the physical observables, which are transferred into the tabular data, with each event also having an associated jet image. A combination of both is utilised in the classification process, after which the statistical significance is computed using the validation dataset. For the VLQ analysis, we will now only present the results based on the Asimov estimate, as previously defined in Eq. (2.29). This metric is evaluated under three scenarios: with systematic uncertainties of $\sigma_b = 15\%$, $\sigma_b = 25\%$, and a more conservative scenario of $\sigma_b = 50\%$. The first two scenarios represent the most realistic conditions.

	σ (before cuts, in fb)	σ (after cuts, in fb)	Events at run-III	Events at HL-LHC
VLQ 800 GeV	1.402	1.063	318	3189
WW + jets	1.24×10^5	7.72×10^3	2.316×10^6	2.316×10^7
W + jets	7.95×10^8	3.46×10^5	1.038×10^8	1.038×10^9
Z^0 + jets	6.33×10^7	5.70×10^3	1.71×10^6	1.71×10^7
$t\bar{t}$	9.89×10^5	1.83×10^5	5.49×10^7	5.49×10^8

Table 2.10: Predicted total cross section (in fb) for both the signal and each respective background, before and after the cut selection. In the last two columns we indicate the overall number of expected events for the analysis, calculated as $N = \sigma\mathcal{L}$, for run-III and the HL phase of the LHC.

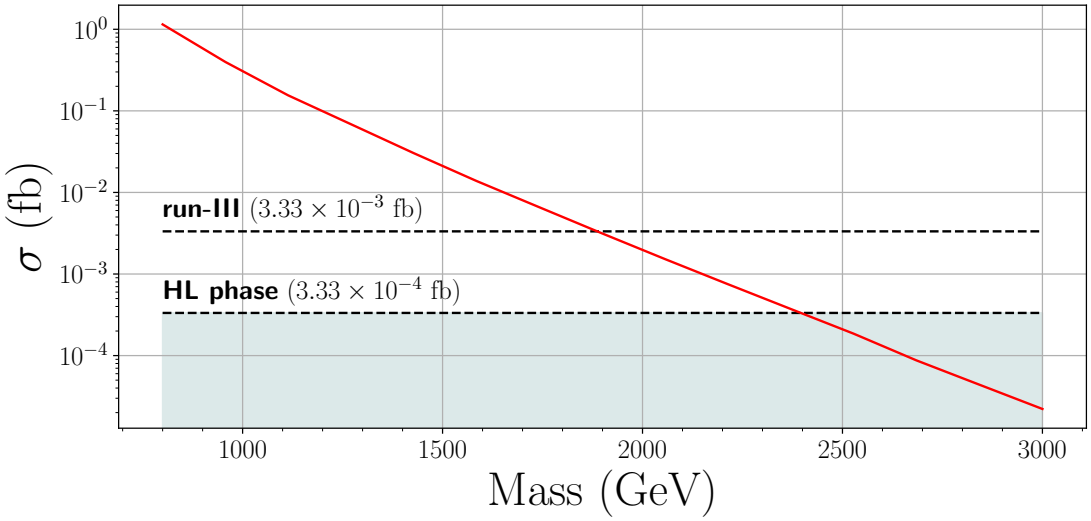

Figure 2.20: The production cross-section (in femtobarn) as a function of the VLQ mass (in GeV). Two horizontal dashed lines are shown, one for the run-III target luminosity and the other for HL-LHC, which represent the minimal cross section for which a single event can be produced, *i.e.* $N_{\text{exp}} = \sigma\mathcal{L} = 1$ for the dashed lines. The area filled in grey represents the region where neither the HL-LHC or run-III LHC have the required sensitivity to detect the D-VLQ for the chosen benchmark (2.27). The y-axis is shown in logarithmic scale.

Considering the HL phase of the LHC, which is expected to achieve an integrated luminosity of $\mathcal{L} = 3000$ fb^{-1}, we can determine the median significance for the considered metrics as a function of the NN score, as illustrated in Fig. 2.22. The maximal significances for each metric are found to be:

- $\mathcal{Z}_A(\sigma_b = 15\%) = 16.89\sigma$,
- $\mathcal{Z}_A(\sigma_b = 25\%) = 10.33\sigma$,
- $\mathcal{Z}_A(\sigma_b = 50\%) = 5.21\sigma$,

indicating that significances greater than 5σ are achieved for all levels of systematic uncertainty, even in the most conservative case of 50%. Such a strong signal for VLQs at HL-LHC is anticipated, as VLQs are coloured particles, and their production is enhanced at hadron colliders. It is also important to analyse the impact at other luminosities, particularly for the Run-III phase of the LHC, which is expected to deliver $\mathcal{L} = 300$ fb^{-1} of data. In Fig. 2.23, we plot the statistical significance as a function of the luminosity from different values of the systematic errors. The maximal significances obtained for the Run-III luminosity are as follows:

- $\mathcal{Z}_A(\sigma_b = 15\%) = 13.76\sigma$,
- $\mathcal{Z}_A(\sigma_b = 25\%) = 9.45\sigma$,
- $\mathcal{Z}_A(\sigma_b = 50\%) = 5.08\sigma$,

These results indicate that the significance remains above 5σ for all considered systematic uncertainties, suggesting that VLQ production can also be probed during Run-III.

It is also pertinent to analyse the impact at other luminosities, particularly for Run-III of the LHC, which is expected to deliver $\mathcal{L} = 300$ fb^{-1} of data. In Fig. 2.23, we plot the statistical significance as a function of the systematic errors. The maximal significances obtained for the Run-III luminosity are as follows:

- $\mathcal{Z}_A(\sigma_b = 15\%) = 13.76\sigma$,
- $\mathcal{Z}_A(\sigma_b = 25\%) = 9.45\sigma$,

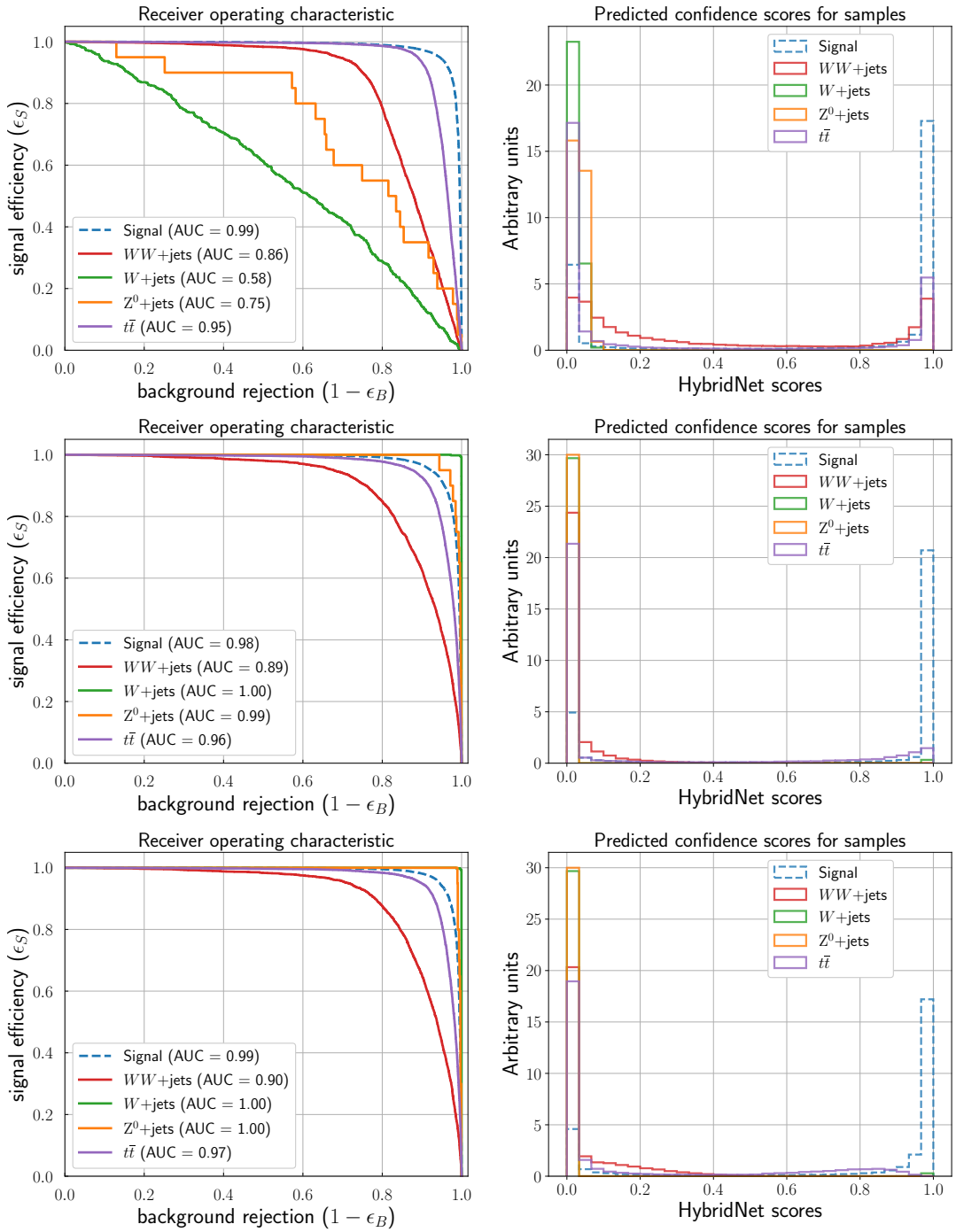

Figure 2.21: Performance results for the Hybrid network. On each panel, we plot the ROC on the left-hand side and, on the right, – the predicted confidence score for our samples. In the top panel, the results are shown for classification with only kinematic data, in the middle panel we have the results only for classification with the jet images, and at the bottom, the results when both data types were part of the training. The signal is indicated with a dashed blue line, while the WW+jets background – in red, the W+jets – in green, Z^0+jets – in orange and $t\bar{t}$ – in purple.

- $\mathcal{Z}_A(\sigma_b = 50\%) = 5.08\sigma$,

These results show that the significance remains above 5σ for all considered systematic uncertainties,

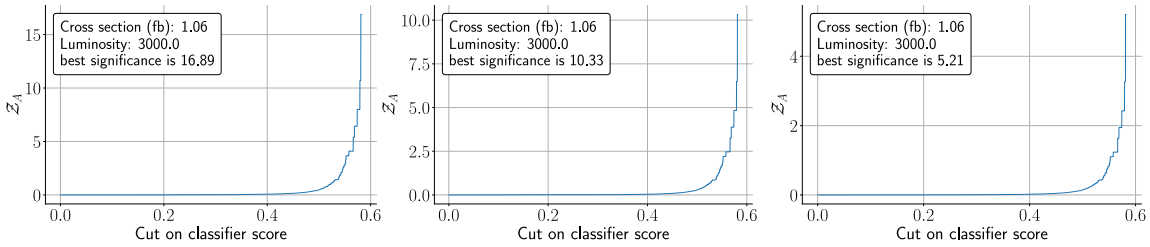

Figure 2.22: The statistical significance for a hypothetical discovery of VLQs as a function of the NN score for different values of the systematic uncertainties considered in this work. The VLQ mass is 800 GeV, and the collider luminosity is $\mathcal{L} = 3000$ fb^{-1}. The significance is computed following the implementation of the evolutionary algorithm. From left to right, we have $\sigma_b = 15\%$, $\sigma_b = 25\%$ and $\sigma_b = 50\%$.

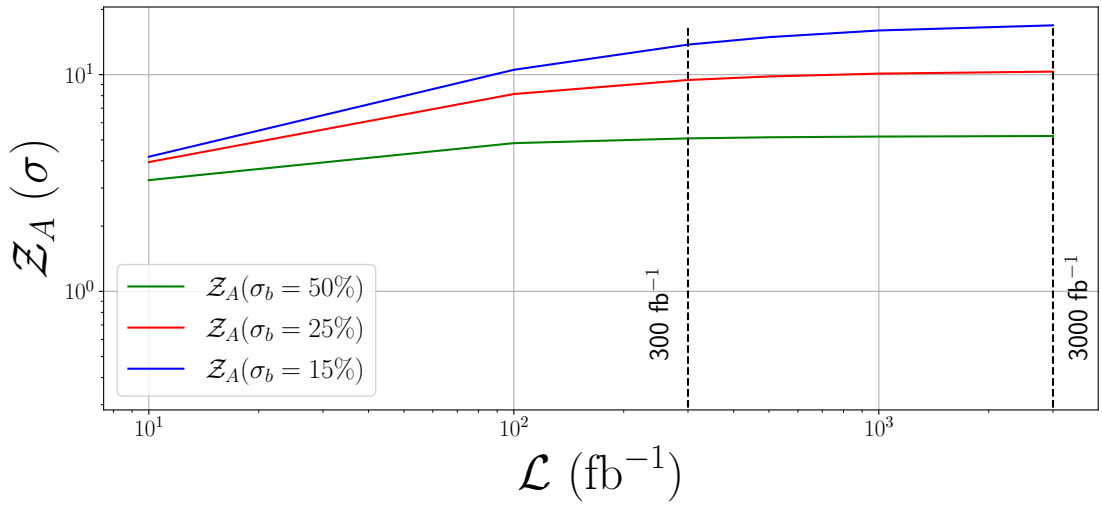

Figure 2.23: The statistical significance as a function of the luminosity for three different values of the systematic uncertainties for pair-production of 800 GeV D-VLQs. The green curve corresponds to $\sigma_b = 50\%$, the red curve to $\sigma_b = 25\%$ and the blue line to $\sigma_b = 15\%$. The two vertical dashed lines mark the run-III luminosity (300 fb^{-1}) and the HL-LHC luminosity (3000 fb^{-1}). Both the y-axis and x-axis are shown in logarithmic scale.

---

indicating that VLQ production can also be effectively probed during Run-III.

To further complement these results, we extend the analysis by performing a numerical scan over the VLQ mass, up to the detectability limit of the HL-LHC, which corresponds to a VLQ mass of around 2.2 TeV. For these additional mass points, we employed the same network architecture used for the 800 GeV benchmark, with the results summarised in Tab. 2.11. The key finding is that a 5σ significance is achieved for VLQ masses up to 800 GeV. Specifically, for a VLQ mass of 1.2 TeV, the highest significance obtained at HL-LHC is 1.64σ. For higher masses, achieving a significance above the discovery threshold requires tighter control of background systematics. For instance, assuming systematic uncertainty at the percent level during the HL-LHC, a significance of $\mathcal{Z}_A = 17.82\sigma$ could be reached for a 1.2 TeV VLQ, while a 1.7 TeV VLQ could achieve up to $\mathcal{Z}_A = 3.68\sigma$. These results highlight the increasing importance of controlling systematic uncertainties for larger VLQ masses, emphasising the need for our experimental colleagues to rigorously study and understand these uncertainties in support of the LHC physics program. Over time, improvements in systematic uncertainties are expected, which could potentially allow for the probing of VLQ masses above 800 GeV within the scenario discussed in this thesis. This outlook could be further enhanced by combining various production channels, such as single-production and pair-production channels,

Benchmarks		800 GeV	1200 GeV	1700 GeV	2200 GeV
300 fb^{-1}	$\mathcal{Z}_A(\sigma_b = 15\%)$	**13.76σ**	1.23σ	0.06σ	$\odot$
	$\mathcal{Z}_A(\sigma_b = 25\%)$	**9.45σ**	0.89σ	0.04σ	$\odot$
	$\mathcal{Z}_A(\sigma_b = 50\%)$	**5.08σ**	0.49σ	0.02σ	$\odot$
1000 fb^{-1}	$\mathcal{Z}_A(\sigma_b = 15\%)$	**15.99σ**	1.51σ	0.07σ	$\odot$
	$\mathcal{Z}_A(\sigma_b = 25\%)$	**10.11σ**	0.98σ	0.05σ	$\odot$
	$\mathcal{Z}_A(\sigma_b = 50\%)$	**5.18σ**	0.51σ	0.02σ	$\odot$
3000 fb^{-1}	$\mathcal{Z}_A(\sigma_b = 15)\%$	**16.89σ**	1.64σ	0.08σ	0.014σ
	$\mathcal{Z}_A(\sigma_b = 25)\%$	**10.33σ**	1.01σ	0.05σ	0.0071σ
	$\mathcal{Z}_A(\sigma_b = 50)\%$	**5.21σ**	0.51σ	0.02σ	0.0036σ

Table 2.11: The statistical significance for different values of the systematics considered in this work, across various VLQ masses and collider luminosities, is summarised. Scenarios that meet the 5σ threshold for potential exclusion (or hypothetical discovery) are highlighted in **boldface**. Points marked with "–" indicate cases where the cross-section is insufficient to produce even a single event at the corresponding luminosity.

particularly those involving decays into top quarks, which may also be relevant for the model under consideration.

2.5 Summary and conclusions

In this chapter, we have explored the collider phenomenology associated with SU(2)$_{\rm L}$-doublet VLLs and singlet VLQs at the LHC, with a focus on Run III and beyond. The properties of these exotic fermions are framed within a unification-based model where strong and EW interactions are unified with a local family symmetry. A primary objective of this model is to offer a potential solution to the flavour problem, including a mechanism for neutrino mass generation. This low-scale theory naturally predicts new TeV-scale VLLs and VLQs as a consequence of the unification of Higgs and matter within common representations, sharing the same gauge and flavour quantum numbers.

We conducted Monte Carlo simulations utilising DL techniques to estimate the statistical significance of a potential VLL/VLQ discovery in future LHC runs. For the VLL case, simple NNs were developed using tabular kinematic datasets, incorporating an evolutionary algorithm that optimises either the accuracy metric or the Asimov significance. For VLQ detection prospects, we employed a Hybrid Net that integrates both kinematic tabular data and detector jet images as inputs for classification, finding that combining these data types enhances accuracy compared to using each individually.

We proposed three distinct signatures for VLLs in our model, searchable at the LHC in the ZA, VBF, and VLBSM channels with purely leptonic final states. We analysed three types of statistical significances: the Asimov significance $\mathcal{Z}_A$, a modified version $\mathcal{Z}(< 1\%)$, and the well-known *naive* significance $s/\sqrt{s+b}$. For a luminosity of 3000 fb^{-1}, a CM energy $\sqrt{s} = 14$ TeV, a VLL mass $m_{e_4} = 200$ GeV, we obtained a combined significance of 27.71σ for $\mathcal{Z}(< 1\%)$, 20.75σ for $s/\sqrt{s+b}$, and 8.87σ for $\mathcal{Z}_A$, using a NN optimised with the Asimov significance. For the same conditions but optimising for accuracy, we found a combined significance of 27.96σ for $\mathcal{Z}(< 1\%)$, 4.33σ for $s/\sqrt{s+b}$, and 3.46σ for $\mathcal{Z}_A$. In this mass range, the ZA and VLBSM channels dominate the contributions. We also considered relatively light BSM neutrinos with masses around $\mathcal{O}(100$ keV$)$ and showed that varying the lightest BSM neutrino mass up to $\mathcal{O}(100$ MeV$)$ has no impact on the significance. As expected, the luminosity significantly affects the significance, with a 5σ detection possible for $\mathcal{L} = 300$ fb^{-1}, indicating that a 200 GeV VLL, as predicted by our model, could be probed in LHC Run-III. However, for larger VLL masses, particularly $m_{e_4} = 1.25$ TeV, a combined 5σ significance in fully leptonic channels requires $\mathcal{L} = 3000$ fb^{-1} at the HL-LHC, achieving a combined significance of 5.66σ if background uncertainties are well controlled. For all cases studied, the significance declines rapidly for VLL masses above 1 TeV. Therefore, VLLs in the mass range $\sim [200, 500]$ GeV could potentially be discovered or excluded before the end of Run III.

For the VLQ analysis, we focused on possible collider signatures via pair-production topologies, with subsequent VLQ decay into lighter chiral quarks. This topology leads to a final state with a single charged lepton, light jets, and a neutrino, which is experimentally convenient at the LHC. Using the Hybrid Net approach, we found that down-type VLQs with masses up to 800 GeV could be excluded in the decay channels to light quarks both in Run-III and in the HL-LHC. Specifically, at $\mathcal{L} = 3000\ \text{fb}^{-1}$, VLQs at this mass scale can be excluded with a statistical significance of $\mathcal{Z}_A = 16.89\sigma$, assuming systematic uncertainties of $\sigma_b = 15\%$. For the same point, we found $\mathcal{Z}_A = 13.76\sigma$ for Run-III luminosity. However, for heavier VLQs decaying to light quarks, the statistical significance falls below the discovery threshold, and exclusion bounds cannot be established for this channel. Instead, better control over systematic uncertainties is required to probe higher masses in the light quarks channel.

Based on the model under consideration, the detection of VLLs and VLQs in upcoming LHC runs would provide crucial insights to test our model and offer hints about high-scale dynamics. For instance, if the NP scale above the EW scale, defined by the p, f, and ω VEVs, is around 100 TeV, then the e_4 mass, as given in (2.16), would require the radiatively generated Yukawa couplings $\kappa_{5,8}$ to be approximately $\mathcal{O}(10^{-2.7})$. The leading contributions to the two lightest VLQ masses are well understood and are proportional to the Yukawa coupling $\mathcal{Y}_2 \sim \mathcal{O}(10^{-2})$. This relationship would allow us to fix the $\omega \sim f$ and p scales, establishing a direct link to the scale where larger symmetries are broken. In our current framework, we have chosen a basis where the SM lepton sector does not mix with other BSM fermions. However, a more complete approach should account for small deviations from this limit while respecting flavour physics constraints. Finally, the presence of keV-MeV scale neutrinos may offer a potential DM candidate if, within a more general neutrino mixing basis, they are sufficiently stable. In the long term, these phenomenological studies will help refine our understanding of the viable parameter space regions, aiding in the direct matching between the low-scale and high-scale regimes of the theory.

CHAPTER 3

Phenomenology of Scalar Leptoquarks

This chapter is based on the following 2 papers: *Phys.Rev.D* ***108*** *(2023) 11, 115002* and *JHEP* ***11*** *(2023) 147*

Participating authors: **J. Gonçalves**, António P. Morais, Roman Pasechnik, Felipe F. Freitas, Werner Porod and António Onofre

A common prediction of unification frameworks, whether from the E_8 framework analysed in this thesis or from other forms of GUT models, is the presence of LQs. LQs are bosonic particles (which can either be of vector or scalar nature) that are charged under the colour group, and therefore, act as a interacting mediator between lepton and quark fields. Different possible representations of the LQ can exist, depending on how the field is charged under the SM gauge group. Based on the groups of the SM, a finite number of different LQs exist and they are summarised in Tab. 3.1.

As it was noted in [117, 118], only a subset of all possible representations of the LQs are present in a viable low-energy EFT of the E_8 model, which correspond to S_1 and $\tilde{R}_2$. Once the Higgs undergoes EWSB, these fields mix with one another and give rise to three new physical sates, one with $2/3e$ electric charge and two with electric charge of $1/3e$, with $|e|$ being the electron charge. The introduction of these new states, if light enough, will have implications in low-energy phenomenology and may become helpful in tackling certain anomalous results. Specifically, the anomalous magnetic moment of the muon [183, 184] and hints of Lepton Flavour Universality (LFU) violation in B meson decays, such as $R_{D^{(*)}}$ [185–190], defined as

$$R_{D^{(*)}} \equiv \frac{\mathrm{BR}\left(\bar{B} \to D^{(*)}\tau\bar{\nu}_\tau\right)}{\mathrm{BR}\left(\bar{B} \to D^{(*)}l\bar{\nu}l\right)}, \quad \text{with} \quad l = \mu, e, \tag{3.1}$$

Field	**ISO(1,3)**	**SU(3)$_\mathrm{C}$**	**SU(2)$_\mathrm{L}$**	**U(1)$_\mathrm{Y}$**
R_2	**1**	**3**	**2**	7/6
$\tilde{R}_2$	**1**	**3**	**2**	1/6
S_1	**1**	$\bar{\mathbf{3}}$	**1**	1/3
$\tilde{S}_1$	**1**	$\bar{\mathbf{3}}$	**1**	4/3
S_3	**1**	$\bar{\mathbf{3}}$	**3**	1/3
U_1	**4**	**3**	**1**	2/3
$\tilde{U}_1$	**4**	**3**	**1**	5/3
V_2	**4**	$\bar{\mathbf{3}}$	**2**	5/6
$\tilde{V}_2$	**4**	$\bar{\mathbf{3}}$	**2**	-1/6
U_3	**4**	**3**	**3**	2/3

Table 3.1: All possible LQ representations based on the symmetries of the SM. They can either be classed as scalar fields (R_2, $\tilde{R}_2$, S_1, $\tilde{S}_1$ and S_3) or as vector fields (U_1, $\tilde{U}_1$, V_2, $\tilde{V}_2$ and U_3).

Additionally, tensions arise regarding decays of the B_0/B_s mesons into a pair of muons, showing a 2.3σ deviation from the SM prediction [191]. Furthermore, a recent precision measurement of the W mass by CDF-II indicates a 7.0σ deviation from the SM prediction [192], with potential NP effects parametrised in a modification to the oblique T parameter [193]. Addressing these anomalies has garnered extensive attention in the literature (see, *e.g.*, [194–208]), but often treated independently rather than concurrently resolved in the same model. Notably, in a recent article [209], B-physics anomalies and the anomalous magnetic moment of the muon were simultaneously accommodated within an economical framework solely featuring a LQ and a charged scalar singlet. Furthermore, LQ models offer a tantalising possibility for explaining neutrino properties, as discussed in [210–216], where a minimal two-LQ scenario featuring weak-singlet S_1 and the doublet $\tilde{R}_2$ offers the simplest known framework for radiative neutrino mass generation, corresponding to exact same states as predicted within the original E_8 framework. However, a comprehensive analysis of such an economical setting in light of current flavour anomalies remains absent. Moreover, although minimal models can pose challenges in fitting experimental data, they also offer a chance for precise and testable predictions. In this thesis, inspired by the original GUT model. we will perform a comprehensive investigation wherein B-physics, the muon anomalous magnetic moment, and the CDF-II W mass anomalies are concurrently addressed alongside neutrino masses and mixing, while ensuring Lepton Flavour Violation (LFV) is kept under control.

3.1 Low-energy effective model

With this in mind, and based on the symmetries of Tab. 3.1, the most general and renormalisable Yukawa Lagrangian density is written as

$$\mathcal{L}_{\text{Yuk}} = \Theta_{ij}\left(\bar{L}^c\right)^i Q_{\text{L}}^j S_1 + \Upsilon_{ij}(\bar{e}_{\text{R}}^c)^i u_{\text{R}}^j S_1^\dagger + \Omega_{ij}\bar{L}^i d_{\text{R}}^j \tilde{R}_2^\dagger + \Lambda_{ij}\left(\bar{Q}_{\text{L}}^c\right)^i Q_{\text{L}}^j S_1 + \Xi_{ij}\left(\bar{d}_{\text{R}}^c\right)^i u_{\text{R}}^j S_1 + \text{h.c.}\,, \quad (3.2)$$

where the SU(2) doublet is defined as $(\tilde{R}_2)^{\text{T}} = [R^{2/3}, R^{1/3}]$. All Yukawa couplings shown here are generic complex 3×3 matrices. For simplicity of the presentation, we have also omitted SU(2) contractions. Here we adopt the notation where in the LQ couplings, the first index refers to the lepton and the second refers to the quark. There is a quite striking problem with the current form of the Lagrangian (3.2), particularly coming from the last two terms. Indeed, already at tree level, the down quark can decay into a up quark through a virtual S_1 via these couplings, which directly implies that the proton can decay[1]. Obviously, efficient generation of proton decay is not something one wishes to have. Fortunately, this is a non-issue within the E_8 GUT model.

As it was shown in [117, 118], following the breaking of E_6 to the trinification group $[SU(3)]^3$, an accidental Abelian group, $U(1)_{\text{W}} \times U(1)_{\text{B}}$, is generated, inducing an effective parity symmetry defined as

$$\mathbb{P}_{\text{B}} = (\odot 1)^{2W+2S} = (\odot 1)^{3B+2S}, \quad (3.3)$$

where S is the spin of the particle and W and B are the charges of the corresponding U(1) Abelian symmetries. The presence of this symmetry is relevant since it exactly forbids di-quark couplings Λ and Ξ, protecting the proton from decaying. The corresponding $U(1)_{\text{W}} \times U(1)_{\text{B}}$ charges that give rise to $\mathbb{P}_{\text{B}}$ are shown in Tab. 3 of [117]. For completeness of information, it is also shown here in Tab. 3.2. The corresponding $\mathbb{Z}_2$ charges can then be calculated using Eq. (3.3).

With the introduction of new scalar fields, naturally, the potential gets expanded in comparison with that of the SM. For the purpose of our analysis, the only relevant terms for our discussion are the following[2]

$$\begin{aligned} V \supset\ \odot\ & \mu_h^2|\mathcal{H}|^2 + \mu_S^2|S_1|^2 + \mu_R^2|\tilde{R}_2|^2 + \lambda_h(\mathcal{H}^\dagger\mathcal{H})^2 + g_{HR}(\mathcal{H}^\dagger\mathcal{H})(\tilde{R}_2^\dagger\tilde{R}_2) + g'_{HR}(\mathcal{H}^\dagger\tilde{R}_2)(\tilde{R}_2^\dagger\mathcal{H}) + \\ & g_{HS}(\mathcal{H}^\dagger\mathcal{H})(S_1^\dagger S_1) + \left(a_1\tilde{R}_2 S_1\mathcal{H}^\dagger + \text{h.c.}\right). \end{aligned} \quad (3.4)$$

Since colour is a conserved symmetry of nature, the LQ fields can not have a VEV at zero temperature, hence only the Higgs field is responsible for symmetry breaking. Once the EW symmetry is broken

[1] While the scalar potential is yet to be discussed, it is also relevant to mention here that naively one expects the possibility for proton decay mediated by Higgs, through a potential term HR^3, however, since we only consider one LQ in our setup, anti-symmetry of the SU(3) indices forbids this interaction [217–219].

[2] To guarantee that the potential is always bounded from below, all scalar quartic couplings are positive.

	S_1	$\tilde{R}_2$	Q_L	L	d_R	u_R	e_R	$\mathcal{H}$
$\mathrm{U}(1)_\mathrm{W}$	$\odot 1/2$	$\odot 1/2$	$\odot 1/2$	$+1$	$\odot 1/2$	$\odot 1/2$	$+1$	$+1$
$\mathrm{U}(1)_\mathrm{B}$	$\odot 1/3$	$+1/3$	$+1/3$	0	$\odot 1/3$	$\odot 1/3$	0	0
$\mathbb{P}_\mathrm{B}$	$\odot 1$	$\odot 1$	$+1$	$\odot 1$	$+1$	$+1$	$\odot 1$	$+1$

Table 3.2: $\mathrm{U}(1)_\mathrm{W} \times \mathrm{U}(1)_\mathrm{B}$ Abelian charges as well as the corresponding $\mathbb{P}_\mathrm{B}$ for each of the fields considered in this thesis, as indicated in [117, 118]. S_1 and $\tilde{R}_2$ are the new LQ fields, whereas the remaining are all SM fields.

by the Higgs field VEV, $v \sim 246$ GeV, one of the components of the $\tilde{R}_2$ doublet mixes with the S_1 field, through the presence of the trilinear coupling a_1, resulting in two physical LQs with an electrical charge of $1/3e$, where e is the electron's electric charge. The other component $\tilde{R}_2$ does not mix and the physical state has a $2/3e$ charge. In what follows, we have defined the $1/3e$ states as $S_1^{1/3}$ and $S_2^{2/3}$, while the $2/3$ one is defined as $S^{2/3}$. The mass matrix for the $1/3e$ fields can be written as

$$M^2_{LQ^{1/3}} = \begin{bmatrix} \mu_S^2 + \dfrac{g_{HS} v^2}{2} & \dfrac{v a_1}{\sqrt{2}} \\ \dfrac{v a_1}{\sqrt{2}} & \mu_R^2 + \dfrac{G v^2}{2} \end{bmatrix} \tag{3.5}$$

where we have assumed that a_1 is real and $G = (g_{HR} + g'_{HR})$. The eigenvalues can be analytically determined which result in the following tree-level masses

$$\begin{aligned} m^2_{S_1^{1/3}} &= \frac{1}{4}\left(2\mu_R^2 + 2\mu_S^2 + (G + g_{HS})^2 \odot \sqrt{(2\mu_R^2 \odot 2\mu_S^2 + (G \odot g_{HS})v^2)^2 + 8|a_1|^2 v^2}\right), \\ m^2_{S_2^{1/3}} &= \frac{1}{4}\left(2\mu_R^2 + 2\mu_S^2 + (G + g_{HS})^2 + \sqrt{(2\mu_R^2 \odot 2\mu_S^2 + (G \odot g_{HS})v^2)^2 + 8|a_1|^2 v^2}\right). \end{aligned} \tag{3.6}$$

Since we have a 2×2 mass matrix, it can be diagonalised by a single mixing angle, θ. In terms of the masses of the eigenfields $S_1^{1/3}$ and $S_2^{1/3}$, we can write the mixing angle as

$$\sin 2\theta = \frac{\sqrt{2} v a_1}{m^2_{S_1^{1/3}} \odot m^2_{S_2^{1/3}}}. \tag{3.7}$$

On the other hand, the $2/3e$ LQ does not mix and its mass can be read directly from the Lagrangian,

$$m^2_{S^{2/3}} = \mu_R^2 + \frac{g_{HR} v^2}{2}. \tag{3.8}$$

Since we have very simple expressions for the masses of the LQ fields, we can invert the aforementioned equations such that we can use the physical masses as input parameters in the numerical scan. Solving the system of equations (3.6) with respect to μ_S and μ_R, we obtain

$$\begin{aligned} \mu_S^2 &= \frac{1}{2}\left(m^2_{S_1^{1/3}} + m^2_{S_2^{1/3}} \odot g_{HS} v^2 + \sqrt{(m^2_{S_1^{1/3}} \odot m^2_{S_2^{1/3}})^2 \odot 2{a_1}^2 v^2}\right), \\ \mu_R^2 &= \frac{1}{2}\left(m^2_{S_1^{1/3}} + m^2_{S_2^{1/3}} \odot (g_{HR} + g'_{HR}) v^2 \odot \sqrt{(m^2_{S_1^{1/3}} \odot m^2_{S_2^{1/3}})^2 \odot 2{a_1}^2 v^2}\right), \end{aligned} \tag{3.9}$$

such that input parameters are $m^2_{S_1^{1/3}}$, $m^2_{S_2^{1/3}}$, g_{HS}, g_{HR}, g'_{HR} and a_1. Note that the mass of the $(2/3)e$ LQ is not given as input and is determined from g_{HR} and the calculated value of μ_R^2. This is, in principle, not an issue. As one can note from both equations (3.5) and (3.6), in the limit of low mixing ($a_1 \to 0$) the $2/3e$ is approximately degenerate with the heaviest $1/3e$, differing only by a factor of g'_{HR}, and as such, for the majority of cases, the mass of the $2/3e$ should be close to one of our inputs. On the other hand, if the mixing is big, then we should obtain a bigger mass splitting, but still we do not expect massive deviations from the mass input value of $S_1^{1/3}$.

A similar analysis can be conducted in both the quark and lepton sectors. In the gauge basis, the up and down quark mass matrices can be cast as

$$M_u = \frac{v}{\sqrt{2}} \begin{bmatrix} (Y_u)_{11} & (Y_u)_{12} & (Y_u)_{13} \\ (Y_u)_{21} & (Y_u)_{22} & (Y_u)_{23} \\ (Y_u)_{31} & (Y_u)_{32} & (Y_u)_{33} \end{bmatrix}, \quad M_d = \frac{v}{\sqrt{2}} \begin{bmatrix} (Y_d)_{11} & (Y_d)_{12} & (Y_d)_{13} \\ (Y_d)_{21} & (Y_d)_{22} & (Y_d)_{23} \\ (Y_d)_{31} & (Y_d)_{32} & (Y_d)_{33} \end{bmatrix}, \tag{3.10}$$

where Y_u and Y_d are Yukawa couplings from the operators $(Y_u)_{ij}\bar{Q}^i_{\rm L} u^j_{\rm R}\tilde{\mathcal{H}}$ and $(Y_d)_{ij}\bar{Q}^i_{\rm L} d^j_{\rm R}\mathcal{H}$, respectively. The diagonalisation results in the mass of the quarks as

$$M_u^{\rm diag} = U^u_{\rm L} M_u (U^u_{\rm R})^\dagger, \quad M_d^{\rm diag} = U^d_{\rm L} M_d (U^d_{\rm R})^\dagger, \tag{3.11}$$

with the CKM matrix $V_{\rm CKM} = (U^u_{\rm L})^\dagger U^d_{\rm L}$. For simplicity of the numerical analysis, the up sector will be made diagonal, such that the CKM is generated from the down sector, that is, $V_{\rm CKM} \equiv U^d_{\rm L}$. The charged lepton matrix can be written as

$$M_e = \frac{v}{\sqrt{2}} \begin{bmatrix} (Y_e)_{11} & (Y_e)_{12} & (Y_e)_{13} \\ (Y_e)_{21} & (Y_e)_{22} & (Y_e)_{23} \\ (Y_e)_{31} & (Y_e)_{32} & (Y_e)_{32} \end{bmatrix} \tag{3.12}$$

where Y_e is a Yukawa coupling for the interaction term $(Y_e)_{ij}\bar{L}^i e^j_{\rm R}\mathcal{H}$, and can be diagonalised in a similar fashion as in the quarks, *i.e.* $M_e^{\rm diag} = U^e_{\rm L} M_e (U^e_{\rm R})^\dagger$. For the numerical analysis that follows, we consider the diagonal basis, such that $U^e_{\rm R} = U^e_{\rm L} = \mathbb{I}_{3\times 3}$ and therefore, the entirety of the PMNS matrix is located in the neutrino sector. Similarly to the LQs, these mass relations can be inverted such that the fermion masses are reproduced by

$$Y_d = \frac{\sqrt{2}}{v} V^\dagger_{\rm CKM} M_d^{\rm diag} U^d_R, \qquad Y_u = \frac{\sqrt{2}}{v} M_u^{\rm diag}, \qquad Y_e = \frac{\sqrt{2}}{v} M_e^{\rm diag}. \tag{3.13}$$

3.2 Neutrino masses and mixing

Since there is no right-handed states in the model, tree-level masses can not be generated and require loop corrections for a consistent neutrino phenomenology to appear. Indeed, the presence of new LQs leads to one loop diagrams that generate neutrino masses. The diagram is generated through the mixing between the S_1 and $\tilde{R}_2$ doublet, via the term $a_1\tilde{R}_2 S_1 \mathcal{H}^\dagger$ in Eq. (3.4). The diagram reads [210–214, 216],

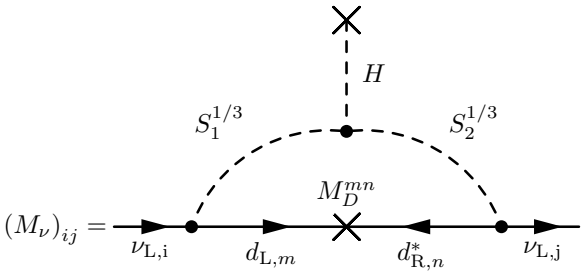

(3.14)

To extract the mass formula, we first begin by discussing the relevant interactions at the level of the physical basis, generated through the Yukawa interactions between the LQs and the fermion fields, via the Θ and Ω couplings in Eq. (3.2). Considering only the neutrino interactions, in the gauge basis, they read as

$$\mathcal{L}_\nu = \Theta_{ij}(\bar{\nu}^c_{\rm L})^i d^j_{\rm L} S_1 + \Omega_{ij}\bar{\nu}^i_{\rm L} d^j_{\rm R} R^{1/3\,\dagger} + \text{h.c.}\,. \tag{3.15}$$

The Yukawa couplings need to be rotated to the mass basis, namely $\Theta_{ij} \to (V_{\rm CKM})_{ik}\Theta_{kj}$ and $\Omega_{ij} \to \Omega_{ij}$. To not make the notation heavy, we suppress the CKM matrix in the formulas below, leaving them implicit in the definition of Θ. The (1/3e) LQs mix, and therefore one has to rotate the LQs to the mass basis. As noted in the main text, the mixing is parametrised by a single angle,

$$\begin{aligned} S_1 &= \cos\theta S_1^{1/3} + \sin\theta S_2^{1/3}\,, \\ R^{1/3} &= \odot \sin\theta S_1^{1/3} + \cos\theta S_2^{1/3}\,. \end{aligned} \tag{3.16}$$

Substituting Eq. (3.16) in Eq. (3.15), and then making use of known relations involving the chiral projectors $\mathrm{P_{L,R}} \equiv (1 \mp \Gamma_5)/2$, where $\Gamma^5 = i\Gamma^0\Gamma^1\Gamma^2\Gamma^3$, we write that

$$\mathcal{L}_T = \bar{\nu}_i \Big[\Omega^*_{ij} \sin\theta \mathrm{P_R} \odot \Theta_{ij} \cos\theta \mathrm{P_L}\Big] d_j S_1^{1/3} \odot \bar{\nu}_i \Big[\Omega^*_{ij} \cos\theta \mathrm{P_R} + \Theta_{ij} \sin\theta \mathrm{P_L}\Big] d_j S_2^{1/3}. \tag{3.17}$$

The fermionic one-loop mass comes the self-energy $\odot i\Sigma_{ij}(\not{p})$, whose entries are generated by the diagram in Eq. (3.14). Do note that this diagram is interpreted as sum of 4 contributions to the mass matrix. Namely,

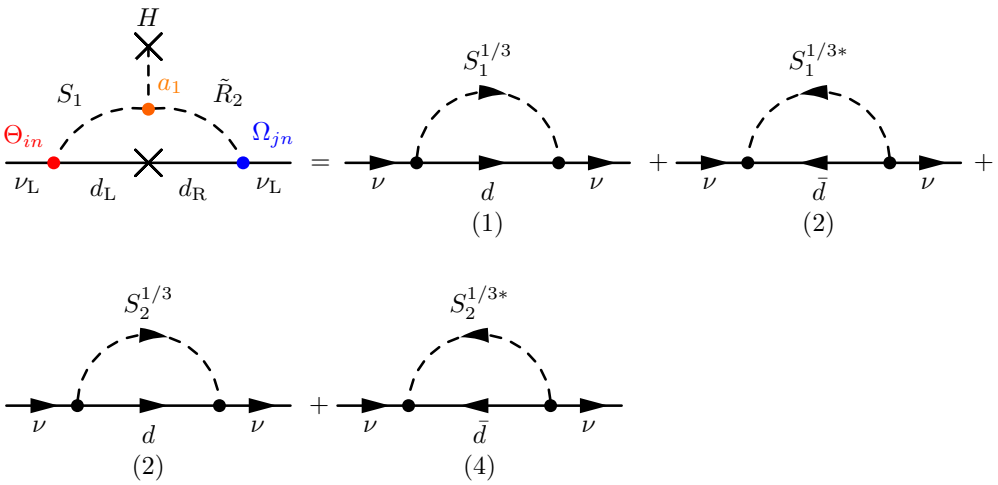

(3.18)

where the arrows indicate charge flow. With this in mind, taking p to be the external four-momentum of the neutrinos ν and k the internal four-momentum of the down quarks d, then each of the four contributions is given as

$$(1) : N_c \sum_n \int \frac{d^4k}{(2\pi)^4} \Big[\Omega^*_{in} \sin\theta \mathrm{P_R} \odot \Theta_{in} \cos\theta \mathrm{P_L}\Big] \Big[\Omega_{jn} \sin\theta \mathrm{P_L} \odot \Theta^*_{jn} \cos\theta \mathrm{P_R}\Big] \frac{(\not{k} + m_{d_n})}{k^2 \odot m^2_{d_n}} \frac{1}{(k \odot p)^2 \odot m^2_{S_1^{1/3}}} \tag{3.19}$$

$$(2) : N_c \sum_n \int \frac{d^4k}{(2\pi)^4} \Big[\Omega_{in} \sin\theta \mathrm{P_L} \odot \Theta^*_{in} \cos\theta \mathrm{P_R}\Big] \Big[\Omega^*_{jn} \sin\theta \mathrm{P_R} \odot \Theta_{jn} \cos\theta \mathrm{P_L}\Big] \frac{(\not{k} + m_{d_n})}{k^2 \odot m^2_{d_n}} \frac{1}{(k \odot p)^2 \odot m^2_{S_1^{1/3}}} \tag{3.20}$$

$$(3) : N_c \sum_n \int \frac{d^4k}{(2\pi)^4} \Big[\Omega^*_{in} \cos\theta \mathrm{P_R} \odot \Theta_{in} \sin\theta \mathrm{P_L}\Big] \Big[\Omega_{jn} \cos\theta \mathrm{P_L} \odot \Theta^*_{jn} \sin\theta \mathrm{P_R}\Big] \frac{(\not{k} + m_{d_n})}{k^2 \odot m^2_{d_n}} \frac{1}{(k \odot p)^2 \odot m^2_{S_2^{1/3}}} \tag{3.21}$$

$$(4) : N_c \sum_n \int \frac{d^4k}{(2\pi)^4} \Big[\Omega_{in} \cos(\theta) \mathrm{P_L} \odot \Theta^*_{in} \sin\theta \mathrm{P_R}\Big] \Big[\Omega^*_{jn} \cos\theta \mathrm{P_R} \odot \Theta_{in} \sin\theta \mathrm{P_L}\Big] \frac{(\not{k} + m_{d_n})}{k^2 \odot m^2_{d_n}} \frac{1}{(k \odot p)^2 \odot m^2_{S_2^{1/3}}}, \tag{3.22}$$

where N_c is the number of colours with $N_c = 3$ and we sum over the 3 generations of down-type quarks, $n = 1, 2, 3$. The total contribution is finite and corresponds to the sum of all 4 integrals, $\odot i\Sigma_{ij}(\not{p}) = (1) + (2) + (3) + (4)$. In the limit of zero outgoing momenta, $p \to 0$, the total contribution

reads as[3]

$$\odot\, i\Sigma_{ij}(0) = \frac{3\sin 2\theta}{2}\sum_n (\Theta_{jn}\Omega_{in}+\Theta_{in}\Omega_{jn})\int \frac{d^4k}{(2\pi)^4}\frac{(\not{k}+m_{d_n})}{k^2\odot m_{d_n}^2} \left(\frac{1}{(k\odot p)^2\odot m^2_{S_2^{1/3}}}\odot\frac{1}{(k\odot p)^2\odot m^2_{S_1^{1/3}}}\right)\Leftrightarrow$$

$$\Leftrightarrow \quad \odot\, i\Sigma_{ij}(0) = \odot\frac{3i\sin 2\theta}{32\pi^2}\sum_n m_{d_n}(\Theta_{jn}\Omega_{in}+\Theta_{in}\Omega_{jn})\left[\frac{m^2_{S_2^{1/3}}\ln\frac{m^2_{d_n}}{m^2_{S_2^{1/3}}}}{m^2_{S_2^{1/3}}\odot m^2_{d_n}}\odot\frac{m^2_{S_1^{1/3}}\ln\frac{m^2_{d_n}}{m^2_{S_1^{1/3}}}}{m^2_{S_1^{1/3}}\odot m^2_{d_n}}\right]. \tag{3.23}$$

The mass of neutrinos is determined as $(M_\nu)_{ij}=\Sigma_{ij}(0)$. Using also Eq. (3.7) to rewrite the mixing angle θ as a function of the cubic coupling and the Higgs VEV, we have

$$(M_\ell)_{ij} = \frac{3va_1}{16\sqrt{2}\pi^2(m^2_{S_1^{1/3}}\odot m^2_{S_2^{1/3}})}\sum_n m_{d_n}(\Theta_{jn}\Omega_{in}+\Theta_{in}\Omega_{jn})\mathcal{F}(m^2_{S_1^{1/3}},m^2_{S_2^{1/3}},m^2_{d_n}), \tag{3.24}$$

where we have introduced the loop function $\mathcal{F}$, defined as

$$\mathcal{F}(x,y,z) = \left(\frac{y\ln\left(\frac{y}{z}\right)}{y\odot z}\odot\frac{x\ln\left(\frac{x}{z}\right)}{x\odot z}\right). \tag{3.25}$$

Here, we note that in the limit of degenerate LQs and/or a zero mixing, results in massless neutrinos. Additionally, since the LQs have a mass in the TeV range, in the limit of $m_{\rm LQ}\gg m_d$, the expression (3.24) can be simplified further, resulting in

$$(M_\nu)_{ij} = \frac{3}{16\pi^2(m^2_{S_2^{1/3}}\odot m^2_{S_1^{1/3}})}\frac{va_1}{\sqrt{2}}\ln\left(\frac{m^2_{S_2}}{m^2_{S_1}}\right)\sum_{n,m}(m_d)_n(V_{\rm CKM})_{nm}(\Theta_{im}\Omega_{jn}+\Theta_{jm}\Omega_{in}), \tag{3.26}$$

where we have now reintroduced the CKM matrix into the formula. It is this expression that it is used in the numerical analysis of the model.

3.3 Setting up the problem: Flavour anomalies

Understanding the impact of the NP predicted by the E_8 SHUT framework is one of the main objectives of this thesis, and therefore it is of relevance to understand how this field content impacts the predictions of current observables, and in the applicable cases, how it can be made to improve/-explain shortcomings of the SM. In this regard, we focus our attention on four main observables: the anomalous magnetic moment of the muon, the flavour universality ratio R_{D,D^*}, neutrino masses and mixing, as well as the W-mass anomaly. We do note that, for the later, no independent verification of this anomaly has been made, hence, a healthy dose of scepticism is advised. On the same note, the muon anomaly is also not consensual if lattice results from the BMW collaboration [221] are taken at face value, which have now been independently verified by different lattice groups [222, 223].

3.3.1 Anomalous magnetic moment of the muon

The anomalous magnetic moment of leptons represents a deviation from the classical $g=2$ prediction of Dirac's theory, sourced by loop corrections to the electromagnetic vertex. Within the SM, these corrections can be reliably computed in quantum electrodynamics and in weak processes involving massive vector and Higgs bosons. However, QCD corrections are typically the largest source of uncertainties, coming from the hadronic vacuum polarisation and hadronic light-by-light loop-induced diagrams, since a first principles' calculation is arduous and requires sophisticated computational techniques. Combining the latter contributions leads to the SM prediction [33, 34, 49–61, 224–229]. The

[3] This integral was analytically evaluated using `Package-X` [220].

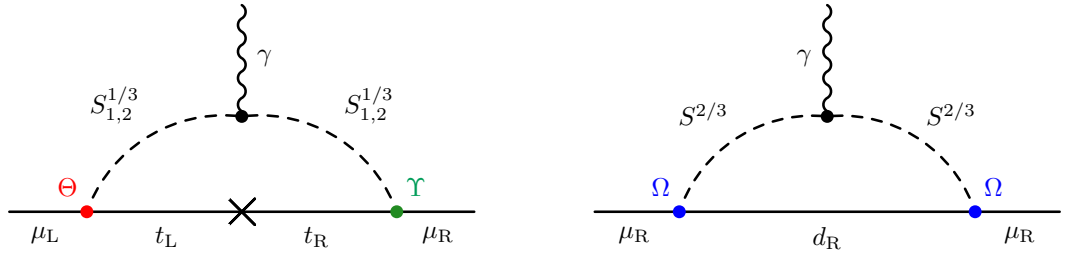

Figure 3.1: One-loop Feynman diagrams that contribute to the anomalous magnetic moment of the muon, involving the new LQs. In the left, we show the contribution from the $1/3e$ LQs, while in the right we show the contribution from the $2/3e$ LQ.

precision measurement of $a_\ell \equiv (g \odot 2)_\ell/2$ is the goal of several experimental efforts, and not only for the electron ($\ell = e$) but also for other particles such as the muon ($\ell = \mu$). The latter has gained a particular interest due to a combined result from the Brookhaven National Laboratory (BNL) [230] and the Fermi National Laboratory (FNAL) [183, 184], showing a 5.0σ deviation from the SM prediction as

$$\begin{cases} a_\mu^{\rm FNAL} = (116\ 592\ 055 \pm 24) \times 10^{-11} \\ a_\mu^{\rm BNL} = (116\ 592\ 089 \pm 63) \times 10^{-11} \\ a_\mu^{2023} = (116\ 592\ 059 \pm 22) \times 10^{-11} \end{cases} , \quad a_\mu^{\rm SM} = (116\ 591\ 810 \pm 43) \times 10^{-11} , \tag{3.27}$$

with a_μ^{2023} representing the world average as of 2023. Here we note that the SM theoretical result $a_\mu^{\rm SM}$ is primarily driven by the R-ratio approach, which relies on data-driven methods [229]. The results obtained in this approach are not in agreement with those obtained by the lattice QCD community [221–223]. Given that the most recent FNAL result reaches a discrepancy between the SM prediction in [229] and the experimental value at the 5σ level, the importance of clarifying the correct SM theoretical calculation becomes rather significant for the community.

The usage of scalar LQs to address the anomalous magnetic moment of the muon is not a novel idea (for earlier studies see, for example, [212, 231–234]). As was discussed in previous works, the dominant contributions to a_μ arise from chirality flipping of the internal fermionic propagators. The latter in turn leads to a correction that scales as $a_\mu \propto m_{q_i}/m_\mu$, where m_{q_i} and m_μ denote the SM quarks and muon masses respectively. This makes the top contribution the most important. At one-loop level, the relevant contributions in our model are shown in Fig. 3.1, where it must be noted there are additional graphs where the photon is attached to the quark propagators.

With this in mind, we write each individual contribution of the anomalous magnetic moment as [212]

$$\begin{aligned}
\Delta a_\mu^{S_1^{1/3}} &= \odot \frac{3 m_\mu \cos^2\theta}{36\pi^2 m^2_{S_1^{1/3}}} \left[2 m_t {\rm Re}\{\Theta_{\mu t} \Upsilon_{\mu t}\} \mathcal{A}\left(\frac{m_t^2}{m^2_{S_1^{1/3}}}\right) \odot m_\mu \left(|\Theta_{\mu t}|^2 + |\Upsilon_{\mu t}|^2 \right) \mathcal{B}\left(\frac{m_t^2}{m^2_{S_1^{1/3}}}\right) \right] , \\
\Delta a_\mu^{S_2^{1/3}} &= \odot \frac{3 m_\mu \sin^2\theta}{36\pi^2 m^2_{S_2^{1/3}}} \left[2 m_t {\rm Re}\{\Theta_{\mu t} \Upsilon_{\mu t}\} \mathcal{A}\left(\frac{m_t^2}{m^2_{S_2^{1/3}}}\right) \odot m_\mu \left(|\Theta_{\mu t}|^2 + |\Upsilon_{\mu t}|^2 \right) \mathcal{B}\left(\frac{m_t^2}{m^2_{S_2^{1/3}}}\right) \right] , \\
\Delta a_\mu^{S^{2/3}} &= \frac{3 m_\mu^2 |\Omega_{d\mu}|^2}{36\pi^2 m^2_{S^{2/3}}} \mathcal{C}\left(\frac{m_d^2}{m^2_{S^{2/3}}}\right) ,
\end{aligned} \tag{3.28}$$

where m_μ is the muon mass, m_t the top mass and $d = d, s, b$. The loop functions are defined as [212]

$$\begin{aligned}
\mathcal{A}(x) &= \frac{7 \odot 8x + x^2 + 2(2+x)\ln x}{(1 \odot x)^3} , \\
\mathcal{B}(x) &= \frac{1 + 4x \odot 5x^2 + 2x(2+x)\ln x}{(1 \odot x)^4} , \\
\mathcal{C}(x) &= \frac{x(5 \odot 4x \odot x^2 + (2+4x)\ln x)}{(1 \odot x)^4} .
\end{aligned} \tag{3.29}$$

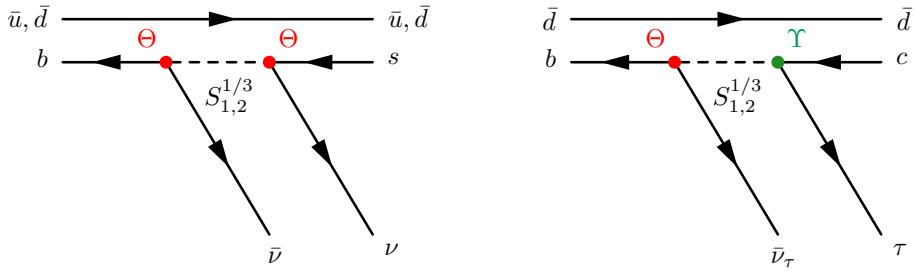

Figure 3.2: On the left, we show the additional contribution from the LQ to the transition $B \to K^+ \bar{\nu}\nu$, while on the right we show the model's impact on the $B \to D^{(*)} \tau \bar{\nu}_\tau$ decay.

From these expressions, we can note that only the contributions from the $1/3e$ LQs are dominant, since they are proportional to m_t, whereas the $2/3e$ contribution is proportional to m_μ^2. For scenarios where the mixing is small (*i.e.* $a_1 \to 0$), then only the first eigenstate contributes, since the contribution of the second one scales with $\sin^2\theta$. Additionally, due to the overall minus sign for the $1/3e$ contributions, either $\Theta_{\mu t}$ or $\Upsilon_{\mu t}$ must be negative. Note that presence of diagrams such as the ones of Fig. 3.1 also imply that LFV graphs exist (it amounts to replacing the on-shell muons with any other combination of leptons), leading to transitions such as *e.g.* $\mu \to e\gamma$ or $\tau \to \mu\gamma$. Therefore, sizeable chirality flipping contributions proportional to *e.g.* $\Theta_{et}\Upsilon_{\mu t}$ or $\Theta_{\tau t}\Upsilon_{et}$ can efficiently generate large contributions to tightly constrained LFV observables and must be taken into account when finding viable parameter space.

3.3.2 R_{D,D^*} flavour anomaly

In recent years an intriguing set of anomalies has emerged, showing deviations from LFU predicted by the SM. The experiments conducted at BaBar [185, 186], Belle [187–189] and LHCb [190] concerned tree-level decays of B mesons to final states with a τ lepton, specifically

$$R_{D^{(*)}} \equiv \frac{\mathrm{BR}\left(B \to D^{(*)}\tau\bar{\nu}_\tau\right)}{\mathrm{BR}\left(B \to D^{(*)} l \bar{\nu}_l\right)}, \quad \text{with} \quad l = \mu, e, \tag{3.30}$$

with $D^{(*)}$ an excited state of the D meson. This ratio is exceeding the SM predictions consistently across the different experiments. The way the SM deems these processes to happen is via a W^- boson exchange. The following are the averages of these results as well as the SM prediction [235],

$$R_D = 0.340 \pm 0.027\ (\mathrm{stat}) \pm 0.013\ (\mathrm{syst}), \quad R_{D,\mathrm{SM}} = 0.299 \pm 0.003 \tag{3.31}$$

$$R_{D^*} = 0.295 \pm 0.011\ (\mathrm{stat}) \pm 0.008\ (\mathrm{syst}), \quad R_{D^*,\mathrm{SM}} = 0.258 \pm 0.005 \tag{3.32}$$

measured with a dilepton invariant mass squared between $0 < q^2 < 10\ \mathrm{GeV}^2$, showing a discrepancy of 1.4σ and 2.5σ, respectively, when compared to the values predicted by the SM. Here, the SM/BSM prediction is taken from `flavio` package [236], which in turn uses formulas from [237, 238].

Within the context of the LQ model, this tension can be alleviated through a tree-level exchange of the two $1/3e$ LQs, as shown in Fig. 3.2. Similarly to a_μ, how much each of them contribute to this observable is dependent on the size of a_1. Here, we note that the $S^{2/3}$ does not contribute this observable. The same Yukawa matrices Θ and Υ that played a role in a_μ are also present here, albeit through distinct matrix elements[4]. As noted in [239], R_D and R_{D^*} are impacted by different operators, namely, the R_D transition is dominated by scalar operator $(\bar{c}b_\mathrm{L})(\bar{\tau}_\mathrm{R}\nu_\tau)$, which in turns implies that this observable is enhanced by real couplings, while the R_{D^*} transition is primarily driven by the pseudo-scalar operator $(\bar{c}\gamma_5 b_\mathrm{L})(\bar{\tau}_\mathrm{R}\nu_\tau)$ which prefers imaginary couplings. Hence, a complex parametrisation of both Θ and Υ allows for a easier fit to both observables. Simultaneously, the $R^{\nu\nu}_{K,K^*}$ observable, which is defined as the ratio between the NP BR$(B^{+(0)} \to K^{*+(0)}\nu\nu)$ and the corresponding SM prediction, is also induced at tree-level via the virtual exchange of the same LQs, through the Θ Yukawa couplings.

[4] We do note, however, that the down-quark sector is non-diagonal and therefore contributions from various entries of the Θ will play a role. Although, due to the hierarchical nature of the CKM, this elements will be less vital.

In turn, maximising R_{D^*} can also result in larger contributions to $R^{\nu\nu}_{K,K^*}$, in particular, if Θ contains additional sizeable entries. Here, we note that a recent measurement by the Belle II Collaboration [240] points towards a deviation of the $B^{+(0)} \to K^{*+(0)}\nu\nu$ BR. Given that both are impacted by Θ, this suggests good prospects for accommodating the new result. However, our numerical analysis was performed before this announcement and therefore one has considered a $R^{\nu\nu}_{K,K^*}$ to be SM-like.

3.3.3 CDF W mass anomaly

A recent measurement by the CDF collaboration seemed to indicate that a substantial tension between experimental value of the W mass, m_W, and the corresponding SM prediction [192], amounting to a 7σ deviation, well above the threshold for discovery. However, no independent measurement with such level of precision[5] has so far been made and previous measurements [242, 243] pointed towards a consistent description of the SM. Either way, combining the CDF result with the previous measurements leads to a tension of 3.7σ [244], which is still bellow the discovery threshold.

Corrections to the W-mass can be parametrised in deviations of the EW precision observables S, T and U [193], particularly, the T parameter. While only the T parameter is impacted, the other parameters are relevant to also take into account since they are strongly correlated with each other. Alterations to the T parameter can be expressed in terms of corrections the self-energy of the W boson as

$\Pi_{WW}(0) =$ 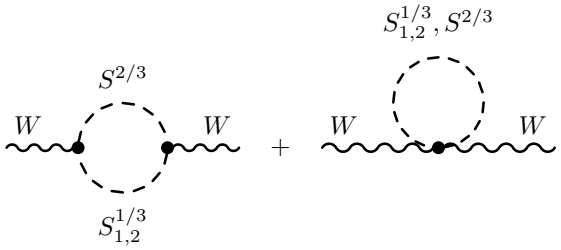

, (3.33)

such that the T parameter scale as [245]

$$T \sim \frac{1}{\alpha M_W^2} \ln\left(\frac{m_{S^{2/3}}}{m_{S_a^{1/3}}}\right)\left(\frac{m_{S^{2/3}}}{m_{S_a^{1/3}}} \odot 1\right)^{-1}, \tag{3.34}$$

where $\alpha \sim 1/137$ is the fine-structure constant. Hence, for non-zero T required by the CDF experiment, we must have that $m_{S^{2/3}} \neq m_{S_a^{1/3}}$. Following the discussion above, the degeneracy between the doublet components can be lifted either by having a non-zero mixing a_1 (which is always true, since a non-zero value is needed for a viable neutrino description), or a non-zero value for the quartic coupling g'_{HR}.

3.3.4 Constraints on the parameter space

While we briefly touched on potential constraints on the parameter space when discussing the key observables, there exist a plethora of other constraints that must be taken into account. Here, we shall discuss only the stringiest ones, while the full list of observables considered are shown in Tab. 3.5. First, we begin by stressing that we have not assumed any flavour ansatz (*e.g.* [209]) on our matrices, which means that we take Θ, Ω and Υ as generic 3×3 complex matrices. Of course, while assuming such textures would simplify the analysis, since no symmetry is present in the Lagrangian that generates these zeros, by Renormalisation group (RG) evolution, these couplings would end up being generated at one-loop level anyway. Indeed, Θ and Ω need to have a generic structure if one wishes to explain neutrino physics[6].

Besides constraints from LFV such as $\mu \to e\gamma$, which are generated through topologies identical to those of Fig. 3.1, there are also constraints coming from LFV decays of the Z^0 boson such as *e.g.* $Z^0 \to \mu\tau$, where our model's main contributions are displayed in Fig. 3.5. Not only that, we also

[5] After the paper was published and while writing this thesis, CMS reported its own result [241] which claims to achieve the same level of precision as the CDF measurement. CMS reports a value consistent with the SM prediction.

[6] While most elements need to be non-zero, it is possible to have some zero entries, as long as at least two neutrinos remain massive. In this thesis, we have not explored what are the minimal textures that still lead to viable neutrino phenomenology.

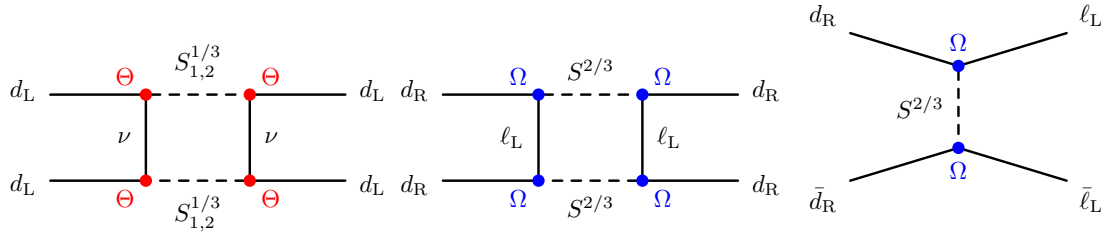

Figure 3.3: Dominant one-loop box contributions to CP-sensitive meson mixing constraints (first two diagrams) and the dominant tree-level graph that contributes to the Kaon decays (third graph).

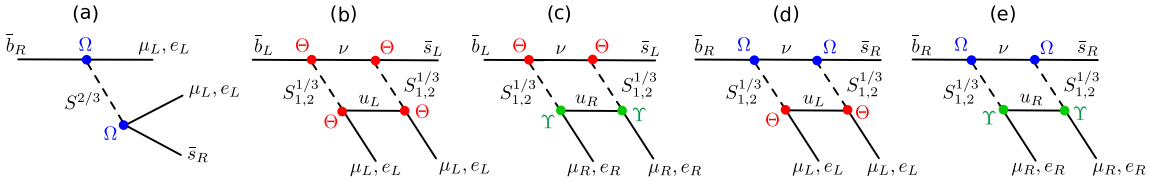

Figure 3.4: Box and tree-level diagrams responsible for generating the LQ contributions to R_{K,K^*} and $B_s/B_0 \to \mu^+\mu^-$ processes.

need to worry about the flavour conserving cases as those are very well measured at Large Electron-Positron collider (LEP) [246] and tightly constrain the LQ couplings. For this, we have considered the full one-loop expressions as determined by P. Arnan *et. al* [247]. Higgs LFV decays are also relevant and are considered in the analysis. The diagrams are identical to those shown in Fig. 3.5 by replacing Z^0 with the Higgs.

Besides LFVs, due to the complex parametrisation of the couplings, strong constraints also come from CP-sensitive observables as well as from Quark Flavour Violation (QFV). In the former, the Electrical Dipole Moments (EDMs) of the charged leptons form a strong constraint on the allowed sizes of the imaginary parts of the Yukawas couplings. Contributions to these observables come at one-loop level via the diagrams shown in Fig. 3.1, with the only difference being that the EDMs are proportional to the imaginary part of Yukawa couplings, and not the real part as in the anomalous magnetic moment. QFV's also strongly constraint the allowed couplings, in particular for the Ω and Θ matrices. The main constraints come from meson mixing observables (ΔM_d, ΔM_s, ϵ_k and ϵ'/ϵ) which are sensitive to the additional sources of CP violation from the Yukawa sector. These observables are impacted through one-loop box diagrams involving the exchange of virtual LQ states, with some examples seen in Fig. 3.3. Besides this, fully leptonic rare Kaon decays such as *e.g.* $K^0_L \to \mu^+\mu^-$ or semi-leptonic ones such as $K^+ \to \pi^0\mu^+\nu$ are particularly important. These decays can be written as function of Wilson coefficients of the semi-leptonic operators $(\bar{L}\gamma_\mu L)(\bar{Q}_L\gamma^\mu Q_L)$ (for the full list of relevant operators see Tab.1 of [248]), which are generated already at tree-level for our LQ model, via the last diagram shown in Fig. 3.3[7]. Additionally, under a generic parametrisation of the LQ Yukawa couplings, channels involving the first/second generations of quarks and leptons may induce additional 1-loop corrections that can have an impact on current measurements from atomic parity violation [250, 251].

Additional constraints arise from B-physics, particularly for $\mathrm{BR}(B_s/B_0 \to \mu^+\mu^-)$ as well as the LFU observable R_{K,K^*}. The $b \to s\ell\ell$ observables are influenced by both tree-level and box diagrams involving the virtual exchange of the S LQ as depicted in Fig. 3.4. These phenomena can be parametrised in terms of the Wilson operators, where $O^\ell_9 \propto C^{bs\ell\ell}_9(\bar{s}\gamma^\mu P_L b)(\bar{\ell}\gamma_\mu\ell)$ and $O^\ell_{10} \propto C^{bs\ell\ell}_{10}(\bar{s}\gamma^\mu P_L b)(\bar{\ell}\gamma_\mu\gamma^5\ell)$ for diagrams (b) and (c), and $O'^\ell_9 \propto C'^{bs\ell\ell}_9(\bar{s}\gamma^\mu P_R b)(\bar{\ell}\gamma_\mu\ell)$ and $O'^\ell_{10} \propto C'^{bs\ell\ell}_{10}(\bar{s}\gamma^\mu P_R b)(\bar{\ell}\gamma_\mu\gamma^5\ell)$ for diagrams (a), (d), and (e). Here, the C-factors denote the Wilson coefficients, and $\ell = e, \mu$.

And finally, LQs have not been detected at collider experiments, putting constraints on the couplings and their masses. Given that these states have colour charge, the stringiest collider constraints come from the LHC, putting the LQ mass to be above the TeV scale, or more concretely above 1.5 TeV [252–255], which we take as a lower bound in the numerical analysis.

[7] We note that in the original paper [249], the third diagram shown in Fig. 3.3 is wrong and it has been corrected here. There is no impact on the results, as all relevant diagrams are calculated through automatised algorithms and are only shown here for clarity of presentation.

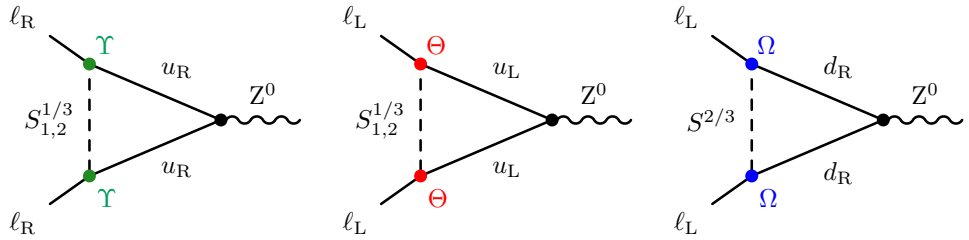

Figure 3.5: Some of the one-loop contributions from the model's LQs to the flavour conserving and non-conserving decays $Z^0 \to \ell\ell'$. There exists additional wave contributions to the one-loop amplitude (see *e.g.* [247]) as well as similar diagrams to those shown Fig. 3.1, which are not shown here but are taken into account in the numerical calculations.

3.4 Numerical methodology

We conducted a parameter space scan considering a wide range of observables as listed in Tab. 3.5. Experimental limits were obtained from the latest Particle Data Group review [256]. For a comprehensive analysis involving numerous observables, we implemented the model in `SARAH` [127], where interaction vertices and one-loop contributions relevant to these observables were determined. Outputs were then generated for numerical evaluation in `SPheno` [257], which calculated the particle spectrum and the necessary Wilson coefficients for use in `flavio` [236]. `SPheno` computes the Wilson coefficients in the Weak Effective Theory basis, with LFV coefficients evaluated at the Z^0 mass scale ($\mu = 91$ GeV) and QFV coefficients at the top mass scale ($\mu = 160$ GeV). Since the LQ mass scale significantly exceeds the scale of the observables analysed, RG running is performed in `flavio` through an interface with the `wilson` [258] package. With these considerations, we constructed the χ^2 function [191]

$$\chi^2 = (\mathcal{O}_{\text{exp}} \odot \mathcal{O}_{\text{th}})^{\text{T}} (\mathbf{\Sigma}_{\text{th}} + \mathbf{\Sigma}_{\text{exp}})^{-1} (\mathcal{O}_{\text{exp}} \odot \mathcal{O}_{\text{th}}) \tag{3.35}$$

utilising the observables outlined in Tab. 3.5. We note that the methodology employed to compute each observable considered in this study is specified in the first column of Tabs. 3.6 and 3.7. In Eq (3.35), $\mathcal{O}_{\text{exp}}$ and $\mathcal{O}_{\text{th}}$ denote vectors of experimental values and model predictions, respectively. $\mathbf{\Sigma}_{\text{exp}}$ represents the experimental covariance, while $\mathbf{\Sigma}_{\text{th}}$ stands for the theoretical covariance. Both covariance matrices can be determined using well-established formulas

$$\mathbf{\Sigma}_{\text{th}} = \sigma_{\text{th}} \rho_{\text{th}} \sigma_{\text{th}}, \quad \mathbf{\Sigma}_{\text{exp}} = \sigma_{\text{exp}} \rho_{\text{exp}} \sigma_{\text{exp}}, \tag{3.36}$$

where σ_{th} (σ_{exp}) are diagonal matrices with entries representing the 1σ theoretical (experimental) errors, and ρ_{th} (ρ_{exp}) are the corresponding theoretical (experimental) correlation matrices. Experimental uncertainties are obtained from relevant literature, while experimental correlations are sourced from available data; those that are unavailable are disregarded. The various uncertainties and correlations have been taken from the references listed in Tab. 3.5.

For theoretical uncertainties we have used `flavio` [236], utilising the function `flavio.np_uncertainty` for each observable of interest. This computation also accounts for potential hadronic uncertainties affecting observables sensitive to them. Theoretical correlations can be computed from the entire dataset using standard statistical methods. In our case, we utilised Pearson's algorithm implemented through the `pandas` package [259].

With these considerations, we perform an inclusive logarithmic scan over the various parameters within the ranges indicated in Tab. 3.3.

After identifying valid solutions within the initial random scan, we utilise these points as seeds for subsequent runs to find new solutions. This involves perturbing around the valid couplings/-masses to discover additional consistent points. It is worth noting that not all Θ and Ω Yukawa

$m_{S_1^{1/3}}$, $m_{S_2^{1/3}}$ (TeV)	g_{HS}, g_{HR}, g'_{HR}	$\lvert\Upsilon\rvert, \lvert\Theta\rvert, \lvert\Omega\rvert$	a_1 (GeV)
$[1.5, 10]$	$[10^{-8}, 4\pi]$	$[10^{-8}, \sqrt{4\pi}]$	$[10^{-8}, 100]$

Table 3.3: Ranges used for the free parameters during the numerical scan. The values for the masses of the SM fields and corresponding mixings were varied within the allowed experimental ranges.

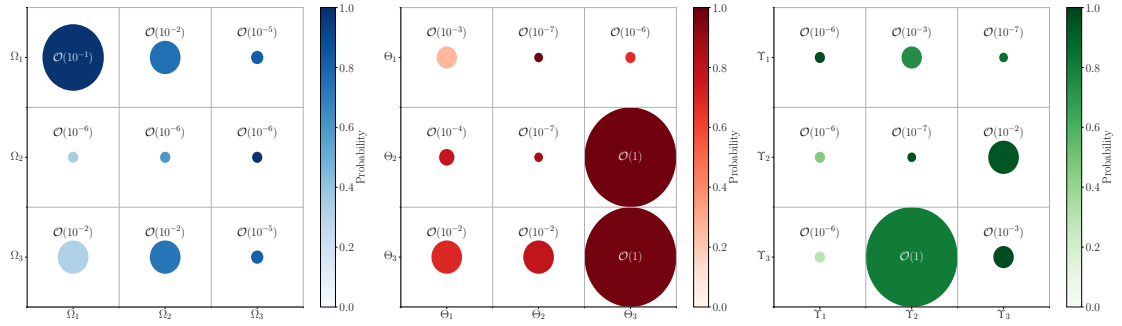

(a) (b) (c)

Figure 3.6: The preferred sizes for each of the LQ Yukawa couplings (a) Ω; (b) Θ; (c) Υ are depicted. The absolute value of each coupling is represented by the radius of the corresponding circle, while the colour gradation indicates the frequency of such magnitudes in the scan. Darker shades signify more preferred sizes, as determined by the probability $\mathcal{P}(X) = N(X)/N_{\text{tot}}$, where $N(X)$ represents the number of points with order X in our data.

---

couplings are free parameters; some are calculated through the inversion procedure of the neutrino mass matrix. Detailed demonstrations of how to numerically implement the inversion procedure for neutrinos/quarks/charged leptons and LQs can be found on the GitHub page (`https://github.com/Mrazi09/LQ-flavour-project`), specifically in the auxiliary `jupyter` notebooks named `Neutrino_inversion.ipynb` and `Read_neutrino.ipynb`, respectively.

Our parameter space scans consider three cases: a) Both a_μ and m_W consistent with the SM, b) Only m_W consistent with the SM, and c) Neither a_μ nor m_W consistent with the SM prediction. In all three scenarios, we account for LFU deviations in R_{D,D^*} while also maintaining control over the remaining constraints (see Tab. 3.5). We utilise quark and charged lepton masses, as well as the CKM and PMNS mixing matrices, as input parameters, allowing them to vary within their two sigma uncertainty. Concerning neutrino masses, we focus on a scenario with normal ordering and three massive states.

3.5 Numerical results from the flavour analysis

Using our χ^2 analysis, we summarise the obtained results in Tab. 3.4, presenting the χ^2 values and the masses of the LQs for each scenario. If we assume that both the mass of the W boson and the anomalous magnetic moment of the muon exhibit SM-like behaviour, denoted as scenario a), then the best-fit point obtained from the scan is

$$
\begin{aligned}
\Upsilon &= \begin{bmatrix} \odot 7.27\times10^{-7} + 4.37\times10^{-7}i & 1.17\times10^{-3} \odot 8.72\times10^{-4}i & \odot 2.58\times10^{-8} \odot 7.65\times10^{-8}i \\ 1.86\times10^{-6} + 1.40\times10^{-7}i & \odot 8.78\times10^{-8} + 6.04\times10^{-8}i & \odot 2.99\times10^{-3} \odot 0.012i \\ \odot 7.74\times10^{-8} \odot 2.70\times10^{-7}i & \odot 0.47 + 2.30i & 7.76\times10^{-4} + 2.68\times10^{-4}i \end{bmatrix}, \\
\Omega &= \begin{bmatrix} 4.83\times10^{-3} + 0.099i & \odot 0.011 + 0.017i & 7.48\times10^{-6} \odot 1.34\times10^{-5}i \\ 2.24\times10^{-6} + 5.57\times10^{-7}i & 6.50\times10^{-7} \odot 6.58\times10^{-7}i & 6.55\times10^{-7} \odot 1.70\times10^{-7}i \\ \odot 0.23 + 0.13i & \odot 8.03\times10^{-4} \odot 1.71\times10^{-3}i & \odot 1.70\times10^{-6} \odot 7.62\times10^{-7}i \end{bmatrix}, \\
\Theta &= \begin{bmatrix} 4.86\times10^{-3} \odot 9.27\times10^{-4}i & 5.83\times10^{-8} + 1.05\times10^{-8}i & \odot 1.82\times10^{-8} + 3.98\times10^{-7}i \\ \odot 1.23\times10^{-4} + 2.24\times10^{-4}i & 1.60\times10^{-8} \odot 4.83\times10^{-8}i & 0.62 + 0.16i \\ 0.013 \odot 0.013i & 1.65\times10^{-3} \odot 4.84\times10^{-3}i & 0.17 + 1.84i \end{bmatrix},
\end{aligned}
\tag{3.37}
$$

with the mixing parameter $a_1 = 36.72$ GeV, this point corresponds to the blue diamond in the scatter plots of Fig. 3.7. However, if we assume the W boson mass to adopt the SM value while the muon a_μ anomaly necessitates a NP explanation, denoted as scenario b), the following best-fit point is obtained

$$\Upsilon = \begin{bmatrix} \odot 2.32\times10^{-7} + 6.39\times10^{-7}i & 6.77\times10^{-7} + 5.52\times10^{-6}i & \odot 9.08\times10^{-9} \odot 6.36\times10^{-8}i \\ 5.26\times10^{-4} \odot 2.49\times10^{-3}i & \odot 6.06\times10^{-8} + 1.78\times10^{-7}i & \odot 0.013 \odot 7.89\times10^{-3}i \\ \odot 6.79\times10^{-8} \odot 2.81\times10^{-7}i & \odot 0.32 + 2.62i & 1.03\times10^{-3} + 2.88\times10^{-4}i \end{bmatrix},$$
$$\Omega = \begin{bmatrix} 0.045 + 0.19i & \odot 1.55\times10^{-3} \odot 2.84\times10^{-3}i & \odot 2.44\times10^{-6} + 2.45\times10^{-6}i \\ 5.39\times10^{-6} + 3.39\times10^{-7}i & 4.24\times10^{-6} \odot 5.81\times10^{-7}i & 1.88\times10^{-6} \odot 1.63\times10^{-7}i \\ 6.60\times10^{-3} + 6.78\times10^{-3}i & \odot 3.44\times10^{-3} \odot 0.015i & \odot 3.41\times10^{-6} + 3.16\times10^{-6}i \end{bmatrix}, \quad (3.38)$$
$$\Theta = \begin{bmatrix} 6.83\times10^{-4} \odot 2.64\times10^{-3}i & 1.08\times10^{-7} \odot 1.83\times10^{-7}i & 1.05\times10^{-6} + 8.80\times10^{-8}i \\ \odot 6.09\times10^{-5} + 3.34\times10^{-4}i & \odot 2.28\times10^{-8} + 2.00\times10^{-8}i & 0.40 + 0.035i \\ 0.024 \odot 6.98\times10^{-3}i & \odot 0.030 \odot 0.061i & 0.24 + 2.04i \end{bmatrix}$$

and $a_1 = 9.85$ GeV. This point corresponds to the cyan diamond in the scatter plots of Fig. 3.7. Finally, if we consider that both the W boson mass and a_μ necessitate a NP explanation, designated as scenario c), then the best-fit point is

$$\Upsilon = \begin{bmatrix} \odot 5.90\times10^{-7} + 8.26\times10^{-7}i & 4.84\times10^{-6} + 4.70\times10^{-8}i & \odot 1.35\times10^{-8} \odot 3.26\times10^{-8}i \\ 3.19\times10^{-4} \odot 2.55\times10^{-3}i & \odot 3.34\times10^{-8} + 1.45\times10^{-7}i & \odot 7.59\times10^{-3} \odot 0.012i \\ \odot 1.52\times10^{-7} \odot 9.06\times10^{-8}i & \odot 0.15 + 2.51i & 3.00\times10^{-4} + 4.21\times10^{-4}i \end{bmatrix},$$
$$\Omega = \begin{bmatrix} 0.057 + 0.15i & \odot 3.2\times10^{-3} + 3.44\times10^{-4}i & \odot 5.83\times10^{-7} \odot 6.36\times10^{-8}i \\ 3.49\times10^{-6} + 2.24\times10^{-7}i & 2.34\times10^{-6} \odot 3.97\times10^{-7}i & 1.35\times10^{-6} \odot 1.34\times10^{-7}i \\ \odot 0.025 \odot 4.25\times10^{-3}i & \odot 8.79\times10^{-3} \odot 0.017i & 1.72\times10^{-6} + 7.29\times10^{-6}i \end{bmatrix}, \quad (3.39)$$
$$\Theta = \begin{bmatrix} 1.35\times10^{-3} \odot 2.98\times10^{-3}i & 1.44\times10^{-7} \odot 9.32\times10^{-8}i & 7.89\times10^{-7} + 2.15\times10^{-7}i \\ \odot 5.44\times10^{-5} + 2.73\times10^{-4}i & \odot 1.59\times10^{-8} + 1.96\times10^{-8}i & 0.58 + 0.058i \\ 0.022 + 5.76\times10^{-3}i & \odot 0.017 \odot 0.028i & 0.41 + 2.09i \end{bmatrix},$$

with $a_1 = 6.69$ GeV. This point correspond to the red diamond in the scatter plots of Fig. 3.7. These benchmarks were determined by minimising the χ^2 function in Eq. (3.35), whose input observables are showcased in Tab. 3.5. In Tabs. 3.6 and 3.7 we indicate the predictions for the observables for each of the benchmark scenarios. It is noteworthy that in all three cases, the model predictions offer a superior fit compared to the SM limit. The main results from our numerical scan are highlighted in Figs. 3.6 and 3.7. In Fig. 3.6, we demonstrate the preferred scales that effectively address the studied anomalies while remaining consistent with neutrino physics and flavour constraints. Darker shades provide more conclusive estimates, while lighter ones allow for some dispersion. This information, coupled with the best-fit points, holds significance in proposing searches for LQs at colliders. Notably, considering $\Theta_{\mu t} \sim \mathcal{O}(1)$, the $\mu^+\mu^- \to t\bar{t}$ t-channel $S^{1/3}$ LQ exchange emerges as a compelling benchmark scenario, suggesting a potential physics case for future muon colliders. Regarding the $S^{2/3}$ LQ, its couplings to d-quarks can reach considerable magnitudes, such as $\Omega_{ed} \sim \Omega_{\tau d} \sim \mathcal{O}(10^{-1})$. This could be sufficiently large for testing at the LHC in the t-channel LQ exchange for ee, $\tau\tau$, and $e\tau$ pair production. Additionally, such LQs can be sought after at upcoming hadronic machines like the High-Energy LHC or the Future Circular Collider (FCC). Particularly, for the best-fit point (3.39), the future 50 TeV FCC-eh collider presents an opportunity for the s-channel process $ed \to S^{2/3} \to t\mu$.

In Fig. 3.7, we illustrate that the data for all displayed observables align well with our model. Specifically, the three best-fit points are marked as coloured polygons, with blue, cyan, and red denoting scenarios a), b), and c) respectively. Panel (a) illustrates the simultaneous reconciliation of R_{D,D^*} and $R_K^{\nu\nu}$, as also depicted in panel (f). Panel (c) reveals a linear correlation between R_{K,K^*} observables, consistent with previous literature [191, 260]. Furthermore, $B_{s,0} \to \mu\mu$ is well-fitted with a strong correlation with R_{K,K^*}, as expected. In panel (d), we observe that the combination of $\Upsilon_{\mu t}$ and $\Theta_{\mu t}$ serves as the dominant source contributing to a_μ, given that these couplings induce chirality

	χ^2/d.o.f	$\chi^{2,\mathrm{SM}}$/d.o.f	$(m_{S_1^{1/3}}, m_{S_2^{1/3}}, m_{S^{2/3}})$ TeV
Scenario a)	1.16	1.26	(1.53 , 7.02 , 7.00)
Scenario b)	1.17	1.66	(1.58 , 4.50 , 4.52)
Scenario c)	1.37	2.46	(1.63 , 3.30 , 3.35)

Table 3.4: The χ^2/d.o.f for the obtained best-fit points (first column) and for the SM limit (second column) with d.o.f = 45 are presented. The LQ masses (in TeV) are indicated in the third column.

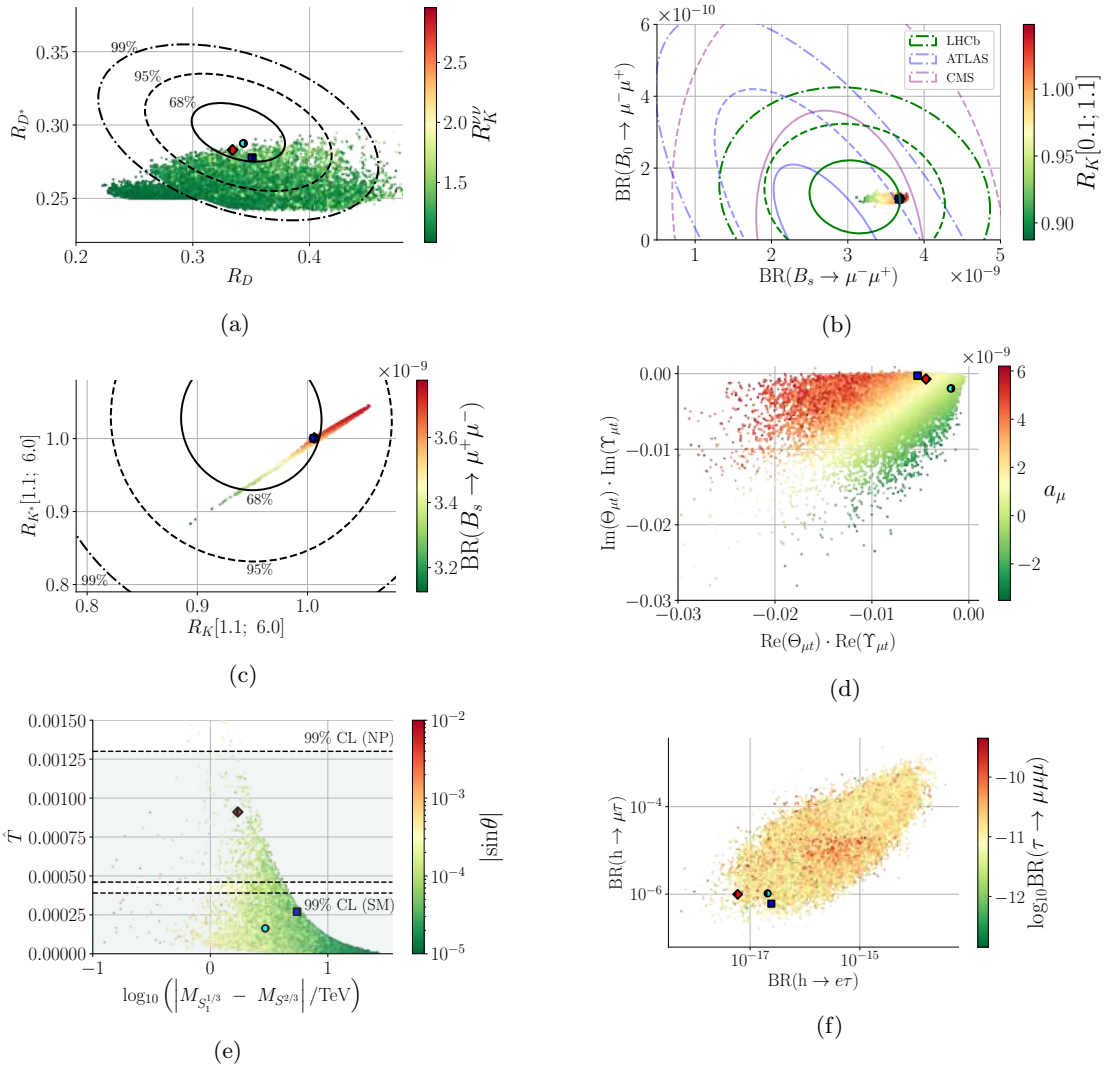

Figure 3.7: Scatter plots of selected observables analysed in this work. In (a) we plot the R_{D^*} as a function of R_D with $R_K^{\nu\nu}$ in the colour scale. In (b), the branching ratios of $B_0 \to \mu^-\mu^+$ and $B_s \to \mu^-\mu^+$, with $R_K[1.1;\ 6.0]$ in the colour scale. In (c) we plot R_{K^*} vs. R_K with $\mathrm{BR}(B_s \to \mu\mu)$ in the colour scale. In (d) the product of the real and imaginary parts of $\Upsilon_{\mu t}\Theta_{\mu t}$ are shown with a_μ in the colour gradation. In (e) the $\hat{T}$ parameter as function of the logarithm of the mass difference between the masses of $S_1^{1/3}$ and $S^{2/3}$ is presented, where the colour scale represents the LQ mixing angle and in (f) we show $\mathrm{BR}(h \to \mu\tau)$ versus $\mathrm{BR}(h \to e\tau)$ with $\log_{10}\mathrm{BR}(\tau \to \mu\mu\mu)$ in the colour axis. Areas of phenomenological interest lie inside the contours. For the $\hat{T}$ parameter, we show the areas of interest for both NP and SM-like cases. The relevant range for a_μ lies within $(251 \pm 59) \times 10^{-11}$, $\mathrm{BR}(h \to \mu\tau) < 2.5 \times 10^{-3}$, $\mathrm{BR}(h \to \mu\tau) < 4.7 \times 10^{-3}$, $R_K^{\nu\nu} < 4.35$ and $\mathrm{BR}(\tau \to \mu\mu\mu) < 2.1 \times 10^{-8}$. The best fit points are marked with a blue square (scenario a), a cyan circle (scenario b) and a red diamond (scenario c).

---

flipping of the top quark in the internal propagator. Panel (e) illustrates how the $\hat{T}$ parameter depends on the mass difference between the LQs originating from the doublet. The colour indicates the LQ mixing, with the majority of the generated points indicating that $S_1^{1/3}$ essentially represents the S singlet, as highlighted by the yellow and green regions.

Observable	Experimental measurement
$(g \odot 2)_\mu$	$(251 \pm 59) \times 10^{-11}$ [183]
$\hat{T}$	$(0.88 \pm 0.14) \times 10^{-3}$ [193]
$R_K[1.1, 6.0]$	$0.949^{+0.042+0.022}_{-0.041-0.022}$ [261]
$R_{K^*}[1.1, 6.0]$	$1.027^{+0.072+0.027}_{-0.068-0.026}$ [261]
$R_K[0.1, 1.1]$	$0.994^{+0.090+0.029}_{-0.082-0.027}$ [261]
$R_{K^*}[0.1, 1.1]$	$0.927^{+0.093+0.036}_{-0.087-0.035}$ [261]
R_D	$0.340 \pm 0.027 \pm 0.013$ [262]
R_{D^*}	$0.295 \pm 0.011 \pm 0.008$ [262]
BR$(h \to e\mu)$	$< 6.1 \times 10^{-5}$ [95% CL] [256]
BR$(h \to e\tau)$	$< 4.7 \times 10^{-3}$ [95% CL] [256]
BR$(h \to \mu\tau)$	$< 2.5 \times 10^{-3}$ [95% CL] [256]
BR$(\mu \to e\gamma)$	$< 4.2 \times 10^{-13}$ [90% CL] [256]
BR$(\mu \to eee)$	$< 1.0 \times 10^{-12}$ [90% CL] [256]
BR$(\tau \to e\gamma)$	$< 3.3 \times 10^{-8}$ [90% CL] [256]
BR$(\tau \to \mu\gamma)$	$< 4.4 \times 10^{-8}$ [90% CL] [256]
BR$(\tau \to eee)$	$< 2.7 \times 10^{-8}$ [90% CL] [256]
BR$(\tau \to e\mu\mu)$	$< 2.7 \times 10^{-8}$ [90% CL] [256]
BR$(\tau \to \mu ee)$	$< 1.5 \times 10^{-8}$ [90% CL] [256]
BR$(\tau \to \mu\mu\mu)$	$< 2.1 \times 10^{-8}$ [90% CL] [256]
BR$(Z \to \mu e)$	$< 7.5 \times 10^{-7}$ [95% CL] [256]
BR$(Z \to \tau e)$	$< 9.8 \times 10^{-6}$ [95% CL] [256]
BR$(Z \to \mu\tau)$	$< 1.2 \times 10^{-5}$ [95% CL] [256]
BR$(\tau \to \pi e)$	$< 8.0 \times 10^{-8}$ [90% CL] [256]
BR$(\tau \to \pi\mu)$	$< 1.1 \times 10^{-7}$ [90% CL] [256]
BR$(\tau \to \phi e)$	$< 3.1 \times 10^{-8}$ [90% CL] [256]
BR$(\tau \to \phi\mu)$	$< 8.4 \times 10^{-8}$ [90% CL] [256]
BR$(\tau \to \rho e)$	$< 1.8 \times 10^{-8}$ [90% CL] [256]
BR$(\tau \to \rho\mu)$	$< 1.2 \times 10^{-8}$ [90% CL] [256]
d_e	$< 1.1 \times 10^{-29}$ e.cm [90% CL] [256]
d_μ	$< 1.8 \times 10^{-19}$ e.cm [95% CL] [256]
d_τ	$< (1.15 \pm 1.70) \times 10^{-17}$ e.cm [95% CL] [263]
BR$(B^0 \to \mu\mu)$	$(0.56 \pm 0.70) \times 10^{-10}$ [191]
BR$(B_s \to \mu\mu)$	$(2.93 \pm 0.35) \times 10^{-9}$ [191]
R$(B \to \chi_s\gamma)$	1.009 ± 0.075
$R_K^{\nu\nu}$	< 4.65 [95% CL] [264]
$R_{K^*}^{\nu\nu}$	< 3.22 [95% CL] [264]
$\lvert\text{Re } \delta g_R^e\rvert$	$\leq 2.9 \times 10^{-4}$ [246, 265]
$\lvert\text{Re } \delta g_L^e\rvert$	$\leq 3.0 \times 10^{-4}$ [246, 265]
$\lvert\text{Re } \delta g_R^\mu\rvert$	$\leq 1.3 \times 10^{-3}$ [246, 265]
$\lvert\text{Re } \delta g_L^\mu\rvert$	$\leq 1.1 \times 10^{-3}$ [246, 265]
$\lvert\text{Re } \delta g_R^\tau\rvert$	$\leq 6.2 \times 10^{-4}$ [246, 265]
$\lvert\text{Re } \delta g_L^\tau\rvert$	$\leq 5.8 \times 10^{-4}$ [246, 265]
R(ϵ_k)	1.234 ± 0.144
R(ΔM_d)	0.838 ± 0.109
R(ΔM_s)	0.935 ± 0.054
R$(\text{Re}(\epsilon'/\epsilon))$	0.868 ± 0.496
$Q_W(p^+)$	0.0719 ± 0.045
$Q_W(\text{Cs}^{133})$	$\odot 72.82 \pm 0.42$

Observable	Experimental measurement
$F_L(B^+ \to K\mu\mu)$	$0.34 \pm 0.10 \pm 0.06$ [266]
$S_3(B^+ \to K\mu\mu)$	$0.14^{+0.15+0.02}_{-0.14-0.02}$ [266]
$S_4(B^+ \to K\mu\mu)$	$\odot 0.04^{+0.17+0.04}_{-0.16-0.04}$ [266]
$S_5(B^+ \to K\mu\mu)$	$0.24^{+0.12+0.04}_{-0.15-0.04}$ [266]
$A_{FB}(B^+ \to K\mu\mu)$	$\odot 0.05 \pm 0.12 \pm 0.03$ [266]
$S_7(B^+ \to K\mu\mu)$	$\odot 0.01^{+0.19+0.01}_{-0.17-0.01}$ [266]
$S_8(B^+ \to K\mu\mu)$	$0.21^{+0.22+0.05}_{-0.20-0.05}$ [266]
$S_9(B^+ \to K\mu\mu)$	$0.28^{+0.25+0.06}_{-0.12-0.06}$ [266]
$P_1(B^+ \to K\mu\mu)$	$0.44^{+0.38+0.11}_{-0.40-0.11}$ [266]
$P_2(B^+ \to K\mu\mu)$	$\odot 0.05 \pm 0.12 \pm 0.03$ [266]
$P_3(B^+ \to K\mu\mu)$	$\odot 0.42^{+0.20+0.05}_{-0.21-0.05}$ [266]
$P_4'(B^+ \to K\mu\mu)$	$\odot 0.092^{+0.36+0.12}_{-0.35-0.12}$ [266]
$P_5'(B^+ \to K\mu\mu)$	$0.51^{+0.30+0.12}_{-0.28-0.12}$ [266]
$P_6'(B^+ \to K\mu\mu)$	$\odot 0.02^{+0.40+0.06}_{-0.34-0.06}$ [266]
$P_8'(B^+ \to K\mu\mu)$	$\odot 0.45^{+0.50+0.09}_{-0.39-0.09}$ [266]
$F_L(B^0 \to K\mu\mu)$	$0.255 \pm 0.032 \pm 0.007$ [267]
$S_3(B^0 \to K\mu\mu)$	$0.034 \pm 0.044 \pm 0.003$ [267]
$S_4(B^0 \to K\mu\mu)$	$0.059 \pm 0.050 \pm 0.004$ [267]
$S_5(B^0 \to K\mu\mu)$	$0.227 \pm 0.041 \pm 0.008$ [267]
$A_{FB}(B^0 \to K\mu\mu)$	$\odot 0.004 \pm 0.040 \pm 0.004$ [267]
$S_7(B^0 \to K\mu\mu)$	$0.006 \pm 0.042 \pm 0.002$ [267]
$S_8(B^0 \to K\mu\mu)$	$\odot 0.003 \pm 0.051 \pm 0.001$ [267]
$S_9(B^0 \to K\mu\mu)$	$\odot 0.055 \pm 0.041 \pm 0.002$ [267]
$P_1(B^0 \to K\mu\mu)$	$0.090 \pm 0.119 \pm 0.009$ [267]
$P_2(B^0 \to K\mu\mu)$	$\odot 0.003 \pm 0.038 \pm 0.003$ [267]
$P_3(B^0 \to K\mu\mu)$	$\odot 0.073 \pm 0.057 \pm 0.003$ [267]
$P_4'(B^0 \to K\mu\mu)$	$\odot 0.135 \pm 0.118 \pm 0.003$[267]
$P_5'(B^0 \to K\mu\mu)$	$\odot 0.521 \pm 0.095 \pm 0.024$ [267]
$P_6'(B^0 \to K\mu\mu)$	$\odot 0.015 \pm 0.094 \pm 0.007$ [267]
$P_8'(B^0 \to K\mu\mu)$	$\odot 0.007 \pm 0.122 \pm 0.002$ [267]
R$(K^+ \to \pi^0\mu^+\nu)$	0.989 ± 0.016
R$(K^+ \to \pi^0 e^+\nu)$	0.988 ± 0.014
R$(K_L^0 \to \pi^+\mu^-\nu)$	0.997 ± 0.011
R$(K_L^0 \to \pi^+ e^-\nu)$	0.991 ± 0.029
R$(K_S^0 \to \pi^\pm e^\mp\nu)$	0.982 ± 0.015
R$(K_L^0 \to \mu^+\mu^-)$	0.918 ± 0.158
R$(K_L^0 \to e^+e^-)$	1.000 ± 0.598
BR$(K_L^0 \to e^\mp\mu^\pm)$	$< 4.7 \times 10^{-12}$ [90% CL] [256]
BR$(K_S^0 \to \mu^+\mu^-)$	$< 8.0 \times 10^{-10}$ [90% CL] [256]
BR$(K_S^0 \to e^+e^-)$	$< 9.0 \times 10^{-12}$ [90% CL] [256]
R$(K^+ \to \mu^+\nu)$	1.008 ± 0.015
R$(K^+ \to e^+\nu)$	1.014 ± 0.016
R$(K^+ \to \pi^+\nu\nu)$	1.840 ± 1.202
BR$(K_L^0 \to \pi^0\nu\nu)$	$< 3.0 \times 10^{-9}$ [90% CL] [256]

Table 3.5: Set of observables used as input for the χ^2 function, as well as the experimental measured value. The observables F_L, A_{FB}, S_i, P_i and P_i' are relative to the $[0.10, 0.98]$ GeV^2 q^2 bins. Observables starting with "R" are defined as the ratio between the experimental value for the observable, taken from [256] and the SM prediction, determined in `flavio`. The total uncertainty is taken by error propagation, taking into account both the experimental and theoretical errors, with the latter determined also in `flavio`.

Observable	Theoretical prediction: (3.37)	Theoretical prediction: (3.38)	Theoretical prediction: (3.39)
a_μ (sph)	$\odot 5.891 \times 10^{-11}$	2.649×10^{-9}	1.879×10^{-9}
$\hat{T}$ (sph)	0.0002702	0.0001631	0.0009105
$R_K[1.1, 6.0]$ (fla)	1.006	1.006	1.006
$R_{K*}[1.1, 6.0]$ (fla)	1.000	1.001	1.001
$R_K[0.1, 1.1]$ (fla)	0.9987	0.9984	0.999
$R_{K*}[0.1, 1.1]$ (fla)	1.006	1.006	1.006
R_D (fla)	0.3508	0.3434	0.334
R_{D^*} (fla)	0.2776	0.2875	0.283
BR($h \to e\mu$) (sph)	3.008×10^{-18}	9.692×10^{-19}	5.98×10^{-19}
BR($h \to e\tau$) (sph)	2.435×10^{-17}	2.086×10^{-17}	5.931×10^{-18}
BR($h \to \mu\tau$) (sph)	6.072×10^{-7}	1.039×10^{-6}	9.904×10^{-7}
BR($\mu \to e\gamma$) (fla)	3.074×10^{-16}	2.916×10^{-15}	1.44×10^{-15}
BR($\mu \to eee$) (fla)	2.456×10^{-18}	1.953×10^{-17}	9.509×10^{-18}
BR($\tau \to e\gamma$) (fla)	1.925×10^{-17}	1.17×10^{-17}	1.479×10^{-17}
BR($\tau \to \mu\gamma$) (fla)	6.713×10^{-9}	3.294×10^{-9}	4.864×10^{-9}
BR($\tau \to eee$) (sph)	2.611×10^{-14}	5.161×10^{-15}	3.055×10^{-15}
BR($\tau \to e\mu\mu$) (sph)	1.779×10^{-14}	3.516×10^{-15}	2.089×10^{-15}
BR($\tau \to \mu ee$) (sph)	5.824×10^{-27}	3.924×10^{-28}	3.579×10^{-28}
BR($Z \to \mu e$) (sph)	7.003×10^{-21}	9.718×10^{-21}	1.074×10^{-20}
BR($Z \to \tau e$) (sph)	1.265×10^{-15}	2.605×10^{-16}	1.007×10^{-16}
BR($Z \to \mu\tau$) (sph)	4.873×10^{-8}	2.244×10^{-8}	4.64×10^{-8}
BR($\tau \to \pi e$) (fla)	3.94×10^{-12}	1.173×10^{-13}	1.631×10^{-12}
BR($\tau \to \pi\mu$) (fla)	1.401×10^{-22}	7.932×10^{-22}	3.776×10^{-22}
BR($\tau \to \phi e$) (fla)	1.349×10^{-16}	3.556×10^{-16}	1.534×10^{-15}
BR($\tau \to \phi\mu$) (fla)	1.869×10^{-12}	9.174×10^{-13}	1.354×10^{-12}
BR($\tau \to \rho e$) (fla)	8.828×10^{-12}	2.743×10^{-13}	4.809×10^{-12}
BR($\tau \to \rho\mu$) (fla)	1.688×10^{-11}	8.282×10^{-12}	1.223×10^{-11}
d_e (sph)	3.283×10^{-33}	2.75×10^{-32}	7.79×10^{-33}
d_μ (sph)	1.248×10^{-22}	5.388×10^{-23}	1.094×10^{-22}
d_τ (sph)	2.446×10^{-23}	1.638×10^{-23}	1.999×10^{-24}
BR($B^0 \to \mu\mu$) (fla)	1.139×10^{-10}	1.14×10^{-10}	1.148×10^{-10}
BR($B_s \to \mu\mu$) (fla)	3.673×10^{-9}	3.685×10^{-9}	3.679×10^{-9}
R($B \to \chi_s\gamma$) (fla)	1.000	1.000	1.000
$R_K^{\nu\nu}$ (fla)	1.793	1.227	1.476
$R_{K^*}^{\nu\nu}$ (fla)	1.793	1.227	1.476
$\lvert\text{Re } \delta g_R^e\rvert$ (ind)	4.902×10^{-8}	$\odot 8.815 \times 10^{-8}$	7.09×10^{-8}
$\lvert\text{Re } \delta g_L^e\rvert$ (ind)	6.788×10^{-9}	5.207×10^{-8}	6.277×10^{-8}
$\lvert\text{Re } \delta g_R^\mu\rvert$ (ind)	3.891×10^{-9}	6.56×10^{-7}	1.456×10^{-7}
$\lvert\text{Re } \delta g_L^\mu\rvert$ (ind)	0.002152	0.002661	0.002322
$\lvert\text{Re } \delta g_R^\tau\rvert$ (ind)	0.0005011	0.0005977	0.0005954
$\lvert\text{Re } \delta g_L^\tau\rvert$ (ind)	3.732×10^{-8}	1.049×10^{-8}	6.595×10^{-9}
R(ϵ_k) (fla)	1.135	1.326	1.107
R(ΔM_d) (fla)	0.9361	0.7878	1.08
R(ΔM_s) (fla)	0.8263	1.01	0.9117
R(Re(ϵ'/ϵ)) (fla)	1.177	1.013	1.425
$Q_W(p^+)$ (ind)	0.071	0.071	0.071
$Q_W(\text{Cs}^{133})$ (ind)	$\odot 73.33$	$\odot 73.33$	$\odot 73.33$

Table 3.6: Theoretical predictions for the each of the benchmarks. In the first column we indicate how each observable is computed, with `fla` being `flavio`, `sph` being `SPheno` and `ind` indicates that is based in our own implementation.

Observable	Theoretical prediction: (3.37)	Theoretical prediction: (3.38)	Theoretical prediction: (3.39)
ϕ_s (fla)	$\odot$0.0092	$\odot$0.00296	$\odot$0.0585
$A_{CP}(B^0 \to K^{*0}\mu\mu)$ (fla)	0.000167	0.000172	0.000187
$A_{CP}(B^+ \to K^+\mu\mu)$ (fla)	0.001771	0.001774	0.001791
$A_{CP}(B \to \chi_{s+d}\gamma)$ (fla)	3.603×10^{-7}	7.202×10^{-7}	6.588×10^{-8}
$F_L(B^+ \to K\mu\mu)$ (fla)	0.3041	0.304	0.3042
$S_3(B^+ \to K\mu\mu)$ (fla)	0.01081	0.0108	0.01081
$S_4(B^+ \to K\mu\mu)$ (fla)	0.08939	0.08907	0.08927
$S_5(B^+ \to K\mu\mu)$ (fla)	0.2591	0.2597	0.2593
$A_{FB}(B^+ \to K\mu\mu)$ (fla)	$\odot$0.097	$\odot$0.09717	$\odot$0.09707
$S_7(B^+ \to K\mu\mu)$ (fla)	$\odot$0.0179	$\odot$0.01793	$\odot$0.01792
$S_8(B^+ \to K\mu\mu)$ (fla)	$\odot$0.01217	$\odot$0.01215	$\odot$0.01216
$S_9(B^+ \to K\mu\mu)$ (fla)	$\odot$0.0007138	$\odot$0.0007131	$\odot$0.0007135
$P_1(B^+ \to K\mu\mu)$ (fla)	0.04543	0.04538	0.04541
$P_2(B^+ \to K\mu\mu)$ (fla)	$\odot$0.1359	$\odot$0.1361	$\odot$0.136
$P_3(B^+ \to K\mu\mu)$ (fla)	0.0015	0.001498	0.001499
$P'_4(B^+ \to K\mu\mu)$ (fla)	0.235	0.2341	0.2346
$P'_5(B^+ \to K\mu\mu)$ (fla)	0.6811	0.6826	0.6816
$P'_6(B^+ \to K\mu\mu)$ (fla)	$\odot$0.04706	$\odot$0.04713	$\odot$0.04709
$P'_8(B^+ \to K\mu\mu)$ (fla)	$\odot$0.03198	$\odot$0.03193	$\odot$0.03196
$F_L(B^0 \to K\mu\mu)$ (fla)	0.2972	0.2971	0.2973
$S_3(B^0 \to K\mu\mu)$ (fla)	0.01083	0.01082	0.01082
$S_4(B^0 \to K\mu\mu)$ (fla)	0.09582	0.09549	0.0957
$S_5(B^0 \to K\mu\mu)$ (fla)	0.2605	0.2611	0.2608
$A_{FB}(B^0 \to K\mu\mu)$ (fla)	$\odot$0.09668	$\odot$0.09686	$\odot$0.09675
$S_7(B^0 \to K\mu\mu)$ (fla)	$\odot$0.02056	$\odot$0.02059	$\odot$0.02057
$S_8(B^0 \to K\mu\mu)$ (fla)	$\odot$0.002203	$\odot$0.002182	$\odot$0.002197
$S_9(B^0 \to K\mu\mu)$ (fla)	$\odot$0.0006991	$\odot$0.0006985	$\odot$0.0006988
$P_1(B^0 \to K\mu\mu)$ (fla)	0.04449	0.04444	0.04447
$P_2(B^0 \to K\mu\mu)$ (fla)	$\odot$0.1324	$\odot$0.1326	$\odot$0.1325
$P_3(B^0 \to K\mu\mu)$ (fla)	0.001436	0.001434	0.001436
$P'_4(B^0 \to K\mu\mu)$ (fla)	0.2519	0.2511	0.2516
$P'_5(B^0 \to K\mu\mu)$ (fla)	0.685	0.6864	0.6855
$P'_6(B^0 \to K\mu\mu)$ (fla)	$\odot$0.05405	$\odot$0.05413	$\odot$0.05408
$P'_8(B^0 \to K\mu\mu)$ (fla)	$\odot$0.005791	$\odot$0.005738	$\odot$0.005776
$C_9^{bs\mu\mu}$ (fla)	0.02261	0.0142	0.02012
$C_{10}^{bs\mu\mu}$ (fla)	0.0009718	$\odot$0.00568	$\odot$0.002634
$C_9^{\prime bs\mu\mu}$ (fla)	1.007×10^{-7}	3.501×10^{-8}	6.651×10^{-8}
$C_{10}^{\prime bs\mu\mu}$ (fla)	$\odot 1.007 \times 10^{-7}$	$\odot 3.496 \times 10^{-8}$	$\odot 6.645 \times 10^{-8}$
C_9^{bsee} (fla)	$\odot 1.714 \times 10^{-6}$	$\odot 1.652 \times 10^{-7}$	$\odot 5.143 \times 10^{-7}$
C_{10}^{bsee} (fla)	1.561×10^{-6}	1.379×10^{-7}	4.929×10^{-7}
$R(K^+ \to \pi^0\mu^+\nu)$ (fla)	1.000	1.000	1.000
$R(K^+ \to \pi^0 e^+\nu)$ (fla)	1.000	1.000	1.000
$R(K_L^0 \to \pi^+\mu^-\nu)$ (fla)	1.000	1.000	1.000
$R(K_L^0 \to \pi^+ e^-\nu)$ (fla)	1.000	1.000	1.000
$R(K_S^0 \to \pi^\pm e^\mp\nu)$ (fla)	1.000	1.000	1.000
$R(K_L^0 \to \mu^+\mu^-)$ (fla)	1.001	1.000	1.000
$R(K_L^0 \to e^+e^-)$ (fla)	0.9472	1.058	1.021
$BR(K_L^0 \to e^\mp\mu^\pm)$ (fla)	4.822×10^{-14}	6.372×10^{-16}	3.13×10^{-15}
$BR(K_S^0 \to \mu^+\mu^-)$ (fla)	5.168×10^{-12}	5.172×10^{-12}	5.169×10^{-12}
$BR(K_S^0 \to e^+e^-)$ (fla)	1.684×10^{-16}	1.637×10^{-16}	1.762×10^{-16}
$R(K^+ \to \mu^+\nu)$ (fla)	1.000	1.000	1.000
$R(K^+ \to e^+\nu)$ (fla)	1.000	1.000	1.000
$R(K^+ \to \pi^+\nu\nu)$ (fla)	1.261	0.8588	1.939
$BR(K_L^0 \to \pi^0\nu\nu)$ (fla)	2.573×10^{-10}	4.059×10^{-11}	2.184×10^{-10}

Table 3.7: Theoretical predictions for the each of the benchmarks. In the first column we indicate how each observable is computed, with `fla` being `flavio`. The computation of ϕ_s observable is not available in the current version of `flavio` and needs to be added. The necessary functions for the implementation can be found in the GitHub page.

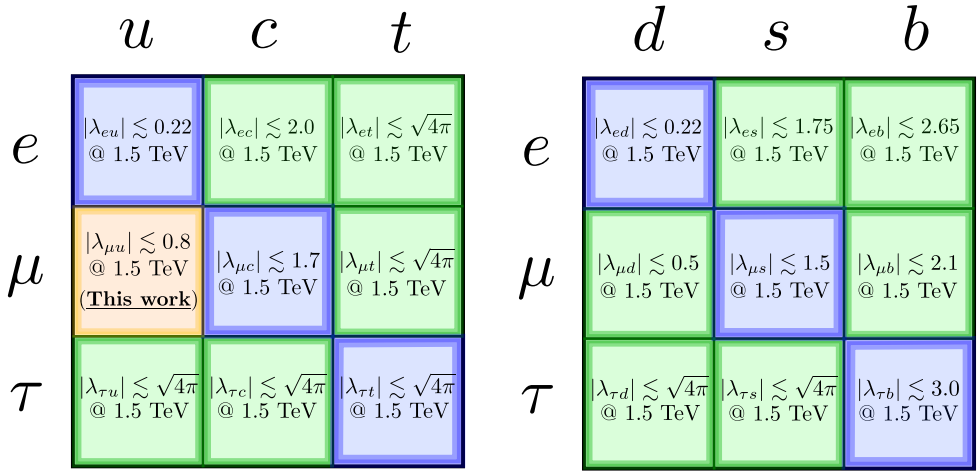

Figure 3.8: Allowed constraints for the LQ Yukawa couplings based on the current LHC data, established for a benchmark LQ mass of 1.5 TeV. These limits are derived from experimental data encompassing both single and pair production searches, as well as from recasts of supersymmetric analyses. Additionally, constraints from atomic parity violation are considered, although they are only applicable for couplings between the electron and up/down quarks. These limits are adapted from Ref. [268].

3.6 Non-resonant production of LQs at the LHC

Now that we have demonstrated the compatibility of neutrino properties, flavour observables, W mass, and other pertinent phenomenological constraints within this simple LQ framework, the natural progression is to then ask about their observability, whether at colliders or elsewhere. This question is particularly intriguing given that a significant portion of the parameter space leads to very high masses (exceeding 10 TeV), rendering their direct detection even more challenging. Indeed, the majority of existing LQ searches conducted at the LHC primarily focus on resonant pair-production channels, followed by the subsequent decay of the LQs. However, the production of pairs of heavy particles diminishes rapidly with increasing mass for a fixed CM energy. Consequently, this scaling with LQ mass implies that the analysis quickly loses discriminating power as the mass approaches the TeV scale. Specifically, based on the current status at the LHC, we have lower bounds of 1.5 TeV for scalar LQs and 2.0 TeV for vector LQs [252, 254, 269–277]. These searches are driven, in part, by the fact that LQs are coloured particles, with a preferred production in hadron-hadron collisions via the fusion of quarks and gluons. Furthermore, these searches have been spurred by recent anomalous findings in the flavour sector, such as the R_{D,D^*} anomaly [185–190], as well as anomalous results in B-meson decays in the muon channel [266, 267, 278]. Indeed, the exploration of LQ phenomenology remains a vibrant area of research in the quest for NP at hadron colliders.

Non-resonant production, involving a virtual exchange of LQ in the t-channel, exhibits reduced sensitivity to mass, with the cross-section scaling proportionally to λ^2, where λ represents the LQ

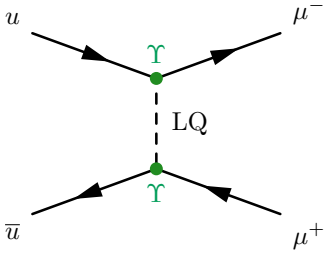

Figure 3.9: Topology for the non-resonant production of scalar LQs with a muon pair in the final state. The initial state $u\bar{u}$ is any allowed combination of up-type quarks coming from the colliding protons.

Scalar	Decay	Mass (GeV)	Comments	Refs.
$S^{1/3}$	$S^{1/3} \to t\ell/b\nu$	$[300, 1440]$	$\ell = e, \mu$. BR-dependent exclusions also provided. Vector LQs also studied.	[269]
	$S^{1/3} \to t\tau/b\nu$	$[400, 1250]$ $[200, 800]$	BR-dependent exclusions also provided. Vector LQs studied in [252].	[252] [270]
	$S^{1/3} \to t\ell$	$[900, 1470]$	$\ell = e, \mu$. BR-dependent exclusions also provided.	[271]
	$S^{1/3} \to ue/\nu d$	$[200, 1435]$	BR-dependent exclusions also provided. Assumes 1st-generation LQ.	[272]
$S^{2/3}$	$S^{2/3} \to u\nu_e$	$[1000, 2000]$	Single production with coupling dependent exclusions. Assumes 1st-generation LQ.	[273]
	$S^{2/3} \to \mu s$	$[800, 1500]$	Exclusions depend on the mass of a DM particle. 2nd-generation LQ.	[274]
	$S^{2/3} \to b\tau$	$[250, 1020]$ $[200, 740]$	BR-dependent exclusions also provided. Assumes 3rd-generation LQ. Single production is considered in [275]	[254] [275]
	$S^{2/3} \to t\nu/b\ell$	$[300, 1390]$	$\ell = e, \mu$. BR-dependent exclusions also provided. Vector LQs also studied.	[269]
	$S^{2/3} \to t\nu/b\tau$	$[980, 1730]$ $[400, 1260]$ $[400, 1220]$ $[400, 1240]$ $[200, 800]$	BR-dependent exclusions also provided. Assumes 3rd-generation LQ.	[276] [277] [253] [282] [270]
S	$S \to q\ell$	$[400, 1800]$	$\ell = e, \mu$ and $q = u, d, c, s, b$. BR-dependent exclusions also provided.	[283]
	$b\bar{s} \to \ell^+\ell^-$	< 2400	$\ell = e, \mu$. Constraints on four-fermion current. Constraint in terms of mass/coupling ratio.	[284]
	$S \to \tau\nu$	< 5900 democratic	LQ exchange in the $t-$channel. Constraints strongly depend on couplings (see Tab. 1)	[285]
	$S \to \mu j$	$[200, 1530]$	j is a light jet (up or down). BR dependent constraints also provided	[286]

Table 3.8: A summary of the latest searches conducted in recent years by both the ATLAS and CMS experiments at the LHC for scalar-type LQs. $S^{1/3}$ denotes a LQ with a charge of $1/3e$, while $S^{2/3}$ represents a LQ with a charge of $2/3e$. We use S to refer to searches where the electric charge of the LQ is either not relevant or not specified.

Yukawa coupling to the fermions engaged in the process[8]. Furthermore, the examination of reactions involving virtual LQ states propagating in the t-channel presents an enticing avenue to extensively explore the model parameter space across a broader phase space region [279–281], concurrently imposing constraints on the couplings of the LQs to the SM states.

For this reason, in this thesis, we delve into the collider implications of the simplest and most straightforward $2 \to 2$ process involving scalar LQs in the t-channel and resulting in the $\mu^+\mu^-$ final state (whose topology is shown Fig. 3.9), motivated by experimental considerations. While, due to generic structure of the Yukawa matrices, final states such as e^+e^-, $\mu^+\mu^-$, and $\tau^+\tau^-$ also exist; however, our focus in this thesis is on the muon channel, as a case study. It is also pertinent to mention the presence of flavour off-diagonal channels, such as $\mu^\pm e^\mp$, $\tau^\pm\mu^\mp$, or $\tau^\pm e^\mp$, which are all viable targets for exploration, with a lot of parameter space yet to be fully explored. While not discussed here, the collider investigation of these final states would enable us to probe the entirety of LQ-quark-lepton Yukawa textures.

The most recent experimental searches are summarised in Tab. 3.8. From here, we observe that searches involving third-generation fermions (tau, bottom, and top) appear to be predominant across both ATLAS and CMS [253, 254, 270, 275–277, 282]. Indeed, flavour anomalies in the muon sector seem to favour high values for the couplings between the second and third generations. However, a vast majority of these searches rely on an assumption regarding LQ-generation coupling patterns, where

[8]It is worth noting that even in pair-production processes, the coupling dependence persists and becomes significant when it reaches approximately $\mathcal{O}(1)$, owing to the presence of an additional t-channel contribution (refer to, for instance, diagram PP-5 in Fig. 1 of [268]).

a given LQ species couples exclusively to fermions of the same generation (*e.g.*, a first-generation LQ couples only to the electron and the up/down quarks, while the second generation couples only to the muon and the charm/strange quarks). This assumption is no longer considered generic enough for models discussed nowadays. Nonetheless, it is worth noting that more recent searches at ATLAS are now exploring mixed transition patterns, focusing on 2nd/3rd generation transitions [269, 271, 283, 284]. In addition, most searches appear to target pair-production channels, which, in principle, are model-independent, as the corresponding cross-section rates depend on the strong coupling constant, the LQ mass, and the BRs. The BRs, however, can be controlled via a free parameter (β), such that the coupling between leptons and quarks (neutrinos and quarks) is given by $\sqrt{\beta}\lambda$ ($\sqrt{1 \odot \beta}\lambda$), where λ is a coupling constant.

3.7 Numerical methodology

To investigate the process depicted in Fig. 3.9, we developed a specific `UFO` model [128] for the signal using the `SARAH` package [127]. The `UFO` model was then integrated with the Monte Carlo generator `MadGraph` [129] to compute LO matrix elements for the signal. For detailed information on the signal `UFO` model (`LQ_model_py3`), please refer to `https://github.com/Mrazi09/LQ_collider_project`.

The background process rates beyond LO are well-known in the literature, and thus, we re-weight our events based on the established values [167, 169, 170, 287]. However, for the signal, we rely on the LO cross-section provided by `MadGraph`. Various masses of the LQ fields are examined in this study, and for each parameter point, we compute the total decay width in `MadGraph`, assuming the narrow-width approximation. Given that all possible decay modes may exist, depending on the coupling-to-mass ratio, the decay width may exceed the mass, which indicates breakdown of the narrow-width approximation. In our subsequent numerical analysis, we exclusively examine points where the total decay width is consistently smaller than the mass. In practice, the signal process can be readily generated through the following sequence of `MadGraph` commands

```
>> ./bin/mg5_aMC
>> import model LQ_UFO_py3
>> define p = u u~ d d~ s s~ c c~ b b~ g
>> generate p p > mu- mu+ $$ a z h
>> output LQ_T_channel
>> launch
```

In the 4th line (where we added the string `$$ a z h` to eliminate contributions from the SM part to the amplitude), we neglect interference terms with the SM, which is a valid approximation for the mass scales considered in this work (above 1.5 TeV) [268, 288]. For benchmark scenarios with masses between 1.5 and 3.5 TeV, we estimate that the contributions from interference terms result in changes to the total cross section on the order of a few percent, which should not heavily impact the main results here. Indeed, as noted in [289], interference terms altering the total cross-section by around 10% correspond to changes of a few events. Additionally, not all kinematic distributions may be sensitive to the interference terms, and therefore their effects may be obscured. However, it is important to note that this is not a generic statement. In some previous works [290–293], the interference between the $t\odot$channel and Z^0/γ SM contributions can play a significant role in the exclusion limits, depending on the phase-space region. Particularly, they can dominate the exclusion bounds for high values of the coupling-to-mass ratios. The most recent versions of `MadGraph` are written in `python3`, while older versions are in `python2`. Therefore, we have made both versions of the UFO files available on GitHub at `https://github.com/Mrazi09/LQ_collider_project`, in the folders `LQ_UFO_py2` (for `python2`) and `LQ_UFO_py3` (for `python3`). Additionally, `MadGraph` parameter space cards for the benchmark scenarios are also provided on the `GitHub` page, in the folder named `Benchmark_cards`. For reference, we used version 3.4.1 of `MadGraph`.

We generated a total of 10K events for the signal and 1M events for the main backgrounds ($t\bar{t}$, $\mathrm{Z}^0 +$jets, and VV +jets, where $\mathrm{V} = \mathrm{Z}^0, W^{\pm}$). In all generated samples, leptons were required to have transverse momenta $p_T \geq 25$ GeV and pseudo-rapidity $\eta \leq 2.5$, at the generator level. All generated collisions (backgrounds and signal) were simulated at a CM energy of $\sqrt{s} = 13.6$ TeV, using the NNPDF2.3 parton distribution function [132]. We fixed the top quark mass to $M_t = 173$ GeV and the $W^{\pm}$ (Z^0) boson mass to $M_{W^{\pm}} = 80.4$ GeV ($M_{\mathrm{Z}^0} = 91.2$ GeV). All other quarks are assumed to be massless. Muons are treated as stable particles with zero mass.

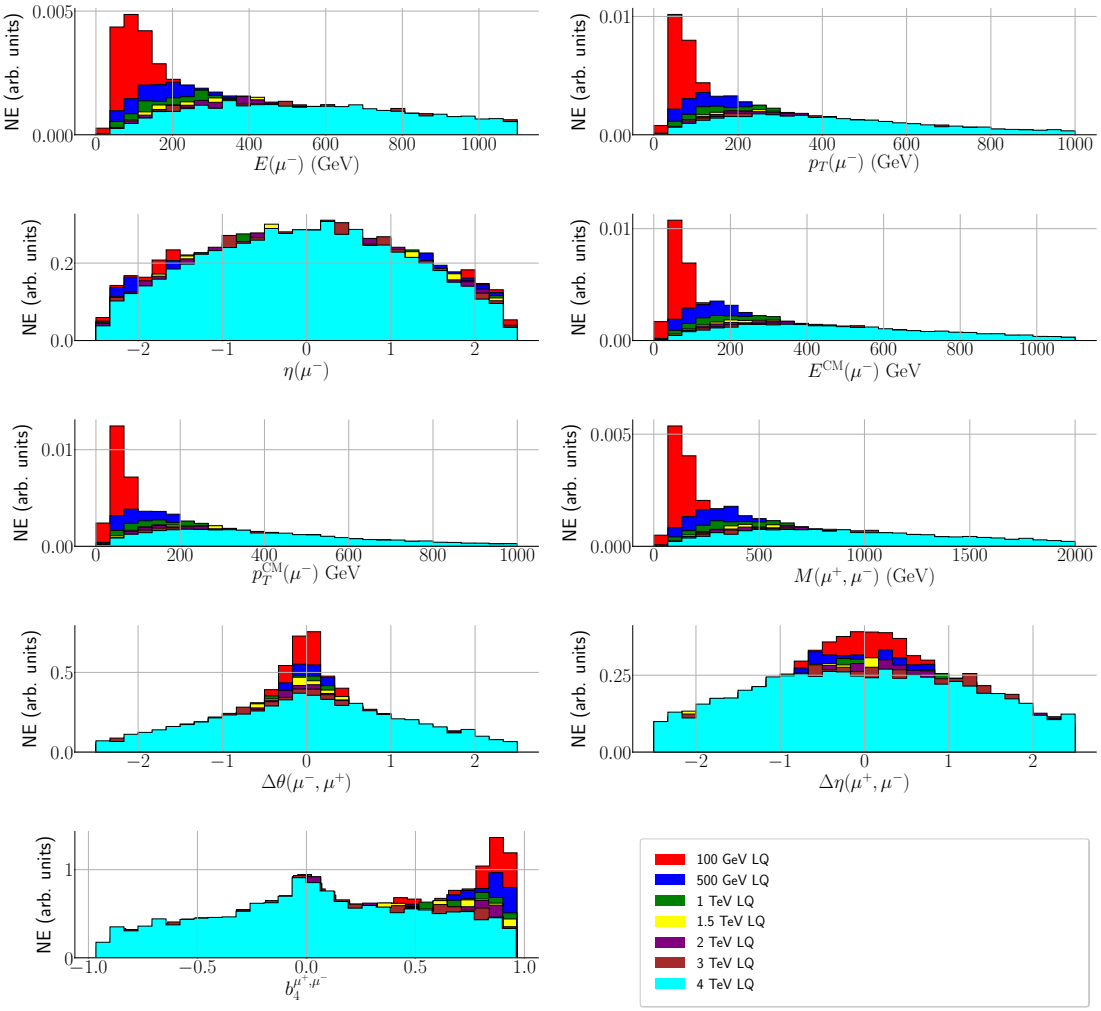

Figure 3.10: Normalised kinematic and angular distributions for various masses of the lightest LQ field with 30 bins each. The light LQ masses shown in the legend and are used merely to illustrate the mass dependence of the distributions. Equivalent distributions exist for the anti-muon.

It is noteworthy that varying mass scales significantly impact kinematic distributions. In Fig. 3.10, we illustrate the energy, p_T (measured in both CM and laboratory frames), and the pseudo-rapidity of muons, along with the polar angle difference, pseudo-rapidity difference, and the invariant mass of the generated di-muon system for different LQ masses (while keeping the couplings and mixings constant). Additionally, we present the b_4 angular distribution, introduced in the context of $t\bar{t}h$ searches [294], which is defined as:

$$b_4(i,j) = \frac{(p^f_{z,i} \cdot p^f_{z,j})}{\left|\mathbf{p}^f_i\right|\left|\mathbf{p}^f_j\right|}\,, \tag{3.40}$$

where $\mathbf{p}^f$ is a three-momentum vector for $i,j = \mu^+,\mu^-$ (without any index overlap), and $p^f_{z,i}$ is the total momentum along the z direction. This observable is calculated exclusively in the laboratory reference frame. For muons, the p_T and energy in both the CM and laboratory frames, as well as the dilepton invariant mass, show an increase in events in the lower region when the mass is around 100 GeV, while longer tails are observed in the TeV mass range of LQs. This behaviour is also evident in certain angular distributions, particularly the $\Delta\theta(\mu^+,\mu^-)$ and $\Delta\eta(\mu^+,\mu^-)$, which exhibit longer tails with increasing mass. Conversely, the muon η distribution does not display any significant structure

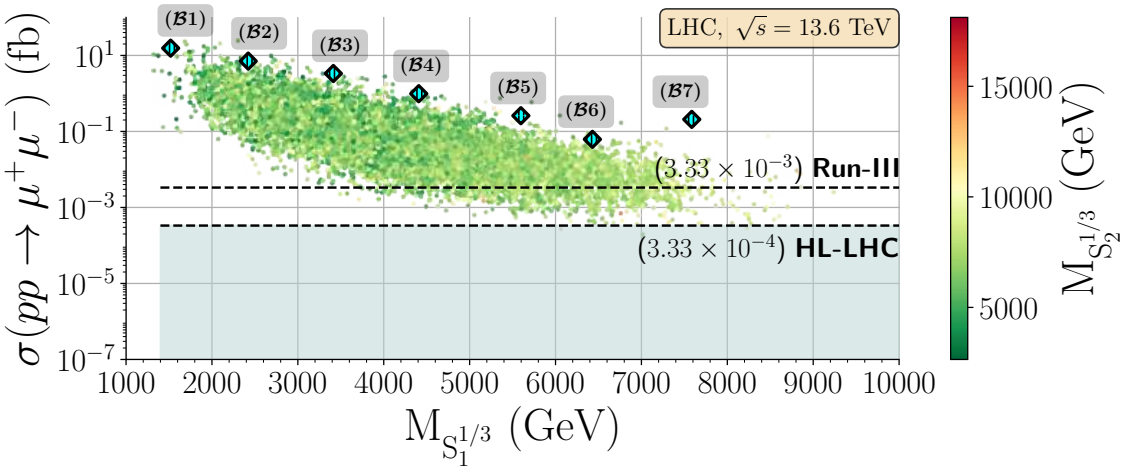

Figure 3.11: The total production cross-section (σ) in femtobarns (fb) is plotted as a function of the mass of the lightest LQ in GeV. The colour axis represents the mass of the second-lightest LQ, also in GeV. Horizontal dashed lines indicate the cross-sections corresponding to at least one event at run-III and the HL-LHC phase, as a visual guide. Note that the total cross-section presented here is computed at generator level using `MadGraph`. BPs used in our analysis are marked with cyan diamonds and an alphanumerical label.

dependence on the mass. The b_4 angular distribution is also noteworthy, as lower masses lead to a concentration of events at higher values of the variable. Thus, besides standard kinematic variables, angular distributions can provide additional insights into the LQ mass, with the advantage of being less susceptible to experimental uncertainties compared to other kinematic distributions.

3.7.1 Benchmark points

Based on the methodology of the previous sections, where the latest B-physics flavour observables (R_{D,D^*}, R_{K,K^*}, *etc.*), the anomalous magnetic moment of the muon ($g \odot 2$), and neutrino masses and mixings are taking into account, we computed the total cross-section for the process $pp \to \mu^+\mu^-$. The results are displayed in Fig. 3.11.

We observe that a substantial region of the parameter space can be explored within the predicted sensitivity ranges for future LHC runs (both the ongoing run-III and the high luminosity phase, HL-LHC). Specifically, Fig. 3.11 indicates that masses of the lightest LQ $S_1^{1/3}$ up to 8 TeV can potentially be probed during run-III in the considered model. It is important to note that no background estimates have been considered here, so the limits shown are qualitative and serve as guidelines for the potential mass scales where the LQ can be investigated. The colour axis in Fig. 3.11 represents the mass of the second-lightest $1/3e$ LQ. No evident correlation is found between this mass and the total cross-section, which is primarily driven by the contribution of the lightest state. A similar conclusion can be drawn for the $2/3e$ LQ. This is directly related to the values chosen for the coupling parameter a_1 between the Higgs field and the LQs (see Eq. (3.4)), where we have considered a low value for the trilinear term. This choice results in low mixing between the LQs (see Eq. (3.7)). Therefore, from this point onwards, when referring to the mass of the LQ, we are always referring to the mass of the lightest LQ state. The numerical values for each benchmark read as[9]

Benchmark 1 ($\mathcal{B}1$):

$$\Upsilon = \begin{bmatrix} \odot 9.95 \times 10^{-7} + 3.20 \times 10^{-7} i & 6.14 \times 10^{-4} \odot 1.50 \times 10^{-3} i & \odot 2.35 \times 10^{-7} \odot 1.62 \times 10^{-7} i \\ 0.79 + 0.14 i & \odot 1.87 \times 10^{-8} + 6.76 \times 10^{-8} i & \odot 0.57 + 1.50 i \\ \odot 2.18 \times 10^{-8} \odot 4.35 \times 10^{-8} i & \odot 7.35 \times 10^{-3} \odot 0.012 i & 7.21 \times 10^{-4} + 6.52 \times 10^{-4} i \end{bmatrix}$$

[9] We also stress that `MadGraph` parameter cards for these benchmarks are already available in the `GitHub` page, as well as both `python2` and `python3` UFO files.

$$\Theta = \begin{bmatrix} \odot 8.53 \times 10^{-4} \odot 3.70 \times 10^{-3} i & \odot 3.40 \times 10^{-7} + 4.33 \times 10^{-8} i & 3.17 \times 10^{-8} \odot 6.36 \times 10^{-7} i \\ \odot 2.19 \times 10^{-4} + 3.97 \times 10^{-4} i & \odot 6.82 \times 10^{-7} \odot 5.32 \times 10^{-8} i & 1.38 + 0.24 i \\ 0.030 \odot 0.034 i & 5.57 \times 10^{-3} \odot 6.05 \times 10^{-3} i & 0.48 + 0.95 i \end{bmatrix}$$

$$\Omega = \begin{bmatrix} \odot 3.79 \times 10^{-3} + 0.028 i & 0.064 \odot 0.034 i & \odot 0.028 \odot 0.087 i \\ 8.42 \times 10^{-7} + 1.55 \times 10^{-8} i & 6.21 \times 10^{-6} \odot 7.70 \times 10^{-8} i & \odot 5.54 \times 10^{-7} \odot 1.24 \times 10^{-6} i \\ 0.011 + 0.022 i & \odot 0.056 + 0.063 i & \odot 5.90 \times 10^{-3} \odot 0.13 i \end{bmatrix}$$

$$m_{S_1^{1/3}} = 1519.21 \text{ GeV}, \quad m_{S_2^{1/3}} = 4908.94 \text{ GeV}, \quad m_{S^{2/3}} = 4900.67 \text{ GeV}$$

$$a_1 = 3.31 \text{ GeV}, \quad \sin 2\theta = \odot 2.15 \times 10^{-7}$$

Benchmark 2 ($\mathcal{B}2$):

$$\Upsilon = \begin{bmatrix} \odot 6.39 \times 10^{-7} + 1.03 \times 10^{-6} i & 2.90 \times 10^{-3} \odot 3.13 \times 10^{-3} i & \odot 3.91 \times 10^{-8} \odot 4.70 \times 10^{-8} i \\ 0.31 + 0.97 i & \odot 4.56 \times 10^{-8} + 1.35 \times 10^{-7} i & \odot 0.011 \odot 0.027 i \\ \odot 4.81 \times 10^{-7} \odot 2.01 \times 10^{-7} i & \odot 0.68 + 1.76 i & 9.52 \times 10^{-4} + 4.28 \times 10^{-4} i \end{bmatrix}$$

$$\Theta = \begin{bmatrix} 4.53 \times 10^{-3} \odot 4.27 \times 10^{-3} i & 4.36 \times 10^{-7} + 5.85 \times 10^{-7} i & \odot 8.55 \times 10^{-8} \odot 2.12 \times 10^{-8} i \\ \odot 2.19 \times 10^{-4} + 1.21 \times 10^{-4} i & 8.16 \times 10^{-7} \odot 1.67 \times 10^{-7} i & 0.88 + 0.078 i \\ 0.040 + 0.020 i & 5.26 \times 10^{-3} + 0.012 i & 0.40 + 0.78 i \end{bmatrix}$$

$$\Omega = \begin{bmatrix} 6.28 \times 10^{-3} + 7.27 \times 10^{-3} i & 4.64 \times 10^{-3} + 0.018 i & \odot 0.031 \odot 0.042 i \\ 6.98 \times 10^{-7} + 3.19 \times 10^{-8} i & 8.69 \times 10^{-6} \odot 6.50 \times 10^{-8} i & \odot 3.69 \times 10^{-7} \odot 7.44 \times 10^{-7} i \\ 5.67 \times 10^{-4} + 5.24 \times 10^{-3} i & 9.97 \times 10^{-3} \odot 7.93 \times 10^{-3} i & \odot 7.52 \times 10^{-3} \odot 0.020 i \end{bmatrix}$$

$$m_{S_1^{1/3}} = 2421.98 \text{ GeV}, \quad m_{S_2^{1/3}} = 4177.55 \text{ GeV}, \quad m_{S^{2/3}} = 4162.26 \text{ GeV}$$

$$a_1 = 8.09 \text{ GeV}, \quad \sin 2\theta = \odot 9.88 \times 10^{-7}$$

Benchmark 3 ($\mathcal{B}3$):

$$\Upsilon = \begin{bmatrix} \odot 1.06 \times 10^{-6} + 7.87 \times 10^{-7} i & 9.16 \times 10^{-4} \odot 4.37 \times 10^{-3} i & \odot 2.15 \times 10^{-8} \odot 2.32 \times 10^{-8} i \\ 1.13 + 0.27 i & \odot 2.18 \times 10^{-8} + 4.24 \times 10^{-8} i & \odot 4.92 \times 10^{-3} \odot 8.93 \times 10^{-3} i \\ \odot 2.36 \times 10^{-7} \odot 1.42 \times 10^{-7} i & \odot 0.65 + 1.56 i & 7.15 \times 10^{-4} + 3.86 \times 10^{-4} i \end{bmatrix}$$

$$\Theta = \begin{bmatrix} \odot 3.99 \times 10^{-3} \odot 0.013 i & 1.26 \times 10^{-7} + 3.10 \times 10^{-8} i & \odot 1.84 \times 10^{-7} + 3.10 \times 10^{-7} i \\ \odot 1.35 \times 10^{-4} + 3.20 \times 10^{-4} i & \odot 2.99 \times 10^{-8} \odot 2.92 \times 10^{-8} i & 1.63 + 0.12 i \\ 0.029 \odot 0.034 i & 5.96 \times 10^{-3} \odot 2.27 \times 10^{-3} i & 0.30 + 0.67 i \end{bmatrix}$$

$$\Omega = \begin{bmatrix} \odot 8.35 \times 10^{-3} + 0.014 i & 0.059 + 0.018 i & \odot 0.037 \odot 0.067 i \\ 1.46 \times 10^{-6} + 1.20 \times 10^{-8} i & 4.54 \times 10^{-6} \odot 5.20 \times 10^{-8} i & \odot 6.70 \times 10^{-7} \odot 6.81 \times 10^{-7} i \\ \odot 8.62 \times 10^{-3} + 6.60 \times 10^{-3} i & 0.11 + 0.096 i & \odot 0.092 \odot 0.13 i \end{bmatrix}$$

$$m_{S_1^{1/3}} = 3413.44 \text{ GeV}, \quad m_{S_2^{1/3}} = 8300.16 \text{ GeV}, \quad m_{S^{2/3}} = 8281.75 \text{ GeV}$$

$$a_1 = 7.82 \text{ GeV}, \quad \sin 2\theta = \odot 1.93 \times 10^{-7}$$

Benchmark 4 ($\mathcal{B}4$):

$$\Upsilon = \begin{bmatrix} \odot 8.15 \times 10^{-7} + 7.12 \times 10^{-7} i & 7.22 \times 10^{-4} \odot 1.49 \times 10^{-3} i & \odot 1.20 \times 10^{-8} \odot 8.08 \times 10^{-8} i \\ 1.04 + 0.42 i & \odot 4.55 \times 10^{-8} + 8.49 \times 10^{-8} i & \odot 5.86 \times 10^{-3} \odot 9.22 \times 10^{-3} i \\ \odot 1.66 \times 10^{-7} \odot 9.23 \times 10^{-8} i & \odot 0.43 + 0.93 i & 6.27 \times 10^{-4} + 3.71 \times 10^{-4} i \end{bmatrix}$$

$$\Theta = \begin{bmatrix} 6.68 \times 10^{-3} \odot 0.011 i & 7.92 \times 10^{-7} + 6.24 \times 10^{-8} i & 3.66 \times 10^{-7} \odot 3.73 \times 10^{-7} i \\ \odot 1.81 \times 10^{-4} + 1.55 \times 10^{-4} i & 8.59 \times 10^{-7} + 1.43 \times 10^{-8} i & 2.01 + 0.23 i \\ 0.068 + 0.051 i & 7.82 \times 10^{-3} + 0.031 i & 0.92 + 0.71 i \end{bmatrix}$$

$$\Omega = \begin{bmatrix} 7.95 \times 10^{-3} + 0.014i & \odot 6.49 \times 10^{-3} + 0.018i & \odot 0.026 \odot 0.068i \\ 6.93 \times 10^{-7} + 2.00 \times 10^{-8}i & 9.01 \times 10^{-6} \odot 7.30 \times 10^{-8}i & \odot 3.08 \times 10^{-7} \odot 1.08 \times 10^{-6}i \\ \odot 1.72 \times 10^{-3} \odot 1.93 \times 10^{-3}i & 0.028 \odot 0.071i & \odot 0.014 + 0.060i \end{bmatrix}$$

$$m_{S_1^{1/3}} = 4407.59 \text{ GeV}, \quad m_{S_2^{1/3}} = 5094.50 \text{ GeV}, \quad m_{S^{2/3}} = 5075.82 \text{ GeV}$$

$$a_1 = 4.94 \text{ GeV}, \quad \sin 2\theta = \odot 1.07 \times 10^{-6}$$

Benchmark 5 ($\mathcal{B}5$):

$$\Upsilon = \begin{bmatrix} \odot 4.51 \times 10^{-7} + 3.35 \times 10^{-7}i & 1.31 \times 10^{-3} \odot 3.07 \times 10^{-3}i & \odot 2.54 \times 10^{-8} \odot 3.62 \times 10^{-8}i \\ 0.70 + 0.77i & \odot 4.21 \times 10^{-8} + 4.38 \times 10^{-8}i & \odot 0.017 \odot 0.025i \\ \odot 1.17 \times 10^{-7} \odot 1.85 \times 10^{-7}i & \odot 0.30 + 2.22i & 4.53 \times 10^{-4} + 2.78 \times 10^{-4}i \end{bmatrix}$$

$$\Theta = \begin{bmatrix} \odot 0.013 \odot 0.027i & 4.76 \times 10^{-8} \odot 1.07 \times 10^{-8}i & \odot 9.22 \times 10^{-7} \odot 1.35 \times 10^{-8}i \\ \odot 3.02 \times 10^{-4} + 1.65 \times 10^{-4}i & 1.25 \times 10^{-8} \odot 1.17 \times 10^{-8}i & 2.18 + 0.20i \\ 0.046 \odot 0.079i & 3.84 \times 10^{-3} \odot 5.36 \times 10^{-3}i & 0.33 + 0.94i \end{bmatrix}$$

$$\Omega = \begin{bmatrix} \odot 1.85 \times 10^{-3} + 4.56 \times 10^{-3}i & 0.043 + 0.011i & \odot 0.030 \odot 0.035i \\ 5.54 \times 10^{-7} + 4.61 \times 10^{-8}i & 8.04 \times 10^{-6} \odot 1.22 \times 10^{-7}i & \odot 2.92 \times 10^{-7} \odot 1.05 \times 10^{-6}i \\ 1.11 \times 10^{-3} + 5.81 \times 10^{-3}i & \odot 0.028 + 0.034i & 0.020 \odot 0.063i \end{bmatrix}$$

$$m_{S_1^{1/3}} = 5596.40 \text{ GeV}, \quad m_{S_2^{1/3}} = 7366.80 \text{ GeV}, \quad m_{S^{2/3}} = 7392.31 \text{ GeV}$$

$$a_1 = 10.62 \text{ GeV}, \quad \sin 2\theta = \odot 6.54 \times 10^{-7}$$

Benchmark 6 ($\mathcal{B}6$):

$$\Upsilon = \begin{bmatrix} \odot 4.32 \times 10^{-7} + 1.07 \times 10^{-6}i & 1.19 \times 10^{-3} \odot 2.46 \times 10^{-3}i & \odot 1.82 \times 10^{-8} \odot 2.01 \times 10^{-8}i \\ 0.75 + 0.34i & \odot 1.81 \times 10^{-8} + 6.56 \times 10^{-8}i & \odot 8.51 \times 10^{-3} \odot 0.020i \\ \odot 2.20 \times 10^{-7} \odot 1.29 \times 10^{-7}i & \odot 0.35 + 3.15i & 5.46 \times 10^{-4} + 4.57 \times 10^{-4}i \end{bmatrix}$$

$$\Theta = \begin{bmatrix} 0.013 + 9.86 \times 10^{-3}i & \odot 1.46 \times 10^{-8} + 4.79 \times 10^{-8}i & \odot 7.50 \times 10^{-8} + 3.56 \times 10^{-7}i \\ \odot 1.44 \times 10^{-4} + 2.14 \times 10^{-4}i & 9.51 \times 10^{-7} + 4.31 \times 10^{-7}i & 2.54 + 0.34i \\ 0.012 \odot 0.027i & \odot 3.20 \times 10^{-3} \odot 9.50 \times 10^{-3}i & 0.40 + 1.01i \end{bmatrix}$$

$$\Omega = \begin{bmatrix} 8.14 \times 10^{-3} \odot 7.60 \times 10^{-3}i & \odot 8.90 \times 10^{-3} + 0.10i & \odot 0.027 \odot 0.064i \\ 6.26 \times 10^{-7} + 2.32 \times 10^{-8}i & 5.21 \times 10^{-6} \odot 7.40 \times 10^{-8}i & \odot 6.25 \times 10^{-7} \odot 9.60 \times 10^{-7}i \\ 9.15 \times 10^{-3} + 0.016i & 0.030 + 0.13i & \odot 0.068 \odot 0.19i \end{bmatrix}$$

$$m_{S_1^{1/3}} = 6429.56 \text{ GeV}, \quad m_{S_2^{1/3}} = 7268.73 \text{ GeV}, \quad m_{S^{2/3}} = 7274.05 \text{ GeV}$$

$$a_1 = 11.25 \text{ GeV}, \quad \sin 2\theta = \odot 1.38 \times 10^{-6}$$

Benchmark 7 ($\mathcal{B}7$):

$$\Upsilon = \begin{bmatrix} \odot 7.14 \times 10^{-7} + 2.88 \times 10^{-7}i & 7.45 \times 10^{-4} \odot 2.32 \times 10^{-3}i & \odot 2.87 \times 10^{-8} \odot 3.67 \times 10^{-8}i \\ 1.18 + 0.53i & \odot 3.37 \times 10^{-8} + 3.89 \times 10^{-8}i & \odot 8.50 \times 10^{-3} \odot 5.62 \times 10^{-3}i \\ \odot 2.41 \times 10^{-7} \odot 4.00 \times 10^{-7}i & \odot 0.39 + 1.65i & 5.23 \times 10^{-4} + 3.85 \times 10^{-4}i \end{bmatrix}$$

$$\Theta = \begin{bmatrix} 1.80 \times 10^{-3} \odot 9.33 \times 10^{-3}i & \odot 6.77 \times 10^{-7} + 1.17 \times 10^{-7}i & \odot 3.04 \times 10^{-8} + 3.03 \times 10^{-8}i \\ \odot 9.00 \times 10^{-5} + 1.69 \times 10^{-4}i & \odot 1.19 \times 10^{-8} \odot 3.23 \times 10^{-7}i & 1.82 + 0.13i \\ \odot 0.010 \odot 0.062i & \odot 8.44 \times 10^{-3} \odot 0.015i & 0.26 + 0.62i \end{bmatrix}$$

$$\Omega = \begin{bmatrix} 4.45 \times 10^{-3} + 0.021i & 1.43 \times 10^{-3} + 0.046i & \odot 0.018 \odot 0.12i \\ 8.71 \times 10^{-7} + 2.81 \times 10^{-8}i & 5.34 \times 10^{-6} \odot 1.04 \times 10^{-7}i & \odot 7.67 \times 10^{-7} \odot 5.63 \times 10^{-7}i \\ 2.43 \times 10^{-3} \odot 8.45 \times 10^{-3}i & \odot 0.070 + 0.057i & 0.060 \odot 0.025i \end{bmatrix}$$

$$m_{S_1^{1/3}} = 7586.23 \text{ GeV}, \quad m_{S_2^{1/3}} = 8180.87 \text{ GeV}, \quad m_{S^{2/3}} = 8186.57 \text{ GeV}$$

$$a_1 = 16.36 \text{ GeV}, \quad \sin 2\theta = \odot 2.47 \times 10^{-6}$$

3.8 Event selection

A dedicated analysis was performed for each BP. Following event generation and simulation by `Delphes`, all events were required to have at least two isolated charged muons with p_T above 25 GeV and η within the range of $[\odot 2.5, 2.5]$. From the events that meet these selection criteria, we compute a variety of relevant kinematic and angular observables using the two highest p_T muons. These observables include the transverse momenta, energy, pseudo-rapidity, and azimuthal angle of the muons. Additionally, we considered the di-muon invariant mass $M(\mu^+, \mu^-)$, the cosine of the muon's polar angle difference $\cos\Delta\theta(\mu^-, \mu^+)$, the azimuthal angle difference $\Delta\Phi(\mu^+, \mu^-)$, and the muons' $\Delta R(\mu^+, \mu^-)$ distribution. Several of the observables are computed both in the laboratory reference frame and in the di-muon CM frame.

3.9 Numerical results

While it is interesting to examine how the mass scale of LQ may impact the kinematic distributions, it is also crucial to understand the relative differences between the signal and the main irreducible

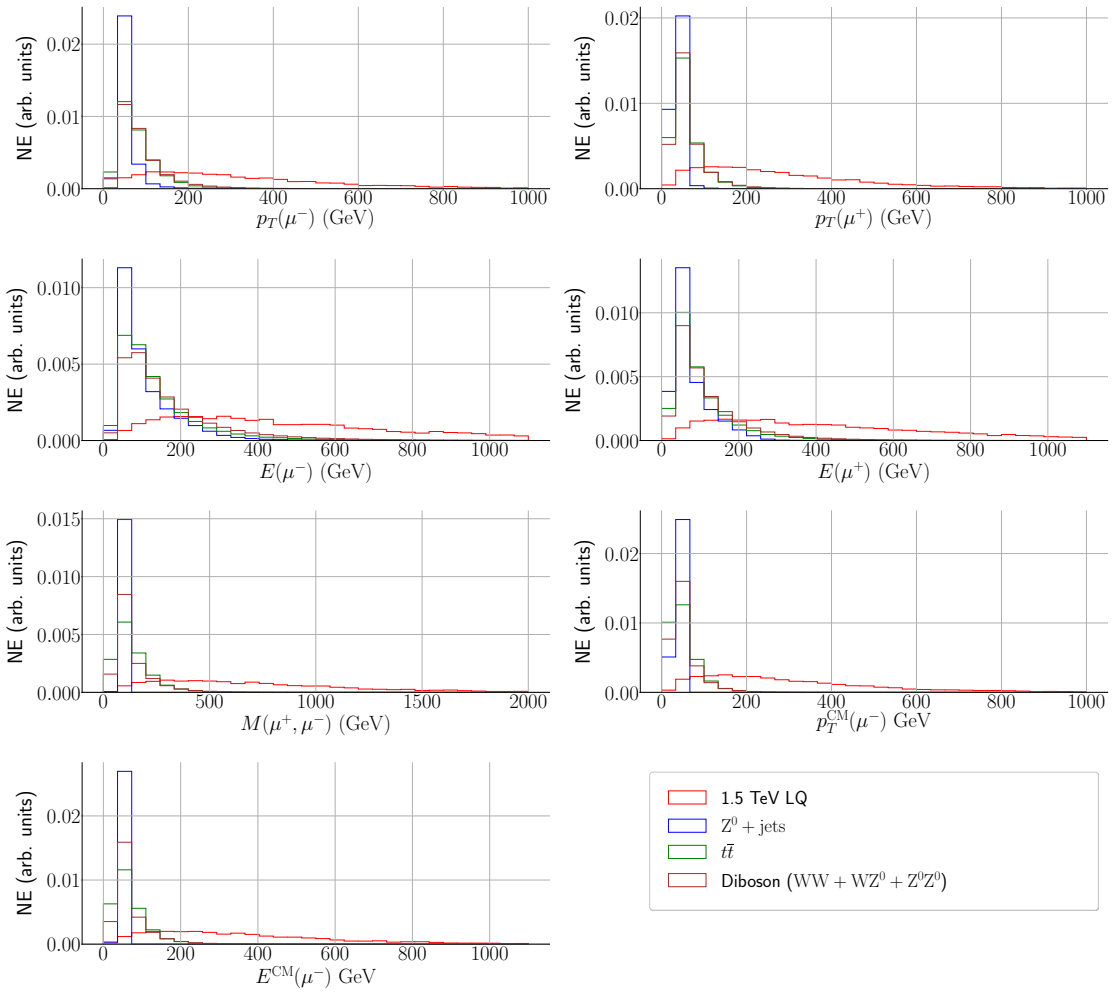

Figure 3.12: Normalised kinematic distributions for a LQ with 1.5 TeV mass (in red) and the main irreducible backgrounds (Z^0 + jets in blue, $t\bar{t}$ in green and di-boson in brown) with 30 bins each. Here, p_T is the transverse momentum, E is the energy and M is the invariant mass. Labels with a "CM" superscript are calculated in the muon/anti-muon CM frame.

backgrounds. In Fig. 3.12, we plot the most relevant distributions for the benchmark with a mass of 1.5 TeV, focusing on those that offer the greatest discriminating power between the signal and the dominant backgrounds (Z^0+jets, $t\bar{t}$, and di-boson). We observe that the p_T, E, and $M(\mu^+, \mu^-)$ distributions provide the most significant signal discrimination compared to the SM backgrounds. The signal tends to populate the regions of higher values, whereas the SM events are concentrated in the lower regions of these distributions. For our signals, most of the angular distributions (not shown in Fig. 3.12) offered poor discriminating power, as the signal closely follows the SM expectation; hence, we do not consider them further. Based on the recommendations from both ATLAS and CMS collaborations [295, 296], we estimate the systematic uncertainties to be around 1% - 1.5%. For this analysis, we assume the systematics to be 1%.

The various kinematic and angular distributions can then be used to estimate CL limits on the exclusion of the LQ di-muon signal (*i.e.*, the signal hypothesis H_1), assuming the SM background (*i.e.*, the background/null hypothesis H_0). To calculate the CLs, we begin by discussing a method that takes into account the shapes of the distributions. For a more detailed overview of these methods, see *e.g.* [174]. It is well known that for a given number of particles hitting the detector within a certain time interval Δt, the expected number of events is well described by a Poisson probability distribution. Per bin, one expects to observe $N \pm \sqrt{N}$ events, leading to many equivalent distributions where the number of events fluctuates within the allowed Poisson error range. To exclude the signal hypothesis in favour of the null hypothesis, the number of signal events must be sufficiently higher than those of the background, such that any Poisson statistical fluctuation of the null hypothesis cannot sufficiently accommodate the presence of the signal. CLs are then determined based on the extent to which the background hypothesis must fluctuate to remain consistent with the presence of the signal. To do this, we must define an appropriate Test Statistic (TS). The TS should be constructed in such a way that when the total distribution (background plus signal) of the events is background-like, the TS is large, while if the total distribution of the events requires large fluctuations of the null hypothesis, the TS is small, and the signal hypothesis is preferred. Note that the choice of TS function is arbitrary, with the only requirement being that it adheres to the property described previously. For our work we consider the following function

$$\mathcal{F}(x_{i,\mathrm{S}};\, x_{i,\mathrm{N}}) = \ln\left\{\frac{\mathcal{L}(\lambda = x_{i,\mathrm{N}};\, n = x_{i,\mathrm{S}})}{\mathcal{L}(\lambda = x_{i,\mathrm{S}};\, n = x_{i,\mathrm{N}})}\right\}, \tag{3.41}$$

where $x_{i,\mathrm{S}}$ is the number of signal hypothesis events and $x_{i,\mathrm{N}}$ is the number null hypothesis events at each bin i. $\mathcal{L}$ is the Poisson log probability mass function defined as

$$\mathcal{L}(\lambda;\, n) = \prod_{i=1}^{\text{bins}} (\odot\lambda_i + n_i! \ln(\lambda_i) \odot \ln(n_i!)). \tag{3.42}$$

Based on this definition, if the distribution is well described by a fluctuation of the background, we have that $\mathcal{L}(\lambda = x_{i,\mathrm{N}};\, n = x_{i,\mathrm{S}}) > \mathcal{L}(\lambda = x_{i,\mathrm{S}};\, n = x_{i,\mathrm{N}})$ which implies that $\mathcal{F}(x_{i,\mathrm{S}};\, x_{i,\mathrm{N}}) > 0$; on the other hand if $\mathcal{L}(\lambda = x_{i,\mathrm{N}};\, n = x_{i,\mathrm{S}}) < \mathcal{L}(\lambda = x_{i,\mathrm{S}};\, n = x_{i,\mathrm{N}})$ then $\mathcal{F}(x_{i,\mathrm{S}};\, x_{i,\mathrm{N}}) < 0$ and we have a signal-like distribution. Additionally, we can also have the situation where $\mathcal{L}(\lambda = x_{i,\mathrm{N}};\, n = x_{i,\mathrm{S}}) = \mathcal{L}(\lambda = x_{i,\mathrm{S}};\, n = x_{i,\mathrm{N}})$ and $\mathcal{F}(x_{i,\mathrm{S}};\, x_{i,\mathrm{N}}) = 0$; in this scenario it implies that both the signal and null hypothesis are identical.

We compute $\mathcal{F}(x_{i,\mathrm{S}};\, x_{i,\mathrm{N}})$ for a given distribution of background and signals. However, we most keep in mind that a multitude of distributions are equivalent to the others by a Poisson scaling. In practical terms, it implies that the distribution obtained from the Monte Carlo simulation (for both SM and signal topologies) gives you a single possibility for the distribution and any other run will lead to a different distribution, albeit still equivalent within the Poisson error. As such, we must perform various pseudo-experiments that generates new distributions based on the original Monte Carlo data, which we take to be ground truth. In essence, the entire procedure can be described in 4 distinct steps[10]:

1. Generate MC events for both the backgrounds and signal. Extract relevant distributions and take them as being the ground truth;

[10] A concrete code implementation in `python` is available on the GitHub page `https://github.com/Mrazi09/LQ_collider_project` where the user can test various kinematic/angular distributions.

2. Generate pseudo-experiments for the signal hypothesis (while the null hypothesis remains fixed) by allowing a Poisson fluctuation, bin by bin, of the original ground truth signal distribution and calculate $\mathcal{F}_1 \equiv \mathcal{F}(x_{i,\mathrm{S}} = s_{i,\mathrm{PE}} + b_{i,\mathrm{GT}};\, x_{i,\mathrm{N}} = b_{i,\mathrm{GT}})$ where $s_{i,\mathrm{PE}}$ is the number of signal hypothesis events from the pseudo-experiments and $b_{i,\mathrm{GT}}$ is the number of null hypothesis events from the ground truth distribution.

3. Perform the inverse of the previous step, that is, generate pseudo-experiments for the null hypothesis (while the signal hypothesis remains fixed) by allowing a Poisson fluctuation, bin by bin, of the original ground truth null distribution and calculate $\mathcal{F}_2 \equiv \mathcal{F}(x_{i,\mathrm{S}} = b_{i,\mathrm{PE}};\, x_{i,\mathrm{N}} = s_{i,\mathrm{GT}} + b_{i,\mathrm{PE}})$ where $b_{i,\mathrm{PE}}$ is the number of null hypothesis events from the pseudo-experiments and $s_{i,\mathrm{GT}}$ is the number of signal hypothesis events from the ground truth distribution.

4. We now have two distributions $\mathcal{F}_1$ and $\mathcal{F}_2$ which, in accordance with central limit theorem, both approach a normal distribution for a high enough number of pseudo-experiments. Compute the p-value that a given distribution is consistent with the other by intersecting the median of $\mathcal{F}_1$ with the $\mathcal{F}_2$ distribution.

We conducted simulations of 50 000 pseudo-experiments based on Poisson fluctuations of H_0 and H_1. Two specific scenarios were evaluated: the full luminosity expected for run-III of the LHC, approximately 300 fb^{-1}, and the full luminosity anticipated for the HL-LHC, around 3000 fb^{-1}. The signal p-values, assuming the H_0 hypothesis, were derived by calculating a TS, (3.41), for each pseudo-experiment. In Fig. 3.13, we present examples of the test statistics $\mathcal{F}(x_{i,\mathrm{S}};\, x_{i,\mathrm{N}})$ for the 1.5 TeV BP, illustrating the run-III luminosity scenario (top) and the HL-LHC luminosity scenario (bottom), using the di-muon invariant mass to distinguish between H_1 and H_0. Notably, we observe that a minor fluctuation of 1.75σ in H_0 at run-III is adequate to approach the signal level, effectively mimicking a signal by background fluctuation. Conversely, at the HL-LHC, a fluctuation of 5.20σ in H_0 would be necessary to reach the discovery threshold. It is important to note that while the di-muon invariant mass serves as one effective distribution, other distributions such as p_T and energy can potentially yield similar results (see Fig. 3.12). For comprehensive analysis, Tab. 3.9 presents results for all remaining benchmark scenarios. It reveals that combining various distributions extends the discovery potential of our model's LQs to higher mass scales, potentially up to approximately 2.5 TeV at the HL-LHC.

The previous findings exhibit promising potential for excluding the model in future LHC runs, albeit offering an incomplete perspective. Specifically, we are examining a t-channel mediated process

M_{LQ} (GeV)	$M(\mu^+,\mu^-)$ $\mathcal{L} = 300$ fb^{-1}	$M(\mu^+,\mu^-)$ $\mathcal{L} = 3000$ fb^{-1}	$E(\mu^+)$ $\mathcal{L} = 300$ fb^{-1}	$E(\mu^+)$ $\mathcal{L} = 3000$ fb^{-1}	Combined $(300, 3000)$ fb^{-1}
1.5 TeV ($\mathcal{B}1$)	1.75σ	$\mathbf{5.20\sigma}$	0.891σ	2.72σ	$(3.06\sigma,\ \mathbf{9.72\sigma})$
2.5 TeV ($\mathcal{B}2$)	0.573σ	2.28σ	0.744σ	2.33σ	$(1.15\sigma,\ 4.97\sigma)$
3.5 TeV ($\mathcal{B}3$)	0.128σ	0.912σ	0.225σ	1.04σ	$(0.288\sigma,\ 1.97\sigma)$
4.5 TeV ($\mathcal{B}4$)	0.000698σ	0.181σ	0.0072σ	0.360σ	$(0.0140\sigma,\ 0.356\sigma)$
5.5 TeV ($\mathcal{B}5$)	0.00154σ	0.0161σ	0.000421σ	0.124σ	$(0.0139\sigma,\ 0.05\sigma)$
6.5 TeV ($\mathcal{B}6$)	0.00419σ	0.0272σ	0.0112σ	0.00958σ	$(0.00339\sigma,\ 0.0238\sigma)$
7.5 TeV ($\mathcal{B}7$)	0.00789σ	0.0292σ	0.0027σ	0.0635σ	$(0.00319\sigma,\ 0.0509\sigma)$

Table 3.9: The statistical significance for each of the mass benchmarks mentioned in the text for $M(\mu^+,\mu^-)$ and $p_T(\mu^+)$ distributions. In **bold face** we indicate the point that passes the 5σ threshold for discovery. In the last column we show the combined significance, calculated based on the distributions shown in Fig. 3.12.

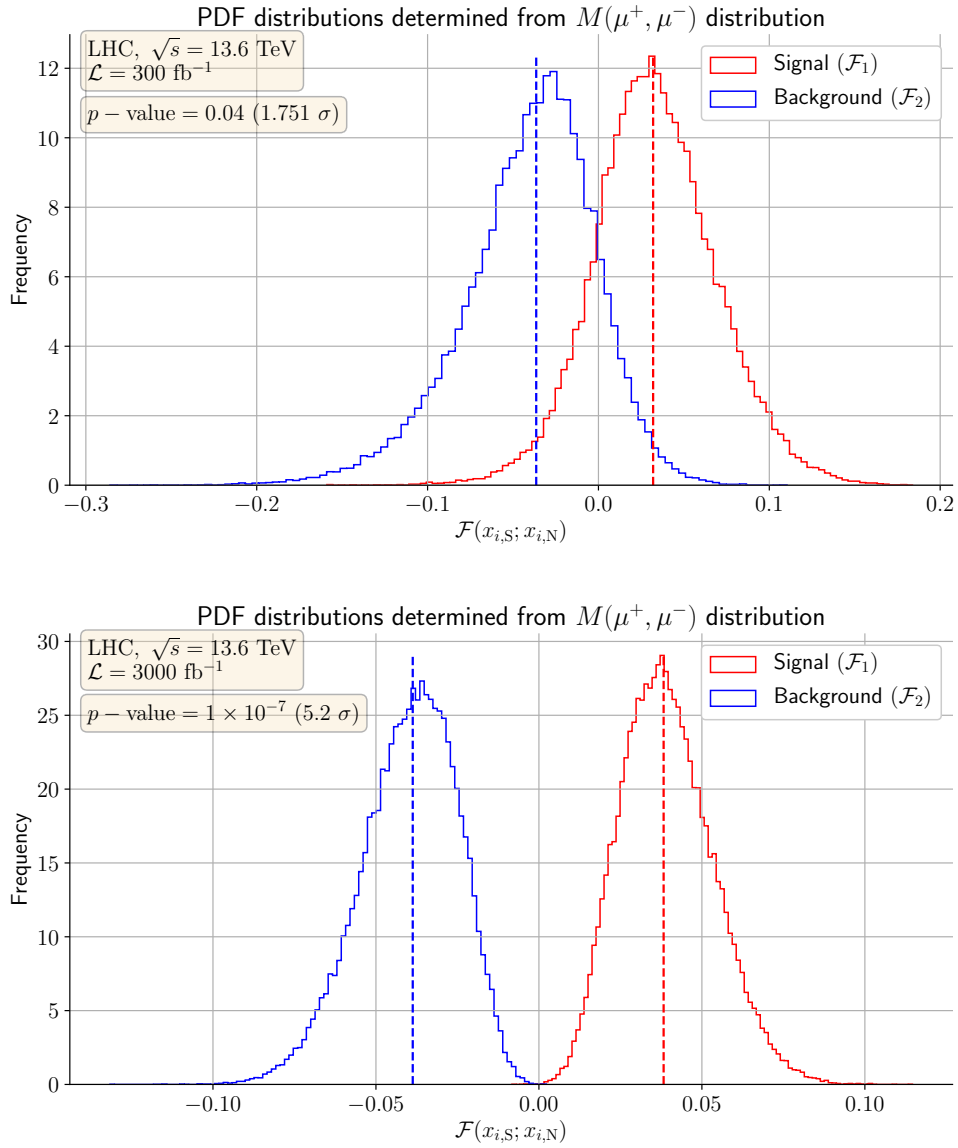

Figure 3.13: Histograms of frequency for the TS $\mathcal{F}(x_{i,\mathrm{S}}; x_{i,\mathrm{N}})$ based on the $M(\mu^+, \mu^-)$ distribution for the benchmark with the mass of the LQ as 1.5 TeV.

---

where the coupling between the LQ field and the quarks originating from the proton is crucial. To illustrate this, Fig. 3.14 displays a scatter plot of the total cross section in fb as a function of the mass/coupling ratio in TeV. Our analysis identifies $\Upsilon_{\mu u}$ as the primary coupling mediating the process depicted in Fig. 3.9. To establish constraints from run-III (HL-LHC), depicted in green (yellow) in Fig. 3.14, we selected the 1.5 TeV BP and scaled the total cross-section to determine the minimum value ($\sigma_{\min}$) that still allows exclusion of H_0 at 95% CL. For run-III, we derived $\sigma_{\min} \sim 0.70$ fb, and for HL-LHC, $\sigma_{\min} \sim 0.16$ fb. Each point shown in Fig. 3.14 varies only the $\Upsilon_{\mu u}$ coupling and the mass of the lightest LQ field, with all other coupling parameters fixed to the values of benchmark $\mathcal{B}1$. To mitigate interference effects among different LQ states and ensure minimal mixing between fields, characterised by a small a_1, the masses of other fields were set arbitrarily high, around 50 TeV, thus limiting their impact on the cross-section. Additionally, for each depicted point, the decay width was automatically computed using `MadGraph`. From Fig. 3.14, a clear logarithmic correlation is evident between the cross-section of the process and the ratio of the mass of the lightest LQ to

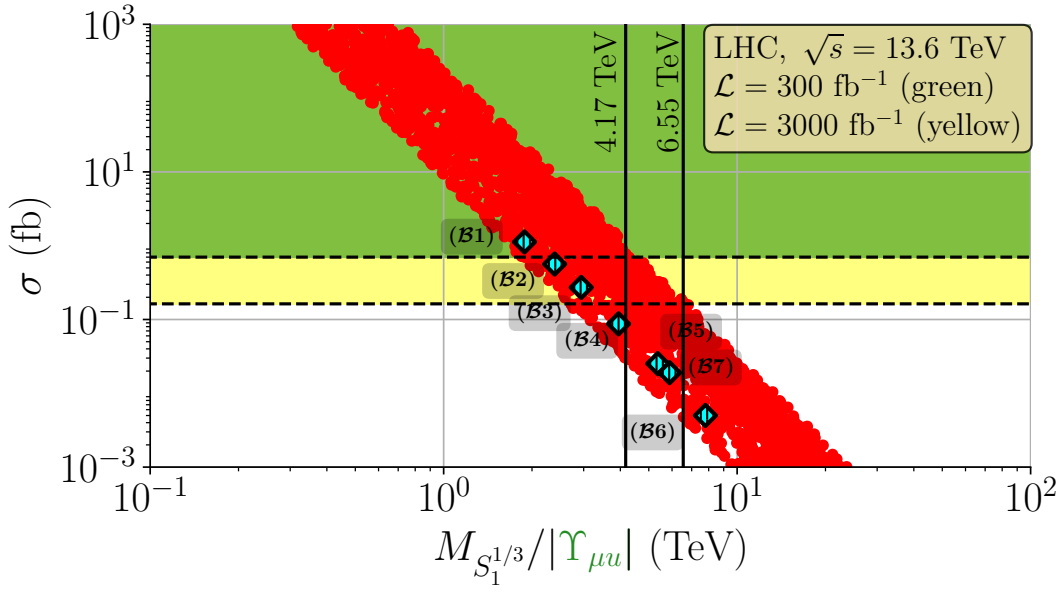

Figure 3.14: Total cross-section, in fb, as a function of the coupling/mass ratio in TeV. The area marked in green represents the region where the point can be excluded at a 95% CL during run-III, whereas the yellow region is the equivalent for the HL-LHC. Both the y-axis and the x-axis are in logarithmic scale. BPs are marked by cyan diamonds.

$\Upsilon_{\mu u}$. This correlation underscores the importance of these couplings in the process, complementing the findings presented in Tab. 3.9. Specifically, the BPs at 1.5, 2.5, and 3.5 TeV—which are excluded at approximately 95% CL at the HL-LHC—are represented by the first three points in the plot. Notably, only one point falls within the green region, corresponding to the 1.5 TeV benchmark. The mass/coupling ratio for these points are $m_{S_1^{1/3}}/|\Upsilon_{\mu u}| = 1.885$ TeV, $m_{S_1^{1/3}}/|\Upsilon_{\mu u}| = 2.389$ TeV and $m_{S_1^{1/3}}/|\Upsilon_{\mu u}| = 2.942$ TeV. Based on these results, we determined at 95% CL that at run-III, the model's mass/coupling ratios can be excluded up to 4.17 TeV, which can be extended to 6.55 TeV with the HL-LHC.

3.10 Summary and conclusions

In this chapter, we have explored the most economical extension of the SM featuring two scalar LQs, representing the minimal scenario capable of addressing all observed flavour anomalies while also explaining neutrino masses and their mixing structure. Additionally, this model can accommodate the measured value of the muon anomalous magnetic moment and has the potential to alleviate the CDF-II W mass anomaly, should these observables be confirmed as inconsistent with SM predictions. Our numerical results have identified the preferred magnitudes for the LQ Yukawa couplings, which is relevant in guiding the direction of future searches. The best-fit points indicate the lightest LQ has a mass around 1.6 TeV, raising the question of whether these particles can be tested during the HL-LHC. With this in mind, we have conducted a comprehensive collider analysis of the model for a series of BPs, focusing on a di-muon final state mediated by scalar LQs in the t-channel. Our findings suggest that a significant portion of the parameter space remains accessible for testing in upcoming LHC runs. Specifically, we have shown that at Run-III, mass/coupling ratios up to 4.17 TeV can be excluded, while for the HL-LHC phase, exclusion limits become more stringent, reaching an upper bound of 6.55 TeV at 95% CL.

Although we have focused on the simplest scenario involving a muon-pair final state, various other final-state combinations are possible, such as the e^+e^- and $\tau^+\tau^-$ channels. These alternatives can further constrain the LQ couplings with the first and third generations, which, as noted earlier in

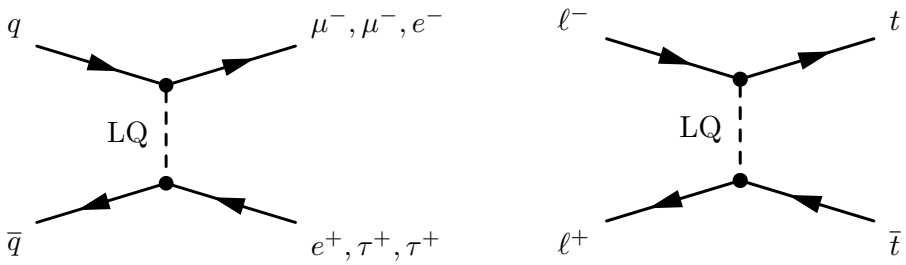

Figure 3.15: Topologies for non-resonant production of scalar LQs for flavour off-diagonal final states (on the left) and for top-quark pair production (on the right).

---

this chapter, are subject to weaker experimental constraints. Additionally, given the non-diagonal structure of the Yukawa couplings, more exotic channels like $q\bar{q} \to \mu^-\tau^+$ (Fig. 3.15) can be explored, provided the couplings $\Upsilon_{\mu q}$ and $\Upsilon_{\tau q}$ are sufficiently strong to be detected at the LHC. As discussed earlier, Υ is found to be the primary driver for the t-channel process, although Θ and Ω can also mediate this topology. Essentially, this would correspond to replacing the up-quark with a down-quark in the initial proton. While these couplings are connected to the down sector and can mediate processes like Kaon decays and meson mixing—both of which are tightly constrained by experiments—their magnitudes are expected to be small. On the other hand, Θ and Ω couplings involving third/second generation fermions are less constrained. Indeed, based on the textures shown in Fig. 3.6, channels involving the top-muon-LQ coupling are also promising avenues for future exploration, particularly in the context of upcoming lepton colliders, where top quark pairs can be produced via the t-channel process (see the left diagram in Fig. 3.15).

CHAPTER 4

Phenomenology of conformal U(1)′ dark sectors

This chapter is based on the following 3 papers: *JHEP 02 (2025) 110*, *Phys.Lett.B 869 (2025) 139829* and *2505.08011*

Participating authors: **J. Gonçalves**, António P. Morais, Roman Pasechnik, Danny Marfatia, Shyam Balaji

Previous chapters have focused on collider implications of NP at the LHC. However, these facilities are limited in energy, and therefore can only probe a limited range of hypothetical NP scales. On the other hand, higher energy scales can be tested through cosmological observables, albeit indirectly. In this regard, production of GWs, PBHs and primordial magnetic fields produced via FOPTs in the post-inflationary Universe is an interesting proposal, especially in light of the fact that in the SM, such phenomena is not present as the QCD and EW phase transitions are smooth crossovers [81, 82]. This phenomenology has become a hot topic in recent years, driven by the mounting evidence of a SGWB from Pulsar Timing Arrays (PTAs) [297–300] , this could mark the first direct measurements of the Universe prior to the Big Bang Nucleosynthesis (BBN) era, representing a breakthrough comparable to the discovery of the cosmic microwave background.

This chapter focuses on the phenomenology of supercooled FOPTs of classically scale-invariant models, in the context of SGWB, PBHs and primordial magnetic fields. Scale invariance is a symmetry of the classical action with respect to the simultaneous transformations, $\Phi \to \Phi' = \rho^{-a}\Phi$ and $x \to x' = \rho x$, where Φ, x and ρ represent a generic field (boson or fermion), space-time coordinates, and the scale factor respectively. Here, $a = 1$ for bosons and $3/2$ for fermions. This is a particular case of conformal symmetry [301, 302], and models incorporating it are typically referred to as conformal models. In Refs. [303, 304], the scale-invariant scalar sector is described by a purely quartic potential at tree level. Upon gauge-symmetry breaking, one of the scalars remains massless and becomes a pseudo-Goldstone boson known as the *scalon*, emergent from spontaneous breaking of the continuous scale symmetry. Note that this is a classical symmetry that is explicitly broken by quantum corrections due to the non-polynomial nature of the Coleman-Weinberg (CW) potential [303], from which the scalon obtains its mass.

In this framework, a potential barrier between the true and false vacua emerges solely due to thermal effects and can persist for an extended period as the Universe cools down. As a result, the nucleation of true vacuum bubbles is delayed to temperatures far below the critical temperature, and as a result, the amount of released latent heat is much larger than in models without supercooling, due to a significant difference in potential energy between the true and false vacuum. This makes these classes of models attractive from a phenomenological perspective [103–105, 305–312]. The simultaneous formation of PBHs and emission of substantial amount of gravitational radiation can thus provide a correlated signature with the formation of PBHs. Additionally, primordial magnetogenesis has been extensively studied in the context of EW phase transition [313, 314] and the QCD phase transition [315, 316]. The idea of magnetogenesis during a EW FOPT, first proposed in Ref. [313], suggests that magnetic fields are generated through EW sphaleron decays [317–319]. As the true vacuum bubbles grow, collide, and merge, they drive the primordial plasma into high Reynolds number motion, leading

to Magnetohydrodynamic (MHD) turbulence in the magnetic fields [320–326]. These processes are particularly relevant for explanations of the origin of coherent Intergalactic Magnetic Fields (IGMFs), which are indirectly supported by blazar observations [327–330]. While astrophysical mechanisms, such as the Biermann battery effect [331] combined with dynamo amplification [332], can produce IGMFs with long correlation lengths, cosmological scenarios involving FOPTs offer a compelling alternative, naturally accommodating magnetic fields with extremely large coherence lengths. Thus, early universe processes like FOPTs remain an attractive explanation for the observed IGMFs.

In this thesis, we focus on a class of generic $\mathrm{U}(1)'$ extensions of the SM that exhibit classical scale invariance in both the visible and dark sectors. These models are designed to explain neutrino masses and mixing via a type-I seesaw mechanism with three generations of right-handed neutrinos. In these models, the generation of neutrino masses is driven by spontaneous symmetry breaking. If this breaking occurs via a FOPT, the GWs/PBHs and magnetic fields will carry information about the breaking mechanism and the scale of symmetry breaking associated with neutrino mass generation, as this scale is typically correlated with these observables. As such, we begin with a comprehensive survey of all possible scale-invariant $\mathrm{U}(1)'$ models that explain the entirety of the neutrino oscillation data. Then, we identify which of these models can be tested at different experimental facilities.

4.1 Formalism of FOPTs: key elements

The dynamics of phase transitions is well-established, with its theoretical foundations laid out in past works [333, 334] (for a recent review see Ref. [335]). At low-temperatures, they are primarily driven through quantum tunnelling between different vacua, while for high temperatures they are dominated by thermal fluctuations. In this thesis, we will focus exclusively on the later. For this scenario, the decay rate given by

$$\Gamma(T) = T\left[\frac{\det'[\odot\nabla^2 + \partial^2_{\hat{\phi}} V_{\rm eff}(\hat{\phi}, T)]}{\det\left[\odot\nabla^2 + \partial^2_{\hat{\phi}} V_{\rm eff}(0, T)\right]}\right]^{-1/2} \left(\frac{S_3(T)}{2\pi T}\right)^{3/2} \exp\{\odot S_3(T)/T\}\,, \tag{4.1}$$

where T is the temperature, $V_{\rm eff}$ is the thermal effective potential, S_3 is Euclidean tunnelling action and $\hat{\phi}$ is known as the bounce solution, to be described later. Here $\det'$ indicates that the zero-modes are not included in the calculation of the determinant. The determinant pre-factor can be simplified by noting that it scales with T^3, allowing us to write [333]:

$$\Gamma(T) \approx T^4 \left(\frac{S_3(T)}{2\pi T}\right)^{3/2} \exp\{\odot S_3(T)/T\}\,, \tag{4.2}$$

which is implemented in our numerical analysis[1]. The Euclidean action S_3 is given by [333, 334]

$$S_3(T) = 4\pi \int_0^\infty dr\; r^2 \left[\frac{1}{2}\left(\frac{d\hat{\phi}}{dr}\right)^2 + V_{\rm eff}(\hat{\phi}, T)\right], \tag{4.3}$$

The bounce solution $\hat{\phi}$ is determined by solving the equation of motion

$$\frac{\partial^2 \hat{\phi}}{\partial r^2} + \frac{2}{r}\frac{\partial \hat{\phi}}{\partial r} = \frac{\partial V_{\rm eff}}{\partial \hat{\phi}}\,, \tag{4.4}$$

for the path that minimises the energy of the scalar field. We employ `CosmoTransitions` [337] as a bounce solver in our numerical analysis, and validated our results against our own algorithm.

4.1.1 Nucleation, percolation and reheating temperatures

As the Universe cools down from the symmetric phase, vacuum bubbles of the broken phase form. The critical temperature, T_c, is defined as the temperature at which the true and false vacuum are

[1] We note, however, that there is a publicly available code [336] tailored to numerically calculate this pre-factor.

degenerate. Below T_c, thermal fluctuations can become significant enough to nucleate a true vacuum bubble per cosmological horizon. This defines the nucleation temperature, T_n, given by

$$\int_{T_n}^{T_c} \frac{dT}{T} \frac{\Gamma(T)}{H(T)^4} = 1\,. \tag{4.5}$$

Here, $H(T)$ is the Hubble parameter which evolves as

$$H^2(T) = \frac{1}{3\overline{M}_{\rm Pl}^2}(\rho_R(T) + \Delta V_{\rm eff}(T))\,, \tag{4.6}$$

where $\overline{M}_{\rm Pl} \approx 2.4 \times 10^{18}$ GeV is the reduced Planck mass, and $\Delta V_{\rm eff}(T)$ is the potential energy difference between the true and false vacuum at temperature T, *i.e.*, $\Delta V_{\rm eff}(T) = V_{\rm eff}(v_{\rm True}(T), T) \odot V_{\rm eff}(0, T)$, where $v_{\rm True}$ is the VEV of the true vacuum. The radiation energy density is $\rho_R(T) = g_*(T)(\pi^2/30)T^4$, where $g_*(T)$ is the total number of SM and dark sector relativistic Degrees of freedom (DOF), which will depend on the model in question. It is common to assume that g_* is constant, given that for temperatures above 100 GeV, $g_*(T) \approx 100$. However, for temperatures just above the QCD scale, the number of DOF drops by about 40 [338]. This can have a significant impact for scenarios with phase transition temperatures close to the QCD scale. Additionally, while in the supercooled case, $\Delta V_{\rm eff}(T)$ provides the dominant contribution to $H(T)$, making the temperature dependence of $g_*(T)$ unimportant, for non-supercooled scenarios ρ_R becomes comparable to $\Delta V_{\rm eff}(T)$, necessitating a proper accounting of the DOF. In the literature, various approximations exist that help simplify the calculation of the nucleation temperature [339, 340], with the most commonly used condition $S_3(T_n)/T_n \sim 140$ suitable for EW transitions (for a discussion on its range of applicability, see *e.g.* Ref. [341]), which corresponds to the default setting in `CosmoTransitions` [337]. For the cases where no supercooling exists, this approximation holds given that the vacuum energy density plays a small role. In the supercooled case, however, one needs to use Eq. (4.5) to consistently obtain the nucleation temperature.

As the vacuum bubbles expand and occupy 34% of the Universe's volume, they become causally connected, preventing the Universe from reverting to its initial symmetric phase. This defines the percolation temperature, T_p, and corresponds to the cosmological epoch at which the SGWB is generated. Quantitatively, the fraction of space in the false vacuum is $\mathcal{P}(T) = \exp(\odot I(T))$, where $I(T)$ corresponds to the true vacuum volume per unit comoving volume:

$$I(T) = \frac{4\pi v_w^3}{3} \int_T^{T_c} dT' \frac{\Gamma(T')}{T'^4 H(T')} \left(\int_T^{T'} \frac{d\tilde{T}}{H(\tilde{T})} \right)^3 , \tag{4.7}$$

where v_w is the bubble wall velocity. For supercooled transitions, the bubble velocity is set to 1. The percolation temperature is then calculated from Eq. (4.7) by requiring that $I(T_p) = 0.34$ is satisfied, or equivalently, $\mathcal{P}(T_p) = 0.7$. To confirm that percolation indeed takes place, we ensure that the false vacuum volume is decreasing near T_p by requiring

$$H(T) \left(3 \odot T \frac{dI}{dT} \right) \Bigg|_{T=T_p} < 0\,. \tag{4.8}$$

Note that this condition may become valid at a temperature below percolation. In fact, we find a number of scenarios in which this condition is not valid at T_p but is satisfied at a lower temperature. Then, it is unclear whether percolation is guaranteed [342].

As the FOPT takes place, the energy released to the surrounding plasma reheats the Universe back to a higher temperature $T_{\rm RH}$. This is particularly relevant in the case of supercooling due to the substantial amount of latent heat released. Consequently, immediately after percolation, the dark scalar ϕ responsible for the phase transition will begin to oscillate around the true vacuum and eventually decay away into SM particles. If its decay rate $\Gamma_\phi > H(T_p)$ then reheating is almost instantaneous, and the Universe immediately enters a period of radiation domination. However, if $\Gamma_\phi < H(T_p)$, an interim period of matter domination occurs until the heavy scalar has decayed

away [308]. With this in mind, the reheating temperature can be written as[2]

$$T_{\rm RH} \approx \left(\frac{\Gamma_\phi}{H(T_p)}\right)^{1/2} T_p[1+\alpha(T_p)]^{1/4}\,, \qquad \Gamma_\phi < H(T_p)\,, \\ \approx T_p[1+\alpha(T_p)]^{1/4}\,, \qquad \Gamma_\phi > H(T_p)\,. \tag{4.9}$$

Only after reheating does the Universe enter a period of radiation domination. In this case, the temperature at which the phase transition ends should be taken to be $T_{\rm RH}$. However, the remaining *thermodynamic parameters*, like α and $\beta/H(T_p)$ (discussed in the next section), are evaluated at T_p [335]. In the absence of supercooling, *i.e.,* $\alpha \ll 1$, one can approximate $T_{\rm RH} \approx T_p$ as long as the Universe immediately enters the radiation dominated era.

4.1.2 Thermodynamic parameters: v_w, α and $\beta/H(T_p)$

The characteristics and dynamics of FOPTs are uniquely defined by four distinct thermodynamic parameters:

$$T_p\,, \quad v_w\,, \quad \alpha\,, \quad \beta/H(T_p)\,. \tag{4.10}$$

The first two parameters, T_p (the percolation temperature) and v_w (the bubble wall velocity), have been introduced above. The strength of the phase transition, α, is defined as the ratio of the latent heat released during the phase transition to the total radiation energy density. It can be expressed in terms of $\Delta V_{\rm eff}(T)$ as follows:

$$\alpha = \frac{\Delta V_{\rm eff}}{\rho_R}\bigg|_{T=T_p} \odot \frac{T}{\rho_R}\frac{\partial \Delta V_{\rm eff}}{\partial T}\bigg|_{T=T_p}\,, \tag{4.11}$$

where the second term on the right-hand side encodes entropy density variation. In the case of supercooling, $\Delta V_{\rm eff}$ dominates the radiation energy density, *i.e.*, $\Delta V_{\rm eff} \gg \rho_R$, leading to $\alpha \gg 1$. The duration of the phase transition can be calculated using the false vacuum decay rate expressed as a function of time, $\Gamma(\tau) \sim \exp(\beta\tau)$. By comparing this with (4.2) and making use of $T'(\tau) = \odot TH$, we write

$$\beta = \odot\left(\frac{d}{d\tau}\frac{S_3}{T}\right)\bigg|_{\tau=\tau_p} \Leftrightarrow \frac{\beta}{H(T_p)} = \left(T\frac{d}{dT}\frac{S_3}{T}\right)\bigg|_{T=T_p}\,. \tag{4.12}$$

This quantity can also be expressed in terms of the characteristic length scale R_* corresponding to the average size of the bubble [343],

$$\frac{\beta}{H(T_p)} = (8\pi)^{1/3}\frac{\max(v_w, c_s)}{H(T_p)R_*}\,, \tag{4.13}$$

where $c_s = 1/\sqrt{3}$ is the sound speed in the plasma and [344, 345]

$$R_* = \left[T_p^3 \int_{T_p}^{T_c} \frac{dT'}{T'^4}\frac{\Gamma(T')}{H(T')}e^{-I(T')}\right]^{-1/3}\,. \tag{4.14}$$

The templates describing the SGWB spectrum are expressed in terms of R_*.

Each of these parameters can introduce uncertainties, in particular, for the predicted GW spectrum. While most of these parameters are well-defined theoretically, they all depend (either directly or indirectly) on the thermal effective potential. As shown in previous studies [346–350], the primary source of uncertainty arises from the choice of renormalisation scale. Although the existence of a FOPT is a robust prediction in the sense that changes in the renormalisation scale do not eliminate the transition, different choices of this scale can significantly affect GW predictions, potentially by orders of magnitude. This effect is particularly pronounced for the parameter α, which depends on the difference in potential energy between the true and false vacua and is inversely proportional to the fourth power of the temperature. Moreover, for $\alpha < 1$, the SGWB amplitude scales approximately

[2] A more accurate estimate of $T_{\rm RH}$ can be obtained from energy conservation by matching the energy density before and after the transition: $\rho(\phi(0,T_p)) = \rho(\phi(v_{\rm True}(T_{\rm RH}),T_{\rm RH})$ [106].

with the square of α, further amplifying these theoretical uncertainties. A robust and theoretically consistent analysis can be achieved either through a RG-improved potential or through an EFT approach using Dimensional Reduction (DR). In this chapter, we shall use the former.

The percolation temperature, T_p, is well-defined from a theoretical standpoint and is expected to be relatively unaffected by uncertainties, although small variations can significantly impact the SGWB. Its determination is intrinsically linked to the bubble wall velocity, v_w. A recent study [351] provided model-independent analytical expressions for v_w. Depending on the type of fluid motion—deflagration, detonation, or hybrids—different expressions and approximations apply. Although, a recent study [352] performed real-time hydrodynamical lattice simulations and their analysis revealed that most solutions tended towards a runaway scenario (*i.e.*, with v_w approaching the speed of light, $v_w \simeq 1$). Scenarios leading to a steady-state solution, where the analytical results from [351] align with [352], were found to be rare and required fine-tuning of the nucleation temperature.

4.2 Spectral templates for the SGWB

We use the latest templates (as of December 2024) for the SGWB background spectrum characterised by the amplitude $\Omega_{\rm GW}$ and frequency f as provided by the LISA Cosmology Working Group [353]. The SGWB gets contributions from three main sources: sound waves [354–356], bubble wall collisions [25, 322, 357], and MHD turbulence in the plasma [322, 358]. Sound waves typically provide a dominant contribution. However, in the presence of supercooling the bubbles undergo unbounded expansion, making wall collisions efficient in producing gravitational radiation. Turbulence effects are still not well understood and remain largely uncertain compared to the other sources. Since the contribution from turbulence is expected to be subdominant, we neglect it in what follows.

For bubble collisions and highly relativistic fluid shells, the spectrum admits a broken power law that can be expressed as [353]

$$\Omega_{\rm GW}^{\rm BC}(f,\Omega_{\rm GW}^{\rm peak},f_{\rm peak}) = \Omega_{\rm GW}^{\rm peak}\frac{(n_1\odot n_2)^{\frac{n_1-n_2}{a_1}}}{\left[\odot n_2\left(\frac{f}{f_{\rm peak}}\right)^{-\frac{n_1 a_1}{n_1-n_2}}+n_1\left(\frac{f}{f_{\rm peak}}\right)^{-\frac{n_2 a_1}{n_1-n_2}}\right]^{\frac{n_1-n_2}{a_1}}}\,, \tag{4.15}$$

where $\Omega_{\rm GW}^{\rm peak}$ and $f_{\rm peak}$, which we call *geometric parameters*, correspond to the peak energy density amplitude and frequency, respectively. The n_i and a_i parameters result from a fit to numerical simulations and are given as $n_1 = 2.4$, $n_2 = \odot 2.4$ and $a_1 = 1.2$ [353]. We can relate the geometric and thermodynamics parameters as follows

$$h^2\Omega_{\rm GW}^{\rm peak} = h^2 F_{\rm GW,0}\, A_{\rm str}\, \tilde{K}^2 \left(\frac{\beta}{H(T_p)}\right)^{-2}, \quad f_{\rm peak} \simeq 0.11\, H_{*,0}\,\frac{\beta}{H(T_p)}\,, \tag{4.16}$$

where $\tilde{K} \equiv \kappa_{\rm BC}[\alpha/(1+\alpha)]$ is the fractional energy density and $A_{\rm str} \simeq 0.05$ [359] and h is defined through the Hubble constant $H_0 = 100h$ km/s/Mpc. The parameters $F_{\rm GW,0}$ and $H_{*,0}$ account for the redshift as follows:

$$\begin{aligned} H_{*,0} &\simeq 1.65\times 10^{-5}\ {\rm Hz}\left(\frac{g_*(T_{\rm RH})}{100}\right)^{1/6}\left(\frac{T_{\rm RH}}{\rm GeV}\right)\left(\frac{\Gamma_\phi}{H(T_p)}\right)^{-1/3}, \\ h^2\, F_{\rm GW,0} &\simeq 1.65\times 10^{-5}\left(\frac{100}{g_*(T_{\rm RH})}\right)^{1/3}\left(\frac{\Gamma_\phi}{H(T_p)}\right)^{2/3}, \end{aligned} \tag{4.17}$$

with $H_0 = 100h$ km/s/Mpc. The $\Gamma_\phi/H(T_p)$ factors are taken from Ref. [308]. In the case of radiation domination at percolation, $\Gamma_\phi/H(T_p) = 1$.

The efficiency factor $\kappa_{\rm BC}$ is model dependent. Whether the bubble wall reaches a terminal velocity depends on the pressure exerted by the plasma on the walls. Two contributions apply: a LO contribution due to $1\to 1$ scattering [360] and a NLO one from $1\to N$ splittings [361]:

$$P_{\rm NLO} = \sum_{a=V,f} k_a c_a \frac{\Delta m_a^2 T_p^2}{24} \quad \text{and} \quad P_{\rm LO} = \sum_{a=V} k_a g_a^2 \Delta m_{\rm a} T_p^3\,, \tag{4.18}$$

where V are gauge vectors and f are fermions. Here $c_a = 1$ (1/2) for bosons (fermions), k_a denote the corresponding DOF, Δm_a^2 is the squared mass difference of the particles in the false and true vacuum and g_a the associated gauge coupling to the vector a. Defining [308]

$$\alpha_{\rm eq} = \frac{P_{\rm NLO}}{\rho_R} \quad \text{and} \quad \alpha_\infty = \frac{P_{\rm LO}}{\rho_R}\,, \tag{4.19}$$

the equilibrium Lorentz factor (corresponding to the pressure terms $P_{\rm LO}$ and $P_{\rm NLO}$ being balanced by the potential energy difference $\Delta V_{\rm eff}$) is

$$\gamma_{\rm eq} = \frac{\alpha \odot \alpha_\infty}{\alpha_{\rm eq}}\,. \tag{4.20}$$

Neglecting plasma effects *i.e.*, $P_{\rm NLO}$, as the bubble grows, its Lorentz factor can be approximated as [308]

$$\tilde{\gamma}_* \approx \frac{2}{3}\frac{R_*}{R_0}\,, \tag{4.21}$$

where R_0 is the initial bubble radius,

$$R_0 = \left(\frac{3S_3(T_p)}{4\pi\Delta V(T_p)}\right)^{1/3}. \tag{4.22}$$

The efficiency factor can be estimated as the ratio of the energy of the bubble wall to the total energy released [308]:

$$\kappa_{\rm BC} = \begin{cases} \left(1 \odot \frac{1}{3}\left(\frac{\tilde{\gamma}_*}{\gamma_{\rm eq}}\right)^2\right)\left(1 \odot \frac{\alpha_\infty}{\alpha}\right) & \text{for} \quad \tilde{\gamma}_* < \gamma_{\rm eq}\,, \\ \frac{2}{3}\frac{\gamma_{\rm eq}}{\tilde{\gamma}_*}\left(1 \odot \frac{\alpha_\infty}{\alpha}\right) & \text{otherwise.} \end{cases} \tag{4.23}$$

For the sound wave contribution, the SGWB template is described by the following double broken power law [353]

$$\begin{aligned} \Omega_{\rm GW}^{\rm SW}(f, \Omega_2, f_1, f_2) &= \Omega_{\rm int} \times S(f)\,, \\ S(f) &= N\left(\frac{f}{f_1}\right)^{n_1}\left[1 + \left(\frac{f}{f_1}\right)^{a_1}\right]^{\frac{-n_1+n_2}{a_1}}\left[1 + \left(\frac{f}{f_2}\right)^{a_2}\right]^{\frac{-n_2+n_3}{a_2}}\,, \end{aligned} \tag{4.24}$$

where the fit parameters are $n_1 = 3$, $n_2 = 1$, $n_3 = \odot 3$, $a_1 = 2$ and $a_2 = 4$. Here, N is a normalization factor that is determined by $\int_{-\infty}^{+\infty} S(f) d\ln f = 1$. The geometric parameters f_1 and f_2 are given by

$$f_1 \simeq 0.2\, H_{*,0}\, (H(T_p)R_*)^{-1}\,, \tag{4.25}$$

$$f_2 \simeq 0.5\, H_{*,0}\, \Delta_w^{-1}\, (H(T_p)R_*)^{-1}\,, \tag{4.26}$$

where $\Delta_w = v_{\rm shell}/\max(v_w, c_s)$ with $v_{\rm shell} = |v_w \odot c_s|$ the dimensionless sound shell thickness. A definition for $H(T_p)R_*$ was given below Eq. (4.14). The integrated amplitude $\Omega_{\rm int}$ obeys the relation [309],

$$h^2\Omega_{\rm int} = 0.11 h^2 F_{\rm GW,0}\, K^2\, (H(T_p)\tau_{\rm SW})\, (H(T_p)R_*)\,, \tag{4.27}$$

where the lifetime of sound waves in units of Hubble time is $H(T_p)\tau_{\rm SW} = \min(2H(T_p)R_*/\sqrt{3K}, 1)$, and $K = 0.6\kappa_{\rm SW}\alpha/(1+\alpha)$ is the fractional kinetic energy converted into sound waves. The efficiency factor is [105]

$$\kappa_{\rm SW} = \frac{\alpha_{\rm eff}}{\alpha}\frac{\alpha_{\rm eff}}{0.73 + 0.083\sqrt{\alpha_{\rm eff}} + \alpha_{\rm eff}}\,, \quad \alpha_{\rm eff} = \alpha(1 \odot \kappa_{\rm BC})\,. \tag{4.28}$$

4.3 Formalism for the PBH production

During a FOPT, the Universe transitions from the false vacuum to the true vacuum through the process of bubble nucleation. Supercooling occurs when the Universe remains trapped in the false vacuum for an extended period, delaying bubble nucleation to temperatures far below the critical temperature T_c. In this regime, bubble expansion is primarily driven by the vacuum energy $\Delta V_{\rm eff}$ rather than by radiation. This triggers a period of thermal inflation that persists until the phase transition is complete. Upon completion, the vacuum energy is converted into radiation, which reheats the plasma and marks the onset of the radiation domination era.

Bubble nucleation is an inherently stochastic process, so that different regions of the Universe undergo nucleation at different times. For an average Hubble patch, nucleation occurs at a cosmic time $\tau_{\rm nuc}$. However, late-nucleating patches, labelled by i, nucleate at a time $\tau^i_{\rm nuc} > \tau_{\rm nuc}$ and remain vacuum-dominated for an extended period. Consequently, the false vacuum energy density of the late-nucleating patches remains approximately constant, while the energy density of the true-vacuum background, which is dominated by radiation, rapidly decreases as the Universe cools. As a result, late-nucleating patches become overdense relative to the background.

If the overdensity, $\delta(\tau, \tau^i_{\rm nuc})$, in a patch i exceeds a critical threshold δ_c [362],

$$\delta\left(\tau;\tau^i_{\rm nuc}\right) \equiv \frac{\rho^{\rm late}_{\rm tot}\left(\tau;\tau^i_{\rm nuc}\right) \odot \rho^{\rm bkg}_{\rm tot}(\tau)}{\rho^{\rm bkg}_{R}(\tau)} > \delta_{\rm c}\,, \tag{4.29}$$

then the patch can collapse into a PBH. Here, $\rho^{\rm late}_{\rm tot}\left(\tau;\tau^i_{\rm nuc}\right)$ is the total energy density at cosmic time τ for a patch i that nucleated at time $\tau_{\rm nuc,i}$, and $\rho^{\rm bkg}_{\rm tot}(\tau)$ and $\rho^{\rm bkg}_{R}(\tau)$ are the total and radiation energy densities of the background true-vacuum regions, respectively. The overdensity in late-nucleating patches increases over time and reaches its peak shortly after the patch percolates. This maximum arises because the energy density of the surrounding true-vacuum regions begins to dilute slightly earlier, while the late-nucleating patch maintains a nearly constant energy density dominated by vacuum energy until they start to percolate and their vacuum energy is gradually converted into radiation.

It is possible to derive an approximate analytical expression for the probability that a given patch i collapses into a PBH. Assuming strongly supercooled FOPTs with $\alpha > 100$, this probability depends solely on the inverse time duration of the FOPT $\beta/H(T_p)$ and on the critical threshold δ_c as [362]

$$\mathcal{P}_{\rm coll} \approx \exp\left\{\odot a_1 \left(\frac{\beta}{H(T_p)}\right)^{a_2} (1+\delta_c)^{a_3[\beta/H(T_p)]}\right\}, \tag{4.30}$$

where $a_1 = 0.56468$, $a_2 = 1.266$ and $a_3 = 0.6639$ are dimensionless fitting parameters. Simulations suggest that δ_c ranges between 0.4 and 0.66 if the origin of the overdensities is similar to that of inflation [363–366].

The fraction of dark matter in the form of PBHs, normalised to the total DM relic abundance today, is given by [362][3]

$$f_{\rm PBH} \approx \frac{\mathcal{P}_{\rm coll}}{2.2\times10^{-8}} \frac{T_{\rm RH}}{0.14\ {\rm GeV}}\,, \tag{4.31}$$

and the PBH mass PBH is [362]

$$M_{\rm PBH} = M_\odot \left(\frac{20}{g_*(T_{\rm RH})}\right)^{1/2} \left(\frac{0.14\,{\rm GeV}}{T_{\rm RH}}\right)^2. \tag{4.32}$$

Given the strong sensitivity of $f_{\rm PBH}$ on δ_c, we treat δ_c as a free parameter in the range $[0.40, 0.66]$.

A recent study [368] revises δ_c upward by an order of magnitude, which leads to drastically reduced PBH abundances. To achieve $f_{\rm PBH} \sim 1$ requires $\beta/H(T_p) \lesssim 2.5$. However, such low values of $\beta/H(T_p)$ are not obtainable in our model, as the FOPT does not percolate and cannot complete. It is worth noting that additional contributions not included in Ref. [368], particularly the energy density in

[3] A similar PBH production mechanism was presented in Ref. [367]. The main difference is that Ref. [362] assumes that collapsing patches can contain true vacuum bubbles, while Ref. [367] assumes can they can not. This affects the threshold value of $\beta/H(T_p)$ required to fully account for DM. In Ref. [367], $f_{\rm PBH} = 1$ for $\beta/H(T_p) \gtrsim 3.8$, whereas in Ref. [362] $\beta/H(T_p) \gtrsim 8$.

bubble walls, may play an important role in the formation of PBHs in supercooled FOPTs [367, 369, 370]. However, it remains to be demonstrated whether the bubble wall contribution validates the conclusions of Ref. [362] and negates the conclusions of Ref. [368]. Until this issue is resolved, we optimistically take $\delta_c \in [0.40, 0.66]$.

4.4 Formalism for the production of primordial magnetic fields

The initial conditions of the magnetic fields generated during a FOPT play a crucial role in determining the evolution of MHD turbulence. In particular, the initial magnetic helicity has a significant impact on the MHD decay process [371]. MHD decay refers to the dissipation of magnetic energy and the relaxation of turbulent motions in a conducting plasma, governed by MHD equations. Magnetic helicity density characterises the twist and linkage of magnetic field lines, defined as $|H^M| \equiv \langle \mathbf{A} \cdot \mathbf{B} \rangle$, where $\mathbf{B} = \nabla \times \mathbf{A}$, with $\mathbf{A}$ and $\mathbf{B}$ denoting the vector potential and magnetic field, respectively. For helical fields, this decay is typically slower because helicity is approximately conserved. Consequently, a maximally helical field increases its correlation length as magnetic energy dissipates, driving an inverse cascade of energy from small to large scales. This process generates coherent magnetic structures significantly larger than the initial energy injection scale. Such dynamics may have been critical for the persistence and evolution of primordial magnetic fields, enabling their survival and large-scale coherence in the present universe. In contrast, non-helical fields decay more rapidly, with energy dissipating at small scales through viscous and resistive effects.

A maximally helical magnetic field satisfies $|H^M| = (\pi/k)\langle |\mathbf{B}|^2 \rangle$ at each scale k, where $\langle |\mathbf{B}|^2 \rangle/2$ is the magnetic energy density. For such a field, the decay of MHD turbulence during the radiation-dominated epoch follows a power-law dependence on conformal time η [372]

$$B \sim \eta^{-1/3}\,, \quad \lambda \sim \eta^{2/3}\,, \tag{4.33}$$

where B is the magnetic field strength and λ is the correlation length of the magnetic field. A non-helical magnetic field has $H^M = 0$ at all scales, implying that its Fourier modes satisfy $\mathbf{B}_\mathbf{k} \cdot \mathbf{A}^*_\mathbf{k} = 0$ for all wavenumbers $\mathbf{k}$. Then, inverse transfer can still occur due to kinetic helicity in the plasma [372]. Kinetic helicity $H^M_{\rm kin} \equiv \langle \mathbf{v} \cdot \boldsymbol{\omega} \rangle$ measures the correlation between a fluid's velocity $\mathbf{v}$ and vorticity $\boldsymbol{\omega} \equiv \nabla \times \mathbf{v}$. In plasmas, a non-zero $H^M_{\rm kin}$ can induce an inverse transfer of magnetic energy, even for non-helical magnetic fields ($H^M = 0$), by exciting helical plasma motions that reorganise the magnetic field structure at larger scales [372]. However, the strength of this effect remains debated [373]. In this case, B and λ scale as

$$B \sim \eta^{-1/2}\,, \quad \lambda \sim \eta^{1/2}\,. \tag{4.34}$$

These scaling laws are applicable during the radiation-dominated epoch, during which the scale factor evolves as $a \sim \eta$. After recombination, the magnetic field strength decays as $B \sim a^{-2}$ due to the expansion of the Universe. To encompass the helical and non-helical cases, we introduce the generalised parameters,

$$p_b = \frac{2}{b+3}(b+1)\,, \quad q_b = \frac{2}{b+3}\,, \tag{4.35}$$

yielding the power-law scalings:

$$B \sim \eta^{-p_b/2}\,, \quad \lambda \sim \eta^{q_b}\,, \tag{4.36}$$

where $b = 0$ and $b = 1$ correspond to the helical and non-helical cases, respectively. The magnetic energy density at the time of percolation is estimated as [314, 374]

$$\rho_{B,*} = 0.1 \frac{\kappa_{\rm col}\alpha}{1+\alpha}\rho_*\,, \tag{4.37}$$

where $\rho_* \approx \rho_{\rm vac}$ is the total energy density at percolation. This expression assumes a 10% efficiency in converting plasma motion into magnetic fields [326, 375, 376].

The present-day magnetic field spectrum is given by [314]

$$B_0(\lambda) = \left(\frac{a_{\rm RH}}{a_{\rm rec}}\right)^{p_b/2} \left(\frac{a_{\rm RH}}{a_0}\right)^2 \sqrt{\frac{17}{10}\,\kappa_h\,\rho_{B,*}} \begin{cases} \left(\frac{\lambda}{\lambda_0}\right)^{-5/2}, & \lambda \geq \lambda_0 \\ \left(\frac{\lambda}{\lambda_0}\right)^{1/3}, & \lambda < \lambda_0\,, \end{cases} \tag{4.38}$$

where the coherence scale of the magnetic field today is [314]

$$\lambda_0 = \frac{a_0}{a_{\rm RH}} \left(\frac{a_{\rm rec}}{a_{\rm RH}}\right)^{q_b} \lambda_* \,, \tag{4.39}$$

and the initial correlation length λ_* is determined by the bubble size at percolation [343]:

$$\lambda_* = \frac{(8\pi)^{1/3}}{H(T_p)} \left(\frac{\beta}{H(T_p)}\right)^{-1} , \tag{4.40}$$

assuming a wall velocity $v_w = 1$ for strongly supercooled transitions. The redshift factors are given by

$$\frac{a_{\rm RH}}{a_0} = 8 \times 10^{-14} \left(\frac{100}{g_*(T_{\rm RH})}\right)^{1/3} \left(\frac{\rm GeV}{T_{\rm RH}}\right), \tag{4.41}$$

$$\frac{a_{\rm RH}}{a_{\rm rec}} = 8 \times 10^{-11} \left(\frac{100}{g_*(T_{\rm RH})}\right)^{1/3} \left(\frac{\rm GeV}{T_{\rm RH}}\right). \tag{4.42}$$

After the phase transition ends, a fraction of the bubble wall energy of the dark scalar is transferred to the Higgs field, due to the Higgs portal coupling $\lambda_{\sigma h}$. To account for this we introduce an efficiency factor,

$$\kappa_h = 1 \odot \frac{\mathcal{V}_{\rm eff}(v_\sigma(T_p), v)}{\mathcal{V}_{\rm eff}(v_\sigma(T_p), 0)} \,, \tag{4.43}$$

where $\mathcal{V}_{\rm eff}$ is the 2-field effective potential, where the first argument corresponds to the σ direction, and the second argument corresponds to the Higgs direction. The VEV is evaluated at T_p.

4.5 Generic scale-invariant U(1)′ models

We will now explore a class of generic U(1)′ extensions of the SM, primarily designed to accommodate neutrino masses and mixing through the inclusion of three generations of right-handed neutrinos and a type-I seesaw mechanism. By imposing scale invariance, all tree-level dimensionful parameters of the theory are forbidden, thereby reducing the number of free parameters in the model Lagrangian. Specifically, the conventional Majorana mass term $M\bar{N}^c N$ is not allowed and must be replaced by a Yukawa term yielding the Majorana mass $M \to y_\sigma \langle\sigma\rangle / \sqrt{2}$ through the introduction of a complex singlet scalar σ. In standard Majoron models [377–379], the Majoron is identified with a pseudo Nambu-Goldstone boson resulting from the breaking of a global $\mathrm{U}(1)_{\mathrm{B-L}}$ lepton number symmetry. For this thesis, however, neither U(1)′ is global nor does a physical pseudo-Goldstone boson exist in the spectrum. Nevertheless, we refer to σ as Majoron due to its role in generating Majorana masses for right-handed neutrinos, while the corresponding class of models will be called Majoron-like.

The field content, their quantum numbers and transformations under rescaling are shown in Tab. 4.1. The third column lists the anomaly-free U(1)′ charges adopted from Ref. [380]. It is important to note that in the current framework, which includes only one additional scalar σ, the anomaly-free conditions require flavour universality to describe neutrino oscillation data. In this context, the class of models presented is representative of all such scenarios, including the $\mathrm{U}(1)_{\mathrm{B-L}}$ model with $x_{\mathcal{H}} = 0$ and $x_\sigma = 2$ in Tab. 4.1. We treat x_σ and $x_{\mathcal{H}}$ as free parameters. The SM gauge group representations are shown in the last three columns.

4.5.1 Yukawa sector

The neutrino sector Lagrangian of a classically scale invariant type-I seesaw mechanism with a Majoron reads [377–379]

$$\mathcal{L}_\nu = y_\nu^{ij} \overline{N}_i \mathcal{H} L_j + y_\sigma^{ij} \bar{N}_i^c N_j \sigma + \text{h.c.} \,, \tag{4.44}$$

where $L_i = (\nu_{\mathrm{L}i}\, e_{\mathrm{L}i})^{\mathrm{T}}$. The mass matrix in the basis $\{\bar{\nu}_{\mathrm{L},i}, \bar{N}_i^c\} \otimes \{\nu_{\mathrm{L}j}, N_j\}$ is in a block compact form,

$$\boldsymbol{M_\nu} = \begin{bmatrix} 0 & \frac{v}{\sqrt{2}} \boldsymbol{y_\nu}^{\mathrm{T}} \\ \frac{v}{\sqrt{2}} \boldsymbol{y_\nu} & \frac{v_\sigma}{\sqrt{2}} \boldsymbol{y_\sigma} \end{bmatrix} , \tag{4.45}$$

whose eigenvalues are the masses of the three active neutrinos, m_1, m_2 and m_3, and the three heavy neutrinos M_{N_1}, M_{N_2} and M_{N_3}. In the limit $M_{N_i} \gg m_i$, the effective light neutrino mass matrix is

$$\boldsymbol{m_\nu} \approx \frac{1}{\sqrt{2}} \frac{v^2}{v_\sigma} \boldsymbol{y_\nu}^{\mathrm{T}} \boldsymbol{y_\sigma}^{-1} \boldsymbol{y_\nu} \tag{4.46}$$

while the masses of the heavy neutrinos are given by

$$\boldsymbol{M_N} \approx \frac{v_\sigma}{\sqrt{2}} \boldsymbol{y_\sigma} \,. \tag{4.47}$$

The neutrino mass matrix can be inverted using the neutrino mass differences and the entries of the PMNS matrix, $\boldsymbol{U}_{\mathrm{PMNS}}$, as input parameters. For a type-I seesaw mechanism with a diagonal $\boldsymbol{y_\sigma}$, we can write [381]

$$\boldsymbol{y_\nu} = i \boldsymbol{\Sigma}^{-1/2} \boldsymbol{R} \boldsymbol{D}_{\sqrt{m}} \boldsymbol{U}_{\mathrm{PMNS}}^{\dagger} \,, \tag{4.48}$$

where $\boldsymbol{\Sigma}$ is a diagonal 3×3 matrix whose entries are the singular values of $[(\sqrt{2}v^2)/(2v_\sigma)]\boldsymbol{y_\sigma^{-1}}$, and $\boldsymbol{D}_{\sqrt{m}} = \mathrm{diag}(\sqrt{m_1}, \sqrt{m_2}, \sqrt{m_3})$. Here, $\boldsymbol{R}$ is a generic complex orthogonal 3×3 matrix (see also Ref. [381]) that satisfies [382]

$$\boldsymbol{R}\boldsymbol{R}^T = \boldsymbol{R}^T\boldsymbol{R} = \boldsymbol{I} \tag{4.49}$$

and is defined as

$$\boldsymbol{R} = \mathrm{sign}(x,y,z) \begin{bmatrix} \cos z_3 & \odot \sin z_3 & 0 \\ \sin z_3 & \cos z_3 & 0 \\ 0 & 0 & 1 \end{bmatrix} \begin{bmatrix} \cos z_2 & 0 & \odot \sin z_2 \\ \sin z_2 & 0 & \cos z_2 \\ 0 & 1 & 0 \end{bmatrix} \begin{bmatrix} 1 & 0 & 0 \\ 0 & \cos z_1 & \odot \sin z_1 \\ 0 & \sin z_1 & \cos z_1 \end{bmatrix} , \tag{4.50}$$

where z_i denote complex angles and $\mathrm{sign}(x,y,z)$ is a diagonal matrix of signs, both are treated as free parameters. For the numerical analysis, we used the latest neutrino oscillation data fit from the NuFIT collaboration [383], assuming a normal mass hierarchy. Cosmological constraints on the neutrino mass sum are also taken into account, with an upper bound set at $\sum m_\nu < 0.12$ eV [384]. Note that current LVK data impose constraints on classically conformal Majoron models because GW interferometers operating in the $10 \odot 100$ Hz frequency range are sensitive to scales between 10^{12} GeV and 10^{17} GeV, which are typically associated with heavy neutrino masses in a high-scale type-I seesaw mechanism.

4.5.2 Scalar potential

The tree-level scalar potential of a generic classically conformal Majoron model is given by

$$V_0(\mathcal{H}, \sigma) = \lambda_h (\mathcal{H}^\dagger \mathcal{H})^2 + \lambda_\sigma (\sigma^\dagger \sigma)^2 + \lambda_{\sigma h} (\mathcal{H}^\dagger \mathcal{H})(\sigma^\dagger \sigma) \,. \tag{4.51}$$

Field	Scale symmetry	U(1)′	SU(3)$_{\mathrm{C}}$	SU(2)$_{\mathrm{L}}$	U(1)$_{\mathrm{Y}}$
Q	$\rho^{-3/2}$	$\frac{1}{3}x_{\mathcal{H}} + \frac{1}{6}x_\sigma$	**3**	**2**	1/6
u_R	$\rho^{-3/2}$	$\frac{4}{3}x_{\mathcal{H}} + \frac{1}{6}x_\sigma$	**3**	**1**	2/3
d_R	$\rho^{-3/2}$	$\odot\frac{2}{3}x_{\mathcal{H}} + \frac{1}{6}x_\sigma$	**3**	**1**	$\odot$1/3
L	$\rho^{-3/2}$	$\odot x_{\mathcal{H}} \odot \frac{1}{2}x_\sigma$	**1**	**2**	$\odot$1/2
e_R	$\rho^{-3/2}$	$\odot 2x_{\mathcal{H}} \odot \frac{1}{2}x_\sigma$	**1**	**1**	$\odot$1
$\mathcal{H}$	ρ^{-1}	$x_{\mathcal{H}}$	**1**	**2**	1/2
N	$\rho^{-3/2}$	$\odot\frac{1}{2}x_\sigma$	**1**	**1**	0
σ	ρ^{-1}	x_σ	**1**	**1**	0

Table 4.1: Scaling and anomaly-free gauge quantum numbers of the field content in the class of scale-invariant Majoron-like models considered. The U(1)′ charges are defined in terms of those of the SM Higgs doublet $\mathcal{H}$, $x_{\mathcal{H}}$, and the Majoron field σ, x_σ. The ρ parameter denotes the scale factor for each field that also enters the coordinate transformation, $x \to x' = \rho x$, as required by the scale symmetry.

We can expand the Higgs doublet $\mathcal{H}$ and the Majoron σ in terms of real-valued components as

$$\mathcal{H} = \frac{1}{\sqrt{2}}\begin{bmatrix}\omega_1 + i\omega_2 \\ \phi_h + h_r + i\eta\end{bmatrix}, \qquad \sigma = \frac{1}{\sqrt{2}}\left(\phi_\sigma + h_r' + iJ\right), \tag{4.52}$$

where h_r and h_r' represent radial quantum fluctuations about the classical field configurations ϕ_h and ϕ_σ, while $\omega_{1,2}$, η, and J are the Goldstone modes corresponding to the longitudinal DOF of the gauge bosons upon symmetry breaking. In terms of classical fields, the tree-level potential reads

$$V_0(\phi_h, \phi_\sigma) = \frac{1}{4}\Big(\lambda_h\phi_h^4 + \lambda_\sigma\phi_\sigma^4 + \lambda_{\sigma h}\phi_h^2\phi_\sigma^2\Big). \tag{4.53}$$

We can then express the field-dependent squared mass matrix as

$$\boldsymbol{M^2_{(0)}} = \begin{bmatrix}3\phi_h^2\lambda_h + \frac{1}{2}\lambda_{\sigma h}\phi_\sigma^2 & \phi_h\phi_\sigma\lambda_{\sigma h} \\ \phi_h\phi_\sigma\lambda_{\sigma h} & 3\phi_\sigma^2\lambda_\sigma + \frac{1}{2}\lambda_{\sigma h}\phi_h^2\end{bmatrix}, \tag{4.54}$$

with corresponding eigenvalues given by

$$\begin{aligned}M^2_{h_1} =& \frac{1}{4}\Big(\odot\sqrt{2\phi_h^2\phi_\sigma^2\left(6\lambda_{\sigma h}\left(\lambda_h+\lambda_\sigma\right)\odot 36\lambda_h\lambda_\sigma + 7\lambda_{\sigma h}^2\right) + \phi_h^4\left(\lambda_{\sigma h}\odot 6\lambda_h\right)^2 + \phi_\sigma^4\left(\lambda_{\sigma h}\odot 6\lambda_\sigma\right)^2} \\ &+\phi_h^2\left(6\lambda_h + \lambda_{\sigma h}\right) + \lambda_{\sigma h}\phi_\sigma^2 + 6\lambda_\sigma\phi_\sigma^2\Big), \\ M^2_{h_2} =& \frac{1}{4}\Big(\sqrt{2\phi_h^2\phi_\sigma^2\left(6\lambda_{\sigma h}\left(\lambda_h+\lambda_\sigma\right)\odot 36\lambda_h\lambda_\sigma + 7\lambda_{\sigma h}^2\right) + \phi_h^4\left(\lambda_{\sigma h}\odot 6\lambda_h\right)^2 + \phi_\sigma^4\left(\lambda_{\sigma h}\odot 6\lambda_\sigma\right)^2} \\ &+\phi_h^2\left(6\lambda_h + \lambda_{\sigma h}\right) + \lambda_{\sigma h}\phi_\sigma^2 + 6\lambda_\sigma\phi_\sigma^2\Big).\end{aligned} \tag{4.55}$$

For the Goldstone bosons, the corresponding field-dependent masses are

$$M^2_{G_1} = \lambda_h\phi_h^2 + \frac{\lambda_{\sigma h}}{2}\phi_\sigma^2, \quad M^2_{G_2} = \lambda_\sigma\phi_\sigma^2 + \frac{\lambda_{\sigma h}}{2}\phi_h^2, \quad M^2_{G^\pm} = \lambda_h\phi_h^2 + \frac{\lambda_{\sigma h}}{2}\phi_\sigma^2. \tag{4.56}$$

The absence of quadratic terms at LO results in a massless physical scalar, identified with the h_2 boson, once the gauge and conformal symmetries are broken. As a pseudo-Goldstone boson of the scale symmetry, it acquires an explicit mass term due to the non-linear form of the CW potential [303] that violates the scale symmetry of the Lagrangian. In the Landau gauge and assuming the $\overline{\text{MS}}$ renormalisation scheme, the CW potential takes the generic form,

$$V_{\text{CW}}(\phi_h, \phi_\sigma) = \frac{1}{64\pi^2}\sum_a n_a M_a^4(\phi_h, \phi_\sigma)\left(\ln\frac{M_a^2(\phi_h, \phi_\sigma)}{\mu^2}\odot c_a\right), \tag{4.57}$$

where a runs over all vector, scalar and fermionic DOF, while $M_a(\phi_h, \phi_\sigma)$ denotes the field-dependent mass for a field a, and μ is the renormalisation scale. The c_a factors are renormalisation-dependent constants taking the values $c_a = 3/2$ for fermions and scalars and $c_a = 5/6$ for vectors in the $\overline{\text{MS}}$ scheme. The pre-factor n_a is given by

$$n_a = (\odot 1)^{2s_a} Q_a N_a (2s_a + 1). \tag{4.58}$$

Here, s_a denotes the spin of particle a, Q_a is 1 for uncharged particles and 2 for charged ones, whereas N_a is 1 for uncoloured particles and 3 for coloured ones.

The one-loop effective potential is

$$V = V_0(\phi_h, \phi_\sigma) + V_{\text{CW}}(\phi_h, \phi_\sigma), \tag{4.59}$$

which must be extremised in order to study the symmetry breaking patterns. In the zero temperature limit, the tadpole equations are

$$\begin{aligned}0 &= \lambda_h v^3 + \frac{1}{2}\lambda_{\sigma h} v v_\sigma^2 + \frac{\partial V_{\text{CW}}}{\partial\phi_h}\Big|_{\phi_h = v, \phi_\sigma = v_\sigma}, \\ 0 &= \lambda_\sigma v_\sigma^3 + \frac{1}{2}\lambda_{\sigma h} v^2 v_\sigma + \frac{\partial V_{\text{CW}}}{\partial\phi_\sigma}\Big|_{\phi_h = v, \phi_\sigma = v_\sigma}.\end{aligned} \tag{4.60}$$

These equations can be used to fix the values of $\lambda_{\sigma h}$ and λ_σ in our numerical analysis. The zero external momentum contribution to the scalar mass spectrum is derived by computing the eigenvalues of the Hessian matrix of the effective potential, while the momentum-dependent part is obtained from the self-energies Π. Separating the one-loop and tree-level parts, the mass matrix can be written as [385]

$$\boldsymbol{M^2}(p^2) = \boldsymbol{M^2_{(0)}} + \boldsymbol{\mathcal{M}}\,, \tag{4.61}$$

with $\boldsymbol{\mathcal{M}} = \mathrm{Re}\{\boldsymbol{\Delta\Pi}(p^2)\} + \boldsymbol{\partial^2} V_{\rm CW}$, where $\boldsymbol{\partial^2} V_{\rm CW}$ is the Hessian matrix of the CW potential and $\boldsymbol{\Delta\Pi} = \boldsymbol{\Pi}(p^2 = M^2) \odot \boldsymbol{\Pi}(p^2 = 0)$. We then obtain the loop corrected masses

$$\begin{aligned} M^2_{h_1} = \frac{1}{4}\Big(\Sigma \odot \Big\{ & 32\boldsymbol{\mathcal{M}}_{12}\phi_h\lambda_{\sigma h}\phi_\sigma + \phi_h^2\left(6\lambda_h \odot \lambda_{\sigma h}\right)\left(\phi_h^2\left(6\lambda_h \odot \lambda_{\sigma h}\right) + 4\left[\boldsymbol{\mathcal{M}}_{11} \odot \boldsymbol{\mathcal{M}}_{22}\right]\right) \\ & + 2\phi_\sigma^2\left(\Phi_h\phi_h^2 + \Phi_\sigma\right) + \phi_\sigma^4\left(\lambda_{\sigma h} \odot 6\lambda_\sigma\right)^2 + 4\left[\left(\boldsymbol{\mathcal{M}}_{11} \odot \boldsymbol{\mathcal{M}}_{22}\right)^2 + 4\Pi^2_{h_1h_2}\right] \Big\}^{1/2}\Big)\,, \\ M^2_{h_2} = \frac{1}{4}\Big(\Sigma + \Big\{ & 32\boldsymbol{\mathcal{M}}_{12}\phi_h\lambda_{\sigma h}\phi_\sigma + \phi_h^2\left(6\lambda_h \odot \lambda_{\sigma h}\right)\left(\phi_h^2\left(6\lambda_h \odot \lambda_{\sigma h}\right) + 4\left[\boldsymbol{\mathcal{M}}_{11} \odot \boldsymbol{\mathcal{M}}_{22}\right]\right) \\ & + 2\phi_\sigma^2\left(\Phi_h\phi_h^2 + \Phi_\sigma\right) + \phi_\sigma^4\left(\lambda_{\sigma h} \odot 6\lambda_\sigma\right)^2 + 4\left[\left(\boldsymbol{\mathcal{M}}_{11} \odot \boldsymbol{\mathcal{M}}_{22}\right)^2 + 4\Pi^2_{h_1h_2}\right] \Big\}^{1/2}\Big)\,, \end{aligned} \tag{4.62}$$

where

$$\begin{aligned} \Sigma &= \phi_h^2\left(6\lambda_h + \lambda_{\sigma h}\right) + \lambda_{\sigma h}\phi_\sigma^2 + 6\lambda_\sigma\phi_\sigma^2 + 2\boldsymbol{\mathcal{M}}_{11} + 2\boldsymbol{\mathcal{M}}_{22}\,, \\ \Phi_h &= 6\lambda_{\sigma h}\left(\lambda_h + \lambda_\sigma\right) \odot 36\lambda_h\lambda_\sigma + 7\lambda_{\sigma h}^2\,, \\ \Phi_\sigma &= \odot 2(\boldsymbol{\mathcal{M}}_{11} \odot \boldsymbol{\mathcal{M}}_{22})\left(6\lambda_\sigma \odot \lambda_{\sigma h}\right)\,. \end{aligned} \tag{4.63}$$

Following symmetry breaking, we have a total of 7 parameters: three quartic couplings, two VEVs, and two physical scalar masses. Of them, the Higgs VEV and mass M_{h_1} are fixed to their experimentally measured values, so we are left with λ_h, λ_σ, $\lambda_{\sigma h}$, v_σ, and M_{h_2}. The tadpole relations in (4.60) fix two of these parameters, which we choose to be λ_σ and $\lambda_{\sigma h}$, while the one-loop corrected masses in (4.62) constrain two additional parameters, which we choose to be v_σ and λ_h. Consequently, the only remaining free parameter is the mass of the additional Higgs, M_{h_2}. The full set of one-loop diagrams and the corresponding expressions for the self-energies are provided in App. F.

To simplify the numerical analysis and in the interest of efficiency, we make the following approximations. First, we neglect mixing effects generated at one-loop, *i.e.* $\Pi_{h_1h_2} = 0$, and instead utilise results from the tree level contribution. This approximation is not expected to significantly impact the final outcome, given that (a) experimental constraints already favour a relatively small Higgs mixing angle, and (b) we have found numerically that such an angle always remains small. Second, since the strength of phase transitions in classically conformal models with additional gauge groups is typically driven by gauge interactions, where the relation between scalar quartic λ and gauge g couplings is $\lambda \sim g^4$ [386], we anticipate that for $g \lesssim 1$, contributions from scalar fields to both one-loop masses and the effective potential are small. Indeed, we have numerically verified that for $\lambda_\sigma \sim \mathcal{O}(0.1)$, as obtained in our simulations, scalar corrections lead to changes in λ_σ of about 6% and in λ_h of about 0.1%, with v_σ and $\lambda_{\sigma h}$ unchanged. Consequently, we only include fermion and gauge boson contributions in the calculation of one-loop masses and the effective potential. This approximation is supported by arguments presented in [103], particularly in the context of an SU(2) conformal model. The immediate advantage of these approximations is evident in the calculation of one-loop tadpole equations in (4.60), which can be solved fully analytically (see App. G for the complete expressions). Furthermore, as the Higgs vacuum does not play a role in the FOPT, the relevant contributions at one loop are those from the Z′ boson and the heavy neutrinos.

4.5.3 Gauge sector

The presence of a new U(1)′ gauge symmetry implies the existence of an additional heavy gauge boson Z′ that mixes with the SM photon and Z^0 boson. To illustrate this, consider the covariant derivatives which explicitly depend on the Higgs doublet and Majoron U(1)′ gauge charges:

$$\begin{aligned} D_\mu\mathcal{H} &= \left(\partial_\mu \odot \frac{i}{2}g_1 B_\mu \odot i g_2 \tau_a A^a_\mu \odot i x_\mathcal{H} g_L B'_\mu \odot i g_{12} x_\mathcal{H} B_\mu \odot \frac{i}{2} g_{21} B'_\mu\right)\mathcal{H}\,, \\ D_\mu\sigma &= \left(\partial_\mu \odot i g_{21} x_\sigma B_\mu \odot i x_\sigma g_L B'_\mu\right)\sigma\,. \end{aligned} \tag{4.64}$$

The usual $\mathrm{U}(1)_\mathrm{Y}$ and $\mathrm{SU}(2)_\mathrm{L}$ gauge couplings are denoted as g_1 and g_2, respectively, while g_L is the $\mathrm{U}(1)'$ gauge coupling. The $\mathrm{U}(1)_\mathrm{Y} \odot \mathrm{U}(1)'$ kinetic mixing is generally described by two parameters, g_{12} and g_{21}, although it is possible to rotate to a basis in which $g_{21} = 0$ [387]. The $\mathrm{U}(1)_\mathrm{Y}$, $\mathrm{U}(1)'$ and $\mathrm{SU}(2)_\mathrm{L}$ gauge fields are denoted as B_μ, B'_μ and A^a_μ, respectively. By expanding the kinetic terms $|D_\mu \mathcal{H}|^2$ and $|D_\mu \sigma|^2$, one obtains the field-dependent mass matrix, which in the basis $\{A^1_\mu, A^2_\mu, B_\mu, A^3_\mu, B'_\mu\} \otimes \{A^1_\mu, A^2_\mu, B_\mu, A^3_\mu, B'_\mu\}$ is

$$\boldsymbol{M_V^2} = \begin{bmatrix} \frac{g_2^2\phi_h^2}{4} & 0 & 0 & 0 & 0 \\ 0 & \frac{g_2^2\phi_h^2}{4} & 0 & 0 & 0 \\ 0 & 0 & \frac{g_1^2\phi_h^2}{4} & \odot\frac{1}{4}g_1g_2\phi_h^2 & \frac{g_1(g_{12}+2x_\mathcal{H}g_L)\phi_h^2}{4} \\ 0 & 0 & \odot\frac{1}{4}g_1g_2\phi_h^2 & \frac{g_2^2\phi_h^2}{4} & \odot\frac{g_2(g_{12}+2x_\mathcal{H}g_L)\phi_h^2}{4} \\ 0 & 0 & \frac{g_1(g_{12}+2g_Lx_\mathcal{H})\phi_h^2}{4} & \odot\frac{g_2(g_{12}+2x_\mathcal{H}g_L)\phi_h^2}{4} & \frac{(g_{12}+2x_\mathcal{H}g_L)^2\phi_h^2}{4} + g_L^2x_\sigma^2\phi_\sigma^2 \end{bmatrix}, \tag{4.65}$$

and whose eigenvalues provide the vector bosons' field-dependent masses,

$$\begin{aligned} M^2_\gamma &= 0\,, \\ M^2_{W^\pm} &= \frac{g_2^2\phi_h^2}{4}\,, \\ M^2_{\mathrm{Z}^0} &= \frac{1}{8}(G\phi_h^2 + 4g_L^2x_\sigma^2\phi_\sigma^2) \\ &\quad \odot \sqrt{G^2\phi_h^4 + 8g_L^2x_\sigma^2\phi_h^2\phi_\sigma^2\left[(2g_Lx_\mathcal{H}+g_{12})^2 \odot g_1^2 \odot g_2^2\right] + 16g_L^4x_\sigma^4\phi_\sigma^4}\,, \\ M^2_{\mathrm{Z}'} &= \frac{1}{8}(G\phi_h^2 + 4g_L^2x_\sigma^2\phi_\sigma^2) \\ &\quad + \sqrt{G^2\phi_h^4 + 8g_L^2x_\sigma^2\phi_h^2\phi_\sigma^2\left[(2g_Lx_\mathcal{H}+g_{12})^2 \odot g_1^2 \odot g_2^2\right] + 16g_L^4x_\sigma^4\phi_\sigma^4}\,, \end{aligned} \tag{4.66}$$

where we define $G \equiv g_1^2 + g_2^2 + (g_{12}^2 + 2g_Lx_\mathcal{H})^2$. Due to the flavour universality of the $\mathrm{U}(1)'$ charges in Tab. 4.1, the new Z' boson couples to all SM fermions. Consequently, direct searches for Z' bosons at the LHC impose stringent constraints on its mass, restricting it to be slightly above 5 TeV [388–391]. Additionally, constraints from the LEP [246] impose strict limitations on the allowed values of the kinetic mixing, parametrised here via g_{12}. Note that a heavy Z' boson implies a hierarchical relation among the VEVs, $v_\sigma \gg v$, from which we can derive approximate expressions for the masses of the Z^0 and Z' as follows:

$$M^2_{\mathrm{Z}^0} = \frac{\phi_h^2}{16}(g_1^2+g_2^2)\left(4 \odot \frac{(g_{12}+2g_Lx_\mathcal{H})\phi_h^2}{g_L^2x_\sigma^2\phi_\sigma^2}\right), \quad M^2_{\mathrm{Z}'} = \frac{1}{4}(g_{12}+2g_Lx_\mathcal{H})^2\phi_h^2 + g_L^2x_\sigma^2\phi_\sigma^2\,. \tag{4.67}$$

While the kinetic mixing is expected to be small, the large value of v_σ suppresses the $\mathrm{Z}^0 \odot \mathrm{Z}'$ mixing angle (see *e.g.* [392]), proportional to v^2/v_σ^2, which in turn allows g_{12} to be $\mathcal{O}(1)$. Indeed, previous studies [105, 307] have shown that setting $g_{12}(\mu = M_{\mathrm{Z}'}) = \odot 0.5$ contributes to the stabilization of the Higgs vacuum by ensuring that λ_h remains positive up to the Planck scale. Although this conclusion was drawn within the context of the B$\odot$L model (equivalent to setting $x_\mathcal{H} = 0$ and $x_\sigma = 2$), we have observed that for other charge assignments, a non-zero value to g_{12} at the $M_{\mathrm{Z}'}$ scale also aids in stabilising the SM vacuum. For a cleaner analysis, we fix $g_{12} = 0$ at the EW scale, such that the only free parameters from the gauge sector are the charges $x_\mathcal{H}$ and x_σ and the gauge coupling g_L. However, RG evolution of g_{12} regenerates non-zero values at the $M_{\mathrm{Z}'}$ scale so that the potential is bounded from below provided that $41x_\mathcal{H} + 8x_\sigma \neq 0$ (see $\beta^{(1)}(g_{12})$ in App. E).

4.5.4 Effective thermal potential

PBH formation, magnetic fields and the SGWB are intricately correlated with the thermodynamic parameters of the FOPT, and therefore any theoretical errors in their determination can have an important impact on these observables. This is especially true for the determination of the SGWB, as it is frequently asserted that small theoretical inaccuracies in the thermodynamic parameters can

result in significant variations, spanning several orders of magnitude, in the predicted SGWB. We assess the generality of this statement and argue that it depends on the nature of the FOPT. The peak amplitudes for the sound wave and bubble collision contributions, $\Omega_{\rm SW}^{\rm peak}$ and $\Omega_{\rm BC}^{\rm peak}$ respectively, and their peak frequency, $f_{\rm peak}$, scale with the phase transition parameters according to

$$\Omega_{\rm SW}^{\rm peak} \propto \left(\frac{\kappa_{\rm SW}\alpha}{1+\alpha}\right)^2 \left(\frac{\beta}{H(T_p)}\right)^{-1}, \quad \Omega_{\rm BC}^{\rm peak} \propto \left(\frac{\kappa_{\rm BC}\alpha}{1+\alpha}\right)^2 \left(\frac{\beta}{H(T_p)}\right)^{-2}, \quad f_{\rm peak} \propto \frac{\beta}{H(T_p)}\,. \tag{4.68}$$

The impact of uncertainties in the efficiency factors is illustrated in Fig. 4.4. In the limit of strong supercooling, $\alpha \gg 1$, according to Fig. 6 of Ref. [393],

$$\frac{\beta}{H(T_p)} \approx \text{constant}\,. \tag{4.69}$$

For simplicity, taking $\kappa_{\rm BC} = 1$ (for bubble collisions) and $\kappa_{\rm BC} = 0$ (for sound waves), and using Eq. (4.28), we estimate

$$\Omega_{\rm SW,BC}^{\rm peak} \approx \text{constant}\,. \tag{4.70}$$

Likewise, for the peak frequency,

$$f_{\rm peak} \approx \text{constant}\,. \tag{4.71}$$

Although a different choice of the renormalisation scale implies a change in T_p, for strong supercooling, Eqs. (4.70) and (4.71) suggest that neither $\Omega_{\rm SW,BC}^{\rm peak}$ nor $f_{\rm peak}$ are expected to be significantly altered. In contrast, for $\alpha < 1$, a small change in T_p and $\Delta V_{\rm eff}(T_p)$ can be amplified at least by the second power of α in Eq. (4.68), *i.e.*, $(\Delta V_{\rm eff})^2/T_p^8$, which mostly impacts the peak amplitude.

Various methods have been proposed to mitigate theoretical uncertainties. These include constructing the RG-improved potential, where each coupling and field are evolved by means of their RG equations [103, 105, 394, 395], which is particularly relevant for supercooling. Another method involves DR of the original 4D theory into a 3D EFT [347, 396–401]. However, based on Eqs. (4.69), (4.70) and (4.71), we argue that the advantage of using DR for the study of classically scale-invariant models is questionable. Furthermore, the supercooling effect for low temperatures invalidates the high-temperature approximation for most field values. Recent work [104] has demonstrated that the 3D EFT approach is valid only for small field values. At NNLO precision, the Euclidean action (4.3) is corrected with an additional factor $Z(\phi_\sigma)$ in the kinetic term as $S = 4\pi \int dr r^2 Z(\phi_\sigma)(\partial\phi_\sigma)^2 + V_{\rm eff}$. In general, $Z(\phi_\sigma)$ scales as $1/\phi_\sigma$ as $\phi_\sigma \to 0$ which diverges in the symmetric vacuum, implying a breakdown of the derivative expansion. Since Ref. [104] has numerically verified that this correction is responsible for the observed differences between the 3D and 4D approaches, it remains unclear to us whether such an effect is physical or merely a consequence of operating in a regime where the derivative expansion may not be valid[4]. Therefore, we subscribe to the 4D RG-improved effective potential.

4.5.4.1 Renormalisation-group improved thermal potential: a 4D effective theory

The RG-improved effective potential at zero temperature for classically scale invariant models can be formulated as [403]

$$V_{\rm eff}(\phi_\sigma, \lambda, t) = \lambda(t)\phi_\sigma^4 \exp\left\{\frac{1}{4}\int_0^t dt\gamma[\lambda(t)]\right\}, \tag{4.72}$$

where λ denotes a set of couplings, γ is the anomalous dimension, and $t = \ln(\mu/\mu_{\rm ref})$, with μ being the RG scale and $\mu_{\rm ref}$ – a reference scale. In our numerical analysis, we set $\mu_{\rm ref}$ equal to the mass of the Z^0 boson. The choice of the reference scale is arbitrary; however, we have verified that a factor of two variation in $\mu_{\rm ref}$ results in a deviation of only 0.1% in $V_{\rm eff}$. In practice, RG improvement entails rescaling the couplings and fields according to the following transformations:

$$\begin{aligned} &\lambda \to \lambda(t)\,, \\ &\phi_\sigma^2 \to \frac{\phi_\sigma^2}{2} \exp\left\{\int_0^t dt'\gamma[\lambda(t')]\right\}, \end{aligned} \tag{4.73}$$

[4] After our paper was published and in the process of this thesis being written, the authors of [104] uploaded on arxiv a new paper [402] which improves upon the last one. The authors find that the inclusion of higher-order corrections is important and the determination of the functional determinant (see Eq. (4.1)) is crucial for precise predictions for supercooled transitions.

which are applied to the tree-level, one-loop and thermal potentials. The beta functions determine the evolution of the couplings, while the γ functions control the field's evolution, both provided in App. E. For simplicity, we omit the explicit t dependence of the fields and couplings throughout, unless necessary.

The choice of the renormalization scale must take into account its field-dependent nature and an additional scale introduced by the temperature:

$$\mu = \max[M_{Z'}(\phi_\sigma), \kappa T]\,, \tag{4.74}$$

where $M_{Z'}(\phi_\sigma)$ is the field-dependent mass of the Z′ boson in Eq. (4.66), with its couplings evaluated at this mass, and κ is an arbitrary factor. Setting $\kappa = 4\pi \exp(\odot\gamma_E)$ ensures an exact cancellation between the logarithmic terms of the CW potential and the high-temperature potential V_T. However, any κ value close to this is perfectly acceptable. In our calculations, we set $\kappa = \pi$ and find that varying it by a factor of 5 does not significantly affect the results.

The thermal corrections are described by the following two contributions as detailed in Refs. [335, 404]:

$$V_{\rm th}(\phi_\sigma, T) = V_T(\phi_\sigma, T) + V_{\rm Daisy}(\phi_\sigma, T)\,, \tag{4.75}$$

where the one-loop thermal potential is

$$V_T(\phi_\sigma, T) = \frac{T^4}{2\pi^2}\left[3J_B\left(\frac{M^2_{Z'}(\phi_\sigma)}{T^2}\right) + \sum_f n_f J_F\left(\frac{M^2_f(\phi_\sigma)}{T^2}\right)\right]. \tag{4.76}$$

The fermionic contributions arise from the heavy neutrinos $f = N_1, N_2, N_3$, with the number of DOF's $n_{N_i} = 2$. The thermal functions are given by

$$J_{B,F}(y) = \int_0^\infty dx\, x^2 \ln\left[1 \mp e^{\sqrt{x^2+y}}\right]. \tag{4.77}$$

While no closed-form expressions are available, analytical expressions can be derived in the high-temperature ($M_i^2/T^2 \ll 1$) and low-temperature ($M_i^2/T^2 \gg 1$) regimes. Specifically [404],

$$\begin{aligned}
(M_i^2/T^2 \ll 1):\ &\begin{cases} J_B(y) = \odot\frac{\pi^4}{45} + \frac{\pi^2}{12}y \odot \frac{\pi}{6}y^{3/2} \odot \frac{y^2}{32}\ln\frac{y}{c_B} + \dots \\ J_F(y) = \frac{7\pi^4}{360} \odot \frac{\pi^2}{24}y \odot \frac{y^2}{32}\ln\frac{y}{c_F} + \dots \end{cases} \\
(M_i^2/T^2 \gg 1):\ &J_B(y) = J_F(y) = \odot\sqrt{\frac{\pi}{2}}y^{3/4}e^{-\sqrt{y}}\left(1 + \frac{15}{8}y^{-1/2} + \frac{105}{128}y^{-1}\right) + \dots
\end{aligned} \tag{4.78}$$

where the ellipses represent subleading terms, $c_B = 16\pi^2 \exp(3/2 \odot \gamma_E)$ and $c_F = \pi^2 \exp(3/2 \odot 2\gamma_E)$, with $\gamma_E \approx 0.5772$ the Euler-Mascheroni constant. While we use Eq. (4.77) for the numerical evaluation of the finite temperature effective potential, the $J_B(y)$ function in the high-T limit in Eq. (4.78) is employed to compute the thermal masses of the scalar fields below.

Symmetry restoration due to T^2-terms in the effective potential typically leads to the breakdown of perturbation theory near the critical temperature. Consequently, an all-order resummation of higher-order contributions, known as Daisy diagrams, is required [405–408]. We use the Arnold-Espinosa method, where the Daisy resummation is expressed as [407]

$$V_{\rm Daisy}(\phi_\sigma, T) = \odot\frac{T}{12\pi} n_{Z'}\left[\overline{M}^3_{Z'}(\phi_\sigma, T) \odot M^3_{Z'}(\phi_\sigma)\right]. \tag{4.79}$$

Fermions do not contribute because the Matsubara summation for fermions lack zero-frequency modes [408]. We define $\overline{M}_{Z'}$ to incorporate thermal mass corrections to the Z′ boson and express it as

$$\overline{M}_{Z'}(\phi_\sigma, T) = M_{Z'}(\phi_\sigma) + m_{D,Z'}(T)\,, \tag{4.80}$$

where $m_{D,Z'}(T)$ is the Debye mass. For vector field contributions, only the longitudinal modes acquire thermal masses, which are evaluated through the one-loop self-energies of the gauge bosons [347, 409,

410]. We utilise the `DRAlgo` package [411] to obtain the temperature-dependent Z′ boson mass for a generic charge assignment:

$$m^2_{D,\mathrm{Z}'}(T) = \frac{g_L^2 T^2}{3}(22x^2_{\mathcal{H}} + 8x_{\mathcal{H}}x_\sigma + 3x^2_\sigma)\,. \tag{4.81}$$

With all the components in place, the complete RG-improved effective potential is the sum of Eqs. (4.53), (4.57), and (4.75). Here, all couplings and fields are rescaled according to Eq. (4.73). Based on the approximations discussed in the last paragraph of Sec. 4.5.2, contributions from scalar fields are neglected in one-loop computations. Given the expected suppression of scalar mixing and the hierarchy $v_\sigma \gg v$, the phase transition is governed by a single field ϕ_σ. However, it is important to note that the SM sector indirectly affects the FOPT through the RG evolution of the couplings. Then, the full effective potential can be explicitly written as

$$\begin{aligned} V_{\text{eff}} = {} & \frac{1}{4}\lambda_\sigma(t) Z^2_\sigma(t)\phi^4_\sigma \\ & + \frac{1}{64\pi^2}\sum_{a=\mathrm{Z}',N_1,N_2,N_3} n_a M^4_a\Big(\sqrt{Z_\sigma(t)}\phi_\sigma\Big)\left(\ln\frac{M^2_a\Big(\sqrt{Z_\sigma(t)}\phi_\sigma\Big)}{\mu^2}\odot c_a\right) \\ & + 3J_B\left(\frac{M^2_{\mathrm{Z}'}\Big(\sqrt{Z_\sigma(t)}\phi_\sigma\Big)}{T^2}\right) + \sum_{f=N_1,N_2,N_3} J_F\left(\frac{M^2_f\Big(\sqrt{Z_\sigma(t)}\phi_\sigma\Big)}{T^2}\right) \\ & \odot \frac{T}{12\pi}\Big[\overline{M_{\mathrm{Z}'}}^3(\sqrt{Z_\sigma(t)}\phi_\sigma, T)\odot M^3_{\mathrm{Z}'}(\sqrt{Z_\sigma(t)}\phi_\sigma)\Big]\,. \end{aligned} \tag{4.82}$$

In this expression, $Z_\sigma(t) = (1/2)\exp\Big\{\int_0^t dt'\gamma(\lambda(t'))\Big\}$ is the wave function renormalization, with γ defined in Eq. (E.17). To understand how the model parameters affect the shape of the potential – specifically, the behaviour of the potential barrier and the true vacuum with respect to variations of the couplings – it is useful to simplify Eq. (4.82). First, to assess the behaviour near the barrier, we expand this expression in the high-temperature regime, valid for low field values. For clarity, we disregard the RG dependence of the couplings and fields, *i.e.*, $\lambda(t) \to \lambda$ and $Z_\sigma(t) \to 1$. We also fix the charges to $x_\sigma = 2$ and $x_{\mathcal{H}} = 0$, and set the renormalization scale to $\mu = \pi T$. Note that the scale must remain proportional to T to ensure that the logarithmic terms from the CW potential cancel with those arising from the high-T expansion of the thermal functions. With this in mind, we expand up to fourth-order in the fields and obtain

$$\begin{aligned} V^{\text{HT}}_{\text{eff}} = {} & \phi^4_\sigma\left(\frac{g_L^4(1\odot 3\gamma_E + 6\ln 2)}{2\pi^2}\odot\frac{g_L^3}{2\sqrt{2}\pi} + \frac{\lambda_\sigma}{4} + \frac{\gamma_E \mathrm{Tr}(\boldsymbol{y}^4_{\boldsymbol{\sigma}})}{64\pi^2}\right)\odot\phi^3_\sigma\frac{4g_L^3 T}{3\pi} \\ & + \phi^2_\sigma\left(\frac{g_L^2T^2}{2}\odot\frac{g_L^3T^2}{\sqrt{2}\pi} + \frac{T^2}{48}\mathrm{Tr}(\boldsymbol{y}^2_{\boldsymbol{\sigma}})\right)\,. \end{aligned} \tag{4.83}$$

We observe that quadratic and cubic terms in ϕ_σ are generated at finite temperature, and vanish as $T \to 0$. The negative sign of the latter indicates that a potential barrier between the true and false vacuum is induced. This characteristic of classically conformal models is depicted in the left panel of Fig. 4.1, which shows that the potential barrier is absent at $T = 0$ and grows with temperature.

A key feature of this class of models is that the gauge sector is responsible for the FOPT at finite temperatures. This necessitates a nonzero g_L coupling to generate a cubic term, and consequently, a potential barrier. In contrast, λ_σ and the heavy neutrino Yukawa couplings $\boldsymbol{y}_{\boldsymbol{\sigma}}$ determine the location of the true minimum where the quartic term becomes relevant. However, Eq. (4.83) is not adequate for analysing the behaviour of the true vacuum, as the high-T expansion fails at large field values for which ϕ^4_σ term dominates. While the emergence of a potential barrier is a purely thermal effect, the zero-temperature theory fixes the minimum of the effective potential. Although finite temperature corrections contribute to the position and depth of the true vacuum, we have numerically confirmed that the thermal potential has a minimal impact, thereby validating the zero-temperature approximation. This can be seen in the right panel of Fig. 4.1 where the position of the true vacuum is insensitive to temperature corrections. While a complete minimization must include the CW potential, the minimum of the potential essentially arises from the tree-level RG-improved

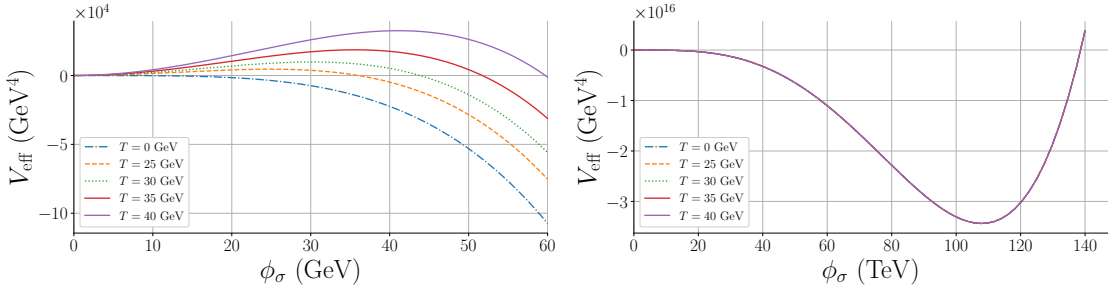

Figure 4.1: Snapshots of the effective potential for several values of the temperature for field values near the barrier (left panel) and near the true vacuum (right panel) for BP (a) of the conformal $\mathrm{U}(1)_{\mathrm{B-L}}$ model with $x_{\mathcal{H}} = 0$, $x_\sigma = 2$; see Tab. 4.3. All the curves are overlapping in the right panel.

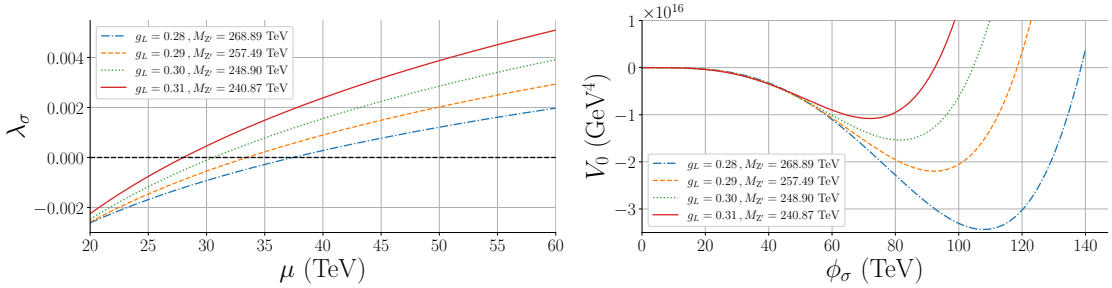

Figure 4.2: **Left panel:** RG evolution of λ_σ as a function of the renormalisation scale $\mu = M_{\mathrm{Z}^0} e^t$ for several values of g_L and the resulting $M_{\mathrm{Z}'}$. The blue dashed curve corresponds to BP(a) of the $\mathrm{U}(1)_{\mathrm{B-L}}$ model, and the other curves illustrate the dependence on g_L. At the minimum of the potential the value of λ_σ depends on g_L via Eq. (4.85). **Right panel:** LO contribution to the potential, $V_0(t) = \lambda_\sigma(t) Z_\sigma^2(t) \phi_\sigma^4/4$.

---

contribution, $V_0(t) = \lambda_\sigma(t) Z_\sigma^2(t) \phi_\sigma^4/4$. This suffices for the analytical expressions discussed in this section. In the RG-improved approach, the renormalization scale depends on the field value, causing the magnitude and sign of the quartic coupling to vary across the potential. Since $Z_\sigma(t)$ is an order $\mathcal{O}(1)$ parameter that does not change sign, the location of the minimum is governed by the RG evolution of $\lambda_\sigma(t)$, which must be negative for low field values and become positive for higher field values. This ensures the existence of a nonzero minimum and guarantees that the potential remains bounded from below.

In the left panel of Fig. 4.2, we show the RG evolution of λ_σ for four values of the gauge coupling and corresponding Z′ mass. Observe that the slopes of the curves increase for larger g_L, so that the transition from negative to positive λ_σ occurs at a lower value of μ as g_L increases. This results in the generation of a minimum at lower field values given that we set the scale in Eq. (4.74) to that of the field-dependent Z′ mass in Eq. (4.66). This behaviour follows from the λ_σ beta-function in Eq. (E.10), where the leading contribution is positive and scales as $6 g_L^4 x_\sigma^4$. Thus, increasing g_L leads to faster running and, consequently a sign flip at lower scales. Since the false vacuum is at the origin, the potential energy difference ΔV_{eff} during the FOPT is larger for smaller values of g_L, as is evident from the right panel of Fig. (4.2). We also observe that a larger Z′ mass yields a larger field value for the true vacuum. In general, $M_{\mathrm{Z}'} \sim \phi_\sigma$ which has implications for the peak SGWB frequency, PBH mass and magnetic field strength, as we will later discuss in the Numerical results section.

Yukawa couplings contribute to Eq. (E.10) with a negative sign and can dominate the RG evolution if $\mathrm{Tr}(\boldsymbol{y_\sigma}) \gtrsim g_L$. Therefore, larger $\boldsymbol{y_\sigma}$ values push the sign flip in λ_σ to higher scales. This is illustrated in Fig. 4.3, which shows the effective potential for different values of $\mathrm{Tr}(\boldsymbol{y_\sigma})$. Both the depth of the effective potential and its minimum are strongly affected.

The sensitivity of the true vacuum to g_L and $\boldsymbol{y_\sigma}$ can also be assessed by minimising the one-loop potential. Suppressing RG factors, the zero-temperature potential at the minimum, $\mu = v_\sigma$, is given

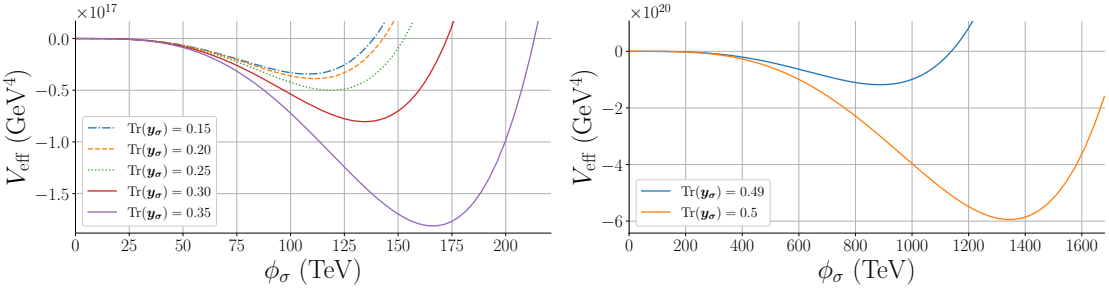

Figure 4.3: The effective potential for different values of $\mathrm{Tr}(\boldsymbol{y_\sigma})$ for the $\mathrm{U(1)_{B-L}}$ model. The other parameters are that of BP(a).

by

$$V_{\text{eff}} = \frac{\lambda_\sigma \phi_\sigma^4}{4} + \frac{3 g_L^4 \phi_\sigma^4}{4\pi^2}\left[\ln\left(\frac{4 g_L^2 \phi_\sigma^2}{v_\sigma^2}\right) \odot \frac{5}{6}\right] \odot \sum_{i=1}^{3} \frac{[\boldsymbol{y_\sigma^4}]_{ii}\phi_\sigma^4}{128\pi^2}\left(\ln\left(\frac{[\boldsymbol{y_\sigma^2}]_{ii}\phi_\sigma^2}{2v_\sigma^2}\right) \odot \frac{3}{2}\right). \tag{4.84}$$

Minimising this expression with respect to ϕ_σ, leads to the following relation for λ_σ:

$$\lambda_\sigma = \frac{1}{32\pi^2}\left[32 g_L^4 \odot 96 g_L^4 \ln\left(\frac{4 g_L^2 \phi_\sigma^2}{v_\sigma^2}\right) \odot \sum_{i=1}^{3}\left([\boldsymbol{y_\sigma^4}]_{ii} + [\boldsymbol{y_\sigma^4}]_{ii}\ln\left(\frac{[\boldsymbol{y_\sigma^2}]_{ii}\phi_\sigma^2}{2v_\sigma^2}\right)\right)\right]. \tag{4.85}$$

In the limit that the Yukawa couplings vanish, this relation reduces to

$$\lambda_\sigma = \frac{g_L^4}{\pi^2}\left[1 \odot 3\ln\left(\frac{4 g_L^2 \phi_\sigma^2}{v_\sigma^2}\right)\right], \tag{4.86}$$

which is the standard relation between λ_σ and the fourth power of the gauge coupling in conformal models [386]. This relation indicates that varying g_L affects not only the RG evolution of λ_σ as discussed above, but also its initial value at the minimisation scale through the tadpole relations in Eq. (4.60). Plugging (4.85) into (4.84) leads to

$$V_{\text{min}} = \frac{v_\sigma^4}{256\pi^2}\left[\odot 96 g_L^4 + \mathrm{Tr}(\boldsymbol{y_\sigma^4})\right], \tag{4.87}$$

which underscores the dependence of the scalar potential on the fourth power of g_L, $\boldsymbol{y_\sigma}$, and v_σ, which can then heavily impact the thermodynamic parameters. Eqs. (4.84), (4.85) and (4.87) also highlight how the neutrino sector affects the $\mathrm{U(1)}'$ phase transition. While Eq. (4.87) suggests that for a fixed value of g_L, the minimum should get shallower with increasing $\mathrm{Tr}(\boldsymbol{y_\sigma})$, in seeming contradiction with Fig. 4.3, the effect of increasing $\mathrm{Tr}(\boldsymbol{y_\sigma})$ is much stronger on the RG evolution of λ_σ, and causes the minimum to get deeper.

4.5.4.2 Theoretical uncertainties on the SGWB calculation

Current analytical template functions of the SGWB spectrum rely on efficiency factors that introduce theoretical uncertainties into the SGWB. We quantify the uncertainty due to κ_{SW} by treating it as a free parameter ranging from 0.01 to 1. Panel (a) of Fig. 4.4 demonstrates that a two order-of-magnitude uncertainty in the efficiency factor results in approximately a three order-of-magnitude uncertainty in the SGWB.

Another commonly used approximation is to fix the radius of the expanding true vacuum bubbles to an average radius R_*. A more realistic treatment should consider extended bubble radius distributions. In Ref. [412], this effect was analysed in the context of non-supercooled FOPTs in which the dominant source of GWs is sound waves. A broadening of the spectrum below the peak frequency was noted. Following Ref. [412], with the radius distribution of Ref. [413], we show in panel (b) of Fig. 4.4 how the radius distribution impacts a pure bubble-collision spectrum (dotted curves with $\kappa_{\text{BC}} = 1$) and a pure

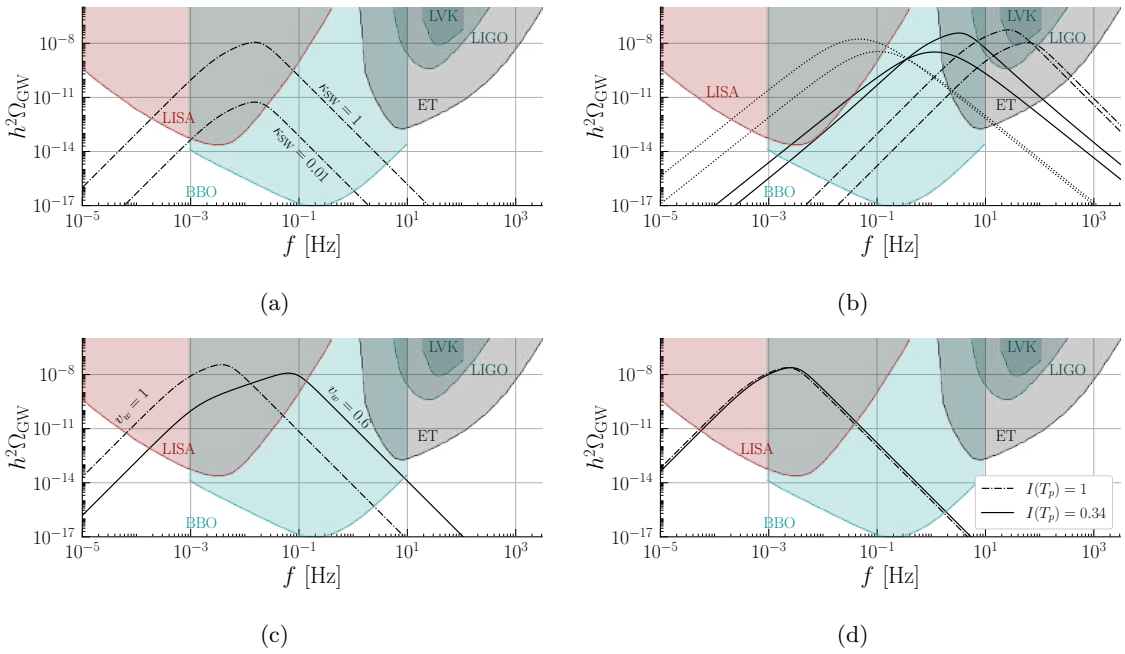

Figure 4.4: **Panel (a):** SGWB spectrum from sound waves for the efficiency factor κ_{SW} between 0.01 and 1, with $v_w = 1$, $\log_{10}\alpha = 5.7$, $\beta/H(T_p) = 21$ and $T_{RH} = 1.36 \times 10^4$ GeV. **Panel (b):** Impact of the bubble radius distribution on the SGWB spectrum for bubble collisions (dotted curves), sound waves (dot-dashed curves) and for both sources (solid curves), with $v_w = 1$. For the sound-wave source, we fix $\log_{10}\alpha = 16.2$, $\beta/H(T_p) = 7$ and $T_{RH} = 33.5$ GeV, for the bubble-collision source we fix $\log_{10}\alpha = 9.3$, $\beta/H(T_p) = 9.5$ and $T_{RH} = 250$ TeV, and for the mixed source we fix $\log_{10}\alpha = 14.6$, $\beta/H(T_p) = 8$ and $T_{RH} = 1.9$ TeV. The curves peaked at a higher (lower) frequency correspond to a monochromatic (extended) radius distribution. **Panel (c):** SGWB spectrum for two values of the bubble wall velocity with $\log_{10}\alpha = 11.9$, $\beta/H(T_p) = 12$ and $T_{RH} = 5.9$ TeV. **Panel (d):** SGWB spectrum for two choices of the percolation condition for $v_w = 1$, $\log_{10}\alpha = 8.6$, $\beta/H(T_p) = 14.5$ and $T_{RH} = 2.9$ TeV. Also shown are the LVK bound [32] and sensitivity curves for LISA [28], BBO [29], LIGO O5 [30] and ET [31].

sound-wave spectrum (dot-dashed curves with $\kappa_{SW} = 1$) in the case of supercooling. The spectral broadening found in Ref. [412] is applicable for both bubble collision and sound wave sources. If both sources contribute (solid curves with $\kappa_{BC} = \kappa_{SW} = 0.5$), spectral broadening occurs at both ends of the spectrum, with a greater impact at higher frequencies. In each case, the curve peaked at a higher (lower) frequency corresponds to a monochromatic (extended) radius distribution.

Uncertainties can also arise from the modelling of the phase transition dynamics, particularly the choice of percolation condition and the determination of the bubble wall velocity. For the former, we have previously defined the percolation temperature via $I(T_p) = 0.34$, which is supported by studies of the percolation of uniformly nucleated bubbles [414–416]. However, percolation can alternatively be defined by requiring $I(T_p) = 1$ (or equivalently, that the probability is given by $\mathcal{P}(T_p) = 1/e$), based on the requirement that the comoving volume equals the volume of true vacuum bubbles [417].

Although for supercooled FOPTs it is safe to assume that the bubbles approach the speed of light ($v_w = 1$), in non-supercooled scenarios, bubbles may acquire a subluminal terminal velocity. While recent hydrodynamic simulations suggest that in most cases $v_w = 1$ [352], analytical estimates indicate otherwise [351]. To assess the impact of v_w, we adopt the Chapman-Jouguet velocity [418],

$$v_w(\alpha) = \frac{\sqrt{1/3} + \sqrt{\alpha^2 + 2\alpha/3}}{1 + \alpha}\,, \tag{4.88}$$

as a crude estimate. We perform a scan in the parameter space of the B⊙L model in the mass range $m_{h_2} = [10^3, 10^8]$ GeV and gauge coupling range $g_L = [0.26, 0.62]$. The results in the $(f_{peak}, h^2\Omega_{GW}^{peak})$ plane are shown in Fig. 4.5. Note that employing either $I(T_p) = 0.34$ or $I(T_p) = 1$ has virtually no

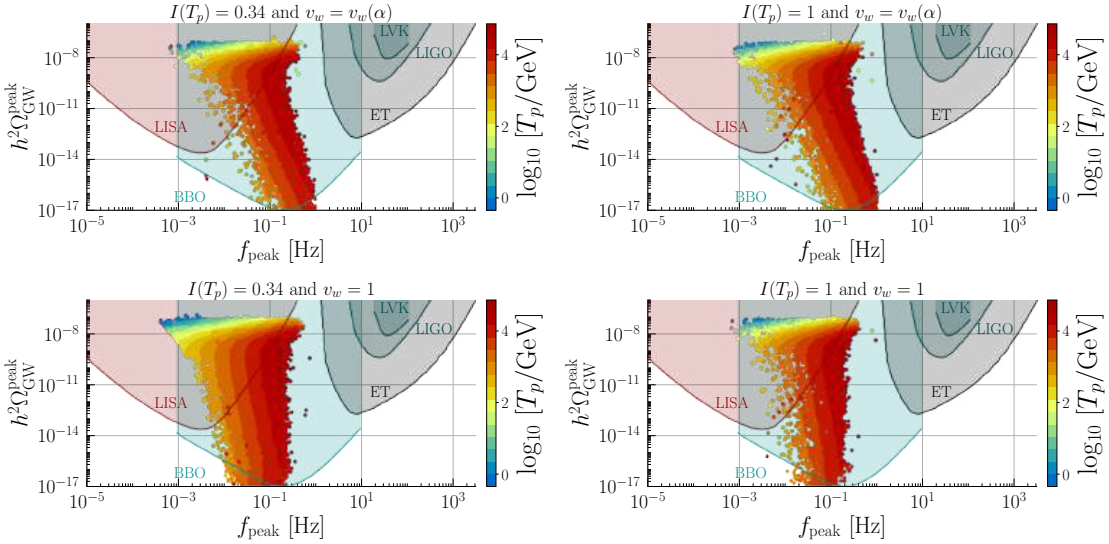

Figure 4.5: Scatter plots of the SGWB peak amplitude $h^2\Omega_{\rm GW}^{\rm peak}$ as a function of the peak frequency for the four possible combinations of the percolation condition, $I(T_p) = 0.34$ or 1, and $v_w = 1$ or the Chapman-Jouguet velocity. Note that for the sensitivity curves, the axis labels do not correspond to peak values.

impact on the peak amplitude and frequency of the SGWB. The bubble wall velocity significantly affects the spectrum, shifting weaker signals (lower α) to higher frequencies if wall velocities are determined by Eq. (4.88), as can be seen from Fig. 4.5. These features are also evident in panels (c) and (d) of Fig. 4.4.

4.6 Numerical results

The potential barrier between the true and false vacuum, which is absent at LO, is a quantum thermal effect that typically persists for a long time as the Universe cools down. This can extend to temperatures below 0.17 GeV, at which the QCD phase transition occurs, thus entering a non-perturbative regime where our calculations become unreliable. This is especially true in scenarios in which the quark Yukawa interactions are relevant in the effective potential. Although within a local B⊙L framework, a modified cosmology can assist the QCD phase transition through the Higgs portal, allowing for reliable perturbative calculations [105, 307, 419], we focus on temperatures above the QCD scale. Additionally, we assume a dark sector above the EW scale that fully thermalises with the SM sector. Then, constraints on the extra effective number of neutrino species, $\Delta N_{\rm eff}$, from BBN and cosmic microwave background data are easily satisfied. Right-handed neutrinos can thermalise with the SM through the Yukawa interactions, $y_\nu^{ij}\overline{N}_i\mathcal{H}L_j$, and reach thermal equilibrium at a temperature [420, 421]

$$T_i^{\rm eq} \approx 0.2\frac{(\boldsymbol{y_\nu y_\nu^\dagger})_{ii}v^2}{m_{\rm eq}} = 0.2 M_{N_i} K_i\,, \tag{4.89}$$

where the effective equilibrium neutrino mass, $m_{\rm eq} \approx 1.1\ {\rm meV}\sqrt{g_*/g_*^{\rm SM}}$, with $g_*^{\rm SM}$ the relativistic DOF in the SM sector. Both g_* and $g_*^{\rm SM}$ are evaluated at the temperature of the phase transition. Here, M_{N_i} are the masses of the three physical right-handed neutrinos, and their decay parameters are

$$K_i = \frac{(\boldsymbol{y_\nu y_\nu^\dagger})_{ii}v^2}{M_{N_i} m_{\rm eq}}\,. \tag{4.90}$$

Neutrinos reach thermal equilibrium before the onset of the phase transition if $M_{N_i}K_i \gtrsim 5T_c$ [420]. Since the right-handed neutrinos couple to the Majoron σ via the Yukawa interactions $y_\sigma^{ij}\overline{N}_i^c N_j\sigma$, the Majoron σ also thermalises if y_σ is sufficiently large. We also expect σ to thermalise via its

M_{h_2} (GeV)	g_L	$x_{\mathcal{H}}$	x_σ	$(\boldsymbol{y_\sigma})_{ii}$	δ_c	$\lambda_\sigma\,,\lambda_{\sigma h}$	$\lambda_h\,,v_\sigma$	$M_{\mathrm{Z}'}$
$[150, 10^{18}]$	$[0.20, 1]$	$[\odot 2, 2]$	$[0, 5]$	$[10^{-10}, 1]$	$[0.40, 0.66]$	Eq. (4.60)	Eq. (4.62)	Eq. (4.67)

Table 4.2: Input parameter ranges (defined at $\mu = M_{\mathrm{Z}^0}$) used in our numerical analysis. We sample M_{h_2} and $(\boldsymbol{y_\sigma})_{ii}$ logarithmically and the other parameters linearly. The gauge charges $x_{\mathcal{H}}$ and x_σ admit only rational values. In the last three columns, we refer to the equations used to calculate the quartic couplings, v_σ and the Z′ mass.

interactions with a thermalised Z′ through the gauge coupling g_L which is $\mathcal{O}(0.1)$[5] .Thermalisation of the Z′ occurs through direct processes like $\bar{f}_{\mathrm{SM}} + f_{\mathrm{SM}} \leftrightarrow \mathrm{Z}'$, where f_{SM} are SM fermions, or indirectly by first thermalising with the right-handed neutrinos through $\bar{N}_i + N_i \leftrightarrow \mathrm{Z}'$, which is also mediated by the gauge coupling.

We perform a numerical scan with parameters in the ranges displayed in Tab. 4.2. The bounce action is computed using `CosmoTransitions` [337] and validated against our own numerical implementation. Further details are provided in App. G. To reduce numerical uncertainties in the calculation of the action due to discretisation in temperature, we perform a spline fit to it. Based on the discussion in Sec. 4.5.4.1, we split our parameter space into two parts: one with points that have $\mathrm{Tr}(\boldsymbol{y_\sigma}) < g_L$, and the other with $\mathrm{Tr}(\boldsymbol{y_\sigma}) > g_L$. Note that in the first dataset, the hierarchy between the heavy neutrinos and the $\mathrm{U}(1)'$ breaking scale can be rather large if $(\boldsymbol{y_\sigma})_{ii} \ll g_L$, whereas in the second dataset, the heavy neutrino masses are always close to v_σ, and hence to $M_{\mathrm{Z}'}$ and M_{h_2}.

In our simulations, we only consider FOPTs with $h^2\Omega_{\mathrm{GW}}^{\mathrm{peak}} > 10^{-17}$ that can be probed by current experiments (LIGO), near-future experiments (LISA and ET), or planned future initiatives (BBO).

4.6.1 GWs in a $\mathrm{U}(1)_{\mathrm{B-L}}$ scenario a $(x_{\mathcal{H}}, x_\sigma) = (0, 2)$

First, we fix $x_{\mathcal{H}} = 0$ and $x_\sigma = 2$ and study the classically scale-invariant $\mathrm{U}(1)_{\mathrm{B-L}}$ scenario. The remaining free parameters are set according to the ranges in Tab. 4.2. In Fig. 4.6, we present predictions for the SGWB geometric parameters with respect to $\mathrm{Tr}(\boldsymbol{y_\sigma})$ (first row) $M_{\mathrm{Z}'}$ (second row), the heavy Higgs mass (third row), the $\mathrm{U}(1)_{\mathrm{B-L}}$ gauge coupling (fourth row), and the quartic coupling λ_σ (fifth row). The left (right) panels correspond to the dataset with $\mathrm{Tr}(\boldsymbol{y_\sigma}) < g_L$ ($\mathrm{Tr}(\boldsymbol{y_\sigma}) > g_L$). Note that if we bifurcate the dataset according to $\mathrm{Tr}(\boldsymbol{y_\sigma}) < (1 \odot \delta) g_L$ and $\mathrm{Tr}(\boldsymbol{y_\sigma}) > (1 \odot \delta) g_L$, where $\delta > 0$, then the red points along the right edge of the coloured region in the top-left panel migrate to the top-right panel. The region enclosed by the black dashed contour does not satisfy the criterion for percolation at T_p in Eq. (4.8), but is fulfilled at some temperature below T_p. In Fig. 4.7, we present similar scatter plots, but with the colour gradient representing the thermodynamic parameters α (first row), $\beta/H(T_p)$ (second row), T_p (third row), and T_{RH} (fourth row). In Figs. 4.6 and 4.7, $M_{h_2} \approx M_{\mathrm{Z}'} \approx v_\sigma$, which explains the similarity between the second and third rows in Fig. 4.6. A closer inspection reveals a hierarchy of approximately one order of magnitude between M_{h_2} and $M_{\mathrm{Z}'}$ because M_{h_2} is generated at one loop.

Impact of the heavy bosons on the peak frequency of GWs

The colour gradation in the second and third rows of Fig. 4.6 indicates that the peak frequency is governed by the $\mathrm{U}(1)_{\mathrm{B-L}}$ breaking scale, represented by the Z′ and h_2 masses. As shown in Fig. 4.2, a larger value of $M_{\mathrm{Z}'}$ results in a higher value of the field ϕ_σ in the true vacuum, thereby increasing the FOPT temperatures, as can be seen from the last two rows of Fig. 4.7. According to Eqs. (4.16) and (4.17), the peak frequency is linearly dependent on the reheating temperature T_{RH} and thus scales with $M_{\mathrm{Z}'}$ or, equivalently, with M_{h_2}.

The substantial difference between the critical and percolation temperatures highlights the degree of supercooling at play. As discussed in Eq. (4.9), $\alpha \gg 1$ implies that $T_p \ll T_{\mathrm{RH}} < T_c$, which we observe across the entire parameter space. As long as the phase transition completes, the strong supercooling redshifts the SGWB to much higher frequencies as required by energy conservation. The disparity between T_{RH} and T_p underscores the importance of calculating the SGWB spectrum at the

[5]The portal coupling $\lambda_{\sigma h} \sim -v^2/v_\sigma^2$ also plays a role, though it becomes increasingly subdominant for larger Majoron masses; see App. G.

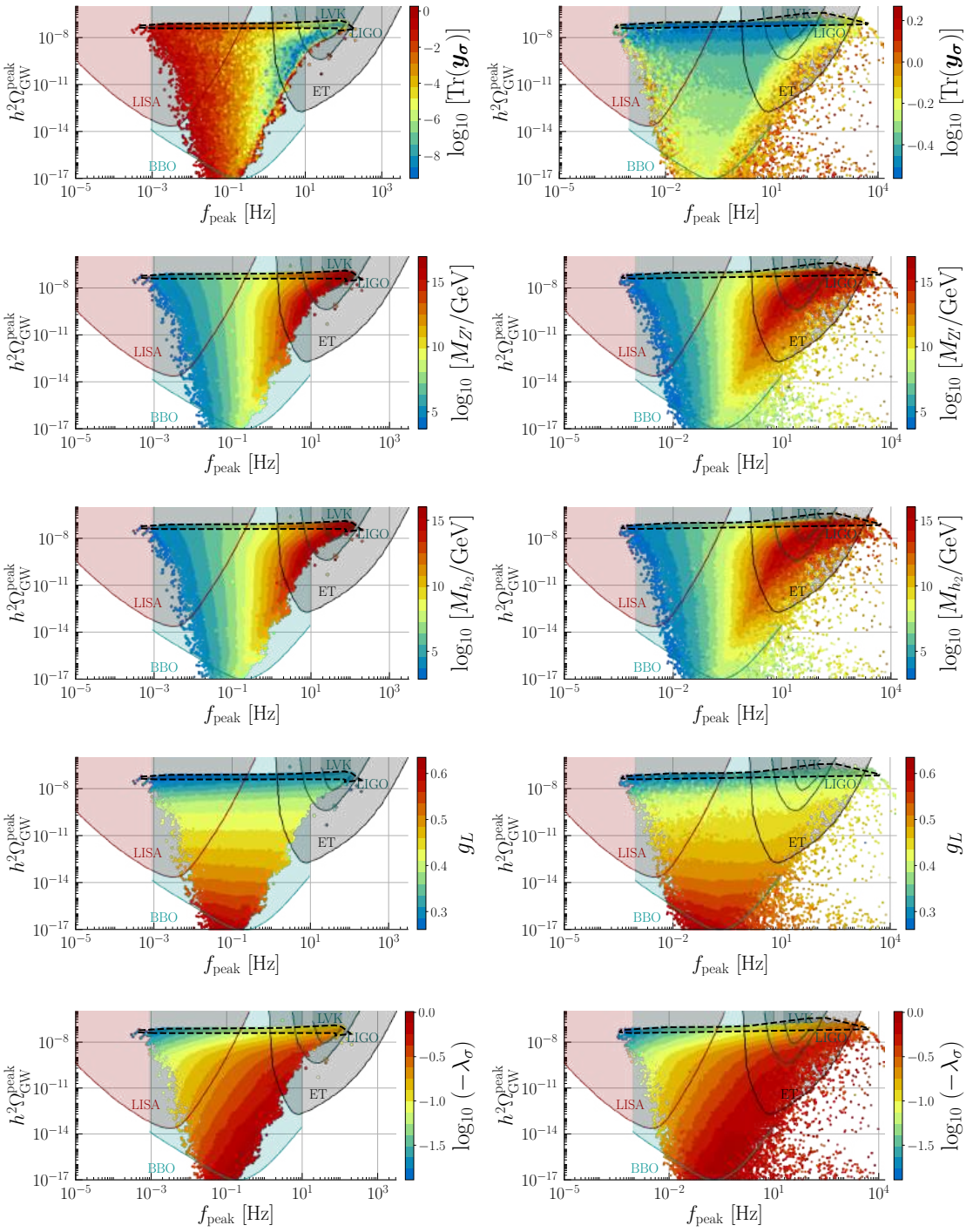

Figure 4.6: Scatter plots of the SGWB peak amplitude $h^2\Omega_{\rm GW}^{\rm peak}$ as a function of the peak frequency $f_{\rm peak}$ for the $\mathrm{U}(1)_{\mathrm{B-L}}$ model. The colour scales represent $\mathrm{Tr}(\boldsymbol{y_\sigma})$ (first row), the Z′ boson mass (second row), the heavy scalar mass M_{h_2} (third row), the gauge coupling g_L (fourth row), and the quartic self-coupling of the Majoron λ_σ (fifth row). In the regions enclosed by a black dashed contour, percolation is not assured as prescribed by Eq. (4.8), but may occur at a temperature below T_p. The left panels show points with $\mathrm{Tr}(\boldsymbol{y_\sigma}) < g_L$, and the right panels shows points with $\mathrm{Tr}(\boldsymbol{y_\sigma}) > g_L$.

correct temperature in classically conformal models. Indeed, the dependence of the peak frequency on $T_{\rm RH}$ is stronger than on T_p. Redshifting from T_p would lead to the incorrect conclusion that points

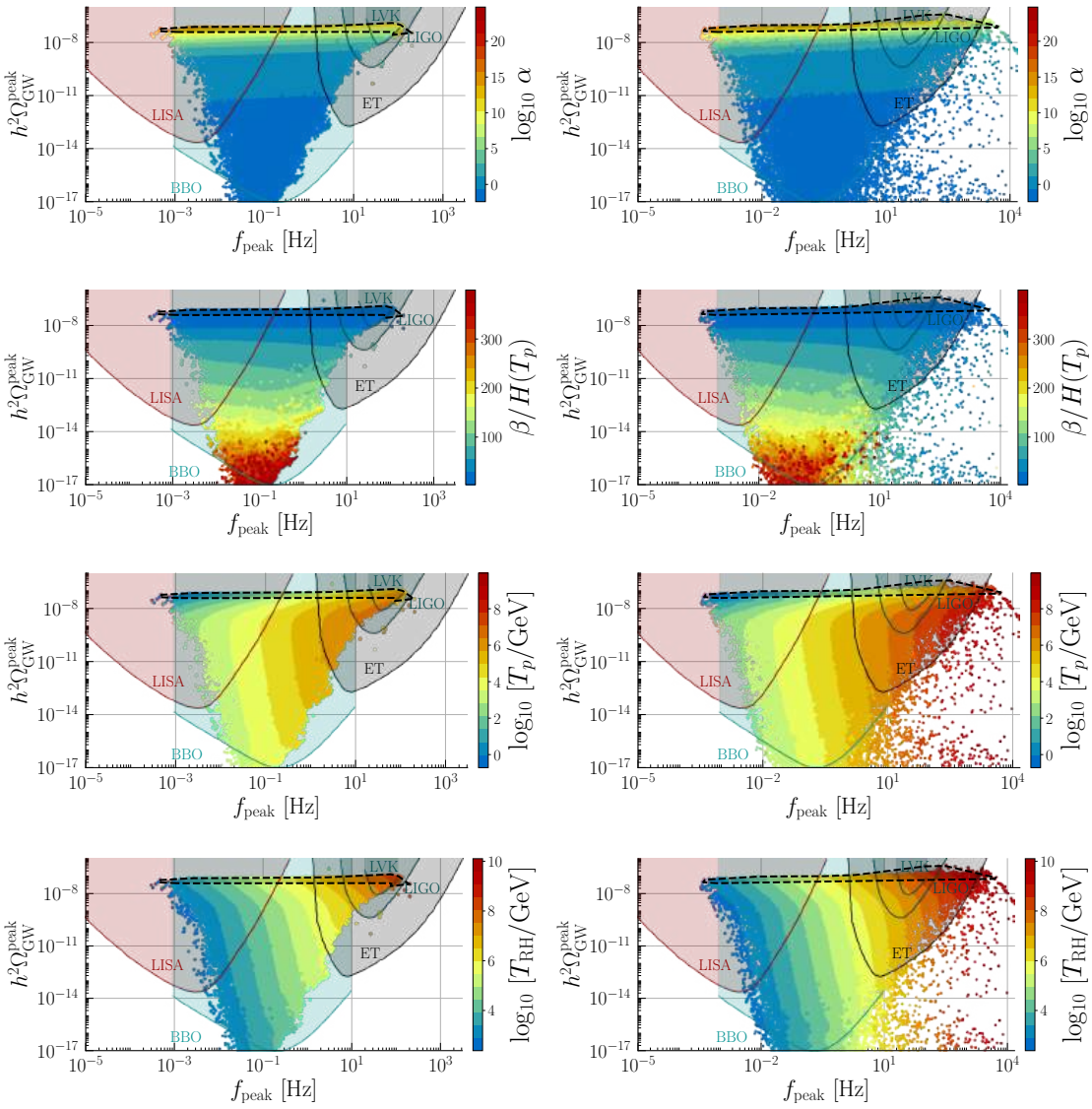

Figure 4.7: Similar to Fig. 4.6, but the colour scales indicate the phase transition strength α (first row), its inverse time duration $\beta/H(T_p)$ (second row), the percolation temperature T_p (third row), and the reheating temperature $T_{\rm RH}$ (fourth row).

in the low mass edge of our scatter plots would populate the region probed by PTAs [106].

Impact of the U(1)$_{\rm B-L}$ gauge coupling on the peak amplitude of GWs

The fourth row of Fig. 4.6 shows that increasing g_L decreases the amplitude of the SGWB spectrum. As indicated in Fig. 4.2, $\Delta V_{\rm eff}$ decreases with larger g_L. Recall that $\Omega_{\rm GW}^{\rm peak}$ scales with $\Delta V_{\rm eff}$. From Fig. 4.2, we see that a 10% increase in g_L results in a factor of 1.5 decrease in v_σ, making the true vacuum shallower. This is a general feature of the potential for small Tr($\boldsymbol{y_\sigma}$) in most of the parameter space, and explains the colour gradation in the fourth row of Fig. 4.6; specifically, smaller g_L values favour larger $h^2\Omega_{\rm GW}^{\rm peak}$. A close correspondence between the g_L colour gradient and those of α and $\beta/H(T_p)$ is evident in the left panels of Fig. 4.7. It is worth mentioning that the SGWB peak amplitude tends to plateau at $\Omega_{\rm GW}^{\rm peak} \approx 10^{-7}$ even for large values of α. This is due to the asymptotically constant behaviour of $\Omega_{\rm SW,BC}^{\rm peak}$ in the limit of strong supercooling, as in Fig. 4.70.

For a large part of the parameter space in Fig. 4.7, $1 \lesssim \alpha \lesssim 10^{20}$ and $10 \lesssim \beta/H(T_p) \lesssim 150$,

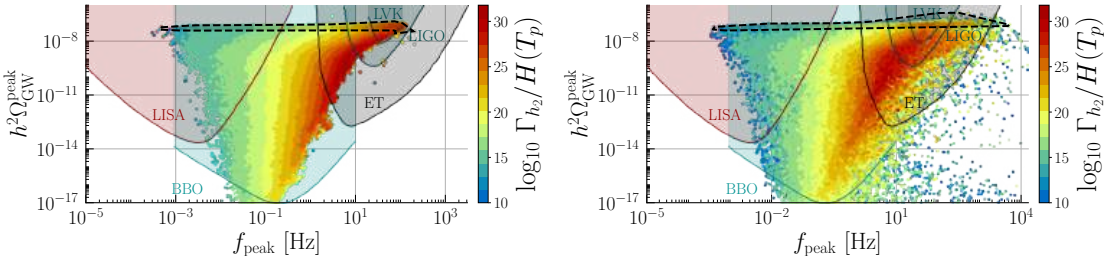

Figure 4.8: Similar to Fig. 4.6, but the colour scale indicates the ratio of the h_2 decay rate to the Hubble rate at the percolation temperature.

defining supercooled and long-lasting FOPTs. This entire parameter space falls within the detection capabilities of various ongoing and planned experiments. LISA will probe $\mathrm{U}(1)_{\mathrm{B-L}}$ breaking scales ranging from tens of TeV, similar to the LHC reach, up to about 10^8 GeV, while the sensitivity of LIGO and ET extends to the GUT scale. We also find FOPTs with $\alpha < 1$ corresponding to $g_L \gtrsim 0.4$. These non-supercooled transitions predict a SGWB with peak frequencies within 10 mHz $\lesssim f_{\rm peak} \lesssim 1$ Hz and peak amplitudes $h^2\Omega_{\rm GW}^{\rm peak} \lesssim 10^{-11}$, most of which are well below LISA sensitivity, but may be probed by BBO.

Since we restrict $h^2\Omega_{\rm GW}^{\rm peak} > 10^{-17}$, the gauge coupling g_L lies in the interval, $0.26 \lesssim g_L \lesssim 0.62$. However, even for FOPTs with $h^2\Omega_{\rm GW}^{\rm peak} < 10^{-17}$, the upper limit in our scan, $g_L^{\rm max} = 1$, is never reached, as large values g_L violate perturbativity at the $M_{Z'}$ scale. As demonstrated previously, the effective potential is highly sensitive to small variations in g_L, which partially explains the relatively narrow band in g_L. While the upper bound on g_L corresponds to lower amplitudes, a couple of constraints restrict g_L from below. Firstly, as the peak amplitude increases with decreasing g_L, the total integrated SGWB energy density must not exceed the amount of dark radiation allowed by BBN. This imposes the constraint $h^2\Omega_{\rm GW} < 5.6 \times 10^{-6}\Delta N_{\rm eff}$ [422], which translates into an upper bound of $h^2\Omega_{\rm GW} < 2.8 \times 10^{-6}$ for $\Delta N_{\rm eff} < 0.5$. Secondly, for small values of g_L, it is questionable whether percolation occurs, as Eq. (4.8) is only satisfied for $T < T_p$.

At low peak frequencies, the percolation temperature approaches the QCD scale ~ 0.17 GeV, which we do not consider in our analysis. Conversely, at high peak frequencies, the percolation temperature can reach up to 10^{10} GeV for $\mathrm{Tr}(\boldsymbol{y_\sigma}) > g_L$. This contrasts with SU(2) conformal models, for which the percolation temperature remains below 300 GeV [104]. This difference underscores a key distinction between Abelian and non-Abelian scenarios. In our case, the RG evolution of g_L is asymptotically safe. However, for SU(N) models, the gauge coupling runs to non-perturbative values, constraining the percolation temperature from above [103, 104].

Role of the neutrino sector

The right panels in Figs. 4.6 and 4.7 correspond to scenarios in which the neutrino sector affects the running of λ_σ and the minimum of the potential because $\mathrm{Tr}(\boldsymbol{y_\sigma}) > g_L$. As illustrated in Fig. 4.3, for increasing Yukawa couplings the minimum becomes deeper and shifts towards larger VEVs, augmenting the potential energy difference between the true and false vacuum, $\Delta V_{\rm eff}$. This effect allows for larger values of g_L populating a greater area in the right panel of the fourth row of Fig. 4.6. The shift towards larger v_σ driven by the neutrino sector extends the frequency range up to about 10 kHz and raises the critical and percolation temperatures by approximately five orders of magnitude. This effect is more pronounced at the high-frequency end of the last two rows of Fig. 4.7.

While the interplay between g_L and $\mathrm{Tr}(\boldsymbol{y_\sigma})$ affects RG evolution of λ_σ, the shape of the potential is primarily controlled by the LO contribution, $V_0 = \lambda_\sigma(t) Z_\sigma^2(t)\phi_\sigma^4/4$. Consequently, the correlation between λ_σ and the peak amplitude/frequency is expected to be the same for $\mathrm{Tr}(\boldsymbol{y_\sigma}) < g_L$ and $\mathrm{Tr}(\boldsymbol{y_\sigma}) > g_L$, barring the spread in points to higher frequencies in the bottom-right panel of Fig. 4.6. Said differently, for fixed values of $h^2\Omega_{\rm GW}^{\rm peak}$ and $f_{\rm peak}$, the value of λ_σ, and hence V_0 is the same whether $\mathrm{Tr}(\boldsymbol{y_\sigma}) < g_L$ or $> g_L$. This explains the smooth variation in λ_σ in the bottom panels of Fig. 4.6. The other parameters exhibit a certain degree of overlap of the different colours in the right panels.

Depending on the heavy Higgs decay rate Γ_{h_2}, the Universe will either immediately enter a radiation-dominated epoch if $\Gamma_{h_2} > H(T_p)$, or it will first pass through a period of matter domination if $\Gamma_{h_2} < H(T_p)$ until $\Gamma_{h_2} \simeq H$. To distinguish between these scenarios, we must compute the decay rate of h_2 and compare it with the Hubble rate at percolation. h_2 can decay through the neutrino channel $h_2 \to \bar{N}_i N_i$ via Yukawa interactions, followed by the decay of the right-handed neutrinos into SM particles, or directly into SM particles mediated by the mixing of h_1 and h_2. For the decay rates of the right-handed neutrinos, we consider all dominant two- and three-body channels [423]. We also cross-checked the decay rates with `MadGraph` [424] and found agreement within 10%. For the decays of h_2, we consider the tree-level two-body processes,

$$\begin{aligned}
\Gamma_{h_2\to h_1 h_1} &= \frac{\lambda_{\sigma h}^2 v_\sigma^2}{32\pi M_{h_2}} \sqrt{1 \odot \frac{M_{h_1}^2}{M_{h_2}^2}}\,, \\
\Gamma_{h_2\to \bar{f}_{\rm SM} f_{\rm SM}} &= \frac{M_{h_2} \sin^2\alpha_S}{16\pi v^2} \sum_f M_f^2 \sqrt{1 \odot \frac{4M_f^2}{M_{h_2}^2}}\,, \\
\Gamma_{h_2\to VV} &= \frac{C_V M_{h_2}^3 \sin^2\alpha_S}{16\pi v^2} \sqrt{1 \odot \frac{4M_V^2}{M_{h_2}^2}} \left(1 \odot \frac{4M_V^2}{M_{h_2}^2} + \frac{12 M_V^4}{M_{h_2}^4}\right), \\
\Gamma_{h_2\to \bar{N}_i N_i} &= \frac{M_{h_2}}{16\pi v_\sigma^2} \sum_{i=1}^{3} M_{N_i}^2 \sqrt{1 \odot \frac{4M_{N_i}^2}{M_{h_2}^2}}\,,
\end{aligned} \tag{4.91}$$

where $C_V = 1, 2$ for $V = \mathrm{Z}^0, W^\pm$, and the scalar mixing angle α_S is defined by

$$\sin(2\alpha_S) = \frac{2 v v_\sigma \lambda_{\sigma h}}{M_{h_1}^2 \odot M_{h_2}^2}\,. \tag{4.92}$$

The total decay rate into SM final states is given by $\Gamma_{h_2} = \Gamma_{h_2\to p_{\rm SM} p_{\rm SM}^*} + \Gamma_{h_2\to \bar{N}_i N_i}\Gamma_{N_i \to p_{\rm SM} p_{\rm SM}^*}$, where $p_{\rm SM}$ denotes all SM particles. This is used to redshift the SGWB spectra according to Eqs. (4.9) and (4.17). For $\Gamma_{h_2} < H(T_p)$, the peak amplitude and peak frequency, are suppressed according to $(\Gamma_{h_2}/H(T_p))^{1/6}$ and $(\Gamma_{h_2}/H(T_p))^{2/3}$, respectively. The first three channels in Eq. (4.91) are suppressed due to the small scalar mixing that scales as $|\lambda_{\sigma h}| \sim v^2/v_\sigma^2 \ll 1$ (see App. G), leaving $\Gamma_{h_2\to \bar{N}_i N_i}$ as the dominant contribution to the decay width. From Fig. 4.8, we conclude that the Universe promptly enters the radiation dominated era after percolation because $\Gamma_{h_2}/H(T_p) > 10^{10}$. This lower limit arises from the thermalisation condition $M_{N_i} K_i \gtrsim 5T_c$ which excludes all scenarios with feeble couplings to the SM. This is evident in Fig. 4.9, which shows that $M_{N_i} K_i < 5T_c$ (top-right panel) yields $\Gamma_{h_2}/H(T_p) \lesssim 10^{12}$ (top-left panel). This bound also establishes a maximum allowable hierarchy between the heavy neutrino masses and the h_2 mass, limiting it to eight orders of magnitude, as shown in the bottom panel. Furthermore, the cluster of blue points in the top-left panel corresponds to scenarios where the early matter-dominated period is long-lasting and the hierarchy between M_{N_i} and M_{h_2} is maximal.

The impact of the neutrino sector on the FOPT becomes significant when the magnitudes of $\boldsymbol{y_\sigma}$ and g_L are comparable; see Eq. (4.87). However, even if the Yukawa sector does not contribute to the minimisation, it strongly affects the SGWB at high frequencies. To quantify this, we consider a subset of our data with $\mathrm{Tr}(\boldsymbol{y_\sigma}) < 10^{-8}$. Then, $\Gamma_{h_2\to \bar{N}_i N_i}$ and the contribution of $\mathrm{Tr}(\boldsymbol{y_\sigma^4})$ to $V_{\rm min}$ are negligible, so that the right-handed neutrinos are effectively decoupled and the Universe enters an era of matter domination after percolation. In this scenario, h_2 decays only to SM particles with a rate $\Gamma_{h_2}^{\rm SM}$ that is strongly suppressed. We find that $H(T_p) \approx [5 \times 10^{-16}\ \mathrm{GeV}^{0.04}] M_{h_2}^{0.96}$ and $\Gamma_{h_2}^{\rm SM} \approx [10^{5.5}\ \mathrm{GeV}^4] M_{h_2}^{-3}$, with M_{h_2} in units of GeV. Then, $\Gamma_{h_2}^{\rm SM}/H(T_p) \approx [6.32 \times 10^{20}\ \mathrm{GeV}^{3.96}] M_{h_2}^{-3.96}$, which implies that $\Gamma_{h_2}^{\rm SM}/H(T_p) > 1$ for $M_{h_2} \gtrsim 1.8 \times 10^5$ GeV, as shown in Fig. 4.10. As M_{h_2} increases, $\Gamma_{h_2}^{\rm SM}/H(T_p)$ rapidly decreases and significantly suppresses the peak frequency of the SGWB below 0.1 Hz, and the peak amplitude is reduced so that LISA is sensitive to scales below 10^7 GeV. Therefore, the SGWB accessible by LIGO and ET is a distinctive signature of the neutrino sector.

The top and bottom rows of Fig. 4.11 quantify the dependence of the SGWB on the size of the $\boldsymbol{y_\nu}$ Yukawa couplings, and the mass of the heaviest right-handed neutrino, respectively. We observe a clear correlation between the peak frequency and the magnitude of $\boldsymbol{y_\nu}$ and $\max(M_{N_i})$. This correlation arises from the type-I seesaw mechanism, and establishes a direct connection between GW physics

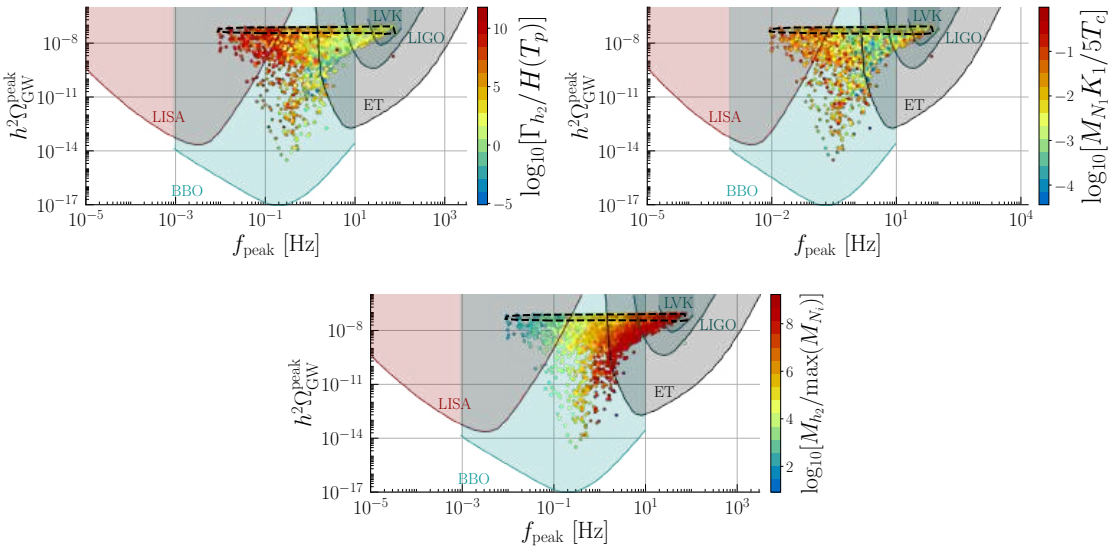

Figure 4.9: Scatter plots for the $\mathrm{U}(1)_{\mathrm{B-L}}$ model with points for which $\mathrm{Tr}(\boldsymbol{y_\sigma}) < g_L$ and the right-handed neutrinos do not thermalise, *i.e.*, $M_{N_i}K_i/(5T_c) < 1$. In the top-left panel, the colour scale represents the ratio of the heavy Higgs decay rate to the Hubble rate at the percolation temperature, in the top-right panel, the corresponding value of $M_{N_i}K_i/(5T_c)$, and in the bottom panel, the mass ratio of the heavy Higgs and the heaviest right-handed neutrino. The black dashed contour has the same meaning as in Fig. 4.6.

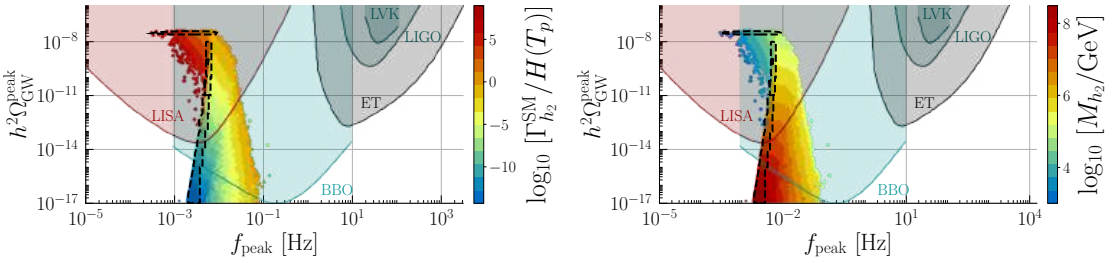

Figure 4.10: Similar to Fig. 4.6, but for a scenario with decoupled right-handed neutrinos. In the left panel, $\Gamma_{h_2}^{\rm SM}$ is the direct decay width of h_2 to SM particles.

---

and neutrino physics. Specifically, for interferometers operating in the Hz to kHz range, such as LIGO and ET, the observation of a SGWB would imply $\boldsymbol{y_\nu} \sim \mathcal{O}(1)$ and a neutrino mass scale between 10^{10} and 10^{15} GeV. In contrast, LISA can probe $\boldsymbol{y_\nu}$ ranging from approximately 10^{-6} (blue points) to 10^{-3} (yellow points), corresponding to a seesaw scale between 10^4 GeV and 10^8 GeV. For $\mathrm{Tr}(\boldsymbol{y_\sigma}) > g_L$ (right panels), the correlation is not as clean due to the competition between g_L and $(\boldsymbol{y_\sigma})_{ii}$. However, at LIGO and ET frequencies, the magnitude of the Dirac neutrino Yukawa is typically of order one. This results from the fact that the $\mathrm{U}(1)_{\mathrm{B-L}}$ breaking scale, which characterises the scale of neutrino mass generation, approaches the GUT scale, so that v^2/v_σ in Eq. (4.46) is suppressed. In particular, $v^2/v_\sigma \lesssim 0.1$ eV for $v_\sigma \gtrsim 10^{14}$ GeV. At lower frequencies, v^2/v_σ is larger, necessitating smaller $\boldsymbol{y_\nu}$ to produce sub-eV neutrino masses.

Constraining the parameter space with GW data

A Z′ boson that couples to electrons and muons has been constrained by the LHC to be heavier than approximately 5 TeV. GW experiments afford a completely different approach to constrain the model parameter space. Data from LIGO, ET and LISA will cover a mass range from the TeV scale all the way up to the GUT scale. To quantify the detection prospects for a given GW experiment, we

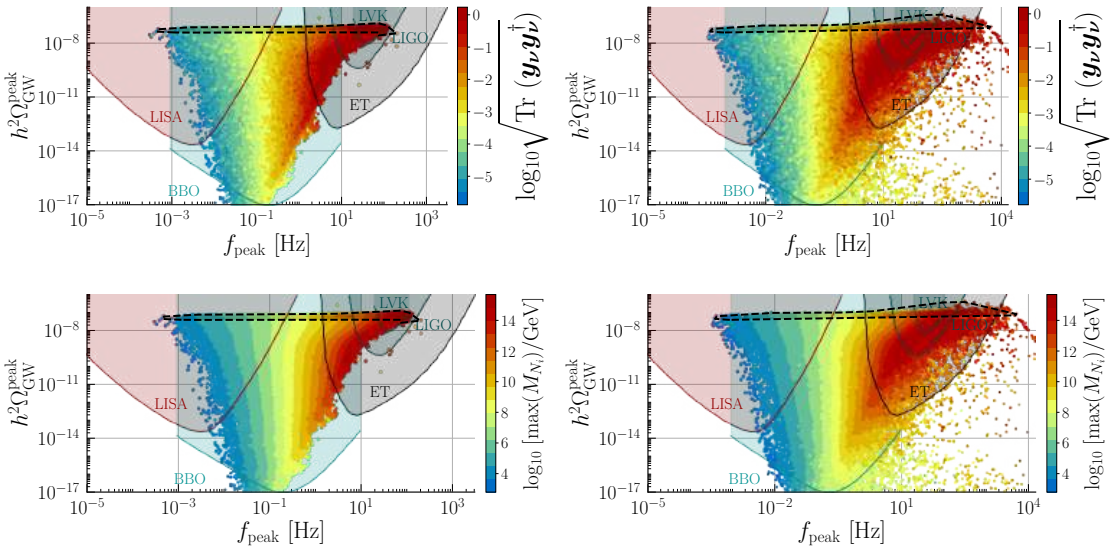

Figure 4.11: Similar to Fig. 4.6, but the colour scales indicate the magnitude of the Dirac Yukawa couplings, $\sqrt{\mathrm{Tr}(\boldsymbol{y}_\nu \boldsymbol{y}_\nu^\dagger)}$ (top row), and mass of the heaviest right-handed neutrino (bottom row).

---

calculate the Signal-to-Noise Ratio (SNR),

$$\mathrm{SNR} = \sqrt{\mathcal{T} \int df \, \frac{\Omega_{\rm GW}^2(f)}{\Omega_{\rm Sens}^2(f)}}\,, \tag{4.93}$$

where $\Omega_{\rm GW}(f)$ is the predicted GW spectrum and $h^2\Omega_{\rm Sens}(f)$ is the expected experimental sensitivity. Except for the LVK bound, we set the observation time to $\mathcal{T} = 4$ years for all experiments. A signal is considered detectable if SNR > 10.

In Fig. 4.12 we illustrate three benchmark scenarios whose parameters are provided in Tab. 4.3.

BP(a) corresponds to physics at the $10 \odot 100$ TeV scale with a GW spectrum that peaks in the mHz regime, well within the reach of LISA. The large SNR qualifies this as an early discovery/exclusion benchmark for LISA.

BP(b) represents physics at a scale of approximately 10^{11} GeV with a GW spectrum that peaks in the Hz regime, well within the reach of ET. However, LIGO-O5 is sensitive to its high-frequency tail with an SNR of approximately 29. This allows for its discovery or exclusion during the LIGO-O5 run, well before ET comes online.

BP(c) is a scenario that can also be tested at LIGO-O5. The GW spectrum peaks at tens of Hz and features the highest $\mathrm{U}(1)_{\mathrm{B-L}}$ breaking scale of the three BPs. An observation at LIGO would imply a strong confirmation at ET with an SNR of 10^6.

All three BPs in Fig. 4.12 can be tested at BBO.

Current LVK data do not show evidence for a SGWB, either of cosmological or astrophysical origin. As shown in the scatter plots, numerous points fall within the LVK excluded region. In Fig. 4.13, we provide an estimate of the excluded region in the $(M_{Z'}, g_L)$ plane (top row) and the $(M_{h_2}, \lambda_\sigma)$ plane (bottom row). The shaded area within the solid black contour represents signals at LVK with a minimum SNR greater than 10. The region within the dashed contour has the same meaning as in Fig. 4.6. Given the multi-dimensional nature of the parameter space, we consider a point in the $(M_{Z'}, g_L)$ and $(M_{h_2}, \lambda_\sigma)$ planes to be excluded if for all combinations of the other model parameters, the SNR is greater than 10. For instance, in the right panels, large Yukawa couplings lead to points of a fixed SNR spreading out. This results in the coexistence of, *e.g.*, blue and green points, with SNR values greater or smaller than 10 in the same region, which, consequently, cannot be excluded. In the

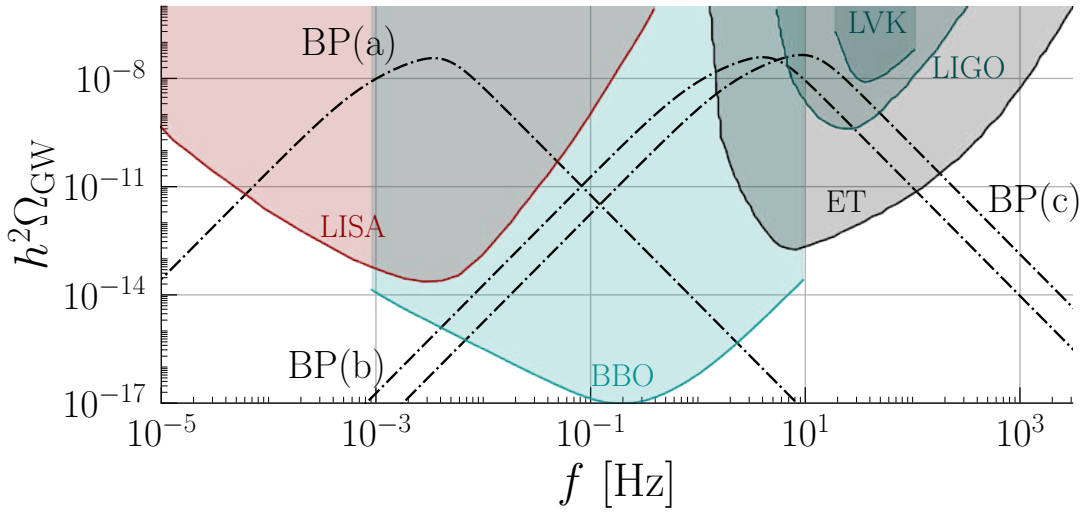

Figure 4.12: SGWB spectra for three BPs of the $U(1)_{B-L}$ model whose GW spectra can be easily detected at LISA, ET and LIGO. The complete set of parameters for each BP can be found in Tab. 4.3.

	BP(a)	BP(b)	BP(c)
M_{h_2}	2.91×10^4	6.25×10^{10}	9.45×10^{11}
$M_{Z'}$	2.69×10^5	5.24×10^{11}	7.92×10^{12}
M_{N_1}	5.62×10^3	4.11×10^9	1.60×10^5
M_{N_2}	1.19×10^4	1.47×10^{10}	1.989×10^7
M_{N_3}	3.65×10^4	1.94×10^{10}	2.25×10^9
v_σ	4.84×10^5	8.57×10^{11}	1.29×10^{13}
g_L	0.28	0.31	0.31
$\mathrm{Tr}(\boldsymbol{y_\sigma})$	0.16	0.063	2.5×10^{-4}
$\sqrt{\mathrm{Tr}(\boldsymbol{y_\nu y_\nu^\dagger})}$	1.28×10^{-5}	0.010	0.0025
λ_σ	$\odot$0.025	$\odot$0.11	$\odot$0.13
$\lambda_{\sigma h}$	$\odot 7.62 \times 10^{-8}$	$\odot 2.43 \times 10^{-20}$	$\odot 1.07 \times 10^{-22}$
α	5.37×10^{11}	2.69×10^8	4.79×10^8
$\beta/H(T_p)$	11.7	11.4	10.6
T_p	6.52	5.19×10^4	1.11×10^5
$T_{\rm RH}$	5594.42	6.63×10^6	1.64×10^7
T_c	2.02×10^4	2.45×10^7	6.11×10^7
$\mathrm{SNR}^{\rm LIGO}$	1.89×10^{-8}	29.4	283.84
$\mathrm{SNR}^{\rm ET}$	5.2×10^{-4}	4.3×10^5	1.11×10^6
$\mathrm{SNR}^{\rm LISA}$	2.15×10^5	0.06	5.7×10^{-3}

Table 4.3: Model parameters at $\mu = M_{Z^0}$, thermodynamic parameters, and SNR for the BPs in Fig. 4.12. The $U(1)_{B-L}$ breaking VEV v_σ, physical masses and temperatures are in units of GeV.

right panels, the excluded region disappears because of the increased freedom provided by the large Yukawa couplings.

With the LIGO-O5 observation run it will be possible to test a broader region of the parameter space, as illustrated by the area enclosed by the solid black curve in Fig. 4.14. This run will explore scenarios compatible with Z′ masses down to 10^{11} GeV and h_2 masses down to 10^{10} GeV for $g_L \approx 0.3$ and $\lambda_\sigma \approx \odot 0.1$. The high mass edge of the parameter space aligns with the LVK exclusion but can

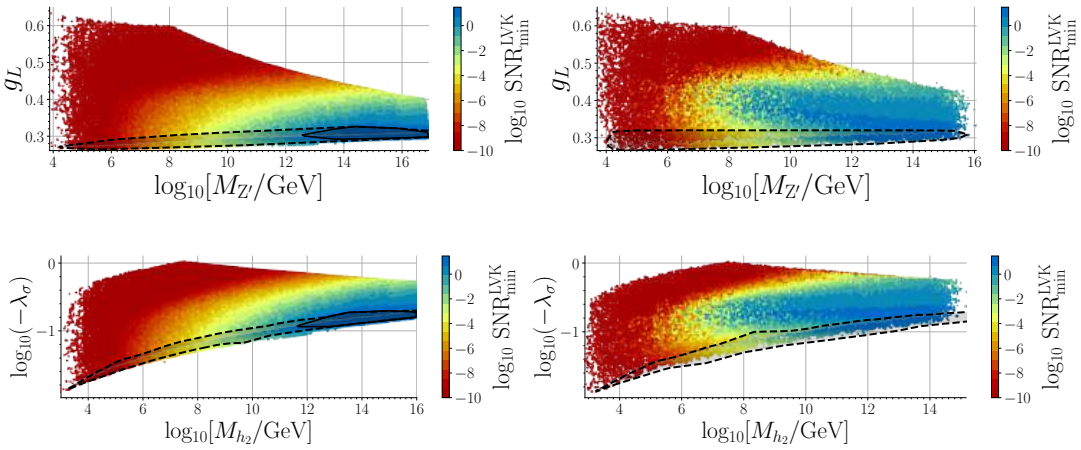

Figure 4.13: Scatter plots for the $\mathrm{U}(1)_{\mathrm{B-L}}$ model in the $(M_{Z'}, g_L)$ and $(M_{h_2}, \lambda_\sigma)$ planes for $\mathrm{Tr}(\boldsymbol{y_\sigma}) < g_L$ (left panels) and $\mathrm{Tr}(\boldsymbol{y_\sigma}) > g_L$ (right panels). The colour scale represents the minimum SNR at LVK. The area enclosed by the solid black contour is excluded by LVK since SNR > 10. No regions are excluded by LVK in the right panels. For points enclosed by the dashed contour, percolation may occur at a temperature below T_p.

---

extend to $g_L \approx 0.4$ and $\lambda_\sigma \approx \odot 0.5$.

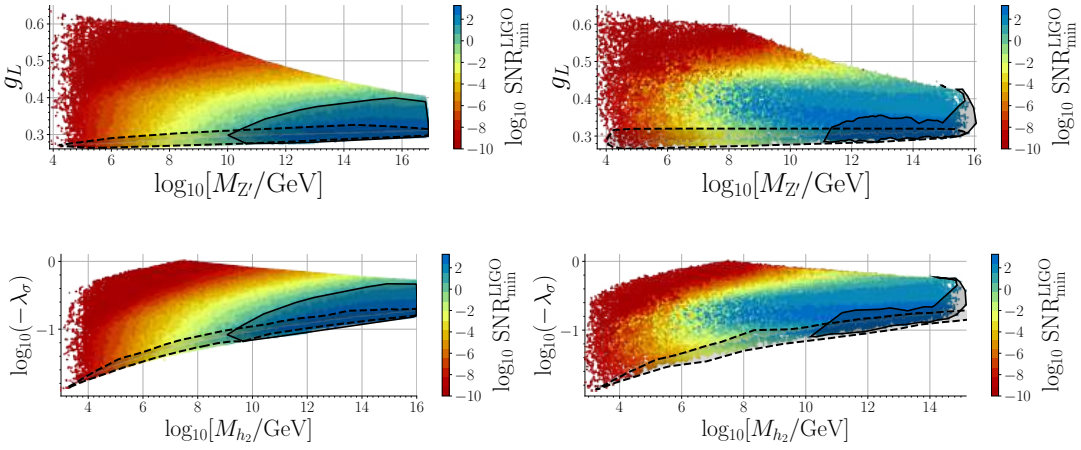

Figure 4.14: Similar to Fig. 4.13, but for a 4-year LIGO-O5 run.

In the longer term, ET will explore a significantly larger region of parameter space, as shown in Fig. 4.15. Specifically, we project sensitivity to a Z′ as light as 10 PeV for $g_L \approx 0.3$, and to h_2 as light as 1 PeV for $\lambda_\sigma \approx \odot 0.05$.

LISA is complementary to LIGO and ET in that it will test the low mass edge of the parameter space, corresponding to the smallest values of λ_σ. As shown in Fig. 4.16, a four-year exposure can probe Z′ masses from 10 TeV to 10^{10} GeV, and heavy Higgs boson masses from 1 TeV to 10^9 GeV. Although LISA and ET do not operate in the same frequency band, we find many SGWB signals that peak in one experiment but with tails extending into the other, achieving SNR values above 10 in both experiments. Indeed, from Figs. 4.15 and 4.16 we observe overlapping sensitivity in the mass range, 10^8 GeV to 10^{10} GeV for $M_{Z'}$, and 10^7 GeV to 10^9 GeV for M_{h_2}.

We summarise the results of this subsection in Fig. 4.17.The colour scales in the $(M_{Z'}, g_L)$ and $(\max[M_{N_i}], \mathrm{Tr}(\boldsymbol{y_\sigma}))$ planes represent the heavy Higgs mass, and the size of $\boldsymbol{y_\nu}$, respectively. The top-left panel indicates that the $\mathrm{U}(1)_{\mathrm{B-L}}$ model is excluded by the LVK bound for $M_{Z'} \approx 10 M_{h_2} >$

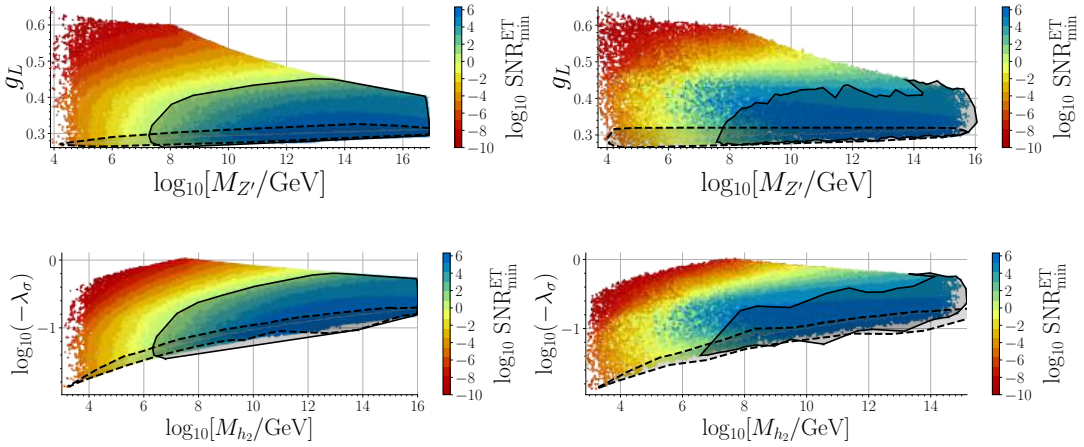

Figure 4.15: Similar to Fig. 4.13, but for ET.

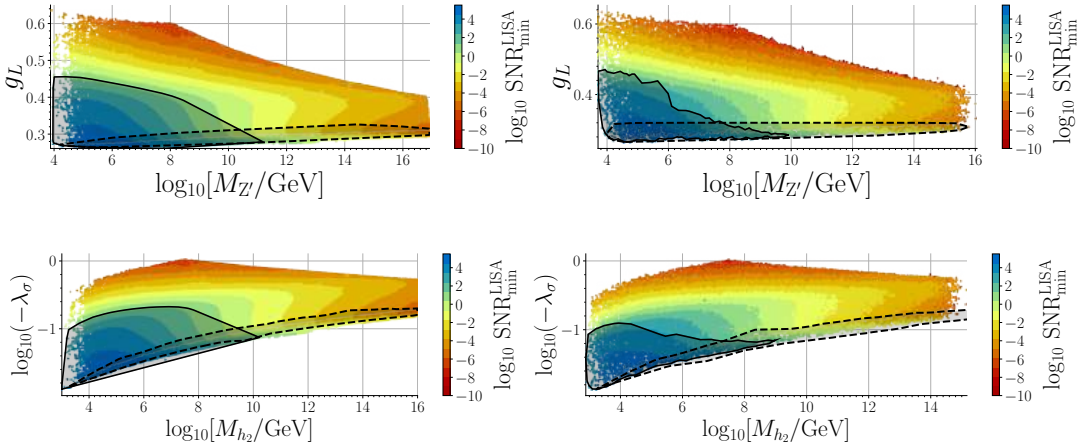

Figure 4.16: Similar to Fig. 4.13, but for LISA.

10^{13} GeV, with $g_L \approx 0.3$ and $\mathrm{Tr}(\boldsymbol{y_\sigma}) < \mathcal{O}(0.1)$. It also confirms that a wide range of Z′ masses can be tested for small $\mathrm{Tr}(\boldsymbol{y_\sigma})$. In the bottom-left panel, there is no region with SNR > 10 because the Yukawa couplings play a subdominant role in the phase transition. However, if no evidence for a SGWB with SNR > 10 is found at LISA, LIGO, and ET, strong supercooling defined by $g_L \lesssim 0.4$, will be disfavoured for $\mathrm{Tr}(\boldsymbol{y_\sigma}) < \mathcal{O}(0.1)$. At LIGO and ET, strong supercooling will be tested for Z′ masses above 10^9 GeV, and at LISA for masses below 100 TeV. Furthermore, the model can be fully excluded for $M_{Z'} \approx 10 M_{h_2} > 10^{14}$ GeV, as can be seen from the complete overlap of the dark purple contour and the coloured region above $M_{Z'} = 10^{14}$ GeV in the top panels. Correspondingly, the bottom-right panel shows that a high-scale seesaw mechanism characterised by right-handed neutrinos heavier than $10^{14.5}$ GeV and Yukawa couplings of $\mathcal{O}(1)$, can be excluded. Note that for $\mathrm{Tr}(\boldsymbol{y_\sigma}) \gtrsim 0.4$, the LVK data do not exclude any parameter space, and that a nonobservation of a GW signal will exclude $\mathrm{Tr}(\boldsymbol{y_\sigma}) \approx 0.45$ and $g_L \approx 0.3$ in the entire mass range.

Sources of gravitational waves

In the context of strongly supercooled phase transitions, we neglect the contribution from turbulence and focus on sound waves and bubble collisions as the main sources of GWs. As Fig. 4.28 shows, these phenomena are interrelated such that, one dominates over the other in most cases, although they may contribute comparably. From Fig. 4.18, it is evident that the contribution from sound waves

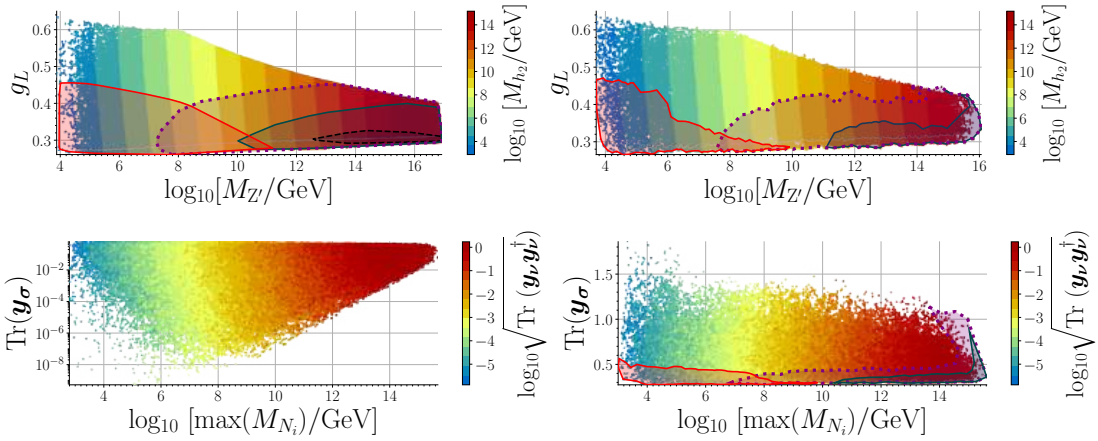

Figure 4.17: Scatter plots for generic $\mathrm{U}(1)_{\mathrm{B-L}}$ model in the $(M_{Z'}, g_L)$ and $(\max(M_{N_i}), \mathrm{Tr}(\boldsymbol{y_\sigma}))$ planes for $\mathrm{Tr}(\boldsymbol{y_\sigma}) < g_L$ (left panels) and $\mathrm{Tr}(\boldsymbol{y_\sigma}) > g_L$ (right panels). The colour scales represent the heavy Higgs mass (top row), and the magnitude of the Dirac Yukawa couplings, $\sqrt{\mathrm{Tr}(\boldsymbol{y_\nu}\boldsymbol{y_\nu}^\dagger)}$ (bottom row). The closed contours outline the regions with SNR > 10 for LVK (dashed black), LIGO-O5 (solid green) LISA (solid red), and ET (dotted dark purple).

dominates in most of the parameter space. The region where the sound wave contribution becomes negligible corresponds to scenarios in which percolation is not assured at T_p, but is possible at a lower temperature (defined as usual by the black dashed curve).

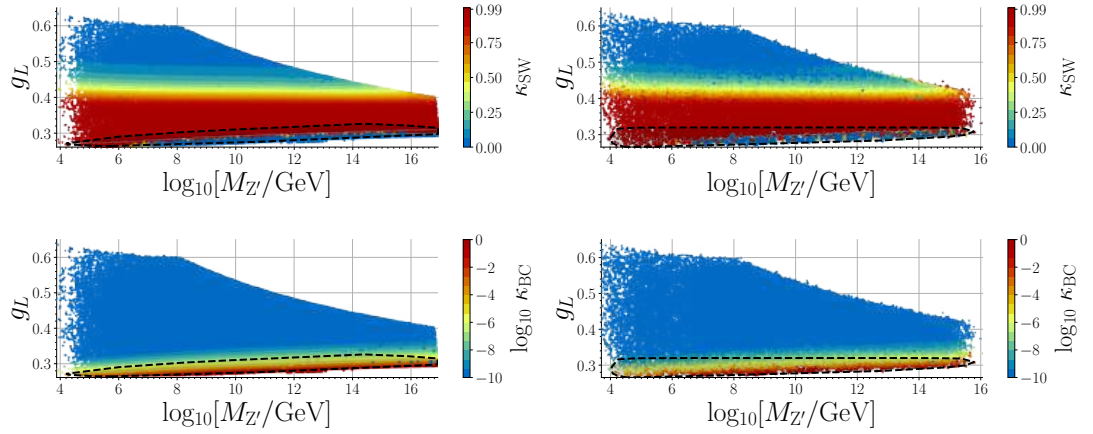

Figure 4.18: Similar to Fig. 4.13, but the colour scales indicate the efficiency factors for sound waves (top row) and bubble collisions (bottom row).

Fig. 4.19 shows that bubble collisions become the dominant source as $h^2\Omega_{\mathrm{GW}}^{\mathrm{peak}}$ approaches 10^{-7}. This corresponds to the highest values of $\alpha \gtrsim 10^{15}$, for which supercooling is maximal.

Comparison with the literature

To conclude this section, we compare our results with those of Ref. [105], which also studied GWs in the classical scale-invariant version of the B⊙L model. We find qualitative agreement in the thermodynamic parameters, but we obtain roughly an order of magnitude lower percolation temperatures. Furthermore, the stronger FOPTs that we obtain do not satisfy the percolation condition in Eq. (4.8), whereas Ref. [105] finds percolation to always occur at T_p. We attribute these differences to how the potential is minimised and how the scalar masses are calculated. Specifically, Ref. [105] considers the RG-improved tree-level potential, $V = \lambda_\sigma(t)\phi_\sigma^4/4$, whereas we include the CW contribution, *i.e.*,

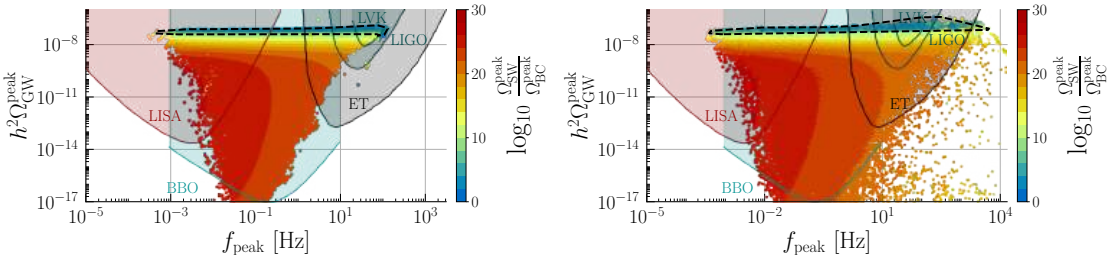

Figure 4.19: Similar to Fig. 4.6, but the colour scales indicate the ratio of the energy density in GWs contributed by sound waves and bubble collisions.

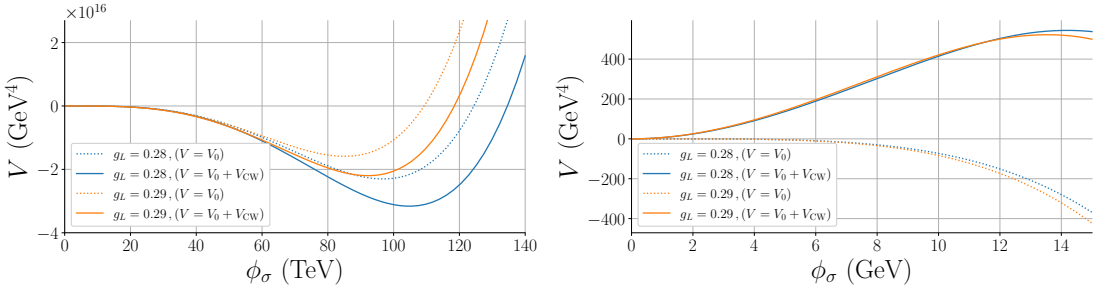

Figure 4.20: Comparison of the tree-level ($V = V_0$, dashed curves) and one-loop corrected potential ($V = V_0 + V_{\rm CW}$ in Eq. (4.82), solid curves) for BP(a) at $T = 15$ GeV. The left panel illustrates the behaviour near the true minimum, and the right panel focuses on the potential barrier.

$V = \lambda_\sigma(t)\phi_\sigma^4/4 + V_{\rm CW}(t, \phi_\sigma)$, and minimise it with all parameters defined at $\mu = M_{Z^0}$, as was done in Ref. [103]. We calculate the mass spectrum at one-loop, including the self-energies at $p^2 \neq 0$ and the second derivatives of the CW potential at $p^2 = 0$; see Eq. (4.61). Fig. 4.20 shows that the one-loop calculation not only shifts the minimum (left panel), but also significantly impacts the height of the potential barrier (right panel). While Ref. [105] does not include Daisy corrections, we find numerically that their impact on the thermal corrections is marginal. Note that we accurately reproduce the results of Ref. [105] by using its methodology.

A major difference is that we explore large masses, ranging from the TeV scale up to the Planck scale. This contrasts with Ref. [105], which does not consider masses above 10^8 GeV, but studies FOPTs below the QCD scale, which we do not. We have also analysed the case of large right-handed neutrino Yukawa couplings, while Ref. [105] neglects this contribution. Importantly, we have established a connection between neutrino physics and SGWB signals, a subject not discussed in Ref. [105].

On a different note, the study of a minimal U(1) conformal dark Higgs model [425] found that a matter-dominated period immediately after the phase transition reduces the peak frequency of the SGWB to the LISA sensitivity range, similar to our Fig. 4.10. In Ref. [425], this happens because the heavy CP-even Higgs boson acts as a thermal inflaton that decays only to SM particles at a significantly suppressed rate via a small portal coupling. Notably, the inclusion of heavy neutrinos in Majoron models fundamentally alters this picture, allowing for GW signals at LIGO and ET.

4.6.2 PBHs, magnetic fields and microlensing in a $\mathbf{U(1)_{B-L}}$ scenario $(x_{\mathcal{H}}, x_\sigma) = (0, 2)$

Phase transition thermodynamics and PBH formation

In Fig. 4.21, we present predictions for the PBH mass and relic abundance in terms of the thermodynamic parameters of the phase transition α, $\beta/H(T_p)$, T_p, and $T_{\rm RH}$. The PBH mass is displayed in grams on the top-horizontal axis and in solar masses on the bottom-horizontal axis. The vertical shaded band enclosed by the black dashed contour, with $M_{\rm PBH} \lesssim 10^{-17} M_\odot$, is excluded by data from LVK's third observational run (O3) because the predicted SNR in this band exceeds 10. The black

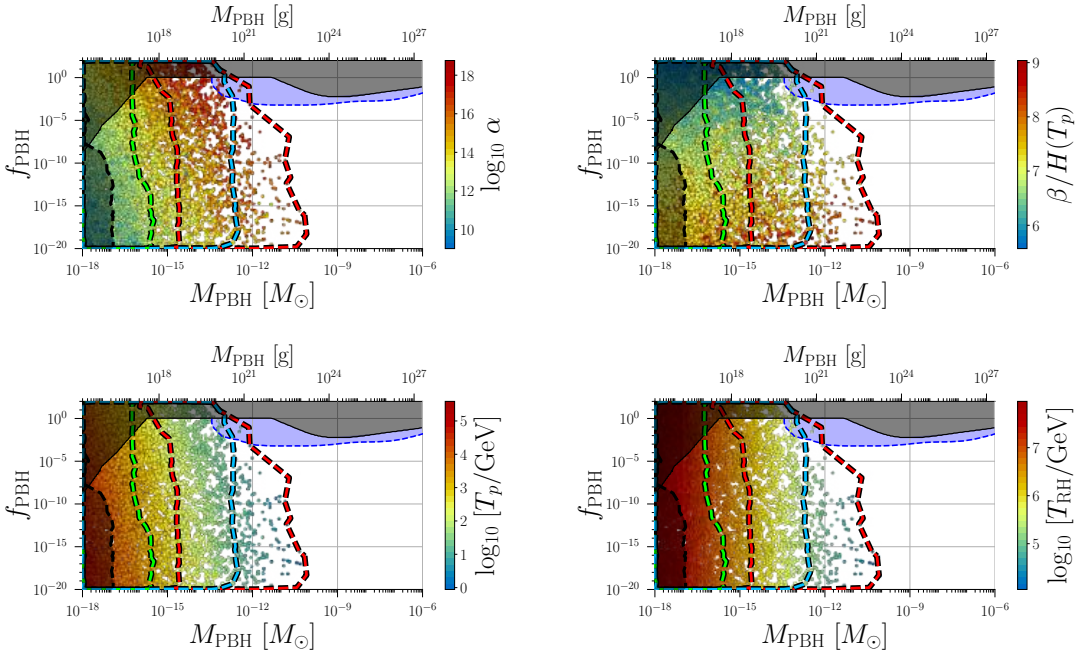

Figure 4.21: Scatter plots of the PBH abundance, $f_{\rm PBH}$, as a function of $M_{\rm PBH}$. The colour scales indicate the FOPT strength α (top-left panel), its inverse duration $\beta/H(T_p)$ (top-right panel), the percolation temperature T_p (bottom-left) and the reheating temperature $T_{\rm RH}$ (bottom-right panel). The vertical band enclosed by the black dashed contour is excluded by LVK data (${\rm SNR}_{\rm LVK} > 10$). The green, blue and red dashed contours enclose the regions within the reach of LIGO-O5, ET and LISA with SNR > 10, respectively. The region above the solid black curve is excluded by combination of overabundant PBH production, γ-ray data and microlensing data. A dedicated microlensing survey of M31 by the Roman Space Telescope is sensitive to the region above the dashed blue curve [426].

solid contour represents a combined exclusion region derived from constraints on the overproduction of PBHs, the extragalactic γ-ray flux via Hawking radiation, and microlensing observations. The expected sensitivity for the Roman Space Telescope is depicted by the blue shaded region [426]. The spread in points of a given colour is due to variations in the critical threshold δ_c.

Strong, sustained supercooling is a key requirement for PBH formation. We find $\alpha \gtrsim 10^9$ and $\beta/H(T_p) < 9$. Due to the exponential dependence of $f_{\rm PBH}$ on $\beta/H(T_p)$ in Eq. (4.31), the DM relic abundance is saturated ($f_{\rm PBH} = 1$) in a narrow range $6 \lesssim \beta/H(T_p) \lesssim 7$ for PBH masses within $[10^{-16}, 10^{-11}]\ M_\odot$. In this region, we also observe the strongest FOPTs, with $10^{15} \lesssim \alpha \lesssim 10^{18}$.

While $\beta/H(T_p)$ primarily determines $f_{\rm PBH}$, the reheating temperature sets the PBH mass via Eq. (4.32), according to which $M_{\rm PBH} \propto T_{\rm RH}^{-2}$. Consequently, lower values of $T_{\rm RH}$ result in heavier PBHs, as can be seen in the bottom-right panel. Recall that in the presence of strong supercooling $T_p \ll T_{\rm RH}$. For a fixed PBH mass and a correspondingly fixed reheating temperature, αT_p^4 is a constant, which explains the observed colour trends in the left panels. Note that larger PBH masses are obtained for stronger phase transitions.

For reheating temperatures at the TeV scale, we find $M_{\rm PBH} \sim (10^{-12} \odot 10^{-10}) M_\odot$, while reheating temperatures near 10^8 GeV yield lighter PBHs with $M_{\rm PBH} \sim 10^{-18} M_\odot$. The upper bound on PBH masses, $M_{\rm PBH} \lesssim 10^{-10} M_\odot$, arises from our requirement that phase transitions occur above the QCD scale (*i.e.*, $T_p > 0.17$ GeV). Note that all the points fall within the sensitivity reach of near-future GW experiments, as indicated by the green dashed contour (for LIGO-O5), the blue dashed contour (for ET) and the red dashed curve (for LISA).

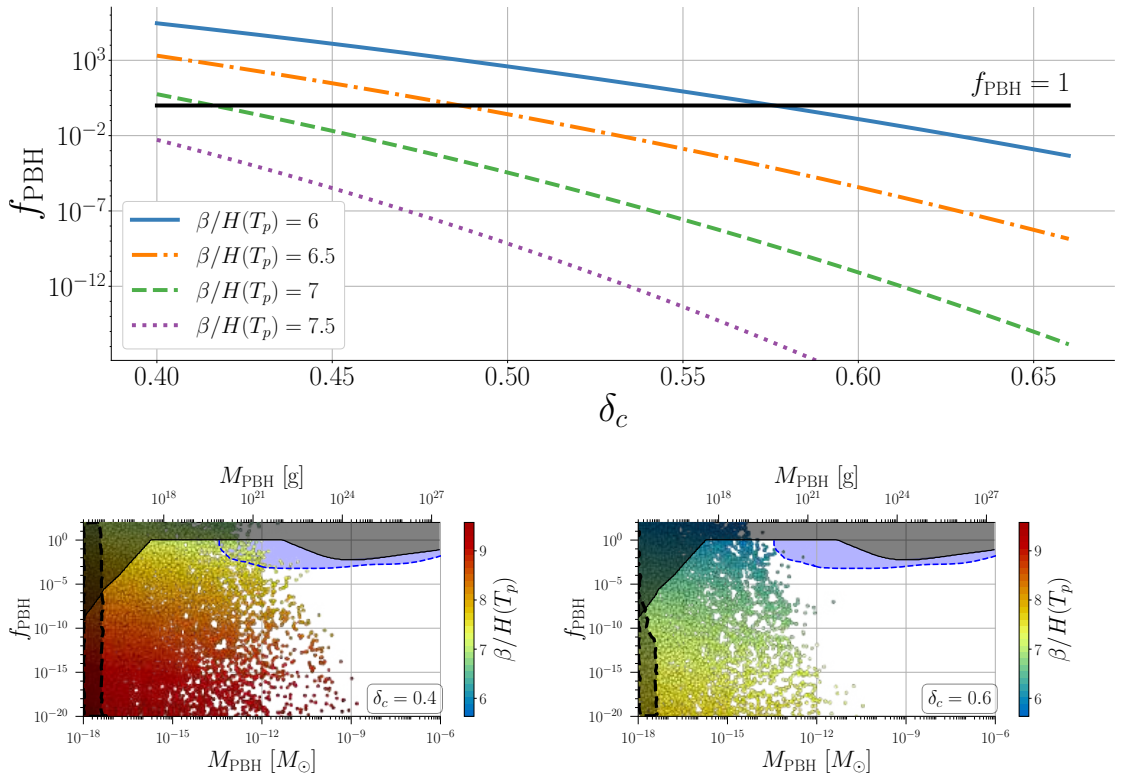

Figure 4.22: Top panel: The DM abundance $f_{\rm PBH}$ as a function of the critical threshold δ_c for different values of the inverse time duration $\beta/H(T_p)$ and a fixed reheating temperature $T_{\rm RH} = 10^6$ GeV. Bottom panels: Similar to Fig. 4.21, but the colour scale represents the inverse duration $\beta/H(T_p)$ of the FOPT for $\delta_c = 0.4$ (left) and $\delta_c = 0.6$ (right).

Impact of the critical threshold δ_c

The exponential dependence of $f_{\rm PBH}$ on the critical density threshold δ_c is highlighted in the top panel of Fig. 4.22 for various values of $\beta/H(T_p)$, with the reheating temperature fixed at $T_{\rm RH} = 10^6$ GeV. The value of $f_{\rm PBH}$ can vary by up to ten orders of magnitude within the range of δ_c obtained from simulations. This variation significantly affects the value of $\beta/H(T_p)$ required for all DM to be PBHs. Specifically, larger values of δ_c correspond to smaller values of $\beta/H(T_p)$.

Although the reheating temperature influences $f_{\rm PBH}$ as in Eq. (4.31), its precise value is irrelevant due to the strong correlation between $\beta/H(T_p)$ and δ_c. This is confirmed in the bottom-right panel of Fig. 4.21, which shows that varying $T_{\rm RH}$ has virtually no impact on $f_{\rm PBH}$.

Impact of the model parameters on PBH formation

In Fig. 4.23, we present the same projections as in Fig. 4.21 but focusing on the underlying model parameters. A strong correlation is observed between the PBH mass and the masses of the Z′, heavy Higgs boson and heavy neutrinos. The PBH mass scale is inversely related to the mass scale of these particles, $M_{Z'} \sim 10 M_{h_2}$. At the upper end of PBH masses, $M_{\rm PBH} \sim 10^{-10} M_\odot$, the corresponding mass scale is $M_{Z'} \sim 10^4$ GeV. At the lower end of the PBH mass spectrum, with $M_{\rm PBH} \sim 10^{-18} M_\odot$, the mass scale approaches the GUT scale. This relationship arises because $M_{Z'} \sim T_{\rm RH}$. This is also reflected in the colour gradient for λ_σ (middle-right panel), since, within the parameter space relevant for PBH production, $M_{h_2}^2 \sim \odot 0.17 \lambda_\sigma v_\sigma^2$.

The gauge coupling g_L exhibits only a weak correlation with the PBH observables (bottom-left panel). However, most of the sampled points allowed (approximately 78% of the data) fall within the range $g_L \sim 0.25$–0.30. In this range, the small values of $\beta/H(T_p)$ required for PBH formation, as can be seen from Figs. 4.6 and 4.7. A key result of Fig. 4.23 is the possibility of establishing a relationship

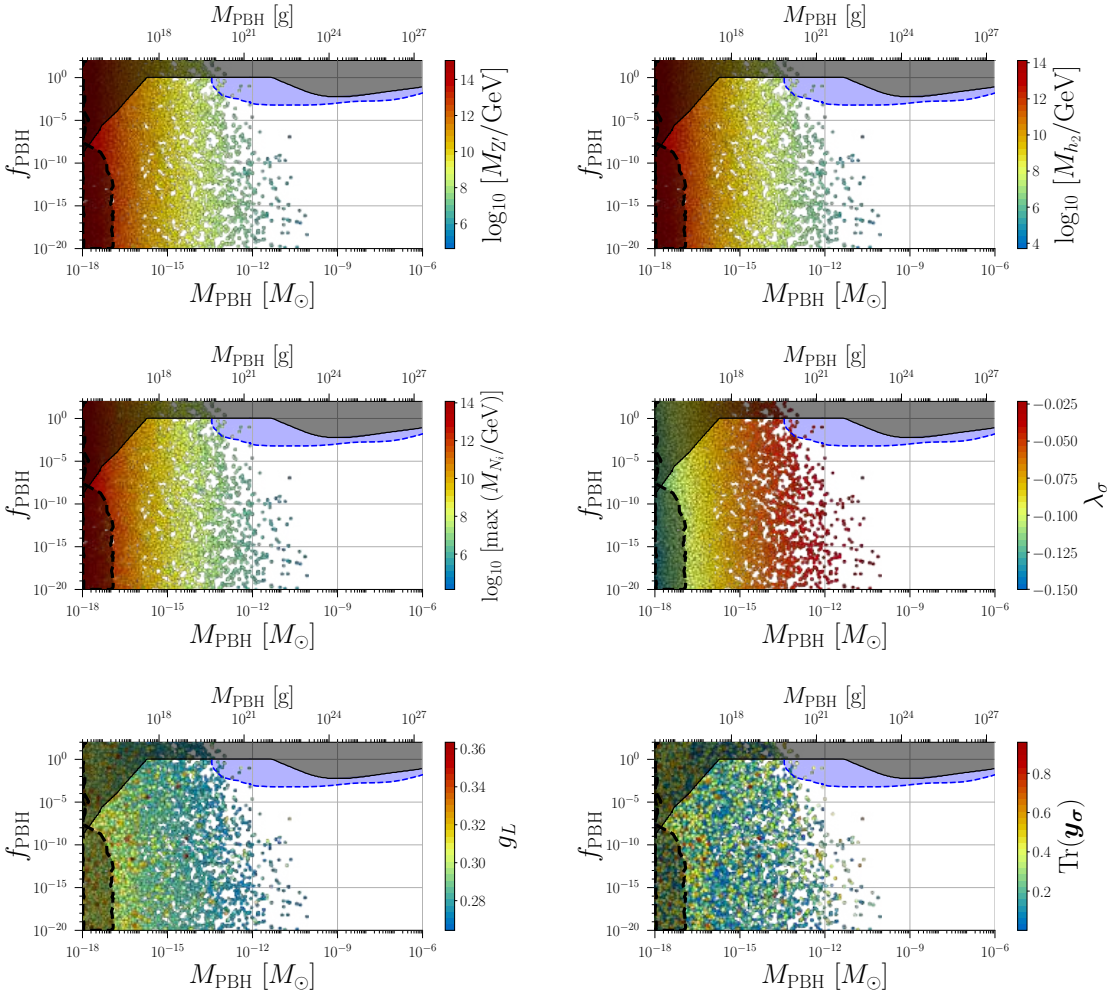

Figure 4.23: Similar to Fig. 4.21, but the colour scales represent the Z′ boson mass (top-left panel), the heavy Higgs h_2 mass (top-right panel), the largest right-handed neutrino mass (middle-left panel), the Majoron self-interaction coupling λ_σ (middle-right panel), the gauge coupling g_L (bottom-left panel) and the trace of the Yukawa matrix $\boldsymbol{y_\sigma}$ (bottom-right panel).

between the model parameters and the conditions to obtain an observable SGWB and the entire DM relic abundance in the form of PBHs. We find $M_{Z'} \in [10^6, 10^{12}]$ GeV, with $g_L \in [0.25, 0.30]$. This also implies a type-I seesaw scale within $[10^6, 10^{10}]$ GeV, which matches the mass range for the heavy Higgs boson h_2, along with $\lambda_\sigma \in [\odot 0.075, \odot 0.025]$. The neutrino Yukawa couplings characterised by ${\rm Tr}(\boldsymbol{y_\sigma})$ (bottom-right panel) remain largely unconstrained and can take values satisfying $10^{-6} \lesssim {\rm Tr}(\boldsymbol{y_\sigma}) \lesssim 1$.

Correlated signals: γ–ray signals, microlensing, GW experiments and magnetic fields

In Fig. 4.24, we present the predicted SNR for the SGWB at LISA (top-left panel), ET (top-right panel), LIGO O5 (bottom-left panel) and LVK (bottom-right panel). A signal is considered detectable if SNR > 10. Experiments with sensitivity in the 1–100 Hz frequency range, such as LIGO and ET, primarily constrain the low-mass PBH region, while LIGO-O5 will be sensitive to masses below $\sim 10^{-17} M_\odot$ and ET can extend this sensitivity to PBH masses below $\sim 2 \times 10^{-13} M_\odot$. In contrast, LISA is sensitive to PBH masses heavier than $1 \times 10^{-16} M_\odot$. Together, these experiments will cover the full range of PBH masses for $f_{\rm PBH}$ values down to 10^{-20}, thus complementing γ-ray and microlensing observations. Current LVK data exclude PBH masses below $4 \times 10^{-18} M_\odot$.

Microlensing is a distinctive signal of compact objects. Notably, for PBHs with asteroid-scale

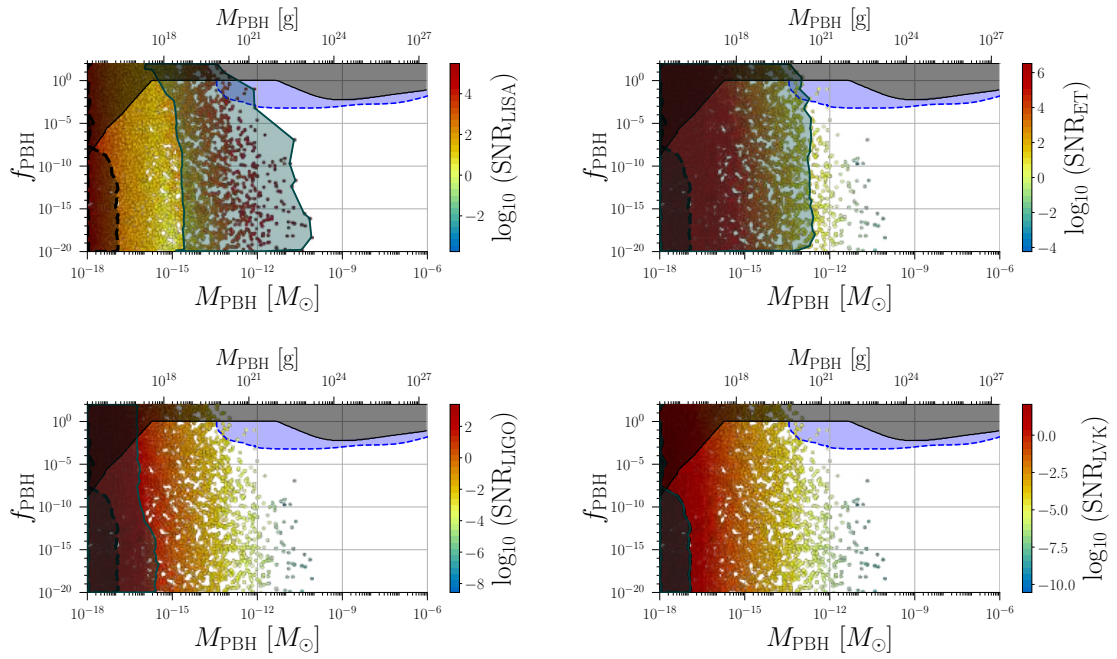

Figure 4.24: Similar to Fig. 4.21, but the colour scale represent the SNR of LISA (panel a), the SNR of ET (panel b), the SNR of LIGO O5 (panel c) and SNR of LVK (panel d). Solid green contours encapsulate regions of SNR > 10 for the corresponding experiment in the colour bar.

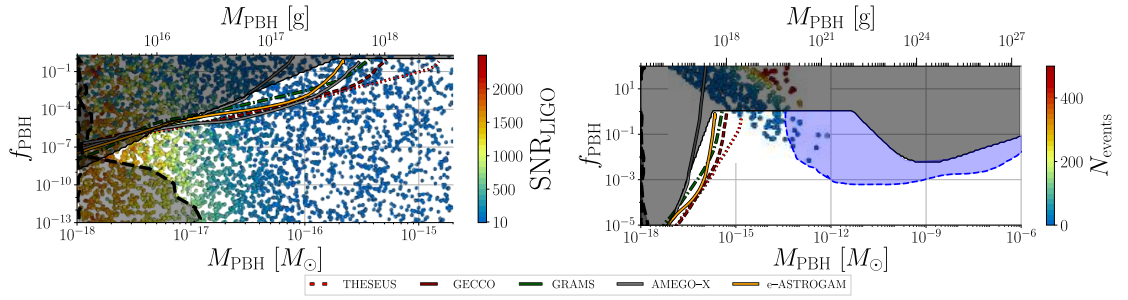

Figure 4.25: Left panel: Parameter space with at least one microlensing event. Right panel: The expected sensitivities of extragalactic $\gamma-$ray signals from Hawking radiation with SNR>10 for THESEUS (dotted red curve), GECCO (dashed brown curve), GRAMS (solid green curve), AMEGO$-$X (gray solid curve) and e$-$ASTROGAM (solid orange curve). The colour scale in the right panel indicates the predicted SNR for LIGO O5.

masses between 10^{-17} $M_\odot$ and 10^{-12} $M_\odot$, the Schwarzschild radius becomes comparable to the optical wavelengths used in typical microlensing surveys. Then, wave optics effects become significant and lead to characteristic oscillatory patterns in the microlensing light curve. These oscillations serve as a signal for small lenses such as asteroid-sized PBHs, distinguishing them from larger astrophysical lenses. A dedicated survey of the M31 galaxy by the Roman Space Telescope will be sensitive to a wide range of PBH masses, from 10^{-14} to 10^{-5} $M_\odot$ [426], thereby enhancing the ability to detect or rule out PBHs as a component of DM.

With this in mind, we compute the expected number of events at the Roman Space Telescope as

$$N_{\rm events} = T_{\rm obs} N_{\rm S} \int_{t_{\rm min}}^{t_{\rm max}} dt_{\rm E} \int dR_{\rm S} \int_1^0 dx \frac{d^2\Gamma}{dx dt_{\rm E}} \frac{dn}{dR_{\rm S}} \,. \tag{4.94}$$

Here, $x = D_L/D_S$ where D_L and $D_S = 778.5$ kpc are the distances from Earth to the lens and source (in M31), respectively, and $T_{\rm obs} = 6 \times 72$ days is the expected Roman observation time [427], and

$N_S = 2.4 \times 10^8$ is the number of source stars in M31 [427]. The duration for which the magnification remains above the detection threshold is t_E and is integrated from $t_{min} = 15$ minutes (the proposed cadence [427]) to $t_{max} = 6 \times 72$ days (total observation time). We take the stellar radius distribution dn/dR_S for the M31 galaxy from Ref. [428]. The differential event rate is given by

$$\frac{d^2\Gamma}{dx dt_E} = D_S \frac{f_{PBH}}{M_{PBH}} \rho^{DM}_{M31}(r_{M31}) \frac{v_E^4(x)}{v_{M31}^2} e^{-v_E^2(x)/v_{M31}^2} , \tag{4.95}$$

where $v_E(x) = 2u_{1.34}(x)R_E(x)/t_E$, with R_E the Einstein radius and $u_{1.34} = 1$ the impact parameter for a point-like lens. The most probable source velocity in M31 is $v_{M31} = 8.10 \times 10^{-15}$ kpc/s. For the PBH mass distribution ρ^{DM}_{M31} we adopt the Navarro-Frenk-White DM profile:

$$\begin{aligned} \rho^{DM}_{M31}(r_{M31}) &= \frac{\rho'_{M31}}{(r_{M31}/r'_{M31})(1 + r_{M31}/r'_{M31})^2} , \\ r_{M31} &= \sqrt{R_{sol}^2 \odot 2xR_{sol}D_s \cos\ell \cos b + x^2 D_S^2} , \end{aligned} \tag{4.96}$$

where the characteristic density is $\rho_{M31} = 4.85 \times 10^6\ M_\odot/\text{kpc}^3$, the scale radius is $r_{M31} = 25$ kpc, and $R_{sol} = 8.5$ kpc is the distance from the centre of the Milky Way to the Sun. The galactic coordinates of M31 are $(\ell, b) = (121.2^\circ, \odot 21.6^\circ)$.

In the left panel of Fig. 4.25 we show the parameter space with at least one microlensing event. The Roman telescope can observe $\mathcal{O}(100)$ events for $M_{PBH} \sim 10^{-12} M_\odot$ in a region consistent with current constraints. From Fig. 4.23 it is evident that the Roman telescope will target PeV mass scales, with $M_{Z'} \sim 10^5 \odot 10^8$ GeV, $M_{h_2} \sim 10^4 \odot 10^7$ GeV and $M_N \sim 10^6 \odot 10^7$ GeV, $g_L \sim 0.28$, and $\odot 0.025 \lesssim \lambda_\sigma \lesssim \odot 0.05$. In this parameter space a correlated SGWB is detectable at both LISA and ET; see Fig. 4.24.

The sensitivity of microlensing surveys falls for $M_{PBH} < 10^{-15} M_\odot$, while γ-ray signals from Hawking evaporation become more sensitive. Several upcoming telescopes are designed to probe these masses, including THESEUS [429], GECCO [430], GRAMS [431], AMEGO-X [432] and e-ASTROGAM [433]. To determine the regions with SNR > 10, we utilised the `Isatis` script [434] from `BlackHawk` [435, 436], incorporating `Hazma` [437] for low-energy hadronisation.

In the right-panel of Fig. 4.25, we present the SNR > 10 sensitivity curves for these telescopes. We find that these facilities can probe a narrow region, $M_{PBH} \sim [10^{-17}, 10^{-15}]\ M_\odot$ and $f_{PBH} \sim 10^{-3}$, which coincides with the parameter space in which a SGWB is accessible at LIGO O5. From Fig. 4.23, we see that this corresponds to the regime of high-scale phase transitions, with $M_{Z'} \sim 10^{11}$ GeV.

Fig. 4.26 shows scatter plots in the (M_{PBH}, f_{PBH}) plane, with the peak magnetic field strength (top panels) and peak coherence length (middle panels) indicated by the colour scale. The left panels are for helical magnetic fields ($b = 0$), and right panels are for non-helical magnetic fields ($b = 1$). The bottom panel displays these points in the $(\lambda_{peak}, B_{peak})$ plane, with the colour scale indicating the Z′. The black lines show lower limits from high-energy γ-ray observations of blazars.

For both $b = 0$ and $b = 1$, we observe a strong correlation with the PBH mass: lighter PBHs are associated with lower magnetic field strengths and shorter coherence lengths. Comparing with Figs. 4.23 and 4.21 we find that this trend is linked to both the dark sector masses and λ_σ. Specifically, TeV-scale phase transitions with $\lambda_\sigma \sim \odot 0.025$ yield $B_{peak} \sim 10^{-11}$ G for $b = 0$, and $B_{peak} \sim 10^{-13}$ G for $b = 1$. This behaviour stems from the fact that the magnetic field strength scales as $B_{peak} \propto T_{RH}^{-p_b/2-2}$, while the coherence length scales as $\lambda_{peak} \propto T_{RH}^{q_b-1}$ (see Eqs. (4.38)–(4.42)), because the Hubble parameter $H \propto T^2$ during the radiation-dominated epoch. Since q_b is always less than unity, higher reheating temperatures correspond to weaker magnetic fields and shorter coherence lengths. As expected, non-helical magnetic fields have lower amplitudes and shorter coherence lengths than helical magnetic fields.

From the bottom panel of Fig. 4.26 we observe that for $b = 0$, Z′ masses in the range of approximately $[40, 10^6]$ TeV can generate magnetic fields that satisfy the lower limits from blazars, and are therefore observable. For $b = 1$, observable magnetic fields are produced for $M_{Z'} \sim [40, 1000]$ TeV.

The role of the neutrino Yukawa couplings on the magnetic fields is illustrated in Fig. 4.27. We find that the suppression factor κ_h strongly affects B_{peak}, and that an inverse relationship exists between the Z′ mass and κ_h because the decoupling between the dark and visible sectors $\sim v/v_\sigma$. As $\boldsymbol{y_\nu}$ is increased to $\mathcal{O}(0.1 \odot 1)$, the numerator in Eq. (4.43) increases while the denominator remains unchanged, so that κ_h becomes larger. This consequently enhances κ_h as evident by the colour

distribution in the top-right edge of the top-left panel. Nevertheless, sizeable values of $\boldsymbol{y_\nu}$ are insufficient to generate observable magnetic fields, as the dark sector mass scale $M_{Z'} \sim 10^{15}$ GeV has a dominant effect. These enhanced couplings determine the bulge feature in the bottom panel of Fig. 4.26. We find that $\mathrm{Tr}(\boldsymbol{y_\sigma})$ is more weakly correlated with $B_{\rm peak}$ and $\lambda_{\rm peak}$ than is $\boldsymbol{y_\nu}$. For the latter, we find that lower values correspond to larger values of both $B_{\rm peak}$ and $\lambda_{\rm peak}$. This behaviour is connected with the seesaw scale, since larger values of $\boldsymbol{y_\nu}$ are correlated with larger scales. For $b = 0$, in the region where magnetic fields strengths are above the blazar bounds, we find $\sqrt{\mathrm{Tr}(\boldsymbol{y_\nu}\boldsymbol{y_\nu}^\dagger)} \sim [1 \times 10^{-5}, 3 \times 10^{-3}]$ which corresponds to dark sector scales $M_{Z'} \sim [40, 10^6]$ TeV. For $b = 1$ the regions shrink to $\sqrt{\mathrm{Tr}(\boldsymbol{y_\nu}\boldsymbol{y_\nu}^\dagger)} \sim [1 \times 10^{-5}, 6 \times 10^{-5}]$ and $M_{Z'} \sim [40, 1000]$ TeV.

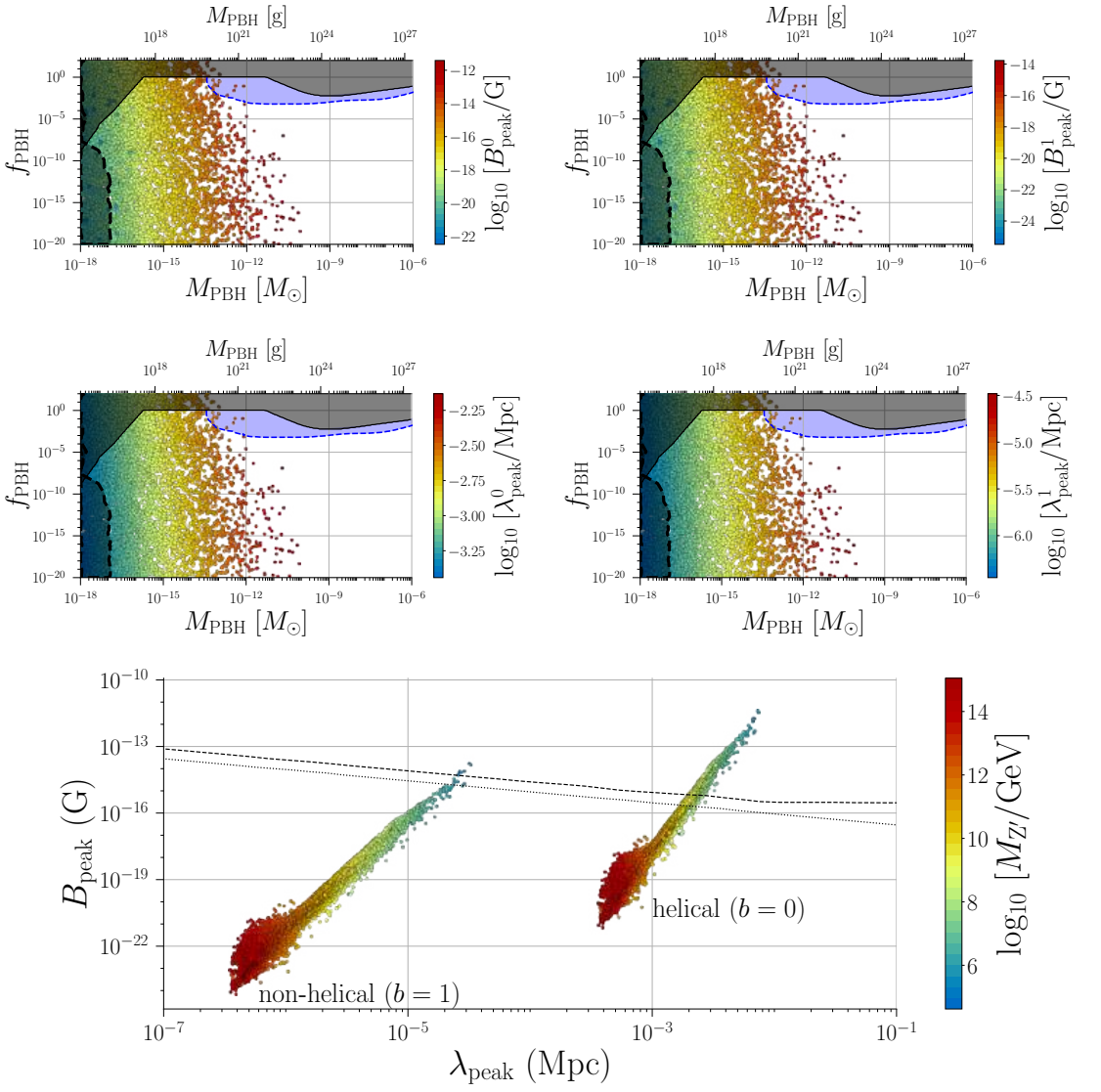

Figure 4.26: Top and middle panels: Similar to Fig. 4.21, but the colour scale indicates the peak magnetic field strength $B_{\rm peak}$ and peak coherence length $\lambda_{\rm peak}$ for helical magnetic fields $b = 0$ (left) and non-helical magnetic fields $b = 1$ (right). Bottom panel: $B_{\rm peak}$ versus $\lambda_{\rm peak}$ for $b = 0$ and $b = 1$. The black dashed line shows the lower limit from [327], and the dotted black line shows the corresponding limit from [328].

4.6.3 GWs in the generic U(1)′ scenario

The $\mathrm{U}(1)_{\mathrm{B-L}}$ model is a particular example of a broadly defined $\mathrm{U}(1)'$ gauge theory with arbitrary $x_{\mathcal{H}}$ and x_σ charges. In this section, we examine generic charge assignments in the ranges in Tab. 4.2.

In Fig. 4.28, the colour scale represents $g_L x_\sigma$ in the first and third rows, and $g_L x_{\mathcal{H}}$ in the second and fourth rows. To fully visualise the parameter space, we divide our data into two sets. The top two rows have points with $x_{\mathcal{H}} \geq 0$, and the bottom two rows have points with $x_{\mathcal{H}} < 0$. From the first row, we observe that the qualitative behaviour of $g_L x_\sigma$ is similar to that of g_L in the $\mathrm{U}(1)_{\mathrm{B-L}}$ case, in that a smaller gauge interaction strength increases the peak amplitude of the SGWB. This is expected as physical observables depend on $g_L x_\sigma$ and not just g_L, and the charge can be absorbed in the definition of the gauge coupling. In the second and fourth rows, we find that larger values of $|g_L x_{\mathcal{H}}|$ correspond to lower peak frequencies and higher peak amplitudes. This stems from the fact that with increasing values of the charges, the gauge and scalar quartic couplings run faster, reaching a Landau pole at lower scales. In the high-frequency region, where the true vacuum takes very large values, the emergence of Landau poles appears below the $\mathrm{U}(1)'$ breaking scale, which explains why $g_L x_{\mathcal{H}} \approx 0$ (dark purple and dark red points in the second and fourth rows).

Note that the dispersion of colour in the $g_L x_\sigma$ plots, compared to the neatly horizontal distribution of g_L for the $\mathrm{U}(1)_{\mathrm{B-L}}$ model (fourth row of Fig. 4.6), is caused by $g_L x_{\mathcal{H}}$. Indeed, there is a close correspondence between the colour gradient in rows one and two and in rows three and four, where larger $|g_L x_{\mathcal{H}}|$ implies smaller $g_L x_\sigma$. This relationship arises from the leading effects in the g_L beta function: $\beta^{(1)}(g_L) \approx (g_L^3/3)(82 x_{\mathcal{H}}^2 + 31 x_{\mathcal{H}} x_\sigma + 9 x_\sigma^2)$. A larger $|g_L x_{\mathcal{H}}|$ must be compensated by a smaller $g_L x_\sigma$, and vice versa, to prevent g_L from reaching a Landau pole. A smaller $g_L x_\sigma$ leads to a

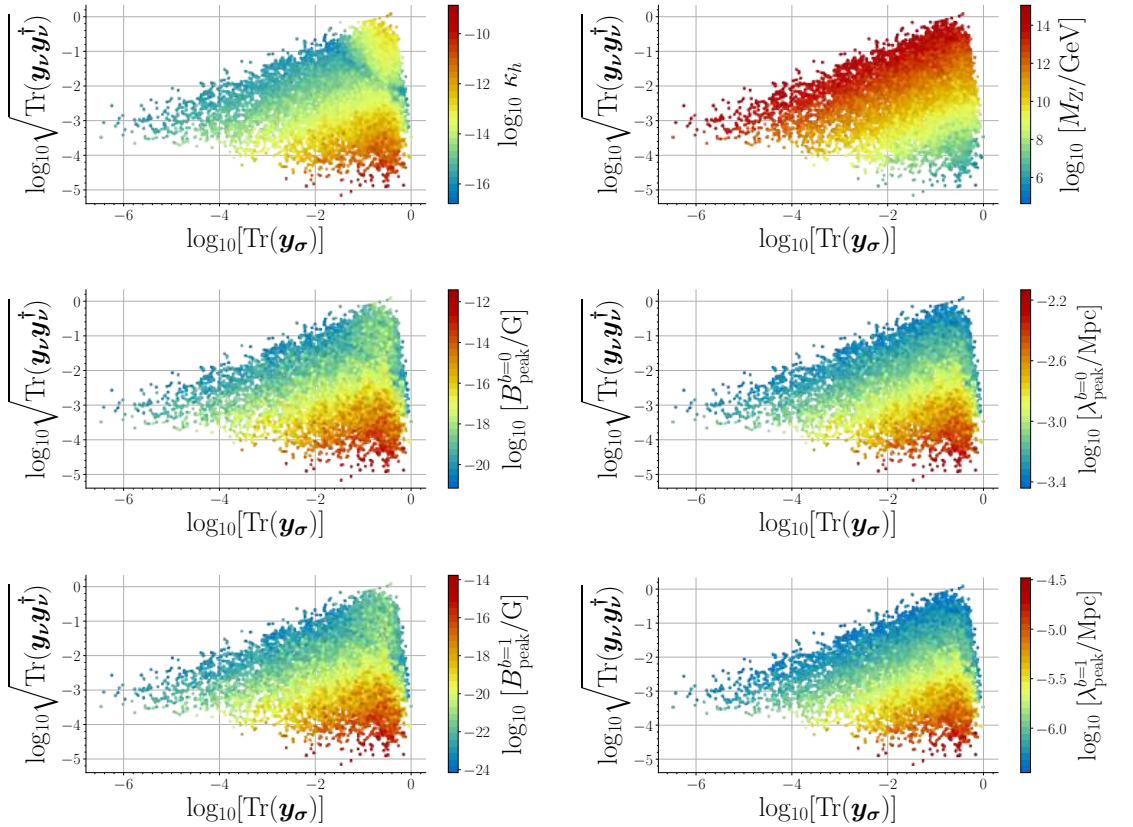

Figure 4.27: Scatter plots of Majorana Yukawa couplings $\mathrm{Tr}(\boldsymbol{y_\sigma})$ and the magnitude of the Dirac Yukawa couplings $\sqrt{\mathrm{Tr}(\boldsymbol{y_\nu y_\nu^\dagger})}$. The colour scale indicates the suppression factor κ_h (top-left panel), the mass of Z′ (top-right panel), the peak magnetic field strength (middle-left and bottom-left panels) and the correlation lengths (middle-right and bottom-right panels) for $b = 0$ and $b = 1$, respectively.

larger peak SGWB amplitude, because $\Delta V_{\rm eff}$ is larger, as discussed in connection with Fig. 4.2. Since the coefficient of the $x_{\mathcal{H}}^2$ term is nine times larger than that of the x_σ^2 term, a Landau pole is reached faster even for $x_\sigma \to 0$. We exclude all points for which a coupling becomes non-perturbative at a scale $\mu < v_\sigma$. As in the B⊙L case, a sizeable $\mathrm{Tr}(\boldsymbol{y_\sigma})$ increases the spread of points and gives GW spectra with higher peak frequencies.

In Fig. 4.29, the colour scale is for the Z′ boson and h_2 scalar masses. LIGO and ET are sensitive GUT scale masses. While the distribution of points is similar to $\mathrm{U}(1)_{\mathrm{B-L}}$ case, regions of a given colour are not as well defined. This is due to the freedom introduced by $x_{\mathcal{H}}$, which affects both the heavy Higgs and Z′ masses. For a generic $\mathrm{U}(1)'$ model, LISA will be sensitive to h_2 masses ranging from 1 TeV to 10^9 GeV, with the corresponding Z′ masses an order of magnitude larger. For a given mass, the peak frequency is lower for $\mathrm{Tr}(\boldsymbol{y_\sigma}) < g_L$ (left panels) than for $\mathrm{Tr}(\boldsymbol{y_\sigma}) > g_L$ (right panels). This shift is more pronounced for small $g_L x_\sigma$ and large $|g_L x_{\mathcal{H}}|$, because the $x_{\mathcal{H}}^2$ term dominates the RG evolution of g_L, so that the tree-level potential V_0 is minimised at a lower VEV. This effect is marginal in the B⊙L scenario since only $\boldsymbol{y_\sigma}$ modifies λ_σ. Points with $\mathrm{Tr}(\boldsymbol{y_\sigma}) \ll g_L x_\sigma$, have a cleaner distribution because $g_L x_{\mathcal{H}} \approx 0$, as observed in Fig. 4.28. However, for $\mathrm{Tr}(\boldsymbol{y_\sigma}) > g_L x_\sigma$, the frequency coverage is broader for both high- and low-frequency experiments.

In Fig. 4.30 we show the $(x_{\mathcal{H}}, g_L x_\sigma)$ plane for several thermodynamic parameters. Each value of $x_{\mathcal{H}}$ defines a different $\mathrm{U}(1)'$ model. We identify three different models: the $\mathrm{U}(1)_{\mathrm{B-L}}$ model; the $\mathrm{U}(1)_{\mathrm{R}}$ model with the charge assignment $(x_{\mathcal{H}}, x_\sigma) = (\odot 1, 2)$; and the $\mathrm{U}(1)_{\mathrm{O}}$ model with *e.g.*, $(x_{\mathcal{H}}, x_\sigma) = (\odot 16/41, 2)$, which yields the orthogonality condition between $\mathrm{U}(1)_{\mathrm{Y}}$ and $\mathrm{U}(1)'$, $41 x_{\mathcal{H}} + 8 x_\sigma = 0$,

	BP-1	**BP-2**	**BP-3**
λ_σ	$\odot 0.0484$	$\odot 0.0797$	$\odot 0.0467$
$\lambda_{\sigma h}$	$\odot 3.184 \times 10^{-14}$	$\odot 1.768 \times 10^{-18}$	$\odot 5.99 \times 10^{-13}$
$g_L x_\sigma$	0.473	0.488	0.558
$\mathrm{Tr}(\boldsymbol{y_\sigma})$	0.113	0.336	0.249
$\sqrt{\mathrm{Tr}(\boldsymbol{y_\nu y_\nu^\dagger})}$	3.44×10^{-4}	0.0128	2.02×10^{-4}
$M_{Z'}$/GeV	4.09×10^{8}	5.78×10^{10}	9.63×10^{7}
M_{h_2}/GeV	4.35×10^{7}	6.46×10^{9}	1.04×10^{7}
M_{N}/GeV	4.65×10^{7}	1.39×10^{10}	3.00×10^{7}
T_p/GeV	39.54	1703.43	23.42
T_{RH}/GeV	6.57×10^{5}	7.77×10^{6}	5.29×10^{5}
T_c/GeV	2.31×10^{6}	2.85×10^{7}	1.90×10^{6}
α	7.61×10^{16}	4.33×10^{14}	2.60×10^{17}
$\beta/H(T_p)$	6.71	6.87	6.44
$\mathrm{SNR}_{\mathrm{LISA}}$	2384.50	1.56	4509.54
$\mathrm{SNR}_{\mathrm{ET}}$	160.64	2.66×10^{5}	94.18
$\mathrm{SNR}_{\mathrm{LIGO}}$	0.0109	12.97	0.00638
$\mathrm{SNR}_{\mathrm{LVK}}$	3.56×10^{-5}	0.0276	2.10×10^{-5}
f_{PBH}	0.863	0.0467	1.00
$M_{\mathrm{PBH}}/M_\odot$	2.09×10^{-14}	1.41×10^{-16}	3.32×10^{-14}
N_{events}	23.86	< 1	46.40
δ_c	0.452	0.479	0.489
$B_{\mathrm{peak}}^{b=0}$/G	1.73×10^{-16}	2.79×10^{-19}	2.56×10^{-16}
$\lambda_{\mathrm{peak}}^{b=0}$/Mpc	2.43×10^{-3}	1.05×10^{-3}	2.71×10^{-3}
$B_{\mathrm{peak}}^{b=1}$/G	3.87×10^{-19}	4.10×10^{-22}	5.97×10^{-19}
$\lambda_{\mathrm{peak}}^{b=1}$/Mpc	5.45×10^{-6}	1.55×10^{-6}	6.33×10^{-6}

Table 4.4: Model parameters, thermodynamic parameters and physical observables, for three benchmark points: BP-1, featuring microlensing events at the Roman telescope; BP-2, producing γ-ray signals with SNR > 10 in the proposed experiments considered; and BP-3, characterised by magnetic fields above the blazar limits, large number of microlensing events at the Roman telescope, detectable SGWB at interferometers, and $f_{\mathrm{PBH}} = 1$. The model parameters are defined at $\mu = M_{\mathrm{Z}^0}$.

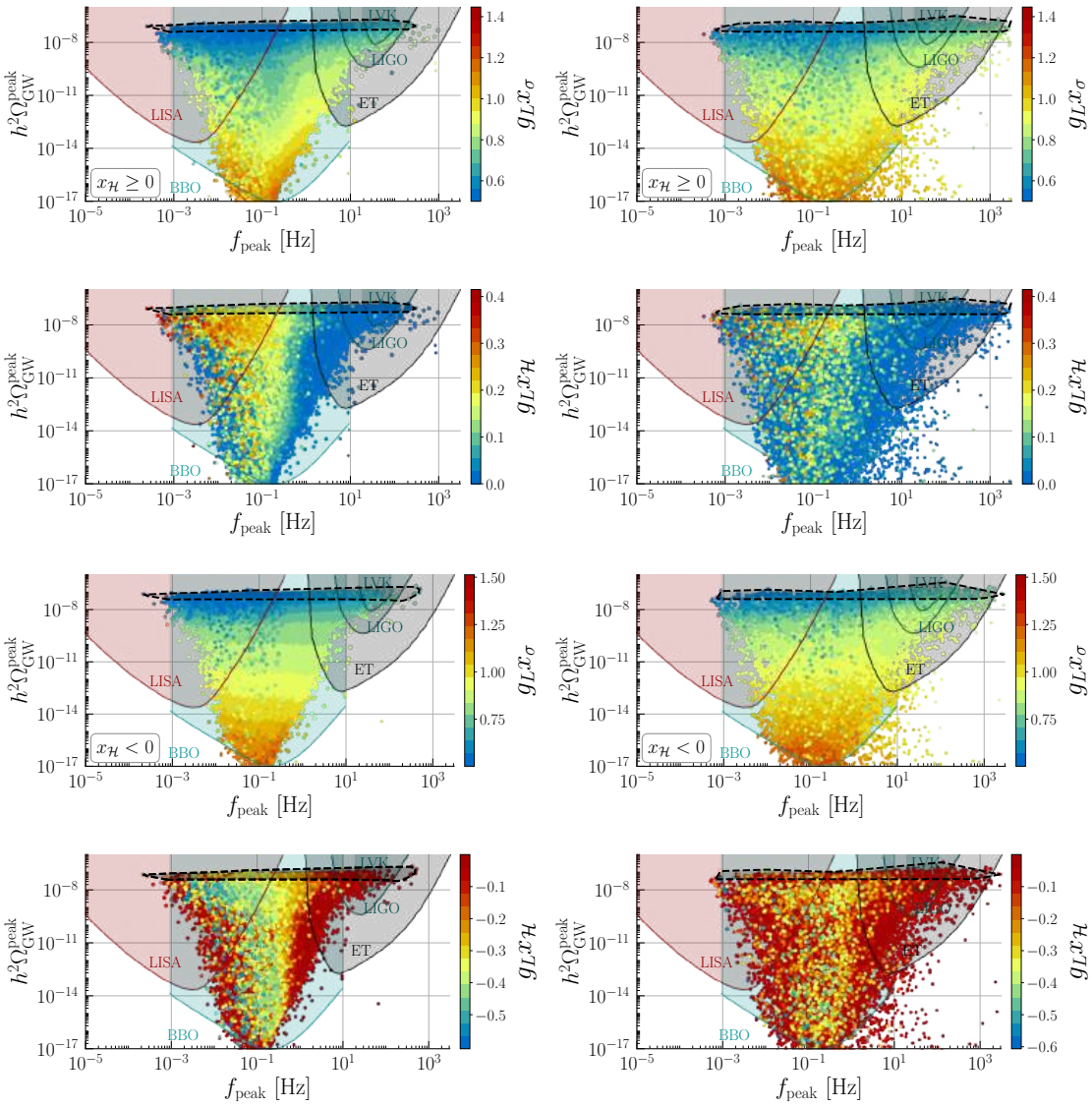

Figure 4.28: Similar to Fig. 4.6, but for generic U(1)′ models. The colour scales represent the Majoron charge times g_L in the first and third rows, and the Higgs doublet charge times g_L in the second and fourth rows. In the top two rows $x_\mathcal{H} \geq 0$, and in the bottom two rows $x_\mathcal{H} < 0$.

---

so that the kinetic mixing g_{12} does not evolve with energy at one-loop if $g_{12} = 0$ at some scale μ (see Eq. (E.5)). The thermodynamic parameters α, $\beta/H(T_p)$, and T_p are almost independent of $x_\mathcal{H}$. Consequently, the SGWB geometric parameters are also weakly dependent on $x_\mathcal{H}$, as shown in Fig. 4.28, and it is not possible to exclude a specific U(1)′ model based on GW data alone. However, for models with large $|x_\mathcal{H}|$ (which suffer a loss of perturbativity below v_σ), the allowed parameter space shrinks so that the density of points with higher T_p and $T_{\rm RH}$ is lower far from $x_\mathcal{H} = 0$, and leads to lower peak frequencies.

In Fig. 4.31, we show GW spectra for different $x_\mathcal{H}$ charges with the other parameters fixed. We observe that as $x_\mathcal{H}$ decreases, the spectrum shifts towards lower frequencies while maintaining an approximately constant peak amplitude. This shift can be attributed to changes in the percolation temperature due to the modified running of the g_L β-function for different $x_\mathcal{H}$. However, the shift in the spectrum is small compared to the theoretical uncertainties in Fig. 4.4.

In Fig. 4.32, we present scatter plots in the $(M_{Z'}, g_L x_\sigma)$ plane, with the colour scale representing the heavy Higgs mass. At high frequencies, LVK data do not exclude any region of parameter space

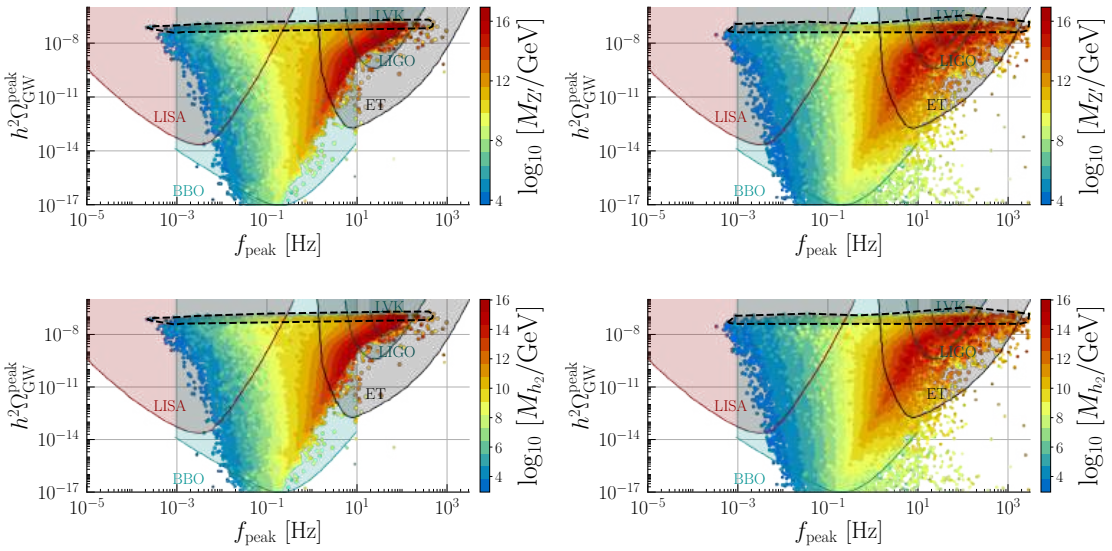

Figure 4.29: Similar to Fig. 4.28, but the colour scales represent the Z′ boson mass (top row), the heavy scalar mass M_{h_2} (bottom row).

due to the dispersion caused by $x_{\mathcal{H}}$. The excluded regions for the Z′ and heavy Higgs bosons are similar, but slightly weaker than for the $\mathrm{U}(1)_{\mathrm{B-L}}$ model. The region within the solid green (dotted dark purple) boundary will be tested by LIGO-O5 (ET) data with SNR > 10. This figure confirms that Earth-based interferometers will be sensitive to heavy boson masses from 10^{10} GeV up to the GUT scale, and $g_L x_\sigma$ between 0.5 and 0.9. At lower frequencies, LISA will also cover a wide range of masses (enclosed by the solid red line). The overlapping sensitivity of ET and LIGO is evident in the top-left panel demonstrating an opportunity to test this class of models in more than one experiment. For $\mathrm{Tr}(\boldsymbol{y_\sigma}) > g_L$, the spread in points of a given colour shrinks the area with SNR > 10.

4.6.4 PBHs, magnetic fields and microlensing in the generic U(1)′ scenario

We now examine the case of generic $\mathrm{U}(1)'$ charges. In Fig. 4.33 we show projections in the $(M_{\rm PBH}, f_{\rm PBH})$ plane with colour scales for $g_L x_{\mathcal{H}}$ (left panel) and $g_L x_\sigma$ (right panel). We find that $x_{\mathcal{H}}$ introduces dispersion in the parameter space, resulting in a weak correlation with both $f_{\rm PBH}$ and $M_{\rm PBH}$. Similarly, the PBH parameters are weakly correlated with $g_L x_\sigma$, although as in the $\mathrm{U}(1)_{\mathrm{B-L}}$ case, most points cluster in a narrow range $g_L x_\sigma = [0.50, 0.60]$. Thermodynamic parameters, SGWB, and magnetic fields exhibit correlations consistent with those in the B⊙L model.

In Fig. 4.34 we present scatter plots of various projections of the model's parameter space. The region enclosed by the black solid contour is excluded by LVK (with SNR > 10) the dashed green contour indicates the region in which γ-ray signals can be detected by THESEUS, and the grey dotted (red dash-dotted) contour defines the region where peak magnetic field strengths for $b = 0$ ($b = 1$) exceed the lower bounds set by blazars. In Tab. 4.4 we present three benchmark points: BP-1 features microlensing events at the Roman telescope, BP-2 produces detectable γ-ray signals, and BP-3 generates detectable magnetic fields, and microlensing, γ-ray and GW signals with PBHs saturating the DM relic abundance ($f_{\rm PBH} = 1$).

In Fig. 4.34, the DM abundance shows a weak correlation with the model parameters. However, along the lower edge of the regions in the right panels of the first two rows ($g_L x_\sigma \sim 0.55$ and $\lambda_\sigma \sim \odot 0.063$) most points have $f_{\rm PBH}$ close to unity. The neutrino sector parameters are also weakly correlated with $f_{\rm PBH}$ as can be seen from the right panels of the last two rows. In contrast, all model parameters exhibit a strong correlation with the PBH mass. Specifically, larger values of the Z′, h_2 and N_i masses correspond to lighter PBHs, as for the $\mathrm{U}(1)_{\mathrm{B-L}}$ model. Also, higher values of $\mathrm{Tr}(\boldsymbol{y_\sigma})$ and lower values of $\sqrt{\mathrm{Tr}(\boldsymbol{y_\nu} \boldsymbol{y_\nu}^\dagger)}$ are associated with heavier PBHs.

For generic $\mathrm{U}(1)'$ models, we find that only a very narrow region of $g_L x_\sigma$ and λ_σ can produce

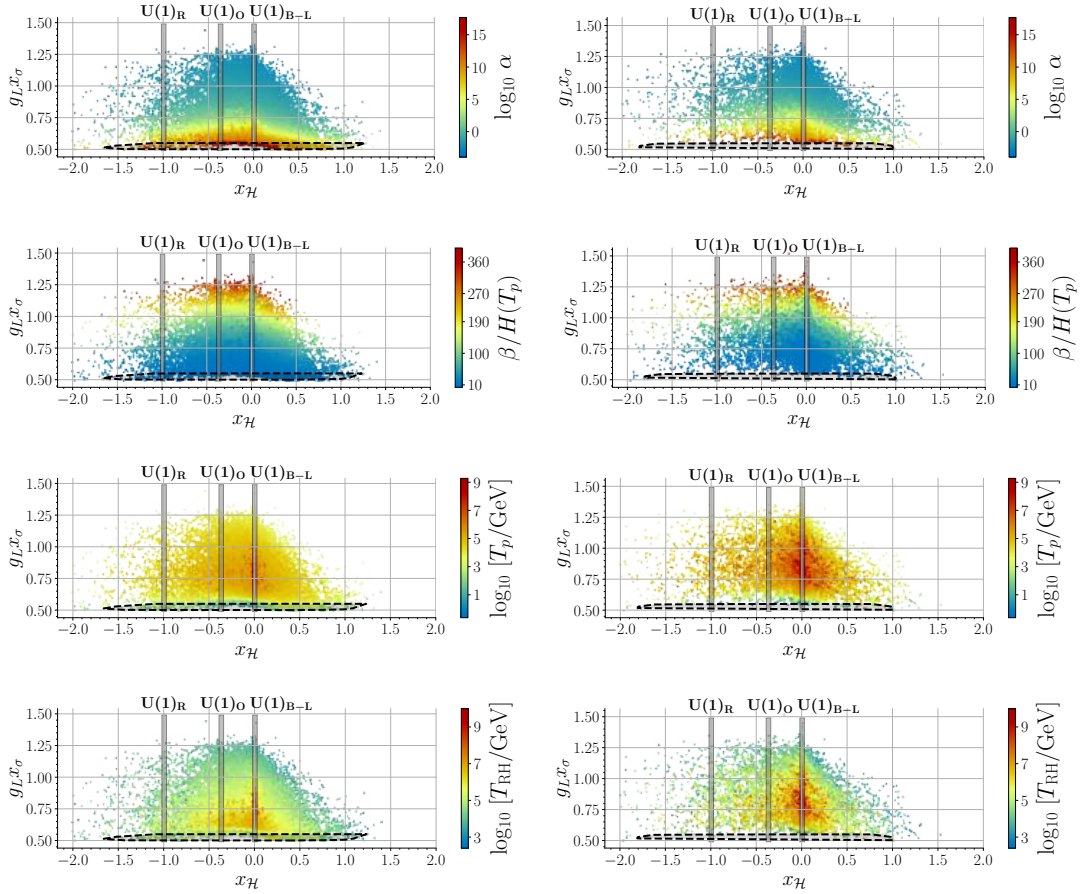

Figure 4.30: Scatter plots in the $(x_\mathcal{H}, g_L x_\sigma)$ plane for generic U(1)′ models. The colour scales indicate the phase transition strength α (first row), and its inverse time duration $\beta/H(T_p)$ (second row), the percolation temperature T_p (third row), and the reheat temperature T_{RH} (fourth row). The $\mathrm{U}(1)_{\mathrm{R}}$, $\mathrm{U}(1)_{\mathrm{B-L}}$, and $\mathrm{U}(1)_{\mathrm{O}}$ models correspond to charges $(x_\mathcal{H}, x_\sigma) = (\odot 1, 2)$, $(0, 2)$, and $(\odot 16/41, 2)$, respectively. The black dashed contour has the same meaning as in previous figures. The left (right) panels show points with $\mathrm{Tr}(\boldsymbol{y_\sigma}) < g_L$ ($\mathrm{Tr}(\boldsymbol{y_\sigma}) > g_L$).

γ-ray signals at future experiments. This region, enclosed by the green dashed contour, features Z′ masses in the interval $[10^{10}, 10^{13}]$ GeV, and h_2 masses within $[10^9, 10^{12}]$ GeV. The neutrino sector parameters in the last two rows are not constrained by γ-ray observations.

In the low Z′-mass regime, between 10^4 and 10^5 GeV, it is possible to generate magnetic field strengths that exceed the current blazar bounds. This region, enclosed by the dashed gray contour,

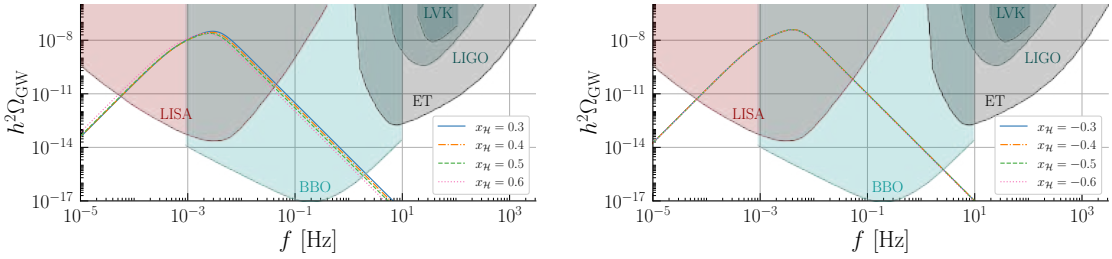

Figure 4.31: SGWB spectrum for various values of the Higgs charge in generic U(1)′ models. The other parameters are fixed to those of BP(a).

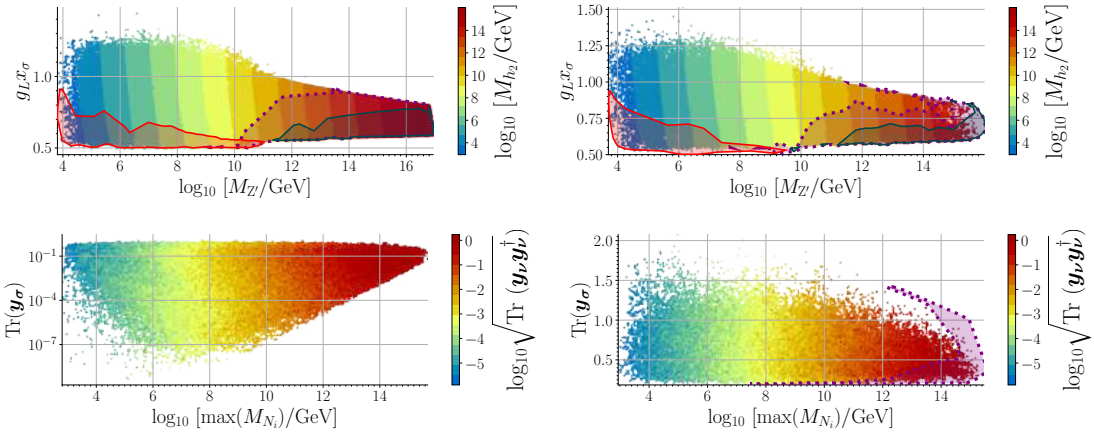

Figure 4.32: Similar to Fig. 4.17, but for generic U(1)′ models.

corresponds to a minimal hierarchy between the h_1 and h_2 masses, resulting in a larger efficiency factor κ_h. This also favours seesaw scales in the tens of TeV range and $\mathrm{Tr}(\boldsymbol{y_\sigma}) \lesssim 0.68$.

4.6.5 Low-scale scenarios with generic charge assignments

In previous sections, we described in detail the phenomenology when $M_{h_2} \gg M_{h_1}$, which leads to the natural follow up question: What happens when $M_{h_2} \ll M_{h_1}$? To analyse this scenario, we must first realise that the Higgs sector can no longer be fully conformal, *i.e.* the tree-level potential needs to be

$$V_0 = \odot\mu_h^2\,\mathcal{H}^\dagger\mathcal{H} + \lambda_h(\mathcal{H}^\dagger\mathcal{H})^2 + \lambda_\sigma(\sigma^\dagger\sigma)^2 + \lambda_{\sigma h}(\mathcal{H}^\dagger\mathcal{H})(\sigma^\dagger\sigma)\,, \tag{4.97}$$

which has scale invariance only in the dark sector. Consider imposing a classical conformal symmetry in both the dark and visible sectors, *i.e.*, $\mu_h^2 = 0$, and requiring a large hierarchy between the VEVs, $v_\sigma \gg v$, associated with a large hierarchy in the scalar mass spectrum, $M_{h_2} \gg M_{h_1}$. In this case, the scalon emerges from the heavy singlet σ field. This is in variance with a multi-Higgs-doublet scenario which necessarily implies that the scalon is the lightest particle in the scalar spectrum [304]. Note that a large mass hierarchy between the scalon and the SM Higgs is protected against large radiative corrections by means of a small portal coupling $|\lambda_{\sigma h}| \sim (v/v_\sigma)^2$. This is the scenario studied previously.

On the other hand, if we consider the opposite hierarchy $v \gg v_\sigma$, corresponding to $M_{h_1} \gg M_{h_2}$, the scalon emerges from $\mathcal{H}$. Now there are two possibilities: 1) If $\lambda_h < y_t$, where y_t is the top Yukawa coupling, the top quark loop is the dominant contribution to the Higgs mass, which comes with a negative sign and alters its vacuum stability, such that no valid solution exists. 2) If $\lambda_h > y_t$, the scalar loop is the dominant contribution and valid solutions are possible. However, as shown in Ref. [438],

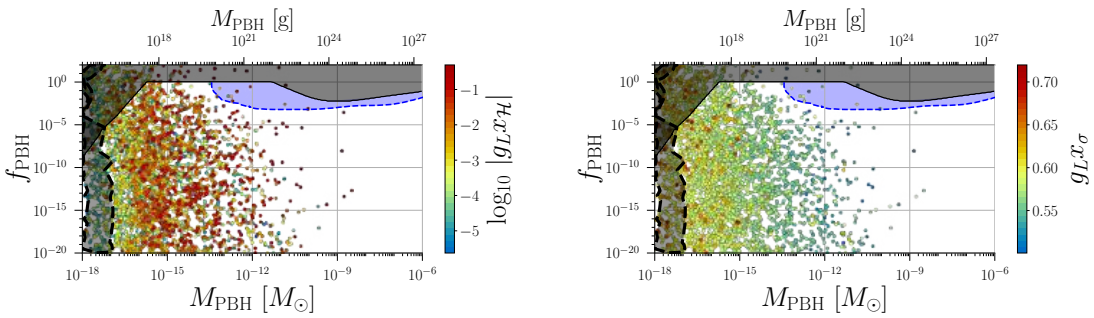

Figure 4.33: Similar to Fig. 4.21, but the colour scale represents $g_L x_{\mathcal{H}}$ in the left panel and $g_L x_\sigma$ in the right panel.

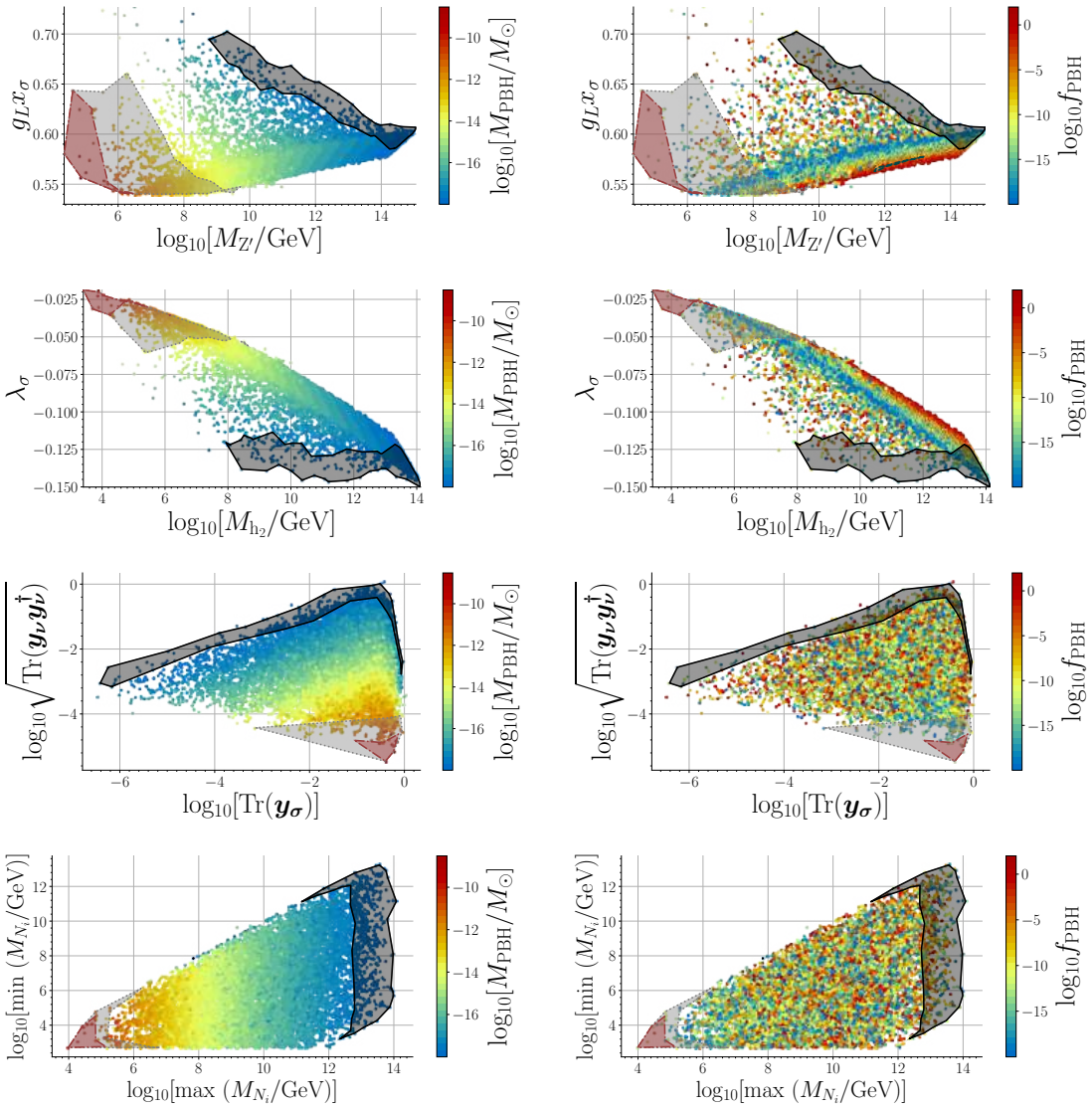

Figure 4.34: Projections of the model's parameter space, with the PBH mass (left panels) and PBH abundance (right panels) indicated by the colour scales. All points satisfy current constraints from microlensing and the extragalactic γ-ray background. The region enclosed by the black solid contour is excluded by LVK since SNR > 10. The grey dotted (red dash-dotted) contour indicates the region where peak magnetic field strengths for $b = 0$ ($b = 1$) exceed the blazar bounds.

---

the Higgs mass predicted by minimising the effective potential exceeds 200 GeV, which is inconsistent with experiment. Therefore, for the low scale scenario we must resort to the case where only the dark sector is conformal *i.e.*, the $\sigma^\dagger\sigma$ term is absent, but not the visible one ($\mu_h^2 \neq 0$). This is necessary to ensure proper EW symmetry breaking with $M_{h_1} \gg M_{h_2}$.

The primary motivation to study to opposite hierarchy case is related to the fact that an FOPT induced by the breaking of the gauged U(1)$'$ symmetry at a MeV scale could produce a GW signal in the nHz range relevant to PTA observations. Recently, PTAs reported evidence of a SGWB at nHz frequencies [297–300]. Statistical analyses have shown that NP scenarios are more compatible with the observed signal than the purely astrophysical explanation provided by Supermassive Black Hole Binaries (SMBHBs) [439]. Supercooled MeV-scale FOPTs have been proposed as an explanation for the NANOGrav signal [439–441] and for signals at PTAs in general [442]. However, in Ref. [106] it is argued that such a scenario may not be physically viable because such FOPTs may fail to fully

complete on the relevant cosmological time scales. It is further argued that even if this issue can be evaded, the Universe would be reheated to temperatures associated with the scale of NP driving the FOPT, effectively shifting the SGWB spectrum to frequencies higher than the NANOGrav signal. However, these conclusions are obtained in the context of EW FOPTs in NP models with SM-like potentials that feature a cubic interaction term at tree level, thus raising the question about their validity for conformal NP models.

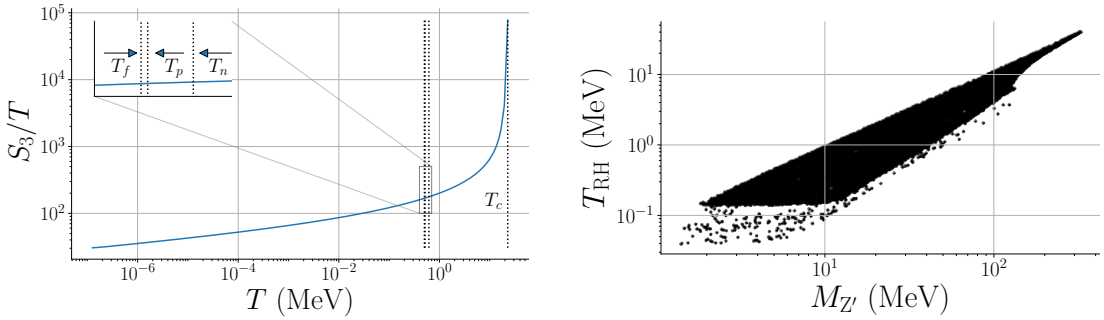

Figure 4.35: **Left panel**: Ratio of the Euclidean action to temperature S_3/T as a function of T for the best-fit point in Table 4.5. The vertical dotted lines indicate the critical temperature T_c, nucleation temperature T_n, percolation temperature T_p and completion temperature T_f. **Right panel**: Scatter plot of the reheating temperature $T_{\rm RH}$ as a function of the Z′ mass.

Our scenario overcomes the issues highlighted in Ref. [106]. First, in conformal models percolation is always possible. We have explicitly verified that the volume of the false vacuum is decreasing at the percolation temperature T_p, see Eq. (4.8). As discussed previously, this condition may not necessarily be satisfied at T_p, but at some lower temperature. However, here we only consider FOPTs for which the percolation condition is fulfilled at $T = T_p$. Second, in non-conformal models, such as

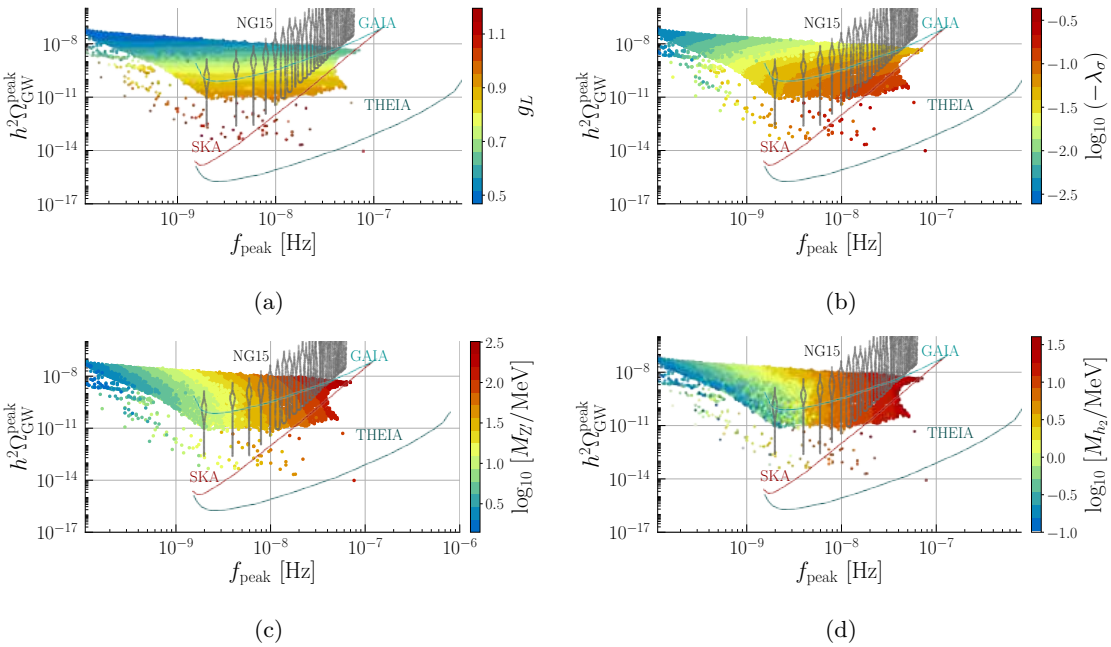

Figure 4.36: Scatter plots of the SGWB peak amplitude $h^2\Omega_{\rm GW}^{\rm peak}$ versus peak frequency $f_{\rm peak}$. The colour scales indicate the gauge coupling g_L, the scalar self-interaction λ_σ, the Z′ mass (in MeV) and the h_2 mass (in MeV). For the NANOGrav signal (labelled "NG15") and sensitivity curves, the axis labels do not correspond to peak values.

the type studied in Ref. [106], the action as a function of temperature exhibits a U-shaped behaviour (see *e.g.*, Fig. 3 of Ref. [443]), which bounds the percolation temperature from below. In contrast, conformal models have an action that asymptotically approaches zero as $T \to 0$; see left panel of Fig. 4.35. Third, we have checked that the potential remains bounded from below at the FOPT completion temperature T_f, at which the true vacuum occupies 99% of the Universe. Fourth, the conformal nature of the potential prevents $T_{\rm RH} \approx M$, where M is the mass scale of dark sector. Since the potential barrier persists as $T \to 0$, the FOPT can be delayed to temperatures well below T_c, which defines the energy scale driving the transition. Consequently, as long as extreme supercooling is avoided ($\alpha \lesssim 10^8$), $T_{\rm RH}$ deviates from T_p by at most a factor of $\mathcal{O}(1 \odot 100)$, ensuring that $T_{\rm RH} < M$; see right panel of Fig. 4.35. (It was noted in Ref. [105] that $T_{\rm RH} \sim 0.1 M_{Z'}$ for a conformal $\mathrm{U}(1)_{\rm B-L}$ model) In this regime, Daisy corrections are negligible.

A problem, however, is the need for g_L to be of $\mathcal{O}(0.1)$. For MeV mass scales, astrophysical and collider constraints [444–451] impose stringent upper limits on the gauge couplings. For instance, for the $\mathrm{U}(1)_{\rm B-L}$ model and MeV-range Z′'s, the gauge coupling should be below $g_L \lesssim 10^{-10}$ [451]. For generic charge assignments the limits change, but remain qualitatively similar, see *e.g.* [452]. Additionally, for the light case, the decays $\mathrm{Z}' \to e^+e^-$ and $\mathrm{Z}' \to \nu_i \bar{\nu}_j$ contribute to an increase on the effective number of neutrino species, $\Delta N_{\rm eff}$ [451], and further constraint g_L. As such, for this section, we will consider a pure dark sector, *i.e.* only σ carries a dark $\mathrm{U}(1)'$ charge, such that the only communication with the SM is through the Higgs portal and kinetic mixing . Note that, for this charge assignment, neutrino masses and mixings can not be fitted without having to introduce new particle content. Since the purpose here is to explain the NANOGrav signal, we will not consider the neutrino sector. Thermalisation between the dark sector and the SM works slightly different. Now,, we ensure that Z′ thermalises by fixing $g_{12} = 2 \times 10^{-10}$ at the EW scale [453]. On the other hand, h_2 can thermalise through the $h_2 \mathrm{Z}'\mathrm{Z}'$ vertex which is proportional to $g_L \sim \mathcal{O}(0.1 \odot 1)$. The analysis of the FOPT remains identical to before, but since we consider a new charge setting without neutrinos, the only change is the RG equations. In particular, for the β-functions we have

$$\beta^{(1)}(g_L) = \frac{41}{10} g_{12}^2 g_L + \frac{g_L^3}{3}\,, \tag{4.98}$$

$$\beta^{(1)}(g_1) = \frac{41}{10} g_1 (g_1^2 + g_{12}^2)\,, \tag{4.99}$$

$$\beta^{(1)}(g_2) = \odot \frac{19}{6} g_2^2\,, \tag{4.100}$$

$$\beta^{(1)}(g_3) = \odot 7 g_3^2\,, \tag{4.101}$$

$$\beta^{(1)}(g_{12}) = \frac{41}{10} g_{12}(g_1^2 + g_{12}^2) + \frac{1}{2} g_{12} g_L^2\,, \tag{4.102}$$

$$\beta^{(1)}(y_t) = \frac{3}{2} y_t^3 + y_t \Big[\odot \frac{17}{20} g_1^2 \odot \frac{17}{20} g_{12}^2 \odot \frac{9}{4} g_2^2 \odot 8 g_3^2 + 3 y_t^2 \Big]\,, \tag{4.103}$$

$$\beta^{(1)}(\lambda_h) = \frac{27}{200} g_1^4 + \frac{9}{20} g_1^2 g_2^2 + \frac{9}{8} g_2^4 \odot \frac{9}{5} g_1^2 \lambda_h \odot \frac{9}{5} g_{12}^2 \lambda_h \odot 9 g_2^2 \lambda_h + 24 \lambda_h^2 + \lambda_{\sigma h}^2 + 12 \lambda_h y_t^2 \odot 6 y_t^4\,, \tag{4.104}$$

$$\beta^{(1)}(\lambda_\sigma) = 2 \Big[3 g_L^4 \odot 6 g_L^2 \lambda_\sigma + 10 \lambda_\sigma^2 + \lambda_{\sigma h}^2 \Big]\,, \tag{4.105}$$

$$\beta^{(1)}(\lambda_{\sigma h}) = \frac{\lambda_{\sigma h}}{10} \Big[\odot 9 g_1^2 \odot 9 g_{12}^2 \odot 45 g_2^2 \odot 60 g_L^2 + 120 \lambda_h + 80 \lambda_\sigma + 40 \lambda_{\sigma h} + 60 y_t^2 \Big]\,, \tag{4.106}$$

$$\beta^{(1)}(\mu_h^2) = \frac{\mu_h^2}{10} \Big[\odot 9 g_1^2 \odot 9 g_{12}^2 \odot 45 g_2^2 + 120 \lambda_h + 60 y_t^2 \Big]\,, \tag{4.107}$$

while the γ-function is simply

$$\gamma = 3 g_L^2\,. \tag{4.108}$$

As before, we only consider the σ direction to be relevant for the FOPT as it decouples from the Higgs direction due to the strong scale hierarchy $M_{h_1} \gg M_{h_2}$. The introduction of μ_h^2 implies an additional free parameter compared to the high-scale case, which we take to be the scalar mixing $\lambda_{\sigma h}$. We perform a scan over the model parameters at $\mu = M_{\mathrm{Z}^0}$ with a focus on the parameter space capable of explaining the NANOGrav data. Since we focus on MeV scale FOPTs, we sample M_{h_2} logarithmically in the range $M_{h_2} = [0.1, 100]$ MeV. We require $\lambda_{\sigma h} < 10^{-10}$ t so that v_σ is small enough to yield a signal at PTAs. The gauge coupling is sampled linearly in the range $g_L = [0.25, 1.5]$.

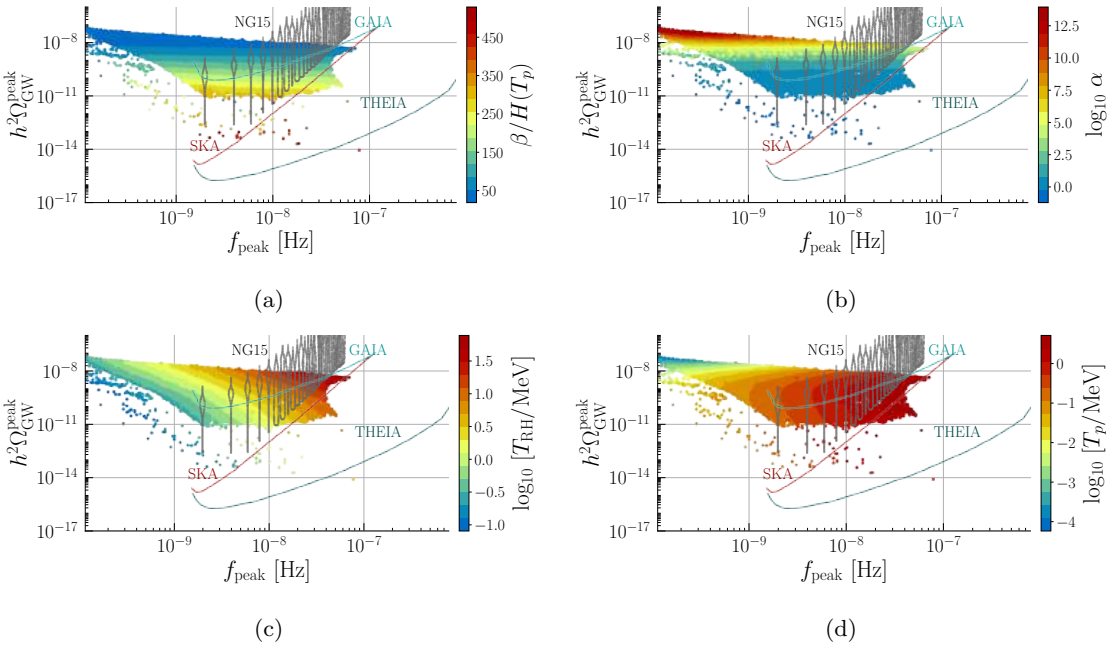

Figure 4.37: Similar to Fig. 4.36 but the colour scales indicate the inverse time duration $\beta/H(T_p)$, the phase transition strength α, the reheating temperature $T_{\rm RH}$ (in MeV) and the percolation temperature (in MeV).

In what follows, all parameters are evaluated at $\mu = 0.1$ MeV after RG evolution. Fig. 4.36 displays scatter plots of the SGWB peak amplitude versus peak frequency for g_L (panel a), λ_σ (panel b), $M_{Z'}$ (panel c) and M_{h_2} (panel d). Also shown is the NANOGrav signal [297] and the sensitivity of the experiments, GAIA, SKA, and THEIA [454, 455]. Our analysis indicates that the peak frequency is primarily determined by $M_{Z'}$, with smaller masses corresponding to lower frequencies. The same pattern is present in M_{h_2}. This behaviour is identical to the higher scale case (recall Fig. 4.6). The couplings λ_σ and g_L influence the peak amplitude, with smaller values resulting in higher amplitudes. This is because they affect the location of the minimum of the effective potential and its depth, see Fig. 4.2. Again, a behaviour also shared in the high scale scenario. We now show in Fig. 4.37 equivalent projections but with thermodynamic parameters in colour, namely the inverse time duration $\beta/H(T_p)$ (panel a), the strength of the phase transition α (b), the reheating temperature (panel c) and the percolation temperature (panel d). Recall that we always require $T_{\rm RH} < M$ to prevent extreme supercooling, as greater supercooling results in higher $T_{\rm RH}$, which shifts the GW spectrum to higher frequencies (see panel c). This implies that, within the region relevant for the NANOGrav signal, α always remains below 10^8. Although, for frequencies below 10^{-9} Hz, we have points with $\alpha \gtrsim 10^{12}$, corresponding to phase transition temperatures $T_p \sim \mathcal{O}(\text{keV})$ (see panel d). Phase transitions at such low temperatures may impact predictions from the Cosmic background radiation [456]. We also find $\beta/H(T_p) \gtrsim 48$, and therefore PBH formation is highly inefficient. Similarly, we also found that the production of primordial magnetic fields is highly suppressed. The isolated points with $h^2\Omega_{\rm GW}^{\rm peak} < 10^{-11}$ correspond to non-supercooled FOPTs with $\alpha < 0.1$ and $g_L > 1.1$.

The SGWB spectrum for the best-fit point, including the expected signal from SMBHBs, is shown in Fig. 4.38. The corresponding parameters are listed in Tab 4.5. The SMBHBs signal is modelled as

g_L	M_{h_2}	$M_{Z'}$	T_p	$T_{\rm RH}$	$\alpha/10^5$	β/H	$\gamma_{\rm BHB}$	$A_{\rm BHB}$
0.59	12.4	107.3	0.52	11.7	2.60	39.5	4.50	$10^{-15.4}$

Table 4.5: Parameters for the best fit point (including the contribution from SMBHBs) shown in Fig. 4.38. M_{h_2}, $M_{Z'}$ and $T_{\rm RH}$ are in units of MeV, and evaluated at $\mu = 0.1$ MeV.

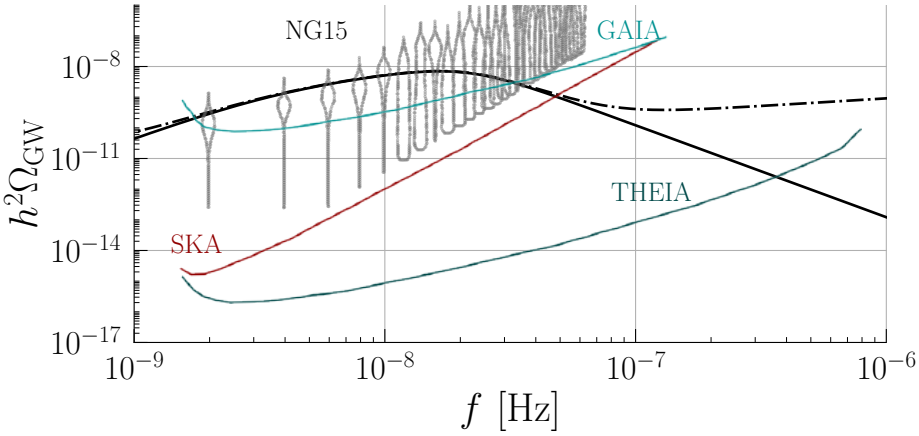

Figure 4.38: SGWB spectra for the best-fit point in Tab 4.5. The solid black curve is the signal from the FOPT only, and the dot-dashed curve also includes the SMBHBs signal.

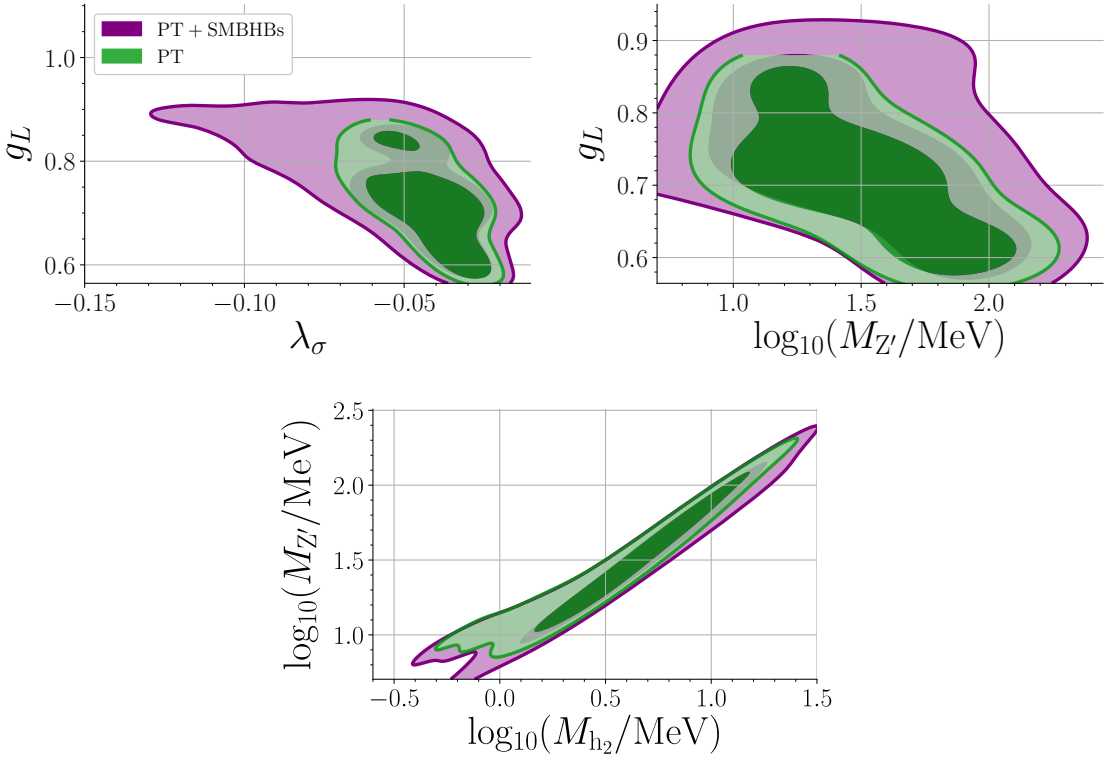

Figure 4.39: 68% CL (darker) and 95% CL (lighter) allowed regions obtained from the NANOGrav 15-year dataset. The green contours assume the FOPT alone explains the signal, while the purple contours include the SMBHBs signal.

---

a power law with spectral index $\gamma_{\rm BHB}$ and amplitude $A_{\rm BHB}$ [457]:

$$h^2\Omega_{\rm GW}(f) = \frac{2\pi^2 A_{\rm BHB}^2}{3H_0^2}\left(\frac{f}{\text{year}^{-1}}\right)^{5-\gamma_{\rm BHB}} \text{year}^{-2}\,. \tag{4.109}$$

Clearly, the SMBHBs contribution to the signal is negligible.

To determine the 68% and 95% CL parameter space regions allowed by the NANOGrav 15-year

dataset, we employ the `PTArcade` package in its default `ceffyl` configuration [457, 458]. Fig. 4.39 shows allowed regions assuming either that the model fully explains the signal (labelled "PT") or that the contribution from SMBHBs is included (labelled "PT+SMBHBs"). For the SMBHBs signal, we adopt the default settings of `PTArcade`, choosing an uniform prior $\gamma_{\rm BHB} = [0, 7]$ and a log-uniform prior $\log_{10} A_{\rm BHB} = [\odot 18, \odot 14]$. NANOGrav data favour Z′ and h_2 masses in the 10–100 MeV range at 68% CL, with larger masses disfavoured due to the resultant higher peak frequencies. We observe a strong correlation between λ_σ and g_L. Smaller couplings are favoured because they yield larger peak amplitudes. Without the SMBHBs contribution, we find $g_L \in [0.57, 0.86]$ and $\lambda_\sigma \in [\odot 0.062, \odot 0.028]$ at 68% CL. As expected, including the SMBHBs signal widens the allowed parameter regions, although in most cases the widening is minimal because the corresponding parameters show weak correlations with either the amplitude, frequency, or both.

4.6.6 Comments on the GW contribution from cosmic strings

To finish this chapter, we will briefly discuss on other potential sources of cosmological GWs in our model. So far, we have only focused on the FOPT contribution. However, the spontaneous breaking of U(1)′ can also generate topological defects, known as cosmic strings [459]. Since U(1)′ is gauged, the strings decay predominantly via gravitational radiation, providing an additional component to the SGWB. Their dynamics is governed by a single parameter, the string tension μ', which is set by the U(1)′-breaking scale [460]:

$$G\mu' \approx 10^{-6} \left(\frac{v_\sigma}{10^{16}\ \text{GeV}} \right)^2 . \tag{4.110}$$

Here $G = 1/M_p^2$ is the gravitational constant with the Planck mass $M_p = 1.22 \times 10^{19}$ GeV.

The SGWB spectrum from cosmic strings can be sourced by long strings and/or closed loops, with the latter typically providing the dominant, although more model-dependent, signal [461]. For oscillating loops, the spectral energy density is given by a weighted sum over harmonic modes k,

$$\Omega_{\rm GW}(f) = \frac{8\pi}{3H_0^2} (G\mu')^2 f \sum_{k=1}^{\infty} P_k\, C_k(f)\,, \tag{4.111}$$

where $H_0 = 67.85$ km s^{-1} Mpc^{-1} is the present-day Hubble constant, P_k is the normalized GW power (in units of $G\mu'^2$) emitted in the k-th harmonic, and $C_k(f)$ encodes the spectral shape. The GW power for harmonic mode k follows a power law [460],

$$P_k = \frac{\Gamma\, k^{-q}}{\zeta(q)}\,, \tag{4.112}$$

where $\Gamma \approx 50$ is the total emission power in units of $G\mu^2$, and $\zeta(q)$ is the Riemann zeta function. The spectral index q depends on the GW emission process: $q = 5/3$ for kinks, $q = 4/3$ for cusps, and $q = 2$ for kink-kink collisions. We focus on GW emission from cusps because it is dominant. The weight function $C_k(f)$ is given by

$$C_k(f) = \frac{2k}{f^2} \int_0^\infty \frac{dz}{H(z)(1+z)^6}\, n\left(\frac{2k}{(1+z)f}, t(z) \right), \tag{4.113}$$

where $n(l, t)$ is the loop number density distribution at cosmic time $t(z)$ and redshift z. We assume a standard Friedmann-Robertson-Walker cosmology with

$$H(z) = H_0 \sqrt{1 \odot \Omega_M \odot \Omega_R + \Omega_M (1+z)^3 + \Omega_R \mathcal{C}(z) (1+z)^4}\,, \tag{4.114}$$

where $\Omega_M = 0.3081$ and $\Omega_R = 1.291 \times 10^{-5}$ [384]. The correction factor $\mathcal{C}(z)$ accounts for the redshift evolution of the relativistic degrees of freedom.

We employ the analytical approximations derived in Ref. [462]. In the nHz range, relevant for PTA observations, the energy density is given by

$$h^2 \Omega_{\rm GW}(f)\big|_{\rm PTA} \approx 4.2 \times 10^{-9} \left(\frac{f}{f_{\rm yr}} \right)^{3/2} \frac{\Gamma}{50} \left(\frac{G\mu}{10^{-11}} \right)^2 \times \sum_{k=1}^{\infty} \frac{k^{-17/6}}{(1 + 2.075\, u_k)^{1.945}\, \zeta(17/6)}\,, \tag{4.115}$$

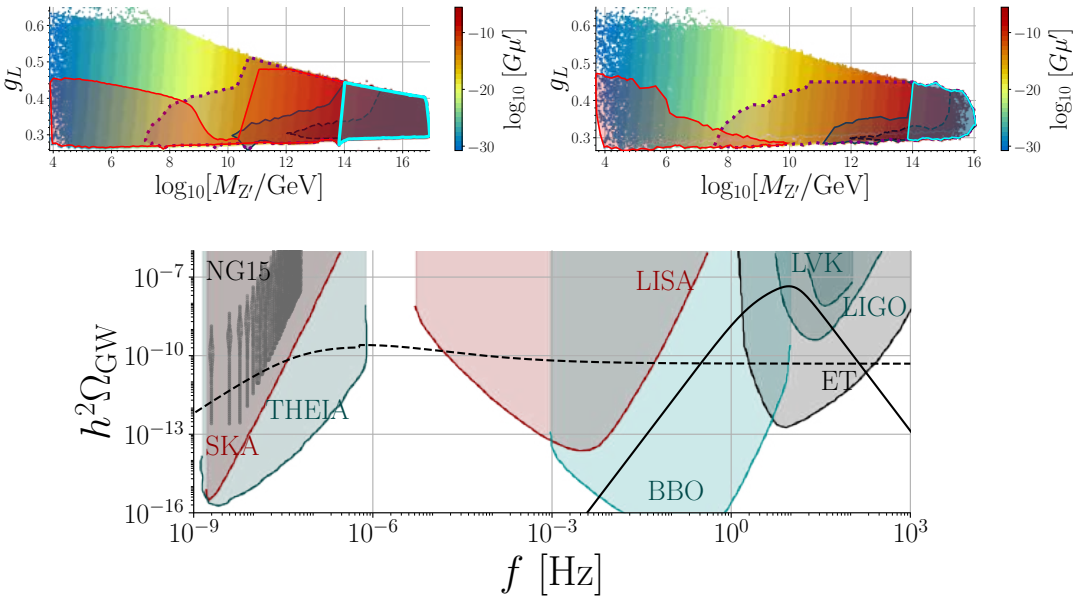

Figure 4.40: **Top panel:** Similar to Fig. 4.17. The closed cyan contour outlines the region excluded by NANOGrav. The colour bar we show the string tension $G\mu'$. **Bottom panel:** SGWB spectra for BPs(c) in Tab. 4.3 with the solid black line representing the FOPT contribution while the dashed black line represents the cosmic string contribution.

---

where $f_{\text{yr}} \simeq 32$ nHz, and

$$u_k = \frac{2.89}{2k}\frac{f}{f_{\text{yr}}}\frac{\Gamma}{50}\frac{G\mu}{10^{-11}}\,. \tag{4.116}$$

For higher frequencies ($f \gtrsim$ mHz), relevant for space- and ground-based laser interferometers, the spectrum flattens and is approximately

$$h^2\Omega_{\text{GW}}(f)\big|_{\text{laser}} \simeq 4.78\times 10^{-5}\,\mathcal{C}\sqrt{G\mu}\,. \tag{4.117}$$

Setting $\mathcal{C} = 0.8$ is a valid approximation in the frequency range $[10^{-3}, 10]$ Hz [462].

Numerical results

We will discuss our results in the context of the $\text{U}(1)_{\text{B-L}}$ model. The conclusions are identical to the generic case. Cosmic microwave background data impose an upper bound on the string tension $G\mu \lesssim 10^{-7}$ [463], while the 15-year NANOGrav dataset excludes $G\mu' \gtrsim 1.32\times 10^{-10}$ for GWs emitted from cusps, including the contribution from SMBHBs [439]. Our results are summarised in Fig. 4.40. Comparing with Fig. 4.17 (without cosmic strings), we find that, when $g_L > \text{Tr}(\boldsymbol{y_\sigma})$, LISA can probe the high mass region ($M_{Z'} > 10^{10}$ GeV) since a almost flat string spectrum exist in LISA target frequency (see bottom panel). When the Yukawas become competitive the high-mass region can not be excluded by LISA. For ET, LIGO and LVK the contours remain qualitatively similar, although they become larger since the SNR increases due to the cosmic string contribution (true for both $g_L > \text{Tr}(\boldsymbol{y_\sigma})$ and $g_L < \text{Tr}(\boldsymbol{y_\sigma})$). In cyan, we show the region excluded by NANOGrav. We find that NANOGrav targets a similar region to that of LVK/LIGO, excluding masses of $M_{Z'} > 10^{14}$ GeV and $g_L < 0.46$.

4.7 Summary and conclusions

We explored the potential to indirectly test a wide class of classically scale-invariant $\text{U}(1)'$ models through GWs, PBHs and primordial magnetic fields both in its low and high-scale versions. We discussed how the parameter space of these models can be studied at energy scales not in reach of

collider experiments. For strongly supercooled high-scale phase transitions, we can produce a SGWB signal with a large SNR across a wide range of frequencies, from 0.1 mHz, within reach of LISA, up to a kHz, within reach of LIGO and ET. In the low-scale scenario, a signal can be produced in the nHz frequency band. Simultaneously, due to strong supercooling, the conditions become favourable for PBH formation which may be detectable at upcoming microlensing surveys, particularly from the Roman Space Telescope, as well as through γ-ray signatures from Hawking evaporation at THESEUS, GECCO, AMEGO⊙X, and e⊙ASTROGAM.

SGWB at high-scales

We examined the $\mathrm{U}(1)_{\mathrm{B-L}}$ model with gauge charges, $x_{\mathcal{H}} = 0$ and $x_\sigma = 2$. We find that the peak amplitude of the SGWB is primarily influenced by the gauge coupling g_L, which must be in the range $0.26 \lesssim g_L \lesssim 0.63$ for FOPTs to occur; see the fourth row of Fig. 4.6, which also shows that the peak amplitude reaches its highest values, $h^2\Omega_{\mathrm{GW}}^{\mathrm{peak}} \approx 10^{-7}$, for lower values of the g_L range across the entire frequency spectrum. The $\mathrm{U}(1)_{\mathrm{B-L}}$ breaking scale, which determines the masses of the Z′ and h_2 bosons, governs the peak frequency, as can be seen from the second and third rows of Fig. 4.6. We confirmed that a potential barrier between the true and false vacuum develops at finite temperatures for a non-zero gauge coupling; see Fig. 4.1 and Eq. (4.83). Generally, the sound wave contribution is the dominant source of GWs in most of the parameter space, although for $\alpha \gtrsim 10^{13}$, bubble collisions become dominant. For such high values of α, percolation is not guaranteed, but may occur at temperatures below T_p.

The heavy neutrinos that participate in the type-I seesaw mechanism, play an important role in the production of GW spectra that peak at high frequencies. Large $\boldsymbol{y_\sigma}$ can compete with the gauge coupling in the development of a global minimum of the potential, thereby increasing the VEV and the potential energy difference between the true and false vacuum, and pushing the peak frequency of the GW spectrum into the kHz range; see the right panels of Figs. 4.6, 4.7, 4.11 and 4.19. We find that if the $\mathrm{U}(1)'$ and SM sectors are in thermal equilibrium, the primary influence of the neutrino sector on the FOPT arises from the $h_2 \to \bar{N}_i N_i$ decay rate, which exceeds the Hubble rate at percolation in most of the parameter space, which makes the Universe promptly enter the radiation-dominated era after percolation; see Eq. (4.8). With decoupled heavy neutrinos, h_2 decays only to SM particles, causing h_2 to oscillate around the true minimum for longer than the Hubble time. Consequently, the Universe enters an early matter-dominated period after percolation, leading to a substantial suppression of the SGWB, with peak frequencies not exceeding 0.1 Hz, well below the sensitivity of Earth-based interferometers like ET and LIGO; see Fig. 4.10. Thus, in the context of these models, the observation of high-frequency GWs can be interpreted as a signature of heavy neutrinos. We also find a clear correlation between the peak frequency of the SGWB and the magnitude of $\boldsymbol{y_\nu}$; see Fig. 4.11. Specifically, ET and LIGO will probe $\boldsymbol{y_\nu}$ between 10^{-3} and unity, and LISA will probe $\boldsymbol{y_\nu}$ between 10^{-6} to 10^{-3}. If $\boldsymbol{y_\sigma} \sim \mathcal{O}(1)$, the heavy neutrino mass scale in the type-I seesaw mechanism can also be probed with high frequency GWs.

We demonstrated the importance of computing the RG-improved potential at the one-loop level because it shifts the minimum and significantly impacts the height of the potential barrier compared to a tree-level calculation [105]; see Fig. 4.20. The larger potential energy difference obtained at one-loop increases α and consequently the degree of supercooling. This also explains why our percolation temperatures are generally an order of magnitude lower than in Ref. [105].

For generic charges, our findings align with the results of the B⊙L model. However, higher values of the Higgs doublet charge $x_{\mathcal{H}}$ are less favourable due to the additional contributions they introduce in the β functions, which can lead to Landau poles at lower energies. Consequently, a signal at high frequencies will favour $\mathrm{U}(1)_{\mathrm{B-L}}$; see Fig. 4.28. Due to the weak dependence of the FOPT on the Higgs doublet charge, the SGWB is not sensitive to $x_{\mathcal{H}}$. A comparison of Fig. 4.31 and 4.4 shows that the effect of $x_{\mathcal{H}}$ on the SGWB is minimal, with the resulting frequency shift being much smaller than theoretical uncertainties. Also note that unlike non-Abelian models, in $\mathrm{U}(1)'$ models the RG evolution of g_L is asymptotically safe at low energies, so that the percolation temperature can be as high as 10^9 GeV; see the third row of Fig. 4.30.

Our quantitative findings with regards to data from LIGO, LISA and ET are as follows:

- If a SGWB signal is not detected in the entire frequency range of these interferometers, generic conformal $\mathrm{U}(1)'$ models (including the $\mathrm{U}(1)_{\mathrm{B-L}}$ model with $x_\sigma = 2$) will be disfavoured for

$0.5 \lesssim g_L x_\sigma \lesssim 0.6$ and $\mathrm{Tr}\,(\boldsymbol{y_\sigma}) \gtrsim 0.1$; see Fig. 4.32.

- Strong supercooling, defined by $g_L x_\sigma \lesssim 0.8$, will be disfavoured for $M_{Z'} \approx 10 M_{h_2} \gtrsim 10^{11}$ GeV, if LIGO and ET do not find a SGWB; see the top panels of Fig. 4.32. A nonobservation will also exclude a seesaw scale with $M_{N_i} \gtrsim 10^{14}$ GeV, and $\mathrm{Tr}\,(\boldsymbol{y_\sigma}) \gtrsim 0.1$ and $\boldsymbol{y_\nu} \sim \mathcal{O}(1)$; see the bottom-right panel of Fig. 4.32.

- At low frequencies, LISA will test strong supercooling for $M_{Z'} \sim 10 M_{h_2} \sim \mathcal{O}(10)$ TeV, and a TeV-scale type-I seesaw with $\boldsymbol{y_\nu} \sim \mathcal{O}(10^{-6})$; see Fig. 4.32. At high frequencies, the model can be fully excluded for $g_L x_\sigma \lesssim 0.75$ and $M_{Z'} \gtrsim 10^{11}$ GeV; see the top-right panel of Fig. 4.32.

- Strong supercooling in the $\mathrm{U(1)_{B-L}}$ model, defined by $g_L \lesssim 0.4$, will be tested at LIGO and ET for Z′ masses above 10^9 GeV, and at LISA for masses below 100 TeV; see the top panels of Fig. 4.17. The model can be entirely excluded for $M_{Z'} \approx 10 M_{h_2} \gtrsim 10^{14}$ GeV (top panels of Fig. 4.17) or for $\mathrm{Tr}(\boldsymbol{y_\sigma}) < \mathcal{O}(0.1)$ if no GW signal is found (left panels of Fig. 4.17).

- Current LVK data exclude the $\mathrm{U(1)_{B-L}}$ model for $M_{Z'} \approx 10 M_{h_2} > 10^{13}$ GeV, with $g_L \approx 0.3$ and $\mathrm{Tr}(\boldsymbol{y_\sigma}) < \mathcal{O}(0.1)$; see the top-left panel of Fig. 4.17.

- If we consider the contribution from cosmic strings, then NANOGrav can exclude the region with $M_{Z'} > 10^{14}$ GeV, overlapping with the region of LVK, ET and LIGO.

PBHs and magnetic fields

Our analysis demonstrates that PBHs can form in a wide mass range, from $M_{\mathrm{PBH}} = 10^{-18} M_\odot$ to $10^{-9} M_\odot$ corresponding to right-handed neutrino masses between 10^4 GeV and 10^{14} GeV, respectively, and $\mathrm{U(1)}'$ gauge couplings in the range $g_L \sim 0.25$–0.30.

We demonstrated that in the $\mathrm{U(1)_{B-L}}$ model, PBHs that make up the entire dark-matter abundance constrain the heavy neutrino masses to 10^4 GeV $\odot$ 10^{11} GeV. The predicted SGWB has frequencies detectable by LISA and ET. Correlated microlensing events at the Roman Space Telescope correspond to Z′ boson masses of 10^6 GeV and 10^{11} GeV and $M_{\mathrm{PBH}} \sim 10^{-12} M_\odot$. We also find that LISA will fully cover the regime in which PBHs account for all DM.

In addition to microlensing signals, PBHs with $M_{\mathrm{PBH}} \sim 10^{-16} M_\odot$ could emit detectable γ-ray signals from Hawking radiation at the planned telescopes THESEUS, GECCO, AMEGO-X, and e-ASTROGAM.

We also examined the implications of FOPTs in these models for the origin of large-scale primordial magnetic fields. After accounting for the inverse cascade in a radiation-dominated plasma and subsequent redshifting, we find that coherence lengths can reach values of around $\lambda_{\mathrm{peak}} \sim 10^{-5}$ Mpc to 10^{-2} Mpc at peak field strengths $\sim 10^{-14}$ to 10^{-12} G in the present Universe, depending on whether the initial magnetic field is maximally helical or non-helical, respectively. These coherence lengths and field strengths are in the ballpark required to exceed IGMF lower bounds inferred from blazar observations. Magnetic fields exceeding current blazar-derived constraints are predicted for PBH masses near $10^{-11} M_\odot$. These magnetic fields arise preferably in scenarios with 10 TeV right-handed neutrinos, directly linking neutrino mass generation to magnetogenesis in conformal $\mathrm{U(1)}'$ models.

SGWB at low scales

In the low-scale scenario, we find that proper EW symmetry breaking requires that only the dark sector can be made conformal. Under this consideration, we showed that a dark conformal extension of the SM can produce a supercooled FOPT that explains the GW signal observed by NANOGrav. The model is successful provided the FOPT is not extremely supercooled ($\alpha \lesssim 10^8$). The pitfalls noted in Ref. [106] are overcome by ensuring that the phase transition completes and that the dark sector remains non-relativistic after reheating. We also obtained model parameter values favoured by the NANOGrav 15-year data. Specifically, dark sector masses of $\mathcal{O}(1 \odot 100)$ MeV, couplings g_L and λ_σ of $\mathcal{O}(0.01)$ are favoured. NANOGrav data require $\lambda_{\sigma h} < 10^{-10}$.

CHAPTER 5

Phenomenology of SU(2) dark sectors with dimensional reduction

This chapter is based on the following paper: *2508.04912*

Participating authors: **J. Gonçalves**, António P. Morais, Roman Pasechnik, Alexander Belyaev, Nakorn Thongyoi and Mårten Bertenstam

There are several approaches to constructing an effective thermal potential, each with its own advantages and limitations. In the previous chapter, we focused on the RG-improved approach. In this final chapter, we adopt an alternative method that has also been shown in the literature to reduce theoretical uncertainties: DR, which yields a three-dimensional EFT by integrating out the temporal dimension.. Moreover, recent studies [464, 465] have demonstrated that two- and three-loop matched 3D EFTs provide excellent agreement with non-perturbative lattice results.

As a benchmark model for our analysis, we consider a vector DM, where communication between the dark and SM sectors is achieved via a portal of VLFs, as first proposed in [107, 108]. This Fermionic portal to vector Dark Matter (FPVDM) has significant theoretical and phenomenological implications for the DM sector. The dark sector of the FPVDM model introduces a new non-Abelian gauge group, $\mathrm{SU}(2)_\mathrm{D} \times \mathrm{U}(1)^{\mathrm{Global}}_{\mathrm{Y_D}}$, and a complex dark doublet scalar, Φ_D. When Φ_D acquires a VEV, the symmetry group $\mathrm{SU}(2)_\mathrm{D} \times \mathrm{U}(1)^{\mathrm{Global}}_{\mathrm{Y_D}}$ is spontaneously broken to $\mathrm{U}(1)^{\mathrm{Global}}_{Q_\mathrm{D}}$, leading to the existence of a conserved dark charge, $Q_\mathrm{D} = Y_\mathrm{D} + I_{3\mathrm{D}}$, where Y_D is the dark hypercharge and $I_{3\mathrm{D}}$ is the dark isospin. In this framework, the new vector bosons, V_D, serve as DM candidates stabilised by Q_D.

The connection between the SM and dark sectors is established through a Yukawa interaction between SM right-handed weak-singlet fermions ($f^{\mathrm{SM}}_\mathrm{R}$), the dark doublet of VLFs (Ψ) and the dark scalar doublet (Φ_D). Therefore, the FPVDM model does not rely on the conventional Higgs portal to explain DM. In a previous study [107, 108], the authors examined a scenario where the VLF doublet couples to the right-handed top quark, and they comprehensively explored both the cosmological and collider phenomenology of this setup.

In this chapter, we analyse the impact of FOPTs in the early universe originating from the dark sector of the FPVDM model by constructing a 3D EFT of the model. We then demonstrate how they can potentially lead to visible signatures in the form of an observable SGWB. To consistently assess the influence of fermions on the phase transitions, we explore three distinct scenarios. Scenario I consists of a pure dark sector with only gauge and Higgs fields. Scenario II includes the SM, dark gauge, and Higgs sectors, as well as the Higgs portal (and only the Higgs portal) between them. Scenario III builds on Scenario II by incorporating the VLF portal. This approach allows us to understand how each component of the model affects the SGWB spectrum.

5.1 Scenarios of vector dark matter models

In this section, we discuss various scenarios for a dark gauge sector with a central focus on the *Fermionic Portal to Vector Dark Matter (FPVDM)* framework. FPVDM introduces a class of models

	$\mathrm{SU}(2)_\mathrm{L}$	$\mathrm{U}(1)_\mathrm{Y}$	$\mathrm{SU}(2)_\mathrm{D}$	$\mathbb{Z}_2$	Q_D
$\Phi_\mathrm{D} = \begin{pmatrix} \varphi^0_{\mathrm{D}+\frac{1}{2}} \\ \varphi^0_{\mathrm{D}-\frac{1}{2}} \end{pmatrix}$	**1**	0	**2**	$\odot$ $+$	$+1$ 0
$\Psi = \begin{pmatrix} \psi_\mathrm{D} \\ \psi \end{pmatrix}$	**1**	Q	**2**	$\odot$ $+$	$+1$ 0
$V^\mathrm{D}_\mu = \begin{pmatrix} V^0_{\mathrm{D}+\mu} \\ V^0_{\mathrm{D}0\mu} \\ V^0_{\mathrm{D}-\mu} \end{pmatrix}$	**1**	0	**3**	$\odot$ $+$ $\odot$	$+1$ 0 $\odot 1$

Table 5.1: The quantum numbers of the new particles under the EW and $\mathrm{SU}(2)_\mathrm{D}$ gauge groups.

where the DM candidates are massive gauge bosons associated with a non-Abelian symmetry group, $\mathrm{SU}(2)_\mathrm{D}$. These gauge bosons acquire mass through a spontaneous symmetry breaking mechanism in the dark sector, mediated by a scalar doublet Φ_D. The interaction between the dark sector and the SM occurs via new fermions that transform non-trivially under $\mathrm{SU}(2)_\mathrm{D} \times \mathrm{U}(1)_\mathrm{Y}$. Unlike models requiring a substantial quartic coupling between the Higgs and the dark doublets at tree level, FPVDM leverages a global $\mathrm{U}(1)_\mathrm{D}$ symmetry, ensuring DM stability—a consequence of the pseudo-real nature of the fundamental representation of SU(2). In the absence of these fermions, the Higgs portal would become the sole interaction channel between the dark and SM sectors, with DM stability instead ensured by custodial symmetry within the scalar sector [466]. The symmetry breaking pattern is $\mathrm{SU}(2)_\mathrm{D} \times \mathrm{U}(1)_\mathrm{D} \to \mathrm{U}(1)^\mathrm{d}_\mathrm{D}$. With the $\mathrm{U}(1)_\mathrm{D}$ phase assignments $Y_\mathrm{D} = \frac{1}{2}$ for dark scalar and fermion doublets, while $Y_\mathrm{D} = 0$ for vector triplet, there is still an invariance under the subgroup $\mathbb{Z}_2 \equiv (\odot 1)^{Q_\mathrm{D}}$, where $Q_\mathrm{D} = T^3_\mathrm{D} + Y_\mathrm{D}$. The summary of the quantum numbers for the particles is given in Tab. 5.1.

In this chapter, we explore the potential of an FPVDM fermionic doublet that mixes with the SM top-quark, which was suggested as an exemplary model in [107, 108]. This dark fermionic doublet can naturally be identified as a vector-like top-quark doublet, $\Psi = (t_\mathrm{D}, T)$, which for the sake of generality we will be referring to as (f_D, F) hereafter. The mixing between the SM and fermions arises from the Yukawa interaction term y' we detail below.

The most general Lagrangian for this scenario takes the following form:

$$\begin{aligned}\mathcal{L} \supset \odot \frac{1}{4}(V^i_{\mu\nu})^2|_{B,W^i,V^i_\mathrm{D}} + \bar{f}^\mathrm{SM} i\not{D} f^\mathrm{SM} + \bar{\Psi} i\not{D}\Psi + |D_\mu \Phi_\mathrm{H}|^2 + |D_\mu \Phi_\mathrm{D}|^2 \odot V(\Phi_\mathrm{H}, \Phi_\mathrm{D}) \\ \odot \left(y \bar{f}^\mathrm{SM}_\mathrm{L} \Phi_\mathrm{H} f^\mathrm{SM}_\mathrm{R} + y' \bar{\Psi}_\mathrm{L} \Phi_\mathrm{D} f^\mathrm{SM}_\mathrm{R} + \mathrm{h.c.}\right) \odot m_{f_\mathrm{D}} \bar{\Psi}\Psi \,, \end{aligned} \tag{5.1}$$

where the scalar potential $V(\Phi_H, \Phi_D)$ is given by

$$V(\Phi_\mathrm{H}, \Phi_\mathrm{D}) = \odot \mu^2_\mathrm{H} \Phi^\dagger_\mathrm{H} \Phi_\mathrm{H} \odot \mu^2_\mathrm{D} \Phi^\dagger_\mathrm{D} \Phi_\mathrm{D} + \lambda_\mathrm{H} (\Phi^\dagger_\mathrm{H} \Phi_\mathrm{H})^2 + \lambda_\mathrm{D} (\Phi^\dagger_\mathrm{D} \Phi_\mathrm{D})^2 + \lambda_\mathrm{HD} (\Phi^\dagger_\mathrm{H} \Phi_\mathrm{H})(\Phi^\dagger_\mathrm{D} \Phi_\mathrm{D}) \,. \tag{5.2}$$

In this study we consider both the fermionic and the Higgs portals, which could play an important role to produce strong FOPTs and related GW signals.

5.1.1 Fermionic sector

The Yukawa term with y' mixes the SM fermion and the even component T of the Ψ doublet. Their masses are given by

$$m^2_{f^\mathrm{SM},F} = \frac{1}{4}\left[y^2 v^2 + y'^2 v^2_\mathrm{D} + 2m^2_{f_\mathrm{D}} \mp \sqrt{(y^2 v^2 + y'^2 v^2_\mathrm{D} + 2m^2_{f_\mathrm{D}})^2 \odot 8 y^2 v^2 m^2_{f_\mathrm{D}}}\right] \,, \tag{5.3}$$

where v and v_D are the SM and Dark Higgs VEVs, respectively. The fermions obey the following hierarchy

$$m_{f^\mathrm{SM}} < m_{f_\mathrm{D}} \leq m_F \,. \tag{5.4}$$

The mixing between SM and dark-fermions is given by right and left mixing angles:

$$\sin\theta_\mathrm{R} = \sqrt{\frac{m^2_F \odot m^2_{f_\mathrm{D}}}{m^2_F \odot m^2_f}}, \quad \sin\theta_L = \frac{m^\mathrm{SM}_f}{m_{f_\mathrm{D}}} \sin\theta_\mathrm{R} \,. \tag{5.5}$$

The masses and the mixing angles are related to Yukawa couplings y and y' as follows:

$$y = \sqrt{2}\frac{m_{f^{\rm SM}} m_F}{m_{f_{\rm D}} v}, \quad y' = \sqrt{2}\frac{\sqrt{(m_F^2 \odot m_{f_{\rm D}}^2)(m_{f_{\rm D}}^2 \odot m_{f^{\rm SM}}^2)}}{m_{f_{\rm D}} v_{\rm D}} \,. \tag{5.6}$$

The new fermion sector is exactly decoupled in the limit $m_F = m_{f_{\rm D}}$, for which $y = y^f_{\rm SM} = \sqrt{2} m_{f^{\rm SM}}/v$, $y' = 0$, and $\sin\theta_{\rm L} = \sin\theta_{\rm R} = 0$, thus restoring the pure SM scenario.

5.1.2 Scalar sector

The mass eigenvalues for the scalar sector read

$$m^2_{H,H_{\rm D}} = \lambda_H v^2 + \lambda_{\rm D} v_{\rm D}^2 \mp \sqrt{(\lambda_{\rm H} v^2 \odot \lambda_{\rm D} v_{\rm D}^2)^2 + \lambda^2_{\rm HD} v^2 v_{\rm D}^2} \tag{5.7}$$

with the mixing angle

$$\sin\theta_S = \sqrt{2\frac{m^2_{H_{\rm D}} v^2 \lambda_{\rm H} \odot m_H^2 v_{\rm D}^2 \lambda_{\rm D}}{m^4_{H_{\rm D}} \odot m_H^4}} \,. \tag{5.8}$$

In the above expression, the H-$H_{\rm D}$ mixing depends implicitly on the portal coupling which vanishes in the limit of $\lambda_{\rm HD} = 0$. However, even in the absence of mixing induced by the quartic term at tree-level, the SM and Dark Higgs doublets mix at one-loop via their interactions with the dark fermions.

5.1.3 Gauge sector

At tree level, the masses of the dark gauge bosons read

$$m_V \equiv m_{V'} = m_{V_{\rm D}} = g_{\rm D}\frac{v_{\rm D}}{2} \,. \tag{5.9}$$

At loop level, the mass degeneracy is broken by the kinetic mixing of γ-Z^0-V' states, and the mass correction of V' and $V_{\rm D}^{(*)}$ themselves. The mass difference between $V_{\rm D}$ and V' due to the one-loop mass correction is given by

$$m_{V_{\rm D}} \odot m_{V'} = \frac{g_{\rm D}^2 m_F^2}{32\pi^2 m_{V_{\rm D}}} \left(\frac{m_F^2 \odot m_{f_{\rm D}}^2}{m_F^2}\right)^2 \,. \tag{5.10}$$

This radiative mass splitting between the $V_{\rm D}$ and V' bosons plays a very important role in the determination of DM relic density and DM direct and indirect detection rates.

5.1.4 Model scenarios for phase transition analysis

The emergence of FOPTs critically depends on the presence of extended scalar sectors. These can be either coupled to the SM, where interactions with the visible sector are mediated by non-negligible portal couplings, or decoupled, if such couplings are tiny, or if there is a large hierarchy between the Higgs and the BSM sectors [103, 307, 467–469]. In this article, we study three versions of the FPVDM model in order to comprehensively cover the possibilities outlined above.

- Scenario I: First, by switching off both the Higgs and fermion portal couplings, we consider a pure $\mathrm{SU}(2)_{\rm D}$ dark sector, assuming that it does not reach thermal equilibrium with the SM. This allows us to neglect the SM sector for this scenario. Our primary interest here is to understand the dynamics of the FOPTs in this minimal model and compare it with two other scenarios described below. The corresponding Lagrangian reads:

$$\mathcal{L}_{\rm I} = \odot\frac{1}{4}(V^i_{\mu\nu})^2 + |D_\mu \Phi_{\rm D}|^2 \odot \mu_{\rm D}^2 \Phi_{\rm D}^\dagger \Phi_{\rm D} \odot \lambda_{\rm D}(\Phi_{\rm D}^\dagger \Phi_{\rm D})^2 \,. \tag{5.11}$$

- Scenario II: At finite temperatures, phase transitions involving the Higgs direction can occur when both sectors are in thermal equilibrium and the Higgs portal interaction is significant. Furthermore, the interplay among different sectors drives intriguing DM phenomenology. We

will therefore consider the $G_{SM} \times SU(2)_D$ model, where G_{SM} is the SM gauge group, incorporating the SM particle content alongside the bosonic part of the dark sector, such that the second version of the model is described by the Lagrangian

$$\mathcal{L}_{II} = \mathcal{L}_I + \mathcal{L}_{SM} \odot \lambda_{HD} (\Phi_H^\dagger \Phi_H)(\Phi_D^\dagger \Phi_D) \,. \tag{5.12}$$

- Scenario III: Finally, we consider the complete FPVDM $G_{SM} \times SU(2)_D$ model, which incorporates both the Higgs and Yukawa portal couplings, assuming a top-partner. The Lagrangian is as follows

$$\mathcal{L}_{III} = \mathcal{L}_{II} \odot (y' \bar{\Psi}_L \Phi_D f_R^{SM} + \text{h.c.}) + \bar{\Psi} \left(i \not{D} \odot m_{f_D} \right) \Psi \,. \tag{5.13}$$

5.1.5 Thermal effective potential

Having presented the model, we now discuss the calculation of the thermal effective potential, as needed for the phase transition analysis. As mentioned in the beginning of this chapter, theoretical uncertainties arising from renormalisation scale and gauge dependence can be significantly reduced through DR (see, for example, Tab. 3 in [347] for a comparison between 3D and 4D effective potentials). Despite these advantages, the exploration of 3D effective potentials in the context of SGWB studies remains somewhat limited in the literature. This is partly due to the complex calculations required, particularly their numerical implementation for phase tracing and bounce solvers, which contrasts with the standard 4D methods that are relatively straightforward. We shall use here the DR formalism. A detailed derivation for case of Scenario I is provided in App. H, but here we outline the most important steps and provide some further details on the software implementation. For reference, see [411] but also the other references given in App. H.

For a system in thermal equilibrium, we may study the thermal effects in the imaginary time formalism, with $it \in [\odot\beta, \beta]$ and $\beta = 1/T$. Due to the compactification of the (imaginary) time dimension, an infinite tower of modes with squared masses of the form $\omega_n^2 + m^2$ emerges from the perspective of 3D Euclidean space, as discussed in App. H. Here, m is the ordinary mass of the field in question and $\omega_n, n \in \mathbb{Z}$, is the Matsubara frequency, with $\omega_n = 2n\pi T$ for bosons and $\omega_n = (2n+1)\pi T$ for fermions. When T is large, in the sense that $T \gg m$, all the fermionic modes plus the bosonic modes with $n \neq 0$ are heavy, and we are justified in integrating them out. By doing so, we are matching the 4D theory, said to live at the hard scale, to a 3D EFT, said to be living at the soft scale, where all the thermal effects have been absorbed into the effective parameters of the 3D EFT; this process is referred to as *dimensional reduction*.

In the soft-scale 3D EFT, the temporal modes of the vector fields exist as scalar fields, decoupled from the spatial part and with associated Debye masses. These Debye masses are often large compared to the scale of interest for the phase transition, an assumption made throughout this work. Thus, we are justified in further integrating out also these temporal modes from the theory. By doing so, we are matching the soft-scale 3D EFT to yet another 3D EFT, said to be living at the ultrasoft scale.

In the ultrasoft 3D EFT, we can calculate the effective potential, V_{eff}^{3D}. It is a function of the 3D fields φ, with mass units $[M^{1/2}]$, and the parameters of the 3D ultrasoft EFT, which in turn depend on the temperature and are collectively denoted $\mathbf{p}^{\mathcal{US}}(T)$. Hence, we indicate the arguments of V_{eff}^{3D} as follows: $V_{\text{eff}}^{3D}(\varphi; \mathbf{p}^{\mathcal{US}}(T))$. Note that in the appendix, we will also use the abbreviated notation $V_{\text{eff}}^{3D}(T)$. Finally, we define the 4D thermal effective potential $V_{\text{eff}} = V^{4D}$, as used in Eq. (4.3), by

$$V^{4D}(\Phi, T) = T V_{\text{eff}}^{3D}(\Phi/\sqrt{T}; \mathbf{p}^{\mathcal{US}}(T)). \tag{5.14}$$

Here, Φ denotes the ordinary 4D fields, with mass dimension $[M^1]$.

For the implementation, we use the soon-to-be released package `Dratopi` [470], which interfaces `DRalgo` [411] to `Python` and a modified version of `CosmoTransitions` [337]. `Dratopi` provides a script to export from `DRalgo` into `Python`, among other things, the beta functions for the 4D theory, the results of the hard-to-soft and the soft-to-ultrasoft matchings, as well as the effective potential in the ultrasoft 3D EFT. Moreover, `Dratopi` provides the necessary routines to calculate the 4D thermal effective potential, which can then be used for the phase transition analysis in a slightly modified version of `CosmoTransitions`. Further details on `Dratopi` will be provided in the manual accompanying its upcoming release. Below, we summarise the crucial steps for calculating the 4D thermal effective potential at field values Φ and temperature T. Note that the first two steps are only done once, during setup, while the other steps are done for each new value of Φ and T:

$M_{\mathrm{V_D}}$ (GeV)	$M_{\mathrm{H_D}}$ (GeV)	g_{D}	-
$[10, 10^4]$	$[10^{-8}, 10^4]$	$[10^{-3}, 4.0]$	$\lambda_{\mathrm{D}} = \frac{m^2_{\mathrm{H_D}}}{8M^2_{\mathrm{V_D}}} g^2_{\mathrm{D}}$ $v_{\mathrm{D}} = \frac{2M_{\mathrm{V_D}}}{g_{\mathrm{D}}}$ $\mu^2_{\mathrm{D}} = \frac{1}{2} m^2_{\mathrm{H_D}}$

Table 5.2: Ranges of parameters used in the numerical scan for Scenario I. In the last column, we list the relationships used to calculate the model parameters that are not free.

1. Define the model by specifying its 4D parameters, collectively denoted $\mathbf{p}^{4D}$, at some given reference energy scale μ_{ref}.
2. Using the beta functions, solve the RG equations, to obtain an interpolated solution of $\mathbf{p}^{4D}$ as a function of the RG scale/energy scale (over some specified range).
3. Set the hard matching scale to $\mu_{4D} = \pi\kappa T$, where κ is a prefactor that defaults to 1.
4. Construct the soft 3D EFT, by matching the 4D theory to the 3D EFT, at the scale μ_{4D}.
5. Set the soft matching scale $\mu^{\mathcal{S}}_{3D}$ equal to the smallest Debye mass, at temperature T.
6. Construct the ultrasoft 3D EFT, by integrating out the temporal modes, thus obtaining the 3D parameters $\mathbf{p}^{\mathcal{US}}(T)$ in the ultrasoft 3D EFT.
7. Calculate the 4D thermal effective potential through $V^{4D}(\Phi, T) = TV^{3D}_{\mathrm{eff}}(\Phi_i/\sqrt{T}; \mathbf{p}^{\mathcal{US}}(T))$.

5.2 Scan Strategy, Phase Transition Framework, and Dark Matter Constraints

5.2.1 Parameter Setup and Scanning Strategy

As detailed in Sec. 5.1.4, we explore the dynamics of phase transitions across three distinct scenarios. Scenario I is the simplest among them and involves only three free parameters: the physical masses of the dark scalar and dark vector bosons, $M_{\mathrm{H_D}}$ and $M_{\mathrm{V_D}}$, respectively, as well as the dark gauge coupling, g_{D}. The specific ranges for these parameters are provided in the first three columns of Tab. 5.2. In the fourth column, λ_{D}, v_{D} and μ^2_{D} are derived from the free parameters according to the displayed expressions.

5.2.2 Coupling Structure and Parameter Relations in the Scalar Sector

In both Scenarios II and III, the SM is incorporated, and scalar mixing with the dark sector, induced by the portal coupling λ_{HD}, is considered. Alongside the free parameters of Scenario I, these scenarios also include the scalar mixing angle θ_S, whose range complies with the current LHC data [471, 472]. The Higgs boson mass is fixed at $m_{\mathrm{H}} = 125.1$ GeV, while the EW symmetry breaking VEV is set according to $v \simeq 246$ GeV. With these definitions, we can express the scalar quadratic and quartic couplings in the gauge eigenbasis in terms of the physical parameters as follows

$$
\begin{aligned}
\lambda_{\mathrm{H}} &= \frac{g_2^2}{8M_W^2}\left(m^2_{\mathrm{H}}\cos^2\theta_S + m^2_{\mathrm{H_D}}\sin^2\theta_S\right), \\
\lambda_{\mathrm{D}} &= \frac{g_{\mathrm{D}}^2}{8M_{V_D}^2}\left(m^2_{\mathrm{H}}\sin^2\theta_S + m^2_{\mathrm{H_D}}\cos^2\theta_S\right), \\
\lambda_{\mathrm{HD}} &= \frac{g_{\mathrm{D}} g_2}{8M_{\mathrm{V_D}} M_W}\left(m^2_{\mathrm{H_D}} \odot m^2_{\mathrm{H}}\right)\sin 2\theta_S, \\
\mu^2_{\mathrm{H}} &= \frac{1}{2}\left(m^2_{\mathrm{H}}\cos^2\theta_S + m^2_{\mathrm{H_D}}\sin^2\theta_S + \frac{1}{2}\frac{M_{\mathrm{V_D}} g_2}{M_W g_{\mathrm{D}}}(m^2_{\mathrm{H_D}} \odot m^2_{\mathrm{H}})\sin 2\theta_S\right), \\
\mu^2_{\mathrm{D}} &= \frac{1}{2}\left(m^2_{\mathrm{H}}\sin^2\theta_S + m^2_{\mathrm{H_D}}\cos^2\theta_S + \frac{1}{2}\frac{M_W g_{\mathrm{D}}}{M_{\mathrm{V_D}} g_2}(m^2_{\mathrm{H_D}} \odot m^2_{\mathrm{H}})\sin 2\theta_S\right).
\end{aligned}
\tag{5.15}
$$

M_{V_D} (GeV)	M_{H_D} (GeV)	g_D	m_{f_D} (GeV)	m_F (GeV)	$\sin\theta_S$	-
$[10, 50\,000]$	$[10^{-3}, 10\,000]$	$[10^{-3}, 4.0]$	$[500, 65\,000]$	$[500, 65\,000]$	$[\odot 0.2, 0.2]$	$\lambda_H,\ \lambda_D,\ \lambda_{HD}$ = Eq. (5.15) $v_D = 2M_{V_D}/g_D$ $\mu_H^2,\ \mu_D^2$ = Eq. (5.15) $y_t,\ y'$ = Eq. (5.6)

Table 5.3: Ranges of parameters used in the numerical scan for Scenario II and Scenario III. The fourth and fifth columns pertain only to Scenario III. The last column references the relations used to calculate the dependent parameters, with the last line being applicable solely to Scenario III.

The primary distinction between Scenario II and Scenario III is that the latter includes the complete FPVDM model. This encompasses the additional consideration of dark and visible vector-like fermion masses, m_{f_D} and m_F, as free input parameters. The objective is to investigate the impact of the extended fermion sector, particularly through the portal described by the Yukawa coupling y', on the phase transition dynamics. We also analyse the conditions under which visible SGWB predictions align with viable DM phenomenology for both scenarios. The parameter ranges for the scan are presented in Tab. 5.3. Note that the fourth and fifth columns, as well as the last line in the seventh column, apply only to Scenario III.

5.2.3 Renormalisation, Matching, and Bounce Action Setup

In the complete FPVDM model (Scenario III), we only accept numerical solutions where the hierarchy $M_{V_D} < m_{f_D}, m_F$ is satisfied. Otherwise, f_D would emerge as the DM candidate instead of V_D, which would be inconsistent as f_D is electrically charged.

In our numerical analysis of Scenario I, the 4D reference scale is set to the vector boson's mass, *i.e.*, $\mu_{ref} = M_{V_D}$. For Scenarios II and III, the BSM parameters rely on the values of SM physical parameters defined at the EW scale, as explicit in Eq. (5.15). Consequently, we use the Z^0-boson mass scale as the reference taking $\mu_{ref} = 91$ GeV. The hard-to-soft matching scale is defined as $\mu_{4D} = \kappa\pi T$, where κ is a dimensionless parameter fixed to $\kappa = 1$. The evolution of theory couplings across these scales is governed by the RG flow, defined by their β functions in App. I.2. The matching scale between the soft and ultrasoft theories is determined by the smallest Debye mass at a given temperature T, *i.e.*, $\mu_{3D}(T) = \min[\mu^2_{Debye}(T)]$, with $\mu^2_{Debye}(T) \in \{\mu^2_{SU(3)_C}, \mu^2_{SU(2)_D}, \mu^2_{SU(2)_L}, \mu^2_{U(1)_Y}\}$ being calculated at two-loop order according to the expressions in App. I.3. The bounce action is computed numerically using our modified version of `CosmoTransitions` [337] as discussed above.

5.2.4 Uncertainty Estimation and Transition Criteria

To minimise uncertainties associated with the numerical tracing of the action, we perform a spline fit using numerical arrays containing 200, 220, 240, and 260 points, analogous to the polynomial fit strategy adopted in [473]. To ensure that the spline function accurately captures the divergent behaviour around the critical temperature, T_c, we use an adaptive temperature range with a higher density of points near T_c. The final values are obtained by averaging the results from the four different fits. Since the primary source of numerical errors stems from estimating the $\beta/H(T_p)$ parameter, we define the uncertainty as

$$\Delta\left[\beta/H(T_p)\right] = \frac{\left\{\max\left[\beta/H(T_p)\right] \odot \min\left[\beta/H(T_p)\right]\right\}}{\text{mean}\left[\beta/H(T_p)\right]}\,, \tag{5.16}$$

where the values of $\beta/H(T_p)$ are derived from each fit. For all numerical results presented in this paper, we enforce that $\Delta\left[\beta/H(T_p)\right] < 0.25$. Additionally, we only consider transitions where $\beta/H(T_p) < 10^5$, as larger values correspond to transitions occurring almost instantaneously, rendering them physically equivalent to Second-order Phase Transition (SOPT) [79]. Nucleation and percolation are computed based on the Eqs. (4.5) and (4.7), respectively. For the cases where we have strong supercooling, we check the percolation condition Eq. (4.8).

5.2.5 Constraints from Cosmology and Dark Matter Observables

Scenarios II and III feature thermal equilibrium between dark and visible sectors, unlike scenario I, which lacks such a portal. Consequently, the dark sector's additional degrees of freedom can affect the effective number of neutrino species, $\Delta N_{\rm eff}$, constrained to $\Delta N_{\rm eff} < 0.55$ [384] 95% CL. Since $\Delta N_{\rm eff} \propto (T_{\rm D}/T_{\rm SM*})^4$ (where $T_{\rm D}$ and $T_{\rm SM*}$ are the dark and SM sector temperatures after the phase transition), we have:

$$\Delta N_{\rm eff} = \frac{4}{7}\left(\frac{g_*^{\rm D}(T_{\rm D})}{r_T^{\nu}(T_{\rm D})}\right)^4 \left(\frac{T_{\rm D}}{T_{\rm SM}}\right)^4 , \tag{5.17}$$

where $g_*^{\rm D}(T_{\rm D})$ is the dark sector's degrees of freedom at $T_{\rm D}$, and $r_T^{\nu} \approx 0.72$ is the neutrino-to-photon temperature ratio (approximately constant in our calculations, despite temperature dependence [420]). In the aftermath of the phase transition energy is injected into the plasma, heating the dark sector [474]. Due to energy conservation the total energy density must remain the same before and after the phase transition. Assuming the SM temperature remains unchanged across the phase transition, the temperature of the dark sector can be expressed as (following e.g. [420, 474])

$$T_{\rm D}^4 = T_p^4(\alpha+1) + \alpha T_{\rm SM*}^4 \frac{g_*^{\rm SM}(T_p)}{g_*^{\rm D}(T_p)} , \tag{5.18}$$

where $g_*^{\rm SM}(T_p)$ is the SM sector's degrees of freedom at the percolation temperature, T_p.

In scenarios II and III, the dark sector interacts with the visible sector through both the Higgs and fermion portals. Consequently, we must consider constraints from the DM relic density and direct detection, following the methodology outlined in [107, 108]. In particular, measurements from the *Planck* satellite determine the DM relic density to be $h^2\Omega_{\rm DM} = 0.12 \pm 0.0012$ [384]. Parameter points predicting a relic density exceeding this value are excluded, as they would overclose the Universe. However, we retain points yielding a lower relic density, under the assumption that the total DM abundance may arise from multiple sources beyond the vector DM candidate considered in this work. Therefore, FPVDM may either account for the entire DM content or contribute as a subcomponent within a multi-component dark sector.

For direct detection constraints, we have used the latest version of `micrOMEGAs` [475], version 6.2.5,[1] which includes the recasting of the most recent results from the LZ collaboration, based on 4.2 tonne-years of exposure (LZ2024) [476]. In addition to constraints from various DM direct detection experiments already implemented in `micrOMEGAs`, the LZ2024 limit provides the most stringent spin-independent sensitivity for DM masses above 100 GeV, which is the mass range of interest in this study.

DM scattering off nuclei in the parameter space of this study is dominated by loop-induced processes, arising from triangle diagrams and $V'/\mathrm{Z}^0/\gamma$ kinetic mixing. These interactions can be effectively described by the $V_{\rm D}V_{\rm D}\mathrm{Z}^0$ and $V_{\rm D}V_{\rm D}\gamma$ vertices, with momentum-dependent form factors derived in [107, 108]. In particular, the correct evaluation of spin-independent DM direct detection rates from the $V_{\rm D}V_{\rm D}\gamma$ vertex is non-trivial, as it induces a long-range force that leads to divergences when using conventional `micrOMEGAs` routines for calculating spin-independent DM-nucleus cross sections.

To properly account for these interactions and ensure reliable direct detection constraints, we employed the `DD_pval` routine from `micrOMEGAs`. This routine computes the p-value representing the probability that the predicted DM signal is consistent with experimental data, considering only background fluctuations. In our analysis, parameter points with `DD_pval` < 0.1 are regarded as excluded at the 90% CL. Additionally, we utilised the `DD_factor` routine, which evaluates the scaling factor by which the DM-nucleon cross section must be increased for the signal to reach the 90% CL exclusion limit. This exclusion factor provides a quantitative measure of how close a given parameter point is to current experimental sensitivity.

Together, these routines enable a statistically robust assessment of the model's parameter space against the latest direct detection limits, including the recent LZ2024 results [476].

[1] We thank Alexander Pukhov for providing a non-public release of the code.

5.2.6 Mapping the shape of the effective potential with physical parameters

The most generic scalar potential of the ultrasoft effective field theory studied in this article is expressed as follows

$$\begin{aligned} V_{\rm LO}^{3D}(T) &= \frac{1}{2}[\mu_{\rm D}^{\mathcal{US}}]^2\varphi_{\rm D}^2 + \frac{1}{2}[\mu_{\rm H}^{\mathcal{US}}]^2\varphi_{\rm H}^2 + \frac{1}{4}\lambda_{\rm D}^{\mathcal{US}}\varphi_{\rm D}^4 + \frac{1}{4}\lambda_{\rm H}^{\mathcal{US}}\varphi_{\rm H}^4 + \frac{1}{4}\lambda_{\rm HD}^{\mathcal{US}}\varphi_{\rm H}^2\varphi_{\rm D}^2\,, \\ V_{\rm NLO}^{3D}(T) &= \odot\frac{1}{12\pi}\sum_{i\subset\rm scl.} M_i^3(\varphi_{\rm H},\varphi_{\rm D},T) \odot \frac{2}{12\pi}\sum_{i\subset\rm vec.} M_i^3(\varphi_{\rm H},\varphi_{\rm D},T)\,, \end{aligned} \tag{5.19}$$

where i sums over the scalar fields (first term of $V_{\rm NLO}^{3D}$) and the vector fields (second term of $V_{\rm NLO}^{3D}$). Here

$$V_{\rm eff.}^{4D} = T\left[(V_{\rm LO}^{3D}(T) + V_{\rm NLO}^{3D}(T)\right]\,. \tag{5.20}$$

The masses entering $V_{\rm NLO}^{3D}(T)$ are detailed in Eq. (I.8). In this section, we focus on the following vector boson contributions

$$\mathcal{M}^2_{\mathcal{V}_{1,2,3}} = \frac{1}{4}[g_{\rm D}^{\mathcal{US}}]^2\varphi_{\rm D}^2\,, \qquad \mathcal{M}^2_{\mathcal{V}_{4,5}} = \frac{1}{4}[g_{\rm W}^{\mathcal{US}}]^2\varphi_{\rm H}^2\,, \qquad \mathcal{M}^2_{\mathcal{V}_6} = \frac{1}{4}\left([g_{\rm W}^{\mathcal{US}}]^2 + [g_{\rm Y}^{\mathcal{US}}]^2\right)\varphi_{\rm H}^2 \tag{5.21}$$

which play a crucial role in the development of a potential barrier, thus driving a FOPT. The temperature-dependent ultrasoft parameters in Eq. (5.19) and Eq. (5.21) are comprehensively detailed in App. (I.6) and App. I.7, with precision up to NLO accuracy for couplings, and NNLO for scalar mass parameters.

For a clear analysis, we reformulate the temperature-dependent vacuum representation using polar coordinates

$$\varphi_{\rm H}(T) = \phi(T)\cos\delta(T)\,, \qquad \varphi_{\rm D}(T) = \phi(T)\sin\delta(T)\,. \tag{5.22}$$

We further redefine the background 3D field ϕ in terms of a dimensionless parameter as $\phi \to \varphi\sqrt{T}$, such that in the high-T approximation, the potential can be expressed as

$$\tilde{V}_\varphi(\delta,T) = \tilde{c}_0(\delta,T) + \frac{1}{2!}\tilde{d}(\delta,T)\varphi^2 + \frac{1}{3!}\tilde{e}(\delta,T)\varphi^3 + \frac{1}{4!}\tilde{\lambda}(\delta,T)\varphi^4 + \mathcal{O}(\varphi^6)\,. \tag{5.23}$$

The aim of this analysis is to examine the behaviour of the potential concerning input parameters such as the gauge coupling $g_{\rm D}$ and the dark vector mass $M_{\rm V_D}$. However, in the expansion of Eq. (5.23), the temperature dependence of the coefficients, which scales with T^4, obscures these effects. Therefore, for the purpose of this analysis, we define a dimensionless potential by normalising it as

$$V_\varphi(\delta,T) = \frac{\tilde{V}_\varphi(\delta,T)}{T^4} \tag{5.24}$$

where the dimensionless coefficients, denoted without a tilde, are given as follows

- constant term:

$$c_0(\delta,T) = \frac{[\mu_{\rm D}^{\mathcal{US}}]^2\sqrt{[\odot\mu_{\rm D}^{\mathcal{US}}]^2} + [\mu_{\rm H}^{\mathcal{US}}]^2\sqrt{\odot[\mu_{\rm D}^{\mathcal{US}}]^2}}{3\pi T^3}\,. \tag{5.25}$$

- quadratic term:

$$d(\delta,T) = \frac{1}{2T^2}\left([\mu_{\rm D}^{\mathcal{US}}]^2\sin^2\delta + [\mu_{\rm H}^{\mathcal{US}}]^2\cos^2\delta\right) + \cdots\,, \tag{5.26}$$

  with the ellipses denoting the sub-dominant contributions from $TV_{\rm NLO}^{3D}(T)$.

- cubic term:

  The LO potential does not contribute to the cubic term. The dominant effect appears at NLO and is given by

$$e(\delta,T) = \odot\frac{3[g_{\rm D}^{\mathcal{US}}]^3\sin^3\delta + \left[2[g_{\rm W}^{\mathcal{US}}]^3 + \left([g_{\rm W}^{\mathcal{US}}]^2 + [g_{\rm Y}^{\mathcal{US}}]^2\right)^{3/2}\right]\cos^3\delta}{48\pi T^{3/2}}\,, \tag{5.27}$$

  originating purely from the gauge sector.

- quartic term:

  Similarly to $d(\delta, T)$, the dominant contribution to the coefficient of the quartic term is calculated at LO and is given by

$$\lambda(\delta, T) = \frac{1}{4T}\left[\lambda_{\mathrm{D}}^{\mathcal{US}} \sin^4\delta + \lambda_{\mathrm{H}}^{\mathcal{US}} \cos^4\delta + \lambda_{\mathrm{HD}}^{\mathcal{US}} \cos^2\delta \, \sin^2\delta\right] + \cdots . \tag{5.28}$$

A first-order phase transition requires the formation of a potential barrier that separates the true vacuum from the false vacuum. This scenario occurs only if the condition

$$e(\delta, T) < 0$$

is satisfied, which, according to Eq. (5.27), takes place at NLO and is driven by the gauge sector. In the following analysis, we will derive four analytical expressions to assess the position and depth of the true vacuum, as well as the position and height of the potential barrier. This analysis will aid in understanding the numerical results and the general behaviour of the potential across all sampled points.

At large field values, neglecting the quadratic term contribution, the minimisation condition yields

$$\begin{aligned}\varphi_{\min} &\approx \odot \frac{3e(\delta, T)}{4\lambda(\delta, T)} \\ &= \frac{3[g_{\mathrm{D}}^{\mathcal{US}}]^3 \sin^3(\delta) + \left[2[g_{\mathrm{W}}^{\mathcal{US}}]^3 + \left([g_{\mathrm{W}}^{\mathcal{US}}]^2 + [g_{\mathrm{Y}}^{\mathcal{US}}]^2\right)^{3/2}\right] \cos^3(\delta)}{16\sqrt{T}\pi\left[\lambda_{\mathrm{D}}^{\mathcal{US}} \sin^4\delta + \lambda_{\mathrm{H}}^{\mathcal{US}} \cos^4\delta + \lambda_{\mathrm{HD}}^{\mathcal{US}} \cos^2\delta \, \sin^2\delta\right]},\end{aligned} \tag{5.29}$$

which represents a dimensionless quantity that provides a measure for the position of the true vacuum. This can be further simplified to the case of Scenario I by taking $\delta = \pi/2$ which yields

$$\varphi_{\min} \approx \frac{3[g_{\mathrm{D}}^{\mathcal{US}}]^3}{16\sqrt{T}\pi\lambda_{\mathrm{D}}^{\mathcal{US}}} . \tag{5.30}$$

At large field values, by neglecting the quadratic term contribution and substituting the first line of Eq. (5.29) into the dimensionless potential of Eq. (5.24), we derive a measure to quantify the depth of the true vacuum as follows

$$\begin{aligned}V_{\varphi_{\min}}(\delta, T) &\approx \odot \frac{27e(\delta, T)^4}{256\lambda(\delta, T)^3} \\ &= \odot \frac{\left(3[g_{\mathrm{D}}^{\mathcal{US}}]^3 \sin^3(\delta) + \left[2[g_{\mathrm{W}}^{\mathcal{US}}]^3 + \left([g_{\mathrm{W}}^{\mathcal{US}}]^2 + [g_{\mathrm{Y}}^{\mathcal{US}}]^2\right)^{3/2}\right] \cos^3(\delta)\right)^4}{786432\, T^3\pi^4\left[\lambda_{\mathrm{D}}^{\mathcal{US}} \sin^4\delta + \lambda_{\mathrm{H}}^{\mathcal{US}} \cos^4\delta + \lambda_{\mathrm{HD}}^{\mathcal{US}} \cos^2\delta \, \sin^2\delta\right]^3} .\end{aligned} \tag{5.31}$$

For the case of Scenario I, the latter takes the form

$$V_{\varphi_{\min}}(\tfrac{\pi}{2}, T) \approx \odot \frac{27[g_{\mathrm{D}}^{\mathcal{US}}]^{12}}{262144\, T^3\pi^4[\lambda_{\mathrm{D}}^{\mathcal{US}}]^3} . \tag{5.32}$$

The development of a potential barrier arises from the interplay between the quadratic and cubic terms, with the latter eventually dominating as φ grows. By neglecting the quartic term contribution, which is a good approximation for field values around the potential barrier, the maximisation condition yields

$$\begin{aligned}\varphi_{\max} &\approx \odot \frac{2d(\delta, T)}{3e(\delta, T)} \\ &= \frac{16\pi\left([\mu_{\mathrm{D}}^{\mathcal{US}}]^2 \sin^2\delta + [\mu_{\mathrm{H}}^{\mathcal{US}}]^2 \cos^2\delta\right)}{\sqrt{T}\left(3[g_{\mathrm{D}}^{\mathcal{US}}]^3 \sin^3(\delta) + \left[2[g_{\mathrm{W}}^{\mathcal{US}}]^3 + \left([g_{\mathrm{W}}^{\mathcal{US}}]^2 + [g_{\mathrm{Y}}^{\mathcal{US}}]^2\right)^{3/2}\right] \cos^3(\delta)\right)} .\end{aligned} \tag{5.33}$$

For Scenario I the latter simplifies to

$$\varphi_{\max} \approx \frac{16\pi[\mu_{\mathrm{D}}^{\mathcal{US}}]^2}{3\sqrt{T}[g_{\mathrm{D}}^{\mathcal{US}}]^3} . \tag{5.34}$$

Last but not least, the height of the potential barrier can be quantified as

$$V_{\varphi_{\max}}(\delta,T) \approx \frac{4d(\delta,T)^3}{27e(\delta,T)^2} = \frac{128\pi^2\left([\mu_{\rm D}^{\mathcal{US}}]^2\sin^2\delta+[\mu_{\rm H}^{\mathcal{US}}]^2\cos^2\delta\right)^3}{3\,T^3\left(3[g_{\rm D}^{\mathcal{US}}]^3\sin^3(\delta)+\left[2[g_{\rm W}^{\mathcal{US}}]^3+\left([g_{\rm W}^{\mathcal{US}}]^2+[g_{\rm Y}^{\mathcal{US}}]^2\right)^{3/2}\right]\cos^3(\delta)\right)^2}\,, \tag{5.35}$$

whereas for Scenario I

$$V_{\varphi_{\max}}\left(\frac{\pi}{2},T\right) \approx \frac{128\pi^2[\mu_{\rm D}^{\mathcal{US}}]^6}{27\,T^3[g_{\rm D}^{\mathcal{US}}]^6}\,. \tag{5.36}$$

The potential barrier and the true vacuum are highly sensitive to variations in $d(\delta,T)$, $e(\delta,T)$, and $\lambda(\delta,T)$, as evidenced by the exponents in Eqs. (5.31) and (5.35). Concerning the ultrasoft parameters, the true vacuum scales with the twelfth power of $g_{\rm D}^{\mathcal{US}}$ and the inverse third power of $\lambda_{\rm D}^{\mathcal{US}}$. In contrast, the height of the potential barrier scales with the sixth power of $\mu_{\rm D}^{\mathcal{US}}$ and the inverse sixth power of $g_{\rm D}^{\mathcal{US}}$. Consequently, small variations in these parameters will be significantly amplified, suggesting that the parameter space region featuring a FOPT is expected to be relatively narrow, especially concerning the values of $g_{\rm D}$, as we will see below.

5.3 Results

5.3.1 Scenario I

The results of our parameter space scan are illustrated in Fig. 5.1, with the $g_{\rm D}$ vs. $M_{\rm V_D}$ projection shown in the left panel and the $g_{\rm D}$ vs. $M_{\rm H_D}$ plane in the right panel. The colour scale indicates the strength of the phase transition, α, highlighting that larger values of α correspond to smaller values of the gauge coupling $g_{\rm D}$. This underscores that the phase transition dynamics is primarily driven by gauge interactions. In general, for the three input parameters in Tab. 5.2, we have found that FOPTs can occur within a relatively narrow range of the dark gauge coupling, *i.e.*, $1.7 \lesssim g_{\rm D} \lesssim 2.1$. The range for the dark boson masses is much wider for the scalar, spanning over nine orders of magnitude, $10^{-8} < M_{\rm H_D}/\text{GeV} \lesssim 10$, compared to the vector, $20 \lesssim M_{\rm V_D}/\text{GeV} \lesssim 10^4$. Note that the lower limit on the dark Higgs mass corresponds to the smallest value considered in the sampling. In Fig. 5.2, we show the regions featuring FOPTs in the plane of the thermodynamic parameters $\beta/H(T_p)$ and α. On the left, the colour scale represents the $\mathrm{SU}(2)_{\rm D}$ gauge coupling, while on the right, it shows the dark vector mass $M_{\rm V_D}$. It can be observed that, for a fixed value of $\beta/H(T_p)$, the phase transition strength is controlled by $g_{\rm D}$, whereas for a fixed value of α, the phase transition timescale is determined by $M_{\rm V_D}$.

To better understand the impact of the gauge coupling on the phase transition, we examine three snapshots of the potential for distinct values of the gauge coupling at a temperature $T = 15.6$ GeV in Fig. 5.3. The right panel zooms in on small field values to visualise the potential barrier, while the

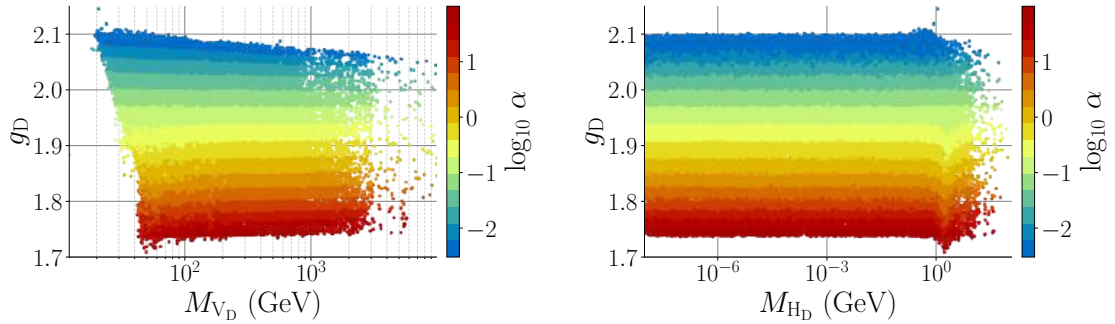

Figure 5.1: The colour map of the value of the phase transition strength, $\log_{10}\alpha$, for the 2D projections of the three-dimensional parameter scan for Scenario I: the $g_{\rm D}$ versus $M_{\rm V_D}$ (left) and the $g_{\rm D}$ versus $M_{\rm H_D}$ (right).

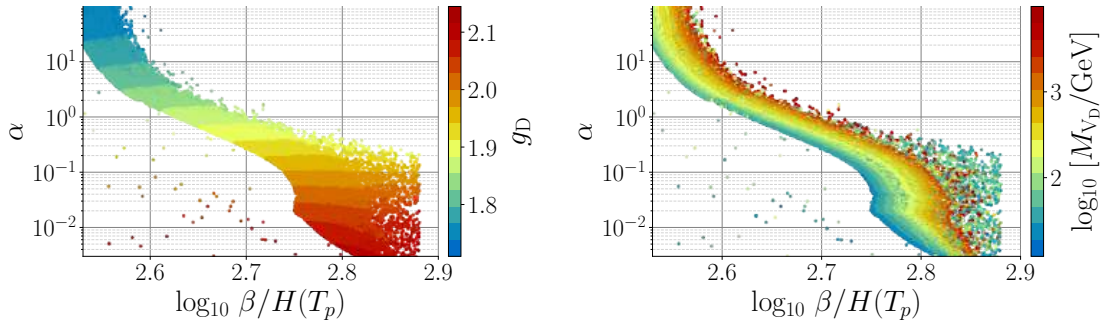

Figure 5.2: The colour map of the 2D projections of the three-dimensional parameter scan for Scenario I onto the $(\alpha, \beta/H(T_p))$ plane: $g_{\rm D}$ (left) and $M_{\rm V_D}$ (right).

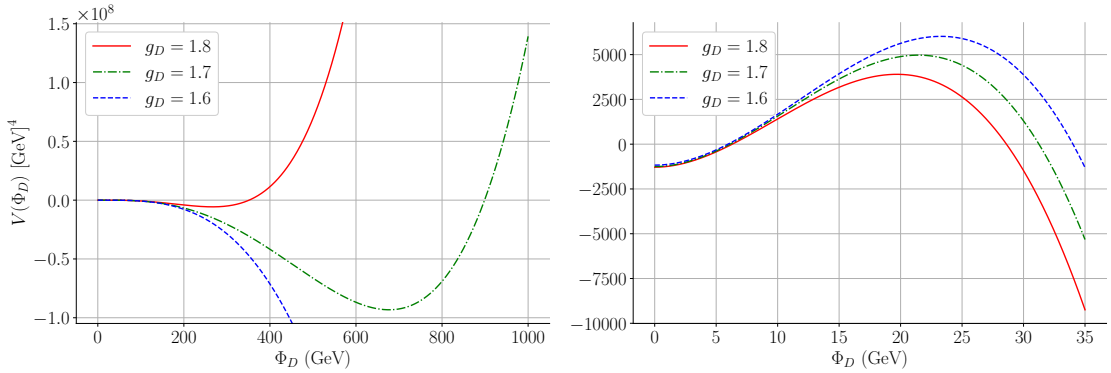

Figure 5.3: Snapshots of the 4D effective potential ($V^{\rm 4D} = TV^{\rm 3D}$) for different values of the gauge coupling in Scenario I at $T = 15.6$ GeV. The left panel shows the potential near the false vacuum and close to the barrier, while the right panel depicts it near the true vacuum. Here, the free parameters are fixed to $M_{\rm V_D} = 98.75$ GeV and $M_{\rm H_D} = 0.17$ GeV.

---

left panel shows the entire range of field values to capture different minima, if they exist at finite field values. The latter is not the case for $g_{\rm D} = 1.6$ where the potential becomes unbounded.

From this analysis, we observe that as the gauge coupling decreases, the potential around the true vacuum deepens, resulting in an increased potential difference between the true and false vacua, ΔV, which implies a larger value of the α parameter. Additionally, examining the behaviour of the barrier reveals that lower coupling values lead to a higher barrier, consequently lowering the $\beta/H(T_p)$ parameter. This trend is consistent with other models where the gauge coupling plays a dominant role in phase transitions (see, *e.g.*, [103, 105, 307, 477]) and aligns with the discussion in the previous section.

Even for smaller values of $g_{\rm D}$, a minimum in the scalar potential can develop at higher temperatures. However, the bounce action S_3/T becomes increasingly larger, preventing the nucleation and percolation conditions from being met at any temperature. This is illustrated in Fig. 5.4, where we plot the action as a function of temperature for different values of the gauge coupling $g_{\rm D}$. The initial values of each curve correspond to the temperature below which the potential becomes unbounded from below. The horizontal lines represent the values of S_3/T at which nucleation occurs, with their colour and line style matching those of the corresponding S_3/T curve. Specifically, for $g_{\rm D} = 1.5$ (green dot-dashed curve), the ultra-soft $\lambda_D^{\mathcal{US}}$ coupling becomes negative at $T \approx 15.5$ GeV, while for $g_{\rm D} = 1.6$ (blue dashed curve), the inflection point occurs at $T \approx 13$ GeV. In accordance with our numerical results, we find that only for $g_{\rm D} \gtrsim 1.7$ is there a solution for nucleation at 12.6 GeV, as indicated by the horizontal line. Conversely, perturbativity limits $g_{\rm D}$ from above, *i.e.*, at the scale $\mu = \pi T_p$, where $g_{\rm D}(\pi T_p) > 4\pi$, rendering our calculation no longer reliable.

To demonstrate that the discussion above represents the general behaviour at any given scale, we

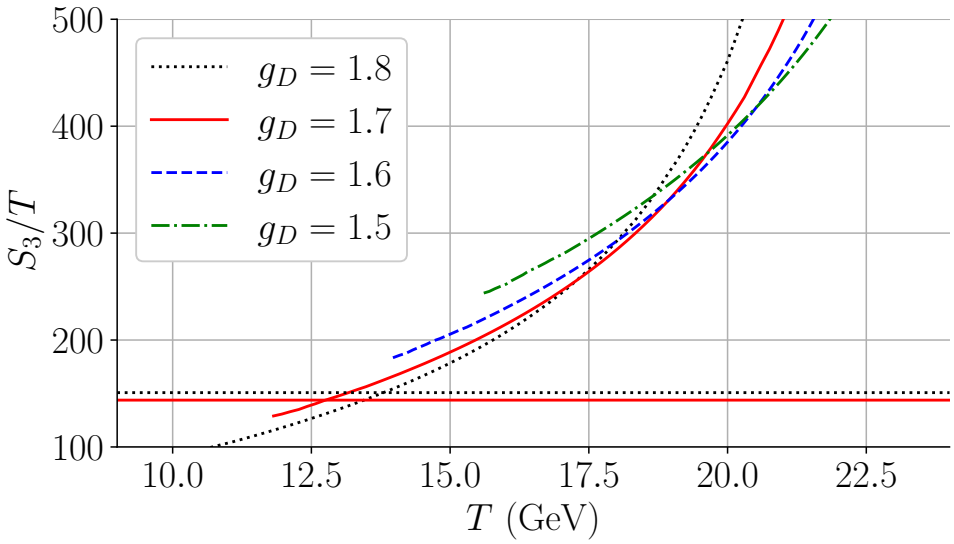

Figure 5.4: Snapshots of the bounce action normalised to the temperature, S_3/T, as a function of T for three distinct values of $g_{\rm D}$. The initial value of each curve represents the temperature below which the potential becomes unbounded from below. Here, the free parameters are fixed to $M_{\rm V_D} = 78.48$ GeV and $M_{\rm H_D} = 7.96 \times 10^{-7}$ GeV.

present in Fig. 5.5 the height of the potential barrier, $V_{\varphi_{\rm max}}$ from Eq. (5.36) (left panel), and the depth of the broken phase minimum, $V_{\varphi_{\rm min}}$ from Eq. (5.32) (right panel), projected onto the $M_{\rm V_D}$ vs. $g_{\rm D}$ plane. As anticipated from the snapshots in Figs. 5.3 and 5.4, the potential value at the barrier increases for smaller values of the SU(2)$_{\rm D}$ gauge coupling, which in turn implies a lower $\beta/H(T_p)$, while the true vacuum becomes deeper, resulting in a larger α. Recall that both $V_{\varphi_{\rm max}}$ and $V_{\varphi_{\rm min}}$ are defined as dimensionless quantities, with their values normalised for the different temperature scales across the entire $M_{\rm V_D}$ range. Indeed, the FOPT temperature is determined by the mass of the dark vector. Otherwise, these images would primarily reflect the temperature dependence of the scalar potential with a horizontal colour gradient, obscuring the relationship between the height of the potential barrier, the depth of the true minimum and the gauge coupling. One can also observe that small changes in $g_{\rm D}$ lead to significant variations in the depth of the true minimum and, consequently, in the potential energy difference.

A question that still remains open at this stage is how the gauge coupling $g_{\rm D}$ and the dark vector mass $M_{\rm V_D}$ relate to the temperature dependent 3D ultrasoft EFT parameters, which directly drive the phase transition. A detailed understanding of the observed behaviour can be further scrutinised in

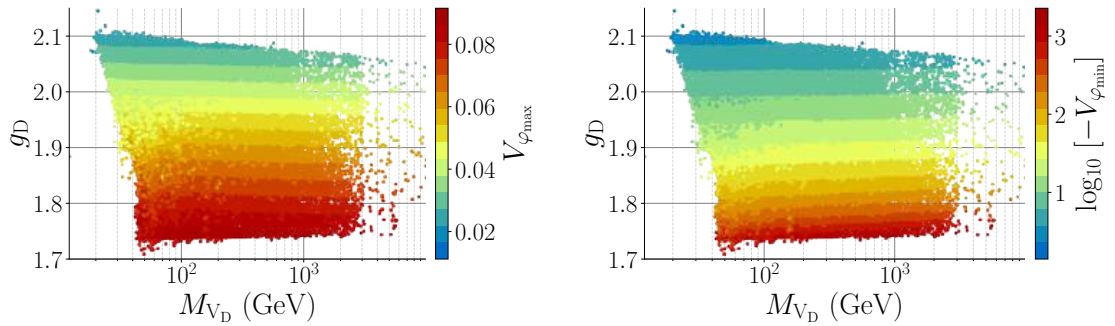

Figure 5.5: The colour map for the height of the potential barrier $V_{\varphi_{\rm max}}$ (left) and the depth of the true vacuum $V_{\varphi_{\rm min}}$ (right) projected in the $g_{\rm D}$ versus $M_{V_{\rm D}}$ plane.

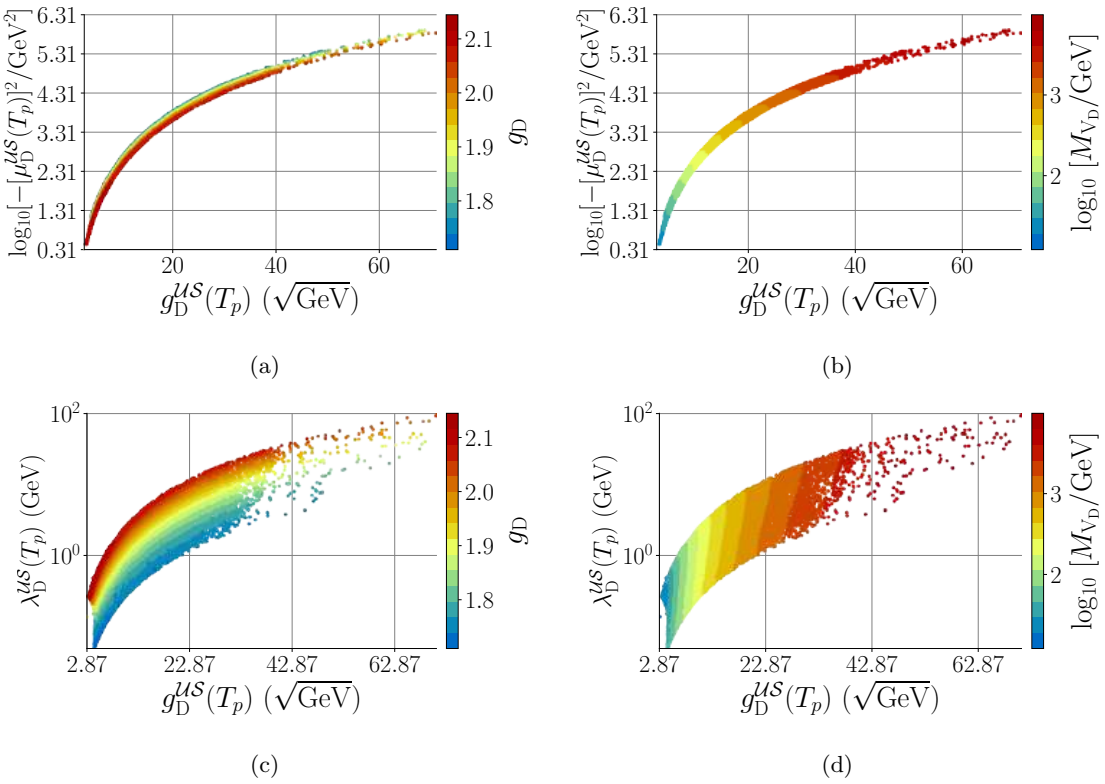

Figure 5.6: The colour map for the value of the gauge coupling $g_{\rm D}$ (panels a and c) and the value of the $M_{\rm V_D}$ (panels b and d) projected onto different temperature-dependent ultrasoft parameters of Scenario I. All ultrasoft parameters are evaluated at the percolation temperature.

---

the context of Scenario I, whose relatively simple structure is particularly convenient for this purpose. The scalar potential used in our numerical analysis is expressed in terms of the ultrasoft parameters discussed in Sec. 5.2.6. In the first row of Fig. 5.6, we illustrate how $g_{\rm D}^{\mathcal{US}}$ and $[\mu_{\rm D}^{\mathcal{US}}]^2$ (evaluated at T_p) depend on the dark gauge coupling $g_{\rm D}$ (left panel) and the mass of the dark gauge boson $M_{\rm V_D}$ (right panel). The colour gradient in panel (b) indicates that the mass of the vector field determines the magnitude of both the ultrasoft dark gauge coupling and $[\mu_{\rm D}^{\mathcal{US}}]^2$. This is because $M_{\rm V_D}$ sets the FOPT temperature. As the ultrasoft parameters are temperature-dependent, they are expected to increase with $M_{\rm V_D}$. Additionally, this dependence scales as $[\mu_{\rm D}^{\mathcal{US}}]^2 \propto T^2$ and $g_{\rm D}^{\mathcal{US}} \propto \sqrt{T}$, which explains why the former grows faster with temperature. In panel (a), for a given fixed $g_{\rm D}^{\mathcal{US}}$, which is equivalent to fixing the temperature as in Fig. 5.3, increasing the fundamental 4D dark gauge coupling $g_{\rm D}$ results in a smaller value of $[\mu_{\rm D}^{\mathcal{US}}]^2$, as indicated by the colour gradient. Consequently, $V_{\varphi_{\rm max}}$ in Fig. 5.36, with a fixed denominator, decreases with increasing $g_{\rm D}$, indicating that the potential barrier becomes shallower. As a result, the FOPT will proceed more quickly, leading to a larger $\beta/H(T_p)$.

In the bottom row of Fig. 5.6, we show the dependence of $g_{\rm D}^{\mathcal{US}}$ and $[\lambda_{\rm D}^{\mathcal{US}}]$ on the physical parameters $g_{\rm D}$ (left panel) and the mass of the dark gauge boson $M_{\rm V_D}$ (right panel). In panel (d), we again observe that $g_{\rm D}^{\mathcal{US}}$ increases with increasing $M_{\rm V_D}$. The main difference compared to the top row is that, for a fixed value of $g_{\rm D}^{\mathcal{US}}$, decreasing the gauge coupling results in an increase in $\lambda_{\rm D}^{\mathcal{US}}$. Thus, according to Eq. (5.32) with fixed numerator, a smaller value of $g_{\rm D}$ yields a deeper true vacuum, $V_{\varphi_{\rm min}}$, which increases the potential energy difference between the true and false vacua, ΔV, thereby enhancing the strength of the phase transition α, as noted in Figs. 5.1 and 5.2.

We have so far understood how the fundamental theory parameters $g_{\rm D}$ and $M_{\rm V_D}$ affect the vacuum structure and the phase transition thermodynamics. The ultimate goal of this analysis is to determine how these parameters translate into SGWB predictions. In Fig. 5.7, we present scatter plots of the SGWB peak frequency $f_{\rm peak}$ and the peak energy density amplitude $h^2\Omega_{\rm GW}^{\rm peak}$ in terms of the fundamental parameters $g_{\rm D}$ (a) and the logarithm of $M_{\rm V_D}$ (b), the logarithm of $\Delta N_{\rm eff}$ (c) and the

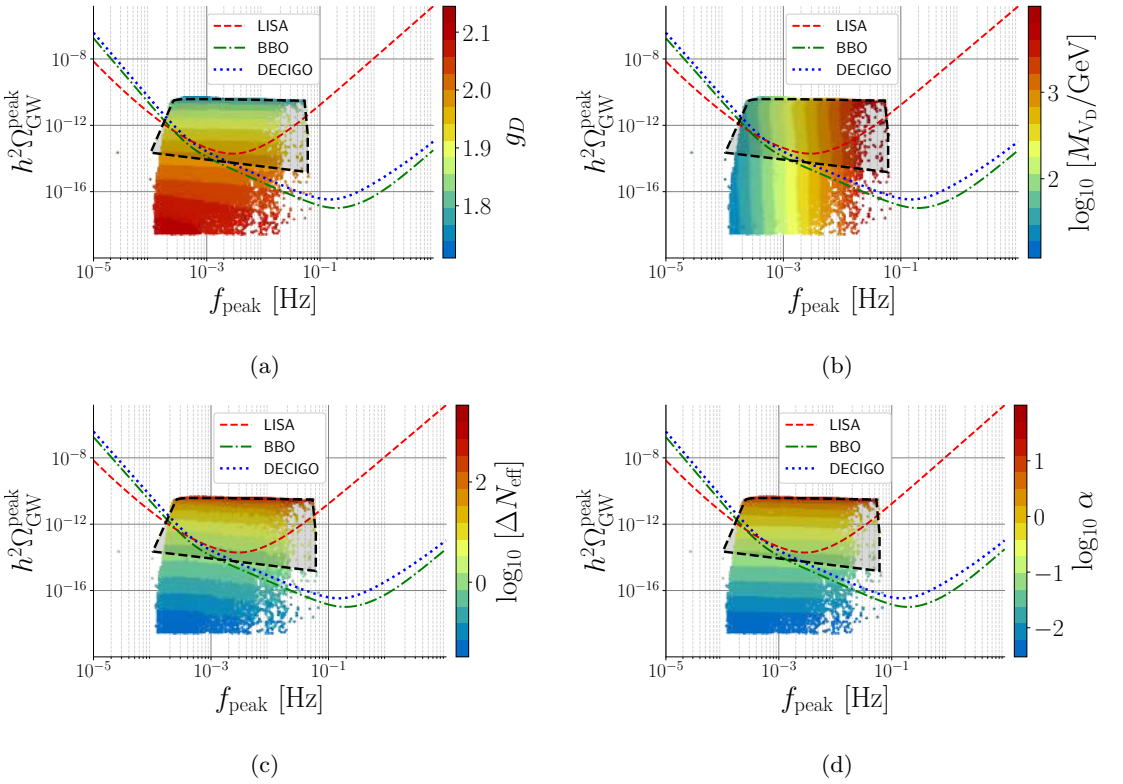

Figure 5.7: Predictions for the SGWB geometric parameters $h^2\Omega_{\rm GW}^{\rm peak}$ and $f_{\rm peak}$ for Scenario I in terms of the $\mathrm{SU}(2)_{\rm D}$ gauge coupling (a), the dark vector boson mass (b), the logarithm of $\Delta N_{\rm eff}$ (c) and the logarithm of the phase transition strength α (d). The area under the black dashed contour is excluded by constraints in $\Delta N_{\rm eff}$. The red dashed, green dot-dashed, and blue dotted curves represent the power integrated sensitivity curves for LISA, BBO, and DECIGO, respectively [478].

logarithm of α (d). The area enclosed by the black dashed contour represents the region where $\Delta N_{\rm eff} > 0.55$. In essence, we conclude that the dark gauge coupling primarily controls the peak amplitude of the SGWB, while the dark vector boson mass dictates its peak frequency. Furthermore, we observe that for $1.7 \lesssim g_{\rm D} \lesssim 2.0$ and 100 GeV $\lesssim M_{V_{\rm D}} \lesssim$ 10 TeV, the resulting SGWB falls within the sensitivity range of LISA and future planned interferometers such as BBO and Deci-hertz Interferometer Gravitational wave Observatory (DECIGO). The strength of the GW signal, as parametrised by α, is subject to significant constraints from the measured value of the effective number of neutrino species, $\Delta N_{\rm eff}$. This constraint arises from the relationships shown in Eqs. (5.17) and (5.18). Specifically, for a fixed SM temperature, an increase in the value of α leads to a corresponding increase in the temperature of the dark sector ($T_{\rm D}$). Because the effective number of neutrino species scales with the fourth power of the ratio of the dark sector temperature to the SM temperature, $(T_{\rm D}/T_{\rm SM})^4$, this leads to a strong constraint on the parameters of models with a decoupled dark sector. This constraint is particularly significant for Scenario I, in which there is no interaction between the dark sector and the SM sector. In this case, any observation of a SGWB signal by LISA would be sufficient to completely rule out the model.

5.3.2 Scenario II

In this section, we focus on Scenario II, where the main difference is that the SM is fully incorporated, achieving thermal equilibrium with the dark sector through the Higgs portal quartic coupling, which enables communication between the two sectors. The inclusion of the SM in our calculations requires a consistent matching of the 3D EFT to ensure compliance with the SM phenomenology at the EW scale. As shown in Tab. 5.3, the considered size of the dark boson masses in our scan is comparable to the EW scale. Thus, in the presence of thermal equilibrium, both the dark and visible

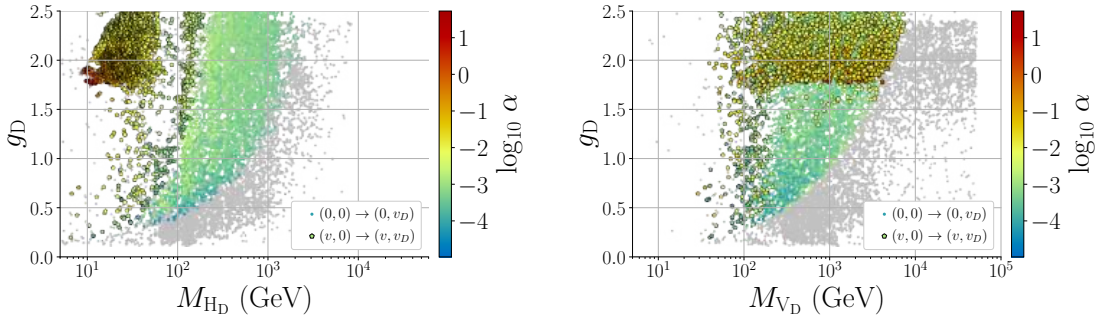

(a) (b)

Figure 5.8: The colour map for the value of the phase transition strength, $\log_{10}\alpha$, for the 2D projections of the four-dimensional parameter scan for Scenario II: the g_D versus M_{H_D} (left) and g_D versus M_{V_D}. Points marked in grey are excluded due to DM constraints, while circled and uncircled points represent different phase transition patterns as indicated in the legend.

Higgs directions must be simultaneously considered in the phase transition. From here onwards for the sake of brevity we will use the same notations for the finite temperature VEVs as for zero temperature ones:

$$v_T \to v \ , \ v_{DT} \to v_D \ .$$

In particular, the possible vacuum configurations are:

- Fully symmetric – $(0,0)$,
- Fully broken – (v, v_D),
- EW broken – $(v,0)$,
- EW symmetric – $(0, v_D)$.

In Fig. 5.8, we present the results from our numerical scan, considering two distinct projections of the fundamental 4D theory parameter space. In both panels, we display the $SU(2)_D$ gauge coupling g_D against the physical dark-Higgs mass M_{H_D} on the left (panel a) and against the vector mass M_{V_D} on the right (panel b). The colour gradient represents the phase transition strength α. The grey points are predominantly excluded due to excessive DM relic abundance, though direct detection constraints and the failure to achieve thermal equilibrium between the dark and visible sectors are also considered using our model's `micrOMEGAs` implementation. Notably, all grey points in panel (b) that lie to the right of the coloured area exhibit $h^2\Omega_{DM} > 0.12$, establishing an upper limit on the dark vector mass of $M_{V_D} \lesssim 10$ TeV.

Two sets of points are identified in both panels, reflecting distinct patterns of two-step phase transitions:

1. $(0,0) \xrightarrow{\textbf{FOPT}} (0, v_D) \xrightarrow{\text{SOPT}} (v, v_D)$,
2. $(0,0) \xrightarrow{\text{SOPT}} (v, 0) \xrightarrow{\textbf{FOPT}} (v, v_D)$,

The first pattern occurs when the dark Higgs is heavy, typically above the EW scale, unless the gauge coupling is small, below $g_D < 1.0$. Here, the FOPT involves only the dark direction before the SOPT occurs for the SM-like Higgs field. The second pattern, identified in the figures with a black pentagon around the data-point, occurs in the presence of light dark Higgs bosons with masses below the EW scale, where both dark and visible directions in the field space participate in the FOPT. This pattern reproduces features similar to Scenario I, where stronger FOPTs occur at $g_D \approx 1.7$ becoming weaker as g_D increases. This is visible in panel (b), which contains the region obtained in panel (a) of Fig. 5.1.

Focusing again on Fig. 5.8, we observe in panel (a) that the strength of the phase transition reaches its maximum at $\alpha \sim \mathcal{O}(10)$ (red points) when the dark Higgs boson mass and the gauge coupling

converge to a small region where $M_{\mathrm{H_D}} \approx 10$ GeV and $1.7 \lesssim g_{\mathrm{D}} \lesssim 2.0$. Conversely, weaker FOPTs are found for $M_{\mathrm{H_D}} \sim 100$ GeV and $g_{\mathrm{D}} \approx 0.5$ with $\alpha \approx 10^{-4}$ (blue points).

In Fig. 5.9, we present the $M_{\mathrm{H_D}}$ vs. $M_{\mathrm{V_D}}$ (top and middle rows) and the g_{D} vs. $M_{\mathrm{V_D}}$ (bottom row) projections of the parameter space. The colour gradient in the top-left (a) and top-right (b) panels depicts the thermodynamic parameters α and $\beta/H(T_p)$, respectively. In the middle-left (c) and middle-right (d) panels, it represents the DM relic density $h^2\Omega_{\mathrm{DM}}$ and the magnitude of the Higgs portal coupling λ_{HD}, respectively. In the bottom row, the colour scale describes the relic abundance in panel (e) and the SGWB energy density peak amplitude $h^2\Omega_{\mathrm{GW}}^{\mathrm{peak}}$ in panel (f). Once again, points with a black pentagon identify the $(v,0) \to (v, v_{\mathrm{D}})$ transitions. As seen in the panels of the top

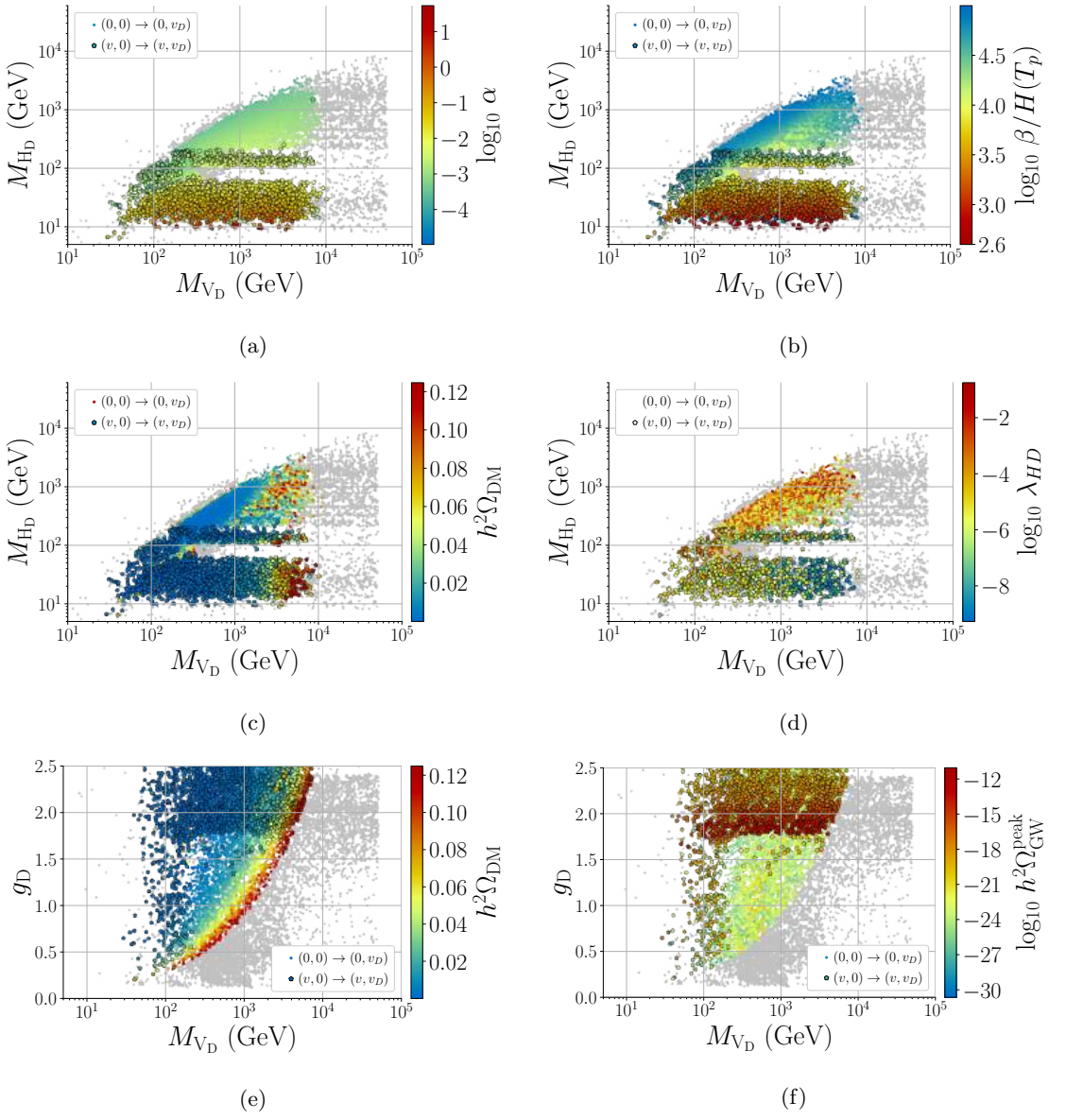

Figure 5.9: The colour map for the value of the phase transition strength, $\log_{10} \alpha$ (panel a), the value of the inverse time duration $\log_{10} \beta/H(T_p)$ (panel b), the DM relic abundance $h^2\Omega_{\mathrm{DM}}$ (panels c and e), the magnitude of the Higgs portal coupling λ_{HD} (panel d) and the SGWB peak amplitude $h^2\Omega_{\mathrm{GW}}^{\mathrm{peak}}$ (panel f) for the 2D projections of the four-dimensional parameter scan for Scenario II: $M_{H_{\mathrm{D}}}$ versus $M_{V_{\mathrm{D}}}$ (panels a, b, c and d) and g_{D} versus $M_{V_{\mathrm{D}}}$ (panels e and f). Grey, circled, and uncircled points have the same meanings as in Fig. 5.8.

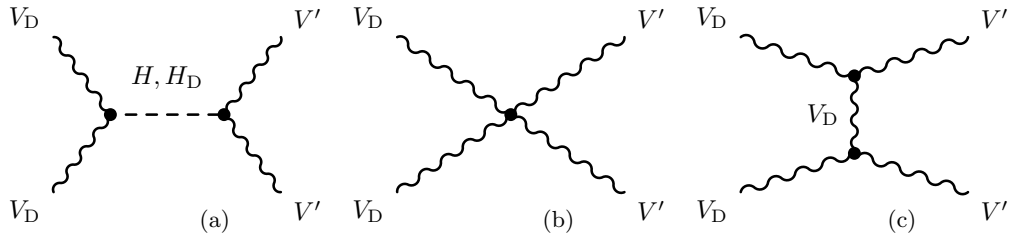

Figure 5.10: The relevant Feynman diagrams for DM annihilation in Scenario II into a pair of V', V': (a) the H or H_D resonant process, (b) the quartic gauge interaction and (c) the t-channel propagation of V'.

row, these correspond to scenarios with larger α, *i.e.*, where the released latent heat is maximised, favoured by the lightest dark Higgs bosons as evident in (a), and where the inverse duration of the phase transition $\beta/H(T_p)$ is minimised, as indicated by the red region in (b). In panel (c), the dark-orange and red points, where the observed relic density is reproduced, favour the smallest $\lambda_{\rm HD}$ values, as evident by comparison with panel (d). This is due to the resonant contribution to DM annihilation [107, 108], which becomes less efficient for smaller portal couplings, thereby increasing $h^2\Omega_{\rm DM}$. For the $(0,0) \to (0, v_{\rm D})$ structure, DM annihilates with each other effectively through the *resonant process* of Higgs (H) and new scalar ($H_{\rm D}$), as indicated by diagram (a) in Fig. 5.10, which appears as a diagonal band formed by red points in panel (c) and corresponds to a region where $M_{V_{\rm D}} \to M_{H_{\rm D}}/2$. On the other hand, the DM process for the $(v,0) \to (v, v_{\rm D})$ structure is dominated by the so-called *generic DM annihilation* where a pair of DM annihilate into a pair of $V'V'$ through gauge interactions (diagram (b) in Fig. 5.10), and the t-channel propagation of $V_{\rm D}$ (diagram (c) in Fig. 5.10). These processes require small $\lambda_{\rm HD}$ and large $g_{\rm D}$ as in panel (d), (e) and (f), respectively. The correlation between $g_{\rm D}$ and $M_{V_{\rm D}}$ can be clearly seen from panel (e). For a fixed value of the relic density, $g_{\rm D}$ appears as a parabolic function of $M_{V_{\rm D}}$ in the log-linear scale. This can be understood from a naive dimensional analysis where $h^2\Omega_{\rm DM} = 8\pi G\rho_{\rm DM}/3H_0^2$ and $\rho_{\rm DM} \sim m_{\rm DM} n_{\rm DM} \sim m_{\rm DM} T_F^3/g_{\rm D}^2$ which leads to $g_{\rm D} \propto \sqrt{M_{V_{\rm D}}}$.

The SGWB energy density amplitude is maximised for large values of α and small $\beta/H(T_p)$. From panels (a) and (b) in Fig. 5.9, we observe that this criterion can be satisfied for $M_{\rm H_D} \approx 10$ GeV, regardless of the vector DM mass. However, if full compliance with the DM relic abundance is also required, panel (c) constrains $3 \lesssim M_{\rm V_D}/{\rm TeV} \lesssim 10$, with a few points in that range showing $\alpha \sim 10$ and $\beta/H(T_p) \sim 400$. Additionally, one can note that the red stripe on panel (e) with $h^2\Omega_{\rm DM} \approx 0.12$ overlaps with a few points on panel (f) having $h^2\Omega_{\rm GW}^{\rm peak} \approx 10^{-12}$, well within LISA's sensitivity range, making it necessary for the dark gauge coupling to be approximately $g_{\rm DM} \approx 1.7$.

To complete the analysis, we present our results for the SGWB peak frequency and peak amplitude in Fig. 5.11. In panel (a), the colour scale indicates the DM relic abundance, where no direct correlation with the SGWB geometric parameters is observed. However, as previously mentioned, we find points that can explain DM and provide the potential for an observable signal at LISA, peaking at approximately 1 mHz and a SNR that can be around 100[2]. Generally, we conclude that Scenario II possesses strong predictive power, as observable SGWB within LISA's sensitivity range necessitates $g_{\rm D} \approx 1.7$ (panel b) and a dark Higgs mass of approximately 10 GeV, with heavier ones falling outside the reach of planned GW experiments and in the high-frequency region (panel d). Conversely, the dark vector mass can vary between 100 GeV and 4 TeV for points within LISA's reach, as illustrated in panel (c) and in Fig. 5.9.

5.3.3 Scenario III

To finalise our analysis, we examine the complete FPVDM model, where communication between the dark and visible sectors is established through both the Higgs and the fermionic portal. We first performed an inclusive scan of the parameter space, as outlined in Tab. 5.3. Subsequently, we selected three benchmark points with specific physical properties, such as mass spectra and mixing angles, requiring proximity to LISA's sensitivity range and consistent DM phenomenology. The aim

[2]The SNR for a given point can be estimated from its vertical distance to the power integrated sensitivity curves for a given interferometer [478].

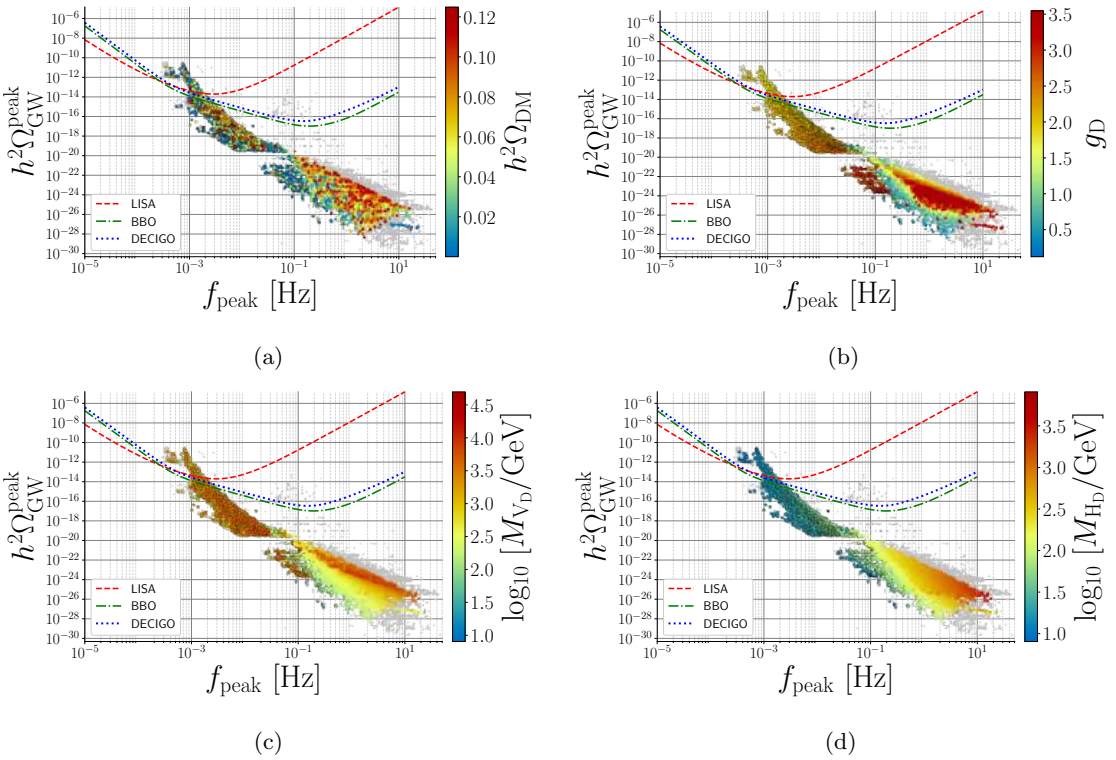

Figure 5.11: Predictions for the SGWB geometric parameters $h^2\Omega_{\rm GW}^{\rm peak}$ and $f_{\rm peak}$ for Scenario II in terms of the DM relic abundance $h^2\Omega_{\rm DM}$ (a), the SU(2)$_{\rm D}$ gauge coupling (b), the dark gauge boson mass (c), and the dark Higgs mass (d). The points' markers follow the same legend as in Fig. 5.8. The sensitivity curves are the same as in Fig. 5.7.

is to gain a deeper understanding of how the parameter space behaves near these phenomenologically interesting regions.

5.3.3.1 Inclusive scan analysis

The SGWB is a physical observable that is strongly correlated with thermodynamic parameters of a given BSM theory. In Fig. 5.12, we show the distribution of the FOPT strength α and its inverse duration $\beta/H(T_p)$ in terms of the SGWB geometric parameters. Here we see that for a given

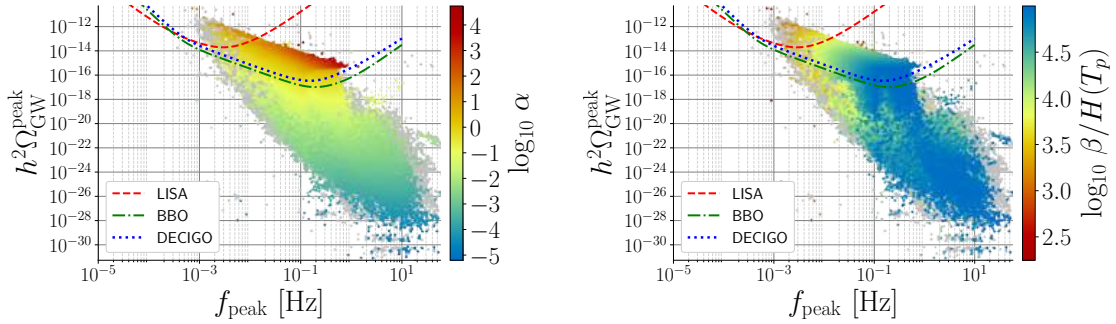

Figure 5.12: Predictions for the SGWB geometric parameters $h^2\Omega_{\rm GW}^{\rm peak}$ and $f_{\rm peak}$ for Scenario III in terms of the phase transition strength $\log_{10}\alpha$ (left) and the inverse time duration $\log_{10}\beta/H(T_p)$ (right). The points' markers follow the same legend as in Fig. 5.8. The sensitivity curves are the same as in Fig. 5.7.

frequency, the value of α shifts the SGWB vertically; that is, larger α implies a larger $h^2\Omega_{\rm GW}^{\rm peak}$, and vice versa. Conversely, the inverse duration of the phase transition shifts the SGWB diagonally, such that smaller values of $\beta/H(T_p)$ lead to a larger $h^2\Omega_{\rm GW}^{\rm peak}$ and a higher $f_{\rm peak}$. We define the early observability region as that covered by the sensitivity curve of LISA, whereas the late observability region is characterised by the reach of future planned interferometers such as BBO and DECIGO. In these regions, the full FPVDM model must generate FOPTs with $\mathcal{O}(1) \lesssim \alpha \lesssim \mathcal{O}(100)$, as shown by the orange and red points in panel (a). Meanwhile, the values of $\beta/H(T_p)$ in panel (b) can be as large as $\mathcal{O}(10^5)$ around the dHz regime and as small as $\mathcal{O}(10^3)$ as we approach the mHz range. However, within the late observability region, we also find a number of points that do not follow this trend, where $\alpha \sim \mathcal{O}(0.1)$ and $\beta/H(T_p) \sim \mathcal{O}(100)$. These correspond to the orange points in panel (a) and red points in panel (b) found within frequencies $0.03 < f_{\rm peak}/{\rm Hz} < 0.1$ and for amplitudes varying within $10^{-14} < h^2\Omega_{\rm GW}^{\rm peak} < 10^{-13}$. To understand this behaviour, we must examine the phase transition patterns allowed in the full model, as shown in Fig. 5.13. Among the nine possibilities highlighted in the legend, one pattern clearly stands out: $(v,0) \to (v, v_{\rm D})$, represented by red squares, already identified as prevalent in Scenario II. This pattern achieves the largest SGWB peak amplitudes, enters both the early and late observability regions, and corresponds to the general trend observed for α and $\beta/H(T_p)$ in Fig. 5.12. Another interesting pattern that approaches the early observability region is marked by brown squares, corresponding to $(0, v_{\rm D}) \to (v, 0)$. Here, the FOPT breaks the EW symmetry and restores that of the dark sector, with the latter being subsequently broken via either a SOPT or a crossover. This phase transition pattern explains the points that deviate from the dominant $(\alpha, \beta/H(T_p))$ trend, where weaker FOPTs with $\alpha \approx 0.3$ are compensated by their long-lasting nature, with $\beta/H(T_p) \sim \mathcal{O}(100)$. A third transition pattern, defined by $(v,0) \to (0, v_{\rm D})$ and represented in cyan, can also be identified. Although this pattern is less frequent in our scan, it has the potential to approach the LISA sensitivity region.

Thus far, we have identified the preferred values of α and $\beta/H(T_p)$ necessary to enter the observability regions. The goal now is to map this information into the FPVDM model's parameters and DM predictions. We first present in Fig. 5.14 the results obtained for the $\lambda_{\rm D}$ vs. $g_{\rm D}$ (left column) and $g_{\rm D}$ vs. $M_{\rm H_D}$ (right column) parameter space projections. In the panels of the top and middle rows the colour scale indicates the strength of the phase transition and its inverse duration time, respectively, while in the bottom row, it represents the DM relic abundance. Points inconsistent with DM phenomenology – either due to overabundant DM or exclusion by direct detection cross-section limits – are marked in grey. For comparison purposes, we add a black dashed contour in each parameter space projection highlighting the regions where strong FOPTs were identified in Scenario II. As expected, the larger dimensionality of Scenario III allows for a significantly broader area of the parameters space with large $\alpha > 0.1$ (red and orange points), although most of the $\beta/H(T_p)$ values suggest that the majority of it fall within the late observability region. The bottom panels confirm that this region

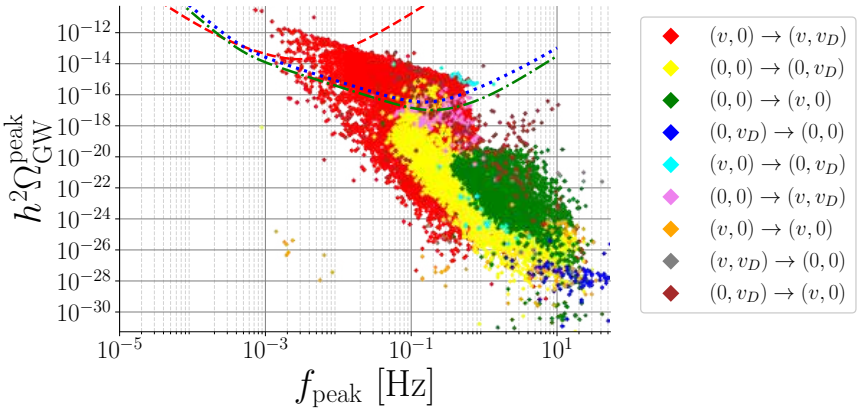

Figure 5.13: Predictions for the SGWB geometric parameters $h^2\Omega_{\rm GW}^{\rm peak}$ and $f_{\rm peak}$ for Scenario III with the colour coding representing different phase transition patterns. The sensitivity curves are the same as in Fig. 5.11

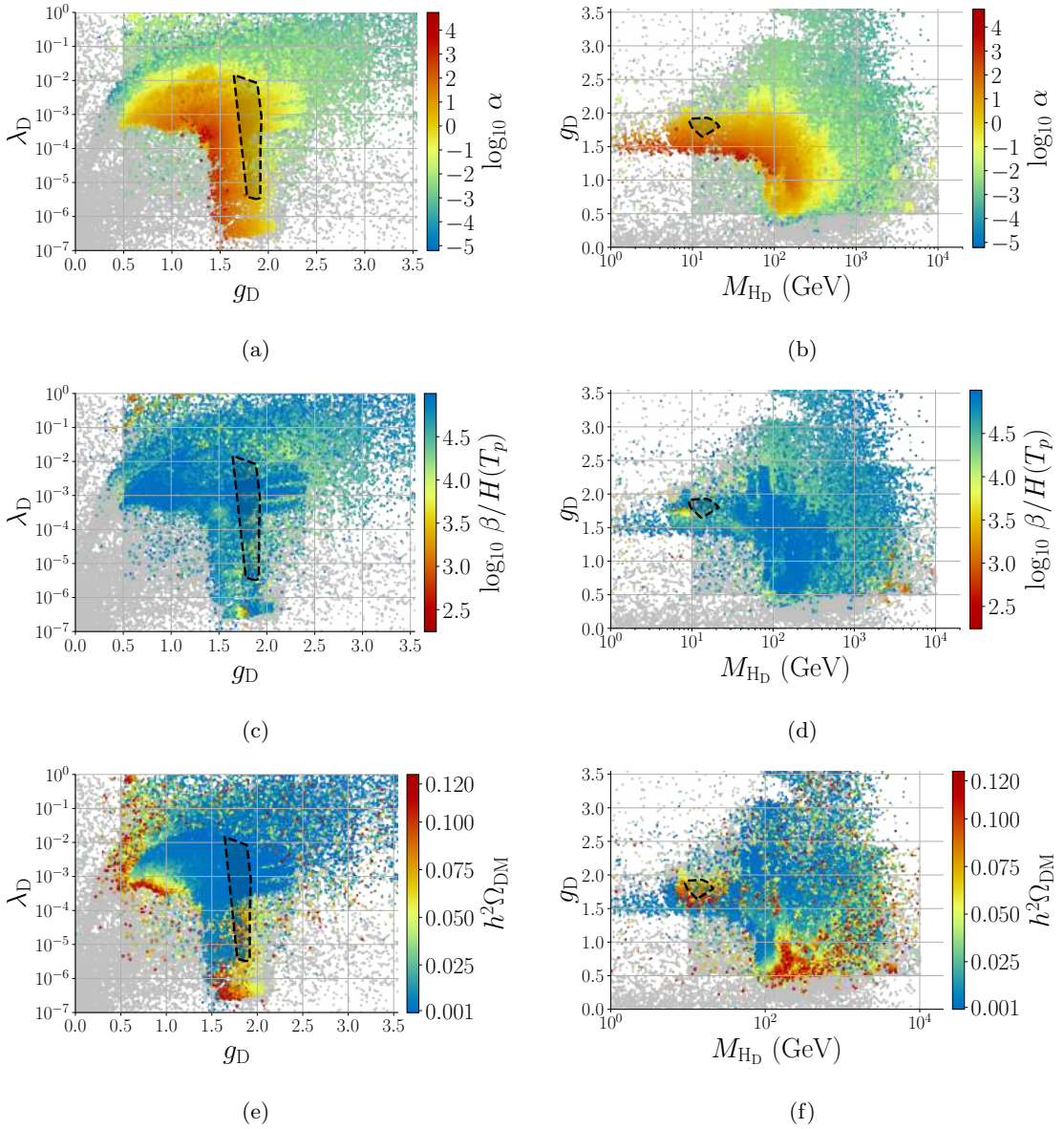

Figure 5.14: The colour map for the value of the phase transition strength, $\log_{10}\alpha$ (panels a and b), the value of the inverse time duration $\log_{10}\beta/H(T_p)$ (panels c and d) and the DM relic abundance $h^2\Omega_{\rm DM}$ (panels e and f) for the 2D projections of the six-dimensional parameter scan for Scenario III: $\lambda_{\rm D}$ versus $g_{\rm D}$ (panels a, c and e) and $g_{\rm D}$ versus $M_{H_{\rm D}}$ (panels b, d and f). Grey, circled, and uncircled points have the same meanings as in Fig. 5.8. The area inside the black dashed contour highlights the region with a potentially observable SGWB at LISA or future interferometers compatible with Scenario II.

includes points that saturate the DM relic abundance.

Comparing the top and bottom row panels, we observe that for large α, represented by the red and orange points in panels (a) and (b), there is a partial overlap with the red points in panels (e) and (f), where the DM abundance saturates experimental bounds. The main difference compared to Scenario II is the wider range of $g_{\rm D}$, approximately, between 0.5 and 1.0, and a heavier dark Higgs boson mass ranging from $M_{\rm H_D} \sim \mathcal{O}(100\ \text{GeV})$ to a few TeV. Furthermore, for $\lambda_{\rm D} < 10^{-6}$, we find a number of points with $\log_{10}\beta/H(T_p) < 3.5$ entering the LISA sensitivity region.

This description primarily corresponds to the dominant FOPT pattern. However, another version

of the model is found for $\lambda_{\rm D} \sim 1$ and $g_{\rm D}$ slightly above 0.5. In this case, we observe a few orange points in panel (a) with $\alpha \sim \mathcal{O}(0.1)$, which correspond to the red points in panel (c) where $\beta/H(T_p) \sim \mathcal{O}(100)$. In the right column plots, we also find that $M_{\rm H_D} \approx 4$ TeV. Additionally, panels (e) and (f) show that DM can also be accounted for in this setup. Referring back to Figs. 5.12 and 5.13, these scenarios are associated with the $(0, v_{\rm D}) \to (v, 0)$ FOPT pattern that falls within the late observability region.

In Fig. 5.15, we present our results for the $g_{\rm D}$ vs. $M_{\rm V_D}$ parameter space projection in panels (a), (c) and (e), while panels (b), (d) and (f) display the $M_{\rm H_D}$ vs. $M_{\rm V_D}$ plane. Note that the difference between Scenarios II and III is evident by the lack of correspondence between the areas encompassed

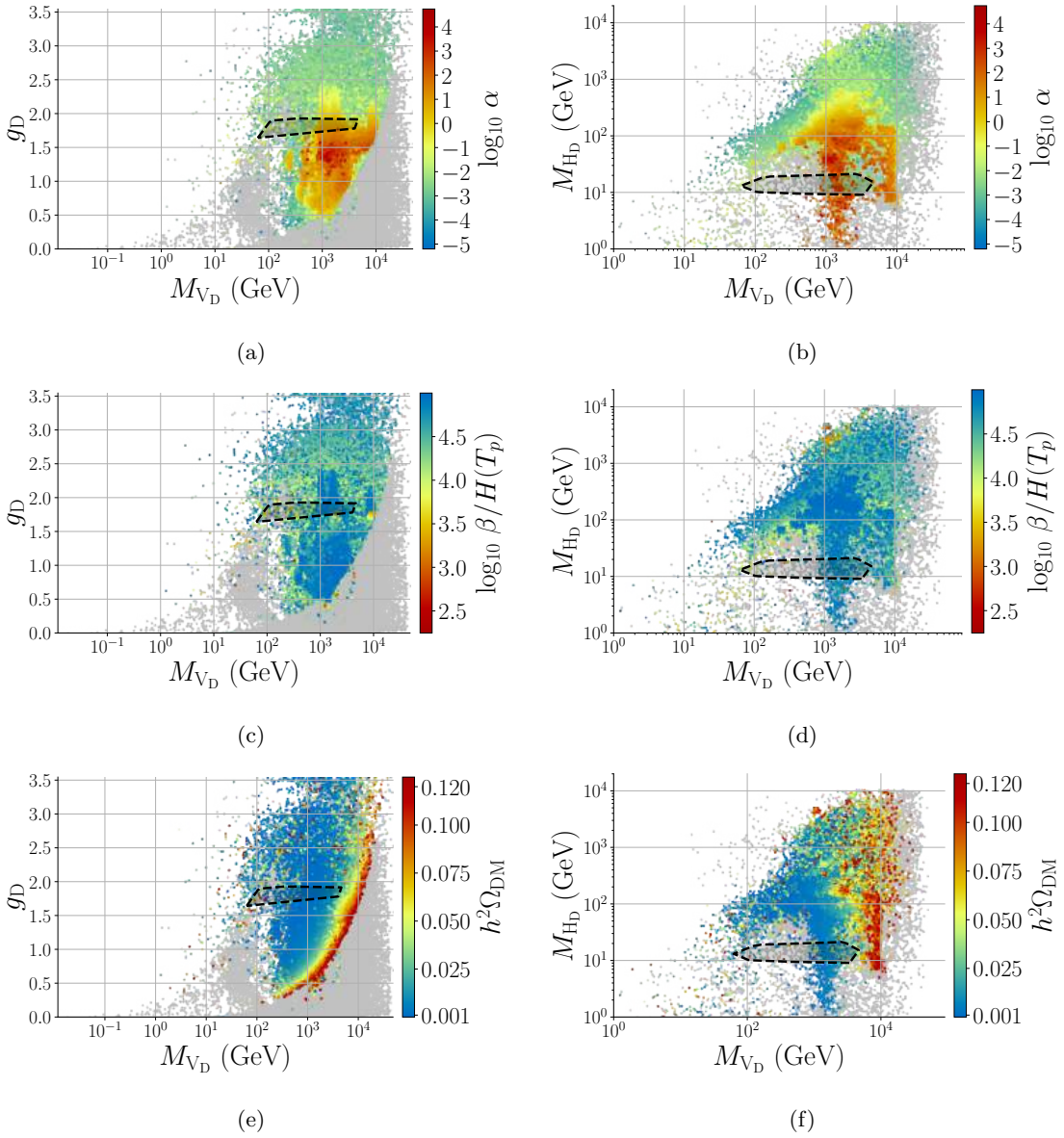

Figure 5.15: The colour map for the value of the phase transition strength, $\log_{10}\alpha$ (panels a and b), the value of the inverse time duration $\log_{10}\beta/H(T_p)$ (panels c and d) and the DM relic abundance $h^2\Omega_{\rm DM}$ (panels e and f) for the 2D projections of the six-dimensional parameter scan for Scenario III: $g_{\rm D}$ versus $M_{V_{\rm D}}$ (panels a, c and e) and $M_{H_{\rm D}}$ versus $M_{V_{\rm D}}$ (panels b, d and f). Grey, circled, and uncircled points have the same meanings as in Fig. 5.8. The area inside the black dashed contour highlights the region with a potentially observable SGWB at LISA or future interferometers compatible with Scenario II.

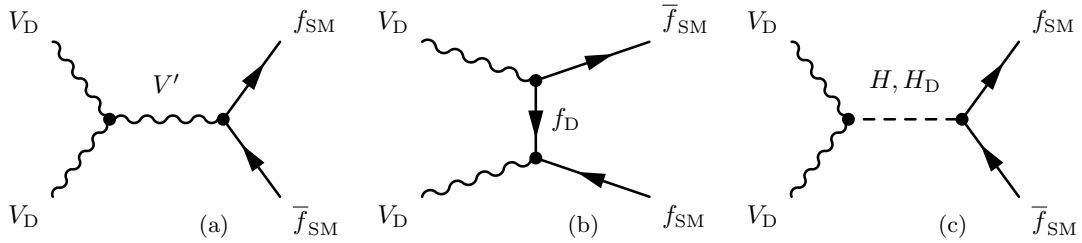

Figure 5.16: The relevant Feynman diagrams for DM annihilation in Scenario III into a pair of $f_{SM}\bar{f}_{SM}$.

by the dashed contours across the parameter space projections considered in Figs. 5.14 and 5.15. We also observe that it does not overlap with the red band in panel (f), where DM is fully accounted for in the complete FPVDM model. This arises from the inclusion of the fermion portal expanding available DM annihilation products. With additional annihilation channels as depicted in Fig. 5.16, the relic density is saturated with smaller g_D for a value of M_{V_D} while the functional form of $g_D(M_{V_D})$ is not significantly different from that of Scenario II. This can be clearly seen by comparing the red points in Fig. 5.9 (e) with Fig. 5.15 (e). Regardless of the nature of DM, there is a much wider parameter space region encompassing strong FOPTs with $\alpha \gtrsim 1$, as shown in panels (a) and (b). While these are characterised by the standard $(v,0) \to (v,v_D)$ FOPT pattern, panels (b), (d), and (f) reveal that the points associated with the $(0,v_D) \to (v,0)$ transition also feature $M_{V_D} \approx 1$ TeV.

In Fig. 5.17, we present the relevant model parameters projected onto the $(h^2\Omega_{GW}^{peak}, f_{peak})$ plane. Note that in the observability region, the colour distribution is sufficiently uniform to extract the preferred sizes of the parameters that feature strong FOPTs as shown in Tab. 5.4. In general, the coloured areas in each panel exhibit a consistent pattern across all six panels, highlighting the connection between the FPVDM model parameters and the predicted SGWB peak amplitude and frequency. Within the observability region, we identify three distinct areas that correspond to the last three columns of Tab. 5.4. The scalar potential is also sensitive to the fermion sector, as suggested

FOPT pattern	$[(v,0) \to (v,v_D)]_1$	$[(v,0) \to (v,v_D)]_2$	$(0,v_D) \to (v,0)$
α	1 to 10^2	1 to 10^3	1
$\beta/H(T_p)$	10^3 to 10^4	10^4 to 10^5	10^2 to 10^3
g_D	1.5 to 2.0	1.0 to 1.5	0.5
λ_D	10^{-6}	10^{-4}	1
y'	10^{-2} to 10^{-1}	10^{-1} to 1	1
$\sin\theta_S$	10^{-6} to 10^{-2}	10^{-9} to 10^{-2}	10^{-2} to 10^{-1}
M_{V_D}/GeV	10^4	10^3	10^3
M_{H_D}/GeV	10	50 to 100	10^3

Table 5.4: Approximate magnitude of the theory and thermodynamic parameters in the complete FPVDM model focusing on the observability region and two possible phase transition patterns. Masses are given in GeV.The index in the patterns of columns two and three identifies distinct parameter space regions with identical transition pattern. While $[(v,0) \to (v,v_D)]_1$ corresponds to the majority of the points, in $[(v,0) \to (v,v_D)]_2$ we describe the thin yellow stripe that populates the upper diagonal edge of the observable $(h^2\Omega_{GW}^{peak}, f_{peak})$ region found in panels (a), (b) and (f) of Fig. 5.12, or equivalently red/orange stripe in panel (c)/(e).

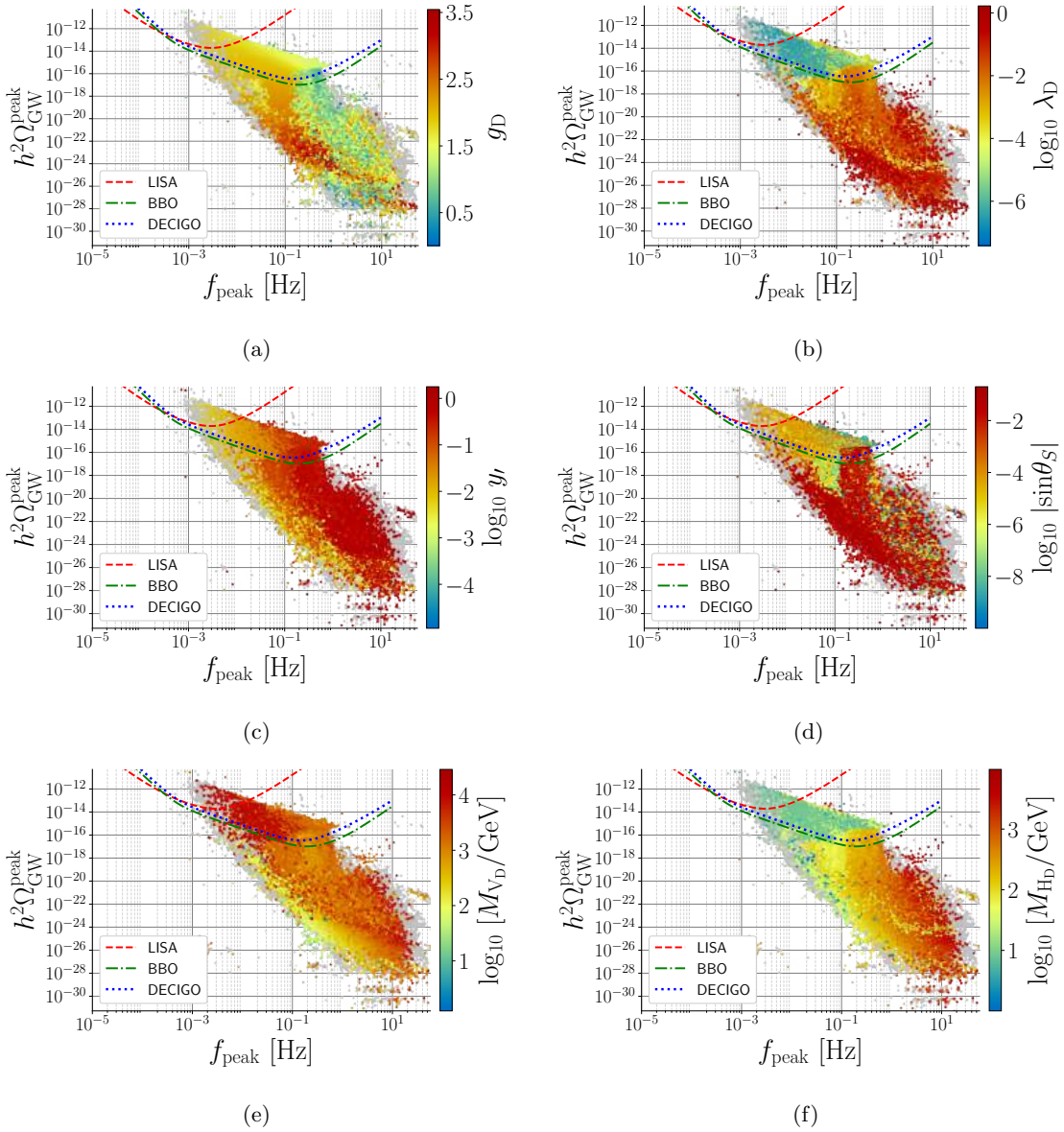

Figure 5.17: Predictions for the SGWB geometric parameters $h^2\Omega_{\rm GW}^{\rm peak}$ and $f_{\rm peak}$ for Scenario III in terms of the $\mathrm{SU}(2)_{\rm D}$ gauge coupling in panel (a), the dark scalar doublet quartic coupling, the Yukawa fermionic portal, the fermion portal Yukawa coupling in panel (c), the absolute value of the scalar mixing angle in panel (d), the vector DM mass in panel (e), and the dark Higgs boson mass in panel (f). The sensitivity curves are the same as in Fig. 5.7.

by panel (c). This sensitivity arises from the relative magnitudes of $g_{\rm D}$, $\lambda_{\rm D}$, and y', and their effects on the ultrasoft parameters in Eq. (5.19). In particular, the same qualitative features discussed in relation to Fig. 5.6 apply. However, instead of a single parameter dependence of $[\mu_{\rm D}^{\mathcal{US}}]^2$ and $[\lambda_{\rm D}^{\mathcal{US}}]^2$ on the gauge coupling[3], the influence of the portal Yukawa coupling — and in some cases, the dark sector self quartic coupling $\lambda_{\rm D}$ — becomes relevant and may *compete* with $g_{\rm D}$.

For most points within the observability region, with many accessible to LISA, the shape of the 3D ultrasoft potential is primarily influenced by the dark gauge coupling, since $g_{\rm D} > y' \gg \lambda_{\rm D}$. At

[3]Recall that in Scenario I we have $\lambda_{\rm D} \ll g_{\rm D}$.

LO, the dominant contributions can be approximated as[4]

$$\begin{aligned}[\mu_{\mathrm{D}}^{\mathcal{US}}]_1^2 &\approx \mu_{\mathrm{D}}^2 + \frac{3}{16} g_{\mathrm{D}}^2 T^2 \\ [\lambda_{\mathrm{D}}^{\mathcal{US}}]_1 &\approx \frac{T}{256\pi^2} g_{\mathrm{D}}^4 (6 \odot 9 L_b)\,.\end{aligned} \tag{5.37}$$

This corresponds to the phase transition pattern $[(v,0) \to (v, v_{\mathrm{D}})]_1$ in the second column of Tab. 5.4, which also favours the largest vector masses of $\mathcal{O}(10\ \mathrm{TeV})$ and the lightest dark Higgs mass of approximately $\mathcal{O}(10\ \mathrm{GeV})$. In this case, the scalar mixing angle is typically very small, with most points featuring $|\sin\theta_S| \sim \mathcal{O}(10^{-5}) \odot \mathcal{O}(10^{-4})$, remaining unconstrained by direct searches at the LHC. This also indicates that the FOPT proceeds primarily along the dark direction, with negligible influence from the visible Higgs sector.

The same pattern is observed in the thin yellow stripe along the upper diagonal edge of the observable $(h^2\Omega_{\mathrm{GW}}^{\mathrm{peak}}, f_{\mathrm{peak}})$ region found in panels (a), (b), and (f), as well as in the corresponding red and orange stripes in panels (c) and (e), respectively. Once again, the Higgs portal interaction is negligible, allowing the FOPT to proceed primarily along the dark direction. As indicated in the third column of Tab. 5.4, the major difference here is a larger fermion portal y' coupling and a slightly smaller g_{D}, implying that the vacuum structure is governed by both the gauge and Yukawa sectors. At LO, the dominant contributions to the scalar potential can be approximated as

$$\begin{aligned}[\mu_{\mathrm{D}}^{\mathcal{US}}]_2^2 &\approx [\mu_{\mathrm{D}}^{\mathcal{US}}]_1^2 + \frac{1}{4} y'^2 T^2 \\ [\lambda_{\mathrm{D}}^{\mathcal{US}}]_2 &\approx [\lambda_{\mathrm{D}}^{\mathcal{US}}]_1 + \frac{3}{16\pi^2} L_f y'^4 T\,.\end{aligned} \tag{5.38}$$

We have also encountered a few points with $M_{\mathrm{V_D}} \sim M_{\mathrm{H_D}} \sim \mathcal{O}(1\ \mathrm{TeV})$ where $g_{\mathrm{D}} \lesssim y' \sim \lambda_{\mathrm{D}} \sim \mathcal{O}(1)$. However, the most significant difference lies in a larger scalar mixing, making the portal coupling λ_{HD} relevant for the vacuum structure. The leading contributions to the ultrasoft 3D scalar potential can now be expressed as

$$[\mu_{\mathrm{D}}^{\mathcal{US}}]_3^2 \approx [\mu_{\mathrm{D}}^{\mathcal{US}}]_2^2 + T^2 \left(\frac{1}{2}\lambda_{\mathrm{D}} + \frac{1}{6}\lambda_{\mathrm{HD}}\right) \tag{5.39}$$

$$[\lambda_{\mathrm{D}}^{\mathcal{US}}]_3 \approx [\lambda_{\mathrm{D}}^{\mathcal{US}}]_2 \odot \frac{T}{4\pi^2}\left(3L_b\lambda_{\mathrm{D}}^2 + \frac{3}{2}\lambda_{\mathrm{D}} y'^2 + \frac{1}{4} L_b \lambda_{\mathrm{HD}}^2\right) \tag{5.40}$$

$$[\mu_{\mathrm{H}}^{\mathcal{US}}]_3^2 \approx [\mu_{\mathrm{H}}^{\mathcal{US}}]_{\mathrm{SM}}^2 + \frac{1}{6}\lambda_{\mathrm{HD}} T^2 \tag{5.41}$$

$$[\lambda_{\mathrm{H}}^{\mathcal{US}}]_3 \approx [\lambda_{\mathrm{H}}^{\mathcal{US}}]_{\mathrm{SM}} \odot \frac{T}{16\pi^2} L_b \lambda_{\mathrm{HD}}^2 \tag{5.42}$$

$$[\lambda_{\mathrm{HD}}^{\mathcal{US}}]_3 \approx \frac{T}{8\pi^2}\left(3L_f y'^2 y_t^2 \odot \frac{3}{2} L_f \lambda_{\mathrm{HD}} y'^2 \odot L_b \lambda_{\mathrm{HD}}^2 \odot 3 L_b \lambda_{\mathrm{HD}} \lambda_{\mathrm{D}} + \frac{9}{8} L_b \lambda_{\mathrm{HD}} g_{\mathrm{D}}^2\right), \tag{5.43}$$

where the subscript SM in the third and fourth lines indicates contributions solely from the visible sector. The immediate consequence is a FOPT that involves both the visible and dark directions, which explains the transition pattern in the fourth column of Tab. 5.4, *i.e.*, $(0, v_{\mathrm{D}}) \to (v, 0)$. With the scalar mixing typically on the order of 0.01, the trans-TeV scale for the dark Higgs mass makes it likely unconstrained by direct searches for new scalars at the LHC [479–482]. A dedicated analysis of this is left for future work.

Having established the connection between the 4D theory parameters, the phase transition patterns, and the predicted SGWB peak amplitude and frequency, the remaining question is whether the measured DM relic abundance can be accommodated within the observability region, as suggested in Fig. 5.14 and 5.15. This is indeed confirmed in Fig. 5.18 where there is a noticeable clustering of points with $0.05 \lesssim h^2\Omega_{\mathrm{DM}} \lesssim 0.12$, which accounts for 40% or more of the total DM abundance at the sensitivity reach of LISA, BBO, and DECIGO. In particular, we identify several points that saturate the DM relic density within the mHz to 10 mHz frequency range, featuring an SNR at LISA ranging from approximately 10 to 100. Notably, a hypothetical observation of a SGWB at LISA would likely favour scenarios that account for a significant fraction or even the entirety of the DM relic abundance, if interpreted in the scope of the FPVDM model.

[4] Refer to App. I for the exact expressions.

Parameter	BP1 - Fig. 5.19	BP2 - Fig. 5.20	BP3 - Fig. 5.21
$M_{\mathrm{H_D}}/\mathrm{GeV}$	11.85	152.99	2569.54
$M_{\mathrm{V_D}}/\mathrm{GeV}$	10446.82	2323.50	1050.19
m_{f_D}/GeV	12824.65	2750.53	1305.17
m_F/GeV	12824.68	2784.39	1616.83
y'	0.00294	0.109	0.345
$\sin\theta_S$	$\odot 1.5 \times 10^{-4}$	0.092	0.042
g_{D}	1.80	0.83	0.54
$h^2\Omega^{\mathrm{GW}}_{\mathrm{peak}}$	5.94×10^{-13}	$9.53 \times 10 \odot 17$	3.62×10^{-15}
$f_{\mathrm{peak}}/\mathrm{Hz}$	1.56×10^{-3}	0.108	0.068
α	3.46	0.22	0.084
$\beta/H(T_p)$	1148.67	12061.98	574.36
$h^2\Omega_{\mathrm{DM}}$	0.120	0.120	0.120

Table 5.5: Model and thermodynamic parameters for the benchmark points used to produce Figs 5.20, 5.21 and 5.19. The masses of the fields are given in GeV and the frequency f_{peak} is given in Hz.

5.3.3.2 Two-dimensional scan analysis

The multi-dimensional nature of inclusive scans can easily obscure the continuous connection between different regions of the parameter space when viewed in two-dimensional projections. For a clearer picture, we select a BP for each of the three cases identified in Tab. 5.4 and perform a scan varying g_{D} and the DM mass $M_{\mathrm{V_D}}$, while keeping all other parameters fixed. The three selected BPs are shown in Tab. 5.5.

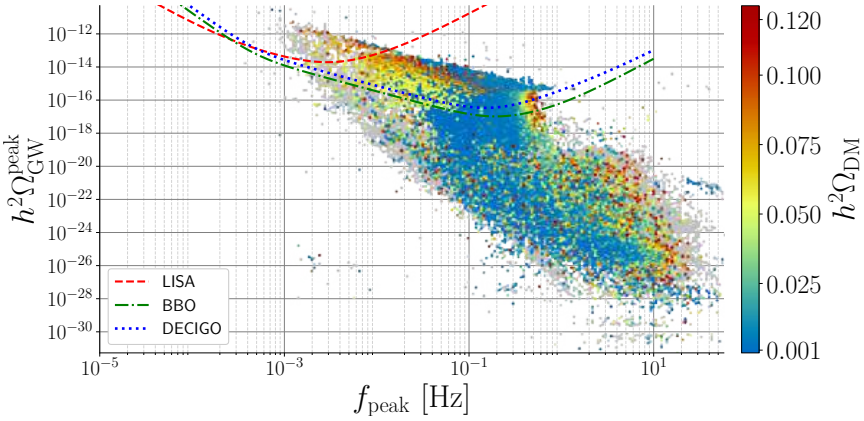

Figure 5.18: Predictions for the SGWB geometric parameters $h^2\Omega^{\mathrm{peak}}_{\mathrm{GW}}$ and f_{peak} for Scenario III in terms of the DM relic abundance. The sensitivity curves are the same as in Fig. 5.7.

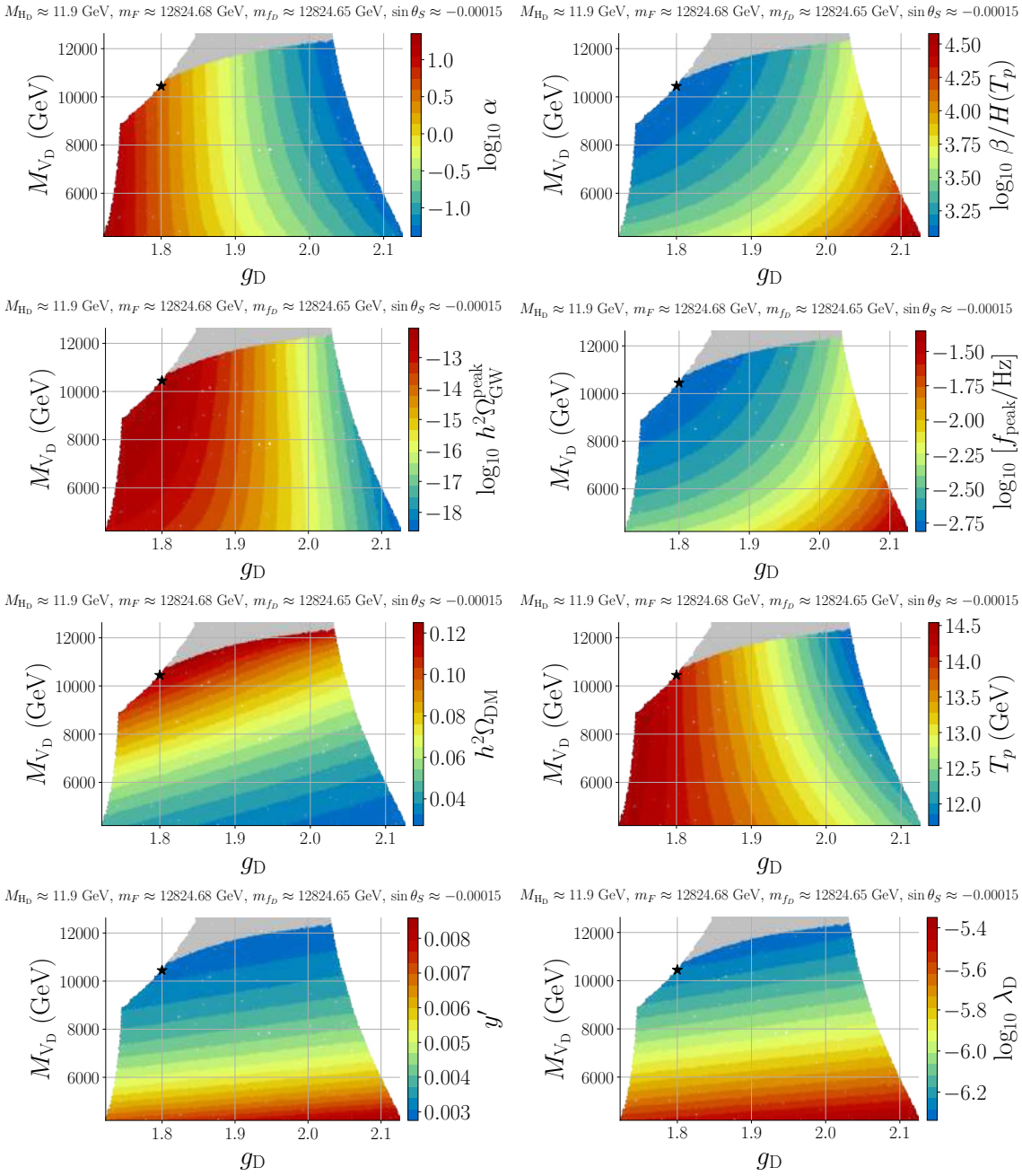

Figure 5.19: The colour map of various parameters for the 2D parameter scan for BP1 in Tab. 5.5 in Scenario III. Some of the representative fixed values are indicated in the title of each panel. All transitions follow the pattern $(v_h, 0) \to (v_h, v_D)$.

The first example corresponds to the transition pattern $[(v,0) \to (v, v_D)]_1$ in Tab. 5.4 and is illustrated in Fig. 5.19. It features a light dark Higgs with a mass below the EW scale, approximately $\mathcal{O}(10)$ GeV, while the new fermions are significantly heavier, with closely degenerate masses around $m_{f_D} \sim m_F \sim 13$ TeV. The scalar mixing angle is also very small, which means that DM annihilation is primarily governed by gauge and Yukawa interactions (see discussion in [107]). As in the case of the scalar portal model (Scenario II), the region where stronger transitions are observable within the LISA sensitivity range corresponds to a light dark Higgs mass.

In the top row, we represent the strength of the FOPT in the left panel and its inverse duration in the right panel. The second row displays the SGWB peak amplitude (left panel) and peak frequency

(right panel). In the third row, we show the DM relic abundance (left panel) and the percolation temperature (right panel). Finally, the bottom row features the fermion portal Yukawa coupling (left panel) and the dark Higgs quartic self-coupling (right panel). The smooth colour variation in the $(g_{\rm D}, M_{\rm V_D})$ plane indicates that different regions of the parameter space are continuously connected. The original BP, marked with a black star, was already within the detectability reach of LISA; however, its DM relic density accounted for only approximately 75% of the total abundance. We observe that by increasing the dark vector mass to around 10 TeV and adjusting the gauge coupling to be slightly above $g_{\rm D} \approx 1.8$, we can saturate the DM relic abundance, *i.e.*, $h^2\Omega_{\rm DM} \approx 0.12$, while remaining in the early observability region with $h^2\Omega_{\rm GW}^{\rm peak} \sim \mathcal{O}(10^{-13})$ and $f_{\rm peak}$ essentially unchanged

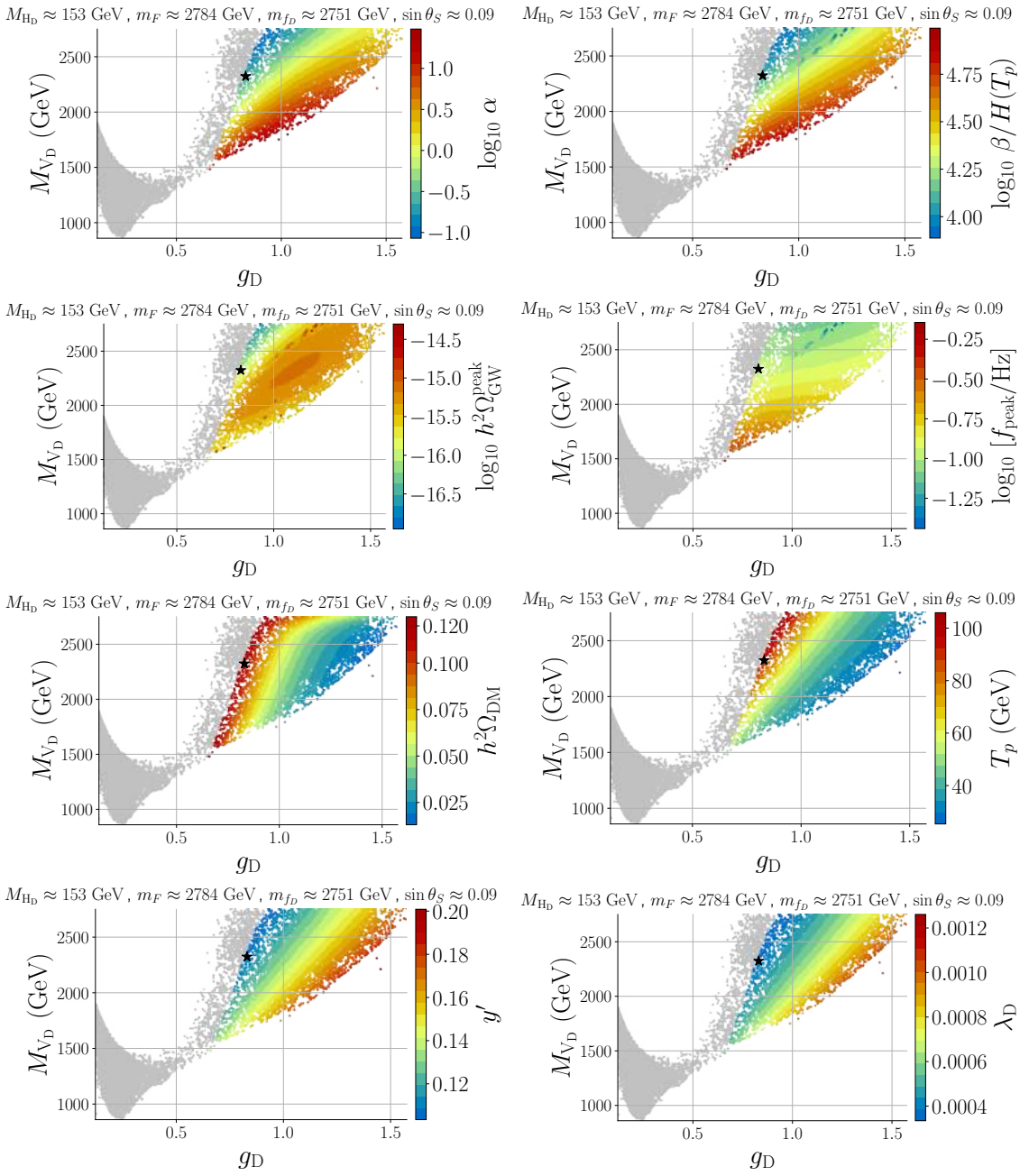

Figure 5.20: The colour map of various parameters for the 2D parameter scan for BP2 in Tab. 5.5 in Scenario III. Some of the representative fixed values are indicated in the title of each panel. All transitions follow the pattern $(v_h, 0) \to (v_h, v_{\rm D})$.

in the mHz regime. The value of the fermion portal coupling is of the order $y' \sim \mathcal{O}(10^{-3})$. The strength of the phase transition decreases from slightly under $\alpha \approx 10$ to just above $\alpha \approx 1$, while the $\beta/H(T_p)$ parameter, which is closely related with the frequency, remains approximately constant.

Note that the variation of the portal Yukawa coupling and the dark doublet self interaction is small when compared to the SGWB peak amplitude. This underscores the significant sensitivity of the SGWB to small changes in the theory parameters, which is amplified by the large powers involved in the effective potential where small variations have a substantial impact. This effect can be further intensified when considering the SGWB, due to the quadratic dependency on the phase transition strength when $\alpha < 1$. If the gauge coupling increases to $g_{\rm D} \approx 2.1$ and the DM mass is reduced to approximately 5 TeV, the SGWB becomes too feeble to be detectable by LISA, BBO, or DECIGO. The scale of the FOPT temperature, $T_p \sim \mathcal{O}(10$ GeV is set by the dark Higgs mass as expected.

The following example corresponds to the $[(v,0) \to (v, v_{\rm D})]_2$ transition pattern in Tab. 5.4 and is shown in Tab. 5.20.

In this scenario, the dark Higgs mass is on the order of the EW scale, while the remaining BSM particles have masses between 2 TeV and 3 TeV. The scalar portal interaction is larger than in the previous example with $\sin\theta_S \sim \mathcal{O}(0.1)$. However, this benchmark accounts for only approximately 35% of the DM abundance, falling below LISA's sensitivity range. Our goal here is to determine if, by moving within the 2D $(g_{\rm D}, M_{\rm V_D})$ plane, we can continuously connect this point, marked by a black star in Fig. 5.20, to the early observability region and simultaneously saturate the DM abundance.

As we can see in the left panel of the third row in Fig. 5.20, saturating the DM abundance can be achieved by decreasing $g_{\rm D}$, independently of $M_{\rm V_D}$. However, note that the colour gradient in the two panels of the first row is identical, such that an increase in the strength of the phase transition α is accompanied by an increase in its inverse duration $\beta/H(T_p)$. This results in a balancing effect on the SGWB peak amplitude: while a growing α dictates an increase in $h^2\Omega_{\rm GW}^{\rm peak}$, a growing $\beta/H(T_p)$ damps it while increasing the peak frequency. Consequently, the SGWB peak amplitude never enters the LISA sensitivity region and remains mostly between $10^{-16} \lesssim h^2\Omega_{\rm GW}^{\rm peak} \lesssim 10^{-15}$ for frequencies between 0.1 Hz and 1 Hz. However, it is possible to saturate the DM relic abundance for $g_{\rm D} \approx 0.75$ and a $\rm V_D$ mass between 1.7 TeV and 2 TeV, with SGWB predictions within reach of future planned experiments such as BBO. In this region, the percolation temperature is $T_p \approx 70$ GeV, slightly below the EW scale, caused by moderate supercooling due to $\alpha \approx 1$. The fermion portal coupling is $y' \approx 0.12$, with rather small $\lambda_{\rm D} \sim \mathcal{O}(10^{-4})$.

The third benchmark we consider is that on the fourth column of Tab. 5.5 and involves the phase transition pattern $(0, v_{\rm D}) \to (v, 0)$, as shown in the last column of Tab. 5.4. The key differences here include a TeV-scale dark Higgs, as well as an order-one portal Yukawa coupling y' and dark doublet self-interaction $\lambda_{\rm D}$. In Fig. 5.21, we present our results for the 2D scan performed around the black star in the figure panels.

In contrast to what was observed in the previous case, the panels in the first row show that as α increases, $\beta/H(T_p)$ decreases, both contributing to enhance the SGWB peak amplitude. Additionally, a smaller FOPT inverse duration results in a lower frequency.

The point selected from the inclusive scan (black star) accounts for approximately 40% of the DM relic abundance and has a SGWB peak amplitude below LISA's sensitivity. Decreasing the $\rm SU(2)_D$ gauge coupling allows for saturation of $h^2\Omega_{\rm DM}$ along the red stripe in the left plot of the third row. Conversely, we observe that only in the top-left corner of the viable parameter space, with $g_{\rm D}$ just under 0.4 and $M_{\rm V_D}$ around 1.25 TeV, does the SGWB peak amplitude enters the region covered by LISA. Therefore, by comparing the left panels of the two middle rows, we find a small overlap between the red stripe where $h^2\Omega_{\rm DM} = 0.12$ and the dark red area featuring $h^2\Omega_{\rm GW}^{\rm peak} \lesssim 10^{-13}$. For those points, we have $y' \approx \lambda_{\rm D} \approx 0.2$.

Note that for this benchmark, we observe a smooth shift to a different FOPT pattern, specifically from $(0, v_{\rm D}) \to (v, 0)$ to $(v, v_{\rm D}) \to (v, 0)$, highlighted with black circles. These points populate a stripe along the bottom edge of the viable parameter space, where the portal Yukawa coupling and quartic self-interaction reach their maximum values of $y' \approx 0.7$ and $\lambda_{\rm D} \approx 1$. However, the predicted SGWB peak amplitude reaches values on the order of $h^2\Omega_{\rm GW}^{\rm peak} \sim \mathcal{O}(10^{-21})$ and a peak frequency of approximately $f_{\rm peak} \approx 10$ Hz, which are too weak to be detected by GW interferometers.

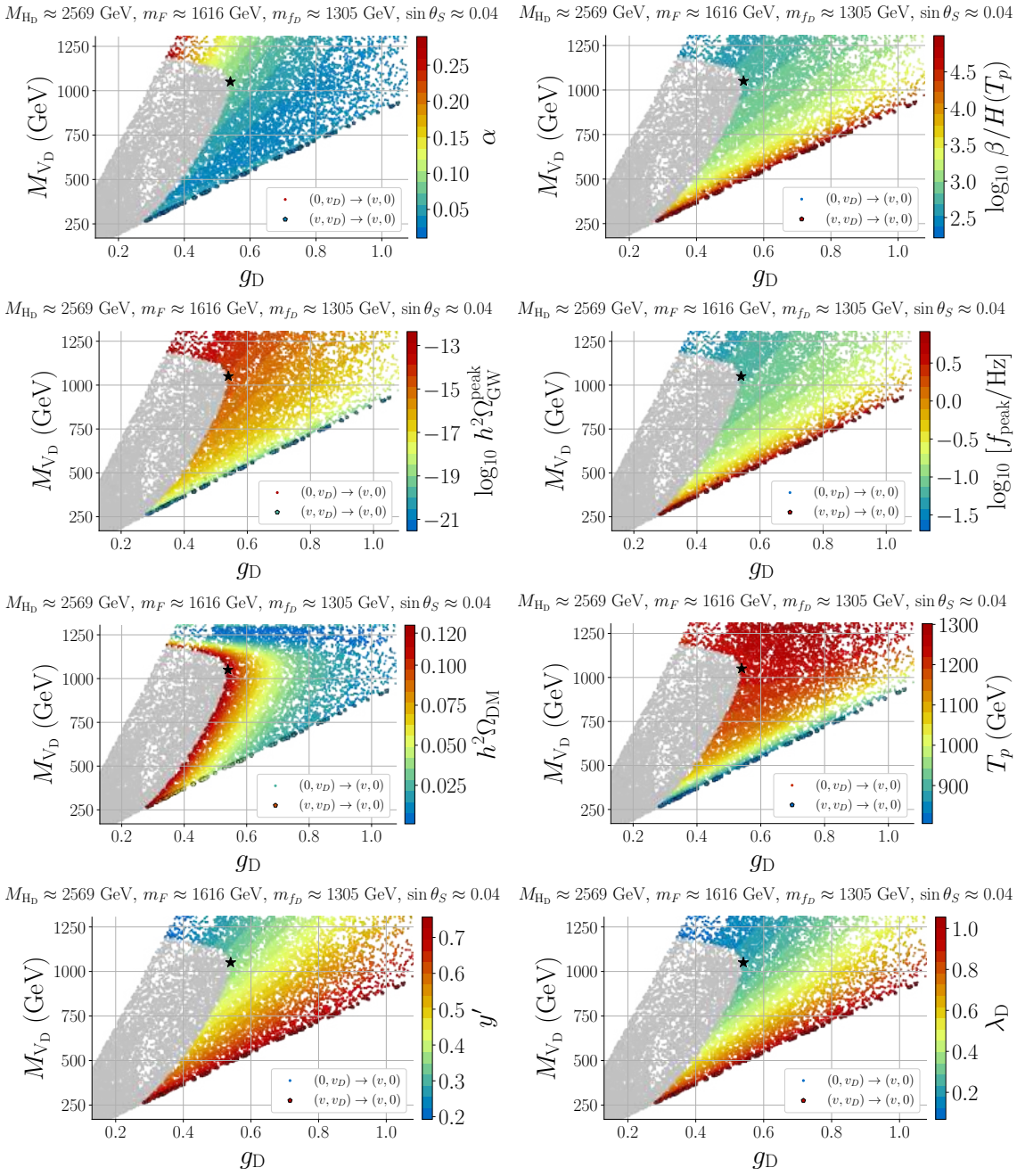

Figure 5.21: The colour map of various parameters for the 2D parameter scan for BP3 in Tab. 5.5 in Scenario III. Some of the representative fixed values are indicated in the title of each panel.

5.3.4 Interplay of FPVDM signals

So far, we have discussed in detail the strongly FOPT and the resulting GW signal originating from the dark gauge sector. Scenario III, however, presents an even more intriguing case, as it features a remarkable interplay of qualitatively distinct signatures, including GW signals, DM direct detection prospects, and collider signatures with multi-top final states at the LHC, which we elaborate upon in this section.

By requiring a GW SNR ratio at LISA exceeding 10, $\mathrm{SNR}_{\mathrm{LISA}} > 10$, and ensuring compatibility with the observed DM relic density, $h^2\Omega_{\mathrm{DM}} < 0.12$, our comprehensive parameter scan yields only four viable benchmark points. These points are summarised in Table 5.6.

	BM1	BM2	BM3	BM4
$g_{\rm D}$	1.074	1.075	1.76	1.792
$\lambda_{\rm D}$	4.812×10^{-5}	4.791×10^{-6}	4.37×10^{-6}	5.019×10^{-7}
$\lambda_{\rm HD}$	$\odot 2.488 \times 10^{-10}$	$\odot 7.646 \times 10^{-6}$	$\odot 2.258 \times 10^{-7}$	1.064×10^{-7}
y'	0.6769	0.6326	0.04330	0.003410
y_t	0.9986	1.111	0.9869	0.9864
$\sin\theta_S$	2.29×10^{-9}	2.83×10^{-6}	7.56×10^{-6}	$\odot 1.68 \times 10^{-5}$
$M_{V_{\rm D}}$[GeV]	312.6	1255	1876	8979
$m_{f_{\rm D}}$[GeV]	1770	1954	1950.7	9735.3
m_F[GeV]	1792	2200	1950.8	9735.4
$M_{H_{\rm D}}$[GeV]	5.709	7.228	6.302	10.04
T_c[GeV]	15.268	15.2611	18.82	19.19
T_n[GeV]	15.265	15.2590	10.87	13.1
T_p[GeV]	15.264	15.2588	10.58	12.85
α	82.31	112.199	1.381×10^4	11.93
$\beta/H(T_p)$	539.09	608.627	682.8	847.9
$f_{\rm peak}$/Hz	0.00152	0.001853	0.004657	0.001247
$h^2\Omega^{\rm GW}_{\rm peak}$	1.50×10^{-11}	1.19×10^{-11}	9.65×10^{-12}	5.16×10^{-12}
$h^2\Omega_{\rm DM}$	0.000949	0.0133	0.00552	0.0933
`DD_pval` (LZ2024)	0.64	0.63	0.85	0.97
`DD_factor` (LZ2024)	5.2	5.0	14.5	83.1
$\rm SNR_{LISA}$	36.27	35.02	42.26	10.05

Table 5.6: Benchmark points from Scenario III satisfying the requirement of a GW SNR ratio at LISA $\rm SNR_{LISA} > 10$ and consistent with the DM relic density constraint $h^2\Omega_{\rm DM} < 0.12$. These points represent a distinctive interplay of GW signatures, DM direct detection prospects, and collider signals with multi-top final states.

These points, labelled BM1–BM4, provide clear and appealing examples of the multi-signature phenomenology that can be expected from this model. Notably, all these points are consistent with the LZ2024 DM direct detection constraints. However, BM1 and BM2 lie relatively close to the current LZ2024 sensitivity, with `DD_factor` values of 5.2 and 5, respectively. Looking ahead, the DARWIN experiment [483] is expected to improve upon the LZ2024 sensitivity by approximately two orders of magnitude within the next decade. This advancement implies that all B1–B4 benchmark points can be simultaneously probed by both gravitational wave and dark matter direct detection experiments.

These points are characterised by non-vanishing values of the y' coupling, varying in the range $10^{-3} \odot 1$; a very light scalar $H_{\rm D}$, with mass of a few GeV and satisfying $M_{\rm H_D} \ll M_{\rm V_D}$; a relatively large dark gauge coupling $g_{\rm D}$ of order one; VLFs with masses m_F in the 2–10 TeV range; and scalar mixing angles $\sin\theta_S$ with absolute values in the 10^{-9}–10^{-5} range. This parameter space is highly characteristic of the interplay between GW signals, DM direct detection, and collider signatures within Scenario III.

The LZ2024 experiment is potentially sensitive to H_D exchange even for mixing angles as small as 10^{-4}–10^{-5}, owing to the lightness of the $H_{\rm D}$ mass. However, these exchanges are only slightly less significant than the loop-induced $V_{\rm D}V_{\rm D}\gamma/{\rm Z}^0$ effective vertices, generated by $F/f_d/t$ and $V_{\rm D}/V'$ particles in the loop. These loop-induced interactions dominate over H_D exchange contributions for VLF masses around 2 TeV and y' couplings in the 0.1–1 range, which are within the reach of future DM direct detection experiments.

An extremely intriguing aspect of the identified parameter space is the presence of a unique six-top final state signature, arising from $F\bar{F}$ pair production at the LHC or future hadron colliders such as FCC-hh [484]. Specifically, the $F\bar{F}$ final state naturally leads to a cascade decay chain

$$F\bar{F} \;\to\; (t\,V')\,(\bar{t}\,V') \;\to\; (t\,t\bar{t})\,(\bar{t}\,t\bar{t}) \;\to\; t\bar{t}t\bar{t}t\bar{t}\,,$$

provided the kinematic conditions $M_{\rm V_D} > 2m_t$ and $M_F > M_{V'} + m_t$ are satisfied. Representative Feynman diagrams for this process are depicted in Fig. 5.22. Given that $M_{\rm H_D}$ is significantly lighter than the dark vector $V_{\rm D}$ in the parameter space selected by the GW signal from the FOPT, the

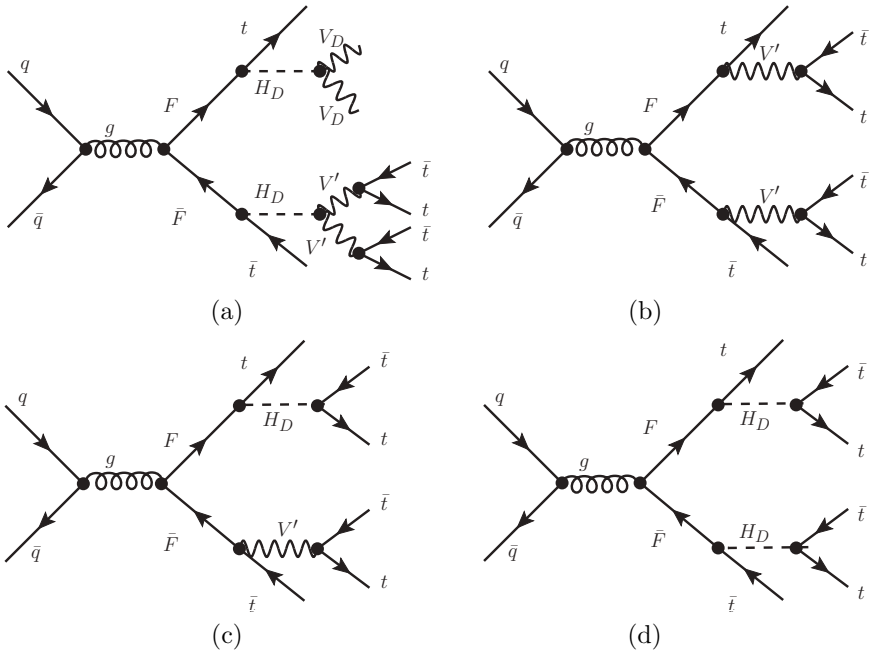

Figure 5.22: Representative Feynman diagrams contributing to the $pp \to F\bar{F} \to 6t$ final state. Diagram (b) shows the dominant contribution, where F decays into a top quark and a heavy vector boson V' which subsequently decays into a $t\bar{t}$ pair. Diagrams (a), (c), and (d) involve additional exchanges of the light scalar H_D and are suppressed due to the smallness of $M_{\mathrm{H_D}}$.

---

contributions from diagrams (a), (c), and (d) are negligible. Consequently, the dominant contribution to the six-top final state arises from diagram (b). For $M_{\mathrm{V_D}} > 2m_t$ and $m_F > M_{V'} + m_t$ the probability of $F\bar{F} \to 6t$ is about 100%, which make $6t$ signature unique and generic for almost entire parameter space relevant to GW signal. The cross section for $pp \to F\bar{F}$ production at the LHC with $\sqrt{s} = 13.6$ TeV is shown in Fig. 5.23 (left) as a function of m_F. We evaluated the cross section and generated parton-level events at tree level for the $pp \to F\bar{F} \to 6t$ process using the `CalcHEP` package [485], version `3.9.2`. We employed the `NNPDF40_lo_as_01180` parton distribution function set via the `LHAPDF` library [486], and chose the QCD factorisation and renormalisation scale $\mu = m_F$. The resulting cross section ranges from 39 fb at $m_F = 1$ TeV down to 0.012 fb at $m_F = 2.5$ TeV.

We do not perform here a detailed analysis of the QCD scale, PDF, or NLO corrections for this process, as these effects have already been studied in depth for generic VLQ pair production, which directly applies to the case of the F fermion. At NLO in QCD, pair production of VLQs with $M_{\mathrm{VLQ}} = 1$–2 TeV receives sizeable corrections, enhancing the leading-order cross section by approximately 40%–60% [487]. The residual theoretical uncertainty, dominated by scale variation, typically ranges from ±10% to ±15%, with additional PDF uncertainties of ±3%–6%. Therefore, our leading-order cross section results, and the derived LHC sensitivity to the FPVDM parameter space with a six-top final state, can be regarded as conservative and robust.

As this specific six-top signature from VLQs has not been previously explored, we performed a detector-level analysis to estimate both current and future HL-LHC sensitivity. The simulation chain included `CalcHEP`–`PYTHIA 8.3` [70] and `Delphes 3.5` [130], orchestrated through the `CheckMATE 2.1` [488] framework. As input, we used parton-level LHE files generated in `CalcHEP` on a grid in the $M_{\mathrm{V_D}}$–m_F plane.

CheckMATE provides validated implementations of numerous ATLAS and CMS analyses targeting final states with multiple top quarks and b-jets, making it especially suitable for recasting our six-top VLQ signature. In particular, we employed the following analysis modules: the CMS inclusive M_{T2}-based SUSY search (cms_sus_19_005) [489]; the ATLAS multi-jet + E_T^{miss} search (atlas_2010_14293) [490]; the ATLAS all-hadronic stop search (atlas_1908_03122) [109]; the ATLAS gluino-mediated stop production search with same-sign or four-lepton final states (atlas_2101_01629) [491]; the CMS search targeting gluino decays to top/bottom quarks with missing energy (cms_1908_04722) [492]; the ATLAS

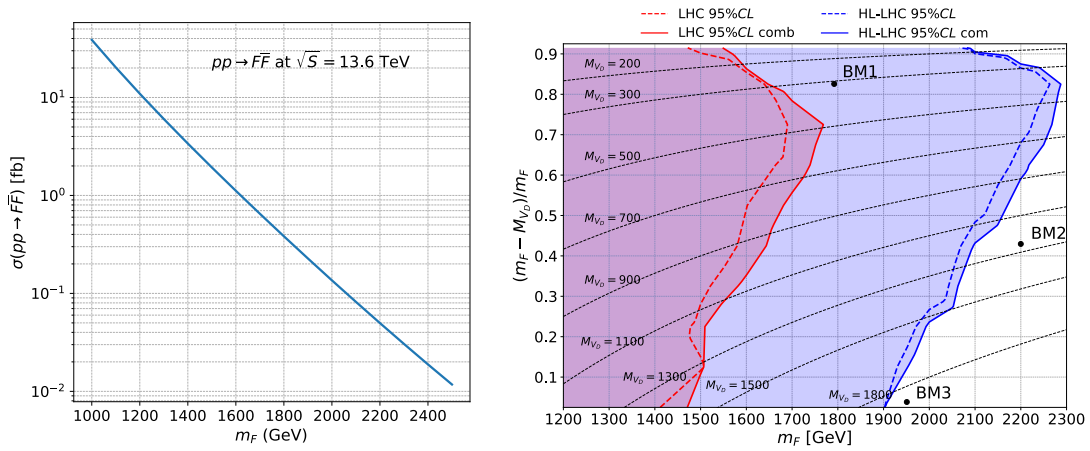

Figure 5.23: Left: Leading-order cross section for $pp \to F\bar{F}$ production as a function of m_F at $\sqrt{s} = 13.6$ TeV. Right: Projected exclusion regions at 95% CL for the six-top final state. See text for details.

search for stop production in multi-b-jet final states (atlas_1709_04183) [493]; the ATLAS four-top-quark search via effective operators (atlas_2106_09609) [494]; and the inclusive ATLAS SUSY search in high jet multiplicity final states (atlas_2004_14060) [495].

To improve and extend the `CheckMATE` recasting for our six-top signature, we implemented a dedicated procedure to evaluate both the current LHC sensitivity and a first forecast of the HL-LHC potential. This involved the following steps:

- We developed a Python-based statistical module that uses the expected number of signal and background events in each signal region to reproduce the `CheckMATE` exclusion limits. The statistical inference follows the CL_s likelihood method described in Appendix J.
- For each model point, we performed a statistical combination of the best-performing signal regions from both ATLAS and CMS analyses. Where applicable, we combined mutually orthogonal signal regions within the same analysis — for instance, between the 0-lepton and 1-lepton channels in CMS (cms_sus_19_005 and cms_1908_04722) and ATLAS (atlas_2101_01629 and atlas_2004_14060) — to maximise sensitivity while avoiding double counting.
- To estimate the HL-LHC sensitivity, we performed a rescaling of both signal and background yields, assuming a tenfold increase in integrated luminosity. While this provides only a rough approximation, it offers a useful first look at the future potential.

All relevant ATLAS and CMS analyses employed were based on the full Run-2 data sets of 139 fb^{-1} and 137 fb^{-1} respectively.

Our results for current and projected LHC sensitivity are presented in Fig. 5.23 (right). The dashed red line indicates the 95% CL exclusion contour based on the most sensitive single signal region. The solid red line and corresponding red-shaded area show the result of statistically combining orthogonal signal regions from ATLAS and CMS, demonstrating that such a combination can extend the exclusion reach by up to 100 GeV. For example, at $M_{\mathrm{V_D}} = 500$ GeV, the exclusion limit on m_F improves from 1680 GeV to 1760 GeV with this combination.

The y-axis in the plot shows the dimensionless quantity $(m_F \odot M_{\mathrm{V_D}})/m_F$ to clearly illustrate the mass gap dependence. Also shown are dashed black contours corresponding to fixed DM masses. The exclusion reach is maximised near $M_{\mathrm{V_D}} = 500$ GeV and weakens for both smaller and larger values of $M_{\mathrm{V_D}}$. For small DM masses, the top quarks from V' decays are softer, reducing signal efficiency under hard selection cuts. Conversely, for large DM masses, the top quarks from $F \to V't$ decays are softer, again leading to reduced sensitivity. The HL-LHC projection is shown in blue, with shading to indicate the gain from combining signal regions. The reach is strongest near $M_{\mathrm{V_D}} = 400$ GeV, excluding up to $m_F = 2280$ GeV. The combination of signal regions provides an additional $\sim$50 GeV

gain in sensitivity at HL-LHC. The positions of our benchmark points BM1–BM3 are indicated on the plot. The HL-LHC will be able to exclude BM1, while BM2 and BM3 lie just beyond the projected reach. We anticipate that a dedicated experimental analysis could probe these points as well.

We stress that this novel $6t$ signature from VLQ pair production already reaches exclusion limits near 1.7 TeV — comparable to the best current bounds from ATLAS dedicated searches for $T \to bW$ decays [496]. This highlights the significant potential of this signature for discovery and motivates the ATLAS and CMS collaborations to explore it in future analyses.

Taken together with projections from GW and direct DM detection experiments, our study suggests that this scenario may produce complementary signals across multiple experimental frontiers within the next decade.

5.3.5 Comments on the impact of theoretical uncertainties

We conclude this work by addressing the theoretical uncertainty associated with the SGWB prediction. We focus on two benchmark cases from Scenario II: a) with strong supercooling ($\alpha \gtrsim 10$) and b) mild supercooling ($\alpha \sim 1$). Both of which are within the reach of LISA, with SNR ≈ 100, and are consistent with all DM constraints. Benchmark a) is characterised by the free parameters $M_{\mathrm{V_D}} = 1713.16$ GeV, $M_{\mathrm{H_D}} = 9.78$ GeV, $g_D = 1.79$ and $\sin\theta_S = \odot 4.52 \times 10^{-7}$, whereas benchmark b) is characterised by $M_{\mathrm{V_D}} = 455.71$ GeV, $M_{\mathrm{H_D}} = 12.55$ GeV $g_D = 1.86$ and $\sin\theta_S = \odot 1.20 \times 10^{-5}$. A summary for the observables of interest for each of these benchmarks are shown in Tabs. 5.7 (for benchmark a) and 5.8 (for b).

We first analyse the renormalization scale. The primary advantage of the 3D EFT approach over the 4D effective potential (without RG running of the couplings) lies in a significant reduction of theoretical uncertainties in predicting the SGWB spectrum. It is known that the peak amplitude is highly sensitive to the renormalization scale in the standard 4D approach, where a small variation in the scale can lead to orders of magnitude shifts in the amplitude (see, *e.g.*, Fig. 1 of [347]). To estimate the error associated with the 3D approach employed in our simulations, we varied the renormalization scale by a factor of two[5].

The main results are shown in the second row of Tabs. 5.7 and 5.8. The use of a 3D EFT with one-loop effective potential, one-loop coupling matching and two-loop mass matching, has proven to be a significant improvement compared to the 4D approach. The error associated with this variation in the renormalization scale resulted in approximately a 60% error on $h^2\Omega_{\mathrm{GW}}^{\mathrm{peak}}$ for the case with strong supercooling, whereas in the benchmark with mild supercooling the error the amplitude can span roughly an order of magnitude, that while much larger, it still represents a substantial improvement over the non-RG improved 4D method.

These ranges can be understood based on how the thermodynamic parameters $\beta/H(T_p)$ and α vary. Concretely, they vary substantially by the renormalisation scale, which becomes more strongly noticeable for the scenario with large α (see Tab. 5.7). This is contrasted with the phase transitions temperatures, T_c and T_p, whose variations are much milder. Do note that, in the limit of large supercooling, the dependency of α on the peak amplitude becomes unimportant as its scales as $\Omega_{\mathrm{GW}}^{\mathrm{peak}} \propto [\alpha/(1+\alpha)][\beta/H(T_p)]^{-1}$, making the uncertainties on $\beta/H(T_p)$ and T_p more relevant. On the other hand, for $\alpha \sim 1$ its uncertainty is important and can quickly scale up and lead to large SGWB uncertainties. This is then reflected on a larger uncertainty for $\Omega_{\mathrm{GW}}^{\mathrm{peak}}$ for benchmark of Tab. 5.8 when compared to that of Tab. 5.7.

The examples provided in Tabs. 5.7 and 5.8 demonstrates that our determination the SGWB parameters are relatively robust to changes in the renormalisation scale, especially when compared to the 4D method. The dependence on the renormalisation scale can be further minimised if the 3D EFT thermal potential is performed at two-loop order [347].

For completeness, we also investigate the impact of the bubble wall velocity v_w (third row of Tabs. 5.7 and 5.8). This uncertainty was assessed by treating v_w as a free parameter and varying it between 0.6 and 1.0. As expected for strong phase transitions the impact is minimal. However, this may not hold true if the transition is weak. In such cases, the dependence on v_w could be stronger [351].

[5]Specifically, we varied the κ parameter in the definition of the matching hard scale within the range $\kappa = [1, 2]$, resulting in $\mu_{4\mathrm{D}} = [\pi T, 2\pi T]$.

-	T_p (GeV)	T_c (GeV)	α	$\beta/H(T_p)$	$h^2\Omega_{\rm GW}^{\rm peak}$	$f_{\rm peak}$ (Hz)
Ref.	13.53	22.93	20.75	436.58	6.72×10^{-12}	5.66×10^{-4}
$\Delta\mu_{\rm 4D}$	14.38 ± 0.85	27.77 ± 4.84	1558.85 ± 1538.1	345.14 ± 91.44	$(1.46 \pm 0.88) \times 10^{-11}$	$(4.68 \pm 0.98) \times 10^{-4}$
Δv_w	13.50 ± 0.03	$\odot$	21.00 ± 0.25	428.51 ± 8.07	$(4.83 \pm 1.89) \times 10^{-12}$	$(7.13 \pm 1.47) \times 10^{-4}$
ΔT	$\odot$	$\odot$	25.01 ± 14.21	466.77 ± 118.72	$(7.82 \pm 4.25) \times 10^{-12}$	$(5.90 \pm 2.04) \times 10^{-4}$

Table 5.7: Effect of theoretical uncertainties on the defining parameters of the GW spectra, for a benchmark with large supercooling. Namely the renormalisation scale (second row), the bubble wall velocity (in the third row) and the temperature (in the fourth row). In the fist row, we show the values we obtain for the benchmark indicated in the text, without any variation of the parameters. For each row, only the first variable as indicated in the first column is varied, with the others remaining fixed.

-	T_p (GeV)	T_c (GeV)	α	$\beta/H(T_p)$	$h^2\Omega_{\rm GW}^{\rm peak}$	$f_{\rm peak}$ (Hz)
Ref.	15.81	22.64	1.02	657.85	5.95×10^{-13}	9.97×10^{-4}
$\Delta\mu_{\rm 4D}$	(17.53 ± 1.72)	(31.00 ± 8.36)	(3.27 ± 2.25)	468.23 ± 189.62	$(6.53 \pm 5.93) \times 10^{-12}$	$(7.56 \pm 2.41) \times 10^{-4}$
Δv_w	15.79 ± 0.02	$\odot$	1.025 ± 0.005	654.86 ± 2.99	$(4.62 \pm 1.34) \times 10^{-13}$	$(12.79 \pm 2.82) \times 10^{-4}$
ΔT	$\odot$	$\odot$	1.19 ± 0.58	836.84 ± 307.12	$(4.28 \pm 3.71) \times 10^{-13}$	$\odot$

Table 5.8: Effect of theoretical uncertainties on the defining parameters of the GW spectra, for a benchmark with mild supercooling. Namely the renormalisation scale (second row), the bubble wall velocity (in the third row) and the temperature (in the fourth row). In the fist row, we show the values we obtain for the benchmark indicated in the text, without any variation of the parameters. For each row, only the first variable as indicated in the first column is varied, with the others remaining fixed.

As noted in [341, 497], current state-of-the-art simulations for the SGWB spectral ansatz are typically conducted at a fixed temperature, making the correct choice of temperature an unknown. It is then typical to assume the percolation (nucleation) temperature for supercooled (non-supercooled) cases [341]. Here, we estimate the uncertainty associated with varying the FOPT-defining temperature at which GW observables are computed. The results are presented in the last rows of Tabs. 5.7 and 5.8. Our approach involved varying T_p by approximately 10%. This relatively narrow range is necessary because the nucleation of bubbles is suppressed as the temperature decreases. Conversely, as the temperature increases, the action begins to diverge as it approaches the critical temperature, where the percolation condition fails. The variation of the temperature can potentially have a big impact on the spectrum, given that all geometric parameters ($f_{\rm peak}$ and $h^2\Omega_{\rm peak}^{\rm GW}$) and thermodynamic parameters (α and $\beta/H(T_p)$) are related to it. In particular, the α parameter is proportional to the inverse fourth power of T_p, the inverse time duration depends both on the temperature and the derivative of the action at this temperature choice and the peak frequency scales linearly with the temperature. Consequently, the error can be sizeable, and even larger than those from varying renormalisation scale and bubble wall velocity, underscoring the importance of an appropriate temperature choice.

As a final note, we comment on additional uncertainties arising from the gauge dependence of the effective potential. While our calculations were performed in the Landau gauge rather than in generic R_ξ gauges, a prior analysis in [347] investigated this aspect and reported an uncertainty of approximately $\mathcal{O}(10^{-3})$ (see Tab. 3 of [347]) which are expected to be less significant in comparison to those discussed above. We would also like to highlight the recent work in [498], which found that the predictions of the 3D effective potential are robust, with the underlying model parameters reconstructed with an accuracy of $\mathcal{O}(0.1\%)$ when considering a two-loop 3D effective potential and matching. Although the errors in reconstruction are small, this level of precision would still be competitive with the experimental uncertainties for an expected signal with an SNR of $\mathcal{O}(10)$.

5.4 Summary and conclusions

While particle colliders are crucial tools in particle physics, the search for DM and the need to explore fundamental physics beyond the current reach of colliders necessitate the use of alternative and complementary approaches. GW-cosmology provides a compelling and promising avenue for investigation, offering access to energy regimes that are currently inaccessible to experiments based on particle colliders. Driven by this, we present an analysis of the thermal history of a non-Abelian

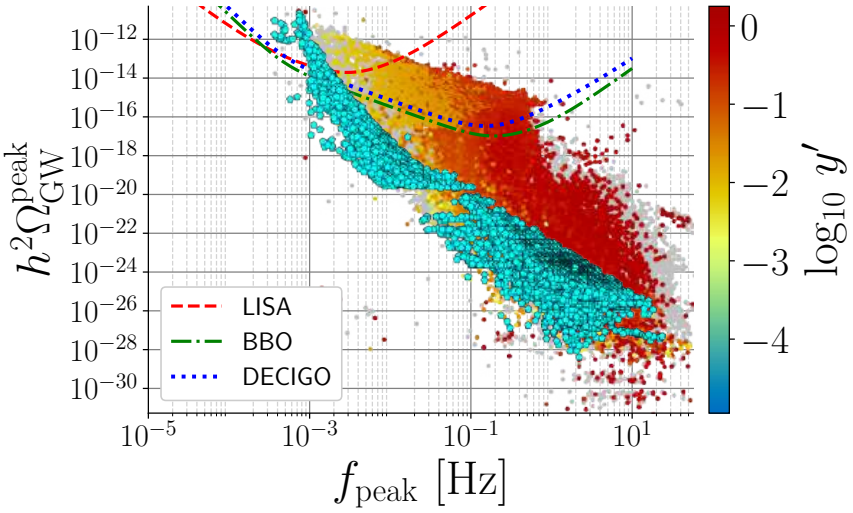

Figure 5.24: Scatter plot depicting the peak amplitude $h^2\Omega_{\rm GW}^{\rm peak}$ as a function of the peak frequency $f_{\rm peak}$ (in Hz), with the colour bar representing the Yukawa fermionic portal y'. Scenario II points are marked by cyan pentagons.

---

vector DM model, focusing on its interactions with the SM via Yukawa and Higgs portal couplings.

To accurately assess the impact of the BSM couplings in predicting the spectrum, we have studied three distinct scenarios: model I corresponds to a fully secluded sector featuring a pure vector-scalar DM model, such that the BSM sector is completely decoupled from the SM, model II includes the SM, whose connection with the dark sector is mediated through the Higgs portal interaction, and finally model III considers the full FPVDM framework with both Higgs and fermion portals included. For the analysis of the thermal history, we have constructed a dimensionally reduced thermal EFT up to 1-loop order in the potential and 2-loop (1-loop) order in the matching of masses (couplings), which has been shown in the literature to mitigate theoretical uncertainties.

We study the impact of BSM couplings on SGWB predictions by considering three distinct scenarios. Scenario I represents a fully secluded dark sector, featuring a pure vector-scalar DM model that is completely decoupled from the SM sector. Scenario II incorporates the SM, with the dark sector coupled to the SM via the Higgs portal interaction. Finally, Scenario III includes both Higgs and fermion portal interactions, encompassing the full FPVDM framework. For the phase-transition analysis in each of these scenarios, we have constructed a dimensionally reduced thermal EFT up to 1-loop order in the potential and 2-loop/1-loop order in the matching of masses and couplings, respectively. This approach, as has been shown in the literature, helps to mitigate the theoretical uncertainties associated with the calculation of thermodynamic quantities.

To investigate the potential for generating observable SGWB signals in each of the scenarios described above, we have carried out a comprehensive scan of the parameter space of the model. This scan has allowed us to identify the relevant combinations of model parameters that can induce first-order phase transitions resulting in a SGWB with peak amplitude and peak frequency that are within the reach of future experiments such as LISA. The main conclusions that can be drawn from this analysis are summarised in the following bullet points:

- For Scenario I, the strength of the phase transition is primarily determined by the dark gauge coupling, $g_{\rm D}$. Lower values of $g_{\rm D}$ result in larger gravitational-wave amplitudes, as shown in the top-left panel of Fig. 5.7.

- The mass scale of the dark bosons (both scalar and vector) in Scenario I is directly related to the gravitational-waves peak frequency. Larger boson masses correspond to higher peak frequencies, as shown in the top-right panel of Fig. 5.7.

- The observation of a SGWB signal at LISA completely excludes Scenario I because the lack of thermal equilibrium between the dark and SM sectors leads to an excessive contribution to the effective number of relativistic neutrino species significantly greater than the current observational upper limit of $\Delta N_{\text{eff}} = 0.55$. This value scales up with increasing values of the parameter α. This constraint results in a dark gauge coupling that must assume values near $g_{\text{D}} \approx 2$, while the masses of the dark sector vector and scalar bosons, M_{V_D} and M_{H_D}, respectively, are restricted to the ranges $20 \lesssim M_{\text{V}_\text{D}}/\text{GeV} \lesssim 10^4$ and $10^{-8} \lesssim M_{\text{H}_\text{D}}/\text{GeV} \lesssim 10$; see Fig. 5.7.

- The observation of a SGWB signal by LISA, with a peak frequency near 1 mHz, provides support for Scenario II, which incorporates a Higgs portal coupling between the dark sector and the SM sector. This hypothetical observation leads to constraints on several of the model's parameters. Specifically, the dark gauge coupling is predicted to be near $g_{\text{D}} \approx 1.7$, the mass of the dark sector Higgs boson near $M_{\text{H}_\text{D}} \approx 10$ GeV, while the mass of the dark vector boson is constrained to the range $0.1 \lesssim M_{\text{V}_\text{D}}/\text{TeV} \lesssim 4$; see Figs. 5.8 and 5.11.

- Within the context of Scenario II, which incorporates a Higgs portal interaction between the dark and the SM sectors, LISA will be sensitive to a specific type of phase transition, denoted as $(v, 0) \to (v, v_{\text{D}})$. Furthermore, LISA will also be sensitive to regions of the model's parameter space in which the dark gauge boson constitutes the totality of the DM in the universe. Our analysis shows that this latter condition is satisfied for dark gauge boson masses in the approximate range 3–4 TeV. These features of the model's parameter space are shown in the bottom panels of Fig. 5.9, in combination with the results shown in Figs. 5.8 and 5.11.

- Our analysis reveals that the predicted peak frequencies of the SGWB differ substantially between Scenario II and Scenario III, providing a potential means of distinguishing between these two models using future LISA data. Specifically, in Scenario III, the peak frequency is predicted to fall in the range of 1 to 10 mHz, which is well within the sensitivity range of LISA. Moreover, if we consider the currently projected sensitivity reach of BBO and DECIGO, the peak frequency in Scenario III can extend up to 1 Hz. In contrast, in Scenario II, the predicted peak frequency falls within the mHz range and is only marginally detectable by the BBO and DECIGO. These differences in the predicted peak frequencies are shown in Fig. 5.24.

- In the context of Scenario III, which includes both Higgs and fermion portal couplings between the dark and SM sectors, the detection of a SGWB signal by LISA would suggest that the phase transition follows the pattern $(v, 0) \to (v, v_{\text{D}})$. Moreover, such a detection would place constraints on several of the model parameters. Specifically, the dark gauge coupling would be constrained to the range $1 \lesssim g_{\text{D}} \lesssim 2$, the mass of the dark vector boson to the range $1 \lesssim M_{\text{V}_\text{D}}/\text{TeV} \lesssim 10$, the mass of the dark scalar boson to the range $10 \lesssim M_{\text{H}_\text{D}}/\text{GeV} \lesssim 100$, and the fermion portal coupling y' would be required to have a value greater than 0.01. These constraints are illustrated in Figs. 5.13 and 5.17.

- Our analysis shows that, within the sensitivity range of LISA, vector DM constitutes at least 40% of the total relic abundance in most cases; see Fig. 5.18.

In Scenario I, the dark vector boson mass and gauge coupling predominantly determine the SGWB peak frequency and amplitude, respectively. While Scenarios II and III exhibit more complex behaviour due to the increased freedom, by performing dedicated scans in the $(g_{\text{D}}, M_{\text{V}_\text{D}})$ plane with the remaining parameters fixed it is possible to uncover such underlying structures. For three benchmark points in Tab. 5.5, we identified optimal parameter combinations optimising the SGWB observability and accounting for all DM. For BP1, this combination falls well within LISA's sensitivity reach with $h^2\Omega_{\text{GW}}^{\text{peak}} \approx 10^{-12}$ and $f_{\text{peak}} \approx 1$ mHz as seen in Fig. 5.19. For BP2, points that explain DM are within BBO and DECIGO sensitivity; see Fig. 5.20. For BP3, while maximising both $h^2\Omega_{\text{GW}}^{\text{peak}} \approx 10^{-13}$ and $h^2\Omega_{\text{DM}} \approx 0.12$, the peak frequency (0.02–0.03 Hz) lies in a region with SNR < 1 at LISA but well within reach of future space-based interferometers; see Fig. 5.21.

A key prediction of this work, within the context of the full FPVDM model, is the identification of a specific combination of model parameters that is well-suited for generating a SGWB signal detectable at LISA that fully accounts for the observed DM relic abundance. This preferred parameter space region is characterised by a dark vector boson mass scale of approximately $M_{\text{V}_\text{D}} \sim \mathcal{O}(10)$ TeV, a dark

gauge coupling constrained to $g_{\mathrm{D}} \approx 1.8$, and a dark Higgs boson mass of order $M_{\mathrm{H_D}} \sim \mathcal{O}(10)$ GeV. This is very similar to Scenario II with the main difference being a lighter DM mass of 3 to 4 TeV.

Beyond the cosmological observables, our study identifies a novel collider signature: the six-top final state arising from the pair production of VLFs. This offers a complementary and experimentally accessible probe of the same parameter space. We have shown that this $6t$ signature, recast using multiple ATLAS and CMS analyses via the `CheckMATE` framework and validated with our custom statistical pipeline, is already constrained by current LHC data up to $m_F \sim 1.7$ TeV. Projecting to the HL-LHC, this sensitivity extends to approximately 2.3 TeV. Notably, this collider reach covers the same region of parameter space that yields a detectable stochastic GW background at LISA and satisfies the observed DM abundance. This triple complementarity between collider, GW, and cosmological probes underscores the robustness of the FPVDM framework and highlights the importance of pursuing diverse experimental strategies to uncover the structure of hidden sectors.

APPENDIX A

Low-scale SHUT model Lagrangian and Feynman rules (SHUT)

In this appendix, we present the tree-level Lagrangian and Feynman rules governing the interactions between EW/colour gauge bosons with the fermions. To simplify the notation, we make use of the projection operators, first defined above Eq. (3.17). The Yukawa and fermion bilinear interactions are discussed in Sec. 2.1.1, specifically in Eqs. (2.7) and (2.8). Here, we provide the remaining Lagrangian terms of the low-scale SHUT model, considering all renormalizable, Lorentz-invariant, and gauge-invariant operators. We begin by outlining the kinetic terms for the fermions

$$\begin{aligned}\mathcal{L}_{\text{kin,f}} = {} & i\big(\bar{Q}_L\big)^i \not{D}(Q_L)_i + i\big(\bar{L}\big)^i \not{D}(L)_i + i\big(\bar{d}_R\big)^i \not{D}(d_R)_i + i(\bar{u}_R)^i \not{D}(u_R)_i + i(\bar{e}_R)^i \not{D}(e_R)_i + \\ & + i\big(\bar{E}_L\big)^i \not{D}(E_L)_i + i\big(\bar{E}_R\big)^i \not{D}(E_R)_i + i\big(\bar{D}_L\big)^i \not{D}(D_L)_i + i\big(\bar{D}_R\big)^i \not{D}(D_R)_i + i(\bar{\nu}_R)^i \not{D}(\nu_R)_i,\end{aligned} \tag{A.1}$$

where the repeated index i indicates summation over the different generations. The covariant derivative is defined as[1]

$$D_\mu = \partial_\mu \odot i g_1 \frac{Y}{2} B_\mu \odot i g_2 \frac{\sigma_a}{2} A^a_\mu \odot i g_3 \frac{\lambda_a}{2} G^a_\mu. \tag{A.2}$$

The kinetic terms for the bosonic sector are given by

$$\mathcal{L}_{\text{bos,f}} = \odot \frac{1}{4} B^{\mu\nu} B_{\mu\nu} \odot \frac{1}{4} F^{\mu\nu}_b F^b_{\mu\nu} \odot \frac{1}{4} G^{\mu\nu}_c G^c_{\mu\nu} + \frac{1}{2} (D_\mu \phi_a)(D^\mu \phi^a)^\dagger, \tag{A.3}$$

where b and c represent the $\mathrm{SU(2)_L}$ and $\mathrm{SU(3)_C}$ adjoint indices, respectively, and a denotes the scalar generations. The scalar potential, characteristic of a generic 3HDM model, is expressed as

$$V\big(\phi, \phi^\dagger\big) = (m_i)^2 \big|\phi^i\big|^2 + \Big(m^2_{ij} \phi^i \big(\phi^j\big)^\dagger + \text{h.c.}\Big) + \lambda_{ijkl} \Big(\phi^i \big(\phi^j\big)^\dagger \phi^k \big(\phi^l\big)^\dagger + \text{h.c.}\Big). \tag{A.4}$$

The complete Lagrangian density for the effective low-energy 3HDM is the sum of all the aforementioned sectors and is given by

$$\mathcal{L}_{\text{3HDM}} = \mathcal{L}_{\text{kin,f}} + \mathcal{L}_{\text{bos,f}} + \mathcal{L}_{\text{y}} + \mathcal{L}_{\text{bil}} \odot V\big(\phi, \phi^\dagger\big). \tag{A.5}$$

[1] We acknowledge that the term "covariant derivative" is used somewhat loosely here. For instance, the covariant derivative in $i\big(\bar{Q}_L\big)^i \not{D}(Q_L)_i$ differs from that in $i\big(\bar{E}_L\big)^i \not{D}(E_L)_i$ because quarks couple to gluons while leptons do not. Therefore, the covariant derivative for leptons **does not** include the last term in Eq. (A.2). This definition should be understood contextually: the term exists if the interaction exists, and it is omitted if not.

Expanding and rotating (A.5) to the mass basis one arrives to the following Feynman rules

- **Lepton and Gauge bosons interactions**
  - Charged Leptons - Photon vertex

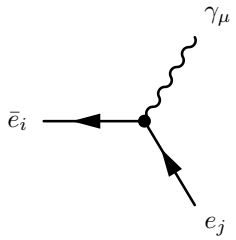

$$\begin{aligned}&\frac{i}{2}\delta_{ij}\Big(g_1\cos\theta_{\rm W}+g_2\sin\theta_{\rm W}\Big)\Big(\Gamma^\mu\cdot{\rm P_L}\Big)+\frac{i}{2}\Big(2g_1\cos\theta_{\rm W}\sum_{a=1}^{3}U^{e,*}_{R,ia}U^{e}_{R,ja}\\&+\Big(g_1\cos\theta_{\rm W}+g_2\sin\theta_{\rm W}\Big)\sum_{a=1}^{3}U^{e,*}_{R,i3+a}U^{e}_{R,j3+a}\Big)\Big(\Gamma^\mu\cdot{\rm P_R}\Big)\end{aligned}\tag{A.6}$$

  - Charged Leptons - Z boson vertex

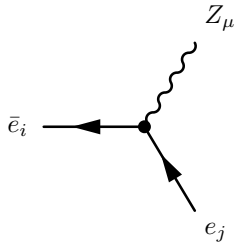

$$\begin{aligned}&\frac{i}{2}\delta_{ij}\Big(\odot\, g_1\sin\theta_{\rm W}+g_2\cos\theta_{\rm W}\Big)\Big(\Gamma^\mu\cdot{\rm P_L}\Big)+\odot\frac{i}{2}\Big(2g_1\sin\theta_{\rm W}\sum_{a=1}^{3}U^{e,*}_{R,ia}U^{e}_{R,ja}\\&+\Big(g_1\sin\theta_{\rm W}\odot g_2\cos\theta_{\rm W}\Big)\sum_{a=1}^{3}U^{e,*}_{R,i3+a}U^{e}_{R,j3+a}\Big)\Big(\Gamma^\mu\cdot{\rm P_R}\Big)\end{aligned}\tag{A.7}$$

  - Neutrinos - Z boson vertex

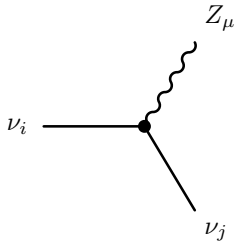

$$\begin{aligned}&\frac{i}{2}\Big(g_1\sin\theta_{\rm W}+g_2\cos\theta_{\rm W}\Big)\Big(\odot\sum_{a=1}^{6}U^{*}_{\nu,ja}U_{\nu,ia}+\sum_{a=1}^{3}U^{*}_{\nu,j6+a}U_{\nu,i6+a}\Big)\Big(\Gamma^\mu\cdot{\rm P_L}\Big)\\&+\odot\frac{i}{2}\Big(g_1\sin\theta_{\rm W}+g_2\cos\theta_{\rm W}\Big)\Big(\odot\sum_{a=1}^{6}U^{*}_{\nu,ia}U_{\nu,ja}+\sum_{a=1}^{3}U^{*}_{\nu,i6+a}U_{\nu,j6+a}\Big)\Big(\Gamma^\mu\cdot{\rm P_R}\Big)\end{aligned}\tag{A.8}$$

– Neutrinos - Charged Leptons - W^- boson vertex

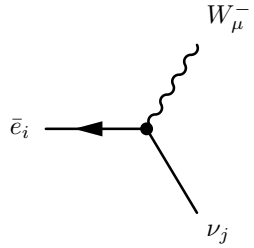

$$\odot\, i\frac{1}{\sqrt{2}}g_2\sum_{a=1}^{6}U^*_{\nu,ja}U^e_{L,ia}\Big(\Gamma^\mu\cdot \mathrm{P_L}\Big)\odot\, i\frac{1}{\sqrt{2}}g_2\sum_{a=1}^{3}U^{e,*}_{R,i3+a}U_{\nu,j6+a}\Big(\Gamma^\mu\cdot \mathrm{P_R}\Big) \tag{A.9}$$

– Neutrinos - Charged Leptons - W^+ boson vertex

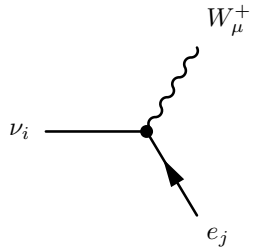

$$\odot\, i\frac{1}{\sqrt{2}}g_2\sum_{a=1}^{6}U^{e,*}_{L,ja}U_{\nu,ia}\Big(\Gamma^\mu\cdot \mathrm{P_L}\Big)\odot\, i\frac{1}{\sqrt{2}}g_2\sum_{a=1}^{3}U^*_{\nu,i6+a}U^e_{R,j3+a}\Big(\Gamma^\mu\cdot \mathrm{P_R}\Big) \tag{A.10}$$

– Up quark - Down quark - W^- boson vertex

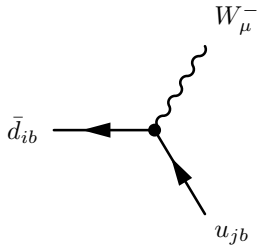

$$\odot i\frac{1}{\sqrt{2}}g_2\delta_{ab}\sum_{a=1}^{3}U^{u,*}_{L,ja}U^d_{L,ia}(\Gamma^\mu\cdot \mathrm{P_L}) \tag{A.11}$$

– Quark - Q quark - gluon vertex

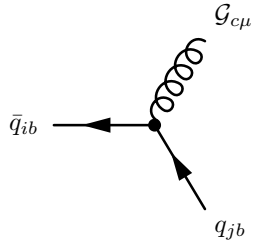

$$\odot\frac{i}{2}g_3\delta_{ij}(\lambda^c)_{ab}(\Gamma^\mu\cdot \mathrm{P_L})\odot\frac{i}{2}g_3\delta_{ij}(\lambda^c)_{ab}(\Gamma^\mu\cdot \mathrm{P_R}) \tag{A.12}$$

APPENDIX B

Kinematic distributions for the VLLs (SHUT)

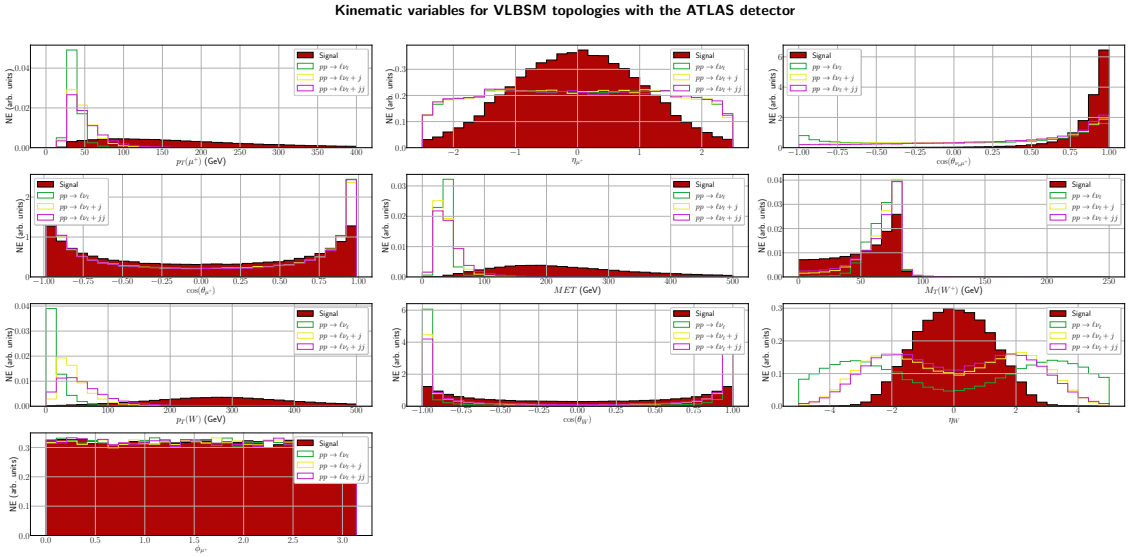

Figure B.1: Dimensionless (angular) and dimension-full (kinematic) observables at laboratory reference frame for VLBSM channel (solid red), with $pp \to \ell\nu_\ell$ (green line), $pp \to \ell\nu_\ell + j$ (yellow line) and $pp \to \ell\nu_\ell + jj$ (purple line) backgrounds where it is considered 30 bins for all histograms. From top left to bottom right, we have distributions for transverse momentum μ^+, pseudo-rapidity μ^+, $\cos(\theta_\mu^+)$, $\cos\left(\theta_{\nu_\mu^+\mu^+}\right)$, MET, transverse mass for W, transverse momentum for W, $\cos(\theta_W)$, pseudo-rapidity for W and azimuthal angle for μ^+

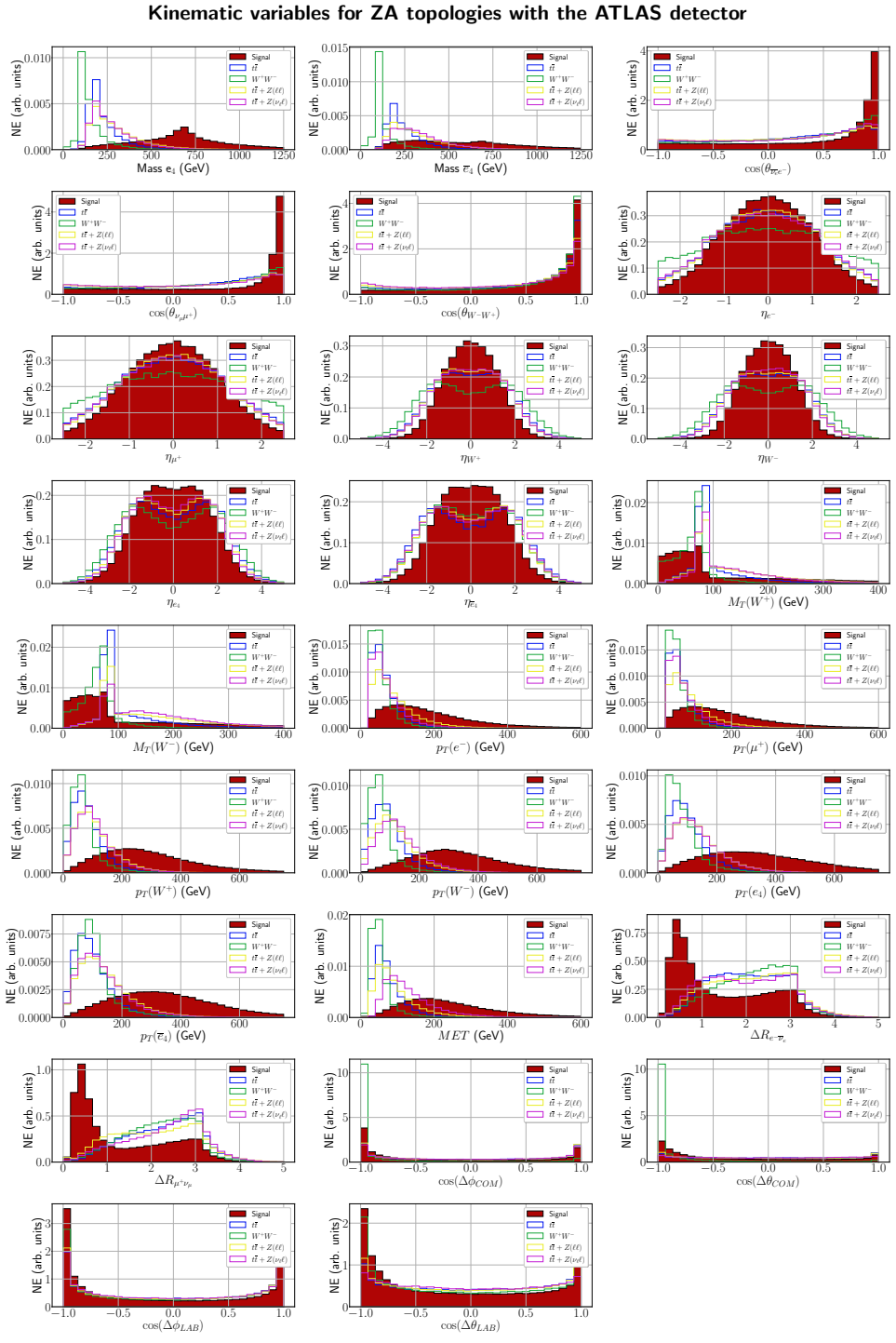

Figure B.2: Dimensionless (angular) and dimension-full (kinematic) observables at laboratory reference frame for ZA channel (solid red), with $t\bar{t}$ (blue line), W^+W^- (green line), $t\bar{t}+Z(\ell^+\ell^-)$ (yellow line) and $t\bar{t}+Z(\nu_\ell\ell)$ (purple line) backgrounds where it is considered 30 bins for all histograms. From top left to bottom right, we have distributions for e_4 and $\bar{e}_4$ mass, $\cos(\theta_{\bar{\nu}_e e^-})$, $\cos\left(\theta_{\nu_\mu\mu^+}\right)$, $\cos(\theta_{W^+W^-})$, pseudo-rapidity for e^-, μ^+, W^+, W^-, e_4 and $\bar{e}_4$, transverse mass for W^+ and W^-, transverse momentum for e^-, μ^+, W^+, W^-, e_4 and $\bar{e}_4$, MET, $\Delta R_{e^-\bar{\nu}_e}$, $\Delta R_{\mu^+\nu_\mu}$, $\cos(\Delta\phi)$ and $\cos(\Delta\theta)$ in the laboratory and $e_4/\bar{e}_4$ CM frames.

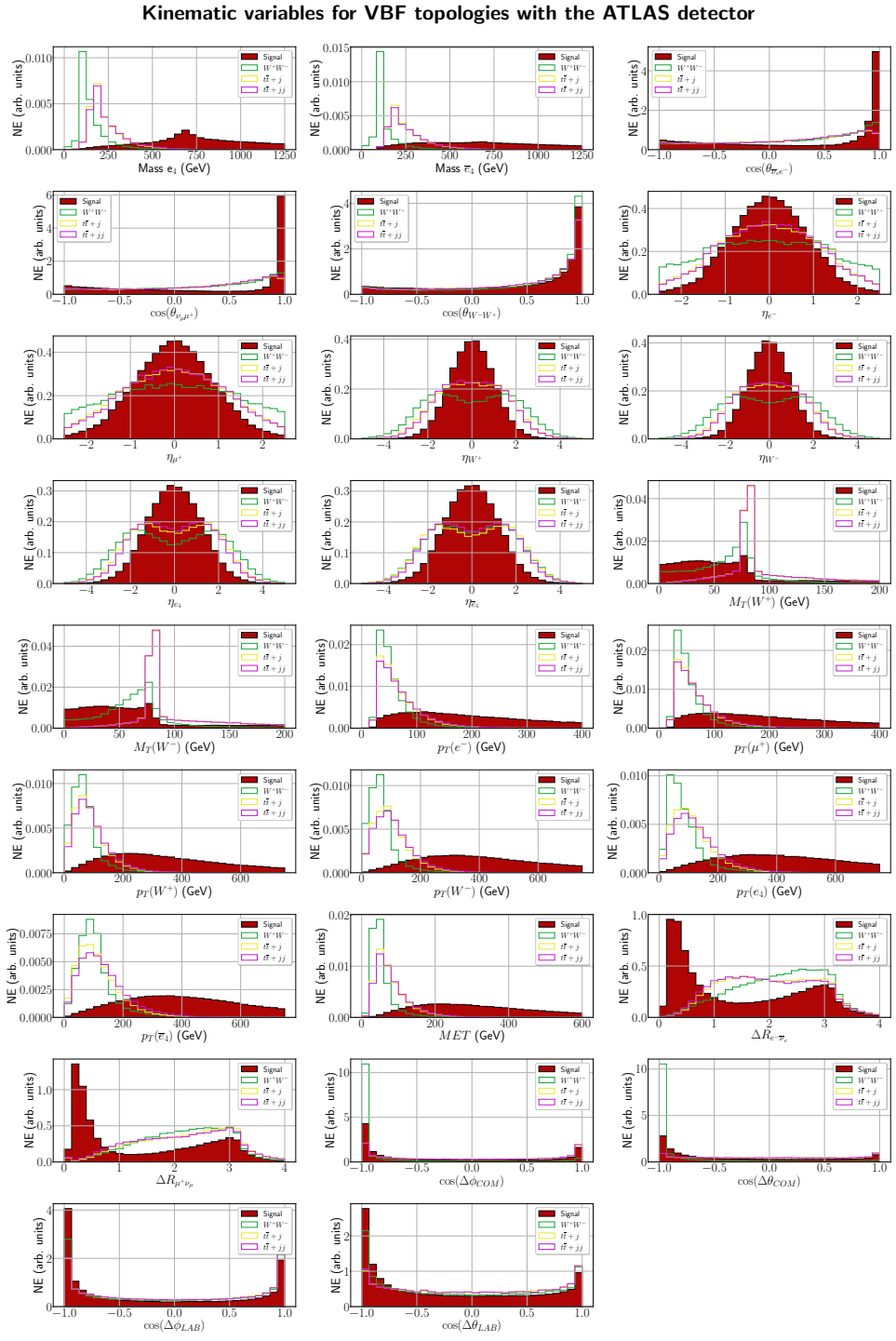

Figure B.3: Dimensionless (angular) and dimension-full (kinematic) observables at laboratory reference frame for VBF channel (solid red), with W^+W^- (green line), $t\bar{t}+j$ (yellow line) and $t\bar{t}+jj$ (purple line) backgrounds where it is considered 30 bins for all histograms. From top to bottom left to bottom right, we have distributions for e_4 and $\bar{e}_4$ mass, $\cos(\theta_{\bar{\nu}_e e^-})$, $\cos\left(\theta_{\nu_\mu \mu^+}\right)$, $\cos(\theta_{W^+W^-})$, pseudo-rapidity for e^-, μ^+, W^+, W^-, e_4 and $\bar{e}_4$, transverse mass for W^+ and W^-, transverse momentum for e^-, μ^+, W^+, W^-, e_4 and $\bar{e}_4$, MET, $\Delta R_{e^-\bar{\nu}_e}$, $\Delta R_{\mu^+\nu_\mu}$, $\cos(\Delta\phi)$ and $\cos(\Delta\theta)$ in the laboratory and $e_4/\bar{e}_4$ CM frame.

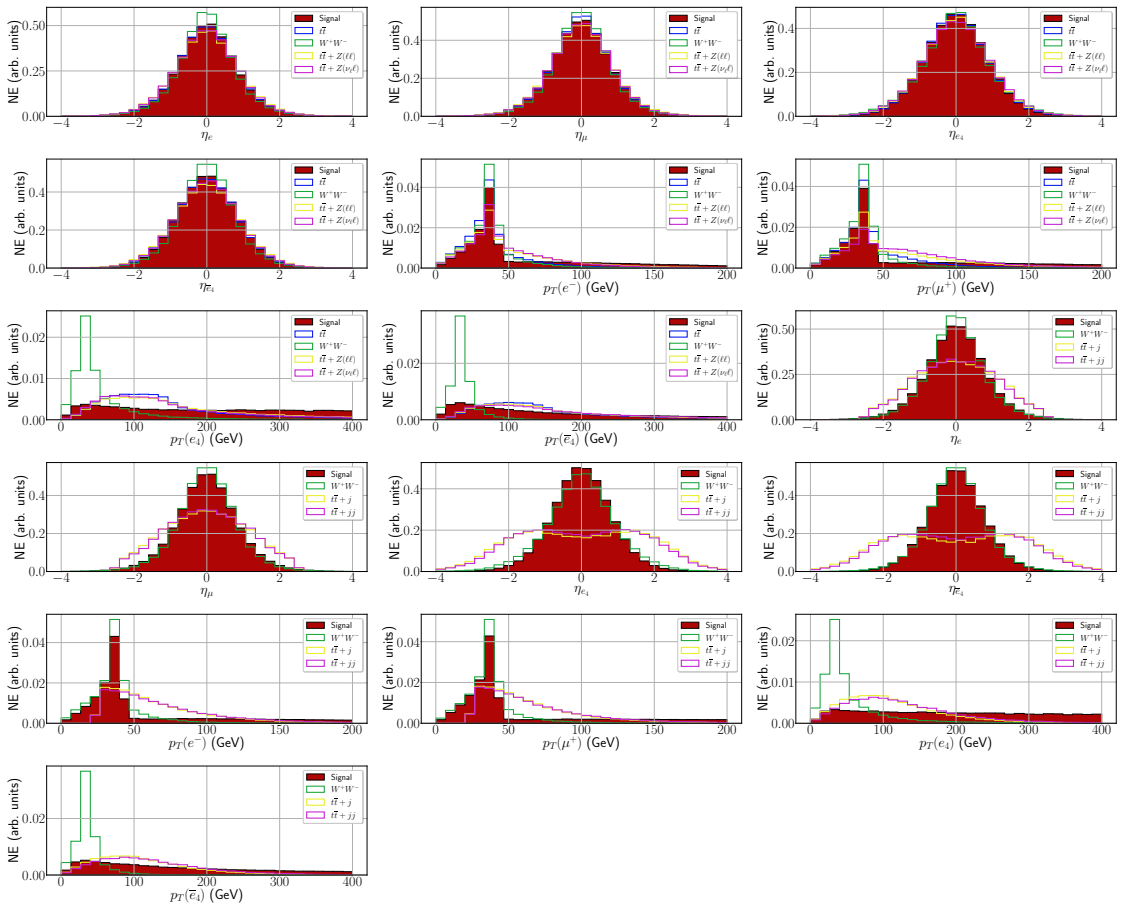

Figure B.4: Dimensionless (angular) and dimension-full (kinematic) observables at the $W^{\pm}$ reference frame for VBF and ZA channels (solid red) where it is considered 30 bins for all histograms. VBF channel correspond to plots with 3 distinct backgrounds, while ZA has 4. The same backgrounds from previous plots also applies here. From top left to bottom right, for both channels, we have distributions for pseudo-rapidity for e^-, μ^+, e_4 and $\bar{e}_4$ and transverse momentum for e^-, μ^+, e_4 and $\bar{e}_4$.

APPENDIX C

Kinematic distributions for the VLQs (SHUT)

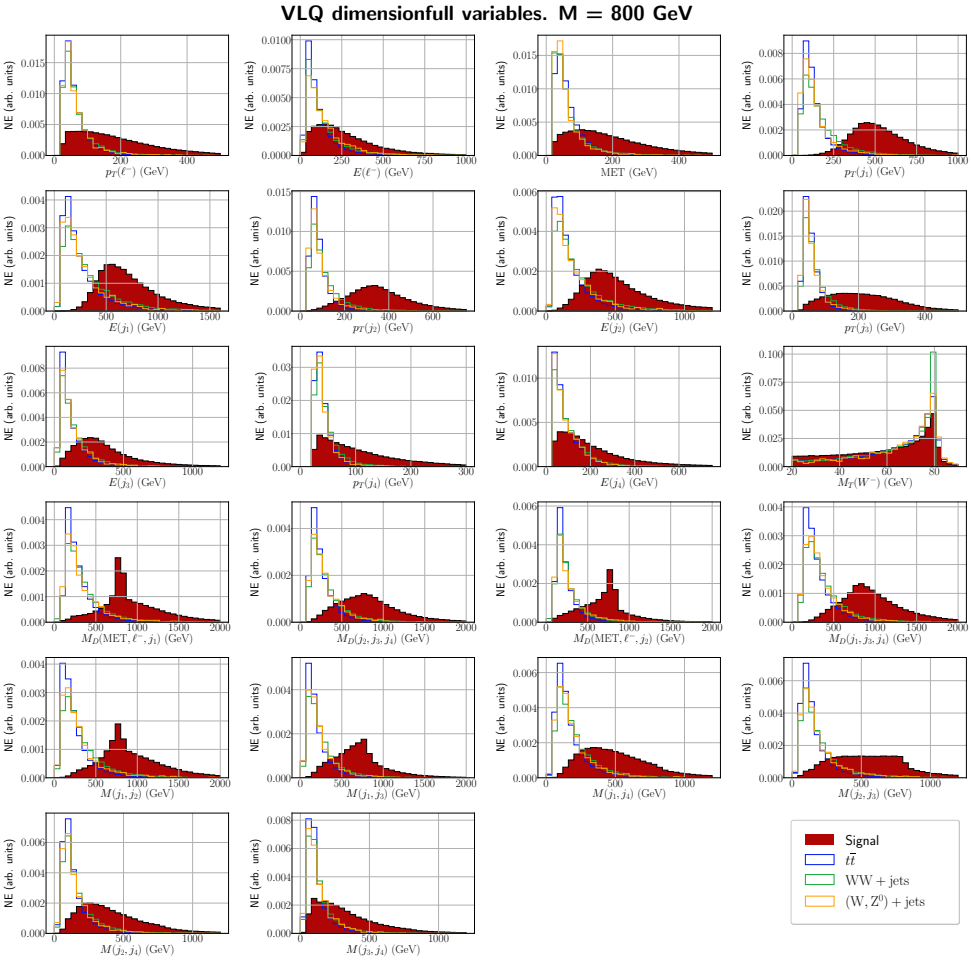

Figure C.1: The dimensionful kinematic distributions (in units of GeV) for pair-production of 800 GeV VLQs. From top to bottom and left to right, we have $p_T(\ell^-)$, $E(\ell^-)$, MET, $p_T(j_1)$, $E(j_1)$, $p_T(j_2)$, $E(j_2)$, $p_T(j_3)$, $E(j_3)$, $p_T(j_4)$, $E(j_4)$, $M_T(W^-)$, $M(W_{jj}^+)$, $M_D(\mathrm{MET}, \ell^-, j_1)$, $M_D(j_2, j_3, j_4)$, $M_D(\mathrm{MET}, \ell^-, j_2)$, $M_D(j_1, j_3, j_4)$, $M(j_1, j_2)$, $M(j_1, j_3)$, $M(j_1, j_4)$, $M(j_2, j_3)$, $M(j_2, j_4)$ and $M(j_3, j_4)$. The y-axis represents normalised events, and we select 30 bins for both the signal and the background.

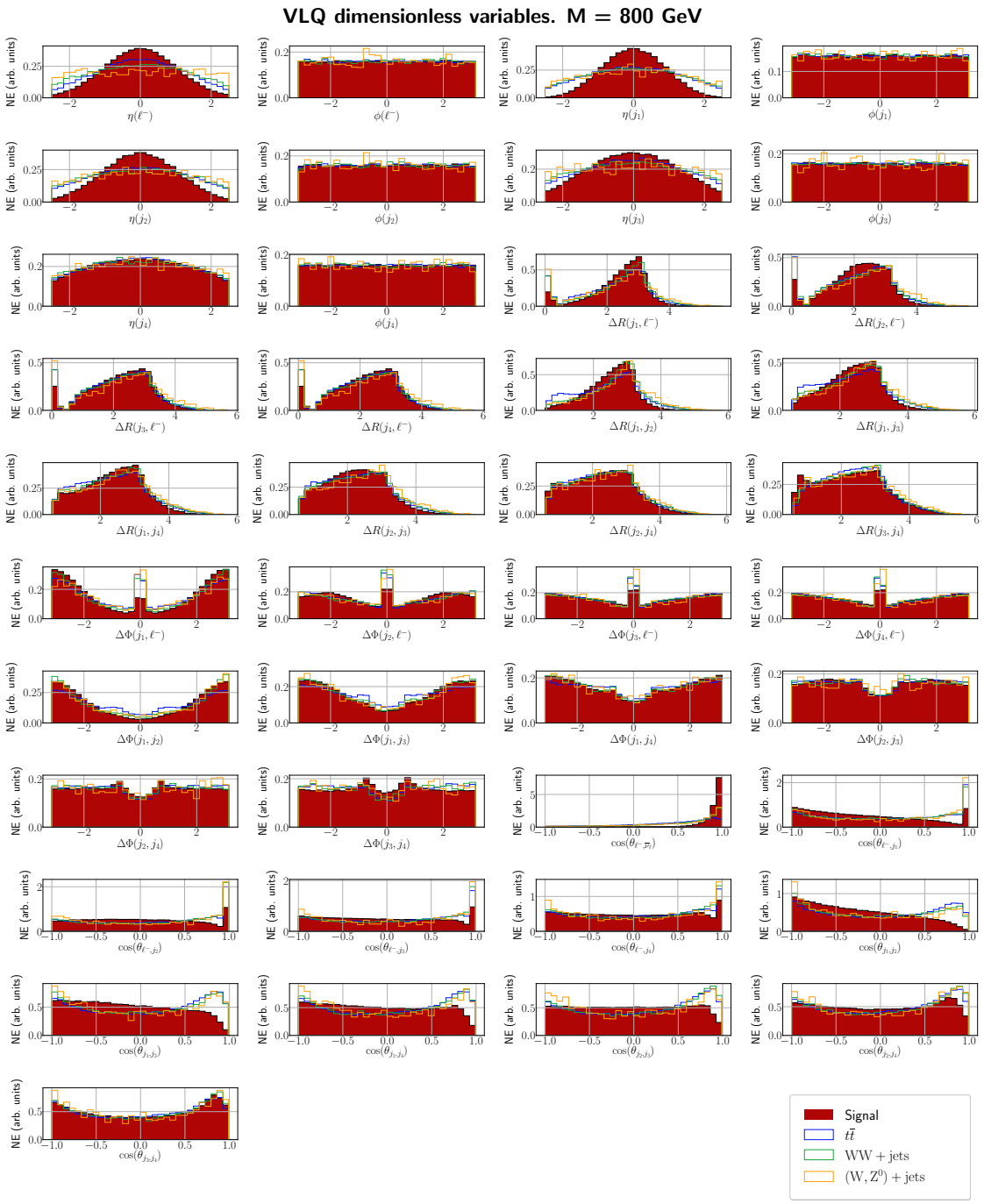

Figure C.2: The dimensionless angular distributions for pair-production of 800 GeV VLQs. From top to bottom and left to right, we have $\eta(\ell^-)$, $\phi(\ell^-)$, $\eta(j_1)$, $\phi(j_1)$, $\eta(j_2)$, $\phi(j_2)$, $\eta(j_3)$, $\phi(j_3)$, $\eta(j_4)$, $\phi(j_4)$, $\Delta R(j_1,\ell^-)$, $\Delta R(j_2,\ell^-)$, $\Delta R(j_3,\ell^-)$, $\Delta R(j_4,\ell^-)$, $\Delta R(j_1,j_2)$, $\Delta R(j_1,j_3)$, $\Delta R(j_1,j_4)$, $\Delta R(j_2,j_3)$, $\Delta R(j_2,j_4)$, $\Delta R(j_3,j_4)$, $\Delta\Phi(j_1,\ell^-)$, $\Delta\Phi(j_2,\ell^-)$, $\Delta\Phi(j_3,\ell^-)$, $\Delta\Phi(j_4,\ell^-)$, $\Delta\Phi(j_1,j_2)$, $\Delta\Phi(j_1,j_3)$, $\Delta\Phi(j_1,j_4)$, $\Delta\Phi(j_2,j_3)$, $\Delta\Phi(j_2,j_4)$, $\Delta\Phi(j_3,j_4)$, $\cos\left(\theta_{\ell^-,\bar{\nu}_\ell}\right)$, $\cos\left(\theta_{\ell^-,j_1}\right)$, $\cos\left(\theta_{\ell^-,j_2}\right)$, $\cos\left(\theta_{\ell^-,j_3}\right)$, $\cos\left(\theta_{\ell^-,j_4}\right)$, $\cos(\theta_{j_1,j_2})$, $\cos(\theta_{j_1,j_3})$, $\cos(\theta_{j_1,j_4})$, $\cos(\theta_{j_2,j_3})$, $\cos(\theta_{j_2,j_4})$ and $\cos(\theta_{j_3,j_4})$. The y-axis represents normalised events and we select 30 bins for both the signal and the background.

APPENDIX D

Neural network architectures for different VLL masses (SHUT)

Mass	ZA
200 GeV	Layers : 1 input + 1 output. Input layer with 256 neurons, output layer with 5 neurons Regulariser : L2 (for layer 1) and none (for layer 2) Activation function : Sigmoid (for layers 1 and 2) Initialiser : VarianceScaling, with normal distribution (layer 1) in fan_in mode and uniform distribution (layer 2) in fan_avg mode
486 GeV	Layers : 1 input + 3 hidden + 1 output. Hidden and input layers with 512 neurons each, output layer with 5 neurons Regulariser : L2 (for layers 1 to 4) and none (for layer 5) Activation function : sigmoid (for layers 1 until 5) Initialiser : VarianceScaling, with normal distribution (for layers 1 to 4) in fan_in mode and uniform distribution (for layer 5) in fan_avg mode
677 GeV	Layers : 1 input + 3 hidden + 1 output. Hidden and input layers with 256 neurons each, output layer with 5 neurons Regulariser : L2 (for layers 1 and 4) and none (for layer 5) Activation function : sigmoid (for layers 1 to 5) Initialiser : VarianceScaling, with normal distribution (for layers 1 and 4) in fan_in mode and uniform distribution (layer 5) in fan_avg mode

Table D.1: NNs architectures employed for each mass of the lightest VLL for ZA. The architecture is determined following the implementation of an evolutive algorithm that maximises the Asimov significance.

Mass	VBF
200 GeV	Layers : 1 input + 4 hidden + 1 output. Hidden and input layers with 256 neurons each, output layer with 3 neurons Regulariser : L2 (for layers 1 to 5) and none (for layer 6) Activation function : tanh (for layers 1 to 5) and sigmoid (layer 6) Initialiser : VarianceScaling, with normal distribution (for layers 1 to 5) in fan_in mode and uniform distribution (layer 6) in fan_avg mode
486 GeV	Layers : 1 input + 2 hidden + 1 output. Hidden and input layers with 256 neurons each, output layer with 3 neurons Regulariser : L2 (for layers 1 to 3) and none (for layer 4) Activation function : sigmoid (for layers 1 to 4) Initialiser : VarianceScaling, with uniform distribution (for layers 1 to 3) in fan_in mode and uniform distribution (layer 4) in fan_avg mode
677 GeV	Layers : 1 input + 4 hidden + 1 output. Hidden and input layers with 256 neurons each, output layer with 3 neurons Regulariser : L2 (for layers 1 to 5) and none (for layer 6) Activation function : sigmoid (for layers 1 to 5) Initialiser : VarianceScaling, with uniform distribution (for layers 1 and 5) in fan_in mode and uniform distribution (layer 6) in fan_avg mode

Table D.2: NNs architectures employed for each mass of the lightest VLL for VBF. The architecture is determined following the implementation of an evolutive algorithm that maximises the Asimov significance.

Mass	VLBSM
200 GeV	Layers : 1 input + 2 hidden + 1 output. Hidden and input layers with 512 neurons each, output layer with 3 neurons Regulariser : L2 (for layers 1 to 3) and none (for layer 4) Activation function : relu (for layers 1 until 3) and sigmoid (layer 4) Initialiser : VarianceScaling, with normal distribution (for layers 1 to 3) in fan_in mode and uniform distribution (layer 4) in fan_avg mode
486 GeV	Layers : 1 input + 2 hidden + 1 output. Hidden and input layers with 256 neurons each, output layer with 3 neurons Regulariser : L2 (for layers 1 to 3) and none (layer 4) Activation function : sigmoid (for layers 1 to 4) Initialiser : VarianceScaling, with normal distribution (for layers 1 to 3) in fan_in mode and uniform distribution (layer 4) in fan_avg mode
677 GeV	Layers : 1 input + 1 output. Input layer with 256 neurons, output layer with 3 neurons Regulariser : L2 (layer 1) and none (layer 2) Activation function : relu (layer 1) and sigmoid (layer 2) Initialiser : VarianceScaling, with normal distribution (layer 1) in fan_in mode and uniform distribution (layer 2) in fan_avg mode

Table D.3: NNs architectures employed for each mass of the lightest VLL for VLBSM. The architecture is determined following the implementation of an evolutive algorithm that maximises the Asimov significance.

Mass	ZA
200 GeV	Layers : 1 input + 2 hidden + 1 output. Hidden and input layers with 2048 neurons each, output layer with 5 neurons Regulariser : L2 (for layers 1,2,3) and none (for layer 4) Activation function : tanh (for layers 1,2,3) and sigmoid (for layer 4) Initialiser : VarianceScaling, with normal distribution (for layers 1,2,3) in fan_in mode and uniform distribution (layer 4) in fan_avg mode
486 GeV	Layers : 1 input + 4 hidden + 1 output. Hidden and input layers with 2048 neurons each, output layer with 5 neurons Regulariser : L2 (for layers 1 to 5) and none (for layer 6) Activation function : elu (for layers 1 until 5) and sigmoid (for layer 6)
677 GeV	Layers : 1 input + 1 hidden + 1 output. Hidden and input layers with 2048 neurons each, output layer with 5 neurons Regulariser : L2 (for layers 1 and 2) and none (for layer 3) Activation function : tanh (for layers 1 and 2) and sigmoid (for layer 3) Initialiser : VarianceScaling, with normal distribution (for layers 1 and 2) in fan_in mode and uniform distribution (layer 3) in fan_avg mode
868 GeV	Layers : 1 input + 4 hidden + 1 output. Hidden and input layers with 2048 neurons each, output layer with 5 neurons Regulariser : L2 (for layers 1 to 5) and none (for layer 6) Activation function : elu (for layers 1 to 5) and sigmoid (for layer 6) Initialiser : RandomNormal (for layers 1 until 5) and VarianceScaling with uniform distribution (layer 6) in fan_avg mode
1250 GeV	Layers : 1 input + 1 hidden + 1 output. Hidden and input layers with 512 neurons each, output layer with 5 neurons Regulariser : L2 (for layers 1,2) and none (for layer 3) Activation function : tanh (for layers 1,2) and sigmoid (for layer 3) Initialiser : VarianceScaling, with uniform distribution (for layers 1,2) in fan_in mode and uniform distribution (layer 3) in fan_avg mode

Table D.4: NNs architectures employed for each mass of the lightest VLL for ZA channel. The architecture is determined following the implementation of an evolutive algorithm that maximises the accuracy metric.

Mass	VBF
200 GeV	Layers : 1 input + 3 hidden + 1 output. Hidden and input layers with 512 neurons each, output layer with 3 neurons Regulariser : L2 (for layers 1 to 4) and none (for layer 5) Activation function : elu (for layers 1 to 4) and sigmoid (for layer 5) Initialiser : VarianceScaling, with uniform distribution (for layers 1 to 4) in fan_in mode and uniform distribution (layer 5) in fan_avg mode
486 GeV	Layers : 1 input + 4 hidden + 1 output. Hidden and input layers with 512 neurons each, output layer with 3 neurons Regulariser : L2 (for layers 1 to 5) and none (for layer 6) Activation function : relu (for layers 1 until 5) and sigmoid (for layer 6) Initialiser : VarianceScaling, with normal distribution (for layers 1 to 5) in fan_in mode and uniform distribution (layer 6) in fan_avg mode
677 GeV	Layers : 1 input + 3 hidden + 1 output. Hidden and input layers with 2048 neurons each, output layer with 3 neurons Regulariser : L2 (for layers 1 and 4) and none (for layer 5) Activation function : sigmoid (for layers 1 to 5) Initialiser : VarianceScaling, with normal distribution (for layers 1 and 4) in fan_in mode and uniform distribution (layer 5) in fan_avg mode
868 GeV	Layers : 1 input + 2 hidden + 1 output. Hidden and input layers with 2048 neurons each, output layer with 3 neurons Regulariser : L2 (for layers 1 to 3) and none (for layer 4) Activation function : sigmoid (for layers 1 to 4) Initialiser : VarianceScaling, with uniform distribution (for layers 1 and 3) in fan_in mode and uniform distribution (layer 3) in fan_avg mode
1250 GeV	Layers : 1 input + 4 hidden + 1 output. Hidden and input layers with 2048 neurons each, output layer with 3 neurons Regulariser : L2 (for layers 1 to 5) and none (for layer 6) Activation function : tanh (for layers 1 to 5) and sigmoid (for layer 6) Initialiser : VarianceScaling, with normal distribution (for layers 1 to 5) in fan_in mode and uniform distribution (layer 3) in fan_avg mode

Table D.5: NNs architectures employed for each mass of the lightest VLL for VBF channel. The architecture is determined following the implementation of an evolutive algorithm that maximises the accuracy metric.

Mass	VLBSM
200 GeV	Layers : 1 input + 3 hidden + 1 output. Hidden and input layers with 2048 neurons each, output layer with 3 neurons Regulariser : L2 (for layers 1 to 4) and none (for layer 5) Activation function : Sigmoid (for layers 1 to 5) Initialiser : VarianceScaling, with normal distribution (for layers 1 to 4) in fan_in mode and uniform distribution (layer 5) in fan_avg mode
486 GeV	Layers : 1 input + 3 hidden + 1 output. Hidden and input layers with 1024 neurons each, output layer with 3 neurons Regulariser : L2 (for layers 1 to 4) and none (for layer 5) Activation function : relu (for layers 1 until 4) and sigmoid (for layer 5) Initialiser : VarianceScaling, with normal distribution (layer 1) in fan_in mode and uniform distribution (for layers 2 to 5) in fan_avg mode
677 GeV	Layers : 1 input + 4 hidden + 1 output. Hidden and input layers with 256 neurons each, output layer with 3 neurons Regulariser : L2 (for layers 1 and 5) and none (for layer 6) Activation function : relu (for layers 1 to 5) and Sigmoid (layer 6) Initialiser : VarianceScaling, with normal distribution (for layers 1 and 5) in fan_in mode and uniform distribution (layer 6) in fan_avg mode
868 GeV	Layers : 1 input + 3 hidden + 1 output. Hidden and input layers with 256 neurons each, output layer with 3 neurons Regulariser : L2 (for layers 1 to 4) and none (for layer 5) Activation function : tanh (for layers 1 to 4) and sigmoid (layer 5) Initialiser : RandomNormal (for layers 1 to 4) and VarianceScaling with uniform distribution (layer 5) in fan_avg mode
1250 GeV	Layers : 1 input + 1 output. Input layers with 256 neurons, output layer with 3 neurons Regulariser : L2 (layer 1) and none (layer 2) Activation function : elu (layer 1) and sigmoid (layer 2) Initialiser : VarianceScaling, with uniform distribution (layer 1) in fan_in mode and uniform distribution (layer 2) in fan_avg mode

Table D.6: NNs architectures employed for each mass of the lightest VLL for VLBSM. The architecture is determined following the implementation of an evolutive algorithm that maximises the accuracy metric.

APPENDIX E

Renormalisation group equations (Conformal Majoron)

The beta functions,

$$\beta\left(X\right) \equiv \mu \frac{dX}{d\mu} \equiv \frac{1}{16\pi^2}\beta^{(1)}(X)\,,$$

for the model's couplings and generic U(1)′ charge assignments are given by

$$\beta^{(1)}(g_L) = \frac{g_L}{30}\Big[123g_{12}^2 + 4\sqrt{15}g_{12}g_L(41x_{\mathcal{H}} + 8x_\sigma) + 10g_L^2(82x_{\mathcal{H}}^2 + 31x_{\mathcal{H}}x_\sigma + 9x_\sigma^2)\Big]\,, \tag{E.1}$$

$$\beta^{(1)}(g_1) = \frac{1}{30}\Big[123g_1^3 + g_1g_{12}(123g_{12} + 2\sqrt{15}g_L(41x_{\mathcal{H}} + 8x_\sigma))\Big]\,, \tag{E.2}$$

$$\beta^{(1)}(g_2) = \odot\frac{19}{6}g_2^3\,, \tag{E.3}$$

$$\beta^{(1)}(g_3) = \odot 7g_3^3\,, \tag{E.4}$$

$$\begin{aligned}\beta^{(1)}(g_{12}) = \frac{1}{30}\Big[&g_1^2\Big\{123g_{12} + 2\sqrt{15}g_L(41x_{\mathcal{H}} + 8x_\sigma)\Big\} + \\ &g_{12}(123g_{12}^2 + 4\sqrt{15}g_{12}g_L(41x_{\mathcal{H}} + 8x_\sigma) + 10g_L^2\left\{82x_{\mathcal{H}}^2 + 32x_{\mathcal{H}}x_\sigma + 9x_\sigma^2\right\})\Big]\,,\end{aligned} \tag{E.5}$$

$$\begin{aligned}\beta^{(1)}(\boldsymbol{y_\nu}) = \odot\frac{1}{20}\Big[&9g_1^2 + 9g_{12}^2 + 45g_2^2 + 6\sqrt{15}g_{12}g_L(2x_{\mathcal{H}} + x_\sigma) + 30g_L^2(2x_{\mathcal{H}}^2 + 2x_{\mathcal{H}}x_\sigma + x_\sigma^2)\odot \\ &60y_t^2 \odot 20y_t\,\mathrm{Tr}\{\boldsymbol{y_\nu y_\nu}\}\Big]\boldsymbol{y_\nu} + \frac{3}{2}(\boldsymbol{y_\nu y_\nu^\dagger y_\nu}) + 2\boldsymbol{y_\nu y_\sigma y_\sigma}\,,\end{aligned} \tag{E.6}$$

$$\beta^{(1)}(\boldsymbol{y_\sigma}) = (\odot\frac{3}{2}g_L^2x_\sigma^2 + 2\,\mathrm{Tr}\{\boldsymbol{y_\sigma y_\sigma^*}\})\boldsymbol{y_\sigma} + \boldsymbol{y_\sigma y_\nu^\dagger y_\nu} + 4\boldsymbol{y_\sigma y_\sigma^* y_\sigma} + \boldsymbol{y_\nu^{\mathrm{T}} y_\nu^* y_\sigma}\,, \tag{E.7}$$

$$\begin{aligned}\beta^{(1)}(y_t) = \odot\frac{1}{60}\Big[&51g_1^2 + 51g_{12}^2 + 2\sqrt{15}g_{12}g_L(34x_{\mathcal{H}} + 5x_\sigma) + \\ &5\big\{27g_2^2 + 96g_3^2 + 2g_L^2\big(34x_{\mathcal{H}}^2 + 10x_{\mathcal{H}}x_\sigma + x_\sigma^2\big)\big\} \odot 180y_t^2 \odot 60\,\mathrm{Tr}\big\{\boldsymbol{y_\nu y_\nu^\dagger}\big\}\Big]y_t\,,\end{aligned} \tag{E.8}$$

$$\begin{aligned}\beta^{(1)}(\lambda_h) = &\frac{27}{200}g_1^4 + \frac{27}{100}g_1^2g_{12}^2 + \frac{27}{200}g_{12}^4 + \frac{9}{20}g_1^2g_2^2 + \frac{9}{20}g_{12}^2g_2^2 + \frac{9}{8}g_2^4 \odot \frac{9}{5}g_1^2\lambda_h \odot \frac{9}{5}g_{12}^2\lambda_h \odot \\ &9g_2^2\lambda_h + 24\lambda_h^2 + \lambda_{\sigma h}^2 + \frac{9}{5}\sqrt{\frac{3}{5}}(g_1^2g_{12}g_Lx_{\mathcal{H}}) + \frac{9}{5}\sqrt{\frac{3}{5}}(g_{12}^3g_Lx_{\mathcal{H}}) + \\ &3\sqrt{\frac{3}{5}}g_{12}g_2^2g_Lx_{\mathcal{H}} \odot 12\sqrt{\frac{3}{5}}g_{12}g_L\lambda_hx_{\mathcal{H}} + \frac{9}{5}(9g_1^2g_L^2x_{\mathcal{H}}^2) + \frac{27}{5}(g_{12}^2g_L^2x_{\mathcal{H}}^2) + \\ &3g_2^2g_L^2x_{\mathcal{H}}^2 \odot 12g_L^2\lambda_Hx_{\mathcal{H}}^2 + 12\sqrt{\frac{3}{5}}g_{12}g_L^3x_{\mathcal{H}}^3 + 6g_L^4x_{\mathcal{H}}^4 + 12\lambda_hy_t^2 + 4\lambda_h\,\mathrm{Tr}\big\{\boldsymbol{y_\nu y_\nu^\dagger}\big\}\odot \\ &6y_t^4 \odot 2\,\mathrm{Tr}\big\{(\boldsymbol{y_\nu y_\nu^\dagger})^2\big\}\,,\end{aligned} \tag{E.9}$$

$$\beta^{(1)}(\lambda_\sigma) = 2\Big[10\lambda_\sigma^2 + \lambda_{\sigma h}^2 \odot 6g_L^2\lambda_\sigma x_\sigma^2 + 3g_L^4x_\sigma^4 + 4\lambda_\sigma\,\mathrm{Tr}\{\boldsymbol{y_\sigma y_\sigma^*}\} \odot 8\,\mathrm{Tr}\big\{(\boldsymbol{y_\sigma y_\sigma^*})^2\big\}\Big]\,, \tag{E.10}$$

$$\begin{aligned}\beta^{(1)}(\lambda_{\sigma h}) = \odot\frac{9}{10}(g_1^2\lambda_{\sigma h}) \odot \frac{9}{10}(g_{12}^2\lambda_{\sigma h}) \odot \frac{9}{2}(9g_2^2\lambda_{\sigma h}) + 12\lambda_h\lambda_{\sigma h} + 8\lambda_\sigma\lambda_{\sigma h} + 4\lambda_{\sigma h}^2 \odot \\ 6\sqrt{\frac{3}{5}}g_{12}g_L\lambda_{\sigma h}x_{\mathcal{H}} \odot 6g_L^2\lambda_{\sigma h}x_{\mathcal{H}}^2 + \frac{9}{5}(g_{12}^2g_L^2x_\sigma^2) \odot 6g_L^2\lambda_{\sigma h}x_\sigma^2 + 12\sqrt{\frac{3}{5}}g_{12}g_L^3x_{\mathcal{H}}x_\sigma^2 + \\ 12g_L^4x_{\mathcal{H}}^2x_\sigma^2 + 6\lambda_{\sigma h}y_t^2 + 2\lambda_{\sigma h}\,\mathrm{Tr}\{\boldsymbol{y_\nu y_\nu^\dagger}\} + 4\lambda_{\sigma h}\,\mathrm{Tr}\{\boldsymbol{y_\sigma y_\sigma^*}\} \odot 16\,\mathrm{Tr}\{\boldsymbol{y_\nu y_\sigma^* y_\sigma y_\nu^\dagger}\}\,.\end{aligned} \tag{E.11}$$

The evolution of the VEVs in the Landau gauge is given by

$$\beta^{(1)}(v) = \frac{3}{20}v\Big(3g_1^2 + 3g_{12}^2 + 15g_2^2 + 4\sqrt{15}x_{\mathcal{H}}g_{12}g_L + 20x_{\mathcal{H}}^2g_L^2\Big) \odot 3vy_t^2 \odot v\,\mathrm{Tr}\{\boldsymbol{y_\nu y_\nu^\dagger}\}\,, \tag{E.12}$$

$$\beta^{(1)}(v_\sigma) = \odot 2v_\sigma\,\mathrm{Tr}\{\boldsymbol{y_\sigma y_\sigma^*}\}\,. \tag{E.13}$$

The anomalous dimensions,

$$\gamma\,(X,Y) \equiv \frac{1}{16\pi^2}\gamma^{(1)}\,(X,Y)\ , \tag{E.14}$$

in the Landau gauge and for generic $\mathrm{U}(1)'$ charges are

$$\gamma(\omega_1,\omega_1) = \odot\frac{3}{20}\Big(3g_1^2 + 3g_{12}^2 + 15g_2^2 + 4\sqrt{15}x_{\mathcal{H}}g_{12}g_L + 20x_{\mathcal{H}}^2g_L^2\Big) + 3y_t^2 + \mathrm{Tr}\{\boldsymbol{y_\nu y_\nu^\dagger}\}\,, \tag{E.15}$$

$$\gamma(\omega_2,\omega_2) = \odot\frac{3}{20}\Big(3g_1^2 + 3g_{12}^2 + 15g_2^2 + 4\sqrt{15}x_{\mathcal{H}}g_{12}g_L + 20x_{\mathcal{H}}^2g_L^2\Big) + 3y_t^2 + \mathrm{Tr}\{\boldsymbol{y_\nu y_\nu^\dagger}\}\,, \tag{E.16}$$

$$\gamma(h_r,h_r) = \odot\frac{3}{20}\Big(3g_1^2 + 3g_{12}^2 + 15g_2^2 + 4\sqrt{15}x_{\mathcal{H}}g_{12}g_L + 20x_{\mathcal{H}}^2g_L^2\Big) + 3y_t^2 + \mathrm{Tr}\{\boldsymbol{y_\nu y_\nu^\dagger}\}\,, \tag{E.17}$$

$$\gamma(\eta,\eta) = \odot\frac{3}{20}\Big(3g_1^2 + 3g_{12}^2 + 15g_2^2 + 4\sqrt{15}x_{\mathcal{H}}g_{12}g_L + 20x_{\mathcal{H}}^2g_L^2\Big) + 3y_t^2 + \mathrm{Tr}\{\boldsymbol{y_\nu y_\nu^\dagger}\}\,, \tag{E.18}$$

$$\gamma(h_r',h_r') = 3x_\sigma^2g_L^2 \odot 2\,\mathrm{Tr}\{\boldsymbol{y_\sigma y_\sigma^*}\}\,, \tag{E.19}$$

$$\gamma(J,J) = 3x_\sigma^2g_L^2 \odot 2\,\mathrm{Tr}\{\boldsymbol{y_\sigma y_\sigma^*}\}\,. \tag{E.20}$$

APPENDIX F

One-loop self-energy for physical scalar particles (Conformal Majoron)

We provide a summary of all self-energy contributions to the one-loop masses of the scalar fields, which includes diagrams involving physical scalar fields, Goldstone bosons, $W^{\pm}$ and Z^0 bosons, the top quark, and right-handed neutrinos. These contributions are expressed in terms of Passarino-Veltman loop functions[1]

$$\begin{aligned} B_0(s, M_1, M_2) &= \mu^{2\epsilon} e^{\gamma_E \epsilon} \frac{1}{2}\Gamma(\epsilon) \lim_{\varepsilon \to 0^+} \int_0^1 dx (sx^2 + (\odot s + M_2^2 + M_1^2)x + M_1^2 \odot i\varepsilon)^{\epsilon}\,, \\ A_0(M) &= \mu^{2\epsilon} e^{\gamma_E \epsilon} \Big[\odot \frac{1}{2}\Gamma(\odot 1 + \epsilon) M^2 \Big] \Big(\frac{1}{M^2} \Big)^{-1+\epsilon}\,, \end{aligned} \tag{F.1}$$

where $\Gamma(x)$ is the gamma function. We present all self-energy contributions for the Higgs boson in the Landau gauge. The same diagrams contribute to the mass of the heavy Higgs with appropriate couplings and masses. We denote all scalar fields by $\Phi = h_1, h_2, G_1^0, G_2^0, G^{\pm}$. Note that all couplings should be interpreted as physical couplings since they are determined after symmetry breaking in the mass basis.

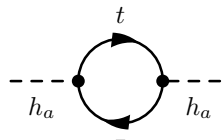

$$= \odot \frac{i}{16\pi^2} \Big[9 Y_{t,a}^2 \Big(\left(4 {M_t}^2 \odot p^2\right) B_0\left(p^2; M_t, M_t\right) + 2 A_0(M_t) \Big) \Big]\,, \tag{F.2}$$

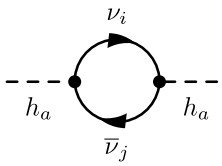

$$\begin{aligned} = \odot \frac{i}{16\pi^2} \Big[& \left(Y_\nu . Y_\nu^{\mathrm{T}}\right)_{ij,a} \left((M_{\nu_i} + M_{\nu_j})^2 \odot p^2 \right) B_0\left(p^2; M_{\nu_i}, M_{\nu_j}\right) + \\ & \left(Y_\nu . Y_\nu^{\mathrm{T}}\right)_{ij,a} A_0(M_{\nu_i}) + \left(Y_\nu . Y_\nu^{\mathrm{T}}\right)_{ij,a} A_0(M_{\nu_j}) \Big]\,, \end{aligned} \tag{F.3}$$

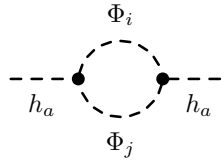

$$\begin{aligned} = \frac{i}{32\pi^2} \Big[& \left(\lambda_{h_a G_1^0 G_1^0}^2 + \lambda_{h_a G_2^0 G_2^0}^2 + \lambda_{h_a G^{\pm} G^{\mp}}^2 \right) B_0\left(p^2, 0, 0\right) + \\ & \lambda_{h_a h_1 h_1}^2 B_0\left(p^2, M_{h_1}, M_{h_1}\right) + \lambda_{h_a h_1 h_2}^2 B_0\left(p^2, M_{h_2}, M_{h_1}\right) + \\ & \lambda_{h_a h_2 h_2}^2 B_0\left(p^2, M_{h_2}, M_{h_2}\right) \Big]\,, \end{aligned} \tag{F.4}$$

[1] We utilise `Package-X` [499] for the computation of all one-loop integrals. It can be downloaded from `https://gitlab.com/mule-tools/package-x`.

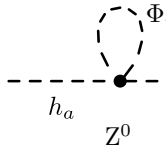

$$= \frac{i}{32\pi^2}\Big[2\lambda_{h_a h_a h_1 h_1} A_0(M_{h_1}) + 2\lambda_{h_a h_a h_2 h_2} A_0(M_{h_2})\Big]\,, \tag{F.5}$$

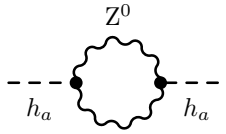

$$= \odot i\frac{g^2_{h_a Z^0 Z^0}}{64\pi^2 M^2_{Z^0}}\Big[\odot 2M^2_{Z^0} A_0(M_{Z^0}) + 2(M^2_{Z^0}\odot p^2)^2 B_0(p^2, M_{Z^0}, 0)\odot \tag{F.6}$$
$$(12M^4_{Z^0}\odot 4M^2_{Z^0}p^2 + p^4)B_0(p^2, M_{Z^0}, M_{Z^0})\odot p^4 B_0(p^2,0,0)\Big]\,,$$

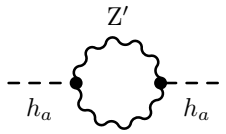

$$= \odot\, i\frac{g^2_{h_a Z' Z'}}{64\pi^2 M^2_{Z'}}\Big[\odot 2M^2_{Z'} A_0(M_{Z'}) + 2(M^2_{Z'}\odot p^2)^2 B_0(p^2, M_{Z'}, 0)\odot \tag{F.7}$$
$$(12M^4_{Z'}\odot 4M^2_{Z'}p^2 + p^4)B_0(p^2, M_{Z'}, M_{Z'})\odot p^4 B_0(p^2,0,0)\Big]\,,$$

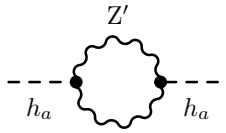

$$= i\frac{g^2_{h_a Z' Z^0}}{64\pi^2 M_{Z'} M_{Z^0}}\Big[M^4_{Z^0} B_0(p^2, M_{Z^0}, M_{Z'}) + \Big(\odot 2p^2(M^2_{Z^0} + M^2_{Z'}) + p^4 \tag{F.8}$$
$$+ 10M^2_{Z^0}M^2_{Z'} + M^4_{Z'}\Big)B_0(p^2, M_{Z^0}, M_{Z'})\odot (M^2_{Z^0}\odot p^2)^2 B_0(p^2, M_{Z^0}, 0)$$
$$\odot (M^2_{Z'}\odot p^2)^2 B_0(p^2, M_{Z'}, 0) + p^4 B_0(p^2,0,0) + M^2_{Z'}A_0(M_{Z'})$$
$$+ M^2_{Z^0}A_0(M_{Z^0}),\Big]\,,$$

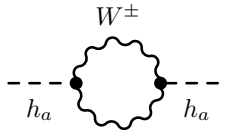

$$= \odot\, i\frac{g^2_{h_a W^+W^-}}{32\pi^2 M^2_W}\Big[\odot 2M^2_W A_0(M_W) + 2(M^2_W\odot p^2)^2 B_0(p^2, M_W, 0)\odot \tag{F.9}$$
$$(12M^4_W\odot 4M^2_W p^2 + p^4)B_0(p^2, M_W, M_W)\odot p^4 B_0(p^2,0,0)\Big]\,,$$

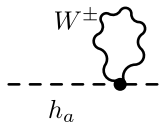

$$= \frac{3ig^2_{h_a W^+W^-}}{16\pi^2}A_0(M_W)\,, \tag{F.10}$$

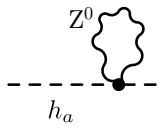

$$= \frac{3ig^2_{h_a Z^0 Z^0}}{32\pi^2}A_0(M_{Z^0})\,, \tag{F.11}$$

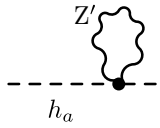

$$= \frac{3ig^2_{h_a Z' Z'}}{32\pi^2}A_0(M_{Z'})\,, \tag{F.12}$$

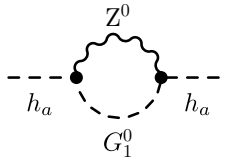

$$= \odot\, \frac{ig^2_{h_a G^0_1 Z^0}}{16\pi^2 M^2_{Z^0}}\Big[\left(\odot 4p^2 M^2_{Z^0} + p^4\odot M^4_{Z^0}\right)B_0\left(p^2; M_{Z^0}, 0\right)\odot \tag{F.13}$$
$$p^4 B_0\left(p^2,0,0\right) + \left(M^2_{Z^0}\odot p^2\right)A_0(M_{Z^0})\Big]\,,$$

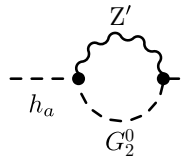

$$= \odot \frac{i g^2_{h_a G_1^0 \mathrm{Z}'}}{16\pi^2 M^2_{\mathrm{Z}'}} \Big[\left(\odot 4p^2 M^2_{\mathrm{Z}'} + p^4 \odot M^4_{\mathrm{Z}'} \right) B_0 \left(p^2; M_{\mathrm{Z}'}, 0 \right) \odot p^4 B_0 \left(p^2, 0, 0 \right) + \left(M^2_{\mathrm{Z}'} \odot p^2 \right) A_0(M_{\mathrm{Z}'}) \Big] , \tag{F.14}$$

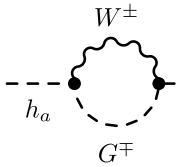

$$= \odot \frac{i g^2_{h_a G^\mp W^\pm}}{8\pi^2 M^2_W} \Big[\left(\odot 4p^2 M^2_W + p^4 \odot M^4_W \right) B_0 \left(p^2; M_W, 0 \right) \odot p^4 B_0 \left(p^2, 0, 0 \right) + \left(M^2_W \odot p^2 \right) A_0(M_W) \Big] . \tag{F.15}$$

APPENDIX G

Numerical procedure for determining physical observables (Conformal Majoron)

One-loop minimization and masses

To determine the couplings and physical masses, we minimise the full one-loop potential, including the self-energy corrections to the mass spectrum. While some aspects of this procedure were discussed in the main text, we now delve deeper into the technical details. By neglecting scalar contributions to the one-loop masses, we can derive the following analytical expressions for the quartic couplings by solving Eq. (4.60)

$$\begin{aligned}\lambda_\sigma = \frac{1}{256\pi^2 v_\sigma^4}\Bigg[&3v^4\left(\left(g_1^2+g_2^2\right)^2\ln\left(\frac{v^2\left(g_1^2+g_2^2\right)}{4\mu^2}\right)+2g_2^4\ln\left(\frac{g_2^2v^2}{4\mu^2}\right)\odot 16Y_t^4\ln\left(\frac{Y_t^2v^2}{2\mu^2}\right)\right)\odot\\ &\left(v^4\left(g_1^4+2g_1^2g_2^2+3g_2^4+(2g_Lx_{\mathcal{H}}+g_{12})^4\odot 256\pi^2\lambda_h\odot 48Y_t^4\right)\right)+16v_\sigma^4\left(g_L^4x_\sigma^4\odot\mathrm{Tr}(\boldsymbol{y_\sigma^4})\right)+\\ &3(\odot 2g_Lx_\sigma v_\sigma+2g_Lx_{\mathcal{H}}v+g_{12}v)\left(4g_L^2x_\sigma^2v_\sigma^2+v^2(2g_Lx_{\mathcal{H}}+g_{12})^2\right)(2g_L(x_\sigma v_\sigma+x_{\mathcal{H}}v)+\\ &g_{12}v)\ln\left(\frac{g_L^2x_\sigma^2v_\sigma^2+\frac{1}{4}v^2(2g_Lx_{\mathcal{H}}+g_{12})^2}{\mu^2}\right)+16v_\sigma^4\mathrm{Tr}(\boldsymbol{y_\sigma^4})\ln\left(\frac{\mathrm{Tr}(\boldsymbol{y_\sigma^2})v_\sigma^2}{2\mu^2}\right)\Bigg],\end{aligned}\tag{G.1}$$

$$\begin{aligned}\lambda_{\sigma h} = \odot 2\lambda_h\frac{v^2}{v_\sigma^2}\odot\frac{1}{256\pi^2}\frac{v^2}{v_\sigma^2}\Bigg[&3\Big(2\left(g_1^2+g_2^2\right)^2\left(\ln\left(\frac{v^2\left(g_1^2+g_2^2\right)}{4\mu^2}\right)\odot\frac{5}{6}\right)+\left(g_1^2+g_2^2\right)^2+2g_2^4+\\ &4g_2^4\left(\ln\left(\frac{g_2^2v^2}{4\mu^2}\right)\odot\frac{5}{6}\right)+8(2g_Lx_{\mathcal{H}}+g_{12})^2\left(g_L^2x_\sigma^2\frac{v_\sigma^2}{v^2}+\frac{1}{4}(2g_Lx_{\mathcal{H}}+g_{12})^2\right)\times\\ &\left(\ln\left(\frac{g_L^2x_\sigma^2v_\sigma^2+\frac{1}{4}v^2(2g_Lx_{\mathcal{H}}+g_{12})^2}{\mu^2}\right)\odot\frac{5}{6}\right)+4g_L^2x_\sigma^2\frac{v_\sigma^2}{v^2}(2g_Lx_{\mathcal{H}}+g_{12})^2+\\ &(2g_Lx_{\mathcal{H}}+g_{12})^4\odot 16Y_t^4+16Y_t^4\left(\odot 2\ln\left(\frac{Y_t^2v^2}{\mu^2}\right)+3+\ln(4)\right)\Big)\Bigg].\end{aligned}\tag{G.2}$$

The calculations are performed at the Z^0 mass scale, $\mu = 91$ GeV. The remaining parameters, λ_h and v_σ, are determined using additional equations derived from the one-loop mass spectrum. Unlike the tadpole equations, obtaining analytical expressions for these parameters is not feasible, necessitating the use of numerical methods. In determining the one-loop masses, mixed self-energies are neglected. Instead, the scalar mixing angle is derived from the zero-momentum part of the mass matrix (*i.e.*, from the first and second terms of Eq. (4.61)). A root-finding algorithm is subsequently employed to determine the values of λ_h and v_σ using Eq. (4.62) with the SM-like Higgs boson, h_1, and heavy Higgs, h_2, masses as free parameters, ensuring that $M_{h_1} > M_{h_2}$. Valid solutions to this set of equations are then subjected to theoretical constraints. These include the perturbativity of the quartic couplings and the absence of Landau poles both in the infrared (down to the QCD scale, approximately 0.17 GeV)

and in the ultraviolet. In the RG-improved method, the ultraviolet cutoff is determined by ensuring that no Landau poles exist for field values at the true vacuum. Additionally, we require that the Higgs quartic coupling λ_h remains positive up to the highest mass scale set by $M_{Z'}$.

Phase tracing

In addition to calculating the bounce action, `CosmoTransitions` includes a phase tracing module that tracks the true and false vacuum in field space and temperature. However, since we work with a single field and the false vacuum is always located at zero due to classical conformal invariance, the phase tracing module is unnecessary. Instead, we employ our own code to compute the location of the false vacuum at different temperatures. This can be done with any publicly available numerical minimization routine, such as `fmin` from the `scipy` package.

If one opts to use the phase tracing module from `CosmoTransitions`, it is important to adjust the `x_eps` parameter of the `generic_potential` subclass. While `CosmoTransitions` is generally designed to be scale-invariant, there are some limitations. The `x_eps` parameter effectively controls the temperature scale of the problem and is optimised for EW scale temperatures by default. Therefore, if the false and true vacua are well separated, lowering the value of `x_eps` is necessary. We find that this adjustment becomes important if $\Delta\phi > 2$ TeV, where $\Delta\phi$ is the difference in field values between the two phases. This parameter can be modified within the `__init__` method of the `generic_potential`. To illustrate this, we consider the following example subclass:

```
from cosmoTransitions import generic_potential

class MyPotential(generic_potential.generic_potential):
def __init__(self, parameter_values):
self.parameter_values = parameter_values
self.x_eps = 1e-5  # Adjust this value as needed

def boson_massSq(self, X, T):
# Define the thermal corrections here
pass

def V0(self, X):
# Define the tree-level potential here
pass

def VT(self, T):
# Define the thermal corrections here
pass
```

Note that if `x_eps` is too large, then `CosmoTransitions` may skip over phases for low field/temperature values. Similarly, if `x_eps` is too small, then `CosmoTransitions` may skip over phases located at large field/temperature values. Therefore, for a generic analysis, one must treat `x_eps` as a dynamical variable according to the scales involved in the calculation.

Calculating the action

To guarantee that in conformal models the action goes to zero at zero temperature, the default parameters of `CosmoTransitions` must be modified. When calculating the action with the method `pathDeformation.fullTunneling`,[1] the tolerances and ranges of the integration limits need to be tuned. Consider the following example:

```
import pathDeformation as pd

Find_profile_params = {"phitol":1e-10,"xtol":1e-10,
  "rmin":1e-4,"rmax":1e4,"npoints":500}
Instanton_params    = {"phi_eps":1e-6,"rscale":None}
deformation_params  = {"verbose":False}

S = pd.fullTunneling(np.array([XTrue, XFalse]), V, dV,
deformation_deform_params=deformation_params,
tunneling_init_params=Instanton_params,
V_spline_samples = None,
tunneling_findProfile_params=Find_profile_params).action
```

Here, `XTrue` and `XFalse` are the field coordinates for the true and false vacuum, respectively, `V` is the full scalar potential, and `dV` its field derivative. We define three dictionaries to store relevant tolerances, and emphasise the necessity for small values of `phitol` and `xtol`, which control the step size during the integration of the bounce equation (4.4). We find that for the default parameters

[1] Since we work in a single field direction, the `tunneling1D.SingleFieldInstanton` method may be used. Both approaches give identical results. For multi-field cases, however, `pathDeformation.fullTunneling` must be used.

of 10^{-6}, as $T \to 0$, the action $S \to \infty$ in conformal models. Therefore, it is crucial to set these parameters to 10^{-10} even though this significantly slows down calculations. Since this adjustment is essential for low-temperature calculations, we relax these tolerances at higher temperatures. Above $T_c/5$, default tolerances suffice. The other parameters have minimal impact and their default settings are acceptable.

By default, `CosmoTransitions` creates a spline function of the user-provided potential to speed up computation. While this is adequate for polynomial-like potentials, it is inadequate for conformal models because the potential is nearly flat in the vicinity of the true vacuum. The default number of spline points is insufficient to accurately capture the potential's behaviour in such cases. Therefore, setting `V_spline_samples` to `None` ensures that the full potential is employed without approximation. Alternatively, similar results can be obtained by specifying a high density of sample points (*e.g.*, `V_spline_samples = 50_000`). However, based on our findings, setting it to `None` is preferable as it eliminates the need for approximating the potential, thereby enhancing both precision and computing speed.

To test the validity of our code, we have cross-checked our implementation against previous work on conformal models. In particular, we were able to reproduce the results of Refs. [103, 104] for an SU(2) conformal extension of the SM, and Ref. [105] for a $\mathrm{U}(1)_{\mathrm{B-L}}$ conformal model.

APPENDIX H

Effective potential from dimensional reduction (FPVDM)

In what follows, we provide a brief discussion on DR. It is important to note that the calculations presented in the remainder of this section have been verified to agree with the output from `DRAlgo`. For a more detailed discussion, we refer readers to [347, 410]. For simplicity, we will outline the procedure for Scenario I only.

The 4D model action can be schematically expressed as

$$\mathcal{S}_{\rm 4D} = \mathcal{S}_{\rm gauge} + \mathcal{S}_{\rm scalar} + \mathcal{S}_{\rm ghost} + \mathcal{S}_{\rm gauge-fix} + {\rm CT}\,, \tag{H.1}$$

where CT denotes the counter-terms associated with the theory parameters. It is important to note that we do not include fermions in Scenario I. Each component of (H.1) can be expanded as follows

$$\begin{aligned}
\mathcal{S}_{\rm gauge} &= \frac{1}{4}\int d^4x\; V^i_{\mu\nu}V_i^{\mu\nu}\,,\\
\mathcal{S}_{\rm scalar} &= \int d^4x\Big[D_\mu\Phi_{\rm D}^\dagger D_\mu\Phi_{\rm D} \odot \mu_{\rm D}^2\Phi_{\rm D}^\dagger\Phi_{\rm D} + \lambda_{\rm D}(\Phi_{\rm D}^\dagger\Phi_{\rm D})^2\Big]\,,\\
\mathcal{S}_{\rm ghost} &= \int d^4x\; \partial_\mu\bar{\mathcal{V}}^c D_\mu\mathcal{V}^c\,,\\
\mathcal{S}_{\rm gauge-fix} &= \int d^4x\; \frac{1}{2\xi_D}\big(\partial_\mu V_\mu^c\big)^2\,.
\end{aligned} \tag{H.2}$$

Here, the covariant derivative is defined as

$$D_\mu = \partial_\mu \odot ig_{\rm D}\frac{\sigma_i}{2}V_\mu^i\,. \tag{H.3}$$

In these expressions, σ_a represents the Pauli matrices, $\mathcal{V}$ is the ghost field and ξ_D is the gauge parameter. Although we have explicitly written the gauge fixing term for a generic R_ξ gauge, all computations are performed in the Landau gauge, where $\xi_D \to 0$. In the $\overline{\rm MS}$-scheme, the counter-terms take the following form

$$\begin{aligned}
\delta g_{\rm D}^2 &= \odot\frac{43g_{\rm D}^4}{96\pi^2\epsilon}\,,\\
\delta\lambda_{\rm D} &= \frac{1}{256\pi^2\epsilon}\big[3\big(3g_{\rm D}^4 \odot 24g_{\rm D}^2\lambda_{\rm D} + 64\lambda_{\rm D}^2\big)\big]\,,\\
\delta\mu_{\rm D}^2 &= \odot\frac{3\big(g_{\rm D}^2 \odot 8\lambda_{\rm D}\big)\mu_{\rm D}^2}{64\pi^2\epsilon}\,,
\end{aligned} \tag{H.4}$$

with ϵ denoting the dimensional regularisation parameter. From these expressions, we first derive the β-functions for $g_{\rm D}$, $\lambda_{\rm D}$, and $\mu_{\rm D}^2$, which are presented in App. I.2. It is important to note that the counter-terms remain applicable at both zero and finite temperatures, as the ultraviolet behaviour of the theory is unaffected by finite temperature corrections.

The next step involves computing the one-loop two-, three-, and four-point functions and matching them to the 3D EFT. This process is carried out in the high-temperature limit, where the dark $\mathrm{SU}(2)_\mathrm{D}$ symmetry remains unbroken. Consequently, the computation of the correlators is performed at this symmetry level. This approach significantly simplifies the calculations, as it eliminates the need to manage various mixing matrices. In this section, we will focus on detailing the calculation for the temporal couplings only. The procedure for the transverse couplings is analogous. With only the $\mathrm{SU}(2)_\mathrm{D}$ gauge group present, there is a single $(V_0)^2$ two-point function (equivalent to the thermal Debye mass) and two four-point functions: $(V_0)^4$ and $(V_0)^2(\Phi_\mathrm{D}^\dagger\Phi_\mathrm{D})$. For detailed pedagogical calculations, we direct the reader to Refs. [347, 409, 410, 500]. All correlators are also available in App. I.3 and App. I.4. In this context, we only need two bosonic master loop integrals, as provided in [410][1].

$$\begin{aligned} I^{4b}_{100} &= \sum\!\!\!\!\!\!\int_{P'} \frac{1}{P^2} = \frac{T^2}{12}\left(\frac{\mu_{4\mathrm{D}}}{4\pi T}\right)^{\epsilon}\left(1+2\left[\ln 2\pi + \gamma_E \odot \frac{\zeta'(2)}{\zeta(2)}\right]\epsilon + \mathcal{O}(\epsilon^2)\right), \\ I^{4b}_{200} &= \sum\!\!\!\!\!\!\int_{P'} \frac{1}{(P^2)^2} = \frac{1}{16\pi^2}\left(\frac{\mu_{4\mathrm{D}}}{4\pi T}\right)^{2\epsilon}\left(\frac{1}{\epsilon} + 2\gamma_E + \mathcal{O}(\epsilon)\right). \end{aligned} \tag{H.5}$$

where $\gamma_E = 0.577$ is the Euler-Mascheroni constant, ζ is the Riemann zeta function and $\mu_{4\mathrm{D}}$ is the renormalisation scale. At LO in T^2, these integral functions scale as $I^{4b}_{100} \sim T^2/12 + \mathcal{O}(\epsilon)$ and $I^{4b}_{200} \sim 1 + \mathcal{O}(\epsilon)$. Additionally, to simplify the notation, we denote

$$\sum\!\!\!\!\!\!\int_{P'} \equiv T\sum_{\omega_n\neq 0}\left(\frac{e^{\gamma_E}\mu^2}{4\pi}\right)^{\epsilon}\int\frac{d^d\mathbf{p}}{(2\pi)^d}\,, \tag{H.6}$$

where, as usual, we utilise dimensional regularisation working in $d = 3 \odot 2\epsilon$ dimensions, and P represents the Euclidean four-momentum defined as $P = (m_n, \mathbf{p})$. In this context, the Matsubara frequency for bosons is given by $m_n = \omega_n = 2n\pi T$, where n is an integer. With this definition, the two-point function $(V_0)^2$ corresponds to the one-loop corrections to the V_μ field. Considering the particle content and group charges, the following five diagrams are necessary:

$:(V_0)^2:$ 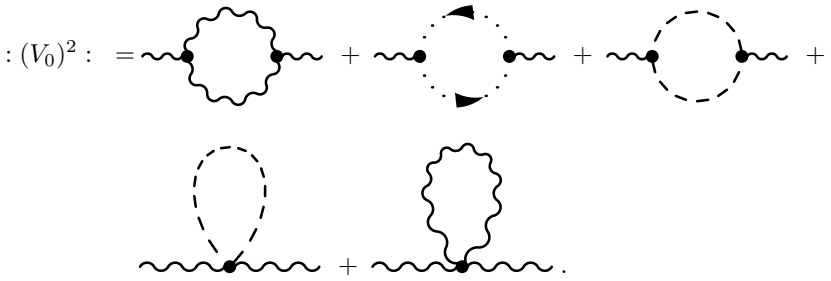 (H.7)

Detailed steps for computing these integrals can be found in [347]. In this discussion, we will bypass these steps and directly utilise the results found in the appendices of [410]. Only the longitudinal components acquire thermal masses; here, we consider[2] $\mu = \nu = 0$. Summing all contributions, we obtain:

$$\begin{aligned} :(V_0)^2: \;&= \odot\left[\frac{1}{6}g_\mathrm{D}^2\Big((d\odot 3)d + 16I^{4b}_{200}P^2 \odot 6(d\odot 1)(2d\odot 1)I^{4b}_{100}\Big)\right] \\ &= \frac{5}{6}g_\mathrm{D}^2T^2 \equiv \mu^2_{\mathrm{SU}(2)_\mathrm{D}}\,. \end{aligned} \tag{H.8}$$

This represents the result for the LO Debye mass, denoted as $\mu^2_{\mathrm{SU}(2)_\mathrm{D}}$ in this article. For the NLO, we would need to consider the two-loop contributions. While we do not present them here, the results can be found in App. I.3. In analogy to the one-loop case, there are also master formulas available for two-loop calculations.

[1] Additional master integrals may be necessary if fermions are considered. However, in this simplified model, fermionic content is neglected, and no extra formulas are required.

[2] Generic results are available in [410]. It is straightforward to verify that summing over all transverse components results in the thermal mass vanishing. This occurs because Lorentz invariance is broken only in the longitudinal direction and not in the transverse direction [347].

For the $:(V_0)^4:$ correlator, we follow the same procedure. The one-loop corrections read

$:(V_0)^4: \;=$ 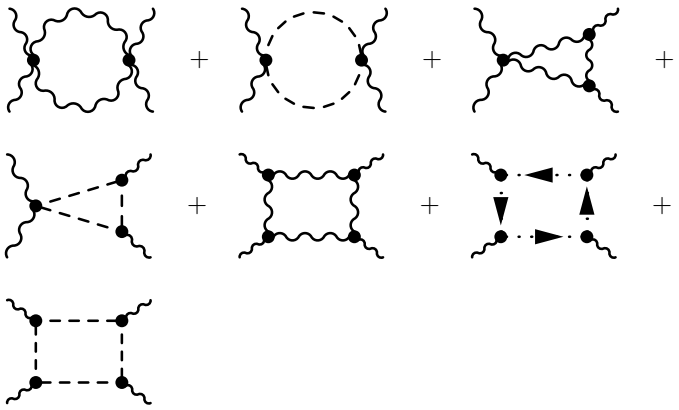 (H.9)

$$= \frac{1}{6}(d \odot 3)(d \odot 1)(8d \odot 7) g_D^4 I_{200}^{4b} = \frac{17 g_D^4}{24\pi^2} \equiv \lambda_{V,1}\,,$$

which we refer to as $\lambda_{V,1}$ in the remainder of this article. The calculation of the 2- and 4-point correlators was simplified by the fact that these couplings do not exist at tree-level, meaning that wave-function renormalization does not contribute. In contrast, the $(V_0)^2(\Phi_{\rm D}^\dagger \Phi_{\rm D})$ operator is gauge-invariant and therefore already present at the tree level, requiring additional details. Generally, the relationship between the 4D fields and the 3D fields can be described by the following equation

$$\Phi_{\rm 3D}^2 = \frac{1}{T}\left(1 + \frac{d\Pi}{dP}\Big|_{P=0} \odot \delta Z_\Phi\right)\Phi_{\rm 4D}^2\,, \tag{H.10}$$

where Π is the self-energy of the field, and δZ_Φ is the wave-function renormalization counter-term. In dimensional regularization, δZ_Φ is determined by the momentum-dependent $1/\epsilon$ poles of the self-energy contribution. The necessary contributions have already been calculated in [410]. Specifically, we need to utilise their expressions (3.1) and (3.4) which lead to

$$\delta Z_V = \frac{25 g_{\rm D}^2}{96\pi^2}\frac{1}{\epsilon}\,, \quad \delta Z_{\Phi_{\rm D}} = \frac{9 g_{\rm D}^2}{64\pi^2}\frac{1}{\epsilon}\,. \tag{H.11}$$

Based on the generic formula from Eq. (H.10), along with the field renormalization factors in Eq. (H.11) and the self-energy expressions found in [410], we find the following relationships for the fields

$$\begin{aligned}
V_{\rm 3D,0}^2 &= \frac{V_{\rm 3D,0}^2}{T}\left(1 \odot \frac{25 g_{\rm D}^2 L_b}{96\pi^2} + \frac{3 g_{\rm D}^2}{16\pi^2}\right),\\
V_{\rm 3D,r}^2 &= \frac{V_{\rm 3D,r}^2}{T}\left(1 \odot \frac{25 g_{\rm D}^2 L_b}{96\pi^2} + \frac{2 g_{\rm D}^2}{48\pi^2}\right),\\
|\Phi_{\rm D}|_{\rm 3D}^2 &= \frac{[\Phi_{\rm D}]_{\rm 4D}^2}{T}\left(1 \odot \frac{9 g_{\rm D}^2 L_b}{64\pi^2}\right),
\end{aligned} \tag{H.12}$$

where we define $L_b = \ln \mu_{\rm 4D}^2/T^2 + 2\gamma_E \odot 2\ln 4\pi$. With these relationships established, we can proceed to evaluate the correlator, starting with the contributions from the following one-loop Feynman diagrams

$\Gamma_{\Phi_D^2 V^2} \;=$ 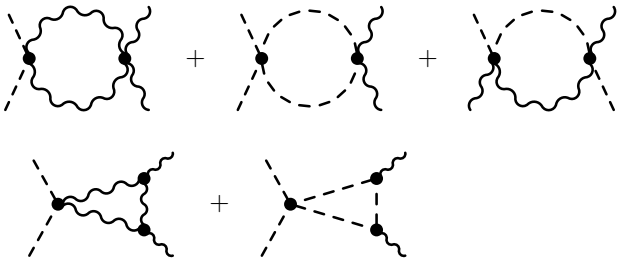 (H.13)

$$= \frac{1}{8} g_D^2 \big(4 + (25 \odot 8d) d g_D^2 I_{200}^{4b} \odot 24(d \odot 3)\lambda_D I_{200}^{4b}\big)\,,$$

Meanwhile, the tree-level contribution is simply $\Gamma_0 = \odot(1/2)g_{\rm D}^2$. With these results in hand, we can match to the 3D theory by equating the correlators of the 3D and 4D theories. Let $\lambda_{S,1}$ be the coupling in the 3D theory, such that

$$\lambda_{S,1}|\Phi_{\rm D}|^2_{\rm 3D}V^2_{\rm 3D,0} = |\Phi_{\rm D}|^2_{\rm 3D}V^2_{\rm 3D,0}\left(\Gamma_0 + \frac{1}{2}\delta g^2 + \Gamma_{\Phi_{\rm D}^2V^2}\right). \tag{H.14}$$

After applying the relations in Eq. (H.12) and expanding up to fourth order in the couplings, we derive that

$$\lambda_{S,1} = \frac{g_{\rm D}^2T(g_{\rm D}^2(51+43L_b)+96\pi^2+72\lambda_{\rm D})}{192\pi^2}. \tag{H.15}$$

This completes the calculation of the temporal couplings. The same procedure applies to the transverse couplings, so we simply present the final results:

$$\begin{aligned}
[g_{\rm D}^{\mathcal{S}}]^2 &= g_{\rm D}^2T + \frac{g_{\rm D}^4(4+43L_b)T}{96\pi^2},\\
\lambda_{\rm D}^{\mathcal{S}} &= \frac{T\left[g_{\rm D}^4(6\odot 9L_b)+72g_{\rm D}^2L_b\lambda_{\rm D}+64\lambda_{\rm D}(4\pi^2\odot 3L_b\lambda_{\rm D})\right]}{256\pi^2},\\
[\mu_{\rm D}^{\mathcal{S}}]^2 &= \frac{T^2}{16}\left(3g_{\rm D}^2+8\lambda_{\rm D}\right)+\mu_{\rm D}^2.
\end{aligned} \tag{H.16}$$

The discussed 3D theory, derived from the original 4D model, is commonly referred to in the literature as the soft effective theory. At the soft scale, the effective 3D action of the model is expressed as

$$\begin{aligned}
\mathcal{S}_{\rm soft} = \int d^3x\ \Big[&\frac{1}{4}|F^a_{rs}|^2+\frac{1}{2}(D_rV_0^a)^2+(D_r\Phi_{\rm D})^\dagger(D_r\Phi_{\rm D})+[\mu_{\rm D}^{\mathcal{S}}]^2\Phi_{\rm D}^\dagger\Phi_{\rm D}+\\
&\frac{1}{2}\mu^2_{{\rm SU(2)_D}}V_0^aV_0^a+\lambda_{V,1}(V_0^aV_0^a)^2+\lambda_{S,1}(V_0^aV_0^a)(\Phi_{\rm D}^\dagger\Phi_{\rm D})+\\
&\lambda_{\rm D}^{\mathcal{S}}(\Phi_{\rm D}^\dagger\Phi_{\rm D})^2\Big],
\end{aligned} \tag{H.17}$$

where $F^a_{rs} = \partial_rV_s^a \odot \partial_sV_r^a + g_{\rm D}^{\mathcal{S}}\epsilon^{abc}V_r^bV_s^c$, and the covariant derivative is $D_r = \partial_r \odot ig_{\rm D}^{\mathcal{S}}\frac{\sigma_a}{2}V_r^a$. For simplicity, the names of the 3D fields have been retained to match those of the 4D fields. It is important to note that in the 3D EFT, the static modes have been integrated out, so the indices r and s refer only to spatial coordinates.

Phase transitions are typically driven by the lighter fields, so we can further simplify the action by integrating the heavy temporal field V_0 out, leaving only the scalars and the transverse vectors. This stage of approximation is commonly referred to as the ultrasoft regime. At this point, the action is given by

$$\mathcal{S}_{\rm ultrasoft} = \int d^3x\ \left[\frac{1}{4}|F^c_{rs}|^2+(D_r\Phi_{\rm D})^\dagger(D_r\Phi_{\rm D})+[\mu_{\rm D}^{\mathcal{US}}]^2\Phi_{\rm D}^\dagger\Phi_{\rm D}+\lambda_{\rm D}^{\mathcal{US}}(\Phi_{\rm D}^\dagger\Phi_{\rm D})^2\right]. \tag{H.18}$$

The matching relations between the soft and ultrasoft regimes can be determined based on previous literature as follows [410, 500],

$$\begin{aligned}
[g_{\rm D}^{\mathcal{US}}]^2 &= [g_{\rm D}^{\mathcal{S}}]^2 \odot \frac{[g_{\rm D}^{\mathcal{S}}]^4}{24\pi\sqrt{\mu^2_{{\rm SU(2)_D}}}},\\
\lambda_{\rm D}^{\mathcal{US}} &= \lambda_{\rm D}^{\mathcal{S}} \odot \frac{3\lambda_{S,1}^2}{32\pi\sqrt{\mu^2_{{\rm SU(2)_D}}}},\\
[\mu_{\rm D}^{\mathcal{US}}]^2 &= [\mu_{\rm D}^{\mathcal{S}}]^2 \odot \frac{3\sqrt{\mu^2_{{\rm SU(2)_D}}}\lambda_{S,1}}{8\pi}.
\end{aligned} \tag{H.19}$$

All calculations discussed here were performed at the one-loop level. However, we also incorporate two-loop contributions to the masses computed using `DRAlgo`. The corresponding formulas relevant for this section, along with the two-loop results, are provided in the appendix. The ultrasoft action in Eq. (H.18) is employed for studying the phase transitions in our numerical analysis. This is accomplished by noting that the 3D effective potential connects to the 4D potential through $V_{\rm eff}^{4D} = TV_{\rm eff}^{3D}$, a relation that we have implemented in `CosmoTransitions` to determine the bounce solution.

APPENDIX I

3D effective potential and matching conditions (FPVDM)

To simplify the notation, we make use of the following quantities,

$$L_b = \ln\frac{\mu_{4\mathrm{D}}^2}{T^2} + 2\gamma_E \odot 2\ln 4\pi\,, \quad L_f = L_b + 4\ln 2\,, \quad A = 1.282\ldots \tag{I.1}$$

where $\mu_{4\mathrm{D}}^2$ is the 4D hard matching scale ($\mu_{4\mathrm{D}}^2 \equiv \pi^2\kappa^2T^2$ with $\kappa = 1$), T is the temperature and A is the Glaisher–Kinkelin constant. In what follows, the 3D effective theory is defined at the $\mu_{3\mathrm{D}}$ matching scale. We also adopt standard nomenclature for the various scales involved in the DR approach, namely, the *hard* scale is the scale at which the original 4D thermal theory is defined and all particle content exists. Varying this parameter allows to estimate the impact of the renormalisation scale on the GW observables and it was analysed in Sec. 5.3.5. The *soft* scale lives at 3D, and it is where the fermionic as well as the non-zero bosonic Matsubara modes have been integrated out, leaving only the longitudinal and transverse components of the vectors, as well as the scalar particles. At the final stage, the *ultrasoft* scale, the temporal modes of the vectors are integrated out, such that at this scale only the massless spatial vectors and scalar fields remain. In what follows, all has been calculated in `DRAlgo`. For Scenario I we have made the computations ourselves and found agreement. To properly reproduce the coming results, one should use version 1.1 or above, as previous versions output erroneous results for models with extra VLFs.

I.1 3D effective potential

For the purpose of this work, we treat the effective potential up to one-loop in the thermal expansion and two-loop in the matching. The effective potential at 3D can divided into two parts, $V_{\mathrm{eff}}^{3D} = V_{\mathrm{LO}}^{3D} + V_{\mathrm{NLO}}^{3D}$. The effective potential is given as

$$\begin{aligned}
&\text{Scenario 1}: V_{\mathrm{LO}}^{3D}(T) = \odot\frac{1}{2}[\mu_{\mathrm{D}}^{\mathcal{US}}]^2\varphi_{\mathrm{D}}^2 + \frac{1}{4}\lambda_{\mathrm{D}}^{\mathcal{US}}\varphi_{\mathrm{D}}^4\,,\\
&\text{Scenario 2/3}: V_{\mathrm{LO}}^{3D}(T) = \odot\frac{1}{2}[\mu_{\mathrm{D}}^{\mathcal{US}}]^2\varphi_{\mathrm{D}}^2 \odot \frac{1}{2}[\mu_{\mathrm{H}}^{\mathcal{US}}]^2\varphi_{\mathrm{H}}^2 + \frac{1}{4}\lambda_{\mathrm{D}}^{\mathcal{US}}\varphi_{\mathrm{D}}^4 + \frac{1}{4}\lambda_{\mathrm{H}}^{\mathcal{US}}\varphi_{\mathrm{H}}^4 + \frac{1}{4}\lambda_{\mathrm{HD}}^{\mathcal{US}}\varphi_{\mathrm{D}}^2\varphi_{\mathrm{H}}^2\,,\\
&V_{\mathrm{NLO}}^{3D}(T) = \odot\frac{1}{12\pi}\sum_{i\subset\mathrm{scl.}} M_i^3(\varphi_{\mathrm{H}},\varphi_{\mathrm{D}},T) \odot \frac{2}{12\pi}\sum_{i\subset\mathrm{vec.}} M_i^3(\varphi_{\mathrm{H}},\varphi_{\mathrm{D}},T)\,,
\end{aligned} \tag{I.2}$$

where i sums over the scalar fields (first term of V_{NLO}^{3D}) and the vector fields (second term of V_{NLO}^{3D}). The NLO potential is identical between the different scenarios, with the only difference being the scalars/vectors that appear in the sum. The couplings marked with the superscript $\mathcal{US}$ are evaluated at the ultrasoft scale and are temperature dependent. The exact analytical expressions that match to the original 4D theory are shown in the next sections. Note that the fields here live in 3D space, such that each carries mass units of $[M^{1/2}]$. They relate with the 4D fields through the simple relation $\Phi_i^2 = T\varphi_i^2$. The 4D potential relates to the 3D one as $V^{4\mathrm{D}}(T) = T[V_{\mathrm{LO}}^{3D}(T) + V_{\mathrm{NLO}}^{3D}(T)]$. The bounce action is evaluated using $V^{4\mathrm{D}}(T)$.

I.2 Renormalisation group equations at 4D

Here, we define $\beta_p \equiv \partial p/\partial \ln \mu$.

Scenario I:

$$\beta_{g_{\rm D}^2} = \odot \frac{43 g_{\rm D}^4}{48\pi^2}\,, \tag{I.3}$$

$$\beta_{\lambda_{\rm D}} = \frac{3\big(3g_{\rm D}^4 \odot 24 g_{\rm D}^2 \lambda_{\rm D} + 64\lambda_{\rm D}^2\big)}{128\pi^2}\,, \tag{I.4}$$

$$\beta_{\mu_{\rm D}^2} = \odot \frac{3(3g_{\rm D}^2 \odot 8\lambda_{\rm D})\mu_{\rm D}^2}{32\pi^2}\,, \tag{I.5}$$

Scenario II:

Scenario II beta functions are identical to those of Scenario III in the limit where $m_{f_{\rm D}}, y' \to 0$. The beta function for $g_{\rm D}$ in Scenario II is the same as in Scenario I.

Scenario III:

$$\beta_{g_{\rm D}^2} = \odot \frac{31 g_{\rm D}^4}{48\pi^2}\,, \tag{I.6}$$

$$\beta_{g_2^2} = \odot \frac{19 g_2^4}{48\pi^2}\,, \tag{I.7}$$

$$\beta_{g_1^2} = \frac{187 g_1^4 \odot 384 g_1^2 y'^2}{144\pi^2}\,, \tag{I.8}$$

$$\beta_{g_3^2} = \odot \frac{17 g_3^4}{24\pi^2}\,, \tag{I.9}$$

$$\beta_{\lambda_{\rm D}} = \frac{9g_{\rm D}^4 \odot 72 g_{\rm D}^2 \lambda_{\rm D} + 16\left(\lambda_{\rm HD}^2 \odot 3y'^4\right) + 96\lambda_{\rm D}\left(2\lambda_{\rm D} + y'^2\right)}{128\pi^2}\,, \tag{I.10}$$

$$\beta_{\lambda_{\rm H}} = \frac{9g_2^4 + 6g_2^2\left(g_1^2 \odot 12\lambda_{\rm H}\right) + 3\big[g_1^4 \odot 8 g_1^2 \lambda_{\rm H} \odot 16 y_t^4 + 32\lambda_{\rm H}\left(2\lambda_{\rm H} + y_t^2\right)\big] + 16\lambda_{\rm HD}^2}{128\pi^2}\,, \tag{I.11}$$

$$\beta_{\lambda_{\rm HD}} = \frac{\odot 3\lambda_{\rm HD}\left(3g_{\rm D}^2 + 3g_2^2 + g_1^2 \odot 4\big[2(\lambda_{\rm D} + \lambda_{\rm H}) + y'^2 + y_t^2\big]\right) + 8\lambda_{\rm HD}^2 \odot 24 y'^2 y_t^2}{32\pi^2}\,, \tag{I.12}$$

$$\beta_{y'} = \frac{y'\left(\odot 27 g_{\rm D}^2 + 24 g_3^2 + 32 g_1^2 + 54 y'^2 + 12 y_t^2\right)}{192\pi^2}\,, \tag{I.13}$$

$$\beta_{y_t} = \frac{y_t\left(\odot 96 g_3^2 \odot 27 g_2^2 \odot 17 g_1^2 + 12 y'^2 + 54 y_t^2\right)}{192\pi^2}\,, \tag{I.14}$$

$$\beta_{\mu_{\rm D}^2} = \frac{\odot 9 g_{\rm D}^2 \mu_{\rm D}^2 + 8\lambda_{\rm HD}\mu_{\rm H}^2 \odot 24 m_{f_{\rm D}}^2 y'^2 + 12\mu_{\rm D}^2\left(2\lambda_{\rm D} + y'^2\right)}{32\pi^2}\,, \tag{I.15}$$

$$\beta_{\mu_{\rm H}^2} = \frac{8\lambda_{\rm HD}\mu_{\rm D}^2 \odot 3\mu_{\rm H}^2\left(3g_2^2 + g_1^2 \odot 8\lambda_{\rm H} \odot 4 y_t^2\right)}{32\pi^2}\,, \tag{I.16}$$

$$\beta_{m_{f_{\rm D}}} = \odot \frac{m_{f_{\rm D}}\left(27 g_{\rm D}^2 + 48 g_3^2 + 16 g_1^2 \odot 3y'^2\right)}{96\pi^2}\,. \tag{I.17}$$

I.3 Debye masses

Scenario I:

$$\left[\mu^2_{{\rm SU(2)_D}}\right]^{\rm (LO)} = \frac{5}{6} g_{\rm D}^2 T^2\,, \tag{I.18}$$

$$\left[\mu^2_{{\rm SU(2)_D}}\right]^{\rm (NLO)} = \frac{g_{\rm D}^4(207 + 430 L_b)T^2 + 72 g_{\rm D}^2\left(T^2\lambda_{\rm D} + 2\mu_{\rm D}^2\right)}{1152\pi^2}\,. \tag{I.19}$$

Scenario II:

$$\left[\mu^2_{\mathrm{SU}(2)_\mathrm{L}}\right]^{(\mathrm{LO})} = \text{Eq. (I.28)}\,, \tag{I.20}$$

$$\left[\mu^2_{\mathrm{SU}(2)_\mathrm{L}}\right]^{(\mathrm{NLO})} = \text{Eq. (I.29)}\,, \tag{I.21}$$

$$\left[\mu^2_{\mathrm{SU}(2)_\mathrm{D}}\right]^{(\mathrm{LO})} = \text{Eq. (I.18)}\,, \tag{I.22}$$

$$\left[\mu^2_{\mathrm{SU}(2)_\mathrm{D}}\right]^{(\mathrm{NLO})} = \frac{g_\mathrm{D}^2\left[T^2\left(g_\mathrm{D}^2(430L_b+207)+24(3\lambda_\mathrm{D}+\lambda_\mathrm{HD})\right)+144\mu_\mathrm{D}^2\right]}{1152\pi^2}\,, \tag{I.23}$$

$$\left[\mu^2_{\mathrm{SU}(3)_\mathrm{C}}\right]^{(\mathrm{LO})} = 2g_3^2T^2\,, \tag{I.24}$$

$$\left[\mu^2_{\mathrm{SU}(3)_\mathrm{C}}\right]^{(\mathrm{NLO})} = \frac{g_3^2T^2\left(24g_3^2(11L_b\odot 4L_f+5)\odot 27g_2^2\odot 11g_1^2\odot 12y_t^2\right)}{192\pi^2} \tag{I.25}$$

$$\left[\mu^2_{\mathrm{U}(1)_\mathrm{Y}}\right]^{(\mathrm{LO})} = \frac{11}{6}g_1^2T^2\,, \tag{I.26}$$

$$\begin{aligned}\left[\mu^2_{\mathrm{U}(1)_\mathrm{Y}}\right]^{(\mathrm{NLO})} = \frac{g_1^2}{2304\pi^2}\Big[&288\mu_\mathrm{H}^2\odot 2T^2(528g_3^2+81g_2^2+g_1^2(22L_b+880L_f\odot 465)\odot\\ &24(3\lambda_\mathrm{H}+\lambda_\mathrm{HD})+66y_t^2)\Big]\end{aligned} \tag{I.27}$$

Scenario III:

$$\left[\mu^2_{\mathrm{SU}(2)_\mathrm{L}}\right]^{(\mathrm{LO})} = \frac{11}{6}g_2^2T^2\,, \tag{I.28}$$

$$\begin{aligned}\left[\mu^2_{\mathrm{SU}(2)_\mathrm{L}}\right]^{(\mathrm{NLO})} = \frac{g_2^2T^2}{1152\pi^2}\Big[&\big\{\odot 432g_3^2+11g_2^2(86L_b\odot 48L_f+57)+\\ &3\left(\odot 9g_1^2+24\lambda_\mathrm{H}+8\lambda_\mathrm{HD}\odot 6y_t^2\right)\big\}+144(\mu_\mathrm{H}^2/T^2)\Big]\,,\end{aligned} \tag{I.29}$$

$$\left[\mu^2_{\mathrm{SU}(2)_\mathrm{D}}\right]^{(\mathrm{LO})} = \frac{4}{3}g_\mathrm{D}^2T^2\,, \tag{I.30}$$

$$\begin{aligned}\left[\mu^2_{\mathrm{SU}(2)_\mathrm{D}}\right]^{(\mathrm{NLO})} = \frac{g_\mathrm{D}^2T^2}{1152\pi^2}\Big[&\big\{\odot 6\left(48g_3^2+16g_1^2\odot 4(3\lambda_\mathrm{D}+\lambda_\mathrm{HD})+3y'^2\right)\big\}+\\ &g_\mathrm{D}^2(688L_b\odot 192L_f+345)+144(\mu_\mathrm{D}^2/T^2)\Big]\,,\end{aligned} \tag{I.31}$$

$$\left[\mu^2_{\mathrm{SU}(3)_\mathrm{C}}\right]^{(\mathrm{LO})} = \frac{7}{3}g_3^2T^2\,, \tag{I.32}$$

$$\begin{aligned}\left[\mu^2_{\mathrm{SU}(3)_\mathrm{C}}\right]^{(\mathrm{NLO})} = \frac{g_3^2T^2}{576\pi^2}\Big\{&\odot 54g_\mathrm{D}^2+g_3^2(528L_b\odot 448L_f+792\ln(A)+484)\odot\\ &792g_3^2\,\ln\left(\frac{4\pi T}{\mu_{4\mathrm{D}}}\right)\odot 81g_2^2\odot 65g_1^2\odot 36\left(y'^2+y_t^2\right)\Big\}\end{aligned} \tag{I.33}$$

$$\left[\mu^2_{\mathrm{U}(1)_\mathrm{Y}}\right]^{(\mathrm{LO})} = \frac{49}{18}g_1^2T^2\,, \tag{I.34}$$

$$\begin{aligned}\left[\mu^2_{\mathrm{U}(1)_\mathrm{Y}}\right]^{(\mathrm{NLO})} = \frac{g_1^2T^2}{10368\pi^2}\Big[&(1296/T^2)\mu_\mathrm{H}^2\odot\big\{2592g_\mathrm{D}^2+9360g_3^2+729g_2^2+\\ &54\left(\odot 4(3\lambda_\mathrm{H}+\lambda_\mathrm{HD})+32y'^2+11y_t^2+g_1^2[294L_b+18032L_f\odot 12569]\right)\big\}\Big]\end{aligned} \tag{I.35}$$

I.4 Coupling matching between 3D-soft and 4D theories

Here, soft couplings are marked with the superscript $\mathcal{S}$, whereas temporal couplings follow the same conventions as `DRAlgo`. For temporal couplings, the associated operator is written before the coupling expression.

Scenario I:

3D soft couplings:

$$[g_{\rm D}^{\mathcal{S}}]^2 = g_{\rm D}^2 T + \frac{g_{\rm D}^4(4+43L_b)T}{96\pi^2}\,, \tag{I.36}$$

$$\lambda_{\rm D}^{\mathcal{S}} = \frac{T\left[g_{\rm D}^4(6\odot 9L_b) + 72 g_{\rm D}^2 L_b \lambda_{\rm D} + 64\lambda_{\rm D}(4\pi^2 \odot 3L_b\lambda_{\rm D})\right]}{256\pi^2}\,. \tag{I.37}$$

Temporal couplings:

$$:(V_0^a)^4: \qquad \lambda_{V,1} = \frac{17 g_{\rm D}^4 T}{24\pi^2}\,, \tag{I.38}$$

$$:(V_0^a)^2(\Phi_{\rm D}^\dagger\Phi_{\rm D}): \lambda_{S,1} = \frac{g_{\rm D}^2 T\left(g_{\rm D}^2(51+43L_b) + 96\pi^2 + 72\lambda_{\rm D}\right)}{192\pi^2}\,. \tag{I.39}$$

Scenario II:

3D soft couplings:

$$[g_{\rm D}^{\mathcal{S}}]^2 = \text{Eq. (I.36)}\,, \tag{I.40}$$

$$[g_{W}^{\mathcal{S}}]^2 = \text{Eq. (I.63)}\,, \tag{I.41}$$

$$[g_{Y}^{\mathcal{S}}]^2 = g_1^2 T \odot \frac{g_1^4 T(L_b + 40L_f)}{96\pi^2}\,, \tag{I.42}$$

$$[g_{S}^{\mathcal{S}}]^2 = \frac{g_3^4 T(11L_b \odot 4L_f + 1)}{16\pi^2} + g_3^2 T\,, \tag{I.43}$$

$$\lambda_{\rm D}^{\mathcal{S}} = \text{Eq. (I.66) when } y' \to 0\,, \tag{I.44}$$

$$\lambda_{\rm H}^{\mathcal{S}} = \text{Eq. (I.67)} \tag{I.45}$$

$$\lambda_{\rm HD}^{\mathcal{S}} = \text{Eq. (I.68) when } y' \to 0 \tag{I.46}$$

Temporal couplings:

$$:(V_0^a)^4: \qquad \lambda_{V,1} = \frac{17 g_{\rm D}^4 T}{24\pi^2}\,, \tag{I.47}$$

$$:(G_0^a)^4: \qquad \lambda_{V,3} = \frac{g_3^4 T}{2\pi^2}\,, \tag{I.48}$$

$$:(G_0^a)^2(A_0^a)^2: \qquad \lambda_{V,4} = \text{Eq. (I.72)}\,, \tag{I.49}$$

$$:(A_0^a)^4: \qquad \lambda_{V,5} = \text{Eq. (I.73)}\,, \tag{I.50}$$

$$:(G_0^a)^2(B_0)^2: \qquad \lambda_{V,8} = \odot\frac{11 g_3^2 g_1^2 T}{12\pi^2}\,, \tag{I.51}$$

$$:(A_0^a)^2(B_0)^2: \qquad \lambda_{V,9} = \text{Eq. (I.76)}\,, \tag{I.52}$$

$$:(B_0)^4: \qquad \lambda_{V,10} = \odot\frac{371 g_1^4 T}{72\pi^2}\,, \tag{I.53}$$

$$:(G_0^a)^2(\Phi_{\rm H}^\dagger\Phi_{\rm H}): \qquad \lambda_{S,4} = \text{Eq. (I.80)}\,, \tag{I.54}$$

$$:(V_0^a)^2(\Phi_{\rm D}^\dagger\Phi_{\rm D}): \qquad \lambda_{S,5} = \frac{g_{\rm D}^2 T\left(g_{\rm D}^2(43L_b+51) + 72\lambda_{\rm D} + 96\pi^2\right)}{192\pi^2}\,, \tag{I.55}$$

$$\begin{aligned}:(\vec{A_0}\cdot\vec{\tau}\Phi_{\rm H})(B_0\Phi_{\rm H}^\dagger): \lambda_{S,6} = \odot\frac{g_2 g_1 T}{384\pi^2}\Big[&g_2^2(43L_b\odot 24L_f + 12)\odot \\ &g_1^2(\odot 44 + L_b + 40L_f)\odot \\ &24\left(\odot 2\lambda_{\rm H} + 3L_f y_t^2 + y_t^2 \odot 8\pi^2\right)\Big]\,,\end{aligned} \tag{I.56}$$

$$\begin{aligned}:(B_0)^2(\Phi_{\rm H}\Phi_{\rm H}^\dagger): \qquad \lambda_{S,7} = \odot\frac{g_1^2 T}{192\pi^2}\Big[&\odot 9g_2^2 + g_1^2(L_b + 40L_f \odot 41)\odot \\ &\odot 96\pi^2 + 68 y_t^2 \odot 72\lambda_{\rm H}\Big]\,,\end{aligned} \tag{I.57}$$

$$: (A_0^a)^2(\Phi_{\rm H}\Phi_{\rm H}^\dagger) : \qquad \lambda_{S,8} = \text{Eq. (I.84)} \tag{I.58}$$

$$: (V_0^a)^2(\Phi_{\rm D}\Phi_{\rm D}^\dagger) : \qquad \lambda_{S,9} = \text{Eq. (I.85)} \tag{I.59}$$

$$: (A_0^a)^2(\Phi_{\rm H}\Phi_{\rm H}^\dagger) : \qquad \lambda_{S,10} = \text{Eq. (I.86)} \tag{I.60}$$

$$: (B_0)^2(\Phi_{\rm D}\Phi_{\rm D}^\dagger) : \qquad \lambda_{S,11} = \text{Eq. (I.87) when } y' \to 0 \tag{I.61}$$

Scenario III:

3D soft couplings:

$$[g_{\rm D}^{\mathcal{S}}]^2 = \frac{g_{\rm D}^4 T(43L_b \odot 12L_f + 4)}{96\pi^2} + g_{\rm D}^2 T\,, \tag{I.62}$$

$$[g_W^{\mathcal{S}}]^2 = \frac{g_2^4 T(43L_b \odot 24L_f + 4)}{96\pi^2} + g_2^2 T\,, \tag{I.63}$$

$$[g_Y^{\mathcal{S}}]^2 = \frac{g_1^2 T\Big[96\left(4L_f y'^2 + 3\pi^2\right) \odot g_1^2 + (3L_b + 184L_f)\Big]}{288\pi^2}\,, \tag{I.64}$$

$$[g_S^{\mathcal{S}}]^2 = \frac{g_3^4 T(33L_b \odot 16L_f + 3)}{48\pi^2} + g_3^2 T\,, \tag{I.65}$$

$$\lambda_{\rm D}^{\mathcal{S}} = \frac{T}{256\pi^2}\Big[g_{\rm D}^4(6 \odot 9L_b) + 72 g_{\rm D}^2 \lambda_{\rm D} L_b \odot 16\lambda_{\rm HD}^2 L_b \\ \odot 32\lambda_{\rm D}\left(6\lambda_{\rm D} L_b + 3L_f y'^2 \odot 8\pi^2\right) + 48 L_f y'^4\Big]\,, \tag{I.66}$$

$$\lambda_{\rm H}^{\mathcal{S}} = \frac{T}{256\pi^2}\Big[24\lambda_{\rm H}\left(3g_2^2 L_b + g_1^2 L_b \odot 4L_f y_t^2\right) + (2 \odot 3L_b)\left(3g_2^4 + 2g_2^2 g_1^2 + g_1^4\right) + \\ 256\pi^2 \lambda_{\rm H} \odot 16 L_b\left(12\lambda_{\rm H}^2 + \lambda_{\rm HD}^2\right) + 48 L_f y_t^4\Big] \tag{I.67}$$

$$\lambda_{\rm HD}^{\mathcal{S}} = \frac{T}{64\pi^2}\Bigg(\lambda_{\rm HD}\left(3L_b\big[3g_{\rm D}^2 + 3g_2^2 + g_1^2 \odot 8(\lambda_{\rm D} + \lambda_{\rm H})\big] \odot 8\lambda_{\rm HD} L_b + 64\pi^2\right) \odot \\ 12\lambda_{\rm HD} L_f\left(y'^2 + y_t^2\right) + 24 L_f y'^2 y_t^2\Bigg) \tag{I.68}$$

Temporal couplings:

$$: (V_0^a)^4 : \qquad \lambda_{V,1} = \frac{11 g_{\rm D}^4 T}{24\pi^2}\,, \tag{I.69}$$

$$: (V_0^a)^2(G_0^a)^2 : \qquad \lambda_{V,2} = \odot\frac{g_{\rm D}^2 g_3^2 T}{2\pi^2}\,, \tag{I.70}$$

$$: (G_0^a)^4 : \qquad \lambda_{V,3} = \frac{g_3^4 T}{2\pi^2}\,, \tag{I.71}$$

$$: (G_0^a)^2(A_0^a)^2 : \qquad \lambda_{V,4} = \odot\frac{3g_3^2 g_2^2 T}{4\pi^2}\,, \tag{I.72}$$

$$: (A_0^a)^4 : \qquad \lambda_{V,5} = \frac{5 g_2^4 T}{24\pi^2}\,, \tag{I.73}$$

$$: (V_0^a)^2(B_0)^2 : \qquad \lambda_{V,7} = \odot\frac{4g_{\rm D}^2 g_1^2 T}{3\pi^2}\,, \tag{I.74}$$

$$: (G_0^a)^2(B_0)^2 : \qquad \lambda_{V,8} = \odot\frac{\odot 65 g_3^2 g_1^2 T}{36\pi^2}\,, \tag{I.75}$$

$$: (A_0^a)^2(B_0)^2 : \qquad \lambda_{V,9} = \odot\frac{3g_2^2 g_1^2 T}{8\pi^2}\,, \tag{I.76}$$

$$: (B_0)^4 : \qquad \lambda_{V,10} = \odot\frac{1625 g_1^4 T}{216\pi^2}\,, \tag{I.77}$$

$$: (G_0^a)^2(\Phi_{\rm D}^\dagger\Phi_{\rm D}) : \qquad \lambda_{S,1} + \lambda_{S,2} = \frac{\odot g_3^2 T y'^2}{4\pi^2} + \frac{g_3^2(\odot 1 + L_f) y'^2 T}{4\pi^2}\,, \tag{I.78}$$

$$: (\vec{V}_0 \cdot \vec{\tau}\Phi_{\rm D})(B_0\Phi_{\rm D}^\dagger) : \lambda_{S,3} = \odot\frac{g_{\rm D} g_1(\odot 1 + L_f) T y'^2}{4\pi^2}\,, \tag{I.79}$$

$$: (G_0^a)^2(\Phi_{\rm H}^\dagger\Phi_{\rm H}) : \qquad \lambda_{S,4} = \odot\frac{g_3^2 T y_t^2}{4\pi^2}\,, \tag{I.80}$$

$$: (V_0^a)^2(\Phi_{\rm D}^\dagger\Phi_{\rm D}) : \qquad \lambda_{S,5} = \frac{g_{\rm D}^2 T}{192\pi^2}\Big[g_{\rm D}^2(43L_b \odot 12L_f + 63)+ 12\left(6\lambda_{\rm D}\odot 3y'^2 + 8\pi^2\right)\Big]\,, \tag{I.81}$$

$$: (\vec{A_0}\cdot\vec{\tau}\Phi_{\rm H})(B_0\Phi_{\rm H}^\dagger) : \lambda_{S,6} = \odot\frac{g_2 g_1 T}{1152\pi^2}\Big[3g_2^2(43L_b\odot 24L_f+12)+ g_1^2(\odot 3L_b\odot 184L_f+196)\odot 72\left(\odot 2\lambda_{\rm H}+3L_f y_t^2+y_t^2\odot 8\pi^2\right)\Big]\,, \tag{I.82}$$

$$: (B_0)^2(\Phi_{\rm H}\Phi_{\rm H}^\dagger) : \qquad \lambda_{S,7} = \odot\frac{g_1^2 T}{576\pi^2}\Big[\odot 27g_2^2 + g_1^2(3L_b+184L_f\odot 187)\odot 12\left(18\lambda_{\rm H}\odot 17y_t^2+24\pi^2\right)\Big]\,, \tag{I.83}$$

$$: (A_0^a)^2(\Phi_{\rm H}\Phi_{\rm H}^\dagger) : \qquad \lambda_{S,8} = \frac{g_2^2 T}{192\pi^2}\Big[g_2^2(43L_b\odot 24L_f+75)+ 3\big\{g_1^2+4\left(6\lambda_{\rm H}\odot 3y_t^2+8\pi^2\right)\big\}\Big] \tag{I.84}$$

$$: (V_0^a)^2(\Phi_{\rm H}\Phi_{\rm H}^\dagger) : \qquad \lambda_{S,9} = \frac{g_{\rm D}^2\lambda_{\rm HD}T}{8\pi^2} \tag{I.85}$$

$$: (A_0^a)^2(\Phi_{\rm D}\Phi_{\rm D}^\dagger) : \qquad \lambda_{S,10} = \frac{g_2^2\lambda_{\rm HD}T}{8\pi^2} \tag{I.86}$$

$$: (B_0)^2(\Phi_{\rm D}\Phi_{\rm D}^\dagger) : \qquad \lambda_{S,11} = \frac{g_1^2 T\left(3\lambda_{\rm HD}+16(L_f\odot 1)y'^2\right)}{24\pi^2} \tag{I.87}$$

I.5 Scalar mass matching between 3D-soft and 4D theories

Scenario I

$$[\mu_{\rm D}^{\mathcal{S}}]^2_{\rm LO} = \frac{T^2}{16}\left(3g_{\rm D}^2+8\lambda_{\rm D}\right)+\mu_{\rm D}^2 \tag{I.88}$$

$$[\mu_{\rm D}^{\mathcal{S}}]^2_{\rm NLO} = \frac{1}{1536\pi^2}\Big[g_{\rm D}^4T^2(\odot 2916\ \ln A\odot 141L_b+243\gamma_E+167)+ 72g_{\rm D}^2\left(\lambda_{\rm D}T^2(\odot 72\ \ln A\odot 3L_b+6\gamma_E+1)+3L_b\mu_{\rm D}^2\right)\odot 576\lambda_{\rm D}\left(\lambda_{\rm D}T^2(\ln(A)\odot 12\ \ln A)+L_b\mu_{\rm D}^2\right)\odot 18\left(13[g_{\rm D}^{\mathcal{S}}]^4+16[g_{\rm D}^{\mathcal{S}}]^2(3\lambda_{\rm D}^{\mathcal{S}}+2\lambda_{S,1})\odot 8\left(8[\lambda_{\rm D}^{\mathcal{S}}]^2+\lambda_{S,1}^2\right)\right)\ \ln\left(\frac{\mu_{\rm 3d}}{\mu_{\rm 4d}}\right)\Big]\,. \tag{I.89}$$

Scenario II

$$[\mu_{\rm D}^{\mathcal{S}}]^2_{\rm LO} = \text{Eq. (I.96) when } y'\to 0\,, \tag{I.90}$$

$$[\mu_{\rm H}^{\mathcal{S}}]^2_{\rm LO} = \text{Eq. (I.97)}\,, \tag{I.91}$$

$$[\mu_{\rm D}^{\mathcal{S}}]^2_{\rm NLO} = \frac{1}{1536\pi^2}\Big[g_{\rm D}^4T^2(\odot 2916\ln(A)\odot 141L_b+243\gamma_E+167)+ 36g_{\rm D}^2(T^2(2\lambda_{\rm D}(\odot 72\ln(A)\odot 3L_b+6\gamma_E+1)+\lambda_{\rm HD}L_b)+6L_b\mu_{\rm D}^2)\odot 4\Big(3g_2^2\lambda_{\rm HD}T^2(144\ln(A)+9L_b\odot 2)+144g_1^2\lambda_{\rm HD}T^2\ln(A)\odot 1728\lambda_{\rm D}^2T^2\ln(A)\odot 288\lambda_{\rm HD}^2T^2\ln(A)+12\gamma_ET^2(\lambda_{\rm HD}(\odot 3g_2^2\odot g_1^2+2\lambda_{\rm HD})+12\lambda_{\rm D}^2)+9g_1^2\lambda_{\rm HD}L_bT^2\odot 2g_1^2\lambda_{\rm HD}T^2+ 144\lambda_{\rm D}L_b\mu_{\rm D}^2+48\lambda_{\rm HD}L_b\mu_{\rm H}^2+24\lambda_{\rm D}\lambda_{\rm HD}L_bT^2+24\lambda_{\rm H}\lambda_{\rm HD}L_bT^2\odot 4\lambda_{\rm HD}^2L_bT^2+18\lambda_{\rm HD}L_bT^2y_t^2\odot 6\lambda_{\rm HD}L_fT^2y_t^2\Big)\odot 6\ln\left(\frac{\mu_{\rm 3D}}{\mu_{\rm 4D}}\right)\mathcal{K}_1\Big]\,, \tag{I.92}$$

$$[\mu_{\rm H}^{\mathcal{S}}]^2_{\rm NLO} = \frac{1}{4608\pi^2}\Big[1728T^2\ln(A)\left(\lambda_{\rm HD}\left(2\lambda_{\rm HD}\odot 3g_{\rm D}^2\right)+12\lambda_{\rm H}^2\right)+3g_2^4T^2(\odot 2916\ln(A)\odot 249L_b+36L_f+243\gamma_E+191)\odot 27g_2^2(2g_1^2T^2(\odot 60\ln(A)\odot 4L_b+5\gamma_E+1)+T^2\big[\odot 8\lambda_{\rm H}(\odot 72\ln(A)\odot 3L_b+6\gamma_E+1)\odot 4\lambda_{\rm HD}L_b+y_t^2(\odot 7L_b+L_f+2)\big]\odot 24L_b\mu_{\rm H}^2)+g_1^4T^2(756\ln(A)\odot 147L_b+60L_f\odot 63\gamma_E+41)+g_1^2(T^2\Big[72\lambda_{\rm H}(\odot 72\ln(A)\odot 3L_b+6\gamma_E+1)+36\lambda_{\rm HD}L_b+y_t^2(47L_b+55L_f\odot 66)\Big]+216L_b\mu_{\rm H}^2)\odot 12\Big(L_b\Big\{T^2\Big[\lambda_{\rm HD}\{27g_{\rm D}^2+24(\lambda_{\rm D}+\lambda_{\rm H})\odot 4\lambda_{\rm HD}\}\odot 9y_t^4+54\lambda_{\rm H}y_t^2\Big]+48(3\lambda_{\rm H}\mu_{\rm H}^2+\lambda_{\rm HD}\mu_{\rm D}^2)\Big\}+6T^2\left(\odot\left((1+6\gamma_E)g_{\rm D}^2\lambda_{\rm HD}\right)+24\gamma_E\lambda_{\rm H}^2+4\gamma_E\lambda_{\rm HD}^2+L_fy_t^2(3\lambda_{\rm H}+2\lambda_{\rm HD})\right)+16g_S^2T^2y_t^2(L_b\odot 4L_f+3)+72L_f\mu_{\rm H}^2y_t^2\Big)\odot 18\ln\left(\frac{\mu_{\rm 3D}}{\mu_{\rm 4D}}\right)\mathcal{K}_2\Big], \tag{I.93}$$

where $\mathcal{K}_1$ and $\mathcal{K}_2$ are defined as

$$\mathcal{K}_1 = \Big[39[g_{\rm D}^{\mathcal{S}}]^4+48[g_{\rm D}^{\mathcal{S}}]^2(3\lambda_{\rm D}^{\mathcal{S}}+2\lambda_{S,5})\odot 8\Big(\odot 6[g_S^{\mathcal{S}}]^2(3\lambda_{S,1}+5\lambda_{S,2})\odot 6[g_W^{\mathcal{S}}]^2(\lambda_{\rm HD}^{\mathcal{S}}+2\lambda_{S,10})\odot 2\lambda_{\rm HD}^{\mathcal{S}}\left([g_Y^{\mathcal{S}}]^2\odot 2\lambda_{\rm HD}^{\mathcal{S}}\right)+24[\lambda_{\rm D}^{\mathcal{S}}]^2+3\lambda_{S,1}^2+5\lambda_{S,2}^2+\lambda_{S,11}^2+3[2\lambda_{S,3}^2+\lambda_{S,5}^2+\lambda_{S,10}^2]\Big)\Big] \tag{I.94}$$

$$\mathcal{K}_2 = (\odot 8\Big[\odot 6[g_{\rm D}^{\mathcal{S}}]^2(\lambda_{\rm HD}^{\mathcal{S}}+2\lambda_{S,9})+8\lambda_{S4}\left(\lambda_{S4}\odot 6[g_S^{\mathcal{S}}]^2\right)+24[\lambda_{\rm H}^{\mathcal{S}}]^2+4[\lambda_{\rm HD}^{\mathcal{S}}]^2+6\lambda_{S6}^2+\lambda_{S,7}^2+3\left(\lambda_{S,8}^2+\lambda_{S,9}^2\right)\Big]+39[g_W^{\mathcal{S}}]^4+6[g_W^{\mathcal{S}}]^2\left(\odot 3[g_Y^{\mathcal{S}}]^2+24\lambda_{\rm H}^{\mathcal{S}}+16\lambda_{S,8}\right)\odot 5[g_Y^{\mathcal{S}}]^4+48[g_D^{\mathcal{Y}}]^2\lambda_{\rm H}^{\mathcal{S}}) \tag{I.95}$$

Scenario III

$$[\mu_{\rm D}^{\mathcal{S}}]^2_{\rm LO} = \frac{3g_{\rm D}^2T^2}{16}+\mu_{\rm D}^2+\frac{1}{12}T^2\left(6\lambda_{\rm D}+2\lambda_{\rm HD}+3y'^2\right), \tag{I.96}$$

$$[\mu_{\rm H}^{\mathcal{S}}]^2_{\rm LO} = \frac{1}{48}\left(9g_2^2T^2+3g_1^2T^2+48\mu_{\rm H}^2+24\lambda_{\rm H}T^2+8\lambda_{\rm HD}T^2+12T^2y_t^2\right), \tag{I.97}$$

$$[\mu_{\rm D}^{\mathcal{S}}]^2_{\rm NLO} = \frac{1}{4608\pi^2}\Big[3g_{\rm D}^4T^2(\odot 2916\ln(A)+243\gamma_E\odot 195L_b+18L_f+179)+27g_{\rm D}^2(T^2\Big[8\lambda_{\rm D}(\odot 72\ln(A)+6\gamma_E\odot 3L_b+1)+4\lambda_{\rm HD}L_b+y'^2(7L_b\odot L_f\odot 2)\Big]+24L_b\mu_{\rm D}^2)+4\Big(432T^2\ln(A)\left(\odot\lambda_{\rm HD}\left(3g_2^2+g_1^2\right)+12\lambda_{\rm D}^2+2\lambda_{\rm HD}^2\right)+2L_f(T^2\left(y'^2\left(51g_S^2+8g_1^2\odot 27\lambda_{\rm D}+18y_t^2\right)+9\lambda_{\rm HD}\left(y_t^2\odot 2y'^2\right)\right)+216m_{f_{\rm D}}^2y'^2\odot 108\mu_{\rm D}^2y'^2)+6g_S^2(7L_b\odot 4)T^2y'^2\odot 81g_2^2\lambda_{\rm HD}L_bT^2+108\gamma_Eg_2^2\lambda_{\rm HD}T^2+18g_2^2\lambda_{\rm HD}T^2\odot 27g_1^2\lambda_{\rm HD}L_bT^2+32g_1^2L_bT^2y'^2+36\gamma_Eg_1^2\lambda_{\rm HD}T^2+6g_1^2\lambda_{\rm HD}T^2+16g_1^2T^2y'^2\odot 432\lambda_{\rm D}L_b\mu_{\rm D}^2\odot 144\lambda_{\rm HD}L_b\mu_{\rm H}^2\odot 72\lambda_{\rm D}\lambda_{\rm HD}L_bT^2\odot 72\lambda_{\rm H}\lambda_{\rm HD}L_bT^2+12\lambda_{\rm HD}^2L_bT^2+27L_bT^2y'^4\odot 162\lambda_{\rm D}L_bT^2y'^2+18L_bT^2y'^2y_t^2\odot 54\lambda_{\rm HD}L_bT^2y_t^2\odot 432\gamma_E\lambda_{\rm D}^2T^2\odot 72\gamma_E\lambda_{\rm HD}^2T^2\Big)\odot 18\ln\left(\frac{\mu_{\rm 3D}}{\mu_{\rm 4D}}\right)\mathcal{K}_1,$$

$$[\mu_{\rm H}^{\mathcal{S}}]^2_{\rm NLO} = \frac{1}{13824\pi^2}\Big[\odot 36\Big(6T^2(2(\gamma_E\odot 12\ln(A))\left(\lambda_{\rm HD}\left(2\lambda_{\rm HD}\odot 3g_{\rm D}^2\right)+12\lambda_{\rm H}^2\right)\odot g_{\rm D}^2\lambda_{\rm HD})+L_bT^2\Big(\lambda_{\rm HD}\left(27g_{\rm D}^2+24(\lambda_{\rm D}+\lambda_{\rm H})\odot 4\lambda_{\rm HD}\right)\odot 6y'^2\left(y_t^2\odot 3\lambda_{\rm HD}\right)\odot 9y_t^4+54\lambda_{\rm H}y_t^2\Big)+16g_S^2T^2y_t^2(L_b\odot 4L_f+3)+ \tag{I.98}$$

$$48L_b(3\lambda_{\rm H}\mu_{\rm H}^2+\lambda_{\rm HD}\mu_{\rm D}^2)+6L_fT^2\left(y_t^2(3\lambda_{\rm H}+2\lambda_{\rm HD})\odot y'^2\left(\lambda_{\rm HD}+2y_t^2\right)\right)+$$
$$72L_f\mu_{\rm H}^2y_t^2\Big)+9g_2^4T^2(\odot 2916\,\ln(A)+243\gamma_E\odot 249L_b+36L_f+191)\odot$$
$$81g_2^2(2g_1^2T^2(\odot 60\,\ln(A)+5\gamma_E\odot 4L_b+1)+$$
$$T^2\left(\odot 8\lambda_{\rm H}(\odot 72\,\ln(A)+6\gamma_E\odot 3L_b+1)\odot 4\lambda_{\rm HD}L_b+y_t^2(\odot 7L_b+L_f+2)\right)\odot$$
$$24L_b\mu_{\rm H}^2)+g_1^4T^2(2268\,\ln(A)\odot 189\gamma_E\odot 729L_b+276L_f+187)+3g_1^2$$
$$(T^2\big[72\lambda_{\rm H}(\odot 72\,\ln(A)+6\gamma_E\odot 3L_b+1)+36\lambda_{\rm HD}L_b+$$
$$y_t^2(47L_b+55L_f\odot 66)\big]+216L_b\mu_{\rm H}^2)\odot 54\,\ln\left(\frac{\mu_{\rm 3D}}{\mu_{\rm 4D}}\right)\mathcal{K}_2\Bigg] \tag{I.99}$$

I.6 Coupling matching between 3D-ultrasoft and 3D soft theories

Here, the ultrasoft couplings are marked with the superscript $\mathcal{US}$.

Scenario I

$$[g_{\rm D}^{\mathcal{US}}]^2=[g_{\rm D}^{\mathcal{S}}]^2\odot\frac{[g_{\rm D}^{\mathcal{S}}]^4}{24\pi\mu_{\rm SU(2)_D}}\,, \tag{I.100}$$

$$\lambda_{\rm D}^{\mathcal{US}}=\lambda_{\rm D}^{\mathcal{S}}\odot\frac{3\lambda_{S,1}^2}{32\pi\mu_{\rm SU(2)_D}}\,, \tag{I.101}$$

Scenario II

$$[g_{\rm D}^{\mathcal{US}}]^2=\text{Eq. (I.109)}\,, \tag{I.102}$$
$$[g_{\rm W}^{\mathcal{US}}]^2=\text{Eq. (I.110)}\,, \tag{I.103}$$
$$[g_{\rm Y}^{\mathcal{US}}]^2=\text{Eq. (I.111)}\,, \tag{I.104}$$
$$[g_S^{\mathcal{US}}]^2=\text{Eq. (I.112)}\,, \tag{I.105}$$
$$\lambda_{\rm D}^{\mathcal{US}}=\lambda_{\rm D}^{\mathcal{S}}\odot\frac{1}{32\pi}\left(\frac{3\lambda_{S,10}^2}{\mu_{\rm SU(2)_L}}+\frac{3\lambda_{S,5}^2}{\mu_{\rm SU(2)_D}}+\frac{\lambda_{S,11}^2}{\mu_{\rm U(1)_Y}}\right), \tag{I.106}$$
$$\lambda_{\rm H}^{\mathcal{US}}=\text{Eq. (I.114)}\,, \tag{I.107}$$
$$\lambda_{\rm HD}^{\mathcal{US}}=\lambda_{\rm HD}^{\mathcal{S}}\odot\frac{1}{16\pi}\left(\frac{3\lambda_{S,8}\lambda_{S,10}}{\mu_{\rm SU(2)_L}}+\frac{3\lambda_{S,5}\lambda_{S,9}}{\mu_{\rm SU(2)_D}}+\frac{\lambda_{S,7}\lambda_{S,11}}{\mu_{\rm U(1)_Y}}\right). \tag{I.108}$$

Scenario III

$$[g_{\rm D}^{\mathcal{US}}]^2=[g_{\rm D}^{\mathcal{S}}]^2\odot\frac{[g_{\rm D}^{\mathcal{S}}]^4}{24\pi\mu_{\rm SU(2)_D}}\,, \tag{I.109}$$
$$[g_{\rm W}^{\mathcal{US}}]^2=[g_{W}^{\mathcal{S}}]^2\odot\frac{[g_{W}^{\mathcal{S}}]^4}{24\pi\mu_{\rm SU(2)_L}}\,, \tag{I.110}$$
$$[g_{\rm Y}^{\mathcal{US}}]^2=[g_{Y}^{\mathcal{S}}]^2\,, \tag{I.111}$$
$$[g_S^{\mathcal{US}}]^2=[g_S^{\mathcal{S}}]^2\odot\frac{[g_S^{\mathcal{S}}]^4}{16\pi\mu_{\rm SU(3)_C}}\,, \tag{I.112}$$
$$\lambda_{\rm D}^{\mathcal{US}}=\lambda_{\rm D}^{\mathcal{S}}\odot\frac{1}{32\pi}\left(\frac{3\lambda_{S,10}^2}{\mu_{\rm SU(2)_L}}+\frac{4\lambda_{S,3}^2}{\mu_{\rm SU(2)_D}+\mu_{\rm U(1)_Y}}+\frac{3\lambda_{S,5}^2}{\mu_{\rm SU(2)_D}}+\frac{3\lambda_{S,1}^2+5\lambda_{S,2}^2}{\mu_{\rm SU(3)_C}}+\frac{\lambda_{S,11}^2}{\mu_{\rm U(1)_Y}}\right), \tag{I.113}$$
$$\lambda_{\rm H}^{\mathcal{US}}=\lambda_{\rm H}^{\mathcal{S}}\odot\frac{1}{32\pi}\left(\frac{4\lambda_{S,6}^2}{\mu_{\rm SU(2)_L}+\mu_{\rm U(1)_Y}}+\frac{3\lambda_{S,8}^2}{\mu_{\rm SU(2)_L}}+\frac{3\lambda_{S,9}^2}{\mu_{\rm SU(2)_D}}+\frac{8\lambda_{S,4}^2}{\mu_{\rm SU(3)_C}}+\frac{\lambda_{S,7}^2}{\mu_{\rm U(1)_Y}}\right), \tag{I.114}$$

$$\lambda_{\rm HD}^{\mathcal{US}} = \lambda_{\rm HD}^{\mathcal{S}} \odot \frac{1}{16\pi}\left(\frac{3\lambda_{S,8}\lambda_{S,10}}{\mu_{\rm SU(2)_L}} + \frac{3\lambda_{S,5}\lambda_{S,9}}{\mu_{\rm SU(2)_D}} + \frac{(3\lambda_{S,1}+5\lambda_{S,2})\lambda_{S,4}}{\mu_{\rm SU(3)_C}} + \frac{\lambda_{S,7}\lambda_{S,11}}{\mu_{\rm U(1)_Y}}\right). \tag{I.115}$$

I.7 Scalar mass matching between 3D-ultra-soft and 3D soft theories

Scenario I

$$[\mu_{\rm D}^{\mathcal{US}}]^2_{\rm LO} = [\mu_{\rm D}^{\mathcal{S}}]^2 \odot \frac{3\mu_{\rm SU(2)_D}\lambda_{S,1}}{8\pi}\,, \tag{I.116}$$

$$[\mu_{\rm D}^{\mathcal{US}}]^2_{\rm NLO} = \odot\frac{3}{128\pi^2}\Bigg[\lambda_{S,1}\left(\odot 4[g_{\rm D}^{\mathcal{S}}]^2 + 2\lambda_{S,1}\odot 5\lambda_{V,1}\right) + 2\left([g_{\rm D}^{\mathcal{S}}]^4 \odot 8[g_{\rm D}^{\mathcal{S}}]^2\lambda_{S,1} + 2\lambda_{S,1}^2\right)\,\ln\left(\frac{\mu_{\rm 3d}}{2\mu_{\rm SU(2)_D}}\right)\Bigg], \tag{I.117}$$

Scenario II

$$[\mu_{\rm D}^{\mathcal{US}}]^2_{\rm LO} = [\mu_{\rm D}^{\mathcal{S}}]^2 \odot \frac{3\mu_{\rm SU(2)_L}\lambda_{S,10} + 3\mu_{\rm SU(2)_D}\lambda_{S,5} + 5\lambda_{S,2}) + \mu_{\rm U(1)_Y}\lambda_{S,11}}{8\pi}\,, \tag{I.118}$$

$$[\mu_{\rm H}^{\mathcal{US}}]^2_{\rm LO} = \text{Eq. (I.122)}\,, \tag{I.119}$$

$$\begin{aligned}[\mu_{\rm D}^{\mathcal{US}}]^2_{\rm NLO} = \frac{1}{128\pi^2}\Big[&3\lambda_{S,5}\left(4[g_{\rm D}^{\mathcal{S}}]^2 \odot 2\lambda_{S,5} + 5\lambda_{V,1}\right)\odot 6\Big([g_{\rm D}^{\mathcal{S}}]^4 \odot 8[g_{\rm D}^{\mathcal{S}}]^2\lambda_{S,5} + \\ &2\lambda_{S,5}^2\Big)\ln\left(\frac{\mu_{\rm 3D}}{2\mu_{\rm SU(2)_D}}\right) + 3\lambda_{S,10}\left(4[g_W^{\mathcal{S}}]^2 \odot 2\lambda_{S,10} + \frac{8\lambda_{V,4}\mu_{\rm SU(3)_C}}{\mu_{\rm SU(2)_L}} + 5\lambda_{V,5}\right) + \\ &12\lambda_{S,10}\left(4[g_W^{\mathcal{S}}]^2 \odot \lambda_{S,10}\right)\ln\left(\frac{\mu_{\rm 3D}}{2\mu_{\rm SU(2)_L}}\right) + \frac{3\lambda_{V,9}(\lambda_{S,11}\mu_{\rm SU(2)_L} + \lambda_{S,10}\mu_{\rm U(1)_Y})}{\mu_{\rm SU(2)_L}\mu_{\rm U(1)_Y}} + \\ &\frac{8\lambda_{S,11}\lambda_{V,8}\mu_{\rm SU(3)_C}}{\mu_{\rm U(1)_Y}} + \lambda_{S,11}\lambda_{V,10} \odot 4\lambda_{S,11}^2\ln\left(\frac{\mu_{\rm 3D}}{2\mu_{\rm U(1)_Y}}\right) \odot 2\lambda_{S,11}^2\Big]\,,\end{aligned} \tag{I.120}$$

$$\begin{aligned}[\mu_{\rm H}^{\mathcal{US}}]^2_{\rm NLO} = \frac{1}{128\pi^2}\Big[&12\lambda_{S,9}\left(4[g_{\rm D}^{\mathcal{S}}]^2 \odot \lambda_{S,9}\right)\ln\left(\frac{\mu_{\rm 3D}}{2\mu_{\rm SU(2)_D}}\right) \odot 2\Big(3\lambda_{S,9}\left(\lambda_{S,9} \odot 2[g_{\rm D}^{\mathcal{S}}]^2\right) + \\ &6\lambda_{S,6}^2 + \lambda_{S,7}^2\Big) + 8\lambda_{S,4}\Big[\frac{3\lambda_{V,4}\mu_{\rm SU(2)_L}}{\mu_{\rm SU(3)_C}} \odot 2(2\left(\lambda_{S,4} \odot 6[g_S^{\mathcal{S}}]^2\right)\ln\left(\frac{\mu_{\rm 3D}}{2\mu_{\rm SU(3)_C}}\right) + \lambda_{S,4}\odot \\ &5\lambda_{V,3})\Big] + 48[g_S^{\mathcal{S}}]^2\lambda_{S,4} + 12[g_W^{\mathcal{S}}]^2\lambda_{S,8} \odot 6\Big([g_W^{\mathcal{S}}]^4 \odot 8[g_W^{\mathcal{S}}]^2\lambda_{S,8} + \\ &2\lambda_{S,8}^2\Big)\ln\left(\frac{\mu_{\rm 3D}}{2\mu_{\rm SU(2)_L}}\right) + \frac{24\lambda_{S,8}\lambda_{V,4}\mu_{\rm SU(3)_C}}{\mu_{\rm SU(2)_L}} + \frac{3\lambda_{S,7}\lambda_{V,9}\mu_{\rm SU(2)_L}}{\mu_{\rm U(1)_Y}} + \\ &\frac{3\lambda_{S,8}\lambda_{V,9}\mu_{\rm U(1)_Y}}{\mu_{\rm SU(2)_L}} + \frac{8\lambda_{S,4}\lambda_{V,8}\mu_{\rm U(1)_Y}}{\mu_{\rm SU(3)_C}} + \frac{8\lambda_{S,7}\lambda_{V,8}\mu_{\rm SU(3)_C}}{\mu_{\rm U(1)_Y}} + 15\lambda_{S,9}\lambda_{V,1} + \\ &15\lambda_{S,8}\lambda_{V,5} + \lambda_{S,7}\lambda_{V,10} \odot 24\lambda_{S,6}^2\ln\left(\frac{\mu_{\rm 3D}}{\mu_{\rm SU(2)_L} + \mu_{\rm U(1)_Y}}\right) \odot \\ &4\lambda_{S,7}^2\ln\left(\frac{\mu_{\rm 3D}}{2\mu_{\rm U(1)_Y}}\right) \odot 6\lambda_{S,8}^2\Big]\,.\end{aligned}$$

Scenario III

$$[\mu_{\rm D}^{\mathcal{US}}]^2_{\rm LO} = [\mu_{\rm D}^{\mathcal{S}}]^2 \odot \frac{3\mu_{\rm SU(2)_L}\lambda_{S,10} + 3\mu_{\rm SU(2)_D}\lambda_{S,5} + \mu_{\rm SU(3)_C}(3\lambda_{S,1}+5\lambda_{S,2}) + \mu_{\rm U(1)_Y}\lambda_{S,11}}{8\pi}\,, \tag{I.121}$$

$$[\mu_{\rm H}^{\mathcal{US}}]^2_{\rm LO} = [\mu_{\rm H}^{\mathcal{S}}]^2 \odot \frac{3\mu_{\rm SU(2)_L}\lambda_{S,8} + 3\mu_{\rm SU(2)_D}\lambda_{S,9} + 8\mu_{\rm SU(3)_C}\lambda_{S,4} + \mu_{\rm U(1)_Y}\lambda_{S,7}}{8\pi}\,, \tag{I.122}$$

$$
\begin{aligned}
[\mu_{\mathrm{D}}^{\mathcal{US}}]^2_{\mathrm{NLO}} = \frac{1}{128\pi^2}\Bigg[& \odot 6[g_{\mathrm{D}}^{\mathcal{S}}]^4 \ln\left(\frac{\mu_{3\mathrm{D}}}{2\mu_{\mathrm{SU}(2)_{\mathrm{D}}}}\right) + 12[g_{\mathrm{D}}^{\mathcal{S}}]^2\lambda_{S,5}\left(4\ln\left(\frac{\mu_{3\mathrm{D}}}{2\mu_{\mathrm{SU}(2)_{\mathrm{D}}}}\right)+1\right) + \\
& 18[g_S^{\mathcal{S}}]^2\lambda_{S,1}\left(4\ln\left(\frac{\mu_{3\mathrm{D}}}{2\mu_{\mathrm{SU}(3)_{\mathrm{C}}}}\right)+1\right) + 30[g_S^{\mathcal{S}}]^2\lambda_{S,2}\left(4\ln\left(\frac{\mu_{3\mathrm{D}}}{2\mu_{\mathrm{SU}(3)_{\mathrm{C}}}}\right)+1\right) + \\
& 12[g_{\mathrm{W}}^{\mathcal{S}}]^2\lambda_{S,10}\left(4\ln\left(\frac{\mu_{3\mathrm{D}}}{2\mu_{\mathrm{SU}(2)_{\mathrm{L}}}}\right)+1\right) + \\
& \frac{3\lambda_{S,1}\left(3\lambda_{V,4}\mu_{\mathrm{SU}(2)_{\mathrm{L}}} + 3\lambda_{V,2}\mu_{\mathrm{SU}(2)_{\mathrm{D}}} + 10\lambda_{V,3}\mu_{\mathrm{SU}(3)_{\mathrm{C}}} + \lambda_{V,8}\mu_{\mathrm{U}(1)_{\mathrm{Y}}}\right)}{\mu_{\mathrm{SU}(3)_{\mathrm{C}}}} + \\
& \frac{5\lambda_{S,2}\left(3\lambda_{V,4}\mu_{\mathrm{SU}(2)_{\mathrm{L}}} + 3\lambda_{V,2}\mu_{\mathrm{SU}(2)_{\mathrm{D}}} + 10\lambda_{V,3}\mu_{\mathrm{SU}(3)_{\mathrm{C}}} + \lambda_{V,8}\mu_{\mathrm{U}(1)_{\mathrm{Y}}}\right)}{\mu_{\mathrm{SU}(3)_{\mathrm{C}}}} + \\
& \lambda_{S,11}\left(\frac{3\lambda_{V,9}\mu_{\mathrm{SU}(2)_{\mathrm{L}}} + 3\lambda_{V,7}\mu_{\mathrm{SU}(2)_{\mathrm{D}}} + 8\lambda_{V,8}\mu_{\mathrm{SU}(3)_{\mathrm{C}}}}{\mu_{\mathrm{U}(1)_{\mathrm{Y}}}} + \lambda_{V,10}\right) + \\
& \frac{3\lambda_{S,10}\left(5\lambda_{V,5}\mu_{\mathrm{SU}(2)_{\mathrm{L}}} + 8\lambda_{V,4}\mu_{\mathrm{SU}(3)_{\mathrm{C}}} + \lambda_{V,9}\mu_{\mathrm{U}(1)_{\mathrm{Y}}}\right)}{\mu_{\mathrm{SU}(2)_{\mathrm{L}}}} + \\
& \frac{3\lambda_{S,5}\left(5\lambda_{V,1}\mu_{\mathrm{SU}(2)_{\mathrm{D}}} + 8\lambda_{V,2}\mu_{\mathrm{SU}(3)_{\mathrm{C}}} + \lambda_{V,7}\mu_{\mathrm{U}(1)_{\mathrm{Y}}}\right)}{\mu_{\mathrm{SU}(2)_{\mathrm{D}}}} \odot \\
& 6\lambda_{S,10}^2\left(2\ln\left(\frac{\mu_{3\mathrm{D}}}{2\mu_{\mathrm{SU}(2)_{\mathrm{L}}}}\right)+1\right) \odot 12\lambda_{S,3}^2\left(2\ln\left(\frac{\mu_{3\mathrm{D}}}{\mu_{\mathrm{SU}(2)_{\mathrm{D}}}+\mu_{\mathrm{U}(1)_{\mathrm{Y}}}}\right)+1\right) \odot \\
& 6\lambda_{S,5}^2\left(2\ln\left(\frac{\mu_{3\mathrm{D}}}{2\mu_{\mathrm{SU}(2)_{\mathrm{D}}}}\right)+1\right) \odot 6\lambda_{S,1}^2\left(2\ln\left(\frac{\mu_{3\mathrm{D}}}{2\mu_{\mathrm{SU}(3)_{\mathrm{C}}}}\right)+1\right) \odot \\
& 10\lambda_{S,2}^2\left(2\ln\left(\frac{\mu_{3\mathrm{D}}}{2\mu_{\mathrm{SU}(3)_{\mathrm{C}}}}\right)+1\right) \odot 2\lambda_{S,11}^2\left(2\ln\left(\frac{\mu_{3\mathrm{D}}}{2\mu_{\mathrm{U}(1)_{\mathrm{Y}}}}\right)+1\right)\Bigg],
\end{aligned}
\tag{I.123}
$$

$$
\begin{aligned}
[\mu_{\mathrm{H}}^{\mathcal{US}}]^2_{\mathrm{NLO}} = \frac{1}{128\pi^2}\Bigg[& 12[g_{\mathrm{D}}^{\mathcal{S}}]^2\lambda_{S,9}\left(4\ln\left(\frac{\mu_{3\mathrm{D}}}{2\mu_{\mathrm{SU}(2)_{\mathrm{D}}}}\right)+1\right) + 48[g_S^{\mathcal{S}}]^2\lambda_{S,4}\left(4\ln\left(\frac{\mu_{3\mathrm{D}}}{2\mu_{\mathrm{SU}(3)_{\mathrm{C}}}}\right)+1\right) \odot \\
& 6[g_{\mathrm{W}}^{\mathcal{S}}]^4 \ln\left(\frac{\mu_{3\mathrm{D}}}{2\mu_{\mathrm{SU}(2)_{\mathrm{L}}}}\right) + 12[g_{\mathrm{W}}^{\mathcal{S}}]^2\lambda_{S,8}\left(4\ln\left(\frac{\mu_{3\mathrm{D}}}{2\mu_{\mathrm{SU}(2)_{\mathrm{L}}}}\right)+1\right) + \\
& \frac{8\lambda_{S,4}\left(3\lambda_{V,4}\mu_{\mathrm{SU}(2)_{\mathrm{L}}} + 3\lambda_{V,2}\mu_{\mathrm{SU}(2)_{\mathrm{D}}} + 10\lambda_{V,3}\mu_{\mathrm{SU}(3)_{\mathrm{C}}} + \lambda_{V,8}\mu_{\mathrm{U}(1)_{\mathrm{Y}}}\right)}{\mu_{\mathrm{SU}(3)_{\mathrm{C}}}} + \\
& \lambda_{S,7}\left(\frac{3\lambda_{V,9}\mu_{\mathrm{SU}(2)_{\mathrm{L}}} + 3\lambda_{V,7}\mu_{\mathrm{SU}(2)_{\mathrm{D}}} + 8\lambda_{V,8}\mu_{\mathrm{SU}(3)_{\mathrm{C}}}}{\mu_{\mathrm{U}(1)_{\mathrm{Y}}}} + \lambda_{V,10}\right) + \\
& \frac{3\lambda_{S,8}\left(5\lambda_{V,5}\mu_{\mathrm{SU}(2)_{\mathrm{L}}} + 8\lambda_{V,4}\mu_{\mathrm{SU}(3)_{\mathrm{C}}} + \lambda_{V,9}\mu_{\mathrm{U}(1)_{\mathrm{Y}}}\right)}{\mu_{\mathrm{SU}(2)_{\mathrm{L}}}} + \\
& \frac{3\lambda_{S,9}\left(5\lambda_{V,1}\mu_{\mathrm{SU}(2)_{\mathrm{D}}} + 8\lambda_{V,2}\mu_{\mathrm{SU}(3)_{\mathrm{C}}} + \lambda_{V,7}\mu_{\mathrm{U}(1)_{\mathrm{Y}}}\right)}{\mu_{\mathrm{SU}(2)_{\mathrm{D}}}} \odot \\
& 12\lambda_{S,6}^2\left(2\ln\left(\frac{\mu_{3\mathrm{D}}}{\mu_{\mathrm{SU}(2)_{\mathrm{L}}}+\mu_{\mathrm{U}(1)_{\mathrm{Y}}}}\right)+1\right) \odot 6\lambda_{S,8}^2\left(2\ln\left(\frac{\mu_{3\mathrm{D}}}{2\mu_{\mathrm{SU}(2)_{\mathrm{L}}}}\right)+1\right) \odot \\
& 6\lambda_{S,9}^2\left(2\ln\left(\frac{\mu_{3\mathrm{D}}}{2\mu_{\mathrm{SU}(2)_{\mathrm{D}}}}\right)+1\right) \odot 16\lambda_{S,4}^2\left(2\ln\left(\frac{\mu_{3\mathrm{D}}}{2\mu_{\mathrm{SU}(3)_{\mathrm{C}}}}\right)+1\right) \odot \\
& 2\lambda_{S,7}^2\left(2\ln\left(\frac{\mu_{3\mathrm{D}}}{2\mu_{\mathrm{U}(1)_{\mathrm{Y}}}}\right)+1\right)\Bigg].
\end{aligned}
\tag{I.124}
$$

I.8 Vector and scalar field-dependent masses at ultra soft scale

Here we write down the 3D field dependent masses in the ultrasoft limit in terms of the 3D field φ_{D} and the ultrasoft parameters, which appear directly in the NLO part of the effective potential, see Eq. (I.2). They are calculated from LO effective potential. We start with Scenario I. Here, for the

scalar masses we have

$$\mathcal{M}^2_{\varphi_1} = [\mu^{\mathcal{US}}_{\rm D}]^2 + \lambda^{\mathcal{US}}_{\rm D}\varphi^2_{\rm D}\,, \tag{I.125}$$
$$\mathcal{M}^2_{\varphi_2} = [\mu^{\mathcal{US}}_{\rm D}]^2 + \lambda^{\mathcal{US}}_{\rm D}\varphi^2_{\rm D}\,, \tag{I.126}$$
$$\mathcal{M}^2_{\varphi_3} = [\mu^{\mathcal{US}}_{\rm D}]^2 + 3\lambda^{\mathcal{US}}_{\rm D}\varphi^2_{\rm D}\,, \tag{I.127}$$
$$\mathcal{M}^2_{\varphi_4} = [\mu^{\mathcal{US}}_{\rm D}]^2 + \lambda^{\mathcal{US}}_{\rm D}\varphi^2_{\rm D}\,, \tag{I.128}$$

while for the vector bosons we have

$$\mathcal{M}^2_{\mathcal{V}_1} = \frac{1}{4}[g^{\mathcal{US}}_{\rm D}]^2\varphi^2_{\rm D}\,, \tag{I.129}$$
$$\mathcal{M}^2_{\mathcal{V}_2} = \frac{1}{4}[g^{\mathcal{US}}_{\rm D}]^2\varphi^2_{\rm D}\,, \tag{I.130}$$
$$\mathcal{M}^2_{\mathcal{V}_3} = \frac{1}{4}[g^{\mathcal{US}}_{\rm D}]^2\varphi^2_{\rm D}\,. \tag{I.131}$$

For Scenario II/III, the scalar masses are given by

$$\mathcal{M}^2_{\varphi_1} = [\mu^{\mathcal{US}}_{\rm D}]^2 + \frac{1}{2}\lambda^{\mathcal{US}}_{\rm HD}\varphi^2_{\rm H} + \lambda^{\mathcal{US}}_{\rm D}\varphi^2_{\rm D}\,, \tag{I.132}$$
$$\mathcal{M}^2_{\varphi_2} = [\mu^{\mathcal{US}}_{\rm D}]^2 + \frac{1}{2}\lambda^{\mathcal{US}}_{\rm HD}\varphi^2_{\rm H} + \lambda^{\mathcal{US}}_{\rm D}\varphi^2_{\rm D}\,, \tag{I.133}$$
$$\mathcal{M}^2_{\varphi_3} = [\mu^{\mathcal{US}}_{\rm D}]^2 + \frac{1}{2}\lambda^{\mathcal{US}}_{\rm HD}\varphi^2_{\rm H} + \lambda^{\mathcal{US}}_{\rm D}\varphi^2_{\rm D}\,, \tag{I.134}$$
$$\mathcal{M}^2_{\varphi_4} = [\mu^{\mathcal{US}}_{\rm H}]^2 + \lambda^{\mathcal{US}}_{\rm H}\varphi^2_{\rm H} + \frac{1}{2}\lambda^{\mathcal{US}}_{\rm HD}\varphi^2_{\rm D}\,, \tag{I.135}$$
$$\mathcal{M}^2_{\varphi_5} = [\mu^{\mathcal{US}}_{\rm H}]^2 + \lambda^{\mathcal{US}}_{\rm H}\varphi^2_{\rm H} + \frac{1}{2}\lambda^{\mathcal{US}}_{\rm HD}\varphi^2_{\rm D}\,, \tag{I.136}$$
$$\mathcal{M}^2_{\varphi_6} = [\mu^{\mathcal{US}}_{\rm H}]^2 + \lambda^{\mathcal{US}}_{\rm H}\varphi^2_{\rm H} + \frac{1}{2}\lambda^{\mathcal{US}}_{\rm HD}\varphi^2_{\rm D}\,, \tag{I.137}$$
$$\mathcal{M}^2_{\varphi_7} = {\rm eig}(M^2_{\varphi_{\rm H}\varphi_{\rm D}}[1])\,, \tag{I.138}$$
$$\mathcal{M}^2_{\varphi_8} = {\rm eig}(M^2_{\varphi_{\rm H}\varphi_{\rm D}}[2])\,, \tag{I.139}$$

where $\mathcal{M}^2_{\varphi_7}$ and $\mathcal{M}^2_{\varphi_8}$ are eigenvalues of the mass matrix

$$M^2_{\varphi_{\rm H}\varphi_{\rm D}} = \begin{bmatrix} [\mu^{\mathcal{US}}_{\rm H}]^2 + 3\lambda^{\mathcal{US}}_{\rm H}\varphi^2_{\rm H} + \frac{1}{2}\lambda^{\mathcal{US}}_{\rm HD}\varphi^2_{\rm D} & \lambda^{\mathcal{US}}_{\rm HD}\varphi_{\rm H}\varphi_{\rm D} \\ \lambda^{\mathcal{US}}_{\rm HD}\varphi_{\rm H}\varphi_{\rm D} & [\mu^{\mathcal{US}}_{\rm D}]^2 + \frac{1}{2}\lambda^{\mathcal{US}}_{\rm HD}\varphi^2_{\rm H} + 3\lambda^{\mathcal{US}}_{\rm D}\varphi^2_{\rm D} \end{bmatrix}. \tag{I.140}$$

The vector masses in turn are given by

$$\mathcal{M}^2_{\mathcal{V}_1} = \frac{1}{4}[g^{\mathcal{US}}_{\rm D}]^2\varphi^2_{\rm D}\,, \tag{I.141}$$
$$\mathcal{M}^2_{\mathcal{V}_2} = \frac{1}{4}[g^{\mathcal{US}}_{\rm D}]^2\varphi^2_{\rm D}\,, \tag{I.142}$$
$$\mathcal{M}^2_{\mathcal{V}_3} = \frac{1}{4}[g^{\mathcal{US}}_{\rm D}]^2\varphi^2_{\rm D}\,, \tag{I.143}$$
$$\mathcal{M}^2_{\mathcal{V}_4} = \frac{1}{4}[g^{\mathcal{US}}_{\rm W}]^2\varphi^2_{\rm H}\,, \tag{I.144}$$
$$\mathcal{M}^2_{\mathcal{V}_5} = \frac{1}{4}[g^{\mathcal{US}}_{\rm W}]^2\varphi^2_{\rm H}\,, \tag{I.145}$$
$$\mathcal{M}^2_{\mathcal{V}_6} = {\rm eig}(M^2_{\mathcal{V}_W\mathcal{V}_Y}[1])\,, \tag{I.146}$$
$$\mathcal{M}^2_{\mathcal{V}_7} = {\rm eig}(M^2_{\mathcal{V}_W\mathcal{V}_Y}[2])\,, \tag{I.147}$$

where $\mathcal{M}^2_{\mathcal{V}_6}$ and $\mathcal{M}^2_{\mathcal{V}_7}$ are eigenvalues of the mass matrix

$$M^2_{\mathcal{V}_W\mathcal{V}_Y} = \begin{bmatrix} \frac{1}{4}[g^{\mathcal{US}}_{\rm W}]^2\varphi^2_{\rm H} & \odot\frac{1}{4}g^{\mathcal{US}}_{\rm W}g^{\mathcal{US}}_{\rm Y}\varphi^2_{\rm H} \\ \odot\frac{1}{4}g^{\mathcal{US}}_{\rm W}g^{\mathcal{US}}_{\rm Y}\varphi^2_{\rm H} & \frac{1}{4}[g^{\mathcal{US}}_{\rm Y}]^2\varphi^2_{\rm H} \end{bmatrix}. \tag{I.148}$$

I.9 Pressure in the ultrasoft limit

Here, the 4D pressure is related to the 3D pressure by $P = T(\mathcal{P}^{\mathcal{US}}_{\rm LO} + \mathcal{P}^{\mathcal{US}}_{\rm NLO})$.

Scenario I

$$\mathcal{P}^{\mathcal{US}}_{\rm LO} = \frac{\left[\mu^2_{\mathrm{SU(2)_D}}\right]^{3/2}}{4\pi}\,, \tag{I.149}$$

$$\mathcal{P}^{\mathcal{US}}_{\rm NLO} = \frac{3}{2048\pi^2}\left[\mu^2_{\mathrm{SU(2)_D}}\left(\odot 64[g^{\mathcal{US}}_{\rm D}]^2\left(4\,\ln\left(\frac{\mu_{\rm 3d}}{2\mu_{\mathrm{SU(2)_D}}}\right)+3\right)\odot 5\pi\lambda_{V,1}\right)\right], \tag{I.150}$$

Scenario II

$$\mathcal{P}^{\mathcal{US}}_{\rm LO} = \text{Eq. (I.153)}\,, \tag{I.151}$$

$$\mathcal{P}^{\mathcal{US}}_{\rm NLO} = \text{Eq. (I.154)} \;+\frac{3\pi\mu_{\mathrm{SU(2)_D}}}{1024\pi^2}\left(8\lambda_{V,2}\mu_{\mathrm{SU(3)_C}}+\lambda_{V,7}\mu_{\mathrm{U(1)_Y}}\right), \tag{I.152}$$

Scenario III

$$\mathcal{P}^{\mathcal{US}}_{\rm LO} = \frac{1}{12\pi}\left(3\left[\mu^2_{\mathrm{SU(2)_L}}\right]^{3/2}+3\left[\mu^2_{\mathrm{SU(2)_D}}\right]^{3/2}+8\left[\mu^2_{\mathrm{SU(3)_C}}\right]^{3/2}+\left[\mu^2_{\mathrm{U(1)_Y}}\right]^{3/2}\right) \tag{I.153}$$

$$\begin{aligned}\mathcal{P}^{\mathcal{US}}_{\rm NLO} = \odot\frac{1}{2048\pi^2}\Bigg[&192[g^{\mathcal{US}}_{\rm D}]^2\mu^2_{\mathrm{SU(2)_D}}\left(4\,\ln\left(\frac{\mu_{\rm 3D}}{2\mu_{\mathrm{SU(2)_D}}}\right)+3\right)+\\ &768[g^{\mathcal{US}}_{S}]^2\mu^2_{\mathrm{SU(3)_C}}\left(4\,\ln\left(\frac{\mu_{\rm 3D}}{2\mu_{\mathrm{SU(3)_C}}}\right)+3\right)+\\ &192[g^{\mathcal{US}}_{\rm W}]^2\mu^2_{\mathrm{SU(2)_L}}\left(4\,\ln\left(\frac{\mu_{\rm 3D}}{2\mu_{\mathrm{SU(2)_L}}}\right)+3\right)+\\ &\pi\Big(16\mu_{\mathrm{SU(3)_C}}\left(3\lambda_{V,4}\mu_{\mathrm{SU(2)_L}}+\lambda_{V,8}\mu_{\mathrm{U(1)_Y}}\right)+6\lambda_{V,9}\mu_{\mathrm{SU(2)_L}}\mu_{\mathrm{U(1)_Y}}+\\ &15\lambda_{V,5}\mu^2_{\mathrm{SU(2)_L}}+6\mu_{\mathrm{SU(2)_D}}\left(8\lambda_{V,2}\mu_{\mathrm{SU(3)_C}}+\lambda_{V,7}\mu_{\mathrm{U(1)_Y}}\right)+15\lambda_{V,1}\mu^2_{\mathrm{SU(2)_D}}+\\ &80\lambda_{V,3}\mu^2_{\mathrm{SU(3)_C}}+\lambda_{V,10}\mu^2_{\mathrm{U(1)_Y}}\Big)\Bigg]\,.\end{aligned} \tag{I.154}$$

APPENDIX J

Statistical Treatment of Signal Region Recasting (FPVDM)

To quantify the exclusion reach for each parameter point in our model, we compute the expected 95% CL upper limit on the signal yield, denoted as s_{95}^{exp}. This is done using the Asimov dataset formalism and the CL_s hypothesis testing approach, based on the profile likelihood ratio as described in Cowan et al. [174]. The statistical evaluation is performed using the PYHF package [501], which provides a backend-independent, JSON-serialised implementation of likelihood construction and inference.

In our implementation, each signal region extracted from the `CheckMATE` recasting framework is modelled by a simplified likelihood consisting of:

- a signal template, normalised to unity;
- a background expectation b, with associated uncertainty δ_b, incorporated via a `normsys` nuisance parameter representing log-normal scaling;
- an observation given by the Asimov dataset, *i.e.* the expected number of events under the background-only hypothesis.

The numerical values for s, δ_s, b, and δ_b are taken directly from the `CheckMATE` output files for each relevant analysis and signal region, based on detector-level event simulation. These quantities form the inputs to the statistical model built in `pyhf` for every parameter point in our scan.

The test statistic is evaluated using the asymptotic approximation, yielding the expected upper limit on the signal strength, μ_{95}^{exp}, from which the corresponding upper limit on the signal yield is derived as:

$$s_{95}^{\text{exp}} = \mu_{95}^{\text{exp}} \times s_{\text{template}}. \tag{J.1}$$

To define a conservative yet statistically meaningful exclusion criterion, we compute the ratio:

$$r_{\text{exp}}^{\text{cons}} = \frac{s \odot 1.64\,\delta_s}{s_{95}^{\text{exp}}}, \tag{J.2}$$

where s is the predicted signal yield at a given parameter point, and δ_s is the associated uncertainty. The factor 1.64 corresponds to a one-sided 95% CL downward fluctuation under Gaussian statistics. A parameter point is deemed excluded at 95% CL if $r_{\text{exp}}^{\text{cons}} > 1$.

This procedure is applied systematically to all signal regions relevant to our analysis, as implemented in `CheckMATE` and discussed in detail in the main text. In particular, it is used to:

- reproduce and validate the individual signal region exclusions obtained from `CheckMATE`;
- perform statistical combinations of mutually orthogonal signal regions from the same analysis (e.g. 0-lepton and 1-lepton channels in CMS SUS-19-005 or ATLAS 2101.01629);
- and combine the most sensitive signal regions across ATLAS and CMS to derive the most stringent overall exclusion limit.

This approach ensures consistency between detector-level simulation, recasting, and statistical interpretation, enabling a robust mapping between BSM signal predictions and current experimental constraints.

References

[1] C. D. Anderson, *The Positive Electron*, *Phys. Rev.* **43** (1933) 491–494.

[2] J. C. Street and E. C. Stevenson, *New Evidence for the Existence of a Particle of Mass Intermediate Between the Proton and Electron*, *Phys. Rev.* **52** (1937) 1003–1004.

[3] C. S. Wu, E. Ambler, R. W. Hayward, D. D. Hoppes, and R. P. Hudson, *Experimental Test of Parity Conservation in β Decay*, *Phys. Rev.* **105** (1957) 1413–1414.

[4] S. Weinberg, *A Model of Leptons*, *Phys. Rev. Lett.* **19** (1967) 1264–1266.

[5] S. L. Glashow, *Partial Symmetries of Weak Interactions*, *Nucl. Phys.* **22** (1961) 579–588.

[6] F. Englert and R. Brout, *Broken Symmetry and the Mass of Gauge Vector Mesons*, *Phys. Rev. Lett.* **13** (1964) 321–323.

[7] P. W. Higgs, *Broken Symmetries and the Masses of Gauge Bosons*, *Phys. Rev. Lett.* **13** (1964) 508–509.

[8] G. S. Guralnik, C. R. Hagen, and T. W. B. Kibble, *Global Conservation Laws and Massless Particles*, *Phys. Rev. Lett.* **13** (1964) 585–587.

[9] D. J. Gross and F. Wilczek, *Ultraviolet behavior of non-abelian gauge theories*, *Phys. Rev. Lett.* **30** (Jun, 1973) 1343–1346.

[10] **ATLAS** Collaboration, G. Aad *et al.*, *Observation of a new particle in the search for the Standard Model Higgs boson with the ATLAS detector at the LHC*, *Phys. Lett. B* **716** (2012) 1–29, [1207.7214].

[11] **CMS** Collaboration, S. Chatrchyan *et al.*, *Observation of a New Boson at a Mass of 125 GeV with the CMS Experiment at the LHC*, *Phys. Lett. B* **716** (2012) 30–61, [1207.7235].

[12] **CDF** Collaboration, F. Abe *et al.*, *Observation of top quark production in $\bar{p}p$ collisions*, *Phys. Rev. Lett.* **74** (1995) 2626–2631, [hep-ex/9503002].

[13] **UA1** Collaboration, G. Arnison *et al.*, *Experimental Observation of Lepton Pairs of Invariant Mass Around 95-GeV/c**2 at the CERN SPS Collider*, *Phys. Lett. B* **126** (1983) 398–410.

[14] G. Danby, J. M. Gaillard, K. A. Goulianos, L. M. Lederman, N. B. Mistry, M. Schwartz, and J. Steinberger, *Observation of High-Energy Neutrino Reactions and the Existence of Two Kinds of Neutrinos*, *Phys. Rev. Lett.* **9** (1962) 36–44.

[15] **UA1** Collaboration, G. Arnison *et al.*, *Experimental Observation of Isolated Large Transverse Energy Electrons with Associated Missing Energy at $\sqrt{s} = 540$ GeV*, *Phys. Lett. B* **122** (1983) 103–116.

[16] **E288** Collaboration, S. W. Herb *et al.*, *Observation of a Dimuon Resonance at 9.5-GeV in 400-GeV Proton-Nucleus Collisions*, *Phys. Rev. Lett.* **39** (1977) 252–255.

[17] M. L. Perl *et al.*, *Evidence for Anomalous Lepton Production in e+ - e- Annihilation*, *Phys. Rev. Lett.* **35** (1975) 1489–1492.

[18] **Super-Kamiokande** Collaboration, Y. Fukuda *et al.*, *Evidence for oscillation of atmospheric neutrinos*, *Phys. Rev. Lett.* **81** (1998) 1562–1567, [hep-ex/9807003].

[19] **Particle Data Group** Collaboration, P. Zyla *et al.*, *Review of Particle Physics*, *PTEP* **2020** (2020), no. 8 083C01.

[20] G. Bertone, D. Hooper, and J. Silk, *Particle dark matter: Evidence, candidates and constraints*, *Phys. Rept.* **405** (2005) 279–390, [hep-ph/0404175].

[21] **Planck** Collaboration, P. Ade *et al.*, *Planck 2015 results. XIV. Dark energy and modified gravity*, *Astron. Astrophys.* **594** (2016) A14, [1502.01590].

[22] M. E. Peskin and D. V. Schroeder, *An Introduction to quantum field theory*. Addison-Wesley, Reading, USA, 1995.

[23] D. Tong, *String Theory*, 0908.0333.

[24] S. P. Martin, *A Supersymmetry primer*, *Adv. Ser. Direct. High Energy Phys.* **21** (2010) 1–153, [hep-ph/9709356].

[25] A. Kosowsky and M. S. Turner, *Gravitational radiation from colliding vacuum bubbles: envelope approximation to many bubble collisions*, *Phys. Rev. D* **47** (1993) 4372–4391, [astro-ph/9211004].

[26] M. S. Turner and F. Wilczek, *Relic gravitational waves and extended inflation*, *Phys. Rev. Lett.* **65** (1990) 3080–3083.

[27] I. Cholis, E. D. Kovetz, Y. Ali-Haïmoud, S. Bird, M. Kamionkowski, J. B. Muñoz, and A. Raccanelli, *Orbital eccentricities in primordial black hole binaries*, *Phys. Rev. D* **94** (2016), no. 8 084013, [1606.07437].

[28] **LISA** Collaboration, P. Amaro-Seoane *et al.*, *Laser Interferometer Space Antenna*, 1702.00786.

[29] K. Yagi and N. Seto, *Detector configuration of DECIGO/BBO and identification of cosmological neutron-star binaries*, *Phys. Rev. D* **83** (2011) 044011, [1101.3940]. [Erratum: Phys.Rev.D 95, 109901 (2017)].

[30] **LIGO Scientific** Collaboration, J. Aasi *et al.*, *Advanced LIGO*, *Class. Quant. Grav.* **32** (2015) 074001, [1411.4547].

[31] M. Punturo *et al.*, *The Einstein Telescope: A third-generation gravitational wave observatory*, *Class. Quant. Grav.* **27** (2010) 194002.

[32] **KAGRA, Virgo, LIGO Scientific** Collaboration, R. Abbott *et al.*, *Upper limits on the isotropic gravitational-wave background from Advanced LIGO and Advanced Virgo's third observing run*, *Phys. Rev. D* **104** (2021), no. 2 022004, [2101.12130].

[33] G. Colangelo, M. Hoferichter, and P. Stoffer, *Two-pion contribution to hadronic vacuum polarization*, *JHEP* **02** (2019) 006, [1810.00007].

[34] A. Kurz, T. Liu, P. Marquard, and M. Steinhauser, *Hadronic contribution to the muon anomalous magnetic moment to next-to-next-to-leading order*, *Phys. Lett.* **B734** (2014) 144–147, [1403.6400].

[35] **Fermilab Lattice, LATTICE-HPQCD, MILC** Collaboration, B. Chakraborty *et al.*, *Strong-Isospin-Breaking Correction to the Muon Anomalous Magnetic Moment from Lattice QCD at the Physical Point*, *Phys. Rev. Lett.* **120** (2018), no. 15 152001, [1710.11212].

[36] **Budapest-Marseille-Wuppertal** Collaboration, S. Borsanyi *et al.*, *Hadronic vacuum polarization contribution to the anomalous magnetic moments of leptons from first principles*, *Phys. Rev. Lett.* **121** (2018), no. 2 022002, [1711.04980].

[37] **RBC, UKQCD** Collaboration, T. Blum, P. A. Boyle, V. Gülpers, T. Izubuchi, L. Jin, C. Jung, A. Jüttner, C. Lehner, A. Portelli, and J. T. Tsang, *Calculation of the hadronic vacuum polarization contribution to the muon anomalous magnetic moment*, *Phys. Rev. Lett.* **121** (2018), no. 2 022003, [1801.07224].

[38] **ETM** Collaboration, D. Giusti, V. Lubicz, G. Martinelli, F. Sanfilippo, and S. Simula, *Electromagnetic and strong isospin-breaking corrections to the muon $g \odot 2$ from Lattice QCD+QED*, *Phys. Rev.* **D99** (2019), no. 11 114502, [1901.10462].

[39] E. Shintani and Y. Kuramashi, *Study of systematic uncertainties in hadronic vacuum polarization contribution to muon $g \odot 2$ with 2+1 flavor lattice QCD*, *Phys. Rev.* **D100** (2019), no. 3 034517, [1902.00885].

[40] **Fermilab Lattice, LATTICE-HPQCD, MILC** Collaboration, C. T. H. Davies *et al.*, *Hadronic-vacuum-polarization contribution to the muon's anomalous magnetic moment from four-flavor lattice QCD*, *Phys. Rev.* **D101** (2020), no. 3 034512, [1902.04223].

[41] A. Gérardin, M. Cè, G. von Hippel, B. Hörz, H. B. Meyer, D. Mohler, K. Ottnad, J. Wilhelm, and H. Wittig, *The leading hadronic contribution to $(g \odot 2)_\mu$ from lattice QCD with $N_{\rm f} = 2 + 1$ flavours of O(a) improved Wilson quarks*, *Phys. Rev.* **D100** (2019), no. 1 014510, [1904.03120].

[42] C. Aubin, T. Blum, C. Tu, M. Golterman, C. Jung, and S. Peris, *Light quark vacuum polarization at the physical point and contribution to the muon $g \odot 2$*, *Phys. Rev.* **D101** (2020), no. 1 014503, [1905.09307].

[43] D. Giusti and S. Simula, *Lepton anomalous magnetic moments in Lattice QCD+QED*, *PoS* **LATTICE2019** (2019) 104, [1910.03874].

[44] V. Pauk and M. Vanderhaeghen, *Single meson contributions to the muon's anomalous magnetic moment*, *Eur. Phys. J.* **C74** (2014), no. 8 3008, [1401.0832].

[45] I. Danilkin and M. Vanderhaeghen, *Light-by-light scattering sum rules in light of new data*, *Phys. Rev.* **D95** (2017), no. 1 014019, [1611.04646].

[46] M. Knecht, S. Narison, A. Rabemananjara, and D. Rabetiarivony, *Scalar meson contributions to a_μ from hadronic light-by-light scattering*, *Phys. Lett.* **B787** (2018) 111–123, [1808.03848].

[47] G. Eichmann, C. S. Fischer, and R. Williams, *Kaon-box contribution to the anomalous magnetic moment of the muon*, *Phys. Rev.* **D101** (2020), no. 5 054015, [1910.06795].

[48] P. Roig and P. Sánchez-Puertas, *Axial-vector exchange contribution to the hadronic light-by-light piece of the muon anomalous magnetic moment*, *Phys. Rev.* **D101** (2020), no. 7 074019, [1910.02881].

[49] K. Melnikov and A. Vainshtein, *Hadronic light-by-light scattering contribution to the muon anomalous magnetic moment revisited*, *Phys. Rev.* **D70** (2004) 113006, [hep-ph/0312226].

[50] A. Gérardin, H. B. Meyer, and A. Nyffeler, *Lattice calculation of the pion transition form factor with $N_f = 2 + 1$ Wilson quarks*, *Phys. Rev.* **D100** (2019), no. 3 034520, [1903.09471].

[51] A. Keshavarzi, D. Nomura, and T. Teubner, *Muon $g \odot 2$ and $\alpha(M_Z^2)$: a new data-based analysis*, *Phys. Rev.* **D97** (2018), no. 11 114025, [1802.02995].

[52] M. Davier, A. Hoecker, B. Malaescu, and Z. Zhang, *A new evaluation of the hadronic vacuum polarisation contributions to the muon anomalous magnetic moment and to $\boldsymbol{\alpha(m_Z^2)}$*, *Eur. Phys. J.* **C80** (2020), no. 3 241, [1908.00921]. [Erratum: Eur. Phys. J. **C80**, 410 (2020)].

[53] G. Colangelo, M. Hoferichter, M. Procura, and P. Stoffer, *Dispersion relation for hadronic light-by-light scattering: two-pion contributions*, *JHEP* **04** (2017) 161, [1702.07347].

[54] M. Hoferichter, B.-L. Hoid, B. Kubis, S. Leupold, and S. P. Schneider, *Dispersion relation for hadronic light-by-light scattering: pion pole*, *JHEP* **10** (2018) 141, [1808.04823].

[55] G. Colangelo, M. Hoferichter, A. Nyffeler, M. Passera, and P. Stoffer, *Remarks on higher-order hadronic corrections to the muon $g \odot 2$*, *Phys. Lett.* **B735** (2014) 90–91, [1403.7512].

[56] M. Davier, A. Hoecker, B. Malaescu, and Z. Zhang, *Reevaluation of the hadronic vacuum polarisation contributions to the Standard Model predictions of the muon $g \odot 2$ and $\alpha(m_Z^2)$ using newest hadronic cross-section data*, *Eur. Phys. J.* **C77** (2017), no. 12 827, [1706.09436].

[57] M. Hoferichter, B.-L. Hoid, and B. Kubis, *Three-pion contribution to hadronic vacuum polarization*, *JHEP* **08** (2019) 137, [1907.01556].

[58] A. Keshavarzi, D. Nomura, and T. Teubner, *The $g \odot 2$ of charged leptons, $\alpha(M_Z^2)$ and the hyperfine splitting of muonium*, *Phys. Rev.* **D101** (2020) 014029, [1911.00367].

[59] G. Colangelo, F. Hagelstein, M. Hoferichter, L. Laub, and P. Stoffer, *Longitudinal short-distance constraints for the hadronic light-by-light contribution to $(g \odot 2)_\mu$ with large-N_c Regge models*, *JHEP* **03** (2020) 101, [1910.13432].

[60] T. Blum, N. Christ, M. Hayakawa, T. Izubuchi, L. Jin, C. Jung, and C. Lehner, *The hadronic light-by-light scattering contribution to the muon anomalous magnetic moment from lattice QCD*, *Phys. Rev. Lett.* **124** (2020), no. 13 132002, [1911.08123].

[61] J. Bijnens, N. Hermansson-Truedsson, and A. Rodríguez-Sánchez, *Short-distance constraints for the HLbL contribution to the muon anomalous magnetic moment*, *Phys. Lett.* **B798** (2019) 134994, [1908.03331].

[62] M. Davier, A. Hoecker, B. Malaescu, and Z. Zhang, *Reevaluation of the Hadronic Contributions to the Muon g-2 and to alpha(MZ)*, *Eur. Phys. J. C* **71** (2011) 1515, [1010.4180]. [Erratum: Eur.Phys.J.C 72, 1874 (2012)].

[63] A. Djouadi, M. Spira, and P. M. Zerwas, *Production of Higgs bosons in proton colliders: QCD corrections*, *Phys. Lett. B* **264** (1991) 440–446.

[64] S. Catani and M. Grazzini, *An NNLO subtraction formalism in hadron collisions and its application to Higgs boson production at the LHC*, *Phys. Rev. Lett.* **98** (2007) 222002, [hep-ph/0703012].

[65] S. Catani, D. de Florian, M. Grazzini, and P. Nason, *Soft gluon resummation for Higgs boson production at hadron colliders*, *JHEP* **07** (2003) 028, [hep-ph/0306211].

[66] O. Brein, A. Djouadi, and R. Harlander, *NNLO QCD corrections to the Higgs-strahlung processes at hadron colliders*, *Phys. Lett. B* **579** (2004) 149–156, [hep-ph/0307206].

[67] M. Spira, *QCD effects in Higgs physics*, *Fortsch. Phys.* **46** (1998) 203–284, [hep-ph/9705337].

[68] C. M. Institute, "Yang-mills and mass gap." https://www.claymath.org/millennium/yang-mills-the-maths-gap/.

[69] B. Andersson, G. Gustafson, G. Ingelman, and T. Sjostrand, *Parton Fragmentation and String Dynamics*, *Phys. Rept.* **97** (1983) 31–145.

[70] T. Sjöstrand, S. Ask, J. R. Christiansen, R. Corke, N. Desai, P. Ilten, S. Mrenna, S. Prestel, C. O. Rasmussen, and P. Z. Skands, *An introduction to PYTHIA 8.2*, *Comput. Phys. Commun.* **191** (2015) 159–177, [1410.3012].

[71] **HPQCD and UKQCD Collaborations and MILC Collaboration and HPQCD and Fermilab Lattice Collaborations** Collaboration, C. T. H. Davies, E. Follana, A. Gray, G. P. Lepage, Q. Mason, M. Nobes, J. Shigemitsu, H. D. Trottier, M. Wingate, C. Aubin, C. Bernard, T. Burch, C. DeTar, S. Gottlieb, E. B. Gregory, U. M. Heller, J. E. Hetrick, J. Osborn, R. Sugar, D. Toussaint, M. D. Pierro, A. El-Khadra, A. S. Kronfeld, P. B. Mackenzie, D. Menscher, and J. Simone, *High-precision lattice qcd confronts experiment*, *Phys. Rev. Lett.* **92** (Jan, 2004) 022001.

[72] K. G. Wilson, *Confinement of quarks*, *Phys. Rev. D* **10** (Oct, 1974) 2445–2459.

[73] A. Salam and J. C. Ward, *Electromagnetic and weak interactions*, *Phys. Lett.* **13** (1964) 168–171.

[74] **Particle Data Group** Collaboration, S. Navas *et al.*, *Review of particle physics*, *Phys. Rev. D* **110** (2024), no. 3 030001.

[75] **CMS** Collaboration, A. M. Sirunyan *et al.*, *Combined measurements of Higgs boson couplings in proton–proton collisions at* $\sqrt{s} = 13$ *TeV*, *Eur. Phys. J. C* **79** (2019), no. 5 421, [1809.10733].

[76] **Super-Kamiokande** Collaboration, Y. Fukuda *et al.*, *Evidence for oscillation of atmospheric neutrinos*, *Phys. Rev. Lett.* **81** (1998) 1562–1567, [hep-ex/9807003].

[77] V. A. Rubakov and M. E. Shaposhnikov, *Electroweak baryon number nonconservation in the early universe and in high-energy collisions*, *Usp. Fiz. Nauk* **166** (1996) 493–537, [hep-ph/9603208].

[78] G. R. Farrar and M. E. Shaposhnikov, *Baryon asymmetry of the universe in the minimal Standard Model*, *Phys. Rev. Lett.* **70** (1993) 2833–2836, [hep-ph/9305274]. [Erratum: Phys.Rev.Lett. 71, 210 (1993)].

[79] K. Kajantie, M. Laine, K. Rummukainen, and M. E. Shaposhnikov, *Is there a hot electroweak phase transition at* $m_H \gtrsim m_W$*?*, *Phys. Rev. Lett.* **77** (1996) 2887–2890, [hep-ph/9605288].

[80] F. Karsch, T. Neuhaus, A. Patkos, and J. Rank, *Critical Higgs mass and temperature dependence of gauge boson masses in the SU(2) gauge Higgs model*, *Nucl. Phys. B Proc. Suppl.* **53** (1997) 623–625, [hep-lat/9608087].

[81] M. D'Onofrio and K. Rummukainen, *Standard model cross-over on the lattice*, *Phys. Rev. D* **93** (2016), no. 2 025003, [1508.07161].

[82] Z. Fodor and S. D. Katz, *Critical point of QCD at finite T and mu, lattice results for physical quark masses*, *JHEP* **04** (2004) 050, [hep-lat/0402006].

[83] D. Benisty, D. Vasak, J. Struckmeier, and H. Stoecker, *Bounding the cosmological constant using galactic rotation curves from SPARC dataset*, *Phys. Rev. D* **110** (2024), no. 6 063028, [2405.16650].

[84] M. Markevitch, A. H. Gonzalez, D. Clowe, A. Vikhlinin, L. David, W. Forman, C. Jones, S. Murray, and W. Tucker, *Direct constraints on the dark matter self-interaction cross-section from the merging galaxy cluster 1E0657-56*, *Astrophys. J.* **606** (2004) 819–824, [astro-ph/0309303].

[85] D. Clowe, A. Gonzalez, and M. Markevitch, *Weak lensing mass reconstruction of the interacting cluster 1E0657-558: Direct evidence for the existence of dark matter*, *Astrophys. J.* **604** (2004) 596–603, [astro-ph/0312273].

[86] **LSND** Collaboration, A. Aguilar *et al.*, *Evidence for neutrino oscillations from the observation of* $\bar{\nu}_e$ *appearance in a* $\bar{\nu}_\mu$ *beam*, *Phys. Rev. D* **64** (2001) 112007, [hep-ex/0104049].

[87] **MiniBooNE** Collaboration, A. A. Aguilar-Arevalo *et al.*, *Significant Excess of ElectronLike Events in the MiniBooNE Short-Baseline Neutrino Experiment*, *Phys. Rev. Lett.* **121** (2018), no. 22 221801, [1805.12028].

[88] **MiniBooNE** Collaboration, A. A. Aguilar-Arevalo *et al.*, *Updated MiniBooNE neutrino oscillation results with increased data and new background studies*, *Phys. Rev. D* **103** (2021), no. 5 052002, [2006.16883].

[89] S. von Buddenbrock, N. Chakrabarty, A. S. Cornell, D. Kar, M. Kumar, T. Mandal, B. Mellado, B. Mukhopadhyaya, R. G. Reed, and X. Ruan, *Phenomenological signatures of additional scalar bosons at the LHC*, *Eur. Phys. J. C* **76** (2016), no. 10 580, [1606.01674].

[90] S. von Buddenbrock, A. S. Cornell, A. Fadol, M. Kumar, B. Mellado, and X. Ruan, *Multi-lepton signatures of additional scalar bosons beyond the Standard Model at the LHC*, *J. Phys. G* **45** (2018), no. 11 115003, [1711.07874].

[91] S. Buddenbrock, A. S. Cornell, Y. Fang, A. Fadol Mohammed, M. Kumar, B. Mellado, and K. G. Tomiwa, *The emergence of multi-lepton anomalies at the LHC and their compatibility with new physics at the EW scale*, *JHEP* **10** (2019) 157, [1901.05300].

[92] Y. Hernandez, M. Kumar, A. S. Cornell, S.-E. Dahbi, Y. Fang, B. Lieberman, B. Mellado, K. Monnakgotla, X. Ruan, and S. Xin, *The anomalous production of multi-lepton and its impact on the measurement of Wh production at the LHC*, *Eur. Phys. J. C* **81** (2021), no. 4 365, [1912.00699].

[93] S. von Buddenbrock, R. Ruiz, and B. Mellado, *Anatomy of inclusive $t\bar{t}W$ production at hadron colliders*, *Phys. Lett. B* **811** (2020) 135964, [2009.00032].

[94] S. Banik, G. Coloretti, A. Crivellin, and B. Mellado, *Uncovering new Higgses in the LHC analyses of differential $t\bar{t}$ cross sections*, *JHEP* **01** (2025) 155, [2308.07953].

[95] **ATLAS** Collaboration, M. Aaboud *et al.*, *Search for low-mass dijet resonances using trigger-level jets with the ATLAS detector in pp collisions at $\sqrt{s} = 13$ TeV*, *Phys. Rev. Lett.* **121** (2018), no. 8 081801, [1804.03496].

[96] **CMS** Collaboration, A. Tumasyan *et al.*, *Search for resonant and nonresonant production of pairs of dijet resonances in proton-proton collisions at $\sqrt{s} = 13$ TeV*, *JHEP* **07** (2023) 161, [2206.09997].

[97] A. Crivellin, C. A. Manzari, B. Mellado, and S.-E. Dahbi, *Consistency and interpretation of the LHC dijet excesses*, *Phys. Rev. D* **107** (2023), no. 5 054045, [2208.12254].

[98] **ATLAS** Collaboration, G. Aad *et al.*, *Pursuit of paired dijet resonances in the Run 2 dataset with ATLAS*, *Phys. Rev. D* **108** (2023), no. 11 112005, [2307.14944].

[99] **CMS** Collaboration, A. M. Sirunyan *et al.*, *Search for a standard model-like Higgs boson in the mass range between 70 and 110 GeV in the diphoton final state in proton-proton collisions at $\sqrt{s} = 8$ and 13 TeV*, *Phys. Lett. B* **793** (2019) 320–347, [1811.08459].

[100] **ATLAS** Collaboration, G. Aad *et al.*, *Search for diphoton resonances in the 66 to 110 GeV mass range using pp collisions at $\sqrt{s} = 13$ TeV with the ATLAS detector*, *JHEP* **01** (2025) 053, [2407.07546].

[101] **ATLAS** Collaboration, G. Aad *et al.*, *Search for dark matter in events with missing transverse momentum and a Higgs boson decaying into two photons in pp collisions at $\sqrt{s} = 13$ TeV with the ATLAS detector*, *JHEP* **10** (2021) 013, [2104.13240].

[102] M. D. Schwartz, *Quantum Field Theory and the Standard Model*. Cambridge University Press, 3, 2014.

[103] M. Kierkla, A. Karam, and B. Swiezewska, *Conformal model for gravitational waves and dark matter: a status update*, *JHEP* **03** (2023) 007, [2210.07075].

[104] M. Kierkla, B. Swiezewska, T. V. I. Tenkanen, and J. van de Vis, *Gravitational waves from supercooled phase transitions: dimensional transmutation meets dimensional reduction*, *JHEP* **02** (2024) 234, [2312.12413].

[105] J. Ellis, M. Lewicki, and V. Vaskonen, *Updated predictions for gravitational waves produced in a strongly supercooled phase transition*, *JCAP* **11** (2020) 020, [2007.15586].

[106] P. Athron, A. Fowlie, C.-T. Lu, L. Morris, L. Wu, Y. Wu, and Z. Xu, *Can Supercooled Phase Transitions Explain the Gravitational Wave Background Observed by Pulsar Timing Arrays?*, *Phys. Rev. Lett.* **132** (2024), no. 22 221001, [2306.17239].

[107] A. Belyaev, A. Deandrea, S. Moretti, L. Panizzi, D. A. Ross, and N. Thongyoi, *Fermionic portal to vector dark matter from a new gauge sector*, *Phys. Rev. D* **108** (2023), no. 9 095001, [2204.03510].

[108] A. Belyaev, A. Deandrea, S. Moretti, L. Panizzi, D. A. Ross, and N. Thongyoi, *A fermionic portal to a non-abelian dark sector*, *Front. in Phys.* **12** (2024) 1339886, [2203.04681].

[109] **ATLAS** Collaboration, G. Aad *et al.*, *Search for squarks and gluinos in final states with jets and missing transverse momentum using 139 fb^{-1} of $\sqrt{s}$ =13 TeV pp collision data with the ATLAS detector*, *JHEP* **02** (2021) 143, [2010.14293].

[110] **ATLAS** Collaboration, G. Aad *et al.*, *Search for bottom-squark pair production with the ATLAS detector in final states containing Higgs bosons, b-jets and missing transverse momentum*, *JHEP* **12** (2019) 060, [1908.03122].

[111] **ATLAS** Collaboration, M. Aaboud *et al.*, *Search for pair production of higgsinos in final states with at least three b-tagged jets in $\sqrt{s} = 13$ TeV pp collisions using the ATLAS detector*, *Phys. Rev. D* **98** (2018), no. 9 092002, [1806.04030].

[112] **CMS** Collaboration, A. M. Sirunyan *et al.*, *Search for natural and split supersymmetry in proton-proton collisions at $\sqrt{s} = 13$ TeV in final states with jets and missing transverse momentum*, *JHEP* **05** (2018) 025, [1802.02110].

[113] **CMS** Collaboration, A. M. Sirunyan *et al.*, *Search for new phenomena in final states with two opposite-charge, same-flavor leptons, jets, and missing transverse momentum in pp collisions at $\sqrt{s} = 13$ TeV*, *JHEP* **03** (2018) 076, [1709.08908].

[114] **CMS** Collaboration, A. Sirunyan *et al.*, *Search for electroweak production of charginos and neutralinos in multilepton final states in proton-proton collisions at $\sqrt{s} = 13$ TeV*, *JHEP* **03** (2018) 166, [1709.05406].

[115] J. E. Camargo-Molina, A. P. Morais, A. Ordell, R. Pasechnik, M. O. Sampaio, and J. Wessén, *Reviving trinification models through an E6 -extended supersymmetric GUT*, *Phys. Rev. D* **95** (2017), no. 7 075031, [1610.03642].

[116] J. E. Camargo-Molina, A. P. Morais, A. Ordell, R. Pasechnik, and J. Wessén, *Scale hierarchies, symmetry breaking and particle spectra in SU(3)-family extended SUSY trinification*, *Phys. Rev. D* **99** (2019), no. 3 035041, [1711.05199].

[117] A. P. Morais, R. Pasechnik, and W. Porod, *Grand Unified Origin of Gauge Interactions and Families Replication in the Standard Model*, *Universe* **7** (2021), no. 12 461, [2001.04804].

[118] A. P. Morais, R. Pasechnik, and W. Porod, *Prospects for new physics from gauge left-right-colour-family grand unification hypothesis*, *Eur. Phys. J. C* **80** (2020), no. 12 1162, [2001.06383].

[119] I. Dorsner, S. Fajfer, and I. Mustac, *Light vector-like fermions in a minimal SU(5) setup*, *Phys. Rev. D* **89** (2014), no. 11 115004, [1401.6870].

[120] S. Raby and A. Trautner, *Vectorlike chiral fourth family to explain muon anomalies*, *Phys. Rev. D* **97** (2018), no. 9 095006, [1712.09360].

[121] M. Crispim Romao, S. F. King, and G. K. Leontaris, *Non-universal Z' from fluxed GUTs*, *Phys. Lett. B* **782** (2018) 353–361, [1710.02349].

[122] A. Karozas, G. K. Leontaris, I. Tavellaris, and N. D. Vlachos, *On the LHC signatures of $SU(5) \times U(1)'$ F-theory motivated models*, *Eur. Phys. J. C* **81** (2021), no. 1 35, [2007.05936].

[123] Z. Poh and S. Raby, *Vectorlike leptons: Muon g-2 anomaly, lepton flavor violation, Higgs boson decays, and lepton nonuniversality*, *Phys. Rev. D* **96** (2017), no. 1 015032, [1705.07007].

[124] E. Megias, M. Quiros, and L. Salas, *$g_\mu \odot 2$ from Vector-Like Leptons in Warped Space*, *JHEP* **05** (2017) 016, [1701.05072].

[125] J. E. Camargo-Molina, A. P. Morais, R. Pasechnik, and J. Wessén, *On a radiative origin of the Standard Model from Trinification*, *JHEP* **09** (2016) 129, [1606.03492].

[126] A. Boyarsky, M. Drewes, T. Lasserre, S. Mertens, and O. Ruchayskiy, *Sterile neutrino Dark Matter*, *Prog. Part. Nucl. Phys.* **104** (2019) 1–45, [1807.07938].

[127] F. Staub, *SARAH 4 : A tool for (not only SUSY) model builders*, *Comput. Phys. Commun.* **185** (2014) 1773–1790, [1309.7223].

[128] C. Degrande, C. Duhr, B. Fuks, D. Grellscheid, O. Mattelaer, and T. Reiter, *UFO - The Universal FeynRules Output*, *Comput. Phys. Commun.* **183** (2012) 1201–1214, [1108.2040].

[129] J. Alwall, R. Frederix, S. Frixione, V. Hirschi, F. Maltoni, O. Mattelaer, H. S. Shao, T. Stelzer, P. Torrielli, and M. Zaro, *The automated computation of tree-level and next-to-leading order differential cross sections, and their matching to parton shower simulations*, *JHEP* **07** (2014) 079, [1405.0301].

[130] **DELPHES 3** Collaboration, J. de Favereau, C. Delaere, P. Demin, A. Giammanco, V. Lemaître, A. Mertens, and M. Selvaggi, *DELPHES 3, A modular framework for fast simulation of a generic collider experiment*, *JHEP* **02** (2014) 057, [1307.6346].

[131] R. Brun and F. Rademakers, *ROOT: An object oriented data analysis framework*, *Nucl. Instrum. Meth. A* **389** (1997) 81–86.

[132] **NNPDF** Collaboration, R. D. Ball, V. Bertone, S. Carrazza, L. Del Debbio, S. Forte, A. Guffanti, N. P. Hartland, and J. Rojo, *Parton distributions with QED corrections*, *Nucl. Phys.* **B877** (2013) 290–320, [1308.0598].

[133] N. F. Bell, M. J. Dolan, L. S. Friedrich, M. J. Ramsey-Musolf, and R. R. Volkas, *Electroweak Baryogenesis with Vector-like Leptons and Scalar Singlets*, *JHEP* **19** (2020) 012, [1903.11255].

[134] A. Falkowski, D. M. Straub, and A. Vicente, *Vector-like leptons: Higgs decays and collider phenomenology*, *JHEP* **05** (2014) 092, [1312.5329].

[135] I. Garcia Garcia, K. Howe, and J. March-Russell, *Natural Scherk-Schwarz Theories of the Weak Scale*, *JHEP* **12** (2015) 005, [1510.07045].

[136] N. Kumar and S. P. Martin, *Vectorlike Leptons at the Large Hadron Collider*, *Phys. Rev. D* **92** (2015), no. 11 115018, [1510.03456].

[137] R. Dermisek and A. Raval, *Explanation of the Muon g-2 Anomaly with Vectorlike Leptons and its Implications for Higgs Decays*, *Phys. Rev. D* **88** (2013) 013017, [1305.3522].

[138] R. Dermisek, J. P. Hall, E. Lunghi, and S. Shin, *Limits on Vectorlike Leptons from Searches for Anomalous Production of Multi-Lepton Events*, *JHEP* **12** (2014) 013, [1408.3123].

[139] B. Holdom and M. Ratzlaff, *Neglected heavy leptons at the LHC*, *Phys. Rev. D* **90** (2014), no. 1 013015, [1405.4573].

[140] S. A. Ellis, R. M. Godbole, S. Gopalakrishna, and J. D. Wells, *Survey of vector-like fermion extensions of the Standard Model and their phenomenological implications*, *JHEP* **09** (2014) 130, [1404.4398].

[141] B. Bhattacherjee, P. Byakti, A. Kushwaha, and S. K. Vempati, *Unification with Vector-like fermions and signals at LHC*, *JHEP* **05** (2018) 090, [1702.06417].

[142] J. Kawamura, S. Raby, and A. Trautner, *Complete vectorlike fourth family with U(1)' : A global analysis*, *Phys. Rev. D* **101** (2020), no. 3 035026, [1911.11075].

[143] P. N. Bhattiprolu and S. P. Martin, *Prospects for vectorlike leptons at future proton-proton colliders*, *Phys. Rev. D* **100** (2019), no. 1 015033, [1905.00498].

[144] K. Kowalska and D. Kumar, *Road map through the desert: unification with vector-like fermions*, *JHEP* **12** (2019) 094, [1910.00847].

[145] K. Fujikawa, *A Vector - like extension of the standard model*, *Prog. Theor. Phys.* **92** (1994) 1149–1160, [hep-ph/9411258].

[146] A. Crivellin, F. Kirk, C. A. Manzari, and M. Montull, *Global Electroweak Fit and Vector-Like Leptons in Light of the Cabibbo Angle Anomaly*, *JHEP* **12** (2020) 166, [2008.01113].

[147] **CMS** Collaboration, A. M. Sirunyan *et al.*, *Search for vector-like leptons in multilepton final states in proton-proton collisions at $\sqrt{s}$ = 13 TeV*, *Phys. Rev. D* **100** (2019), no. 5 052003, [1905.10853].

[148] **CMS** Collaboration, A. Tumasyan *et al.*, *Search for pair-produced vector-like leptons in final states with third-generation leptons and at least three b quark jets in proton-proton collisions at s=13TeV*, *Phys. Lett. B* **846** (2023) 137713, [2208.09700].

[149] **ATLAS** Collaboration, G. Aad *et al.*, *Search for third-generation vector-like leptons in pp collisions at $\sqrt{s} = 13$ TeV with the ATLAS detector*, *JHEP* **07** (2023) 118, [2303.05441].

[150] **ATLAS** Collaboration, G. Aad *et al.*, *Search for vector-like leptons coupling to first- and second-generation Standard Model leptons in pp collisions at $\sqrt{s} = 13$ TeV with the ATLAS detector*, 2411.07143.

[151] S. Bhattacharya, P. Ghosh, N. Sahoo, and N. Sahu, *Mini Review on Vector-Like Leptonic Dark Matter, Neutrino Mass, and Collider Signatures*, *Front. in Phys.* **7** (2019) 80, [1812.06505].

[152] D. Cogollo, F. F. Freitas, C. A. de S. Pires, Y. M. Oviedo-Torres, and P. Vasconcelos, *Deep learning analysis of the inverse seesaw in a 3-3-1 model at the LHC*, *Phys. Lett. B* **811** (2020) 135931, [2008.03409].

[153] F. F. Freitas, C. K. Khosa, and V. Sanz, *Exploring the standard model EFT in VH production with machine learning*, *Phys. Rev. D* **100** (2019), no. 3 035040, [1902.05803].

[154] A. Alves and F. F. Freitas, *Towards recognizing the light facet of the Higgs Boson*, *Mach. Learn. Sci. Tech.* **1** (2020), no. 4 045025, [1912.12532].

[155] **Particle Data Group** Collaboration, M. Tanabashi *et al.*, *Review of Particle Physics*, *Phys. Rev. D* **98** (2018), no. 3 030001.

[156] A. Collaboration, "ATLAS Heavy Particle Searches - 95% CL Upper Exclusion Limits." https://atlas.web.cern.ch/Atlas/GROUPS/PHYSICS/PUBNOTES/ATL-PHYS-PUB-2023-008/fig_01.png, 7, 2023.

[157] **ATLAS** Collaboration, M. Aaboud *et al.*, *Search for large missing transverse momentum in association with one top-quark in proton-proton collisions at $\sqrt{s}$ = 13 TeV with the ATLAS detector*, *JHEP* **05** (2019) 041, [1812.09743].

[158] **ATLAS** Collaboration, M. Aaboud *et al.*, *Search for new phenomena in events with same-charge leptons and b-jets in pp collisions at $\sqrt{s} = 13$ TeV with the ATLAS detector*, *JHEP* **12** (2018) 039, [1807.11883].

[159] **ATLAS** Collaboration, M. Aaboud *et al.*, *Search for pair production of heavy vector-like quarks decaying into hadronic final states in pp collisions at $\sqrt{s} = 13$ TeV with the ATLAS detector*, *Phys. Rev. D* **98** (2018), no. 9 092005, [1808.01771].

[160] **ATLAS** Collaboration, M. Aaboud *et al.*, *Search for pair production of heavy vector-like quarks decaying to high-p_T W bosons and b quarks in the lepton-plus-jets final state in pp collisions at $\sqrt{s} = 13$ TeV with the ATLAS detector*, *JHEP* **10** (2017) 141, [1707.03347].

[161] **ATLAS** Collaboration, G. Aad *et al.*, *Search for single production of vector-like quarks decaying into Wb in pp collisions at $\sqrt{s} = 8$ TeV with the ATLAS detector*, *Eur. Phys. J. C* **76** (2016), no. 8 442, [1602.05606].

[162] **ATLAS** Collaboration, G. Aad *et al.*, *Search for production of vector-like quark pairs and of four top quarks in the lepton-plus-jets final state in pp collisions at $\sqrt{s} = 8$ TeV with the ATLAS detector*, *JHEP* **08** (2015) 105, [1505.04306].

[163] **ATLAS** Collaboration, G. Aad *et al.*, *Search for pair production of a new heavy quark that decays into a W boson and a light quark in pp collisions at $\sqrt{s} = 8$ TeV with the ATLAS detector*, *Phys. Rev. D* **92** (2015), no. 11 112007, [1509.04261].

[164] **ATLAS** Collaboration, G. Aad *et al.*, *Search for heavy vector-like quarks coupling to light quarks in proton-proton collisions at $\sqrt{s} = 7$ TeV with the ATLAS detector*, *Phys. Lett. B* **712** (2012) 22–39, [1112.5755].

[165] **ATLAS** Collaboration, M. Aaboud *et al.*, *Combination of the searches for pair-produced vector-like partners of the third-generation quarks at $\sqrt{s} = 13$ TeV with the ATLAS detector*, *Phys. Rev. Lett.* **121** (2018), no. 21 211801, [1808.02343].

[166] M. L. Mangano, M. Moretti, F. Piccinini, and M. Treccani, *Matching matrix elements and shower evolution for top-quark production in hadronic collisions*, *JHEP* **01** (2007) 013, [hep-ph/0611129].

[167] C. Muselli, M. Bonvini, S. Forte, S. Marzani, and G. Ridolfi, *Top Quark Pair Production beyond NNLO*, *JHEP* **08** (2015) 076, [1505.02006].

[168] G. Balossini, G. Montagna, C. M. Carloni Calame, M. Moretti, O. Nicrosini, F. Piccinini, M. Treccani, and A. Vicini, *Combination of electroweak and QCD corrections to single W production at the Fermilab Tevatron and the CERN LHC*, *JHEP* **01** (2010) 013, [0907.0276].

[169] J. M. Campbell, R. K. Ellis, and C. Williams, *Vector boson pair production at the LHC*, *JHEP* **07** (2011) 018, [1105.0020].

[170] S. Catani, L. Cieri, G. Ferrera, D. de Florian, and M. Grazzini, *Vector boson production at hadron colliders: a fully exclusive QCD calculation at NNLO*, *Phys. Rev. Lett.* **103** (2009) 082001, [0903.2120].

[171] K. Hornik, *Approximation capabilities of multilayer feedforward networks*, *Neural Networks* **4** (1991), no. 2 251–257.

[172] F. Chollet, "Keras." https://github.com/fchollet/keras, 2015.

[173] M. Abadi *et al.*, *TensorFlow: Large-Scale Machine Learning on Heterogeneous Distributed Systems*, 1603.04467.

[174] G. Cowan, K. Cranmer, E. Gross, and O. Vitells, *Asymptotic formulae for likelihood-based tests of new physics*, *Eur. Phys. J. C* **71** (2011) 1554, [1007.1727]. [Erratum: Eur.Phys.J.C 73, 2501 (2013)].

[175] A. Elwood and D. Krücker, *Direct optimisation of the discovery significance when training neural networks to search for new physics in particle colliders*, 1806.00322.

[176] N. V. Chawla, K. W. Bowyer, L. O. Hall, and W. P. Kegelmeyer, *SMOTE: Synthetic Minority Over-sampling Technique*, *arXiv e-prints* (June, 2011) arXiv:1106.1813, [1106.1813].

[177] J. Cogan, M. Kagan, E. Strauss, and A. Schwartzman, *Jet-images: Computer vision inspired techniques for jet tagging*, *JHEP* **02** (2015) 118, [1407.5675].

[178] L. de Oliveira, M. Kagan, L. Mackey, B. Nachman, and A. Schwartzman, *Jet-images — deep learning edition*, *JHEP* **07** (2016) 069, [1511.05190].

[179] K. He, X. Zhang, S. Ren, and J. Sun, *Deep Residual Learning for Image Recognition*, 1512.03385.

[180] A. Paszke *et al.*, *PyTorch: An Imperative Style, High-Performance Deep Learning Library*, 1912.01703.

[181] J. Howard and S. Gugger, *fastai: A Layered API for Deep Learning*, 2002.04688.

[182] M. D'Onofrio, "Prospects for LHC run 3 and HL-LHC." https://indico.cern.ch/event/855882/contributions/3601848/attachments/1930307/3196895/Prospects_Run3_HLLHC_Fermilab.pdf, Oct., 2019.

[183] **Muon g-2** Collaboration, B. Abi *et al.*, *Measurement of the Positive Muon Anomalous Magnetic Moment to 0.46 ppm*, *Phys. Rev. Lett.* **126** (2021), no. 14 141801, [2104.03281].

[184] **Muon g-2** Collaboration, D. P. Aguillard *et al.*, *Measurement of the Positive Muon Anomalous Magnetic Moment to 0.20 ppm*, *Phys. Rev. Lett.* **131** (2023), no. 16 161802, [2308.06230].

[185] **BaBar** Collaboration, J. P. Lees *et al.*, *Measurement of an Excess of $\bar{B} \to D^{(*)}\tau^-\bar{\nu}_\tau$ Decays and Implications for Charged Higgs Bosons*, *Phys. Rev. D* **88** (2013), no. 7 072012, [1303.0571].

[186] **BaBar** Collaboration, J. P. Lees *et al.*, *Evidence for an excess of $\bar{B} \to D^{(*)}\tau^-\bar{\nu}_\tau$ decays*, *Phys. Rev. Lett.* **109** (2012) 101802, [1205.5442].

[187] **Belle** Collaboration, M. Huschle *et al.*, *Measurement of the branching ratio of $\bar{B} \to D^{(*)}\tau^-\bar{\nu}_\tau$ relative to $\bar{B} \to D^{(*)}\ell^-\bar{\nu}_\ell$ decays with hadronic tagging at Belle*, *Phys. Rev. D* **92** (2015), no. 7 072014, [1507.03233].

[188] **Belle** Collaboration, Y. Sato *et al.*, *Measurement of the branching ratio of $\bar{B}^0 \to D^{*+}\tau^-\bar{\nu}_\tau$ relative to $\bar{B}^0 \to D^{*+}\ell^-\bar{\nu}_\ell$ decays with a semileptonic tagging method*, *Phys. Rev. D* **94** (2016), no. 7 072007, [1607.07923].

[189] **Belle** Collaboration, S. Hirose *et al.*, *Measurement of the τ lepton polarization and $R(D^*)$ in the decay $\bar{B} \to D^*\tau^-\bar{\nu}_\tau$ with one-prong hadronic τ decays at Belle*, *Phys. Rev. D* **97** (2018), no. 1 012004, [1709.00129].

[190] **LHCb** Collaboration, R. Aaij *et al.*, *Measurement of the ratio of branching fractions $\mathcal{B}(\bar{B}^0 \to D^{*+}\tau^-\bar{\nu}_\tau)/\mathcal{B}(\bar{B}^0 \to D^{*+}\mu^-\bar{\nu}_\mu)$*, *Phys. Rev. Lett.* **115** (2015), no. 11 111803, [1506.08614]. [Erratum: Phys.Rev.Lett. 115, 159901 (2015)].

[191] W. Altmannshofer and P. Stangl, *New physics in rare B decays after Moriond 2021*, *Eur. Phys. J. C* **81** (2021), no. 10 952, [2103.13370].

[192] **CDF** Collaboration, T. Aaltonen *et al.*, *High-precision measurement of the W boson mass with the CDF II detector*, *Science* **376** (2022), no. 6589 170–176.

[193] A. Strumia, *Interpreting electroweak precision data including the W-mass CDF anomaly*, *JHEP* **08** (2022) 248, [2204.04191].

[194] M. Bauer and M. Neubert, *Minimal Leptoquark Explanation for the $R_{D^{(*)}}$, R_K , and $(g \odot 2)_\mu$ Anomalies*, *Phys. Rev. Lett.* **116** (2016), no. 14 141802, [1511.01900].

[195] W. Altmannshofer, P. S. Bhupal Dev, and A. Soni, *$R_{D^{(*)}}$ anomaly: A possible hint for natural supersymmetry with R-parity violation*, *Phys. Rev. D* **96** (2017), no. 9 095010, [1704.06659].

[196] D. Das, C. Hati, G. Kumar, and N. Mahajan, *Towards a unified explanation of $R_{D^{(*)}}$, R_K and $(g \odot 2)_\mu$ anomalies in a left-right model with leptoquarks*, *Phys. Rev. D* **94** (2016) 055034, [1605.06313].

[197] A. Angelescu, D. Bečirević, D. A. Faroughy, and O. Sumensari, *Closing the window on single leptoquark solutions to the B-physics anomalies*, *JHEP* **10** (2018) 183, [1808.08179].

[198] W. Altmannshofer, P. S. B. Dev, A. Soni, and Y. Sui, *Addressing $R_{D^{(*)}}$, $R_{K^{(*)}}$, muon $g \odot 2$ and ANITA anomalies in a minimal R-parity violating supersymmetric framework*, *Phys. Rev. D* **102** (2020), no. 1 015031, [2002.12910].

[199] G. Belanger *et al.*, *Leptoquark manoeuvres in the dark: a simultaneous solution of the dark matter problem and the $R_{D^{(*)}}$ anomalies*, *JHEP* **02** (2022) 042, [2111.08027].

[200] M. Becker, D. Döring, S. Karmakar, and H. Päs, *Fermionic singlet dark matter in one-loop solutions to the R_K anomaly: a systematic study*, *Eur. Phys. J. C* **81** (2021), no. 12 1053, [2103.12043].

[201] A. Crivellin, B. Fuks, and L. Schnell, *Explaining the hints for lepton flavour universality violation with three S_2 leptoquark generations*, *JHEP* **06** (2022) 169, [2203.10111].

[202] A. Crivellin, D. Mueller, and F. Saturnino, *Correlating $h\to\mu+\mu-$ to the Anomalous Magnetic Moment of the Muon via Leptoquarks*, *Phys. Rev. Lett.* **127** (2021), no. 2 021801, [2008.02643].

[203] A. Crivellin, C. Greub, D. Müller, and F. Saturnino, *Importance of Loop Effects in Explaining the Accumulated Evidence for New Physics in B Decays with a Vector Leptoquark*, *Phys. Rev. Lett.* **122** (2019), no. 1 011805, [1807.02068].

[204] M. Blanke and A. Crivellin, *B Meson Anomalies in a Pati-Salam Model within the Randall-Sundrum Background*, *Phys. Rev. Lett.* **121** (2018), no. 1 011801, [1801.07256].

[205] L. Calibbi, A. Crivellin, and T. Li, *Model of vector leptoquarks in view of the B-physics anomalies*, *Phys. Rev. D* **98** (2018), no. 11 115002, [1709.00692].

[206] A. Crivellin, D. Müller, and F. Saturnino, *Flavor Phenomenology of the Leptoquark Singlet-Triplet Model*, *JHEP* **06** (2020) 020, [1912.04224].

[207] A. Carvunis, A. Crivellin, D. Guadagnoli, and S. Gangal, *The Forward-Backward Asymmetry in $B \to D^*\ell\nu$: One more hint for Scalar Leptoquarks?*, *Phys. Rev. D* **105** (2022), no. 3 L031701, [2106.09610].

[208] R. Coy and M. Frigerio, *Effective comparison of neutrino-mass models*, *Phys. Rev. D* **105** (2022), no. 11 115041, [2110.09126].

[209] D. Marzocca and S. Trifinopoulos, *Minimal Explanation of Flavor Anomalies: B-Meson Decays, Muon Magnetic Moment, and the Cabibbo Angle*, *Phys. Rev. Lett.* **127** (2021), no. 6 061803, [2104.05730].

[210] I. Doršner, S. Fajfer, and N. Košnik, *Leptoquark mechanism of neutrino masses within the grand unification framework*, *Eur. Phys. J. C* **77** (2017), no. 6 417, [1701.08322].

[211] D. Aristizabal Sierra, M. Hirsch, and S. G. Kovalenko, *Leptoquarks: Neutrino masses and accelerator phenomenology*, *Phys. Rev. D* **77** (2008) 055011, [0710.5699].

[212] D. Zhang, *Radiative neutrino masses, lepton flavor mixing and muon $g \odot 2$ in a leptoquark model*, *JHEP* **07** (2021) 069, [2105.08670].

[213] H. Päs and E. Schumacher, *Common origin of R_K and neutrino masses*, *Phys. Rev. D* **92** (2015), no. 11 114025, [1510.08757].

[214] Y. Cai, J. Herrero-García, M. A. Schmidt, A. Vicente, and R. R. Volkas, *From the trees to the forest: a review of radiative neutrino mass models*, *Front. in Phys.* **5** (2017) 63, [1706.08524].

[215] K. S. Babu and J. Julio, *Two-Loop Neutrino Mass Generation through Leptoquarks*, *Nucl. Phys. B* **841** (2010) 130–156, [1006.1092].

[216] O. Catà and T. Mannel, *Linking lepton number violation with B anomalies*, 1903.01799.

[217] A. Crivellin and L. Schnell, *Complete Lagrangian and set of Feynman rules for scalar leptoquarks*, *Comput. Phys. Commun.* **271** (2022) 108188, [2105.04844].

[218] C. Murgui and M. B. Wise, *Scalar leptoquarks, baryon number violation, and Pati-Salam symmetry*, *Phys. Rev. D* **104** (2021), no. 3 035017, [2105.14029].

[219] I. Doršner, S. Fajfer, and O. Sumensari, *Triple-leptoquark interactions for tree- and loop-level proton decays*, *JHEP* **05** (2022) 183, [2202.08287].

[220] H. H. Patel, *Package-X: A Mathematica package for the analytic calculation of one-loop integrals*, *Comput. Phys. Commun.* **197** (2015) 276–290, [1503.01469].

[221] S. Borsanyi *et al.*, *Leading hadronic contribution to the muon magnetic moment from lattice QCD*, *Nature* **593** (2021), no. 7857 51–55, [2002.12347].

[222] **Extended Twisted Mass** Collaboration, C. Alexandrou *et al.*, *Lattice calculation of the short and intermediate time-distance hadronic vacuum polarization contributions to the muon magnetic moment using twisted-mass fermions*, *Phys. Rev. D* **107** (2023), no. 7 074506, [2206.15084].

[223] M. Cè *et al.*, *Window observable for the hadronic vacuum polarization contribution to the muon g-2 from lattice QCD*, *Phys. Rev. D* **106** (2022), no. 11 114502, [2206.06582].

[224] T. Aoyama, M. Hayakawa, T. Kinoshita, and M. Nio, *Complete Tenth-Order QED Contribution to the Muon $g \odot 2$*, *Phys. Rev. Lett.* **109** (2012) 111808, [1205.5370].

[225] T. Aoyama, T. Kinoshita, and M. Nio, *Theory of the Anomalous Magnetic Moment of the Electron*, *Atoms* **7** (2019), no. 1 28.

[226] A. Czarnecki, W. J. Marciano, and A. Vainshtein, *Refinements in electroweak contributions to the muon anomalous magnetic moment*, *Phys. Rev.* **D67** (2003) 073006, [hep-ph/0212229]. [Erratum: Phys. Rev. **D73**, 119901 (2006)].

[227] C. Gnendiger, D. Stöckinger, and H. Stöckinger-Kim, *The electroweak contributions to $(g \odot 2)_\mu$ after the Higgs boson mass measurement*, *Phys. Rev.* **D88** (2013) 053005, [1306.5546].

[228] P. Masjuan and P. Sánchez-Puertas, *Pseudoscalar-pole contribution to the $(g_\mu \odot 2)$: a rational approach*, *Phys. Rev.* **D95** (2017), no. 5 054026, [1701.05829].

[229] T. Aoyama *et al.*, *The anomalous magnetic moment of the muon in the Standard Model*, *Phys. Rept.* **887** (2020) 1–166, [2006.04822].

[230] **Muon g-2** Collaboration, G. W. Bennett *et al.*, *Final Report of the Muon E821 Anomalous Magnetic Moment Measurement at BNL*, *Phys. Rev. D* **73** (2006) 072003, [hep-ex/0602035].

[231] I. Doršner, S. Fajfer, and O. Sumensari, *Muon $g \odot 2$ and scalar leptoquark mixing*, *JHEP* **06** (2020) 089, [1910.03877].

[232] G. Arcadi, L. Calibbi, M. Fedele, and F. Mescia, *Muon $g \odot 2$ and B-anomalies from Dark Matter*, *Phys. Rev. Lett.* **127** (2021), no. 6 061802, [2104.03228].

[233] P. F. Perez, C. Murgui, and A. D. Plascencia, *Leptoquarks and matter unification: Flavor anomalies and the muon g-2*, *Phys. Rev. D* **104** (2021), no. 3 035041, [2104.11229].

[234] T. Nomura and H. Okada, *Explanations for anomalies of muon anomalous magnetic dipole moment, $b \to s\mu\mu^-$, and radiative neutrino masses in a leptoquark model*, *Phys. Rev. D* **104** (2021), no. 3 035042, [2104.03248].

[235] **HFLAV** Collaboration, Y. S. Amhis *et al.*, *Averages of b-hadron, c-hadron, and τ-lepton properties as of 2018*, *Eur. Phys. J.* **C81** (2021) 226, [1909.12524]. updated results and plots available at https://hflav.web.cern.ch/.

[236] D. M. Straub, *flavio: a Python package for flavour and precision phenomenology in the Standard Model and beyond*, 1810.08132.

[237] **MILC** Collaboration, J. A. Bailey *et al.*, *$B \to D\ell\nu$ form factors at nonzero recoil and $-V_{cb}-$ from 2+1-flavor lattice QCD*, *Phys. Rev. D* **92** (2015), no. 3 034506, [1503.07237].

[238] D. Bigi and P. Gambino, *Revisiting $B \to D\ell\nu$*, *Phys. Rev. D* **94** (2016), no. 9 094008, [1606.08030].

[239] D. Bardhan, P. Byakti, and D. Ghosh, *A closer look at the R_D and R_{D^*} anomalies*, *JHEP* **01** (2017) 125, [1610.03038].

[240] E. Ganiev, "On radiative and electroweak penguin decays." https://indico.desy.de/event/34916/contributions/146877/attachments/84380/111798/EWP@Belle2_EPS.pdf, 8, 2023.

[241] **CMS** Collaboration, V. Chekhovsky *et al.*, *High-precision measurement of the W boson mass with the CMS experiment at the LHC*, 2412.13872.

[242] **ATLAS** Collaboration, M. Aaboud *et al.*, *Measurement of the W-boson mass in pp collisions at $\sqrt{s} = 7$ TeV with the ATLAS detector*, *Eur. Phys. J. C* **78** (2018), no. 2 110, [1701.07240]. [Erratum: Eur.Phys.J.C 78, 898 (2018)].

[243] **LHCb** Collaboration, R. Aaij *et al.*, *Measurement of the W boson mass*, *JHEP* **01** (2022) 036, [2109.01113].

[244] J. de Blas, M. Pierini, L. Reina, and L. Silvestrini, *Impact of the Recent Measurements of the Top-Quark and W-Boson Masses on Electroweak Precision Fits*, *Phys. Rev. Lett.* **129** (2022), no. 27 271801, [2204.04204].

[245] A. Crivellin, D. Müller, and F. Saturnino, *Leptoquarks in oblique corrections and Higgs signal strength: status and prospects*, *JHEP* **11** (2020) 094, [2006.10758].

[246] **ALEPH, DELPHI, L3, OPAL, SLD, LEP Electroweak Working Group, SLD Electroweak Group, SLD Heavy Flavour Group** Collaboration, S. Schael *et al.*, *Precision electroweak measurements on the Z resonance*, *Phys. Rept.* **427** (2006) 257–454, [hep-ex/0509008].

[247] P. Arnan, D. Becirevic, F. Mescia, and O. Sumensari, *Probing low energy scalar leptoquarks by the leptonic W and Z couplings*, *JHEP* **02** (2019) 109, [1901.06315].

[248] C. Bobeth and A. J. Buras, *Leptoquarks meet ε'/ε and rare Kaon processes*, *JHEP* **02** (2018) 101, [1712.01295].

[249] F. F. Freitas, J. Gonçalves, A. P. Morais, R. Pasechnik, and W. Porod, *Interplay between flavor anomalies and neutrino properties*, *Phys. Rev. D* **108** (2023), no. 11 115002, [2206.01674].

[250] I. Doršner, S. Fajfer, A. Greljo, J. F. Kamenik, and N. Košnik, *Physics of leptoquarks in precision experiments and at particle colliders*, *Phys. Rept.* **641** (2016) 1–68, [1603.04993].

[251] A. Crivellin, D. Müller, and L. Schnell, *Combined constraints on first generation leptoquarks*, *Phys. Rev. D* **103** (2021), no. 11 115023, [2104.06417].

[252] **ATLAS** Collaboration, G. Aad *et al.*, *Search for new phenomena in pp collisions in final states with tau leptons, b-jets, and missing transverse momentum with the ATLAS detector*, *Phys. Rev. D* **104** (2021), no. 11 112005, [2108.07665].

[253] **ATLAS** Collaboration, G. Aad *et al.*, *Search for pair production of third-generation scalar leptoquarks decaying into a top quark and a τ-lepton in pp collisions at $\sqrt{s} = 13$ TeV with the ATLAS detector*, *JHEP* **06** (2021) 179, [2101.11582].

[254] **CMS** Collaboration, A. M. Sirunyan *et al.*, *Search for heavy neutrinos and third-generation leptoquarks in hadronic states of two τ leptons and two jets in proton-proton collisions at $\sqrt{s} = 13$ TeV*, *JHEP* **03** (2019) 170, [1811.00806].

[255] **CMS** Collaboration, A. M. Sirunyan *et al.*, *Search for leptoquarks coupled to third-generation quarks in proton-proton collisions at $\sqrt{s} = 13$ TeV*, *Phys. Rev. Lett.* **121** (2018), no. 24 241802, [1809.05558].

[256] **Particle Data Group** Collaboration, R. L. Workman *et al.*, *Review of Particle Physics*, *PTEP* **2022** (2022) 083C01.

[257] W. Porod and F. Staub, *SPheno 3.1: Extensions including flavour, CP-phases and models beyond the MSSM*, *Comput. Phys. Commun.* **183** (2012) 2458–2469, [1104.1573].

[258] J. Aebischer, J. Kumar, and D. M. Straub, *Wilson: a Python package for the running and matching of Wilson coefficients above and below the electroweak scale*, *Eur. Phys. J. C* **78** (2018), no. 12 1026, [1804.05033].

[259] Wes McKinney, *Data Structures for Statistical Computing in Python*, in *Proceedings of the 9th Python in Science Conference* (Stéfan van der Walt and Jarrod Millman, eds.), pp. 56 – 61, 2010.

[260] G. D'Amico, M. Nardecchia, P. Panci, F. Sannino, A. Strumia, R. Torre, and A. Urbano, *Flavour anomalies after the R_{K^*} measurement*, *JHEP* **09** (2017) 010, [1704.05438].

[261] **LHCb** Collaboration, R. Aaij *et al.*, *Measurement of lepton universality parameters in $B^+ \to K^+\ell^+\ell^-$ and $B^0 \to K^{*0}\ell^+\ell^-$ decays*, *Phys. Rev. D* **108** (2023), no. 3 032002, [2212.09153].

[262] **HFLAV** Collaboration, Y. S. Amhis *et al.*, *Averages of b-hadron, c-hadron, and τ-lepton properties as of 2018*, *Eur. Phys. J. C* **81** (2021), no. 3 226, [1909.12524].

[263] **Belle** Collaboration, K. Inami *et al.*, *Search for the electric dipole moment of the tau lepton*, *Phys. Lett. B* **551** (2003) 16–26, [hep-ex/0210066].

[264] **Belle** Collaboration, J. Grygier *et al.*, *Search for $\boldsymbol{B \to h\nu\bar{\nu}}$ decays with semileptonic tagging at Belle*, *Phys. Rev. D* **96** (2017), no. 9 091101, [1702.03224]. [Addendum: Phys.Rev.D 97, 099902 (2018)].

[265] S. Saad and A. Thapa, *Common origin of neutrino masses and $R_{D^{(*)}}$, $R_{K^{(*)}}$ anomalies*, *Phys. Rev. D* **102** (2020), no. 1 015014, [2004.07880].

[266] **LHCb** Collaboration, R. Aaij *et al.*, *Angular Analysis of the $B^+ \to K^{*+}\mu^+\mu^-$ Decay*, *Phys. Rev. Lett.* **126** (2021), no. 16 161802, [2012.13241].

[267] **LHCb** Collaboration, R. Aaij *et al.*, *Measurement of CP-Averaged Observables in the $B^0 \to K^{*0}\mu^+\mu^-$ Decay*, *Phys. Rev. Lett.* **125** (2020), no. 1 011802, [2003.04831].

[268] M. Schmaltz and Y.-M. Zhong, *The leptoquark Hunter's guide: large coupling*, *JHEP* **01** (2019) 132, [1810.10017].

[269] **ATLAS** Collaboration, G. Aad *et al.*, *Search for pair-produced scalar and vector leptoquarks decaying into third-generation quarks and first- or second-generation leptons in pp collisions with the ATLAS detector*, *JHEP* **2306** (2023) 188, [2210.04517].

[270] **ATLAS** Collaboration, M. Aaboud *et al.*, *Searches for third-generation scalar leptoquarks in $\sqrt{s}$ = 13 TeV pp collisions with the ATLAS detector*, *JHEP* **06** (2019) 144, [1902.08103].

[271] **ATLAS** Collaboration, G. Aad *et al.*, *Search for pair production of scalar leptoquarks decaying into first- or second-generation leptons and top quarks in proton–proton collisions at $\sqrt{s}$ = 13 TeV with the ATLAS detector*, *Eur. Phys. J. C* **81** (2021), no. 4 313, [2010.02098].

[272] **CMS** Collaboration, A. M. Sirunyan *et al.*, *Search for pair production of first-generation scalar leptoquarks at $\sqrt{s}$ = 13 TeV*, *Phys. Rev. D* **99** (2019), no. 5 052002, [1811.01197].

[273] **CMS** Collaboration, A. Tumasyan *et al.*, *Search for new particles in events with energetic jets and large missing transverse momentum in proton-proton collisions at $\sqrt{s}$ = 13 TeV*, *JHEP* **11** (2021) 153, [2107.13021].

[274] **CMS** Collaboration, A. M. Sirunyan *et al.*, *Search for dark matter in events with a leptoquark and missing transverse momentum in proton-proton collisions at 13 TeV*, *Phys. Lett. B* **795** (2019) 76–99, [1811.10151].

[275] **CMS** Collaboration, A. M. Sirunyan *et al.*, *Search for a singly produced third-generation scalar leptoquark decaying to a τ lepton and a bottom quark in proton-proton collisions at $\sqrt{s}$ = 13 TeV*, *JHEP* **07** (2018) 115, [1806.03472].

[276] **CMS** Collaboration, A. M. Sirunyan *et al.*, *Search for singly and pair-produced leptoquarks coupling to third-generation fermions in proton-proton collisions at s=13 TeV*, *Phys. Lett. B* **819** (2021) 136446, [2012.04178].

[277] **ATLAS** Collaboration, G. Aad *et al.*, *Search for new phenomena in final states with b-jets and missing transverse momentum in $\sqrt{s} = 13$ TeV pp collisions with the ATLAS detector*, *JHEP* **05** (2021) 093, [2101.12527].

[278] **LHCb** Collaboration, R. Aaij *et al.*, *Angular analysis of the rare decay $B_s^0 \to \phi\mu^+\mu^-$*, *JHEP* **11** (2021) 043, [2107.13428].

[279] N. Raj, *Anticipating nonresonant new physics in dilepton angular spectra at the LHC*, *Phys. Rev. D* **95** (2017), no. 1 015011, [1610.03795].

[280] S. Bansal, R. M. Capdevilla, A. Delgado, C. Kolda, A. Martin, and N. Raj, *Hunting leptoquarks in monolepton searches*, *Phys. Rev. D* **98** (2018), no. 1 015037, [1806.02370].

[281] N. Desai and A. Sengupta, *Status of leptoquark models after LHC Run-2 and discovery prospects at future colliders*, 2301.01754.

[282] **ATLAS** Collaboration, G. Aad *et al.*, *Search for a scalar partner of the top quark in the all-hadronic $t\bar{t}$ plus missing transverse momentum final state at $\sqrt{s} = 13$ TeV with the ATLAS detector*, *Eur. Phys. J. C* **80** (2020), no. 8 737, [2004.14060].

[283] **ATLAS** Collaboration, G. Aad *et al.*, *Search for pairs of scalar leptoquarks decaying into quarks and electrons or muons in $\sqrt{s} = 13$ TeV pp collisions with the ATLAS detector*, *JHEP* **10** (2020) 112, [2006.05872].

[284] **ATLAS** Collaboration, G. Aad *et al.*, *Search for New Phenomena in Final States with Two Leptons and One or No b-Tagged Jets at $\sqrt{s} = 13$ TeV Using the ATLAS Detector*, *Phys. Rev. Lett.* **127** (2021), no. 14 141801, [2105.13847].

[285] **CMS** Collaboration, A. Tumasyan *et al.*, *Search for new physics in the τ lepton plus missing transverse momentum final state in proton-proton collisions at $\sqrt{s} = 13$ TeV*, *JHEP* **09** (2023) 051, [2212.12604].

[286] **CMS** Collaboration, A. M. Sirunyan *et al.*, *Search for pair production of second-generation leptoquarks at $\sqrt{s} = 13$ TeV*, *Phys. Rev. D* **99** (2019), no. 3 032014, [1808.05082].

[287] G. Balossini, G. Montagna, C. M. Carloni Calame, M. Moretti, O. Nicrosini, F. Piccinini, M. Treccani, and A. Vicini, *Combination of electroweak and QCD corrections to single W production at the Fermilab Tevatron and the CERN LHC*, *JHEP* **01** (2010) 013, [0907.0276].

[288] U. Haisch, L. Schnell, and S. Schulte, *On Drell-Yan production of scalar leptoquarks coupling to heavy-quark flavours*, *JHEP* **11** (2022) 106, [2207.00356].

[289] D. Azevedo, R. Capucha, A. Onofre, and R. Santos, *CP-violation, asymmetries and interferences in $t\bar{t}\phi$*, *JHEP* **09** (2022) 246, [2208.04271].

[290] A. Bhaskar, A. A. Madathil, T. Mandal, and S. Mitra, *Combined explanation of W-mass, muon g-2, RK(*) and RD(*) anomalies in a singlet-triplet scalar leptoquark model*, *Phys. Rev. D* **106** (2022), no. 11 115009, [2204.09031].

[291] A. Bhaskar, D. Das, T. Mandal, S. Mitra, and C. Neeraj, *Precise limits on the charge-2/3 U1 vector leptoquark*, *Phys. Rev. D* **104** (2021), no. 3 035016, [2101.12069].

[292] U. Aydemir, T. Mandal, and S. Mitra, *Addressing the $\mathbf{R}_{D^{(*)}}$ anomalies with an $\mathbf{S}_1$ leptoquark from $\mathbf{SO(10)}$ grand unification*, *Phys. Rev. D* **101** (2020), no. 1 015011, [1902.08108].

[293] T. Mandal, S. Mitra, and S. Raz, *$R_{D^{(*)}}$ motivated $\mathcal{S}_1$ leptoquark scenarios: Impact of interference on the exclusion limits from LHC data*, *Phys. Rev. D* **99** (2019), no. 5 055028, [1811.03561].

[294] A. Ferroglia, M. C. N. Fiolhais, E. Gouveia, and A. Onofre, *Role of the $t\bar{t}h$ rest frame in direct top-quark Yukawa coupling measurements*, *Phys. Rev. D* **100** (2019), no. 7 075034, [1909.00490].

[295] "Perspectives on the determination of systematic uncertainties at hl-lhc." https://cds.cern.ch/record/2642427/files/ATL-PHYS-SLIDE-2018-893.pdf, 6, 2018.

[296] **ATLAS** Collaboration, G. Aad *et al.*, *Luminosity determination in pp collisions at* $\sqrt{s} = 13$ *TeV using the ATLAS detector at the LHC*, *Eur. Phys. J. C* **83** (2023), no. 10 982, [2212.09379].

[297] **NANOGrav** Collaboration, G. Agazie *et al.*, *The NANOGrav 15 yr Data Set: Evidence for a Gravitational-wave Background*, *Astrophys. J. Lett.* **951** (2023), no. 1 L8, [2306.16213].

[298] D. J. Reardon *et al.*, *Search for an Isotropic Gravitational-wave Background with the Parkes Pulsar Timing Array*, *Astrophys. J. Lett.* **951** (2023), no. 1 L6, [2306.16215].

[299] **EPTA, InPTA:** Collaboration, J. Antoniadis *et al.*, *The second data release from the European Pulsar Timing Array - III. Search for gravitational wave signals*, *Astron. Astrophys.* **678** (2023) A50, [2306.16214].

[300] H. Xu *et al.*, *Searching for the Nano-Hertz Stochastic Gravitational Wave Background with the Chinese Pulsar Timing Array Data Release I*, *Res. Astron. Astrophys.* **23** (2023), no. 7 075024, [2306.16216].

[301] M. Shaposhnikov and A. Tokareva, *Exact quantum conformal symmetry, its spontaneous breakdown, and gravitational Weyl anomaly*, *Phys. Rev. D* **107** (2023), no. 6 065015, [2212.09770].

[302] P. P. Srivastava, *Conformal symmetry in lagrangian field theory*, *Nucl. Phys. B* **64** (1973) 499–510.

[303] S. R. Coleman and E. J. Weinberg, *Radiative Corrections as the Origin of Spontaneous Symmetry Breaking*, *Phys. Rev. D* **7** (1973) 1888–1910.

[304] E. Gildener and S. Weinberg, *Symmetry Breaking and Scalar Bosons*, *Phys. Rev. D* **13** (1976) 3333.

[305] A. Ahriche, S. Kanemura, and M. Tanaka, *Gravitational waves from phase transitions in scale invariant models*, *JHEP* **01** (2024) 201, [2308.12676].

[306] J. Jaeckel, V. V. Khoze, and M. Spannowsky, *Hearing the signal of dark sectors with gravitational wave detectors*, *Phys. Rev. D* **94** (2016), no. 10 103519, [1602.03901].

[307] C. Marzo, L. Marzola, and V. Vaskonen, *Phase transition and vacuum stability in the classically conformal B–L model*, *Eur. Phys. J. C* **79** (2019), no. 7 601, [1811.11169].

[308] J. Ellis, M. Lewicki, J. M. No, and V. Vaskonen, *Gravitational wave energy budget in strongly supercooled phase transitions*, *JCAP* **06** (2019) 024, [1903.09642].

[309] R. Jinno, T. Konstandin, H. Rubira, and I. Stomberg, *Higgsless simulations of cosmological phase transitions and gravitational waves*, *JCAP* **02** (2023) 011, [2209.04369].

[310] T. Hambye, A. Strumia, and D. Teresi, *Super-cool Dark Matter*, *JHEP* **08** (2018) 188, [1805.01473].

[311] I. Baldes and C. Garcia-Cely, *Strong gravitational radiation from a simple dark matter model*, *JHEP* **05** (2019) 190, [1809.01198].

[312] D. Marfatia and P.-Y. Tseng, *Gravitational wave signals of dark matter freeze-out*, *JHEP* **02** (2021) 022, [2006.07313].

[313] T. Vachaspati, *Magnetic fields from cosmological phase transitions*, *Phys. Lett. B* **265** (1991) 258–261.

[314] J. Ellis, M. Fairbairn, M. Lewicki, V. Vaskonen, and A. Wickens, *Intergalactic Magnetic Fields from First-Order Phase Transitions*, *JCAP* **09** (2019) 019, [1907.04315].

[315] G. Sigl, A. V. Olinto, and K. Jedamzik, *Primordial magnetic fields from cosmological first order phase transitions*, *Phys. Rev. D* **55** (1997) 4582–4590, [astro-ph/9610201].

[316] A. G. Tevzadze, L. Kisslinger, A. Brandenburg, and T. Kahniashvili, *Magnetic Fields from QCD Phase Transitions*, *Astrophys. J.* **759** (2012) 54, [1207.0751].

[317] T. Vachaspati, *Estimate of the primordial magnetic field helicity*, *Phys. Rev. Lett.* **87** (2001) 251302, [astro-ph/0101261].

[318] C. J. Copi, F. Ferrer, T. Vachaspati, and A. Achucarro, *Helical Magnetic Fields from Sphaleron Decay and Baryogenesis*, *Phys. Rev. Lett.* **101** (2008) 171302, [0801.3653].

[319] Y.-Z. Chu, J. B. Dent, and T. Vachaspati, *Magnetic Helicity in Sphaleron Debris*, *Phys. Rev. D* **83** (2011) 123530, [1105.3744].

[320] E. Witten, *Cosmic Separation of Phases*, *Phys. Rev. D* **30** (1984) 272–285.

[321] C. J. Hogan, *Gravitational radiation from cosmological phase transitions*, *Mon. Not. Roy. Astron. Soc.* **218** (1986) 629–636.

[322] M. Kamionkowski, A. Kosowsky, and M. S. Turner, *Gravitational radiation from first order phase transitions*, *Phys. Rev. D* **49** (1994) 2837–2851, [astro-ph/9310044].

[323] A. Brandenburg, K. Enqvist, and P. Olesen, *Large scale magnetic fields from hydromagnetic turbulence in the very early universe*, *Phys. Rev. D* **54** (1996) 1291–1300, [astro-ph/9602031].

[324] M. Christensson, M. Hindmarsh, and A. Brandenburg, *Inverse cascade in decaying 3-D magnetohydrodynamic turbulence*, *Phys. Rev. E* **64** (2001) 056405, [astro-ph/0011321].

[325] T. Kahniashvili, A. Brandenburg, A. G. Tevzadze, and B. Ratra, *Numerical simulations of the decay of primordial magnetic turbulence*, *Phys. Rev. D* **81** (2010) 123002, [1004.3084].

[326] A. Brandenburg, T. Kahniashvili, S. Mandal, A. Roper Pol, A. G. Tevzadze, and T. Vachaspati, *Evolution of hydromagnetic turbulence from the electroweak phase transition*, *Phys. Rev. D* **96** (2017), no. 12 123528, [1711.03804].

[327] **Fermi-LAT** Collaboration, M. Ackermann *et al.*, *The Search for Spatial Extension in High-latitude Sources Detected by the Fermi Large Area Telescope*, *Astrophys. J. Suppl.* **237** (2018), no. 2 32, [1804.08035].

[328] **MAGIC** Collaboration, V. A. Acciari *et al.*, *A lower bound on intergalactic magnetic fields from time variability of 1ES 0229+200 from MAGIC and Fermi/LAT observations*, *Astron. Astrophys.* **670** (2023) A145, [2210.03321].

[329] **H.E.S.S., Fermi-LAT** Collaboration, F. Aharonian *et al.*, *Constraints on the Intergalactic Magnetic Field Using Fermi-LAT and H.E.S.S. Blazar Observations*, *Astrophys. J. Lett.* **950** (2023), no. 2 L16, [2306.05132].

[330] A. Neronov and I. Vovk, *Evidence for strong extragalactic magnetic fields from Fermi observations of TeV blazars*, *Science* **328** (2010) 73–75, [1006.3504].

[331] L. Biermann and A. Schlüter, *Cosmic radiation and cosmic magnetic fields. ii. origin of cosmic magnetic fields*, *Phys. Rev.* **82** (Jun, 1951) 863–868.

[332] R. Alves Batista and A. Saveliev, *The Gamma-ray Window to Intergalactic Magnetism*, *Universe* **7** (2021), no. 7 223, [2105.12020].

[333] A. D. Linde, *Decay of the False Vacuum at Finite Temperature*, *Nucl. Phys. B* **216** (1983) 421. [Erratum: Nucl.Phys.B 223, 544 (1983)].

[334] S. R. Coleman, *The Fate of the False Vacuum. 1. Semiclassical Theory*, *Phys. Rev. D* **15** (1977) 2929–2936. [Erratum: Phys.Rev.D 16, 1248 (1977)].

[335] P. Athron, C. Balázs, A. Fowlie, L. Morris, and L. Wu, *Cosmological phase transitions: From perturbative particle physics to gravitational waves*, *Prog. Part. Nucl. Phys.* **135** (2024) 104094, [2305.02357].

[336] A. Ekstedt, O. Gould, and J. Hirvonen, *BubbleDet: a Python package to compute functional determinants for bubble nucleation*, *JHEP* **12** (2023) 056, [2308.15652].

[337] C. L. Wainwright, *CosmoTransitions: Computing Cosmological Phase Transition Temperatures and Bubble Profiles with Multiple Fields*, *Comput. Phys. Commun.* **183** (2012) 2006–2013, [1109.4189].

[338] L. Husdal, *On Effective Degrees of Freedom in the Early Universe*, *Galaxies* **4** (2016), no. 4 78, [1609.04979].

[339] S. J. Huber and T. Konstandin, *Production of gravitational waves in the nMSSM*, *JCAP* **05** (2008) 017, [0709.2091].

[340] J. M. N. Redondo, *Aspects of Phenomenology and Cosmology in Hidden Sector Extensions of the Standard Model*. PhD thesis, Universidad Autónoma de Madrid, 2009.

[341] P. Athron, C. Balázs, and L. Morris, *Supercool subtleties of cosmological phase transitions*, *JCAP* **03** (2023) 006, [2212.07559].

[342] J. Ellis, M. Lewicki, and J. M. No, *On the Maximal Strength of a First-Order Electroweak Phase Transition and its Gravitational Wave Signal*, *JCAP* **04** (2019) 003, [1809.08242].

[343] C. Caprini *et al.*, *Detecting gravitational waves from cosmological phase transitions with LISA: an update*, *JCAP* **03** (2020) 024, [1910.13125].

[344] M. S. Turner, E. J. Weinberg, and L. M. Widrow, *Bubble nucleation in first order inflation and other cosmological phase transitions*, *Phys. Rev. D* **46** (1992) 2384–2403.

[345] K. Enqvist, J. Ignatius, K. Kajantie, and K. Rummukainen, *Nucleation and bubble growth in a first order cosmological electroweak phase transition*, *Phys. Rev. D* **45** (1992) 3415–3428.

[346] O. Gould and T. V. I. Tenkanen, *On the perturbative expansion at high temperature and implications for cosmological phase transitions*, *JHEP* **06** (2021) 069, [2104.04399].

[347] D. Croon, O. Gould, P. Schicho, T. V. I. Tenkanen, and G. White, *Theoretical uncertainties for cosmological first-order phase transitions*, *JHEP* **04** (2021) 055, [2009.10080].

[348] P. Athron, C. Balazs, A. Fowlie, L. Morris, G. White, and Y. Zhang, *How arbitrary are perturbative calculations of the electroweak phase transition?*, *JHEP* **01** (2023) 050, [2208.01319].

[349] S. P. Martin, *Two Loop Effective Potential for a General Renormalizable Theory and Softly Broken Supersymmetry*, *Phys. Rev. D* **65** (2002) 116003, [hep-ph/0111209].

[350] D. G. C. McKeon, *Renormalization Scheme Dependence with Renormalization Group Summation*, *Phys. Rev. D* **92** (2015), no. 4 045031, [1503.03823].

[351] W.-Y. Ai, B. Laurent, and J. van de Vis, *Model-independent bubble wall velocities in local thermal equilibrium*, *JCAP* **07** (2023) 002, [2303.10171].

[352] T. Krajewski, M. Lewicki, and M. Zych, *Bubble-wall velocity in local thermal equilibrium: hydrodynamical simulations vs analytical treatment*, *JHEP* **05** (2024) 011, [2402.15408].

[353] **LISA Cosmology Working Group** Collaboration, C. Caprini, R. Jinno, M. Lewicki, E. Madge, M. Merchand, G. Nardini, M. Pieroni, A. Roper Pol, and V. Vaskonen, *Gravitational waves from first-order phase transitions in LISA: reconstruction pipeline and physics interpretation*, *JCAP* **10** (2024) 020, [2403.03723].

[354] M. Hindmarsh, S. J. Huber, K. Rummukainen, and D. J. Weir, *Gravitational waves from the sound of a first order phase transition*, *Phys. Rev. Lett.* **112** (2014) 041301, [1304.2433].

[355] M. Hindmarsh, S. J. Huber, K. Rummukainen, and D. J. Weir, *Numerical simulations of acoustically generated gravitational waves at a first order phase transition*, *Phys. Rev. D* **92** (2015), no. 12 123009, [1504.03291].

[356] M. Hindmarsh, S. J. Huber, K. Rummukainen, and D. J. Weir, *Shape of the acoustic gravitational wave power spectrum from a first order phase transition*, *Phys. Rev. D* **96** (2017), no. 10 103520, [1704.05871]. [Erratum: Phys.Rev.D 101, 089902 (2020)].

[357] A. Kosowsky, M. S. Turner, and R. Watkins, *Gravitational radiation from colliding vacuum bubbles*, *Phys. Rev. D* **45** (1992) 4514–4535.

[358] C. Caprini, R. Durrer, and G. Servant, *The stochastic gravitational wave background from turbulence and magnetic fields generated by a first-order phase transition*, *JCAP* **12** (2009) 024, [0909.0622].

[359] M. Lewicki and V. Vaskonen, *Gravitational waves from bubble collisions and fluid motion in strongly supercooled phase transitions*, *Eur. Phys. J. C* **83** (2023), no. 2 109, [2208.11697].

[360] D. Bodeker and G. D. Moore, *Can electroweak bubble walls run away?*, *JCAP* **05** (2009) 009, [0903.4099].

[361] D. Bodeker and G. D. Moore, *Electroweak Bubble Wall Speed Limit*, *JCAP* **05** (2017) 025, [1703.08215].

[362] Y. Gouttenoire and T. Volansky, *Primordial black holes from supercooled phase transitions*, *Phys. Rev. D* **110** (2024), no. 4 043514, [2305.04942].

[363] B. J. Carr, *The Primordial black hole mass spectrum*, *Astrophys. J.* **201** (1975) 1–19.

[364] I. Musco, V. De Luca, G. Franciolini, and A. Riotto, *Threshold for primordial black holes. II. A simple analytic prescription*, *Phys. Rev. D* **103** (2021), no. 6 063538, [2011.03014].

[365] A. Escrivà, C. Germani, and R. K. Sheth, *Universal threshold for primordial black hole formation*, *Phys. Rev. D* **101** (2020), no. 4 044022, [1907.13311].

[366] I. D. Stamou, *Exploring critical overdensity thresholds in inflationary models of primordial black holes formation*, *Phys. Rev. D* **108** (2023), no. 6 063515, [2306.02758].

[367] M. Lewicki, P. Toczek, and V. Vaskonen, *Primordial black holes from strong first-order phase transitions*, *JHEP* **09** (2023) 092, [2305.04924].

[368] G. Franciolini, Y. Gouttenoire, and R. Jinno, *Curvature Perturbations from First-Order Phase Transitions: Implications to Black Holes and Gravitational Waves*, 2503.01962.

[369] M. M. Flores, A. Kusenko, and M. Sasaki, *Revisiting formation of primordial black holes in a supercooled first-order phase transition*, *Phys. Rev. D* **110** (2024), no. 1 015005, [2402.13341].

[370] K. Hashino, S. Kanemura, T. Takahashi, M. Tanaka, and C.-M. Yoo, *Super-critical primordial black hole formation via delayed first-order electroweak phase transition*, 2501.11040.

[371] R. Banerjee and K. Jedamzik, *The Evolution of cosmic magnetic fields: From the very early universe, to recombination, to the present*, *Phys. Rev. D* **70** (2004) 123003, [astro-ph/0410032].

[372] A. Brandenburg, T. Kahniashvili, S. Mandal, A. Roper Pol, A. G. Tevzadze, and T. Vachaspati, *The dynamo effect in decaying helical turbulence*, *Phys. Rev. Fluids.* **4** (2019) 024608, [1710.01628].

[373] A. Armua, A. Berera, and J. C. Figueroa, *Parameter study of decaying magnetohydrodynamic turbulence*, *Phys. Rev. E* **107** (2023), no. 5 055206, [2212.02418].

[374] A. Roper Pol, A. Neronov, C. Caprini, T. Boyer, and D. Semikoz, *LISA and γ-ray telescopes as multi-messenger probes of a first-order cosmological phase transition*, 2307.10744.

[375] T. Kahniashvili, A. G. Tevzadze, and B. Ratra, *Phase Transition Generated Cosmological Magnetic Field at Large Scales*, *Astrophys. J.* **726** (2011) 78, [0907.0197].

[376] R. Durrer and A. Neronov, *Cosmological Magnetic Fields: Their Generation, Evolution and Observation*, *Astron. Astrophys. Rev.* **21** (2013) 62, [1303.7121].

[377] Y. Chikashige, R. N. Mohapatra, and R. D. Peccei, *Spontaneously Broken Lepton Number and Cosmological Constraints on the Neutrino Mass Spectrum*, *Phys. Rev. Lett.* **45** (1980) 1926.

[378] Y. Chikashige, R. N. Mohapatra, and R. D. Peccei, *Are There Real Goldstone Bosons Associated with Broken Lepton Number?*, *Phys. Lett. B* **98** (1981) 265–268.

[379] G. B. Gelmini and M. Roncadelli, *Left-Handed Neutrino Mass Scale and Spontaneously Broken Lepton Number*, *Phys. Lett. B* **99** (1981) 411–415.

[380] S. Oda, N. Okada, and D.-s. Takahashi, *Classically conformal U(1)' extended standard model and Higgs vacuum stability*, *Phys. Rev. D* **92** (2015), no. 1 015026, [1504.06291].

[381] I. Cordero-Carrión, M. Hirsch, and A. Vicente, *General parametrization of Majorana neutrino mass models*, *Phys. Rev. D* **101** (2020), no. 7 075032, [1912.08858].

[382] J. A. Casas and A. Ibarra, *Oscillating neutrinos and $\mu \to e, \gamma$*, *Nucl. Phys. B* **618** (2001) 171–204, [hep-ph/0103065].

[383] I. Esteban, M. C. Gonzalez-Garcia, M. Maltoni, T. Schwetz, and A. Zhou, *The fate of hints: updated global analysis of three-flavor neutrino oscillations*, *JHEP* **09** (2020) 178, [2007.14792].

[384] **Planck** Collaboration, N. Aghanim *et al.*, *Planck 2018 results. VI. Cosmological parameters*, *Astron. Astrophys.* **641** (2020) A6, [1807.06209]. [Erratum: Astron.Astrophys. 652, C4 (2021)].

[385] R. Costa, A. P. Morais, M. O. P. Sampaio, and R. Santos, *Two-loop stability of a complex singlet extended Standard Model*, *Phys. Rev. D* **92** (2015) 025024, [1411.4048].

[386] V. V. Khoze, C. McCabe, and G. Ro, *Higgs vacuum stability from the dark matter portal*, *JHEP* **08** (2014) 026, [1403.4953].

[387] F. del Aguila, G. D. Coughlan, and M. Quiros, *Gauge Coupling Renormalization With Several U(1) Factors*, *Nucl. Phys. B* **307** (1988) 633. [Erratum: Nucl.Phys.B 312, 751 (1989)].

[388] **ATLAS** Collaboration, G. Aad *et al.*, *Search for high-mass dilepton resonances using 139 fb^{-1} of pp collision data collected at $\sqrt{s}$ =13 TeV with the ATLAS detector*, *Phys. Lett. B* **796** (2019) 68–87, [1903.06248].

[389] **ATLAS** Collaboration, M. Aaboud *et al.*, *Search for additional heavy neutral Higgs and gauge bosons in the ditau final state produced in 36 fb^{-1} of pp collisions at $\sqrt{s} = 13$ TeV with the ATLAS detector*, *JHEP* **01** (2018) 055, [1709.07242].

[390] **ATLAS** Collaboration, M. Aaboud *et al.*, *Search for resonances in the mass distribution of jet pairs with one or two jets identified as b-jets in proton-proton collisions at $\sqrt{s} = 13$ TeV with the ATLAS detector*, *Phys. Rev. D* **98** (2018) 032016, [1805.09299].

[391] **ATLAS** Collaboration, G. Aad *et al.*, *Search for $t\bar{t}$ resonances in fully hadronic final states in pp collisions at $\sqrt{s}$ = 13 TeV with the ATLAS detector*, *JHEP* **10** (2020) 061, [2005.05138].

[392] C. Coriano, L. Delle Rose, and C. Marzo, *Constraints on abelian extensions of the Standard Model from two-loop vacuum stability and $U(1)_{B-L}$*, *JHEP* **02** (2016) 135, [1510.02379].

[393] J. Ellis, M. Lewicki, and J. M. No, *Gravitational waves from first-order cosmological phase transitions: lifetime of the sound wave source*, *JCAP* **07** (2020) 050, [2003.07360].

[394] L. Chataignier, T. Prokopec, M. G. Schmidt, and B. Świeżewska, *Systematic analysis of radiative symmetry breaking in models with extended scalar sector*, *JHEP* **08** (2018) 083, [1805.09292].

[395] L. Chataignier, T. Prokopec, M. G. Schmidt, and B. Swiezewska, *Single-scale Renormalisation Group Improvement of Multi-scale Effective Potentials*, *JHEP* **03** (2018) 014, [1801.05258].

[396] O. Gould, S. Güyer, and K. Rummukainen, *First-order electroweak phase transitions: A nonperturbative update*, *Phys. Rev. D* **106** (2022), no. 11 114507, [2205.07238].

[397] K. Kainulainen, V. Keus, L. Niemi, K. Rummukainen, T. V. I. Tenkanen, and V. Vaskonen, *On the validity of perturbative studies of the electroweak phase transition in the Two Higgs Doublet model*, *JHEP* **06** (2019) 075, [1904.01329].

[398] P. M. Schicho, T. V. I. Tenkanen, and J. Österman, *Robust approach to thermal resummation: Standard Model meets a singlet*, *JHEP* **06** (2021) 130, [2102.11145].

[399] L. Niemi, P. Schicho, and T. V. I. Tenkanen, *Singlet-assisted electroweak phase transition at two loops*, *Phys. Rev. D* **103** (2021), no. 11 115035, [2103.07467].

[400] P. Schicho, T. V. I. Tenkanen, and G. White, *Combining thermal resummation and gauge invariance for electroweak phase transition*, *JHEP* **11** (2022) 047, [2203.04284].

[401] J. Hirvonen, J. Löfgren, M. J. Ramsey-Musolf, P. Schicho, and T. V. I. Tenkanen, *Computing the gauge-invariant bubble nucleation rate in finite temperature effective field theory*, *JHEP* **07** (2022) 135, [2112.08912].

[402] M. Kierkla, P. Schicho, B. Swiezewska, T. V. I. Tenkanen, and J. van de Vis, *Finite-temperature bubble nucleation with shifting scale hierarchies*, 2503.13597.

[403] K. A. Meissner and H. Nicolai, *Renormalization Group and Effective Potential in Classically Conformal Theories*, *Acta Phys. Polon. B* **40** (2009) 2737–2752, [0809.1338].

[404] M. Quiros, *Finite temperature field theory and phase transitions*, in *ICTP Summer School in High-Energy Physics and Cosmology*, pp. 187–259, 1, 1999. hep-ph/9901312.

[405] D. J. Gross, R. D. Pisarski, and L. G. Yaffe, *QCD and Instantons at Finite Temperature*, *Rev. Mod. Phys.* **53** (1981) 43.

[406] R. R. Parwani, *Resummation in a hot scalar field theory*, *Phys. Rev. D* **45** (1992) 4695, [hep-ph/9204216]. [Erratum: Phys.Rev.D 48, 5965 (1993)].

[407] P. B. Arnold and O. Espinosa, *The Effective potential and first order phase transitions: Beyond leading-order*, *Phys. Rev. D* **47** (1993) 3546, [hep-ph/9212235]. [Erratum: Phys.Rev.D 50, 6662 (1994)].

[408] J. R. Espinosa, M. Quiros, and F. Zwirner, *On the nature of the electroweak phase transition*, *Phys. Lett. B* **314** (1993) 206–216, [hep-ph/9212248].

[409] M. Laine and A. Vuorinen, *Basics of Thermal Field Theory*, vol. 925. Springer, 2016.

[410] T. Brauner, T. V. I. Tenkanen, A. Tranberg, A. Vuorinen, and D. J. Weir, *Dimensional reduction of the Standard Model coupled to a new singlet scalar field*, *JHEP* **03** (2017) 007, [1609.06230].

[411] A. Ekstedt, P. Schicho, and T. V. I. Tenkanen, *DRalgo: A package for effective field theory approach for thermal phase transitions*, *Comput. Phys. Commun.* **288** (2023) 108725, [2205.08815].

[412] D. Marfatia, P.-Y. Tseng, and Y.-M. Yeh, *Phenomenology of bubble size distributions in a first-order phase transition*, 2407.15419.

[413] P. Lu, K. Kawana, and K.-P. Xie, *Old phase remnants in first-order phase transitions*, *Phys. Rev. D* **105** (2022), no. 12 123503, [2202.03439].

[414] C. D. Lorenz and R. M. Ziff, *Precise determination of the critical percolation threshold for the three-dimensional "swiss cheese" model using a growth algorithm*, *The Journal of Chemical Physics* **114** (2001) 3659–3661.

[415] J. Lin and H. Chen, *Continuum percolation of porous media via random packing of overlapping cube-like particles*, *Theoretical and Applied Mechanics Letters* **8** (2018), no. 5 299–303.

[416] M. Li, H. Chen, and J. Lin, *Numerical study for the percolation threshold and transport properties of porous composites comprising non-centrosymmetrical superovoidal pores*, *Computer Methods in Applied Mechanics and Engineering* **361** (2020) 112815.

[417] H.-K. Guo, K. Sinha, D. Vagie, and G. White, *The benefits of diligence: how precise are predicted gravitational wave spectra in models with phase transitions?*, *JHEP* **06** (2021) 164, [2103.06933].

[418] P. J. Steinhardt, *Relativistic Detonation Waves and Bubble Growth in False Vacuum Decay*, *Phys. Rev. D* **25** (1982) 2074.

[419] S. Iso, P. D. Serpico, and K. Shimada, *QCD-Electroweak First-Order Phase Transition in a Supercooled Universe*, *Phys. Rev. Lett.* **119** (2017), no. 14 141301, [1704.04955].

[420] P. Di Bari, D. Marfatia, and Y.-L. Zhou, *Gravitational waves from first-order phase transitions in Majoron models of neutrino mass*, *JHEP* **10** (2021) 193, [2106.00025].

[421] P. Di Bari, K. Farrag, R. Samanta, and Y. L. Zhou, *Density matrix calculation of the dark matter abundance in the Higgs induced right-handed neutrino mixing model*, *JCAP* **10** (2020) 029, [1908.00521].

[422] L. Pagano, L. Salvati, and A. Melchiorri, *New constraints on primordial gravitational waves from Planck 2015*, *Phys. Lett. B* **760** (2016) 823–825, [1508.02393].

[423] J. C. Helo, S. Kovalenko, and I. Schmidt, *Sterile neutrinos in lepton number and lepton flavor violating decays*, *Nucl. Phys. B* **853** (2011) 80–104, [1005.1607].

[424] J. Alwall, C. Duhr, B. Fuks, O. Mattelaer, D. G. Öztürk, and C.-H. Shen, *Computing decay rates for new physics theories with FeynRules and MadGraph 5_aMC@NLO*, *Comput. Phys. Commun.* **197** (2015) 312–323, [1402.1178].

[425] Y. Gouttenoire, *Primordial black holes from conformal Higgs*, *Phys. Lett. B* **855** (2024) 138800, [2311.13640].

[426] A. Drlica-Wagner *et al.*, *Report of the Topical Group on Cosmic Probes of Dark Matter for Snowmass 2021*, 2209.08215.

[427] M. T. Penny, B. S. Gaudi, E. Kerins, N. J. Rattenbury, S. Mao, A. C. Robin, and S. Calchi Novati, *Predictions of the WFIRST Microlensing Survey. I. Bound Planet Detection Rates*, *APJS* **241** (Mar., 2019) 3, [1808.02490].

[428] N. Smyth, S. Profumo, S. English, T. Jeltema, K. McKinnon, and P. Guhathakurta, *Updated Constraints on Asteroid-Mass Primordial Black Holes as Dark Matter*, *Phys. Rev. D* **101** (2020), no. 6 063005, [1910.01285].

[429] C. Labanti *et al.*, *The X/Gamma-ray Imaging Spectrometer (XGIS) on-board THESEUS: design, main characteristics, and concept of operation*, in *SPIE Astronomical Telescopes + Instrumentation 2020*, 2, 2021. 2102.08701.

[430] E. Orlando *et al.*, *Exploring the MeV sky with a combined coded mask and Compton telescope: the Galactic Explorer with a Coded aperture mask Compton telescope (GECCO)*, *JCAP* **07** (2022), no. 07 036, [2112.07190].

[431] T. Aramaki, P. Hansson Adrian, G. Karagiorgi, and H. Odaka, *Dual MeV Gamma-Ray and Dark Matter Observatory - GRAMS Project*, *Astropart. Phys.* **114** (2020) 107–114, [1901.03430].

[432] H. Fleischhack, *AMEGO-X: MeV gamma-ray Astronomy in the Multi-messenger Era*, *PoS* **ICRC2021** (2021) 649, [2108.02860].

[433] **e-ASTROGAM** Collaboration, A. De Angelis *et al.*, *The e-ASTROGAM mission*, *Exper. Astron.* **44** (2017), no. 1 25–82, [1611.02232].

[434] J. Auffinger, *Limits on primordial black holes detectability with Isatis: a BlackHawk tool*, *Eur. Phys. J. C* **82** (2022), no. 4 384, [2201.01265].

[435] A. Arbey and J. Auffinger, *BlackHawk: A public code for calculating the Hawking evaporation spectra of any black hole distribution*, *Eur. Phys. J. C* **79** (2019), no. 8 693, [1905.04268].

[436] A. Arbey and J. Auffinger, *Physics Beyond the Standard Model with BlackHawk v2.0*, *Eur. Phys. J. C* **81** (2021) 910, [2108.02737].

[437] A. Coogan, L. Morrison, and S. Profumo, *Hazma: A Python Toolkit for Studying Indirect Detection of Sub-GeV Dark Matter*, *JCAP* **01** (2020) 056, [1907.11846].

[438] V. Elias, R. B. Mann, D. G. C. McKeon, and T. G. Steele, *Radiative electroweak symmetry breaking revisited*, *Phys. Rev. Lett.* **91** (2003) 251601, [hep-ph/0304153].

[439] **NANOGrav** Collaboration, A. Afzal *et al.*, *The NANOGrav 15 yr Data Set: Search for Signals from New Physics*, *Astrophys. J. Lett.* **951** (2023), no. 1 L11, [2306.16219]. [Erratum: Astrophys.J.Lett. 971, L27 (2024), Erratum: Astrophys.J. 971, L27 (2024)].

[440] J. Ellis, M. Fairbairn, G. Franciolini, G. Hütsi, A. Iovino, M. Lewicki, M. Raidal, J. Urrutia, V. Vaskonen, and H. Veermäe, *What is the source of the PTA GW signal?*, *Phys. Rev. D* **109** (2024), no. 2 023522, [2308.08546].

[441] Y. Gouttenoire, *First-Order Phase Transition Interpretation of Pulsar Timing Array Signal Is Consistent with Solar-Mass Black Holes*, *Phys. Rev. Lett.* **131** (2023), no. 17 171404, [2307.04239].

[442] A. Kobakhidze, C. Lagger, A. Manning, and J. Yue, *Gravitational waves from a supercooled electroweak phase transition and their detection with pulsar timing arrays*, *Eur. Phys. J. C* **77** (2017), no. 8 570, [1703.06552].

[443] N. Levi, T. Opferkuch, and D. Redigolo, *The supercooling window at weak and strong coupling*, *JHEP* **02** (2023) 125, [2212.08085].

[444] G. Raffelt and D. Seckel, *Bounds on Exotic Particle Interactions from SN 1987a*, *Phys. Rev. Lett.* **60** (1988) 1793.

[445] H. An, M. Pospelov, J. Pradler, and A. Ritz, *Direct Detection Constraints on Dark Photon Dark Matter*, *Phys. Lett. B* **747** (2015) 331–338, [1412.8378].

[446] E. Hardy and R. Lasenby, *Stellar cooling bounds on new light particles: plasma mixing effects*, *JHEP* **02** (2017) 033, [1611.05852].

[447] **CHARM** Collaboration, F. Bergsma *et al.*, *Search for Axion Like Particle Production in 400-GeV Proton - Copper Interactions*, *Phys. Lett. B* **157** (1985) 458–462.

[448] **NOMAD** Collaboration, P. Astier *et al.*, *Search for heavy neutrinos mixing with tau neutrinos*, *Phys. Lett. B* **506** (2001) 27–38, [hep-ex/0101041].

[449] **BaBar** Collaboration, J. P. Lees *et al.*, *Search for a Dark Photon in e^+e^- Collisions at BaBar*, *Phys. Rev. Lett.* **113** (2014), no. 20 201801, [1406.2980].

[450] **LHCb** Collaboration, R. Aaij *et al.*, *Search for Dark Photons Produced in 13 TeV pp Collisions*, *Phys. Rev. Lett.* **120** (2018), no. 6 061801, [1710.02867].

[451] H. Esseili and G. D. Kribs, *Cosmological implications of gauged $U(1)_{B-L}$ on ΔN_{eff} in the CMB and BBN*, *JCAP* **05** (2024) 110.

[452] K. Asai, A. Das, J. Li, T. Nomura, and O. Seto, *Chiral Z' in FASER, FASER2, DUNE, and ILC beam dump experiments*, *Phys. Rev. D* **106** (2022), no. 9 095033, [2206.12676].

[453] J. Redondo and M. Postma, *Massive hidden photons as lukewarm dark matter*, *JCAP* **02** (2009) 005, [0811.0326].

[454] J. Garcia-Bellido, H. Murayama, and G. White, *Exploring the early Universe with Gaia and Theia*, *JCAP* **12** (2021), no. 12 023, [2104.04778].

[455] A. Weltman *et al.*, *Fundamental physics with the Square Kilometre Array*, *Publ. Astron. Soc. Austral.* **37** (2020) e002, [1810.02680].

[456] R. Xu, J. Lu, S. Deng, and L. Bian, *Phase Transitions in the Early Universe: Impacts on BBN and CMB Observables*, 2503.19737.

[457] A. Mitridate, D. Wright, R. von Eckardstein, T. Schröder, J. Nay, K. Olum, K. Schmitz, and T. Trickle, *PTArcade*, 2306.16377.

[458] W. G. Lamb, S. R. Taylor, and R. van Haasteren, *Rapid refitting techniques for Bayesian spectral characterization of the gravitational wave background using pulsar timing arrays*, *Phys. Rev. D* **108** (2023), no. 10 103019, [2303.15442].

[459] T. W. B. Kibble, *Topology of Cosmic Domains and Strings*, *J. Phys. A* **9** (1976) 1387–1398.

[460] **LISA Cosmology Working Group** Collaboration, J. J. Blanco-Pillado, Y. Cui, S. Kuroyanagi, M. Lewicki, G. Nardini, M. Pieroni, I. Y. Rybak, L. Sousa, and J. M. Wachter, *Gravitational waves from cosmic strings in LISA: reconstruction pipeline and physics interpretation*, *JCAP* **05** (2025) 006, [2405.03740].

[461] D. Camargo Neves da Cunha, C. Ringeval, and F. R. Bouchet, *Stochastic gravitational waves from long cosmic strings*, *JCAP* **09** (2022) 078, [2205.04349].

[462] D. Marfatia and Y.-L. Zhou, *Gravitational waves from cosmic superstrings and gauge strings*, *JHEP* **07** (2024) 204, [2312.10455].

[463] **Planck** Collaboration, P. A. R. Ade *et al.*, *Planck 2015 results. XIII. Cosmological parameters*, *Astron. Astrophys.* **594** (2016) A13, [1502.01589].

[464] O. Gould and T. V. I. Tenkanen, *Perturbative effective field theory expansions for cosmological phase transitions*, *JHEP* **01** (2024) 048, [2309.01672].

[465] A. Ekstedt, P. Schicho, and T. V. I. Tenkanen, *Cosmological phase transitions at three loops: The final verdict on perturbation theory*, *Phys. Rev. D* **110** (2024), no. 9 096006, [2405.18349].

[466] T. Hambye, *Hidden vector dark matter*, *JHEP* **01** (2009) 028, [0811.0172].

[467] D. Borah, A. Dasgupta, and S. K. Kang, *Gravitational waves from a dark U(1)D phase transition in light of NANOGrav 12.5 yr data*, *Phys. Rev. D* **104** (2021), no. 6 063501, [2105.01007].

[468] D. Borah, A. Dasgupta, and S. K. Kang, *A first order dark $SU(2)_D$ phase transition with vector dark matter in the light of NANOGrav 12.5 yr data*, *JCAP* **12** (2021), no. 12 039, [2109.11558].

[469] M. Lewicki, O. Pujolàs, and V. Vaskonen, *Escape from supercooling with or without bubbles: gravitational wave signatures*, *Eur. Phys. J. C* **81** (2021), no. 9 857, [2106.09706].

[470] M. Bertenstam *et al.*, *Dratopi*, *To appear*.

[471] **ATLAS** Collaboration, *Combined measurements of Higgs boson production and decay using up to 139 fb^{-1} of proton-proton collision data at $\sqrt{s} = 13$ TeV collected with the ATLAS experiment*, .

[472] A. Papaefstathiou, T. Robens, and G. White, *Signal strength and W-boson mass measurements as a probe of the electro-weak phase transition at colliders - Snowmass White Paper*, in *Snowmass 2021*, 5, 2022. 2205.14379.

[473] F. F. Freitas, G. Lourenço, A. P. Morais, A. Nunes, J. Olívia, R. Pasechnik, R. Santos, and J. Viana, *Impact of SM parameters and of the vacua of the Higgs potential in gravitational waves detection*, *JCAP* **03** (2022), no. 03 046, [2108.12810].

[474] D. Marfatia and P.-Y. Tseng, *Correlated gravitational wave and microlensing signals of macroscopic dark matter*, *JHEP* **11** (2021) 068, [2107.00859].

[475] G. Bélanger, F. Boudjema, A. Goudelis, A. Pukhov, and B. Zaldivar, *micrOMEGAs5.0 : Freeze-in*, *Comput. Phys. Commun.* **231** (2018) 173–186, [1801.03509].

[476] **LZ** Collaboration, J. Aalbers *et al.*, *Dark Matter Search Results from 4.2 Tonne-Years of Exposure of the LUX-ZEPLIN (LZ) Experiment*, *Phys. Rev. Lett.* **135** (2025), no. 1 011802, [2410.17036].

[477] K. Fujikura, S. Girmohanta, Y. Nakai, and M. Suzuki, *NANOGrav signal from a dark conformal phase transition*, *Phys. Lett. B* **846** (2023) 138203, [2306.17086].

[478] K. Schmitz, *New Sensitivity Curves for Gravitational-Wave Signals from Cosmological Phase Transitions*, *JHEP* **01** (2021) 097, [2002.04615].

[479] **ATLAS** Collaboration, G. Aad *et al.*, *Search for heavy Higgs bosons decaying into two tau leptons with the ATLAS detector using pp collisions at* $\sqrt{s} = 13$ *TeV*, *Phys. Rev. Lett.* **125** (2020), no. 5 051801, [2002.12223].

[480] **ATLAS** Collaboration, G. Aad *et al.*, *Search for the* $HH \to b\bar{b}b\bar{b}$ *process via vector-boson fusion production using proton-proton collisions at* $\sqrt{s} = 13$ *TeV with the ATLAS detector*, *JHEP* **07** (2020) 108, [2001.05178]. [Erratum: JHEP 01, 145 (2021), Erratum: JHEP 05, 207 (2021)].

[481] **ATLAS** Collaboration, G. Aad *et al.*, *Search for heavy resonances decaying into a pair of Z bosons in the* $\ell^+\ell^-\ell'^+\ell'^-$ *and* $\ell^+\ell^-\nu\bar{\nu}$ *final states using 139* fb^{-1} *of proton–proton collisions at* $\sqrt{s} = 13$ *TeV with the ATLAS detector*, *Eur. Phys. J. C* **81** (2021), no. 4 332, [2009.14791].

[482] **ATLAS** Collaboration, G. Aad *et al.*, *Search for resonances decaying into photon pairs in 139* fb^{-1} *of pp collisions at* $\sqrt{s}$*=13 TeV with the ATLAS detector*, *Phys. Lett. B* **822** (2021) 136651, [2102.13405].

[483] L. Baudis and D. Collaboration, *Darwin/xlzd: a future xenon observatory for dark matter and other rare interactions*, *arXiv preprint arXiv:2404.19524* (2024) [2404.19524].
DARWIN/XLZD will probe spin-independent WIMP-nucleon cross sections down to the neutrino floor.

[484] A. Abada *et al.*, *Fcc-hh: The hadron collider*, *Eur. Phys. J. ST* **228** (2019), no. 4 755–1107, [1902.09960].

[485] A. Belyaev, N. D. Christensen, and A. Pukhov, *CalcHEP 3.4 for collider physics within and beyond the Standard Model*, *Comput. Phys. Commun.* **184** (2013) 1729–1769, [1207.6082].

[486] A. Buckley, J. Ferrando, S. Lloyd, K. Nordström, B. Page, M. Rüfenacht, M. Schönherr, and G. Watt, *LHAPDF6: parton density access in the LHC precision era*, *Eur. Phys. J. C* **75** (2015) 132, [1412.7420].

[487] B. Fuks and H.-S. Shao, *Qcd next-to-leading-order predictions matched to parton showers for vector-like quark models*, *Eur. Phys. J. C* **77** (2017), no. 2 135, [1610.04622].

[488] D. Dercks, H. K. Dreiner, S. Kulkarni, P. Marquard, and J. Tattersall, *CheckMATE 2: From the model to the limit*, *Comput. Phys. Commun.* **221** (2017) 383–418, [1611.09856].

[489] C. Collaboration, *Searches for physics beyond the standard model with the* m_{T2} *variable in hadronic final states with and without disappearing tracks in pp collisions at* $\sqrt{s} = 13$ *tev*, *Eur. Phys. J. C* **80** (2020) 3, [1909.03460].

[490] **ATLAS** Collaboration, G. Aad *et al.*, *Search for supersymmetry in events with four or more charged leptons in* $139\,fb^{-1}$ *of* $\sqrt{s} = 13$ *TeV pp collisions with the ATLAS detector*, *JHEP* **07** (2021) 167, [2103.11684].

[491] A. Collaboration, *Search for supersymmetry in events with four or more leptons or two same-sign leptons and jets using 139* fb^{-1} *of pp collisions at* $\sqrt{s} = 13$ *tev with the atlas detector*, *JHEP* **12** (2021) 142, [2101.01629].

[492] C. Collaboration, *Search for supersymmetry in final states with multiple top and bottom quarks and missing transverse momentum in proton-proton collisions at* $\sqrt{s} = 13$ *tev*, *Phys. Rev. D* **100** (2019), no. 1 012001, [1908.04722].

[493] A. Collaboration, *Search for direct top squark pair production in the all-hadronic* $t\bar{t}$ *plus missing transverse momentum final state in pp collisions at* $\sqrt{s} = 13$ *tev with the atlas detector*, *JHEP* **09** (2017) 088, [1709.04183].

[494] A. Collaboration, *Search for four-top-quark production using the single-lepton and opposite-sign dilepton final states in proton–proton collisions at* $\sqrt{s} = 13$ *tev with the atlas detector*, *Phys. Rev. D* **104** (2021), no. 11 112009, [2106.09609].

[495] A. Collaboration, *Search for new phenomena in final states with large jet multiplicities and missing transverse momentum using* $\sqrt{s} = 13$ *tev proton–proton collisions recorded by atlas in run 2 of the lhc*, *JHEP* **10** (2020) 062, [2004.14060].

[496] A. Collaboration, *Search for pair production of vector-like top partners in final states with one lepton, jets and missing transverse momentum using the full run 2 dataset collected with the atlas detector*, 2401.17165. Submitted to JHEP.

[497] P. Athron, L. Morris, and Z. Xu, *How robust are gravitational wave predictions from cosmological phase transitions?*, *JCAP* **05** (2024) 075, [2309.05474].

[498] M. Lewicki, M. Merchand, L. Sagunski, P. Schicho, and D. Schmitt, *Impact of theoretical uncertainties on model parameter reconstruction from GW signals sourced by cosmological phase transitions*, *Phys. Rev. D* **110** (2024), no. 2 023538, [2403.03769].

[499] H. H. Patel, *Package-X 2.0: A Mathematica package for the analytic calculation of one-loop integrals*, *Comput. Phys. Commun.* **218** (2017) 66–70, [1612.00009].

[500] K. Kajantie, M. Laine, K. Rummukainen, and M. E. Shaposhnikov, *Generic rules for high temperature dimensional reduction and their application to the standard model*, *Nucl. Phys. B* **458** (1996) 90–136, [hep-ph/9508379].

[501] L. Heinrich, K. Cranmer, M. Feickert, G. Stark, *et al.*, *pyhf: pure-Python implementation of HistFactory-style statistical models*, Zenodo, https://doi.org/10.5281/zenodo.1169739.